

Lecture Notes in Mechanical Engineering

Taoufik Boukharouba
Guy Pluinage
Krimo Azouaoui *Editors*

Applied Mechanics, Behavior of Materials, and Engineering Systems

Selected contributions to the 5th Algerian
Congress of Mechanics, CAM2015, El-Oued,
Algeria, October 25–29

 Springer

Lecture Notes in Mechanical Engineering

About this Series

Lecture Notes in Mechanical Engineering (LNME) publishes the latest developments in Mechanical Engineering—quickly, informally and with high quality. Original research reported in proceedings and post-proceedings represents the core of LNME. Also considered for publication are monographs, contributed volumes and lecture notes of exceptionally high quality and interest. Volumes published in LNME embrace all aspects, subfields and new challenges of mechanical engineering. Topics in the series include:

- Engineering Design
- Machinery and Machine Elements
- Mechanical Structures and Stress Analysis
- Automotive Engineering
- Engine Technology
- Aerospace Technology and Astronautics
- Nanotechnology and Microengineering
- Control, Robotics, Mechatronics
- MEMS
- Theoretical and Applied Mechanics
- Dynamical Systems, Control
- Fluid Mechanics
- Engineering Thermodynamics, Heat and Mass Transfer
- Manufacturing
- Precision Engineering, Instrumentation, Measurement
- Materials Engineering
- Tribology and Surface Technology

More information about this series at <http://www.springer.com/series/11236>

Taoufik Boukharouba · Guy Pluinage
Krimo Azouaoui
Editors

Applied Mechanics, Behavior of Materials, and Engineering Systems

Selected contributions to the 5th Algerian
Congress of Mechanics, CAM2015, El-Oued,
Algeria, October 25–29

 Springer

Editors

Taoufik Boukharouba
Laboratory for Advanced Mechanics
USTHB
Bab Ezzouar
Algeria

Krimo Azouaoui
Laboratory for Advanced Mechanics
USTHB
Bab Ezzouar
Algeria

Guy Pluvinage
Metz
France

ISSN 2195-4356 ISSN 2195-4364 (electronic)
Lecture Notes in Mechanical Engineering
ISBN 978-3-319-41467-6 ISBN 978-3-319-41468-3 (eBook)
DOI 10.1007/978-3-319-41468-3

Library of Congress Control Number: 2016943871

© Springer International Publishing Switzerland 2017

This work is subject to copyright. All rights are reserved by the Publisher, whether the whole or part of the material is concerned, specifically the rights of translation, reprinting, reuse of illustrations, recitation, broadcasting, reproduction on microfilms or in any other physical way, and transmission or information storage and retrieval, electronic adaptation, computer software, or by similar or dissimilar methodology now known or hereafter developed.

The use of general descriptive names, registered names, trademarks, service marks, etc. in this publication does not imply, even in the absence of a specific statement, that such names are exempt from the relevant protective laws and regulations and therefore free for general use.

The publisher, the authors and the editors are safe to assume that the advice and information in this book are believed to be true and accurate at the date of publication. Neither the publisher nor the authors or the editors give a warranty, express or implied, with respect to the material contained herein or for any errors or omissions that may have been made.

Printed on acid-free paper

This Springer imprint is published by Springer Nature
The registered company is Springer International Publishing AG Switzerland

Preface

The Algerian Congress of Mechanics *Congrès Algérien de Mécanique CAM*, www.cam-dz.org was started in 2007 by members of the Advanced Mechanics Laboratory (*LMA*) of Houari Boumediene University of Sciences and Technology (*USTHB*, Algiers, Algeria) with the assistance of the Algerian Association for Technology Transfer (*a2t2*). The pioneers were Pr. Taoufik Boukharouba, Pr. Krimo Azouaoui and Pr. Nourdine Ouali from *USTHB*. First time, Pr. Lakhdar Taleb of *INSA Rouen*, Pr. Nacer Hamzaoui of *INSA Lyon*, Pr. Moussa Nait Abdelaziz of *Polytech'Lille*, Pr. Rezak Ayad of the University of Reims, Dr. Salim Benmedakene of *Technip France*, Pr. Nouredine Ouelaa of University 8 May 1945 of Guelma, and Pr. Abdelkrim Liazid of Polytechnic school of Oran joined the scientific plane group; about Dr. Djamel Sais and Dr. Halim Foudi joined logistic plane.

The first edition of *CAM2007* was organized at *USTHB*, Algiers in 2007, the second at Biskra in 2009, the third at Guelma in 2011, and the fourth at Mascara in 2013. *CAM* conferences have just finished its fifth edition in 2015 which took place in the city of El-Oued.

Traditionally *CAM2015* provides a forum bringing together researchers from university, research institutions and industry. One of its major objectives is to develop connections between academic and applied research. For that, *CAM* received its essential help from the Algerian Association for Technology Transfer (*a2t2*). The organization of *CAM2015* provides the frame for constructive exchanges and promoting the development of new ideas in these fields.

CAM is also a place for discussing the major actual world challenges as global warming, decreasing of raw material resources, saving energy, increase of world population and preservation of the environment. To that, *CAM* has organized 10 sessions on the following topics:

1. Cyclic behavior and damage of materials including behavior and fatigue damage of metals, metallic alloys and composites, and high-temperature fatigue. This concerns elastic and plastic behavior by including viscoplasticity, cyclic softening and hardening, shakedown, and ratcheting. Temperature effect

- is also taken into account with mechanical and metallurgical interactions, thermal stresses, and stress corrosion cracking (six contributions)
2. Deep drawing and systems manufacturing by automation in the field of non-conventional machining processes (EDM, laser or ultrasonic machining,) mechanics of surfaces and tribology, contacts, friction and interfaces. Modeling of complex systems and mechanisms is also examined (five contributions)
 3. Transport and logistics with transport engineering, vehicles reliability of urban transport and safety in urban transport (four contributions)
 4. Reagent flows and transport phenomena including mixing phenomena, combustion and reactants turbulence interactions and propulsion systems (six contributions)
 5. Fracture mechanics with special attention to local criteria in fracture mechanics, harmfulness of defects and transferability in fatigue and fracture (seven contributions)
 6. Structural dynamics, acoustics and industrial maintenance including noise and machines vibration, rotating machines, early diagnosis of failure, cyclostationarity, source separation, monitoring and diagnostics, maintenance managing and mechanical reliability, techniques of defect detection such as NDT, vibro-acoustic, thermography, etc. (nine contributions)
 7. Composite materials' advances concerning specially nanocomposites, bio-based natural structural composites, new honeycomb cores and sandwich structures, textile composites and their applications, and fracture and damage mechanics in composite structures and materials. Enhanced methods for composites defects (delamination, matrix and fiber cracks) (13 contributions)
 8. Energy, heat, and mass transfer thermodynamics as energy conversion and storage renewable energy, energy efficiency heat transfer, and numerical simulations and experiments (14 contributions)
 9. Fluid mechanics and systems engineering concerning applications of computational fluid dynamics, algorithms applied for high-performance calculation, cavitation and multiphase flows, fluid-structure interactions, and also microfluidics (11 contributions)
 10. Numerical modeling product-driven simulation design and optimization with simulation of manufacturing processes (including industrial and healthcare applications), materials, multiphysics and multiscale modeling (linear and nonlinear behavior, static and dynamic analysis), advances in finite element numerical methods and software engineering (finite element, finite volume, optimization, meshless, parallel programming, solvers, use of commercial software in multiphysics engineering analysis (12 contributions)

Two workshops were added to the conference; the first entitled *Damage-Behavior coupling: From the initiation to the propagation of macroscopic cracks* was animated by Pr. André Dragon, Univ. Poitiers (France), Pr. Djimédo Kondo Univ. Pierre et Marie Curie (France), Pr. Jean-Jacques Marigo, Polytechnic school (France), Pr. Pierre-Yves Manach, Univ. Bretagne-Sud (France) and Pr. Khemais Saanouni, Univ. Technology of Troyes (France).

The second workshop “Advances in Fracture Mechanics” received contribution from Pr. Píška Miroslav, Brno University of Technology (Czech Republic), Pr. Simon A. Sedmak, University of Belgrade (Serbia), and Pr. Ljubica Milovic, University of Belgrade (Serbia).

The scientific contribution of CAM2015 is important: the total number of papers was 387 and 257 were accepted, this led to an acceptance rate of 80.3 %. The total number of participants was 199, with 33 coming from outside Algeria. Participants came from countries such as France, Tunisia, Canada, China, Serbia, Morocco, and UEA.

Totally 12 plenary lectures, 19 introductory lectures, 81 oral presentations, 47 posters, and 12 conferences in the two workshops were presented.

These facts indicate that *CAM* is a major scientific event in North Africa. Its international audience indicates its high scientific level. The next *CAM* will be organized in 2017.

Since June 13, 2015, *CAM* has an institution called “College of Expert, Monitoring and Deontology” (*Collège d’Experts, de Suivi et de Déontologie*) abbreviated as *CESD*. This college will be responsible for overseeing future editions of *CAM* at the organizational and scientific level. The designation of the topics’ coordinators and the host university for the *CAM*, based on a tender will remain its main charge. The *CESD* is composed of 10 members (9 academicians and one from socioeconomic sector), refer to www.a2t2-dz.org.

Metz, France

Guy Pluvinage

Contents

The Optics Between Theory and Application in Arabic Golden Age . . .	1
Ahmed Djebbar	
Fatigue and Notch Mechanics	9
Bruno Atzori, Giovanni Meneghetti and Mauro Ricotta	
Experimental Disparity Analysis of the Behavior and Fatigue of the 304L Stainless Steel.	25
Kada Mouedden, Adel Belattar and Lakhdar Taleb	
Numerical Investigation on the Anisotropic Behavior of an Aluminum Alloy Type 2017A	41
Mouaad Brik, Malek Chabane Chaouche and Lakhdar Taleb	
History of Microstructure Evolution and Its Effect on the Mechanical Behavior During Friction Welding for AISI 316.	51
Ammar Jabbar Hassan, Ramzi Lechelch, Taoufik Boukharouba, Djamel Miroud, Nacer-eddine Titouche and Nourdine Ouali	
A Study of Selective Laser Melting Technology on the Ultra-High Strength Tool Steel Use—Quality, Mechanical Properties and Fatigue	67
Píška Miroslav, Trubačová Pavlína, Horníková Jana, Šandera Pavel and Klas Boivie	
Transferability of Fracture Toughness with Constraint.	87
Guy Pluvinage, Julien Capelle and Mohamed Hadj Meliani	
Crack Path Stabilisation and T-Stress Estimation in Connection with the Global Approach for Inclined Notches	101
Mohammed Hadj Meliani, Omar Bouledroua, Mohamed Ould-M’beirick, Khled Elmiloudi, Mohamed Sadou and Guy Pluvinage	

Measuring of Strain and Displacements in Welded Joints Subjected to Tensile Load Using Stereometric Methods	117
Branislav Djordjevic, Simon A. Sedmak, Uros Tatic, Milos Milosevic and Filip Vucetic	
Experimental and Numerical Investigations of Friction Stir Welding of Aluminum to Copper	129
Gihad Kerrar, Nesar Merah, Abdelrahman Nasr Shuaib, Fadi AL-Badour and Abdelaziz Bazoune	
Heat-Affected Zone as Critical Location in Pressure Equipment	139
Ljubica Milović	
Mixed Mode Static and Dynamic Modeling in Fracture Mechanics for Plane Composite Materials by X-FEM.	157
Sadam Houcine Habib, Brahim Elkhali Hachi, Mohamed Guesmi and Mohamed Haboussi	
The Preheating Temperature Effects on the Residual Stresses of the Welded Rails Sections	169
Oussama Bouazaoui and Abdelkrim Chouaf	
Dynamic Analysis of Fiber Reinforced Composite Beam Containing a Transverse Crack.	179
Yassine Adjal, Rachid Benzidane and Zouaoui Sereir	
Determination of Elastic-Plastic Parameters of Inconel Arc Sprayed Coating	193
Yamina Mebdoua, Yazid Fizi and Hadj Lahmar	
Study of Noise Inside a Mechanical Shovel Cabin Using a Sound Perception Approach.	205
Nacer Hamzaoui	
Perceptual Study of Simple and Combined Gear Defects	219
Ramdane Younes, Nouredine Ouelaa, Nacer Hamzaoui and Abderrazek Djebala	
Natural Frequencies of Composite Cylindrical Helical Springs	227
Sami Ayadi and Ezzeddine Haj Taïeb	
Improvement of the Sensitivity of the Scalar Indicators Using a Denoising Method by Wavelet Transform	239
Mustapha Merzoug, Khalid Ait Shgir, Abdelhamid Miloudi and Jean Paul Dron	
Fault Diagnosis Through the Application of Cyclostationarity to Signals Measured	251
Tarek Kebabsa, Nouredine Ouelaa, Jerome Antoni, Mohamed Cherif Djamaa, Raid Khettabi and Abderrazek Djebala	

Experimental Study of Real Gear Transmission Defects Using Sound Perception 267
 Nouredine Ouelaa, Ramdane Younes, Nacer Hamzaoui and Abderrazek Djebala

Taguchi Design of Experiments for Optimization and Modeling of Surface Roughness When Dry Turning X210Cr12 Steel 275
 Oussama Zerti, Mohamed Athmane Yaltese, Salim Belhadi and Lakhdar Bouzid

Study Contribution of Surface Quality Parts Machined by Turning Using Hard Materials 289
 Razika Aouad and Idriss Amara

Prediction of Cutting Tool’s Optimal Lifespan Based on the Scalar Indicators and the Wavelet Multi-resolution Analysis 299
 Mohamed Khemissi Babouri, Nouredine Ouelaa, Abderrazek Djebala, Mohamed Cherif Djamaa and Septi Boucherit

Diffusion Modelling of Composite with Permeable Fiber 311
 Djelloul Gueribiz, Frédéric Jacquemin, Hocine Bourenane and Silvain Fréour

Elastic Buckling at the Scale of a Bone Trabecula: The Influence of the Boundary Conditions 323
 Hamza Bennaceur, Salah Ramtani and Toufik Outtas

Dynamic Characterization of MR Damper and Experimental Adjustment of Numerical Model 331
 Said Boukerroum and Nacer Hamzaoui

Evaluation of Nonlinear Seismic Response of Reinforced Concrete Structures 345
 Samira Bouyakoub and Taïeb Branci

A Finite Element Approach for Predicting the Flexural Response of Light Weight FRP-Concrete Beams Under Cyclic Loading 355
 Abdelmadjid Si Salem, Souad Ait Taleb and Kamal Ait Tahar

Study of Composite with Metallic Matrix WC/W₂C–20W–20Ni Realized by Spontaneous Infiltration of the Bronze Alloy Cu–30Mn–3P 365
 Mokrane Gousmine, Djamel Miroud, Mohamed Farid Benlamnouar, Boualeme Demri and Abderrahmane Younes

Investigations on the Residual Shear Properties of a Composite Subjected to Impact Fatigue Loading. 375
 Said Mouhoubi and Krimo Azouaoui

Development of a Reliability-Mechanical: Numerical Model of Mechanical Behavior of a Multilayer Composite Plate 387
 Abdelhakim Maizia, Abdelkader Hocine, Hocine Dehmous and David Chapelle

Analysis of Deflection in Isotropic and Orthotropic Rectangular Plates with Central Opening Under Transverse Static Loading 399
 Ahmed Abdelatif Bouzgou, Abdelouahab Tati and Abdelhak Khechai

Diffusive Behavior in Polymer-Local Organommodified Clay Matrix 411
 Ali Makhloufi, Djelloul Gueribiz, Djamel Boutassouna, Frédéric Jacquemin and Mustapha Zaoui

Effect of Grain Size of Nano Composite on Raman and Magnetic Proprieties 425
 Abderrahmane Younes, Nacer Eddine Bacha, Mourad Zergoug, Mokrane Gousmine, Heider Dehdouh and Amirouche Bouamer

Finite Element Based on Layerwise Approach for Static and Dynamic Analysis of Multi-layered Sandwich Plates 435
 Mohamed-Ouejdi Belarbi, Abdelouahab Tati, Houdayfa Ounis and Abdelhak Khechai

Tool Life Evaluation of Cutting Materials in Turning of X20Cr13 Stainless Steel. 447
 Lakhdar Bouzid, Mohamed Athmane Yaltese, Salim Belhadi and Lakhdar Boulanouar

Importance of Physical Modeling for Simulations of Turbulent Reactive Flows 453
 Vincent Robin, Michel Champion, Arnaud Mura and Q.N. Kim Kha

Influence of Diverging Section Length on the Supersonic Jet Delivered from Micro-nozzle: Application to Cold Spray Coating Process 465
 Abderrahmane Belbaki and Yamina Mebdoua-Lahmar

Turbulent Combustion Modeling in Compression Ignition Engines 475
 Mohamed Bencherif, Rachid Sahnoun and Abdelkrim Liazid

On the Thermal Characterization of a Fire Induced Smoke-Layer in Semi-confined Compartments 491
 Abdallah Benarous, Souhila Agred, Larbi Loukarfi and Abdelkrim Liazid

Numerical Study of Twin-Jets Impinging Against a Smooth and Flat Surface 503
 Rachid Sahnoun and Abdelkrim Liazid

Heat and Mass Transfer into a Porous Annulus Found Between Two Horizontal Concentric Circular Cylinders 511
Karim Ragui, Abdelkader Boutra, Rachid Bennacer and Youb Khaled Benkahla

Heat and Mass Transfer in the Growth of Titanium Doped Sapphire Material with the μ -PD Technique 523
Hanane Azoui, Abdellah Laidoune, Djamel Haddad and Derradji Bahloul

Cooperating Double Diffusion Natural Convection in a Square Enclosure with Partially Active Vertical Wall. 535
Abdennacer Belazizia, Smail Benissaad and Said Abboudi

Increased Risk of Accidents Due to Human Behavior 551
Martina J. Mazankova

Statistic of Police of Czech Republic Influence on Risk Assessment of Road Traffic 561
Martina J. Mazankova

Author Index 569

The Optics Between Theory and Application in Arabic Golden Age

Ahmed Djebbar

Abstract From its birth in Islamic world at the late of eighth century, and throughout its development, the optics has been the concerned technology. To apply it in the actual field, the specialists have made theoretical work by using mathematical methods. They could realize an important document reference which contains original results. But that was only possible after collection, translation and critical comprehension of a rich heritage that had been produced, mainly, during the Hellenistic period (the third century before B.C.) and has been preserved in its mother language (the Greek). It is necessary to remind these sources and their contents were translated originally from Greek to Arabic sciences.

1 The Appropriation of Greek Heritage Age

Early in the ninth century, or perhaps earlier, Greeks have written on different topics about optics began to be translated into Arabic. This trend continued throughout that century, by chance, discovery of manuscripts in different libraries of the Fertile Crescent and Alexandria. Some of the translated books have the general title “Book of optics”, that is to say the study of visual phenomena, or that of “Catoptrics” (geometric study of the reflection phenomenon). Some authors of these writings are known as mathematicians. This is the case of Euclid (third century before B.C.) and Heron of Alexandria (first century). The others like Ptolemy (died at 168) and Theon of Alexandria (died at 405) were astronomers. The second major title treated by Greek scientists was the burning mirrors, instruments, once designed and built, had become an invincible weapon in the hands of the military, since they were intended to burn and destroy forces and enemy ships by remote. Four books about this subject have been translated into Arabic: those of Anthemus of Tralles (died at 558 before B.C.), and Diocles (second century) for the most important, and those of Didyme and Ditrums, two authors have no survived work [1]. The early Muslims

A. Djebbar (✉)

University of Lille for Sciences and Technology, Villeneuve-d’Ascq, France
e-mail: ahmed.djebbar@wanadoo.fr

optical specialists were interested by a third title (the physiology of the eye). Greek knowledge on this subject was available in the writings of the famous Galen (died about 216) [2].

Finally, must sign the contribution of Aristotle (died before 322 B.C.) and his commentator Alexander Aphrodisias (died about 215 B.C.) on linked subjects of the light, like the weather and the color phenomena [3].

Translation and study of various optical, medical and philosophical works that have just been mentioned have allowed first scientists of Islamic countries to have a rich exceptional group in varied and various theories, mathematical analyzes and anatomic descriptions. At the theoretical level, they have acknowledgement about different explanations of the phenomenon of vision developed during the centuries. The first, attributed to Epicurus (around 341–270 before B.C.) says that the vision is the result of the diffusion, by the object, thin films which are containing all features of observed object (theory of eidola).

When we are going inside the eye, these films cause vision. A second theory, known as “the emission” says that the eye diffuse invisible rays forming a circular cone, allowing the vision of any object within the cone. Plato (died at 347 before B.C.) adds to this theory the existence of an external light to the eye that would combine with the rays from the eye. In their theory of “pneuma”, the Stoics (from the 3rd century before B.C.) replace the light cone of column air beam by external light. From the other side, Aristotle says that the essential property of a visible object is the color and considers that light is neither material substance nor a movement [4].

From a mathematical point of view, the first physicists of Islamic countries have benefited from geometric works of great value that allowed explaining the phenomenon of light propagation and the reflection of light rays on surfaces of different shapes. Finally, from the physiology point of view, detailed descriptions of the eye and its connections with the brain exposed by Galen, which opened the new developments way to study the relationship between light and vision.

2 The Arabic Optic Before Ibn Al-Haytham

Without waiting the final translations from Greek to Arabic, some scientists from Islamic countries have studied and taught the content of translated writings. This first effort resulted in the publication of critical comments and then books on the same subjects, as those inherited from the Greek tradition, but with some improvements in the presentation and justification of the results. Regarding the optical system of the eye, the oldest Arab contribution is that for the translator and medicine Hunayn Ibn Ishaq (died at 873), which put two books in this field, entitled “*the ten books on the eye*” and the “*Book of questions on the eye*” [5].

About geometric optics, Al-Kindi the famous philosopher (died about 873) is the first Arab concerning about this field. Al-Kindi interested about the phenomenon of vision, deals this phenomenon in side general and reflection. Al-Kindi devoted four

books. Following the Greek authors as noted previously, Al-Kindi also held student in burning mirrors, in three separate writings, different geometric shapes that could allow to effectively focusing the rays light to burn a remote target. His theoretical studies concerned about plane hexagonal mirrors, particularly, strong one, such as the tapered mirrors, spherical, parabolic and pyramid with 24 faces [6]. But neither bibliographic sources nor optical writings indicate a technological extension of these theoretical studies.

After Al-Kindi, Qusta Ibn Luqa (died at 910), known as a translator from Greek to Arabic, made some new contributions in three fields of optics study of reflection on convex and concave spherical mirrors, justification certain assumptions of Euclid and especially a study mirrors that category distorted images of reflected objects [7]. These two Arabic scientists characterize the first phase of this discipline: Understanding the many heritage of Greek, more rigorous reformulation of certain procedures or certain results and further investigations around old themes.

Not until the tenth century, that shows the first break with the Greek tradition. In an epistle entitled “Book on property of vision” for the great physician and chemist Abu Bakr al-Razi (died at 925) have shown that the vision is not result of spread of rays coming out from the eye, and rejecting, for the first time, the hypothesis unanimously accepted in the Greek tradition optics [8]. Abu Bakr al-Razi also said that pupil dilation is not due to internal pressure when it expands the pneuma, as Galen had explained, but a drop in external light. It is also the first to have said that the movement of the pupil is a mechanism regulating amount of light entering the eye. A century later, the physician and philosopher Ibn Sina (died at 1037) rejected the Greek theories of vision, especially, the spread of the light beam through the eye of the observer [9].

But it's Ibn Sahl (tenth century), from our knowledge, the first great innovator in addressing new problems. In his work “Book of burning mirrors” he studied for the first time, the refracting properties of the plan-convex lenses and biconvex in order to substitute them for burning mirrors. Analysis resulted in the characterization of the environment where the light moves by a certain relationship, which is exactly the inverse of the refracting index. This result does not seem to have attracted the attention of scientists from Islamic countries after Ibn Sahl, and it was not until the sixteenth century it is again established by the Dutch scientist Snell (died at 1626) [10].

3 Optical Work of Ibn Al-Haytham

Most mentioned of optic Arabic works have been circulated after the death of their authors. Their works have been taught and opened the way to new discoveries in this field. This will be the work of Ibn al-Haytham scientist of the tenth–eleventh century. His study in many fields and have enabled to achieve a great synthesis that involves geometry, experimental physics, technology and physiology.

Abu Ali al-Hasan Ibn al-Hasan Ibn al-Haytham is known as its original productions in at least three fields: optics, mathematics and astronomy. But before discussion his optical works, it seems useful to know elements relating to his life, studies and publications in other scientific fields.

This scientist was born in 965 in Basra and died around 1040 in Cairo, spent the first part of his life in his hometown where finished his basic study. But we know nothing about his family, his childhood, his adolescence and the environment in which he grew up. Apparently, he spent some time in other cities such as Baghdad and Ahwaz [11]. At an unspecified date, he moved to Cairo after accepting an invitation from al-Hakim (996–1021), the Fatimid caliph of Egypt [12]. He remained there until his death in 1040.

The known biographical sources do not mention the content of his scientific study. But we can deduce from what has survived of his publications, he has treated reviewing the content of Greek works of geometry, numbers theory, astronomy and optics that had been translated into Arabic in the ninth century [13]. It has also multi knowledge of the production in different field for scientists from Islamic countries that preceded it [14].

The majority physical writings of Ibn al-Haytham are concerned by optics. The titles treat different concerned aspects of that discipline, which had already been the subject of research on the part of Greek scientists or had been treated, for the first time deal physicists of Islamic countries. That is the propagation of light, vision, reflection and refraction, burning mirrors, the rainbow and various astronomical phenomena (halo, eclipses, etc.).

By careful studying various contributions produced before the mid-tenth century. Ibn al-Haytham opened new thinking of research, breaking the usual way of research procedure by interest on several principle points. This research conducted by a three approaching methods: inductive, deductive and experimental. It will lead to the writing of his famous “Book of optics” which remains in the eyes of experts, the most important book written in this field, since from old Greek until the early of seventeenth century Europe.

This book is composed of seven chapters preceded by an introduction [15]. The first chapter presents a general theory of light and vision. After the synthesis of the points of views for the old physicists and mathematicians, he defines the light and its different types of diffusion: primary, secondary, reflected and refracted. Soon thereafter, Ibn al-Haytham describes many experiments using a number of instruments, such as fluorescent tubes and darkrooms, and which establish the rectilinear propagation property.

After finding that the light is inseparable from the vision, Ibn al-Haytham exposed in this chapter the anatomy of the eye based on the research of Greek and Arab physicians, but it innovates by introducing purely geometrical considerations in the form of eye and the position of its various components: crystalline, pupil, cornea, etc. Occasionally, he rejects the explanation of the vision based on the Greek notion by substituting an explanation based on light and its propagation and, specially, he abandoned the old assumption of vision, saying that an object was visible through its illumination by a cone of light from the eye, and says, then it

demonstrates that it is the spread of light rays from the object to the eye that can see the object.

The second chapter sets out a theory of knowledge based on visual perception, while the third deals binocular vision, errors of vision and fourth knowledge. The fourth is deal with reflection. Ibn al-Haytham studied, experimentally, the reflection of essential and accidental lights and it gives a complete formulation of the law of reflection. There is also a description of an instrument for measuring reflections on different surfaces: planes, spherical, cylindrical and conics, according as they are convex or concave. He ends the chapter by showing how to determine the incident ray when you know the positions of the eye and the reflected beam.

The fifth and sixth chapters treated also the reflection but with two different approaches. In the fifth, studied, according to purely geometric approaches, the famous problem which will be known in Europe as the “Problem of Alhazen”: it determines the point or points of reflection on a mirror plane, spherical, conical or cylindrical (convex or concave) of a light ray starting from a given source, and also leading to a given point outside the mirror. In the sixth, Ibn al-Haytham deals by clear way the errors in vision due to reflection.

The seventh chapter and final studies the refraction. For this, the author perfected an instrument that was designed by Ptolemaos and he uses it to measure the refractive air-water, air-glass and water-glass, compared to flat and spherical surfaces. But it does not just bring together all the results of the experiment in tables, as the Greek made. It groups considering eight rules that express the relationship between the angle of incidence and the angle of deviation [16].

Most other optical writings of Ibn al-Haytham are devoted to concrete problems. Indeed, apart from the text entitled “ Letter of Light”, who gets a topic already addressed in his great treatise, ten written on the remaining eleven concern either optical instruments, such as burning mirrors (spherical and parabolic) or some astronomical phenomena related to light (shadows, eclipses, halo, rainbow, moon and stars light).

In each of these studies, Ibn al-Haytham continued to practice, and find a mixing way to the new scientific approach combines mathematical deduction to the experimental method. This did not always enable him to solve the problems that he had proposed to study, but its investigations have prepared the ground for the explanation of physical phenomena. This is the case of the rainbow for which he provided incomplete and partially inaccurate explanations that will bring one of his successors, as we discuss later, to resume the study of the phenomenon and to provide an explanation satisfactory for the time. But his analysis of the propagation of light rays and the formation of the image of an object in the eye that allowed him to give a new view to the optic, with the use, for the first time in history the properties of darkroom.

4 Work Movement of Ibn Al-Haytham in Islam Countries and Europe

The written scientific and survey sources enable us to confirm that the eleventh to the seventeenth century, some works of Ibn al-Haytham devoted to optical circulated in various parts of Muslim empire and even outside its borders. Already, some of own writings in his lifetime had begun to be studied. This is the case of his "Epistle on the moon light" will be copied by his contemporary, Ibn Ridwan, a famous medicine of Cairo [17]. This is same as the case of "Book of optics" a copy will arrive in Zaragoza in the second half of the eleventh century. It will be used by the mathematician al-Mu'taman his "Book of perfection", where there are exposed and solved the famous problem of Ibn al-Haytham on the determination of the projection point on a mirror, beam of light from a given source and terminating at a given point [18].

In the thirteenth century, some optical work of the scientist have interested researchers, like Qutb al-Din al-Shirazi (died at 1311) and his student Kamal ad-Din al-Farisi (died at 1321) who lived in central of Asia. The second scientific studied some of works of Ibn al-Haytham and published an important book, entitled "Optical review for people who have a view and judgment". This book contains a revised wording of some writings of his illustrates predecessor, particularly his "Book of optics". There are also original contributions, for example, full explanation of rainbow phenomenon, which had not had, before him, a satisfactory scientific explanation [19].

In Europe, it is accepted that before the translation phenomenon of Arab scientific works in Latin, optics was virtually non-existent at the level of teaching, research and publications. The few available items were found in encyclopedias, such as Pliny (died at 79), Solinus (three-fourth century) and Isidore of Seville (seventh century). In addition, the information exposed to them were rejected or corrected long ago by the work of Arab physicists at tenth-eleventh century. It says, for example, the view is generated by light scattered from the eye and the seat of vision is the pupil. As for the mathematical analysis of the propagation of light, it is simply absent from the books that deal with this topic. Not until the end of the twelfth century that the situation changed with the translation in Latin, some Greek and Arabic writings. From these translations, there are two books of Ibn al-Haytham: The "Book on burning mirrors made by using conic sections" and, especially, the "Book of optics". This book will be the reference European specialists in this field. The oldest of them, Robert Grosseteste (dead at 1253) is the only one did not have this book. He discovered the Arabic optical by the book of "optical Book" for al-Kindi by translation it to Latin. But, Roger Bacon (dead at 1292), which will give impulse light to the European optical science, thanks to his knowledge of Ibn al-Haytham books. At the same time, Vitello (dead at 1281) will publish *Perspectiva* and John Peckham (dead at 1292) his "Tractatus de perspectiva", which are adaptations and extensions of the Cairo scientist. In the fourteenth century, same works benefit the Italian translation and philosophers, which will be

interested in its content. From the fifteenth century, there is a renewed interest in the work of Ibn al-Haytham, especially after the new edition by Risner, Basel, in 1572. Among the scientists who will be interested again its contents include Leonardo da Vinci (died at 1519) and Huygens (died at 1695) who try to solve with their own way, the famous “problem of Alhazen” [20].

During this long period from early of thirteenth century to late of sixteenth century, we do not see significant progress in the European optical tradition, as highlighted an expert in this period speaks of “striking continuity between Ibn al-Haytham in the eleventh century and Johannes Kepler in the seventeenth century”, in explaining his decision thus: “we have seen interest and important developments in the optical theory during this period, but it is amazing how many have been small changes in questions from the theory in its basic assumptions” [21] and concluding with these words: “When Johannes Kepler solves the problem of vision, in the early of seventeenth century, he began where Ibn al-Haytham was arrested” [22].

5 Conclusions

Researches in recent decades allow new Arabic books on themes of mathematic, astronomy, and physic and thereby improve our information and even rewrite some chapters of the history of science in Islamic countries, especially in the field of optic. Also publishing a number of books, products from the ninth allowed for more detail, concerns, orientations, and contributions originals researchers at that time, such as al-Kindi, Ibn Sahl and especially Ibn al-Haytham. For the latter, the researchers have contextualized his work and the part of a dynamic that began in the ninth century and cleared in the late of tenth and early eleventh century.

Concerning Ibn al-Haytham, a detailed analysis of his contributions helped a better define of his overall methodology, its approaches and tools used in the development of its most important results. He also revealed his vision of scientific activity and the rules of conduct that is applied throughout his life as a researcher: “It is the duty of those who studied scientific works, to know the truth, must adversary of all that study, treating the text and all the comments, putting in question under every conceivable aspect. Also has duty to ask questions, by following this path, that will prove the truth, inadequate and uncertainties that the previous works” [23].

References

1. Rashed, R.: *L’optique géométrique*. In: Rashed, R. (ed.) *Histoire des sciences arabes*, Paris, Seuil, 1997, vol. 2, pp. 293–295 (1997)
2. Russell, G.A.: *La naissance de l’optique physiologique*. In: Rashed, R. (ed.): *Histoire des sciences arabes*, op. cit., pp. 323–324

3. Op. cit., pp. 324–325
4. Op. cit., pp. 320–322
5. Op. cit., pp. 330–331
6. Rashed, R.: *L'optique et la catoptrique d'al-Kindî*. Leiden, Brill (1997)
7. Rashed, R.: *L'optique géométrique*, op. cit., pp. 295–305
8. Rosenfeld, B.A., Ihsanoğlu E.: *Mathematicians, Astronomers and other Scholars*, op.cit., p. 66
9. Russell, G.A.: *La naissance de l'optique physiologique*, op. cit., pp. 331–334
10. Rashed, R.: *Géométrie et dioptrique au X^e siècle*, Paris, Les Belles Lettres, 1993, pp. 1–52; R. Rashed, *L'optique géométrique*, op. cit., pp. 295–309 (1993)
11. Ibn Abî Usaybi'a, 'Uyûn al-anbâ' fî tabaqât al-atibbâ'. In: N. Ridâ (ed.), Beyrouth, Dâr Maktabat al-hayât, non datée, pp. 550–553
12. Ibn al-Qifû, *Kitâb ikhbâr al-'ulamâ' bi akhbâr al-hukamâ'* [Livre qui informe les savants sur la vie des sages], Beyrouth, Dâr al-âthâr, non datée, p. 115
13. Sezgin, F.: *Geschichte des Arabischen Schrifttums*, Leiden, Brill, vol. V, 1974, pp. 158–1; vol. VI, 1978, pp. 73–96
14. Sabra, A.I., Ibn al-Haytham. In: Ch. Gillispie (ed.): *Dictionary of Scientific Biography*, New York, Scribner'sons, pp. 189–210 (1981)
15. Nazîf, M., Al-Hasan Ibn al-Haytham, buhûthuhû wa kushûfuhû al-basariyya [Al-Hasan Ibn al-Haytham, ses recherches et ses découvertes optiques], Le Caire, Matba'at an-Nûrî, 1942. Seconde édition (fac-similé), F. Sezgin (ed.), Frankfurt, Publications of the Institute for the History of Arabic-Islamic Science, Natural Sciences in Islam, n. 35 (2001)
16. Op. cit., pp. 11–36
17. Ibn al-Qifû, *Ikhbâr al-'ulamâ' bi akhbâr al-hukamâ'*, op. cit., p. 288
18. Hogendijk, J.-P.: *Le roi-géomètre al-Mu'taman ibn Hûd et son livre de la perfection (Kitâb al-Istikmâl)*, In: *Actes du premier colloque sur l'histoire des mathématiques arabes*. Algiers, pp. 59–62 (1998)
19. Al-Fârisî, *Kitâb tanqîh al-manâzîr* [Livre de la révision de l'Optique <d'Ibn al-Haytham>], Hijazi, M., Mukhtar, M. (ed.), Le Caire, Al-Hay'a al-misriyya al-'amma li l-kitâb (1983)
20. Lindberg, D.C.: *La réception occidentale de l'optique arabe*. In: Rashed, R. (ed.), *L'Histoire des sciences arabes*, op. cit., pp. 355–367
21. Op. cit., p. 355
22. Op. cit., p. 367
23. Ibn al-Haytham, *Al-Shukûk 'lâ Batlamyûs* [Les doutes sur Ptolémée], A.I. Sabra & N. Shehaby (ed.), Le Caire, Publications de la Bibliothèque Nationale, pp. 3–4 (1996)

Fatigue and Notch Mechanics

Bruno Atzori, Giovanni Meneghetti and Mauro Ricotta

Abstract Linear Elastic Notch Mechanics (LENM) extends the concepts of the well known Linear Elastic Fracture Mechanics (LEFM) to notches having root radius different from zero and arbitrary notch opening angle. LENM is based on fundamental analytical results and definitions introduced by Williams [43] and Gross and Mendelson [17]. From the experimental point of view, it has been applied for the first time by Haibach [18] on pure phenomenological basis to analyse the fatigue strength of welded joints using the strain gauge technique. Subsequently, LENM was developed thanks to the progressively increasing use of the Finite Element Method (FEM). Nowadays, NM has been formalised and applied to structural strength assessment of components. Different application techniques exist, but the theoretical frame remains unchanged [6, 8, 12, 20, 21, 23, 24, 28, 31, 37, 38, 42]. The present paper, after recalling the classic notch fatigue design criterion and the LEFM, aims at illustrating the link between Notch Mechanics and those classic approaches. In particular the aim is two-fold: on one side the use of Notch Mechanics in notch fatigue design will be illustrated, on the other side it will be shown how it can be used to better analyse and explain in deep the fundamentals of the classic approaches mentioned previously.

1 Introduction

Classical methods of fatigue design of mechanical components are based on either stresses, elastically evaluated, or strains calculated in the elasto-plastic field. More recently, the use of different fatigue-relevant parameters has been put forward thanks to the development of numerical and experimental techniques: the finite element method on one side and the thermometric methods on the other side. As an example, the finite-volume strain energy density [22] has been extensively applied

B. Atzori (✉) · G. Meneghetti · M. Ricotta
Department of Industrial Engineering, University of Padova, via Venezia 1,
35131 Padua, Italy
e-mail: bruno.atzori@unipd.it

and has been recently reviewed on some publications [11, 34–36]; an experimental, energy-based approach to notch fatigue was proposed by one of the authors, taking the heat energy dissipated in a unit volume of material per cycle as a fatigue damage indicator [27, 29, 30]. However, these novel approaches have still a limited diffusion in practical applications.

Classical fatigue design approaches are based on material properties generated from fatigue testing of plain specimens under stress or strain control for the stress- or strain-based approaches mentioned previously, respectively. The use of such design curves when assessing mechanical components weakened by stress risers is critical due to two reasons:

1. the highly stressed volume at the notch tip which is smaller and smaller as the notch tip radius is reduced, so that the stress/strain peaks are no longer effective in correlating the fatigue strength;
2. as far as ductile engineering materials are concerned, the plastic redistribution which is present around the notch tip, that is significant particularly in the low cycle regime.

A limit case is represented by cracks that are characterised by a notch opening angle and a tip radius equal to zero, with a singular linear elastic stress distribution; therefore, the classical methods based on finite values of the peak stress/strain quantities are not applicable, but the Fracture Mechanics approach must be adopted. The assessment method of the latter approach is based on the complete local stress distribution, characterised by a stress singularity exponent equal to $1/2$, according to the Linear Elastic Fracture Mechanics. Fatigue characterisation of engineering materials is performed on cracked specimens and the adopted stress parameter is the Stress Intensity Factor that quantifies the intensity of the singular linear elastic stress distribution close to the crack tip. Relying on this theoretical background, the Notch Mechanics extends the stress field intensity approach to pointed V-shaped notches, that are characterised by a decreasing stress singularity exponent as the notch opening angle is increased [43]. If a small notch tip radius is introduced, the linear elastic stress distributions do not change significantly, apart from the finite linear elastic peak stress, causing a plateau in a log-log plot of the stress distribution ahead the notch [16].

2 Stress-Life Approach to Fatigue

Dealing with notch fatigue, the linear elastic stress concentration factor is considered, K_t , that is defined as the ratio between the peak stress and the nominal stress referred to the net-section or the gross section, $K_m = \frac{\sigma_{pe}}{\sigma_n}$ or $K_{Ig} = \frac{\sigma_{pe}}{\sigma_g}$, respectively. If the fatigue strength were correlated by the range of the linear elastic peak stress,

$\Delta\sigma_{pe}$, then the fatigue curve relevant to notched specimens would be shifted downward by a factor equal to K_t as compared to the one generated from plain specimens. However, this does not occur, because of the two reasons aforementioned. Concerning the stress-gradient effect, the influence of the linear elastic peak stress is properly reduced by introducing a fatigue strength reduction factor K_f , that can be defined experimentally as the ratio between the fatigue strength of a plain specimen and that of the notched specimen for the same high number of fatigue cycles, N :

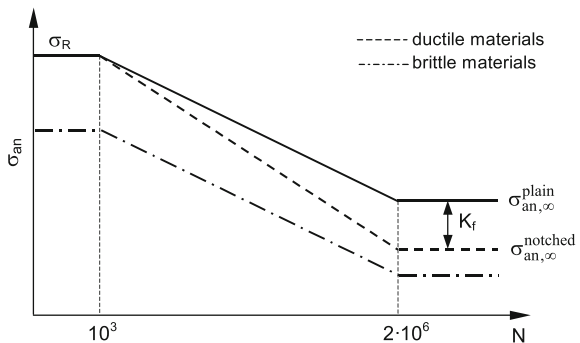
$$(K_f)_N = \left(\frac{\Delta\sigma_{plain}}{\Delta\sigma_{notched}} \right)_N = \left(\frac{\sigma_{eff}}{\sigma_{nom}} \right)_N \tag{1}$$

where, σ_{eff} is the effective stress. In practice, K_f is defined only at the fatigue limit, plastic stress re-distribution becoming more and more effective as the stress level is increased, as shown in Fig. 1 [2] for ductile and brittle materials. For brittle materials also a K'_f should be defined for the static behaviour, since plastic stress re-distribution is not possible or limited. In Fig. 1 it has been assumed a constant K_f , however K_f might change if the stress amplitude of the notched member is increased from the high cycle fatigue to the very low cycle fatigue regime. Concerning the influence of plasticity, which is significant in the low-rather than in the high-cycle fatigue, ductile metals are assumed to fail due to the fully plastic collapse of the net section in the fatigue range up to about 10^3 fatigue cycles. Therefore, the net-section stress amplitude is generally adopted to represent the fatigue design curves, as illustrated in Fig. 1.

The most widely adopted expression to estimate K_f starting from K_t was proposed by Peterson [33]:

$$(K_f - 1) = q(K_t - 1) \tag{2}$$

Fig. 1 Comparison of the fatigue curves for a plain and a notched specimen



However, other formulas are available in literature, many of which formulated subsequently in light of the knowledge progress [9, 10, 13, 19, 23, 25, 26, 32, 37–41].

3 Strain-Life Approach to Fatigue

In principle this approach eliminates the second problem mentioned above, because it is based on the elasto-plastic strain evaluated at the notch tip. Therefore, the strain-life curve derived experimentally on plain specimens, as depicted in Fig. 2, should be directly applicable in design of notched components. However, in case of severely notched specimens (sharp notches, characterised by a reduced notch tip radius), the elasto-plastic peak strain does not correlate the fatigue life and must be reduced or averaged inside a properly defined structural volume.

The elasto-plastic peak strain at the notch tip can be determined starting from a linear elastic stress analysis by using the Neuber’s rule:

$$K_\sigma \cdot K_\epsilon = K_t^2 \tag{3}$$

combined with the stabilised cyclic stress-strain curve, as reported in Fig. 3. Alternative formulations are available in the literature (see as an example [14]). In case of severely notched components, K_t appearing in Eq. (3) is suggested to be substituted by K_f , but all uncertainties in K_f estimation still remains, as illustrated in the previous section dedicated to the stress-life approach.

Fig. 2 Manson-Coffin curves of heat treated ductile cast iron (adapted from [30])

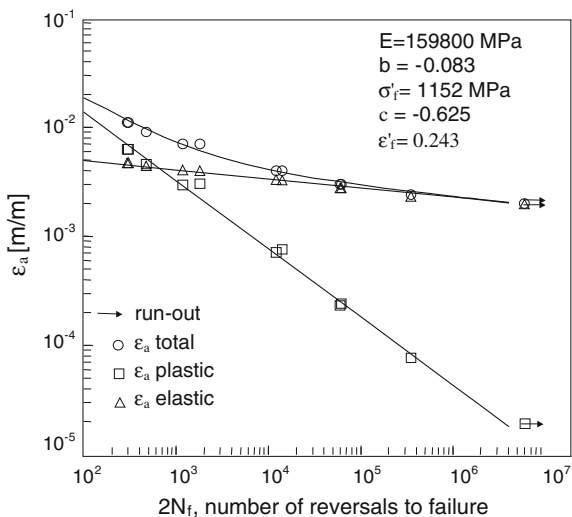
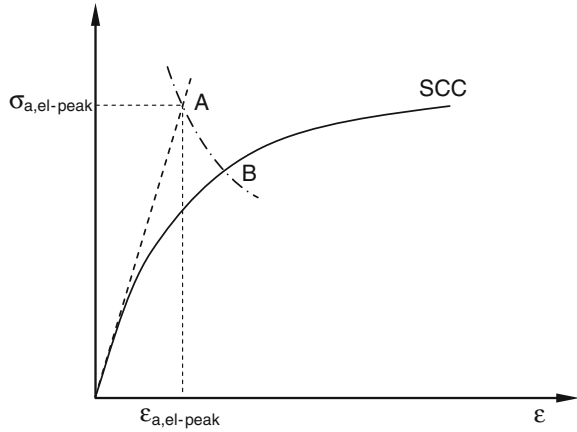


Fig. 3 Graphical representation of the Neuber's rule



4 Linear Elastic Fracture Mechanics (LEFM)

In high cycle fatigue, the *LEFM* is commonly adopted and therefore only this discipline will be analysed here. For the sake of simplicity, only the case of a crack having length equal to $2a$ in an infinitely wide plate subjected to mode I loading will be considered (Fig. 4). The σ_y local stress distribution along the x-axis is given by:

$$\sigma_y = \frac{K_I}{\sqrt{2\pi x}} \tag{4}$$

Fig. 4 A through crack centred in an infinitely wide plate

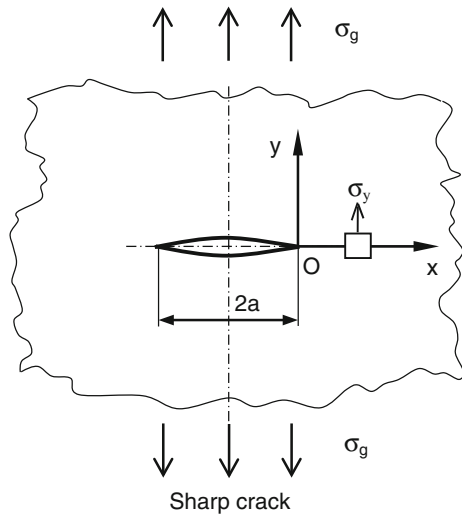
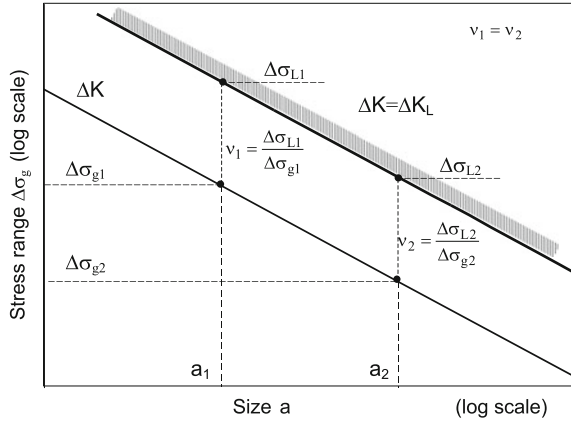


Fig. 5 Interpretation of the Fracture Mechanics Eq. (5) as a nominal stress-based strength criterion



where K_I is the Stress Intensity Factor (*SIF*), that can be calculated using the following expression:

$$K_I = \sigma_g \sqrt{\pi a} \quad (5)$$

where σ_g is the remotely applied nominal gross stress.

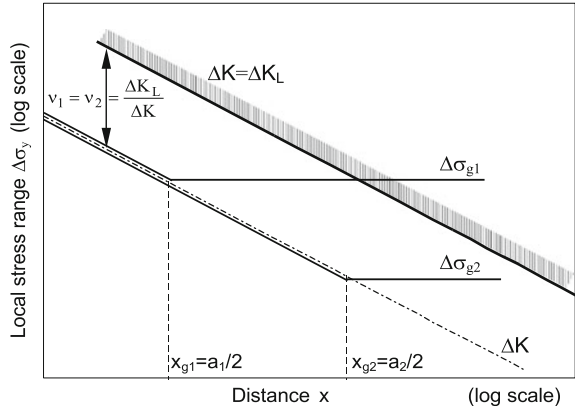
Equations (4) and (5) are often represented in log-log diagrams, as reported in Figs. 5 and 6, and they can be interpreted as an extension to crack problems of the classical approaches presented previously.

In particular, Eq. (5) shows that a nominal stress can be used in fatigue design, thus recalling the stress-based approach, as shown in Fig. 5. Each case analysed is represented in Fig. 5 by a single point, connecting the applied nominal stress to the dimension $2a$ of the crack. The scale effect for two cracks of different a_i but with the same ΔK is shown in this figure, evidencing also that the safety factor v does not change, changing a_i .

Alternately, Eq. (4) shows the local linear elastic stress distribution; because it can be immediately and easily re-converted into local strains due to the linear elastic hypothesis, then Eq. (3) recalls the strain-based approach. Each case analysed is represented in Fig. 6 by the full field of stress (local and nominal): two different crack lengths with the same ΔK give the same local stresses (and the same safety factor v) with two different nominal stresses $\Delta\sigma_g$ evidencing then the scale effect. Both Eqs. (4) and (5) are based on K_I , that is they are based on the asymptotic linear elastic stress distribution, and not on the peak stress; therefore they overcome the first problem of the classic approaches mentioned previously, related to the loss of significance of the linear elastic peak stress as the notch tip radius is reduced.

Concerning the second problem related to the development of plastic strains, as far as the high cycle fatigue behaviour of long cracks is concerned, small plastic zones develop only close to the crack tip, so that linear elastic stresses/strains can be adopted as fatigue relevant parameters. By extending the previous classical approaches to the fatigue crack problems analysed in the present section, Eq. (5)

Fig. 6 Interpretation of the Fracture Mechanics Eq. (4) as a local stress/strain-based strength criterion



will be referred to as stress approach, while Eq. (4) will be referred to as strain approach.

In fatigue design, expressions (4) and (5) along with the crack growth rate equation for long cracks known as Paris' law:

$$\frac{da}{dN} = C \cdot \Delta K^m \tag{6}$$

are adopted to estimate the number of cycles to spread a fatigue crack from an initial size a_i up to a final size a_f [14]:

$$N_f = \frac{a_f^{(1-\frac{m}{2})} - a_i^{(1-\frac{m}{2})}}{C(1-\frac{m}{2})(\Delta\sigma_g \cdot \sqrt{\pi})^m} \tag{7}$$

Concerning the determination of the fatigue limit of a cracked plate, Eq. (5) should be used for the stress approach as illustrated in Fig. 7, while Eq. (4) is valid for the strain approach as depicted in Fig. 8. The idealised trends reported in Figs. 7 and 8 show abrupt changes of the slope, while real trends are smooth, which can be described by proper analytical expressions [9, 13].

Concerning the static strength design, Eqs. (4) and (5) are still valid, provided that the threshold range of the SIF is substituted by the Fracture Toughness ΔK_c and the plain material fatigue limit $\Delta\sigma_0$ is substituted by the material tensile strength σ_R .

Figure 8 shows that the stress field approach according to the *LEFM* requires that the extension of the asymptotic stress field is sufficiently long, i.e. there will be a limitation of applicability as the crack size is reduced. The behaviour of short fatigue cracks is widely investigated in the literature; however, a simple and effective equation to estimate the threshold SIF of short cracks was proposed by El Haddad et al. [15] as follows (see Fig. 7):

Fig. 7 Fatigue limit estimation according to Eq. (5)

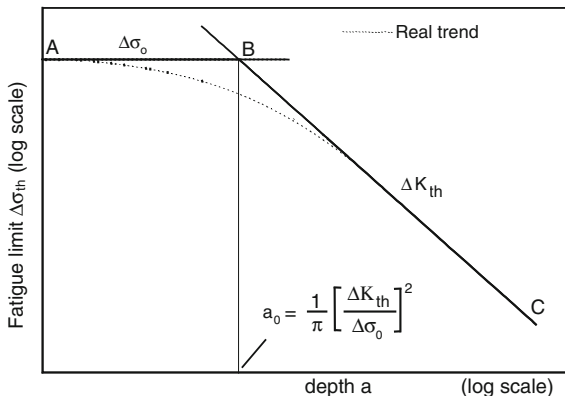
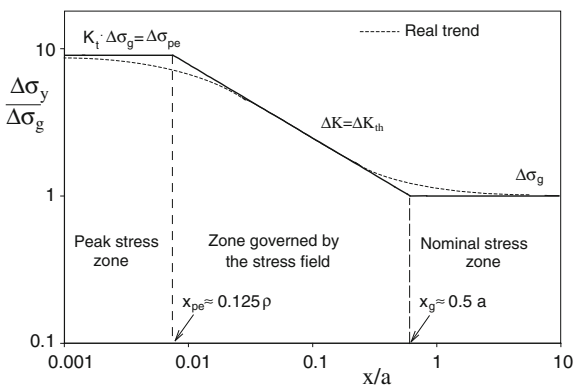


Fig. 8 Fatigue limits estimation according to different weakest link conditions



$$\Delta K_{th} = \Delta \sigma_{g,th} \sqrt{\pi(a + a_0)} \tag{8}$$

Equation (8) is valid for cracks centred in an infinite plate. For real components, Eq. (8) should be re-arranged to account for a shape factor [9].

5 Linear Elastic Notch Mechanics

Linear Elastic Notch Mechanics is a non-conventional extension of the *LEFM* to include also pointed or rounded V-shaped notches, characterised by an arbitrary notch opening angle (*LEFM* considers only the crack case, i.e. the notch opening angle and the tip radius are equal to zero).

One of the main fields of application of the Notch Mechanics is the fatigue design of welded structures. About fifty years ago, Haibach proposed an experimental approach to evaluate the fatigue strength of welded structures, based on the

strain range evaluated at a fixed distance from the weld toe (supposed to be the crack initiation point) by means of a strain gauge having a well defined length [18]. By so doing, Haibach found that the fatigue strength of welded joints in structural steels tested in the as-welded conditions and failing from the weld toe could be synthesised by means of a single scatter band, despite the different plate thicknesses and joints' shape considered. Such an approach has been later applied to welded joints in aluminium alloys [3], but only after twenty years several finite element analyses demonstrated that the stress field close to the tip of sharp V-notches has a singularity exponent lower than $\frac{1}{2}$ and decreasing as the V-notch opening angle increases [1]. These stress analyses provided a theoretical justification to the phenomenological approach introduced by Haibach.

The research concerning the more general theory of notch stresses put in evidence that, several years before the works by Haibach, the stress singularity exponents for open V-notches had been provided by Williams [43], while later on a definition of Notch-Stress Intensity Factor, playing the same role of the *SIF* of the *LEFM*, was introduced by Gross and Mendelson for mode *I* loading [17]:

$$K_I^V = \sqrt{2\pi} \cdot \lim_{x \rightarrow 0} (\sigma_x \cdot x^\gamma) \tag{9}$$

γ being the stress singularity exponent, equal to $\frac{1}{2}$ for the crack case and decreasing to zero as the notch opening angle increases to 180° . On this basis, Lazzarin and Tovo formalised the equations of the linear elastic stress fields for open V-notches and by using the range of the *N-SIF* evaluated at the weld toe they were able to summarise the fatigue strength of welded joints in structural steels, tested in as-welded conditions and failing from the weld toe, as shown in Fig. 9 [20].

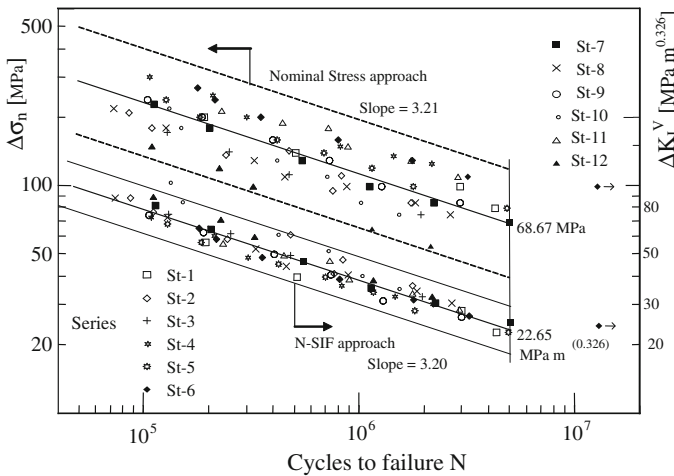


Fig. 9 Synthesis of the fatigue strength of welded joints in steel using the mode I *N-SIF* (from [21])

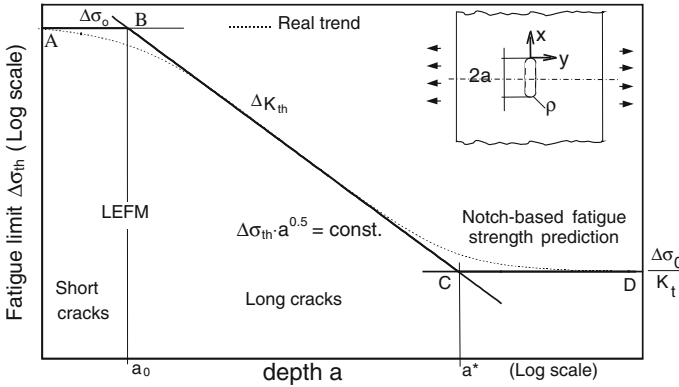


Fig. 10 Atzori-Lazzarin’s diagram for U-shaped notches (from [5])

In the case of U-shaped notches having notch tip radius ρ different from zero, the notch acuity $\zeta = \frac{a}{\rho}$ is not infinite, as it occurs in the crack case. If the notch acuity (and then the K_t) is kept constant and the notch absolute dimensions are scaled in proportion, the threshold stress range $\Delta\sigma_{gth}$ (i.e. the fatigue limit) will vary according to Fig. 10, where the short crack/notch behaviour, the long crack/sharp notch behaviour and the blunt notch behaviour are highlighted [5]. The diagram reported in Fig. 10 has been validated using several experimental data, as shown in Fig. 11 [9].

Subsequently it has been extended and validated to include the V-notch case [10]; moreover, it has been demonstrated that the threshold values of the N -SIF ΔK_{th}^V can be expressed as a function of the material fatigue properties ΔK_{th} of a crack and $\Delta\sigma_0$ of the plain material.

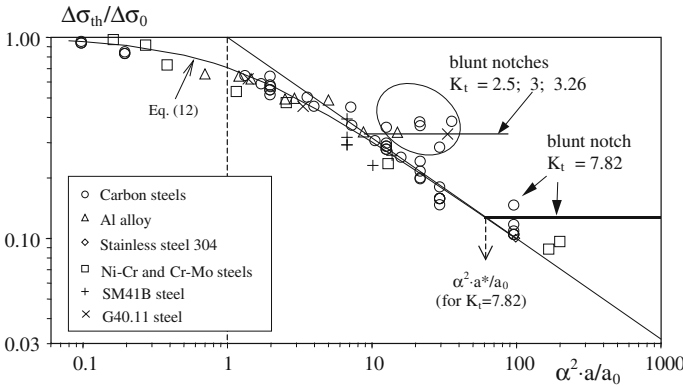


Fig. 11 Fatigue strength of specimens containing defects and notches [9]

6 Sharp Notches, Scale Effect and Woehler Curves

For the sake of brevity, only U-shaped sharp notches characterised by a (small) tip radius, a well defined acuity $\frac{a}{\rho}$, centred in an infinitely wide plate and subjected to pure mode I loading will be considered. Moreover a material characterised by a brittle behaviour will be analysed.

The fatigue model according to the Notch Mechanics is reported in Fig. 12 for the limit conditions corresponding to the fatigue limit ($\Delta K = \Delta K_{th}$) and to the static failure ($\Delta K = \Delta K_c$) [4, 5]. In the form presented in Fig. 12, $\Delta\sigma_g = f(a)$, the method recalls the classic stress-based approach. It is worth noting that Fig. 12 shows an idealised behaviour, the experimental trends generating smooth transitions between two intersecting straight lines.

To generate the Woehler curve of a notch having given acuity and size a_i , different constant amplitude fatigue tests should be performed corresponding to stress levels chosen in the range $\Delta\sigma_{gth}(a_i) - \Delta\sigma_R(a_i)$ (for the same initial notch size a_i). In each one of such tests, the notch-emanated fatigue crack would grow up to the final condition $\Delta K = \Delta K_c$ when $a = a_f$ as reported in Fig. 12. Depending on the size $2a_i$ of the tested notches, we can define different zones as indicated in the figure:

Zone I : $a \leq a_0$

Zone II : $a_0 < a \leq a_{0s}$

Zone III : $a_{0s} < a \leq a^*$

Zone IV : $a^* < a \leq a_s^*$

Zone V : $a > a_s^*$

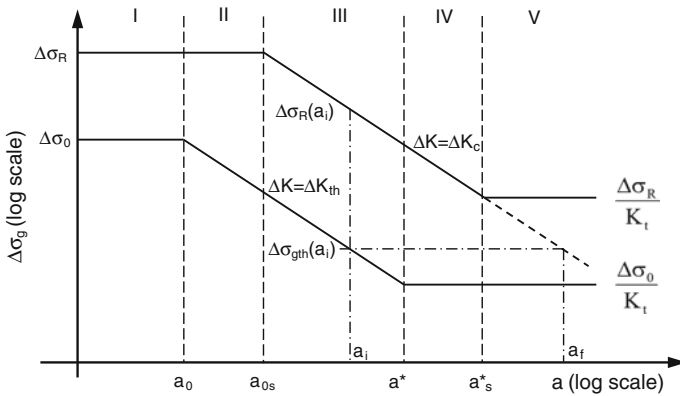


Fig. 12 Application of Linear Elastic Notch Mechanics to a notch having initial size a_i

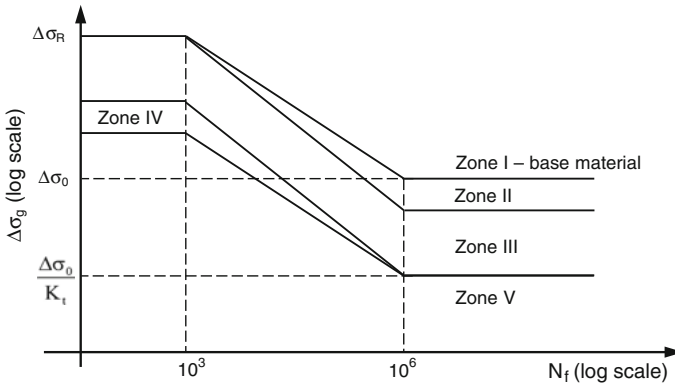


Fig. 13 Fatigue curves generated from testing notches having different initial sizes

A comparison between theoretical estimations and experimental results also for ductile materials has been reported elsewhere [7].

While increasing the notch size $2a_i$, the Woehler curve will modify according to Fig. 13. Starting from the base material fatigue behaviour (*zone I*), the sharp notch behaviour according to the Notch Mechanics is illustrated by *zone III* and finally the full notch sensitivity (in static as well as fatigue behaviour) is the one of *zone V*, where the fatigue curve of the base material is simply shifted downwards of a factor given by the stress concentration factor K_{tg} .

There are also two zones where the slope of the Woehler curve is different from that of the base material: the first is *zone II* where the inverse slope increases because the fatigue limit decreases, the static strength being unchanged; the second is *zone IV*, where the inverse slope decreases because the static strength decreases, the fatigue limit being constant. Figure 13 assumes that the high cycle and the low cycle knees are located at 10^3 and 2×10^6 cycles, respectively, according to the Classic Mechanics.

7 Conclusions

In the present work the fundamental concepts of the Notch Mechanics have been presented, along with its relation to the Fracture Mechanics and Classic Mechanics disciplines. For the sake of brevity, it has not been possible to present in deep all analytical formulations and experimental validations reported in the literature, which the reader is referred to.

Notch Mechanics is a non-conventional extension of the Fracture Mechanics concepts that are included as a particular case. All notch opening angles, notch tip radii and notch acuties are included in Notch Mechanics, thus largely extending the possibility to use Fracture Mechanics concepts in practical design situations. From a

theoretical point of view and considering a progressive reduction of the notch size, Notch Mechanics shows the limitations of applicability for fatigue design purposes of the linear elastic peak stress evaluated at a rounded notch tip and of the stress field evaluated at a sharp notch. The former can be applied as far as $a > a^*$ in the schematic Fig. 10, while the latter can be applied when a is between a_0 and a^* . The schematic diagram shown in Fig. 10 seems to suggest that a small notch having size $a \leq a_0$ behaves as a non-damaging defect. Indeed the experimental trend also reported in the same figure clarifies that there exists a so-called defect sensitivity according to which a fatigue strength decrease can be observed. Such reduction is approximately 40 % when $a = a_0$ and consequently cannot be neglected in practical fatigue design.

References

1. Atzori, B.: Fracture mechanics or notch sensitivity in fatigue design. In: Proceedings of the AIAS National Conference, Bergamo, Italy, (in Italian) (1985)
2. Atzori, B.: Machine Design, Cortina ed. (in Italian) (1999)
3. Atzori, B., Haibach, E.: Local strains at the toe of fillet welds and relationship with the fatigue life. In: VII AIAS National Congress, Cagliari (Italy), (in Italian) (1979)
4. Atzori, B., Lazzarin, P.: Analysis of some problems related to the FE-based assessment of fatigue strength. *La Metallurgia Italiana* **10**, 37–44 (2001). (in Italian)
5. Atzori, B., Lazzarin, P.: Notch sensitivity and defect sensitivity under fatigue loading: two sides of the same medal. *Int. J. Fract.* **107**, L3–L8 (2001)
6. Atzori, B., Meneghetti, G.: Fatigue strength of fillet welded structural steels: finite elements, strain gauges and reality. *Int. J. Fatigue* **23**, 713–721 (2001)
7. Atzori, B., Meneghetti, G.: Static strength of notched and cracked components. In: Proceedings of the 5th International Conference New Trends in Fatigue and Fracture 5 NTFF5, Bari (Italy) (2005)
8. Atzori, B., Lazzarin, P., Tovo, R.: Stress field parameters to predict fatigue strength of notched components. *J. Strain. Anal. Eng.* **34**, 1–17 (1999)
9. Atzori, B., Lazzarin, P., Meneghetti, G.: Fracture Mechanics and Notch Sensitivity. *Fatigue Fract. Eng. Mater. Struct.* **26**, 257–267 (2003)
10. Atzori, B., Lazzarin, P., Meneghetti, G.: A unified treatment of the mode I fatigue limit of components containing notches or defects. *Int. J. Fract.* **133**, 61–87 (2005)
11. Berto, F., Lazzarin, P.: Recent developments in brittle and quasi-brittle failure assessment of engineering materials by means of local approaches. *Mater. Sci. Eng. R Rep.* **75**, 1–48 (2014)
12. Boukharouba, T., Tamine, T., Nui, L., Chehimi, C., Pluvinage, G.: The use of notch stress intensity factor as a fatigue crack initiation parameter. *Eng. Fract. Mech.* **52**, 503–512 (1995)
13. Ciavarella, M., Meneghetti, G.: On fatigue limit in the presence of notches: classical vs. recent unified formulations. *Int. J. Fatigue* **26**, 289–298 (2004)
14. Dowling, N.E.: *Mechanical Behavior of Materials*. Pearson Prentice Hall, Englewood Cliffs (2007)
15. El Haddad, M.H., Topper, T.H., Smith, K.N.: Prediction of non-propagating cracks. *Eng. Fract. Mech.* **11**, 573–584 (1979)
16. Glinka, G., Newport, A.: Universal features of elastic notch-tip stress fields. *Int. J. Fatigue* **9**, 143–150 (1987)
17. Gross, R., Mendelson, A.: Plane elastostatic analysis of V-notched plates. *Int. J. Fract. Mech.* **8**, 267–327 (1972)

18. Haibach, E.: Die Schwingfestigkeit von Schweissverbindungen aus der Sicht einer örtlichen Beanspruchungsmessung. Laboratorium für Betriebsfestigkeit, Darmstadt, Bericht N° FB-77 (1968)
19. Harkegard, G.: An effective stress intensity factor and the determination of the notched fatigue limit. In: Backlund, J., Blom, A.F., Beevers, C.J. (eds.) *Fatigue Thresholds: Fundamentals and Engineering Applications*, vol. 2, pp. 867–879. Chameleon Press Ltd., London (1981)
20. Lazzarin, P., Tovo, R.: A unified approach to the evaluation of linear elastic stress fields in the neighborhood of cracks and notches. *Int. J. Fracture* **78**, 3–19 (1996)
21. Lazzarin, P., Tovo, R.: A notch intensity factor approach to the stress analysis of welds. *Fatigue Fract. Eng. Mater. Struct.* **21**, 1089–1104 (1998)
22. Lazzarin, P., Zambardi, R.: A finite-volume-energy based approach to predict the static and fatigue behavior of components with sharp V-shaped notches. *Int. J. Fract.* **112**, 275–298 (2001)
23. Lazzarin, P., Tovo, R., Meneghetti, G.: Fatigue crack initiation and propagation phases near notches in metals with low notch sensitivity. *Int. J. Fatigue* **19**, 647–657 (1997)
24. Livieri, P., Lazzarin, P.: Fatigue strength of steel and aluminium welded joints based on generalised stress intensity factors and local strain energy values. *Int. J. Fract.* **133**, 247–278 (2005)
25. Lukas, P., Klesnil, M.: Fatigue limit of notched bodies. *Mater. Sci. Eng.* **34**, 61–66 (1978)
26. Lukas, P., Kunz, L., Weiss, B., Stickler, R.: Non-damaging notches in fatigue. *Fatigue Fract. Eng. Mater. Struct.* **9**, 195–204 (1986)
27. Meneghetti, G.: Analysis of the fatigue strength of a stainless steel based on the energy dissipation. *Int. J. Fatigue* **29**, 81–94 (2007)
28. Meneghetti, G., Lazzarin, P.: Significance of the elastic peak stress evaluated by FE analyses at the point of singularity of sharp V-notched components. *Fatigue Fract. Eng. Mater. Struct.* **30**, 95–106 (2007)
29. Meneghetti, G., Ricotta, M., Atzori, B.: A synthesis of the push-pull fatigue behaviour of plain and notched stainless steel specimens by using the specific heat loss. *Fatigue Fract. Eng. Mater. Struct.* **36**, 1306–1322 (2013)
30. Meneghetti, G., Ricotta, M., Masaggia, S., Atzori, B.: Comparison of the low- and high-cycle fatigue behaviour of ferritic, pearlitic, isothermed and austempered ductile irons. *Fatigue Fract. Eng. Mater. Struct.* **36**, 913–929 (2013)
31. Murakami, Y., Endo, M.: Effects of defects, inclusions and inhomogeneities on fatigue strength. *Int. J. Fatigue* **19**, 163–182 (1994)
32. Neuber, H.: *Theory of Notch Stresses*, 2nd edn. Springer, Berlin (1958)
33. Peterson, R.E.: Notch sensitivity. In: Sines, G., Waisman, J.L. (eds.) *Metal Fatigue*. MacGraw-Hill, New York (1959)
34. Radaj, D.: State-of-the-art review on the local strain energy density concept and its relation to the J-integral and peak stress method. *Fatigue Fract. Eng. Mater. Struct.* **38**, 2–28 (2015)
35. Radaj, D., Vormwald, M.: *Advanced Methods of Fatigue Assessment*. Springer, Berlin (2013)
36. Radaj, D., Sonsino, C.M., Fricke, W.: *Fatigue Assessment of Welded Joints by Local Approaches*, 2nd edn. Woodhead Publishing, Cambridge (2006)
37. Tanaka, K.: Engineering formulae for fatigue strength reduction due to crack-like notches. *Int. J. Fract.* **22**, R39–R45 (1983)
38. Taylor, D.: Geometrical effects in fatigue: a unifying theoretical model. *Int. J. Fatigue* **21**, 413–420 (1999)
39. Ting, J.C., Lawrence, F.V.: A crack closure model for predicting the threshold stresses of notches. *Fatigue Fract. Eng. Mater. Struct.* **16**, 93–114 (1993)
40. Usami, S.: Short crack fatigue properties and component life estimation. In: Tanaka, T., Jono, M., Komai K. (eds.) *Current Research on Fatigue Cracks*, pp. 119–147. Elsevier (1987)
41. Verreman, Y., Bailon, J.: Fatigue of V-notched members: short crack behaviour and endurance limit. *Eng. Fract. Mech.* **28**, 773–783 (1987)

42. Verreman, Y., Nie, B.: Early development of fatigue cracking at manual fillet welds. *Fatigue Fract. Eng. Mater. Struct.* **19**, 669–681 (1996)
43. Williams, M.L.: Stress singularities resulting from various boundary conditions in angular corners of plates in extension. *J. Appl. Mech.* **19**, 526–528 (1952)

Experimental Disparity Analysis of the Behavior and Fatigue of the 304L Stainless Steel

Kada Mouedden, Adel Belattar and Lakhdar Taleb

Abstract This present study investigates the fatigue behavior of the 304L austenitic stainless steel at room temperature. We are particularly interested in the consequences of the experimental disparity on the behavior and on the fatigue of such steel. Thus, several specimens were solicited through the application of symmetrical strain controlled tests with amplitude of 0.22 %. The obtained results show that the evolutions of the stress amplitude of the loaded specimens are almost identical, with a specific fatigue life for each specimen. The evolutions of the isotropic (R) and kinematic (X) parts of the cyclic hardening show that these two components have a similar evolution during the fatigue cycles. The evolution of the discharge slope is similar for all the loaded specimens.

1 Introduction

Due to its superior quality of corrosion resistance, tenacity and ductility, the 304L austenitic stainless steel is used in many industrial sectors. Several researchers have been interested at its cyclic and fatigue behavior under different types of loading path [1–7] and others.

Cyclic strain controlled tests have been performed under different loading paths. For a proportional low amplitude strain control, the 304L shows a very limited cyclic hardening (first and second cycle), immediately followed by a cyclic softening [1]. However, under a non proportional load, the metal presents a cyclic hardening; with a slight softening appearing at the end of the cycles.

Therefore, the most powerful cyclic hardening can be obtained for a non proportional loading path, as it significantly increases the hardening period (number of

K. Mouedden (✉) · A. Belattar · L. Taleb
GPM, INSA de Rouen, Normandie Université, CNRS UMR6634,
BP. 8 avenue de l'université, St Etienne du Rouvray, 76800 Rouvray, France
e-mail: kada.mouedden@insa-rouen.fr; kada.mouedden@yahoo.fr

K. Mouedden · A. Belattar
Département des Sciences et Technologie, AMC,
BP 48 Cherchell Terre, 42006 Tipaza, Algeria

cycles), which is very short compared to the proportional loading path. Additionally, a phenomenon called cross-hardening effect has been observed; this phenomenon appears when a proportional cyclic loading at a specific direction is followed by another proportional cyclic loading in a different direction. The cyclic additional hardening is observed immediately after the changing in loading direction, followed by a cyclic softening [1, 8].

The previous work conducted by Belattar [9] were interested in the effects of the cyclic pre-hardening, axial or torsional, on the cyclic behavior and the fatigue lifetime of the 304L stainless steel. The sequential cyclic test carried out with increasing or decreasing of strain amplitude has confirmed the strain memory effect on the cyclic curve of the 304L. The study of the isolated effect of the pre-hardening on the fatigue without the intervention of the mean stress was possible through the application of the sequential loading as pre-hardening loading. Compared to the previous researches with a similar objective [6, 10, 11], the application of a sequential pre-hardening assures a progressive return at zero stress-strain at the end of the process of the pre-hardening, which allows us to study the isolated effect of the pre-hardening. The obtained results show that the lifetime was significantly reduced for the pre-hardened specimens compared with the non pre-hardened ones. This lifetime reduction is related to the formation of dense dislocation structures inherited from the pre-hardening phase. Additionally, it was also shown that increasing of the fatigue strain amplitude reduces this pre-hardening effect especially for the torsion pre-hardening case. However, concerning the axial pre-hardening at a low amplitude fatigue strain (0.22 %), obtained results showed that the axial pre-hardening has almost no effect on the fatigue lifetime of the 304L.

The objective of this present work is to explore these latest results of previous works in order to study the lifetime disparity of the 304L, especially the fatigue strain amplitude of 0.22 %, by analyzing the contribution of the isotropic and kinematic hardening components of each performed test.

2 Material, Specimen and Experimental Procedure

The material used in this study is an austenitic stainless steel 304L grade THYSSEN, commercially obtained in the bars form. The chemical composition of this nuance is reported in Table 1 in percentage by weight transmitted by the provider. After machining, the test specimens were heat treated at 1050 °C (in primary vacuum) for 1 h followed by slow cooling to room temperature to obtain a homogeneous mechanical and metallurgical state. This heat treatment also aims to relax the internal stresses introduced during machining.

Table 1 Chemical composition in weight percent of 304L

C	Cr	Ni	Si	Mn	S	P	N ₂	Mo	Cu	Fe
0.028	18.5	10	0.68	1.54	0.026	0.035	0.085	/	/	Remain

The mechanical tests were performed on tubular cylindrical specimens with the outer and inner diameters are respectively 20 and 17 mm with a length of 46 mm in gauge section. However, axial displacement and strain measurements were made with an MTS extensometer having 12 mm gage length (distance between the knives of the extensometer), this geometry is more suitable for axial loads in ten-sion-compression. This type of tubular specimens is recommended to perform low cycle fatigue tests where the temperature increase is important. Due to its geometry the cooling is easier. The fatigue tests were performed on a servo-hydraulic MTS machine tension-torsion. It has a singular capacity for control of tension and compression tests (± 250 kN, ± 75 mm) or torsion (± 2220 Nm, $\pm 45^\circ$). It allows for testing imposed strain or imposed stress.

In order to realize the given objectives, three tension-compression controlled strain fatigue tests were performed with an amplitude of 0.22 % at room temperature with a frequency of 0.1 Hz for the 100 first cycles and 5 Hz during the rest of the cycles, these tests were performed on virgin specimens of nuance 304L Thyssen.

This study is based on the results of the three fatigue tests, as well as two other tests performed by Belattar [9]. These last two are executed with a frequency of 1 Hz for the first 500 cycles and a frequency of 5 Hz was applied during the remaining cycles. Table 2 includes all tests on 304L-Com nuance.

We sought through the application of a low frequency (1 Hz) during the first cycles of our tests to present the material behavior at the beginning of life. The results obtained by Kpodekon [10] showed that the frequency change did not have a significant influence on the stress response. This change does not alter the strain mechanisms during the fatigue cycles. During the different fatigue tests, the evolutions of displacement and force are recorded in a file according to time and number of cycles. In order to calculate the axial stress, plastic strain, stress amplitude and other parameters we used different expressions presented in Table 3. Figure 1 shows the main characteristic parameters of a hysteresis loop.

In order to confirm the good progress of these axial fatigue tests, the evolution of torque versus time was controlled for five tests. From Fig. 2a, we find that the torque values remain insignificant, so they are not involved during the fatigue tests.

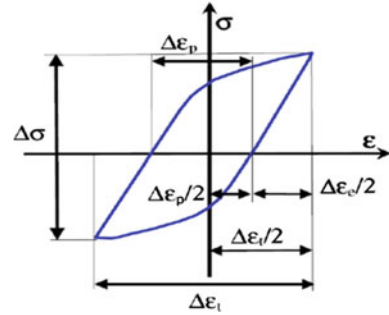
The fatigue tests were performed in zero mean stress conditions. Figure 2b shows the evolution of the mean stress versus number of cycles for the Ax1_0.22 % test, we note that the evolution of the mean stress is not significant during cycles. We can therefore consider that the cyclic test is really performed at zero mean

Table 2 Description of the various tests carried out as part of this study

Nuance	Specimen type	Stress rate (s^{-1})	Reference (%)
304L (nuance THYSSEN)	Specimen tubular (blank)	0.1 Hz for the first hundred cycles; -5 Hz for the rest.	Ax1_0.22 % Ax2_0.22 % Ax3_0.22 %
		-1 Hz for the first 500 cycles; -5 Hz during the remaining cycles.	Ax4_0.22 % [12] Ax5_0.2 % [12]

Table 3 Relationships used to calculate variable analysis obtained from the mechanical tests

Parameters	Formula	Unit
Axial total strain	$\varepsilon = \frac{\Delta l}{l_0}$, $l_0 = 12 \text{ mm}$	unitless
Axial stress	$\sigma_{11} = \frac{F}{S}$, $S = \frac{D_{ext}^2 - D_{int}^2}{4} = 87 \text{ mm}^2$	N/mm ² (MPa)
Axial plastic deformation	$\varepsilon_{11}^p = \varepsilon_{11} - \frac{\sigma_{11}}{E}$, E : Elastic modulus	unitless
Stress amplitude	$\sigma_a = \frac{\Delta \sigma}{2} = \frac{\sigma_{max} - \sigma_{min}}{2}$	N/mm ² (MPa)
Mean stress	$\sigma_{moy} = \frac{\sigma_{max} + \sigma_{min}}{2}$	N/mm ² (MPa)

Fig. 1 The main parameters calculated on a hysteresis loop

stress. We present only the evolution of the mean stress of this test because the other tests have a similar evolution compared to this one. The tests were performed on virgin specimens (without effect of pre-hardening) at room temperature. This shows that tests are carried without any interference parameter on the fatigue behavior of this steel.

3 Results

In order to clarify the cyclic behavior of the different specimens, we are compared in Fig. 3 the evolutions of stress amplitudes according to the number of cycles. The fatigue life time of the specimens 1–5 are respectively 122099, 133199, 84099, 132099 and 154599 cycles. We note an important difference between these life-times. These results show that there is a disparity of different specimens even if their chemical compositions and mechanical stresses were identical.

Regarding the evolution of the stress amplitude, it is observed that the three curves obtained from tests (*Ax_1 to 3*) are very close. The behavior as a function of number of cycles can be decomposed into three phases. The specimens show a first cyclic hardening phase during the first few cycles. Then a gradual decrease in the rate of consolidation to the maximum stress amplitudes was observed and then a cyclic softening. These observations are reflected in reduced stress amplitude at the

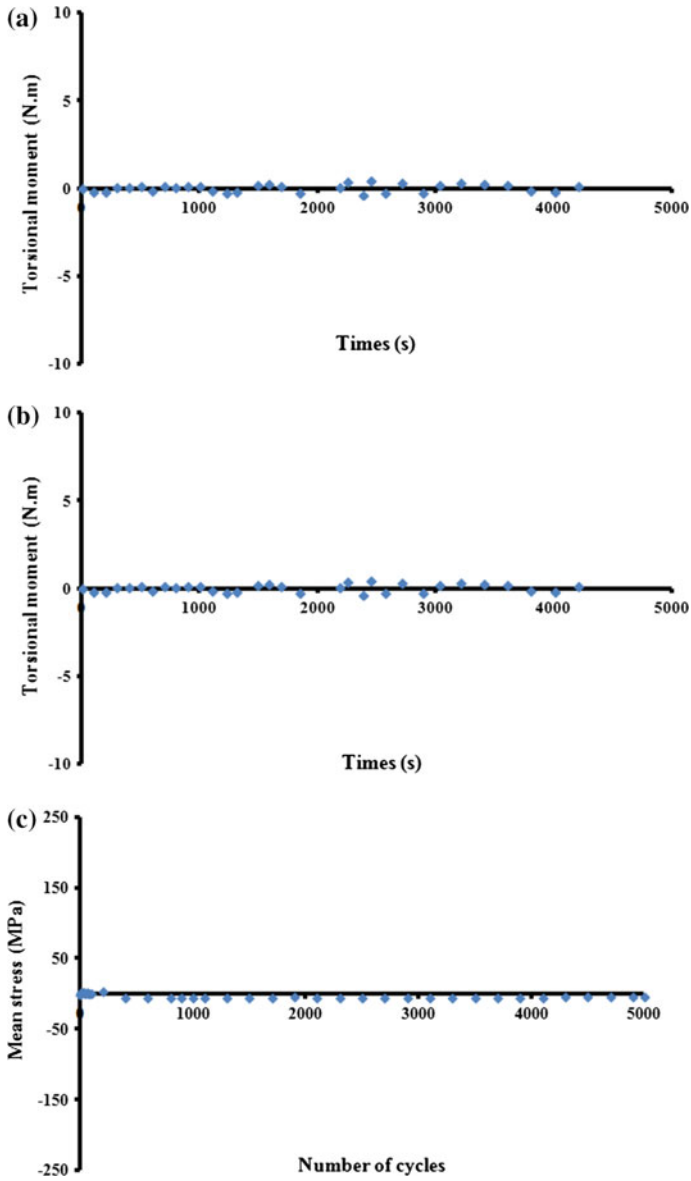


Fig. 2 Evolution of **a** torque as a function of time and **b** the mean stress versus number of cycles for first test

beginning of cyclic loading followed by stabilization from the 1000th cycle. Finally, in the vicinity of the fracture stress amplitude decreases rapidly.

About the two other tests, carried out by Belattar [9, 12], we note that the setpoint has been reached 0.22 % from the 100th cycle. A comparison was made

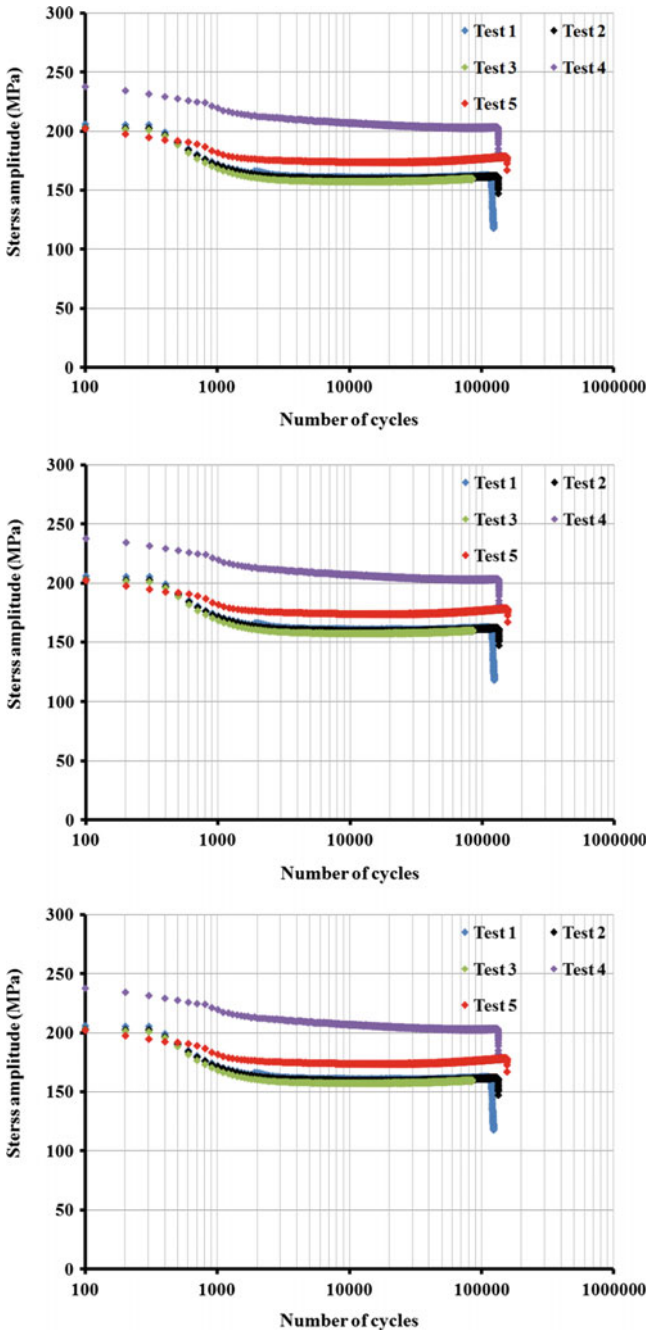


Fig. 3 Evolution of the stress amplitude versus number of cycles for the five fatigue tests

between the evolutions of the amplitude stress for Ax_4 and Ax_5 tests, both specimens exhibit a softening until the stabilization of the stress amplitude. We note that from about the 100th cycle, the five specimens have the same qualitative and quantitative representations. However, the fourth specimen has a gap of the order of 40 MPa during the stabilization phase compared to the other samples. The differences between the stresses amplitudes of three specimens tested in this study are not significant, even if their fatigues lifetimes are different.

In order to analyze the cyclic behavior of the material, we present in Fig. 4 the evolution of hysteresis loops at the beginning, mid-life and near to fracture for the

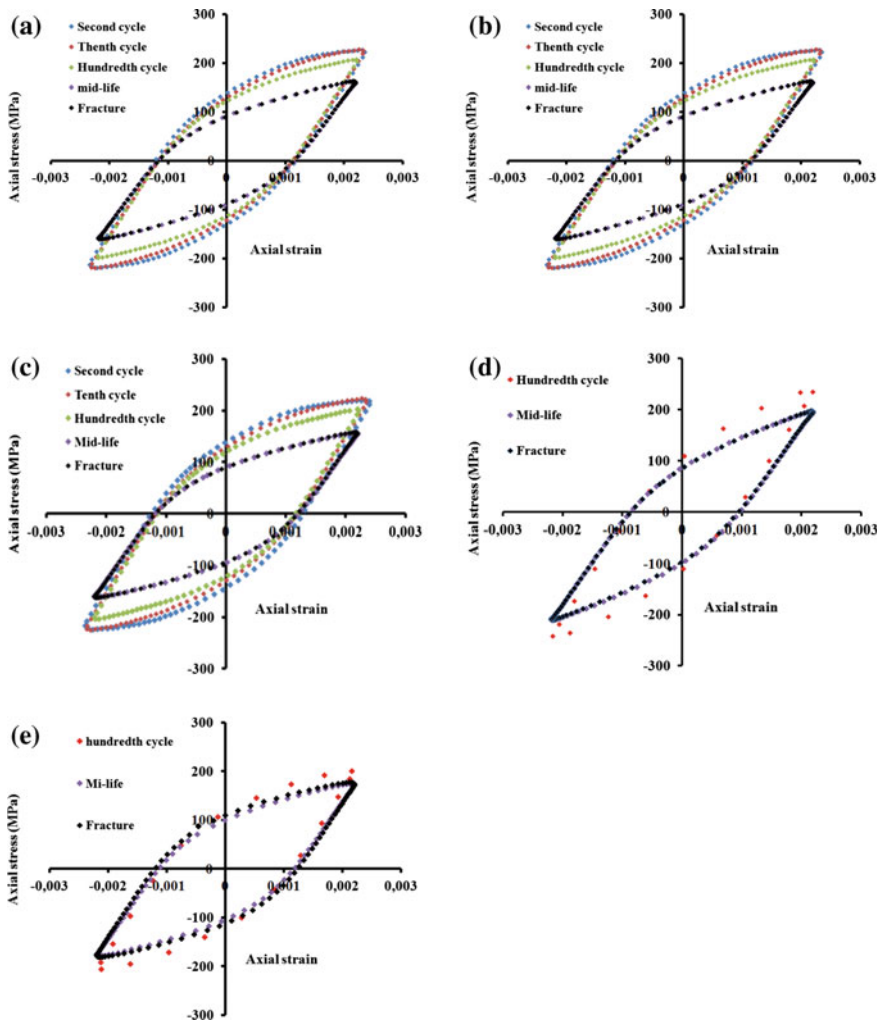


Fig. 4 Evolution and comparisons between hysteresis loops obtained during fatigue testing to 0.22 % **a** Ax_1 , **b** Ax_2 , **c** Ax_3 , **d** Ax_4 and **e** Ax_5

five tested specimens. The observation of Fig. 4 which includes the evolutions axial stresses in function of axial strains, gives the following remarks:

- All loops are perfectly symmetrical attesting to zero mean stress during the tests;
- For Ax_1 , Ax_2 and Ax_3 fatigue tests: we can observe a slight cyclic hardening limited to the first five cycles followed by a progressive cyclic softening up to about 100th cycles. A rapid reduction in axial stress after these cycles is observed which stabilizes until failure;
- Concerning Ax_4 and Ax_5 fatigue tests: the hysteresis loops (d) and (e) show that both specimens show a cyclic softening from about 100th cycles. During the stability the hysteresis loops are superposed;
- The plastic strain amplitude is similar to the five tests specimens. However, any gap between the axial stress in particular from the first three specimens and that of Belattar [9, 12] is observed.

The curve of the evolution of maximum stresses as a function of number of cycles confirms the previous observations. From Fig. 5, we notice a decrease of maximum stress between 100 and 1000 cycles followed by stabilization of the maximum stresses phase until it failure. A small gap is found between Ax_1 , Ax_2 and Ax_3 tests; however there is a difference of about 40 MPa between these tests and the fourth. These results highlight the existence of a disparity lifetimes of 304L grade Thyssen loaded in oligocyclic fatigue in low imposed strain amplitude.

In the following, and in order to explain the recorded observations, we carried out an analysis of the evolution of the kinematic and isotropic cyclic hardening components as well as the elastic modulus. From a macroscopic viewpoint, the evolution of the isotropic hardening represents the variation in the size of the elastic domain. The evolution of X shows the evolution of the elastic domain center.

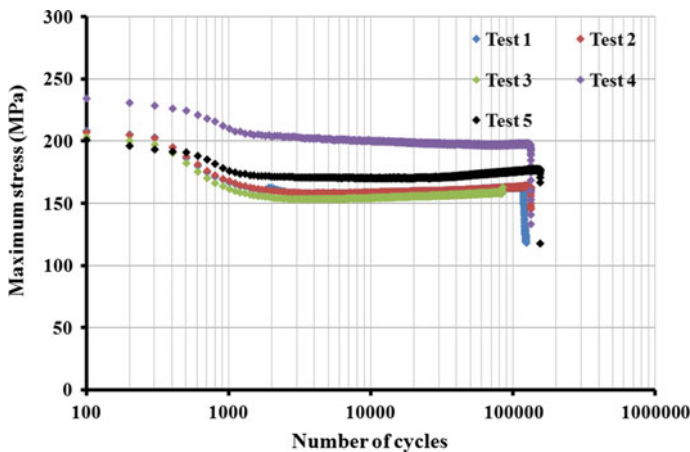
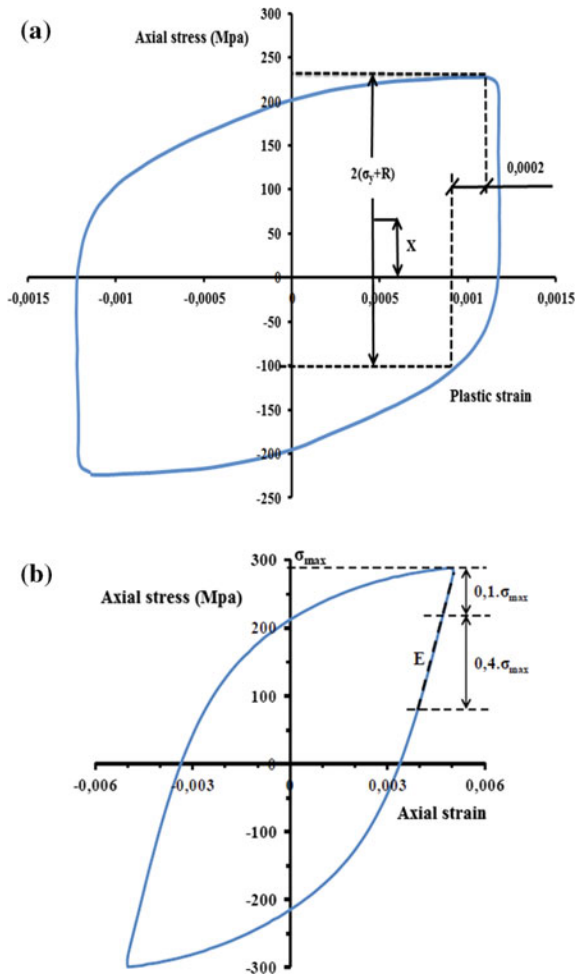


Fig. 5 Evolution of maximum stress as a function of the number of cycles for the five tests

4 Evolution of Cyclic Hardenings

In this section we examine the contribution of the isotropic and kinematic hardening generated during these five fatigue tests. The estimation of parameters for these two types of hardening has been described several times in the literature [13, 14] in tension-compression and in biaxial loading conditions [1]. They are determined from the hysteresis loops generated during the loading cycles, as shown in Fig. 6. Firstly, we identify the maximum stress (σ_{max}). Then, from the point ($\sigma_{max}, \epsilon_{offset}$) an offset is applied corresponding to a plastic strain of 0.0002, ϵ_{offset} is the stress associated with this plastic strain. The determination of X and R also involves the identification of the elastic limit σ_y , which is calculated from the first cycle during discharge. It is noteworthy that the evaluation of R and X has been realized by an

Fig. 6 **a** Estimation of isotropic R and kinematic X cyclic hardening in the case of axial loading. **b** Procedure for the identification pseudo elastic modulus [15]



offset of 10^{-4} and 2×10^{-4} . The kinematic (X) and isotropic (R) cyclic hardening are given by the following relationships:

$$R = \frac{\sigma_{max} - \sigma_{offset}}{2} - \sigma_y \quad \text{and} \quad X = \frac{\sigma_{max} + \sigma_{offset}}{2} \tag{1}$$

However, this identification process presents some limitations. The selection of offset has a great influence on values of kinematic and isotropic cyclic hardening.

For this purpose, we preferred an identification with both offset (0.0001 and 0.0002). The evolutions of X and R of the five tests for an offset of 2×10^{-4} are presented in Figs. 7 and 8, we preferred to exhibit the evolutions of R and X for specimens 1, 2 and 3 from the first cycles in order to show the behavior during the first 100 cycles.

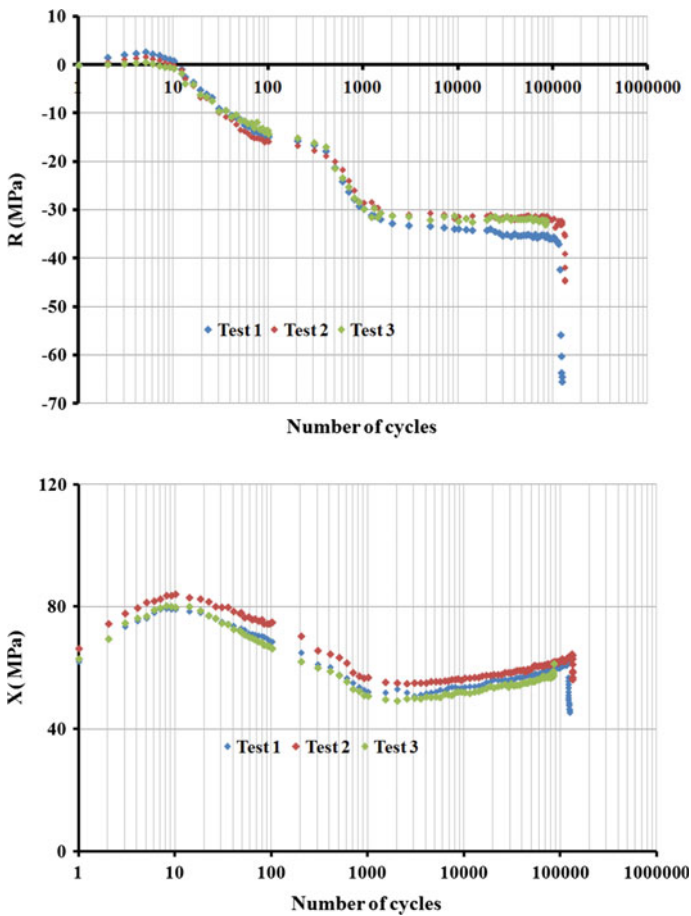


Fig. 7 Comparison between evolutions of R and X (calculated with offset = 0.0002) of first, second and third tests

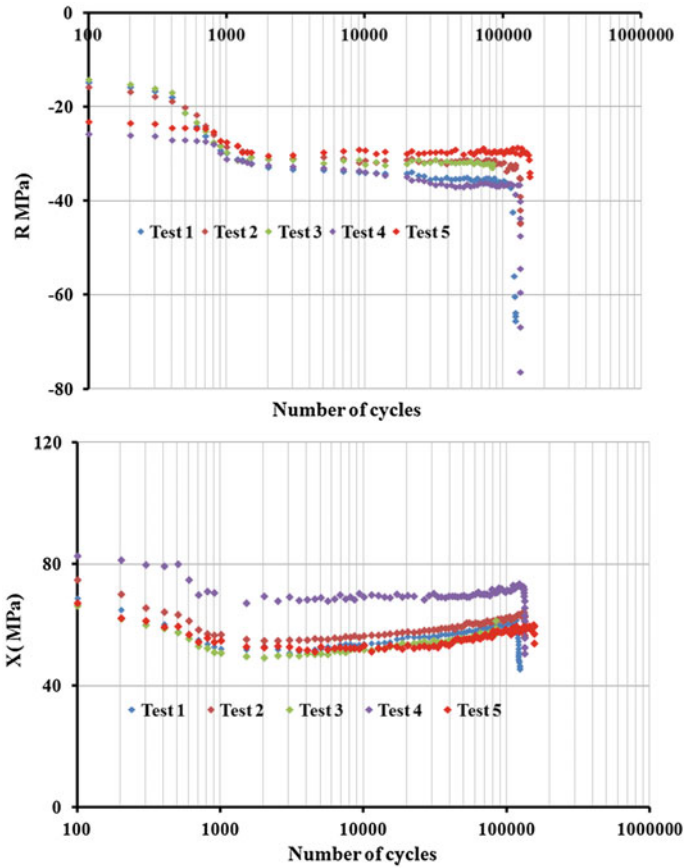


Fig. 8 Comparison between R and X evolutions of the five tests (calculated with offset = 0.0002)

Figures 7, 8, 9 and 10 shows a comparison for evolutions of R and X from the 100th cycles of the five tests. We can do the following findings:

- For the five tests the kinematic hardening is more important than the isotropic hardening;
- The kinematic hardening (X) increases during the first few cycles and then decreases and increases again until failure for the first three tests;
- The kinematic hardening for the fourth and the fifth specimens shows a decrease from the 100th cycles followed by an increase until failure. Nevertheless the evolution of X for the fourth specimen exhibited a small increase after about 1000 cycles;
- From the 100th cycles, the kinematic hardening for the specimens number 1, 2, 3 and 5 is identical, against the specimens number 4 which has a gap about of 10 MPa relative to other specimens;

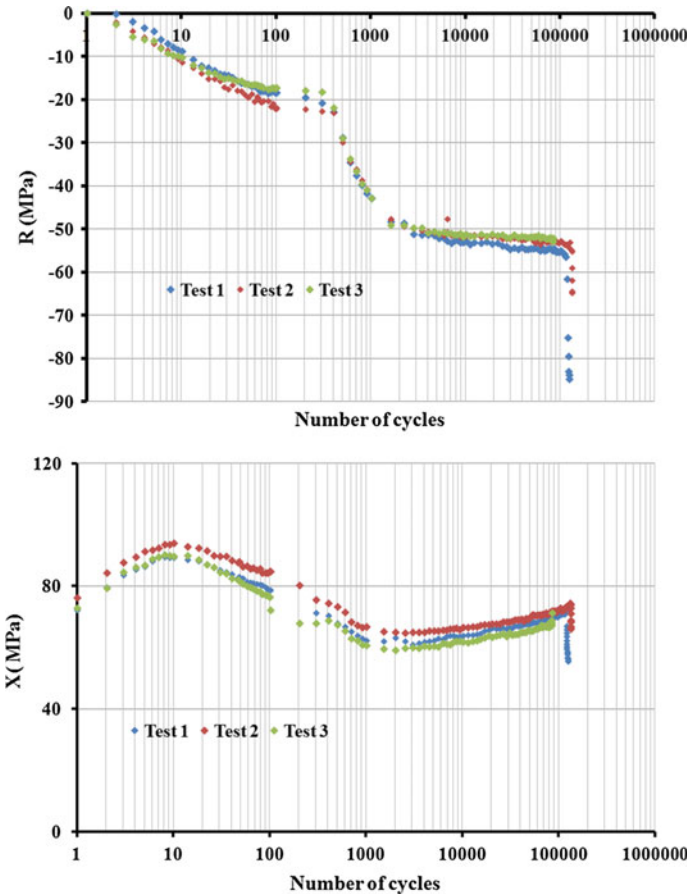


Fig. 9 Comparison between evolutions of R and X (calculated with offset = 0.0001) of first, second and third tests

- The evolution of the isotropic hardening of three first fatigue tests shows that the latter exhibit an increase during the first five cycles which indicates the cyclic hardening observed at the beginning, followed by a decrease for this variable, reflecting the observed cyclic softening. After the 100th cycle a fast decrease of R is observed followed by a phase of stability until failure;

A comparison for R of the five fatigue tests showed that all specimens are similar curves with a small difference, the difference observed between our tests and those of Belattar [12] is of the order of 5 MPa which remains insignificant. Figures 9 and 10 exhibit the evolutions of kinematic and isotropic cyclic hardening estimated with an offset of 0.0001. Figure 9a shows the variation of R as a function of cycles for the first, second and third fatigue tests. We note that this parameter is negative in all cycles which are contrary to the cyclic hardening observed in the first cycles.

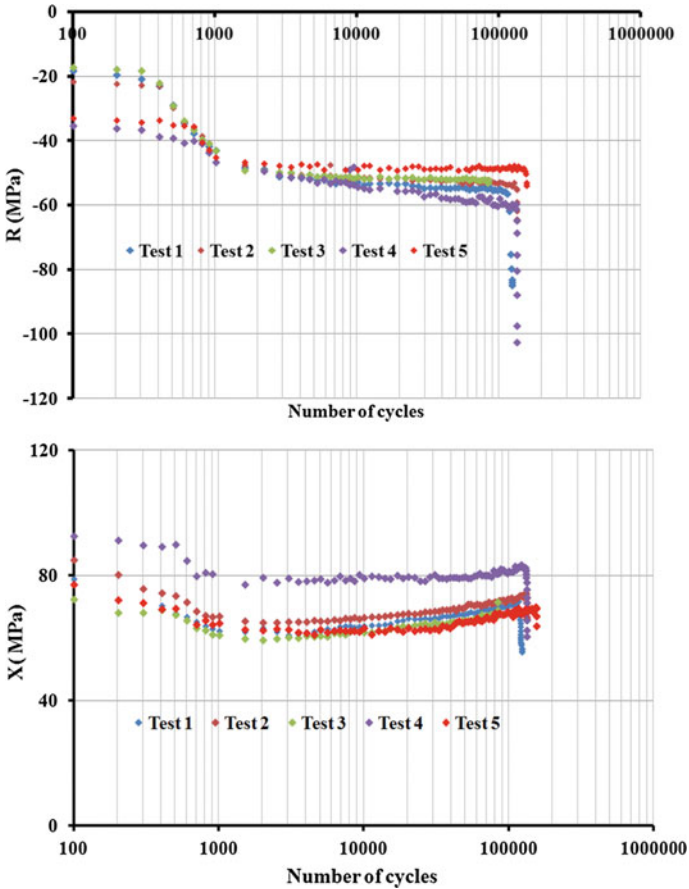


Fig. 10 Comparison between R and X evolutions of the five tests (calculated with offset = 0.0001)

5 Cyclical Evolution of the Discharge Slope

The evolution of the elastic modulus (Young’s modulus) during fatigue test may be an indicator of material damage. We examine in the following the evolution of this parameter according to the number of cycles for the five specimens, his estimate is carried during the discharge on each hysteresis loop. A pseudo elastic modulus was determined by the slope of a regression straight line in a range of 40 % of maximum stress. Figure 11 shows the procedure for identifying of this pseudo elastic modulus. The evolution of the pseudo elastic modulus as a function of number of cycles is similar to the five tests. It can decompose in three phases, a fast decay of

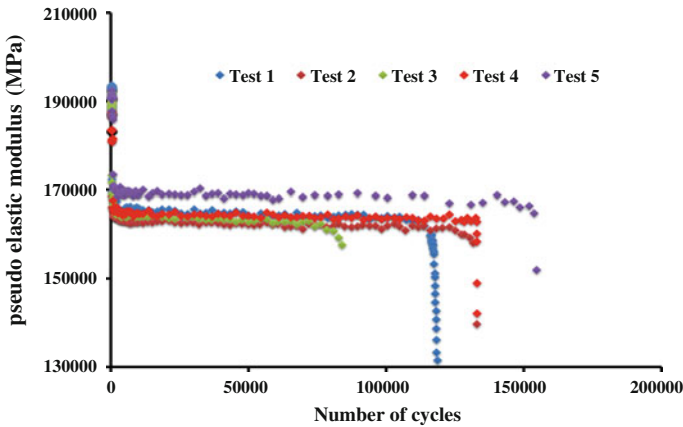


Fig. 11 Evolution of the pseudo elastic modulus during fatigue cycles for the five specimens

the pseudo elastic modulus is observed in the first cycles followed by a saturation phase and finally a new decrease phase. During the saturation phase, the calculated pseudo elastic moduli have a gap between them of the order of 2–3 % which is low.

6 Conclusions

The obtained results of performed fatigue tests at small controlled strain amplitude of 0.22 %, allows us to conclude that:

- The fatigue lifetime of the *304L* stainless steel varies from one specimen to another, even if they are loaded with a same manner;
- The evolution of the stress amplitude of the five specimens is unique. However, a small difference was found;
- The cyclic behavior of the *304L grade THYSSEN* is similar to this level of strain even if the frequencies of solicitation are different at the beginning of fatigue tests;
- The evolutions of X and R as a function of number of cycles show that these two components have a similar evolution during the fatigue cycles;
- The calculation of R taking into account a value of offset 10^{-4} does not render into consideration the behavior at the beginning of cycles for this steel with low applied strain amplitude;
- The evolution of the discharge slope is similar for the five specimens.

References

1. Taleb, L., Hauet, A.: *Int. J. Plast.* **25**(7), 1359–1385 (2009)
2. Vincent, L., Le Roux, J.C., Taheri, S.: *Int. J. Fatigue* **38**, 84–91 (2012)
3. Le Roux, J.C., Taheri, S., Sermage, J.P., Colin, J.F.A.: *Pressure vessels and piping conference*. Chicago, Illinois, USA (2008)
4. Taheri, S., Hauet, A., Taleb, L., Kpodekon, C.: *Int. J. Plast* **27**(12), 1981–2004 (2011)
5. Yoshida, F.: *Int. J. Press. Vessels Pip.* **44**(2), 207–223 (1990)
6. Colin, J., Fatemi, A., Taheri, S.: *J. Eng. Mater. Technol.* **132**(2), 021008–021013 (2010)
7. Colin, J., Fatemi, A., Taheri, S.: *J. Mater. Sci.* **46**(1), 145–154 (2011)
8. Cailletaud, G., Kaczmarek, H., Policella, H.: *Mech. Mater.* **3**(4), 333–347 (1984)
9. Belattar, A.: *INSA de Rouen: Rouen*, **185** (2013)
10. Kpodekon, C.: *INSA de Rouen* (2010)
11. Doquet, V. Taheri, S.: *Revue Française de Mécanique*, pp. 28–33 (2000)
12. Belattar, A., Taleb, L., Hauet, A., Taheri, S.: in *Congrès Algérien de Mécanique*. Guelma, Algérie (2011)
13. Dickson, J.I., Boutin, J., Handfield, L.: *Mater. Sci. Eng.* **64**(1), L7–L11 (1984)
14. Feaugas, X.: *Acta Mater.* **47**(13), 3617–3632 (1999)
15. Belattar, A.: *Mécanique. INSA de Rouen*, **185** (2013)

Numerical Investigation on the Anisotropic Behavior of an Aluminum Alloy Type 2017A

Mouaad Brik, Malek Chabane Chaouche and Lakhdar Taleb

Abstract The study presented in this paper will focus on modeling, via a multi-mechanism model, the behavior of an anisotropic aluminum alloy, type 2017A subjected to complex loading. Numerical simulations are carried out using two parameters sets which take into account this anisotropy. The first parameters set were proposed in [1] based of cyclic tests in controlled deformations mode following proportional and non-proportional paths. The second parameters set have been identified recently on a larger database [2]. In this work, we propose to evaluate the ability of multi-mechanisms model and compare predictions by using one or the other set of parameters. Tests simulation under proportional and non-proportional loads carried out in this object. The experimental identification of the parameters is performed using only test strain imposed tests while evaluation of the model is made on other tests in a controlled stress and strain mode, which were note used for the identification. This point is important taking into account the predictive model.

1 Introduction

During cyclic loading several complex phenomena affect the mechanical behavior of metals. This has driven the researchers to improve several classic models in order to include macroscopic phenomena observed during loading like the Bauschinger effect [3], the structural hardening [4], the microstructural changes introduced by [5], the effect of pre-hardening [6], the effect of non-proportional loading [7] and the ratcheting effect [8–10]. The modeling which includes several sources of inelastic strain without referring to the slip systems gave the opportunity to add new contributions in this field, given birth to the multi-mechanisms model.

M. Brik (✉) · M. Chabane Chaouche · L. Taleb
INSA de Rouen/GPM, UMR CNRS 6634, BP 08, Avenue de l'Université,
76800 St. Etienne du Rouvray, France
e-mail: mouaad.brik@insa-rouen.fr

Cailletaud et al. [11] have deduced that through the coupling of variable kinematics, the variant model referred as “*2MIC*” can describe some original mechanical behavior such as ratcheting effect and the sensitivity to the inversion of the loading. Sai et al. [12] have supposed that the non-linear behavior is the result of the slip of dislocations, through against the hardening is supposed to be the result of the interaction between dislocations.

In 2006, Velay et al. [13] have introduced two additional variables of isotropic work hardening (R_1 and R_2) into the old version of *2MIC* in order to include thermomechanical fatigue of martensitic steels. In 2006, Taleb et al. [14] have modified the term recall of variable kinematics for better representing the phenomenon of ratcheting in unidimensional and into two-dimensional with the same set of parameters and they propose to modify the rule of evolution of the kinematic hardening. In 2007, Sai et al. [15] proposed an improved version of *2MIC* and *2M2C* to take into account the ratcheting effect by introducing two modifications of the constitutive equations. The first concerns the control of the characteristics of kinematic hardening tensor and the second is used to calibrate the multiaxial ratcheting effect. In 2010, Taleb et al. [16] updated the old version of *2MIC* by changing the equation concerning the isotropic hardening, the new model is now called multi-mechanisms. The purpose of this amendment is to take into account the effect of non-proportional loading and the hardening memory effect already observed experimentally by the authors of [17]. This new version of the model includes 17 parameters in the most general version taking into account the viscous effects of both types of hardening, non-proportional loading. In 2012, an extension of the model is carried out in [1] which takes account the anisotropy of this alloy type as the extruded aluminum alloy *2017A*. In the same reference, the model parameters were identified through the given yield strengths in the axial and torsional directions.

In 2015, Taleb et al. [2] have a new identification for multi-mechanisms model using a database of deformations imposed to larger trials.

Our work involves investigating the ability of the model to identify the differences between results that will be obtained using both sets of parameters mentioned above. The evaluation of the model will include its ability to predict the material behavior under imposed stress tests that were not used to identify the parameters.

2 Experimental Methodology

The chemical composition of our study material (*2017A*) is shown in Table 1.

The specimens used in this study have a tubular shape as shown in Fig. 1, the outer and inner diameters are respectively equal to 20 and 17 mm with a gage length of 46 and 25 mm for the working portion on which biaxial extensometer is attached. This allows the monitoring of the evolution of the axial displacement and the torsional rotation (capacity: ± 2.5 mm and $\pm 5^\circ$).

Table 1 Chemical composition of the material (wt%)

Cu (%)	Mg (%)	Mn (%)	Si (%)	Fe (%)	Al (%)
3.95	0.67	0.53	0.76	0.90	Balance

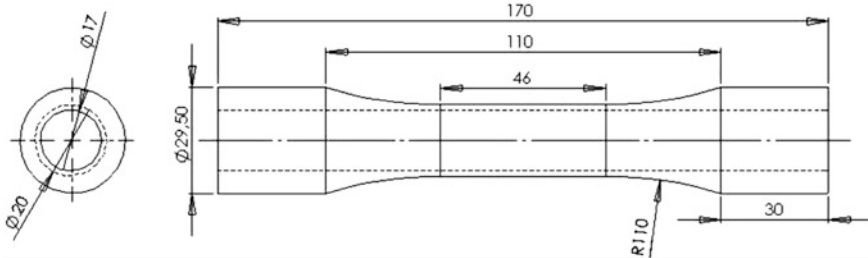


Fig. 1 The geometry of the specimen used in the tests

The tests were made using a hydraulic machine Servo-MTS. The machine can be driven by stress or strain imposed in both directions (axial and torsional). Two types of cycles are carried out in simulated trials: either a combination of a constant traction and a cyclic torsional torque or a combination of a constant traction and a cyclic torsional strain (see Fig. 2) [18]. In these trials the tensor stress and strain in a cylindrical coordinate system are closed to the following form:

$$\underline{\sigma} = \begin{pmatrix} 0 & 0 & 0 \\ 0 & 0 & \sigma_{z\theta} \\ 0 & \sigma_{z\theta} & \sigma_{zz} \end{pmatrix} = \underline{\varepsilon} \begin{pmatrix} \varepsilon_{rr} & 0 & 0 \\ 0 & \varepsilon_{\theta\theta} & \varepsilon_{z\theta} \\ 0 & \varepsilon_{z\theta} & \varepsilon_{zz} \end{pmatrix} \quad (1)$$

The tests are performed in phases described below [18]:

- Test 1 (σ_{zz} constant— σ cyclic) (MPa): (50–190 → 50–230 → 100–230). 50 cycles were applied in each sequence. This test will be marked 50–190.
- Test 2 (σ_{zz} constant— ε cyclic) (MPa—%): (50–0.4 → 5–0.8 → 100–0.8). 50 and 175 cycles were applied in each of the sequences, respectively. This test will be marked 50–0.4.

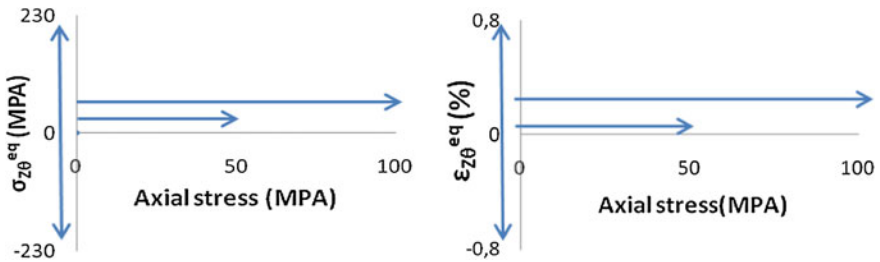


Fig. 2 Loading combined followed in simulated trials [18]

3 The Model Multi Mechanisms

3.1 Constitutive Equations of the Model

The total deformation is decomposed in an elastic and non-elastic part as follows:

$$\dot{\underline{\underline{\varepsilon}}} = \dot{\underline{\underline{\varepsilon}}}^e + \dot{\underline{\underline{\varepsilon}}}^1 + \dot{\underline{\underline{\varepsilon}}}^2 \quad (2)$$

3.2 Criterion

$$f = \sqrt{(J(\underline{\underline{\sigma}} - \underline{\underline{X}}^1))^2 + (J(\underline{\underline{\sigma}} - \underline{\underline{X}}^2))^2} - R - R_0 \quad (3)$$

The elastic part is formulated using the Hooke law as follows:

$\underline{\underline{\sigma}} = \underline{\underline{\Lambda}} : \underline{\underline{\varepsilon}}^e$ or $\underline{\underline{\Lambda}}$ is the Hook's matrix of order 4.

Effect of non-proportionality of loading:

$$\begin{aligned} dQ_2 &= dA(Q_s - Q_2)dv \\ Q_s &= \frac{gAQ_m + (1-A)Q_0}{gA + (1-A)} \\ \cos \alpha &= \frac{\dot{\underline{\underline{\varepsilon}}} : \dot{\underline{\underline{\varepsilon}}}^p}{\sqrt{\dot{\underline{\underline{\varepsilon}}} : \dot{\underline{\underline{\varepsilon}}} \sqrt{\dot{\underline{\underline{\varepsilon}}}^p : \dot{\underline{\underline{\varepsilon}}}^p}} \end{aligned} \quad (4)$$

$$J_{Li} = J_{Li}(\underline{\underline{\sigma}} - X^i) = \sqrt{\frac{3}{2}(\underline{\underline{S}} - \underline{\underline{X}}^i) : (\underline{\underline{S}} - \underline{\underline{X}}^i)} \quad i = 1, 2 \quad (5)$$

Normality rule for each plastic deformation introducing an anisotropy tensor:

$$\begin{cases} \dot{\underline{\underline{\varepsilon}}}^1 = \dot{v}\underline{\underline{n}}^1 & \text{or} & \underline{\underline{n}}^1 = \frac{3}{2}\underline{\underline{L}} \frac{(\underline{\underline{s}} - X^1)}{\sqrt{j_{L1}^2 + j_{L2}^2}} \\ \dot{\underline{\underline{\varepsilon}}}^2 = \dot{v}\underline{\underline{n}}^2 & \text{or} & \underline{\underline{n}}^2 = \frac{3}{2}\underline{\underline{L}} \frac{(\underline{\underline{s}} - X^2)}{\sqrt{j_{L1}^2 + j_{L2}^2}} \end{cases} \quad (6)$$

with: $\begin{cases} j_{L1} = j_L(\underline{\underline{\sigma}} - X^1) \\ j_{L2} = j_L(\underline{\underline{\sigma}} - X^2) \end{cases}$

$$\underline{\underline{L}} = \begin{bmatrix} L_a & 0 & 0 & 0 & 0 & 0 \\ 0 & L_b & 0 & 0 & 0 & 0 \\ 0 & 0 & L_c & 0 & 0 & 0 \\ 0 & 0 & 0 & L_d & 0 & 0 \\ 0 & 0 & 0 & 0 & L_e & 0 \\ 0 & 0 & 0 & 0 & 0 & L_f \end{bmatrix} \quad (7)$$

The kinematic hardening variables \underline{X}^1 , \underline{X}^2 are related to internal variables $\underline{\alpha}^1$, $\underline{\alpha}^2$ using the kinematic hardening matrix [C] such as:

$$\begin{pmatrix} \underline{X}^1 \\ \underline{X}^2 \end{pmatrix} = \frac{2}{3} \begin{pmatrix} C_{11} & C_{1\cdot} \\ C_{12} & C_{\cdot 1} \end{pmatrix} \begin{pmatrix} \underline{\alpha}^1 \\ \underline{\alpha}^2 \end{pmatrix} \quad (8)$$

$$\begin{aligned} \dot{\underline{\alpha}}_1 &= \dot{\nu}(\underline{n}^1 - (3D_1/2C_{11})) \cdot \underline{X}^1 \\ \dot{\underline{\alpha}}_2 &= \dot{\nu}(\underline{n}^2 - (3D_2/2C_{22})) \cdot \underline{X}^2 \end{aligned} \quad (9)$$

3.3 Consistency Condition

$$\dot{\nu} = \frac{(\underline{n}^1 + \underline{n}^2) : \dot{\underline{\alpha}}}{H_R + H_{X1} + H_{X2}} = \frac{(\underline{n}^1 + \underline{n}^2) : \underline{\underline{A}} : \dot{\underline{\underline{E}}}}{H_R + H_{X1} + H_{X2} + H_E} \quad (10)$$

with:

$$\begin{aligned} H_{X1} &= \frac{2}{3} (\underline{n}^1 C_{11} + \underline{n}^2 C_{12}) \cdot \left(\underline{n}^1 - \frac{3D_1}{2C_{11}} \underline{X}^1 \right) \\ H_{X2} &= \frac{2}{3} (\underline{n}^1 C_{12} + \underline{n}^2 C_{22}) \cdot \left(\underline{n}^1 - \frac{3D_2}{2C_{22}} \underline{X}^2 \right) \\ H_R &= Q_1 b_1 e^{-b_1 \nu} + Q_2 b_2 e^{-b_2 \nu} \\ H_E &= (\underline{n}^1 + \underline{n}^2) : \underline{\underline{A}} : (\underline{n}^1 + \underline{n}^2) \end{aligned} \quad (11)$$

The two parameters sets used in the simulations are given in Tables 2 and 3.

Table 2 Parameters (P_1) identified by the authors of [1]

R_0	Q_2	b_2	Q_{3m}	d_3	b_3	C_{11}	C_{22}	C_{12}	d_1	d_2	L_d	L_e
283	92	15.83	71	58.63	18.4	7282	205264	34993	646	440	2.56	1

The simulation results with these settings will be denoted by “ P_1 ”

Table 3 Parameters (P_2) identified by the authors of [2]

R_0	Q_2	b_2	Q_{3m}	d_3	b_3	C_{11}	C_{22}	C_{12}	$d_1 = d_2$	d_2	L_d	L_e
283	92	12.2	500	15	18.5	5026	607427	-35000	0	440	1	2.56

The simulation results with these settings will be denoted by “ P_2 ”: $E = 72000$, $\nu = 0.33$, $L_b = L_c = L_f = 1$ are common values for P_1 and P_2

4 Results and Discussion

In the following illustrations, the results obtained from simulations using the parameters identified by the authors of [2] are shown with red marks. The curves presented with blue marks correspond to simulations obtained by exploiting the parameters identified by the authors of [1], whereas our experimental results are in green. The comparison between the simulation and the experimental one is presented on the Figs. 3, 4, 5 and 6. To simplify the follow up of the inelastic deformation in the axial direction, we are interested in the evolution of the average axial deformation during the tests such as:

$$\epsilon_{zz}^{moy} = \frac{\epsilon_{zz}^{max} + \epsilon_{zz}^{min}}{2} \tag{11}$$

The correlation between the answers simulated with “ P_1 ” and experimental results are satisfactory. We note a good capacity to describe the evolution of work hardening during the simulated tests (Figs. 3 and 4). In contrast with pa1, we cannot

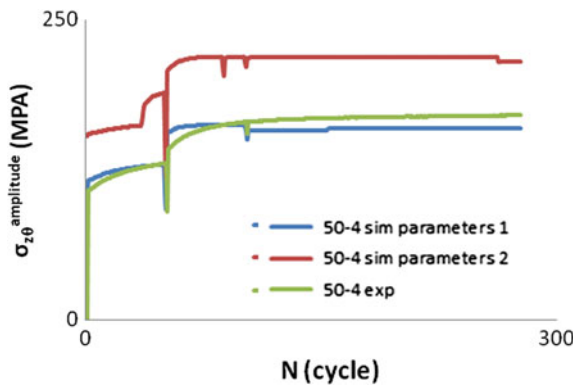


Fig. 3 Evolution of the stress amplitude during the tests 50-4 and 50-8

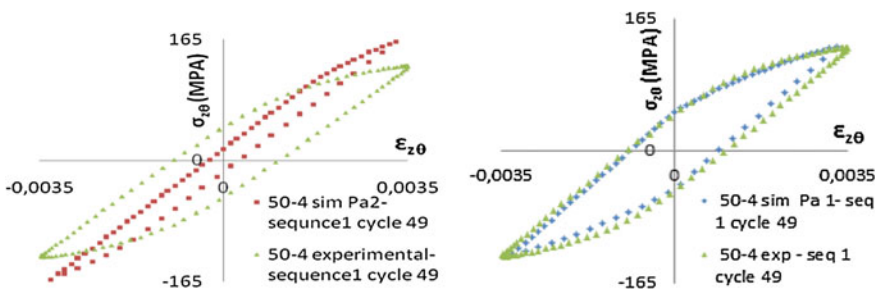


Fig. 4 Stress strain curves for the cycle 49 in the test 50-4

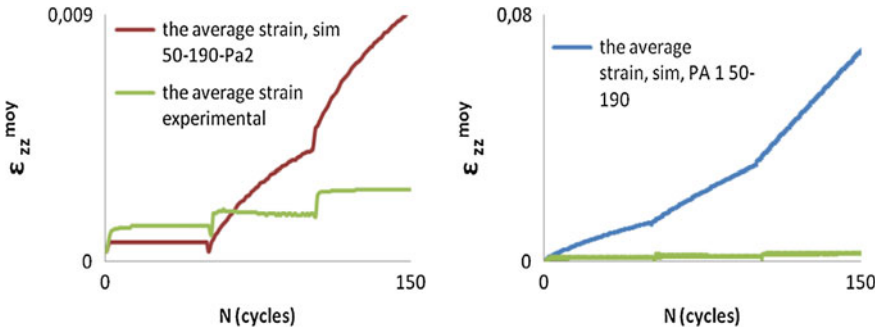


Fig. 5 Accumulation of inelastic strain during the test 50–190

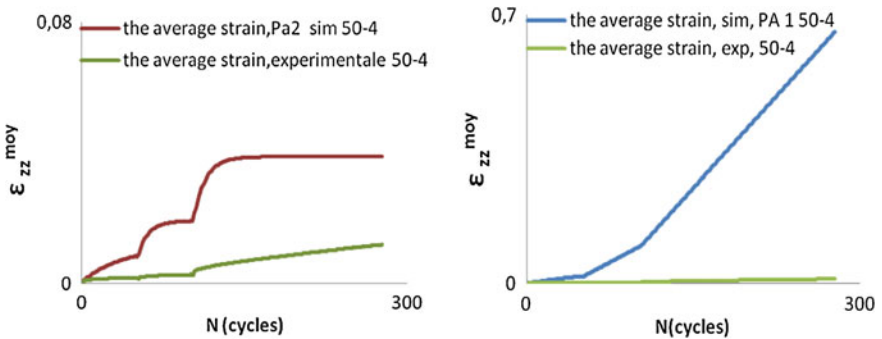


Fig. 6 Accumulation of inelastic strain during the 50–4 test

correctly predict the accumulation of inelastic deformation in the axial direction. The use of parameters “ P_2 ” described better this accumulation and its speed of evolution (Figs. 5 and 6). However, its capacity to predict the evolution of the stress amplitude in the imposed deformation test is not satisfactory.

5 Conclusion

In general, we note the following points:

Test Simulation of 50–4 test:

- The stress-strain twist loop is well represented by the calculation P_1 , unlike the calculation by P_2 which overestimates the cyclic hardening.
- The same applies as regards the evolution of the torsional stress amplitude versus cycles: good prediction for P_1 and overestimation for P_2

- The findings are different regarding the prediction of the evolution of inelastic deformation as a function of number of cycles. The prediction is fairly good in terms of rate of accumulation for the calculation P_2 compared to the calculation by P_1 which leads to a substantial overestimation of the deformation. This result is expected since the calculation P_2 leads to a greater cyclic hardening.

50–190 simulation tests:

The conclusions are similar to those above as P_1 overestimates widely the strain cyclical accumulation; the calculation made by P_2 leads to results somewhat better but still remain quite distant from the experience. In short: the parameters sets P_1 overestimates the cyclic inelastic strain accumulation and correctly provides the cyclic hardening, while the P_2 game overestimates the cyclic hardening and gives better forecasts of the ratcheting. The two parameters sets have been identified on an experimental database that does not include the strain hardening memory effect. The inclusion of the latter phenomenon should improve the quality of predictions; it will be one of the future works.

References

1. Sai, K., Taleb, L., Cailleteaud, G.: Numerical simulation of the anisotropic behavior of 2017 aluminum alloy. *Comput. Mater. Sci.* **65**, 48–57 (2012)
2. Taleb, L., Sai, K., Cailleteaud, G.: Capabilities of the multi-mechanism model in the prediction of the cyclic behaviour of various classes of metals. In: Altenbach, H., Matsuda, T., Okumura, D. (eds.) *Advanced Material Modeling Book in Honor of Professor Ohno 65th Anniversary*. Springer (2015)
3. Chaboche, J.L.: Viscoplastic constitutive equations for the description of cyclic and anisotropic behaviour of metals. *Bull. Acad. Polon. Sci. Ser. Sci. Tech.* **25**(1), 33–42 (1977)
4. Krempl, E.: The role of aging in the modeling of elevated temperature deformation. *Creep Fract. Eng. Mater. Struct.* 201–211 (1981)
5. Cailleteaud, G., Culie, J.P., Kaczmar, K.H.: Thermal fatigue on a thermally unstable alloy. In: *International Conference on Mechanical Behavior of Metals, ICM4, Stockholm*
6. Nouailhas, D., Cailleteaud, G., Policella, H., Marquis, D., Dufailly, J., Lieurade, H.P., Ribes, A., Bollinger, E.: On the description of cyclic hardening and initial cold working. *Eng. Fract. Mech.* **21**, 887–895 (1985)
7. Benallal, A., Marquis, D.: Constitutive equations for non-proportional cyclic elasto-viscoplasticity. *ASME J. Eng. Mater. Technol.* **109**, 326–336 (1987)
8. Chaboche, J.L.: On some modifications of kinematic hardening to improve the description of ratcheting effects. *Int. J. Plast.* **7**, 661–678 (1991)
9. Ohno, N., Wang, J.D.: Kinematic hardening rules with critical state of dynamic recovery, Part I: Formulation and basis features for ratcheting behaviour. *Int. J. Plast.* **9**, 375–390 (1993)
10. Ohno, N., Wang, J.D.: Kinematic hardening rules with critical state of dynamic recovery, Part II: Application to experiments of ratcheting behaviour. *Int. J. Plast.* **9**, 391–403 (1993)
11. Cailleteaud, G., Sai, K.: Study of plastic/viscoplastic models with various inelastic mechanisms. *Int. J. Plast.* **11**, 991–1005 (1995)
12. Sai, K., Aubourg, V., Cailleteaud, G., Strudel, J.: Physical basis for model with various inelastic mechanisms for nickel base superalloy. *Mater. Sci. Technol.* **20**, 747–755 (2004)

13. Velay, V., Bernhart, G., Penazzi, L.: Cyclic behavior modeling of a tempered martensitic hot work tool steel. *Int. J. Plast.* **22**, 459–496 (2006)
14. Taleb, L., Cailletaud, G., Blaj, L.: Numerical simulation of complex ratcheting tests with a multi-mechanism model type. *Int. J. Plast.* **22**, 724–753 (2006)
15. Sai, K., Cailletaud, G.: Multi-mechanism models for the description of ratcheting: effect of the scale transition rule and of the coupling between hardening variables. *Int. J. Plast.* **23**, 1589–1617 (2007)
16. Taleb, L., Cailletaud, G.: An updated version of the multimechanism model for cyclic plasticity. *Int. J. Plast.* **26**, 859–874 (2010)
17. Taleb, L., Hauet, A.: Multiscale experimental investigations about the cyclic behavior of the 304L SS. *Int. J. Plast.* **25**, 1359–1385 (2009)
18. Brik, M., Taleb, L.: Experimental investigations about ratcheting and strain hardening memory of extruded 2017A aluminum alloy. *Eur. J. Mech. A/Solids* (submitted)

History of Microstructure Evolution and Its Effect on the Mechanical Behavior During Friction Welding for AISI 316

Ammar Jabbar Hassan, Ramzi Lechelah, Taoufik Boukharouba, Djamel Miroud, Nacer-eddine Titouche and Nourdine Ouali

Abstract The evolution of the mechanical properties of steel AISI316 during direct drive friction welding depends essentially on the heat flow. The generation of this flow depends on two parameters, rotation speed and friction pressure. In the first time, optimization of welding conditions to obtain a microstructure closest to that of the base metal. This optimization was made for a single parameter, the temperature must remain below the phase transformation line that is 926 °C for AISI 316 [7, 12]. The results show that the microstructure of welded joint is built in the last three steps of the process. During the first step of friction phase, the application of friction pressure causes a cold deformation creates a mechanical deformation zone (MDZ_1). At the second step of friction phase MDZ_1 leaves place for softening zone because of heat diffusion, with still remaining of friction pressure. Thermo-mechanically affected zone (TMAZ) creates at final this step of friction phase. The forging pressure application during the third step defined the microstructure of welded joint; the TMAZ is replaced by the second mechanical deformation zone (MDZ_2). Additionally, forging pressure application creates inside a new MDZ_2 a hard eccentric core around the welding centre, precisely along the rotation axis. The micro-hardness of MDZ_2 is higher than TMAZ and less than MDZ_1. Post weld analysis were investigated by micro-hardness measurements, SEM, XRD, EDX and tensile test, those illustrate the important role of heat flux on the microstructure of joint through the welding process.

A. Jabbar Hassan (✉) · R. Lechelah · T. Boukharouba · N. Ouali
Laboratoire de Mécanique Avancée “LMA”, Université Des Sciences et de
La Technologie Houari Boumediene “USTHB”, BP. 32; El-Alia,
16111 Bab-Ezzouar, Algiers, Algeria
e-mail: jabbarhassan1973@yahoo.fr

D. Miroud
Materials Science and Process Engineering Laboratory (LSGM),
Université Des Sciences et de La Technologie Houari Boumediene “USTHB”,
BP. 32; El-Alia, 16111 Bab-Ezzouar, Algiers, Algeria
e-mail: jamelart@yahoo.fr

N. Titouche
Nuclear Research Center of Birine, OB 180, 17200 Ain Oussera, Djelfa, Algeria
e-mail: netitouche@yahoo.fr

1 Introduction

The advantage of solid state welding is elimination the problem of hot cracking. A filler metal is not necessary, which avoids the formation of hard and brittle phases. The welding joint remains chemically homogeneous; another advantage constitutes low effect of corrosion [8]. The equipment is simple, needs little maintenance and experience. Overall, the process is clean, no smoke, no dangerous, fast and automated which guarantees the control of its parameters [4, 6, 10]. In present work, for example, longest welding operation does not exceed 20 s.

This joining process associated with both mechanical and thermal effect. The mechanical effect is primarily related by friction pressure while thermal effect depends on friction time. The mechanical effect occurs before the elevation of temperature, during accosting phase. This effect ends at the maximum temperature and the thermal effect begins. This last is stopped also at the end of friction phase. The mechanical effect seems again with forging pressure application.

In otherwise, the history of microstructure evolution passes through four stapes, which are forming the three phases of the direct drive friction welding (accosting, friction and forging). Future mechanical properties of welded joint depend on this history of the base metal. This method of proceeding allows separating both mechanical and thermal effect during welding operation, in order to evaluate the effect and role of each step in the microstructure evolution of the welded joint. Can conclude that as following:

- first step of friction phase leads to finer grain size with increase of hardness,
- second step of friction phase occurs grain growth with decrease of hardness,
- unique step of forging phase introduces a second mechanical effect by creating a hard core, benefiting from the remaining thermal effect (second step of friction phase).

2 Experimental Study

2.1 Material

Material used in this process is austenitic stainless steel *AISI 316*, with chemical composition, mechanical, physical and microstructure of base metal shown respectively in Tables 1, 2 and 3 and Fig. 1.

Table 1 Chemical composition of base metal (%)

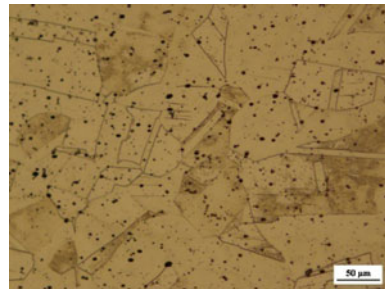
C	Mn	Si	P	S	Mo	Cr	Ni
0.04	1.50	0.67	0.03	0.021	2.93	17.93	9.95

Table 2 Mechanical properties of base metal

Offset yield stress 0.01 % (MPa)	UTS (MPa)	Modulus of elasticity (MPa)	Elongation (%)	Average micro-hardness (Hv0.1)	Strain hardening exponent (n)	Strength coefficient K (MPa)
578	670–680	$\approx 1.93 \times 10^5$	≈ 45	260–263	0.206	1146

Table 3 Physical properties of base metal

Density (g/cm ³)	Electrical resistivity ($\mu\Omega$ -cm) (20 °C)	Specific heat (kJ/kg k) (0–100 °C)	Thermal conductivity (w/m k) at (100 °C) and (500 °C)	Mean coefficient of thermal expansion ($\mu\text{m}/\text{m k}$) (0–871 °C)
8.00	74	0.50	(16.2) and (21.4)	19.9

Fig. 1 Microstructure of base metal

2.2 Welding Process

Welding operations are carried out by a direct drive friction welding machine designed and manufactured by our laboratory (Fig. 2). This process is simple two welded parts are kept in contact, one of them is maintain in rotating (1000–3700 rev/min) [4, 11, 13, 14, 18] during the first of two phases of the welding process, the accosting and friction phase. Present work used a rotation speed of 3000 rpm [2, 5].

This study begins by optimizing the welding parameters which are controlling the flow of heat generated during the process. The temperature is measured in two different positions by using two thermocouples. First one is a thermocouple type K (attached by cold welding), and second one is an infrared thermocouple. The average uncertainty of measurement is 45 °C, observed for 107 operations with 11 conditions have been fulfilled (Fig. 3a). That seems in both X4 and X5 case (Table 4), while the friction pressure and rotation speed used for both cases are the same.

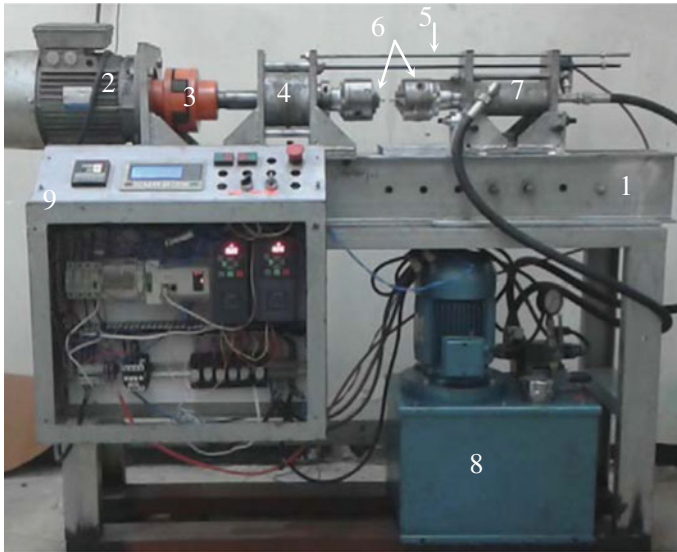


Fig. 2 Scheme of the direct driving friction welding machine (*Designed and Fabricated in LMA of USTHB, Algiers, Algeria*): 1 Main body, 2 main driving motor with brake unit system, 3 clutch, 4 bearing collar, 5 supports, 6 chucks, 7 press, 8 hydraulic unit, 9 control unit box

The welding operations achieved without any preparation of cutting samples. Specimens before welding process were cut directly from 6 m bars for 45 mm length and 12 mm diameter, followed that, the specimens subjected to a face machining for the welding interfaces organization.

The selecting conditions were used in the present study (Fig. 3b) subjected to limiting temperature of 926 °C, which must be remaining below the phase transformation [3]. For example, one of the cases:

1. Rejected case (*X1*, does not exist in the Table 4) maximum temperature 1057 °C > T °C of phase transformation with upset distance 16 mm.
2. Retained case (*X5*, Table 4), maximum temperature 819 °C < T °C of phase transformation with upset distance 8.75 mm (Fig. 3d).

Present study shows the macro and microscopic level for three cases, *X2*, *X4* and *X5* (Fig. 3b and Table 4). Each case represents the mean value of seven or six welding operations. The history of microstructure evolution is subjected to four steps, contained in **three phases** which is defining the welding operation (Table 5), three of them illustrate at Fig. 3c. The temperature level generated by the welding operation depends on the friction pressure, speed of rotation and the physical properties of the material. The welding operation starts by the accosting phase, at moment of friction pressure application. Time of this phase depends on rotation speed, specific heat, friction coefficient and density of welded material. At the end of this first phase, the temperature begins to increase locally at the interface (Fig. 4),

Fig. 3 Welding specimens of AISI 316 with different welding conditions.

a Welding cases with different fash metal according to the parameters. **b** X4, X5 and X2. **c** Steps of X5: (1) E₀-E₁, (2) E₁-E₂ and (3) E₂-E₃. **d** X5, upset distance

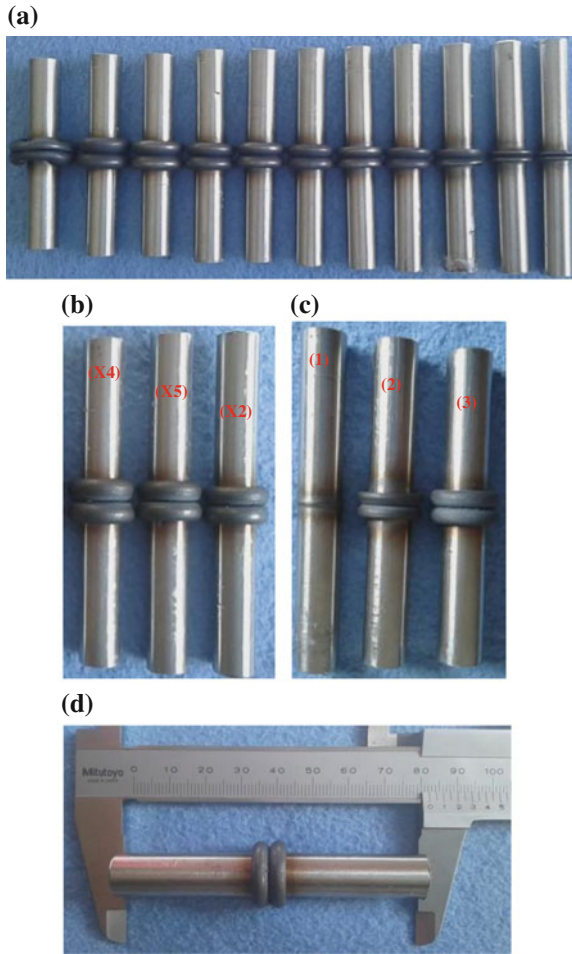


Table 4 Average values results of friction welding selected cases

	RS (rev/min)	AT (s)	FrP (MPa)	FrT (s)	FoP (MPa)	FoT (s)	UD (mm)	Tmax (°C)	AITss [E ₀ -E ₁] (1 °C/s)
X4	3000	3.5	4.00	8.50	8.00	5.00	11.75	870	0.0013789
X2			3.50	8.50	8.00		8.00	790	0.0015187
X5			4.00	6.50	8.00		8.75	819	0.0014703

RS Rotation speed

AT Accosting time

FrP Friction pressure

FrT Friction time

FoP Forging pressure

FoT Forging time

UD Upset distance

Tmax Maximum temperature

AITss Average increasing temperature, solid state

Table 5 Illustration of four steps (three phases) of direct drive friction welding

Steps	Metal state	Description	Phase
1/E ₀ -E ₁	Solid state	Start of friction, this phase ends when the temperature at the interface of the two parts exceeds the room temperature (Fig. 4)	Accosting
2/E ₁ -E ₂		Future microstructure of the metal depends principally on this step. This is clearly seen in the macro-graphic form, large mechanically affected zone along the perpendicular axis to the welding axis. The measured surface temperature reaches its maximum value at the end of this step (Fig. 4)	
3/E ₂ -E ₃	Soft state	The heat dissipation depends on the friction time remaining after the first step of friction. The dissipation can exceed 55 % of the maximum value of the temperature measured at the surface. The flash metal is formed at least 50 % (Fig. 4)	Friction
4/E ₃ -E ₄		Temperature continues to fall up to 75 % of its maximum value at the end of the fourth step (Fig. 4). The flash metal takes its final form at the end of this phase (§4)	

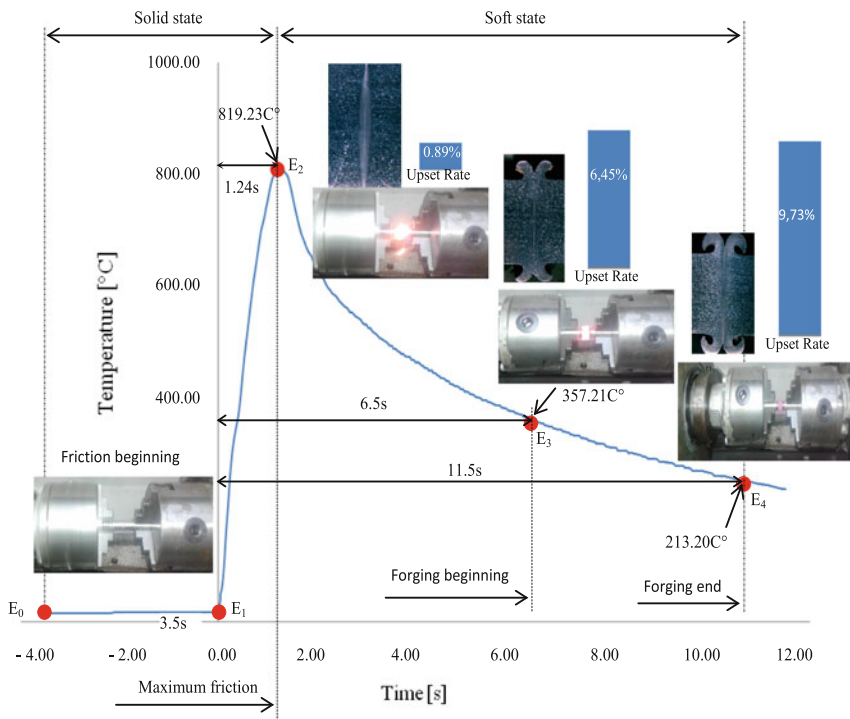


Fig. 4 Diagram illustrates the four stapes (three phases) of direct drive friction welding operation, X5

indicating to begin the most important phase which is called friction phase, this phase is concluding *two steps*. The first step of friction phase occurs when the metal is heated locally to maximum temperature. The upset rate for *AISI316* at this step end can exceed 14 % (Fig. 4), it is the beginning of flash metal formation (Fig. 3c). The change in temperature is roughly linear and the maximum value reached of this temperature depends on the rotation speed and friction pressure (Table 4). Once arrived to the maximum temperature, starts the second step of friction phase. The metal begins to be soft, which is leading to friction and temperature decrease that allow for flash metal formation. The physical flash metal approved by the soft metal which extrude to the free circumference of the welded piece, and this first migration of grains is containing until the end of friction time (Fig. 3c). The upset rate during this second step of friction phase can exceed 57 % of total upset rate and it depends mainly upon the friction time and pressure (Fig. 3d and Table 4). The friction pressure is replaced by forging pressure at stop of rotating suddenly. Under effect of this pressure, the metal is not completely cold yet ($T > 350$ °C, for the case X5), so it has to be continuously discharged from centre to circumference of welded piece [19]. The upset rate during this phase does not exceed 30 % of the total upset rate, X5 case (Fig. 3d).

3 Mechanical Tests

3.1 Tensile Test

In order to compare the overall mechanical properties of the metal before and after welding, tensile tests were performed on the three selected case (X2, X4 and X5). The trials were conducted by a universal test machine with capacity ± 100 kN (Fig. 5a). The tests have been achieved with a constant strain rate of $1.6 \times 10^{-3} \text{ s}^{-1}$. The tensile test specimens were taken from the welding direction. The direction of the position and their geometric form are shown in the Fig. 5b.

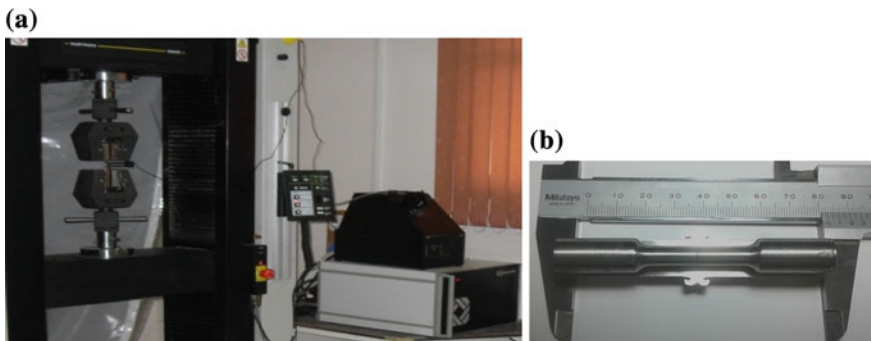
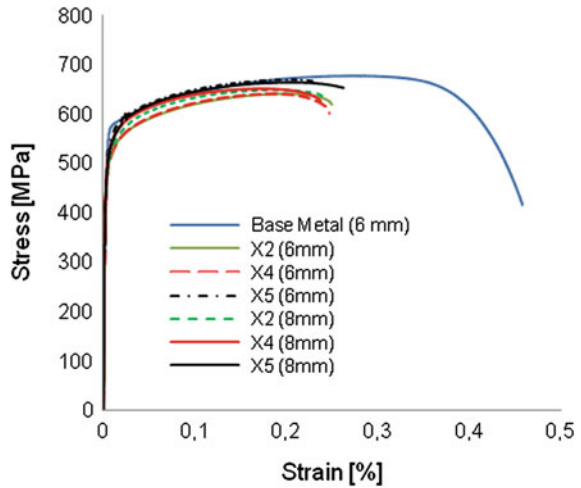


Fig. 5 Tensile test: **a** machine, **b** specimen ISO 6892-1:2009(F)

Fig. 6 Tensile tests curves

The evolution of deformation during the test was measured locally, by using displacement sensor, with open space $19.5 \text{ mm} \pm 2.5$ (Fig. 5a). The sensor was mounted on the test piece around the interface of the welded joint. An example of comparing seven tensile curves is shown in Fig. 6.

For welded specimens, test results show that the plastic deformation tends to be localized beyond the hard core, i.e. in the softest zones (*TMAZ_2*) away from the welded interface [1]. For the three cases, the fracture position is in the stationary part of welding specimens (Fig. 7), which presents more ductility than rotating part.

Disregarding the accuracy of tensile test, there are differences between the results obtained for test specimens of base metal and welded. These differences reveal for three characteristics (Table 6):

- total strain,
- ultimate tensile stress *UTS*,
- strain related to the *UTS*.

Generally, if according to the mechanical properties obtained by tensile tests, the *X5* case is closest to the mechanical properties of the base metal (Table 6).

Fig. 7 Tensile test fracture

Table 6 Tensile tests results

Diameter (mm)	Cas	σ_{max} (MPa)	$\epsilon_{with \sigma_{max}}$	ϵ_{max} (%)	$\frac{\sigma_{max, welded}}{\sigma_{max, base metal}}$ (%)	$\frac{\epsilon_{max, welded}}{\epsilon_{max, base metal}}$ (%)
6	Base metal	678.17	0.274	0.457		
	X2	641.206	0.187	0.25	94.55	54.70
	X4	641.344	0.2	0.247	94.57	54.05
	X5	670.134	0.209	0.231	98.82	50.55
8	X2	649.212	0.191	0.24	95.73	52.52
	X4	651.373	0.172	0.237	95.05	51.86
	X5	663.689	0.202	0.262	97.86	57.33

3.2 Micro-Hardness Test

The micro-hardness measurements along the welding direction allowed estimating of local micromechanical properties around the welding interface. Micro-hardness profiles for X4 and X5 cases are represented by plots both side along the axis of welding center (Fig. 8), the stationary part denoted by (-) side and the rotating part designated by (+) side. The specimens were mechanically polished up to 5 μm . The measurements are carried out by using weight of 100 g (Hv0.1). For the base metal used 7 measurements were performed at different locations with average 17 units of uncertainty.

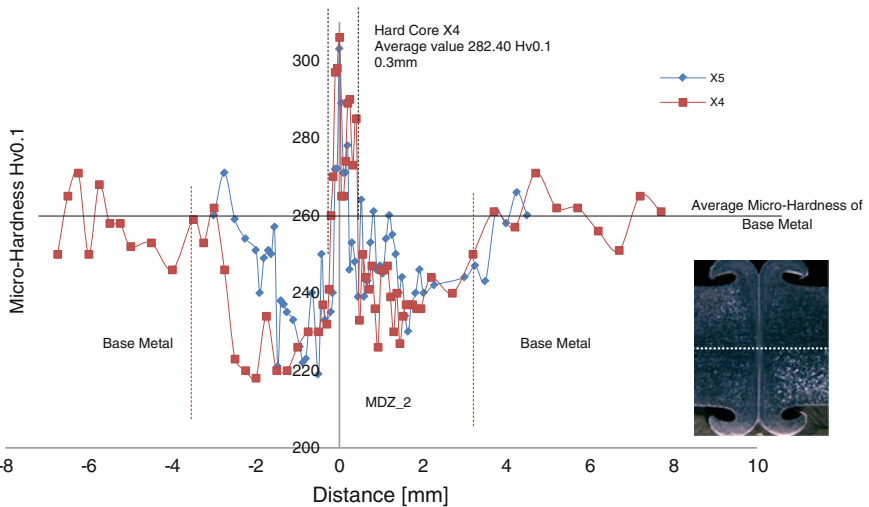


Fig. 8 Comparison between X4 and X5

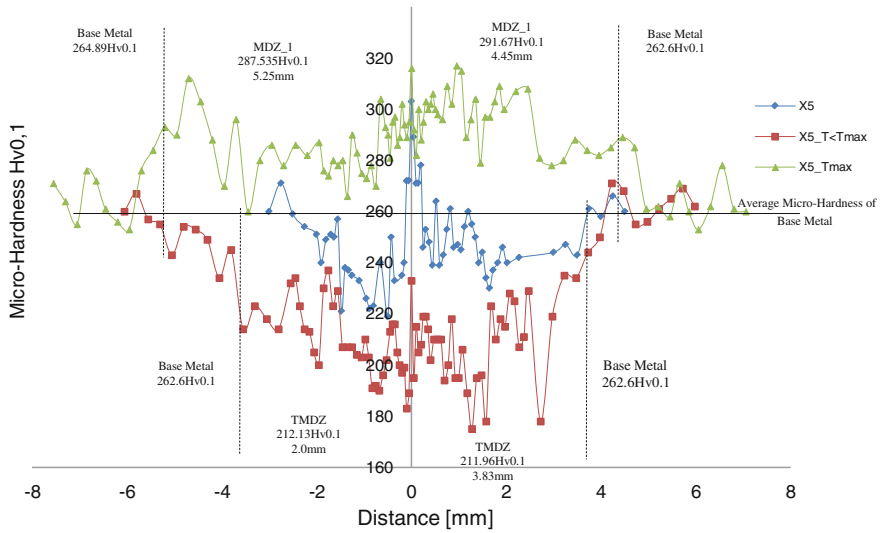


Fig. 9 Hardness profile for three steps, X5

Other measurements were carried out on the X5, but at this time for two steps of friction phase (Fig. 9). These measurements show that the micro-hardness profile changes for each step of welding, and the changes summarized as following:

- general hardening represents first strongly mechanical deformation zone (*MDZ_1*), separated from the base metal by a partially mechanical deformation zone (*P_MDZ*),
- general softening represents combination effect of three parameters: thermal diffusion + friction pressure concentrates at soft part from both side of the interface + angular rotation speed which is about 300 rad/s. This step presents the thermo-mechanical deformation zone (*TMDZ*).
- generate a new hard zone with small dimensions [15] around by region less soften than *TMDZ* and also less large than *TMDZ* and *MDZ_1*. This hard core positioned along two sides of welding axis.

X5 presents a difference between average micro-hardness measurement of *TMDZ* and *MDZ_2* about 35 *Hv0.1* (Fig. 9). On the otherwise, the difference between average micro-hardness measurement of *MDZ_2* for X4 and X5 case about 10 *Hv0.1* (Fig. 8).

The micro-hardness measurements confirm the position of tensile test fracture. The fracture always occurs at the more ductile part of the welding specimen (Fig. 8).

3.3 EDX and XRD Analysis

EDX analysis carried out for 07 points of measurements from thermo-mechanical deformation zone toward welding center (Fig. 10a), confirms uniform distribution for alloying elements toward welding line (Fig. 10b, c).

On the other side, the XRD analysis reveals austenite redistribution for both heat treatment ($T = 820\text{ }^{\circ}\text{C}$, soaking time $\frac{1}{2}$ h and air cooling) and welding case. The XRD shows fine grains in the welding center and relatively fine grains for heat treatment case relative to the base metal (Fig. 11). Notice, absence of phase chngement, i.e. proves a high controlling of welding conditions.

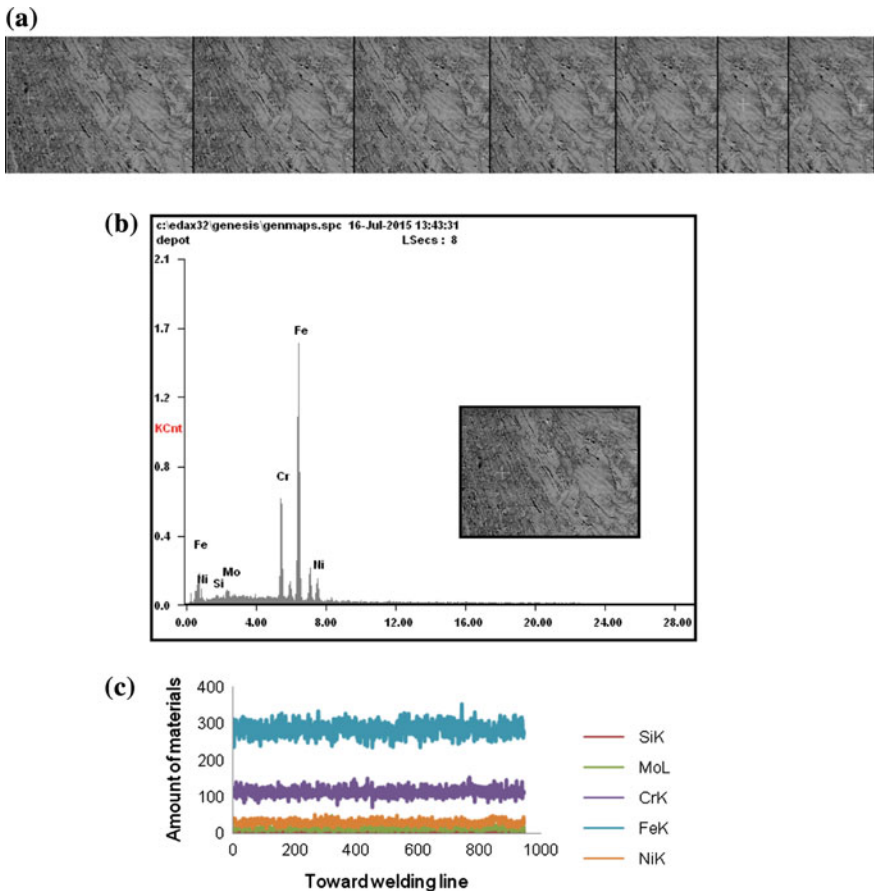


Fig. 10 EDX Analysis, **a** points of measurements, X5, **b** example for EDX analysis toward welding interface, X5, **c** distribution of alloying elements toward welding interface, X5

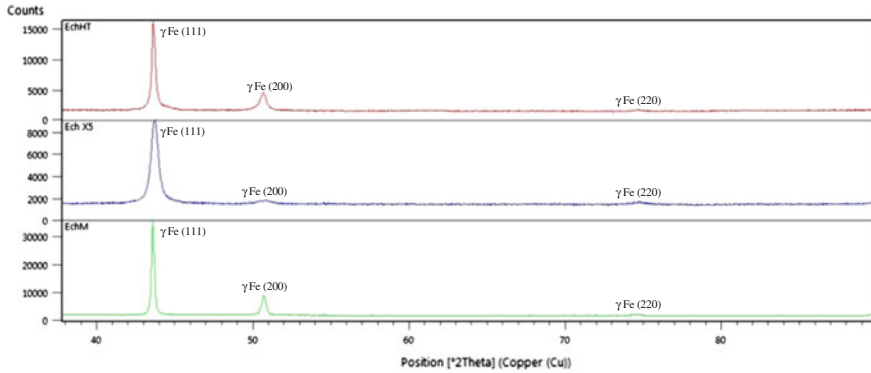


Fig. 11 XRD peaks: base metal (EchM), X5 (Ech X5) and heat treatment (EchHT)

4 Discussion

Present work confirms that during direct drive friction welding process the microstructure of the base metal pass through *three states* (Fig. 9), which starts at E_1 (Fig. 4). During the first step of friction phase (E_1-E_2), the pressure application, and consequently the mechanical action, strongly affected on the microstructure of the base metal. Suggestion it is step of cold deformation [9]. Micro-hardness of this zone (MDZ_1) increased by average of $40Hv0.1$ relative to the average of micro-hardness for the base metal $260Hv0.1$ (Table 2 and Fig. 9).

Conversely, during the second step of friction phase (E_2-E_3), that the action of the temperature is very clear on the microstructure, as shown in micro-hardness profile (Fig. 9). The micro-hardness average decreases by $89Hv0.1$ relative to the MDZ_1 . This decreasing of micro-hardness explained by expose the fine grains from previous step (MDZ_1) to thermal diffusion (+80 % time of friction phase) and mechanical action (friction pressure). What happened in welding zone is a hot

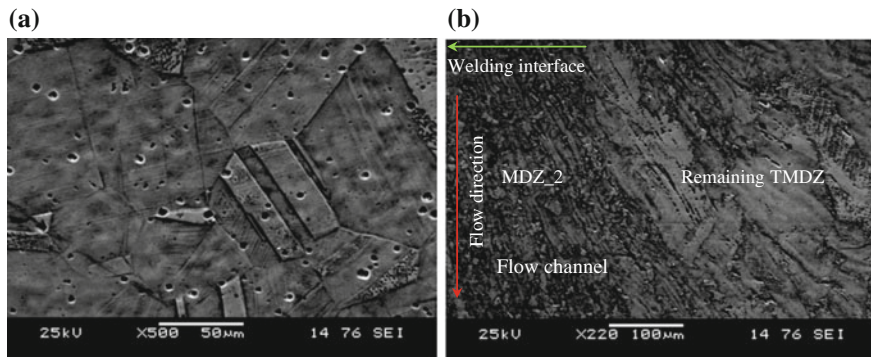


Fig. 12 SEM photographic analysis (new grains formation), **a** base metal (γ phase), **b** welding zone, X5

deformation (*TMAZ*). Therefore, this last under angular speed effect creates new grains by torsion effect (Fig. 12).

During the forging phase ($T = 360\text{ }^{\circ}\text{C}$ + welded metal relatively still soft, see Fig. 4), will form the final future microstructure of welded joint. Which will compose essentially from the grains of *TMAZ* excites away from welding interface. Different form and size grains replace those were excited around welding interface (Fig. 9), expelled outward under compression.

From other side, by forging pressure application the grains still soft absorbs amount of developed energy, that permit to it displaced toward outside circumference to form the final flash metal [16, 17] (Fig. 13). The remaining grains of *TMAZ* form the future of the microstructure joint after subject to second cold deformation (*MDZ_2*).

The remaining energy will give hard core (Fig. 14); with grains size depends on the same time on maximum temperature generated (2nd step) and diffusion time (3rd step) of it (Figs. 8 and 9). For X5 has a cylindrical shape with fine grains hard core (Fig. 15a) and elliptical base with axes diameter 0.3 and 0.4 mm (Fig. 15b).

EDX (Fig. 10) and *XRD* (Fig. 11) analysis, confirm respectively in the same time a good uniform distribution of alloying elements and absence of phase transformation in welding zone. Conversely, these two items have a capable responsibility to reduce the ductility in a welding piece.

From this effect, we think that the hard core influence on the tensile fracture behavior of welding piece. The tests results reveal a ductile fracture formerly by

Fig. 13 Example of flash metal profile, X5

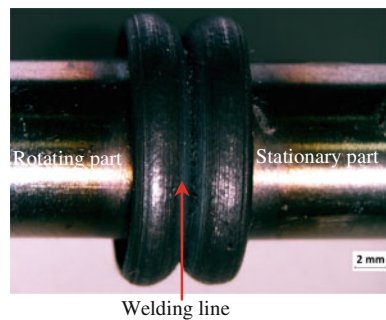
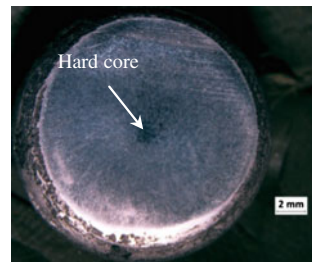


Fig. 14 Macro-graphic illustrates the hard core, cross section of X5



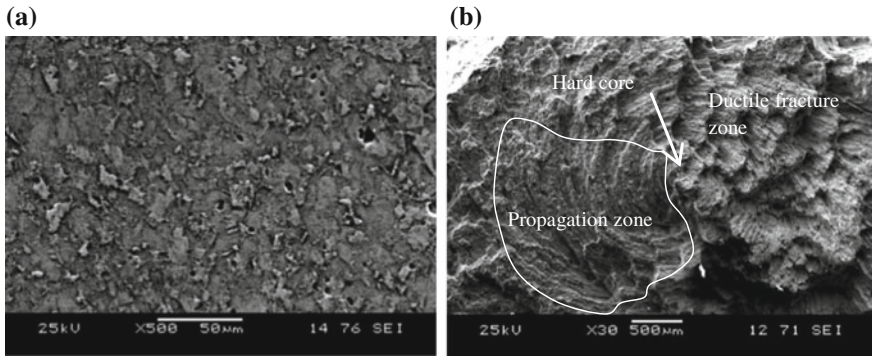


Fig. 15 SEM photographic analysis for welding core and fracture surface (specimen of 8 mm, X5), **a** Welding core, fine grains, **b** fracture surface of tensile test

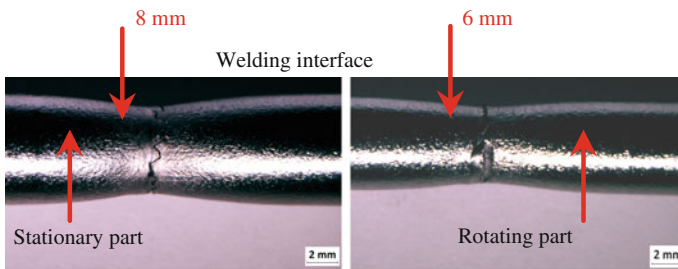


Fig. 16 Fracture position for specimens of 6 and 8 mm, X5

necking smaller than that occurs in the base metal. The fine grains hard core with (Fig. 15a) represents a serious obstacle of necking.

Limitation of necking and stress increasing because of hard core initiate a crack in stationary side of welding piece (Fig. 16). Once crack initiates will propagate on the limiting zone until brittle fracture occurs (Fig. 15b). Therefore, in spite of fracture occurs by maximum necking as in the base metal it occurs by limited necking followed by initiation and propagation of cracks in the soft part of welding specimen.

5 Conclusions

The first view of friction welding was in 1836, while introduces in the manufacture applications in the middle of 20th century. Since that period, many re-researchers concern about this process, using different analysis to explain the mechanism controlling the direct drive friction welding.

Present study by use a simple plane tried to explain the mechanism controlling the microstructure of welding joint obtained by this process. The final structure depends on the last three steps of the process.

Each of three steps provide a new creation of microstructure. The first fin grins zone results by cold deformation under mechanical action and angular rotation speed. This last transformed by diffusion of heat flow associated with mechanical action resulting grain growth zone deformed by torsion. This zone also transform under effect of shear results due to another cold deformation to zone with a grins size near to that of the base metal, which covers a narrow fin grains zone that has a micro-hardness higher than the base metal. Named this fin grains zone of cylindrical form by a hard core.

References

1. Ajith, P.M., Barik, B.K., Sathiya, P., Aravindan, S.: Multiobjective optimization of friction welding of UNS S32205 duplex stainless steel. *Defence Technol.* **11**, 157–165 (2015)
2. Akbari Mousavi, S.A.A., Rahbar Kelishami, A.: Experimental and numerical analysis of the friction welding process for the 4340 steel and mild steel combinations. *Weld. J. USA* **87**, 178s–186s (2008)
3. Asif, M.M., Shrikrishna, K.A., Sathiya, P.: Effects of post weld heat treatment on friction welded duplex stainless steel joints. *J. Manuf. Process.* **21**, 196–200 (2016)
4. Avinash, M., Chaitanya, G.V.K., Giri, D.K., Upadhya, S., Muralidhara, B.K.: Microstructure and mechanical behaviour of rotary friction welded titanium alloys. *World Acad. Sci. Eng. Technol.* **35**, 146–148 (2007)
5. Biljana, S., Svetislav, M.: Physical model of the friction welded joint of different types of steel. *FME Transactions. Fac. Mech. Eng. Belgrade*, **36**, 93–97 (2008)
6. Bonte, D., Derynck, B., De Baets, P., De Waele, W., Faes, K.: Friction Welding of Ceramics to Metals, Day of Research 2010, Ghent University, Laboratory Soete, Belgian Welding Institute, Belgium, pp. 14–20 (2010)
7. Castro, R.J., Cadenet, J.J.: *Welding Metallurgy of Stainless and Heat Resisting Steel*. Cambridge University Press, Cambridge (1974)
8. Cecile, G.: Genèse des microstructures lors du soudage par friction malaxage d’alliages d’aluminium de la série 2000 & 5000 et comportement mécanique résultant. Thèse de Doctorat, Institut National Polytechnique “INPG” de Grenoble, France (2004)
9. Davis, J.R.: *Heat Resistant Materials, ASM Especially Handbook*, Printed in the USA, 1st edn. pp. 144–294 (1997)
10. Faes, K., Dhooge, A., De Baets, P., Afschrift, P.: New friction welding process for pipeline girth welds-welding time optimization. *Int. J. Adv. Manuf. Technol.* **43**, 982–992 (2009)
11. Kurt, A., Uygur I., Paylasan U.: Effect of friction welding parameters on mechanical and microstructural properties of dissimilar AISI 1010-ASTM B22 joints. *Weld. J. USA* **90**, 102s–106s (2011)
12. Nishio, Y., Ohmae, T., Yoshida, Y., Miura, A.: Weld cracking and mechanical properties of 17 % chromium steel weldment. *Weld. J.* **50**(1), 9s–18s (1971)
13. Özdemir, N.: Investigation of the mechanical properties of friction welded joints between AISI 304L and AISI 4340 steel as a function rotational speed. *Mater. Lett.* **59**, 2504–2509 (2005)
14. Sardana, G., Kumar, A.: To study the mechanical behavior of friction welding of HSS M33 & SS 316. *Int. J. Eng. Sci. Adv. Technol.* **3**, 131–134 (2013)

15. Sathiya, P., Aravindan, S., Noorul haq, A.: Raiser Innovation Award for Friction Welding (2011), www.raiser.de/bewerber2011/sathiya
16. Schmicker, D., Persson, P.O., Strackeljan, J.: Implicit geometry meshing for the simulation of rotary friction welding. *J. Comput. Phys.* **270**, 478–489 (2014)
17. Shanjeevi, C., Satish Kumar, S., Sathiya, P.: Evaluation of mechanical and metallurgical properties of dissimilar materials by friction welding. In: International Conference on Design and Manufacturing, IConDM, *Procedia Engineering*, vol. 64, pp. 1514–1523 (2013)
18. Song, Y., Liu, Y., Zhu, X., Yu, S., Zhang, Y.: Strength distribution at interface of rotary-friction-welded aluminum to nodular cast iron. *Trans. Nonferrous Met. Soc. China* **18**, 14–15 (2008)
19. Srinivasa Rao, M.K., Reddy, G.M.: Friction welding of nickel free high nitrogen steel: influence of forge force on microstructure, mechanical properties and pitting corrosion resistance. *J. Mater. Res. Technol.* **3**(1), 90–100 (2014)

A Study of Selective Laser Melting Technology on the Ultra-High Strength Tool Steel Use—Quality, Mechanical Properties and Fatigue

Píška Miroslav, Trubačová Pavlína, Horníková Jana, Šandera Pavel
and Klas Boivie

Abstract During the last few years, laser based powder bed fusion (PBF) processes have received an increasing attention as a section of additive manufacturing technologies with a rapidly growing number of established and potential industrial applications. This paper investigates the effect that key parameters in PBF processes have on critical material properties in high-alloyed steel samples, manufactured under controlled process conditions such as scanning strategy, energy density and orientation of samples in the build chamber. A Concept Laser M2 Cusing Machine, (Concept Laser, Lichtenfels, Germany) was used for the fabrication of samples made from MARLOK[®] C1650, an independent maraging (precipitation hardening) tool steel. This steel is specially designed to be used in highly demanding applications, including tools for aluminum die casting in long series with high requirements for surface quality in the product and high fatigue resistance in the tooling. Two series of samples were made with different hatch spacing of the laser beam and with different orientation and angles in the build chamber. The samples were prepared according to relevant standards including CNC machining, with exception for a few samples that were kept in as-built condition for comparison. Evaluation of the 3D surface quality of the machined samples and the morphology of the fracture were done with the contact-less Alicona Infinite G4 machine and a Tescan Mira 3GM scanning electron microscope. Fatigue testing was performed with an Instron 8874 Servohydraulic Dynamic Testing machine. The investigations include the influence of process parameters on mechanical properties in the final material, as well as the effect on the parameters

P. Miroslav (✉) · T. Pavlína · H. Jana · Š. Pavel
Faculty of Mechanical Engineering, Brno University of Technology,
Technická 2, 616 69 Brno, Czech Republic
e-mail: piska@fme.vutbr.cz

H. Jana · Š. Pavel
Central European Institute of Technology, Brno University of Technology,
Technická 10, 616 00 Brno, Czech Republic

K. Boivie
Department of Production Technology, SINTEF Raufoss Manufacturing AS,
S.P. Andersens vei 5, NO-7465 Trondheim, Norway

measured in cyclic material fatigue tests. A special test for assessment of machinability of the sintered materials with turning in terms of specific cutting force has also been performed. The results confirmed a statistically significant influence of technological variables on the mechanical and fatigue properties. Some porosity found in the material apparently has been the origin of several mechanisms of crack initiation and propagation. However despite this, the results are encouraging since optimized process conditions apparently can produce a material of good quality and high fatigue resistance.

1 Introduction

The area of Additive Manufacturing technologies (*AM*) in metals comprehends a significant number of practical applications, such as fabrication of very demanding end-use products, small tooling parts or surgical implants [1–7]. The *AM* methods propose wide range of technological advantages like direct creation of complex and geometrically difficult parts, an ability to fabricate not only solid material structure, but also a low density, porous and open-celled net structure [1] can be designed too. In addition, the strong individualization of product to specific applications [2] is main issue of *AM* technologies (e.g. customized medical implants).

The Selective Laser Melting is one of the powder bed fusion automatic *AM* technologies. The metallic powder is heated by the laser beam to melting temperature and fused layer by layer [4]. The building of the part is based on *3D CAD* model (*STL format*). This is very suitable for medical application and reverse engineering where the *3D* model of customized implant can be easily acquired by exploitation of Computed Tomography (*CT*) scan or of Magnetic Resonance Image (*MRI*) [6] and then fabricated by *SLM*. However, the *SLM* parts have to reach the best quality in term of mechanical properties, surface quality and competitiveness to the *CNC* parts made from blanks, esp. for the medical implants, car or aeronautic components. Nevertheless, a final machining can be used, because the *SLM* components don't reach high surface quality (surface arithmetic roughness—*Ra*—from 3.2 to 25 μm [6, 8]). Up to now, many researches have carried out the *SLM* and *AM* methods [1–25]. The influences of many process parameters on final component quality have also often been investigated [9–25]. For example, the influence of energy density on porosity and microstructure of a stainless steel [26], the specific impact of the laser power density and of the scan speed on microstructure, microhardness and surface finish of a titanium alloy was investigated in [27], and the effect of specimens position and inclination in the building chamber on similar characteristics was made in [28].

Possibly, no evaluation of machinability of *SLM* components and study of variation of *SLM* process parameters on mechanical and fatigue properties, surface quality, including machinability measured by cutting forces haven't been found yet.

Not only the processing conditions result in wide scale of microstructural and mechanical properties of the materials and *3D* designs, but the material

characteristics are important factor too. The metal powder used in *AM* is important as well; it is assumed to be spherical. However, the particle size distribution undergoes normal distribution [9, 10] that affects the final mechanical properties and density of the structure. Non-equilibrium processes, the high temperature gradients in the melted and cooled area followed by drastic shrinkage [11, 20], the size and shape of the melting pool and cooling rates significantly affect microstructural features of components [11]. These factors can be reduced by increasing the temperature inside the built chamber or by post processing heat treatment [7].

An occurrence of some pores in the structure of the *SLM* parts can be seen in an initial powder contamination, evaporation or local voids due to internal stresses after powder-layer deposition. They can be the initializing points of stress risers which finally lead to failure under fatigue loading [7].

Obviously the type of material determines the final properties and behaviour of *SLM* parts too. Since many *SLM* materials have been investigated in regard of evaluation of their mechanical properties—like Al-alloys [12, 13], Ti-alloys mainly for medical and aerospace applications [13–16], then some more specific materials like glass [17] or copper matrix composites [18].

The mostly studied material for *SLM* is the steel alloys [19–25]. The maraging steel *H13* [33], stainless steels *316L* [24, 25] and martensitic precipitation-hardening stainless steel *17-4PH* are basically used [20].

The sequence of thermal loadings of the part is difficult to predict because there are many acting factors such as the melting point of the material, the temperature of the build chamber, the nature of the atmosphere (vacuum, helium, nitrogen or argon), the particle size and the thermal mass of the surrounding un-melted powder [20].

The key factor studied in this work is the effect of scanning strategy on fatigue properties of the produced parts. The scanning strategy includes the energy density of laser beam, the scanning direction, overlap and hatch spacing strategy. The work continues similar studies [29, 30], but this work deals with machinability and *2D/3D* surface evaluations.

2 Materials and Methods

2.1 *SLM* Fabrication

The system Concept Laser (SINTEF, Trondheim) was used for fabrication of all specimens. This *SLM* installation is equipped with an Nd: YAG fibre laser, which produces the laser beam with a wavelength of 1064 nm. The laser can reach the power from 200–400 W in continuous mode (with supposed Gaussian intensity distribution). The spot diameter of the laser beam can be set in the range of 5–200 μm (15 μm was used) and the scan laser velocity is 7 m/s in maximum. The dimensions of the building chamber were 250 \times 250 \times 280 mm (*x*, *y*, *z*) [5].

Table 1 Chemical composition of MARLOK[®] C1650 [31]

Element	C	Cr	Mo	Ni	Co	Ti	Si	Mn	Fe
(wt%)	<0.008	<0.3	4.5	14.0	10.5	0.2	<0.10	<0.10	rest

Table 2 Physical and mechanical properties of MARLOK[®] [31]

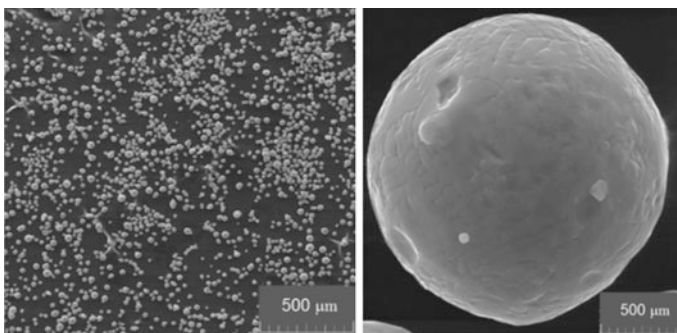
Density, ρ (g/cm ³)	8.9	Fracture elongation, A_5 (%)	5.00–8.12
Tensile strength, R_m (MPa)	1450–1600	Reduction of area, Z (%)	20 and 35–45
Yield strength, R_e (MPa)	1400–1500	Impact energy, CVN (J)	20 and 25–35
Young's Modulus, E (GPa)	186	Fracture toughness, K_{IC} (MPa \sqrt{m})	100
		Hardness, HRC	47–51

The material used for this work was the ultra-high strength die steel MARLOK[®] C1650—Table 1, with a very low carbon content and increased N , Mo and Co contents [31]. The advanced mechanical properties of this material are listed in Table 2.

Due to high corrosion resistance of MARLOK[®] no vacuum or special atmosphere for sintering is needed, just the oxygen limit of 2.2 % and nitrogen atmosphere inside built chamber must be controlled.

The size distribution of grains of MARLOK[®] powder was analysed by the electron beam microscope VEGA 3 TESCAN and programme Particles—Fig. 1. All grains were considered as spherical particles and their size distribution was statistically evaluated by size area distribution—Fig. 2. The mean size of powder grain was about 20 μm .

The hatch spacing h_s of laser beam—Fig. 3—is one of the key factors in the building strategy [29]. In this research each powder layer was re-melted due to reduced hatch spacing—Fig. 3.

**Fig. 1** The powder distribution by EBM VEGA 3

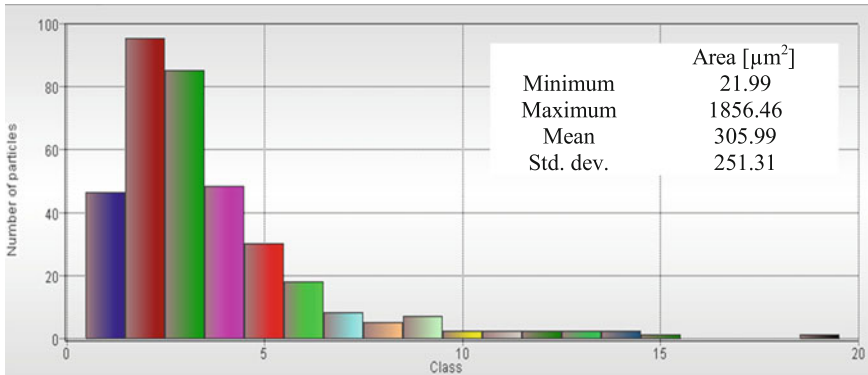
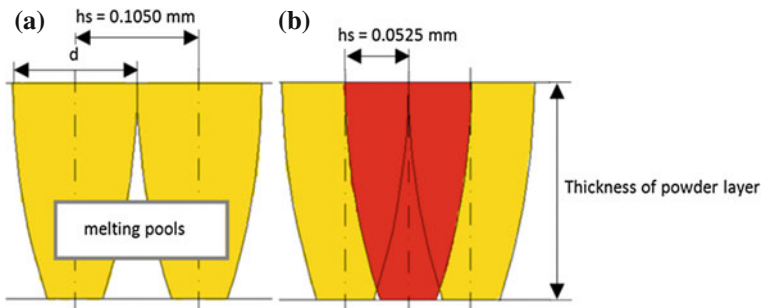


Fig. 2 The size area distribution of powder particles (diameter of one particle ~ 20 μm)



Spot diameter of laser beam: **d = 0.15 mm**

Hatch spacing: **hs = 0.7*d**

hs	hs/2
0.7*d	0.35*d
0.1050 mm	0.0525 mm

Fig. 3 The laser hatch spacings: **a**—standard, **b** reduced

The total energy density of the laser beam changes with the different hatch spacing [32] so some modifications in the microstructure and mechanical properties of material can be expected. Besides hatch spacing the energy density (E) depends on other parameters of laser sintering technology: laser power, scan velocity of laser beam and of layer thickness of powder bed:

$$E = \frac{P}{v \cdot h_{st}} \tag{1}$$

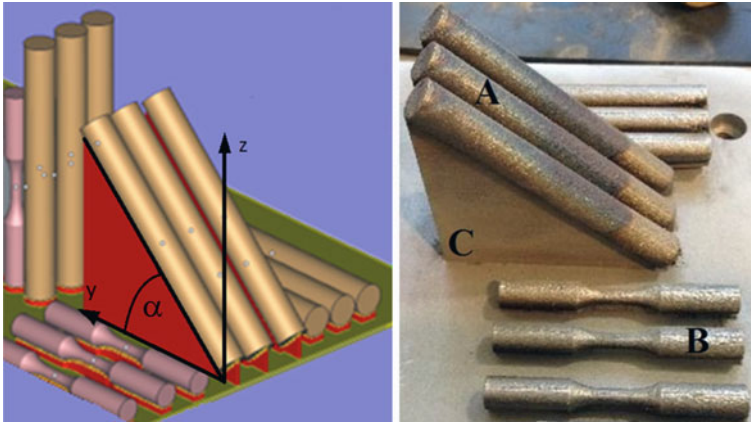


Fig. 4 The orientation of samples in building chamber and final fabricated specimens: *A*—inclined samples with machining allowances, *B*—horizontal as-built samples, *C*—support structure

Table 3 The experimental process parameters

Laser power	Scan velocity	Layer thickness	Hatch spacing	Energy density
P (W)	v (mm s^{-1})	t (mm)	h_s (mm)	E (J mm^{-3})
200	600	0.03	0.1050	105.82
			0.0525	211.64

where E (J mm^{-3}) is density of energy, P (W) means the power of the laser beam, v (mm/s) is the scan velocity, h_s (mm) is the hatch spacing, and t (mm) is the thickness of the monolayer.

The second key factor in the fabrication process was the angle orientation of samples in the building chamber—Fig. 4. Three positions were set: horizontal $\alpha = 0^\circ$, inclined $\alpha = 45^\circ$ and vertical $\alpha = 90^\circ$. Six specimens were built without machining allowances (as-built) and they were oriented only in the horizontal position (three with standard hatch spacing, and three with reduced hatch spacing). The settings of process parameters and the value of energy densities are in the Table 3. An overview of the fabricated specimens can be found in Table 4.

2.2 Machining of Samples

All specimens were CNC machined with the turning centre SPN 12 and the Sinumerik 840D control system. Rounded cutting inserts *ISCAR GIMY 315-UN IC8250*, tool holder *TGDL 2525-3 M* and a special chuck for precise clamping and support was used. Cutting speed 100 m/min, feed 0.02 mm/rev and shallow depth

Table 4 An overview of the fabricated specimens and their markings

CNC machined samples														
Hatch spacing	0.1050													
Orientation	0°			45°			90°		0°			45°		
Marking of samples	A1	A2	A3	B1	B2	B3	C1	C2	D1	D2	D3	E1	E2	E3
As-built samples														
0.1050							0.0525							
0°							0°							
F1		F2		F3			G1		G2			G3		

of cuts $ap = 0.2$ mm, intensive outer cooling with emulsion *CIMCOOL CIMSTAR 597* (volumetric concentration of 10–11 %, chlorine-free and intensity of 10 l/min) were used. After turning, all samples were polished with diamond pastes with grain size 5.0, 2.0, 1.0, 9.25 μm (Struers) to a glossy appearance.

3 Experimental Works, Results

3.1 Testing of Machinability of the SLM Specimens

As a criterion of machinability the specific cutting force was analysed. In general, the variable can be calculated as a ratio of principal cutting force F_c —Fig. 5—and the real chip cross section A_D :

$$k_c = \frac{F_c}{A_D} = \frac{F_c}{\iint_{\Omega} dx.dy} \tag{2}$$

The experimental machining conditions are mentioned in the Table 5. Short tubular chips were made at all cut specimens resembling standard wrought metal alloys. These test showed a strong influence of the hatch spacing and the inclination angle of the sample on the specific cutting force—Figs. 6 and 7.

3.2 Investigation of Produced Surfaces

The surface quality was investigated at each sample prior the fatigue tests. The average roughness R_a and the Abbott-Firestone curve (for the bearing areas measurements) were 6 times measured and statistically evaluated according to the standards ISO 4287 (1997) with the Alicona Infinite Focus G4 microscope.

Fig. 5 The principle of cutting tests—experimental set-up, the chip cross-section, time series of the cutting force

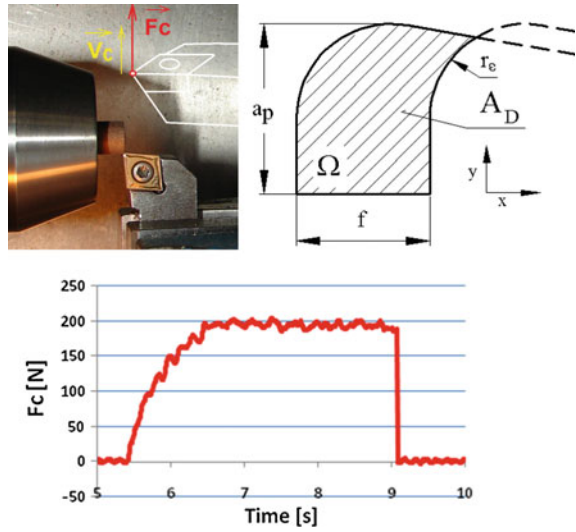


Table 5 Technological conditions for cutting tests (dry cutting)

Indexable insert	CCMT 09T304E-FM 9930 Pramet Tools	Cutting speed v_c (m/min)	100
Tool holder	PCLNR/L 2020 K 12 Pramet Tools	Feed per rotation f (mm)	0.1
Machine	SPN 12 CNC/Sinumerik 840 D	Depth of cut, a_p (mm)	0.25

Fig. 6 Specific force as function of hatch spacing and inclination angle

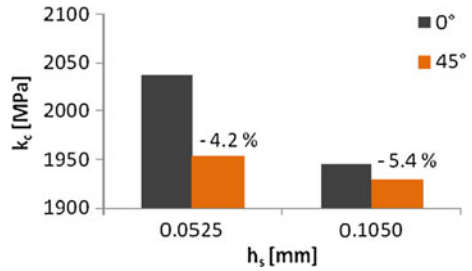
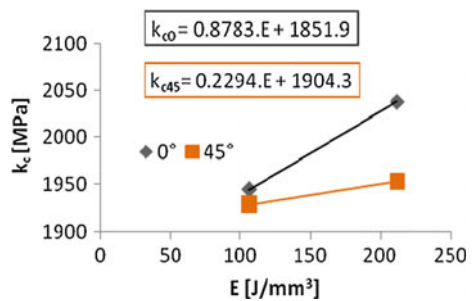


Fig. 7 Specific force as function energy density and inclination angle



The effect of hatch spacing on surface quality of the raw (as-built) specimens is shown in Figs. 8, 9, 10 and 11 and some selected measurements can be seen in Tables 6 and 7. The reduction of the spacing with the same inclination angle reflected in a non-significant deterioration of the surface.

Fig. 8 Average roughness of the raw samples

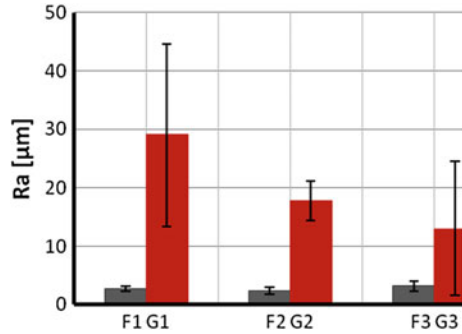


Fig. 9 The material ratios of the surfaces (means ± SD)

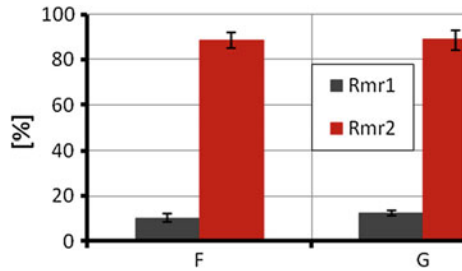


Fig. 10 Average roughness of the raw samples

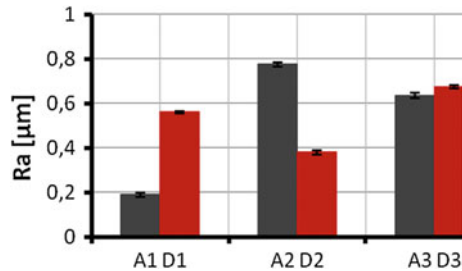


Fig. 11 The material ratios of the surfaces

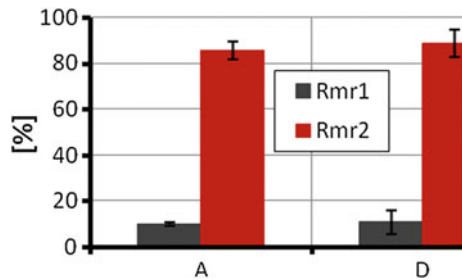
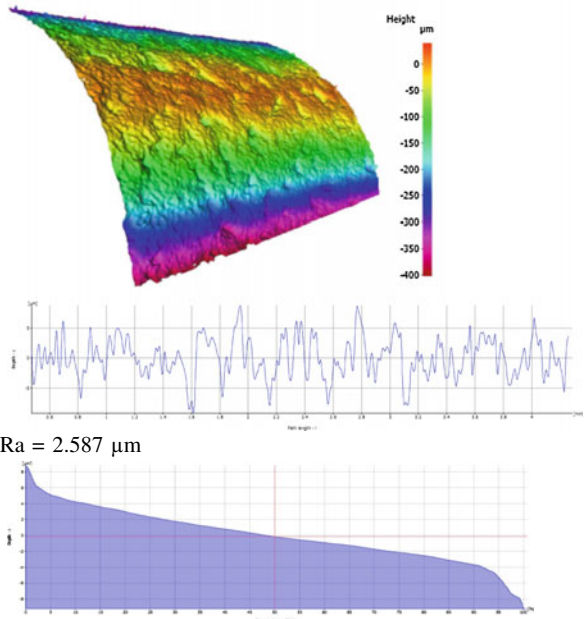


Table 6 The profile data of as-built specimens F3 ($h_s = 0.1050$ mm) and G3 ($h_s = 0.0525$ mm)

F3



G3

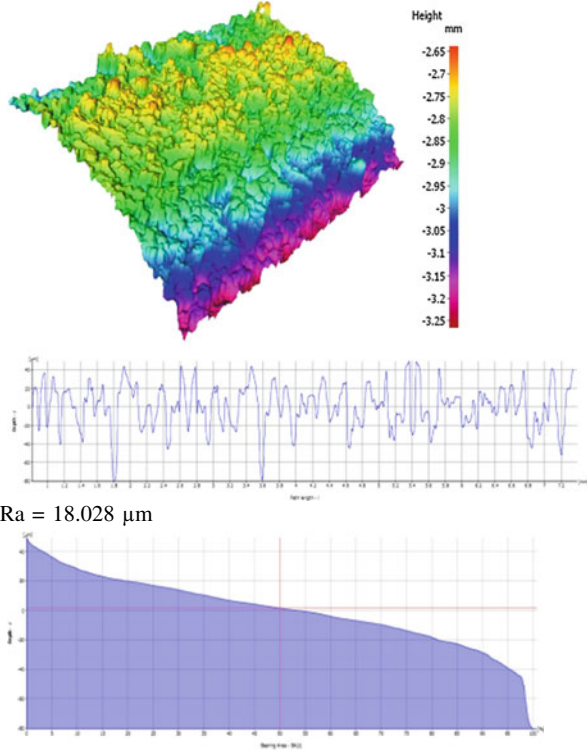
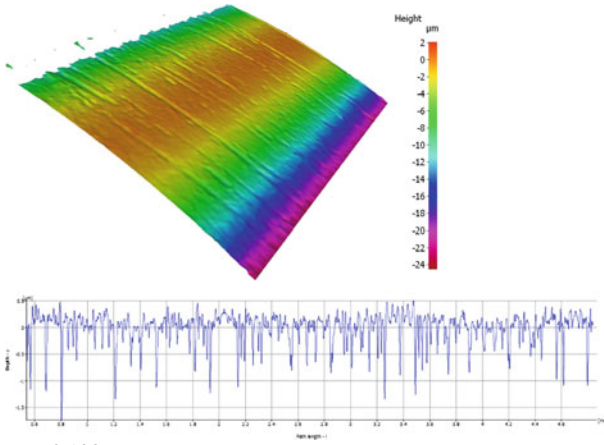
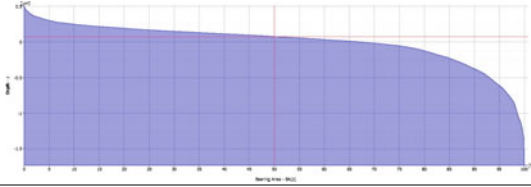


Table 7 The profile data of the machined specimens A1 (hs = 0.1050 mm) and D1 (hs = 0.0525 mm)

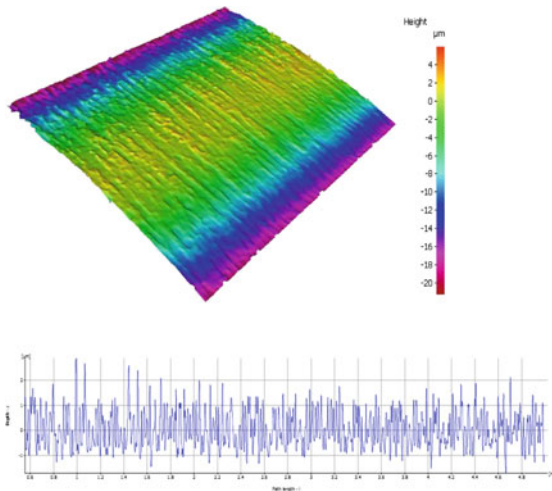
A1



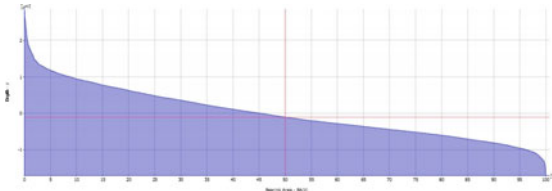
Ra = 0.198 μm



D1



Ra = 0.562 μm



The material ratios R_{mr} according to the ISO 13565-2 can be seen in Figs. 9 and 11 (similar results).

Machining and mechanical polishing of the samples according to the standards for fatigue testing ($R_a \leq 0.8 \mu\text{m}$) proved to have a very beneficial effect on the surface quality—Figs. 8, 9, 10 and 11, Tables 6 and 7.

3.3 Fatigue Testing

A specification of the specimens can be seen in Fig. 12 and Table 4. Fatigue testing was performed using the servo-hydraulic dynamic testing machine Instron 8874—Fig. 13. Testing frequency of 0.2 Hz in the lower range of testing machine was set because of unknown prediction of cycles to failure. In each series of samples different values of load amplitudes—7.7, 6.8, and 6.0 kN with the cycle asymmetry of $R = -1$ were applied. The number of cycles to failure N corresponds to a final fracture of the specimens.

Results of the series *C* were rejected because a sheared crack initiated at the contact with gripping jaws that resulted in a premature failure in the followed testing—(see Fig. 16, in the following fractography part). Final set of acceptable results was presented with 17 values.

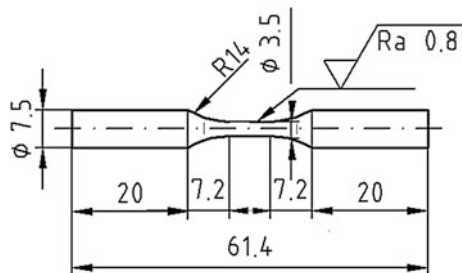
The theoretical relation for the stress amplitude σ_a and fatigue life (*S-N curve*) was supposed as:

$$\sigma_a = A \cdot N^\alpha \quad (3)$$

where A and α are constants.

The method of least squares for *S-N* curves was used. All experimental results were evaluated according to the hatch density of laser sintering and types of surface—as-built and machined. The same value of exponent α (-0.194) was found for all groups. Each group of experimental samples was characterized by corresponding coefficient A and its standard deviation (can be understood as a scatter with reliability about 68 %)—see Table 8, Figs. 14, 15 and 16.

Fig. 12 The dimensions of the tested samples



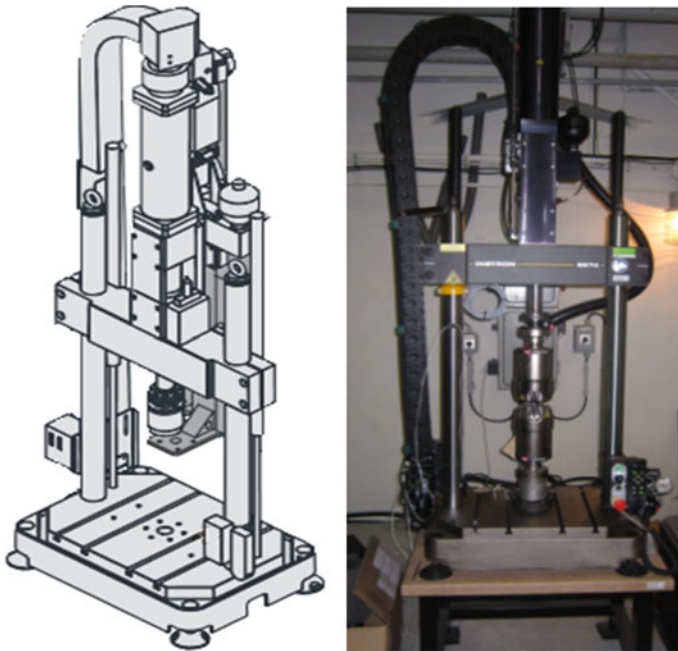


Fig. 13 The fatigue INSTRON 8874 Servohydraulic Dynamic Testing machine

Table 8 Calculated parameters of the S-N curves—Eq. (3)

Group of samples	Coefficient A (GPa)	Standard deviation (GPa)	α
hs = 0.0525 mm, as-built	3.06	± 0.08	-0.194
hs = 0.1050 mm, as-built	2.95	± 0.19	
hs = 0.0525 mm, machined, polished	3.72	± 0.15	
hs = 0.1050 mm, machined, polished	4.10	± 0.40	

3.4 Fractography of the Tested Specimens

The scanning electron microscope Tescan Mira 3GM and Alicona Infinite Focus G4 were used to investigate morphology of the fractured surfaces. A few different types of crack nucleuses were defined:

- outer nucleation, starting mainly in the places of a low surface integrity—e.g. series A, D (but also series F, G partially)—Fig. 17 and 18,

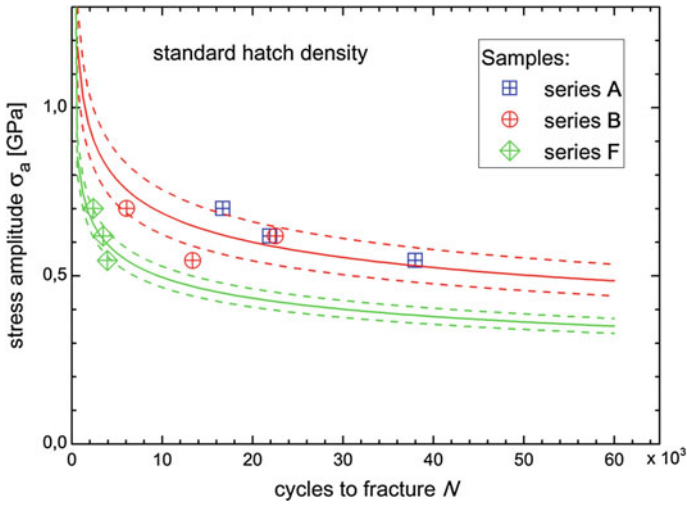


Fig. 14 Experimental data of the fatigue life tests, calculated S-N curves for polished samples (red) and as-built samples (green)

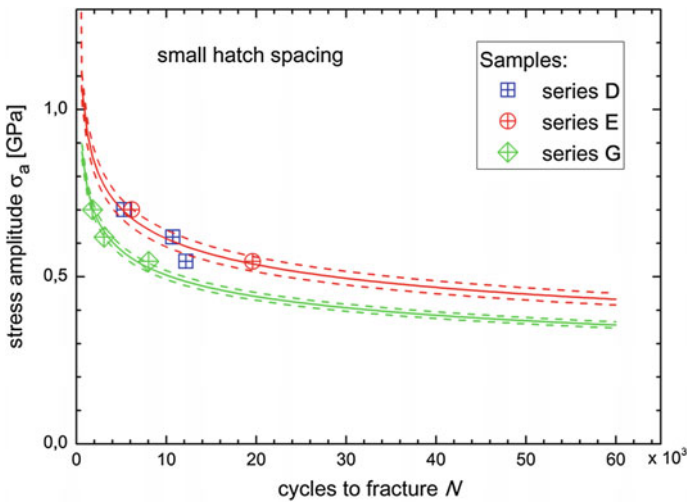


Fig. 15 Experimental data of the fatigue life tests, calculated S-N curves for polished samples (red) and as-built samples (green)

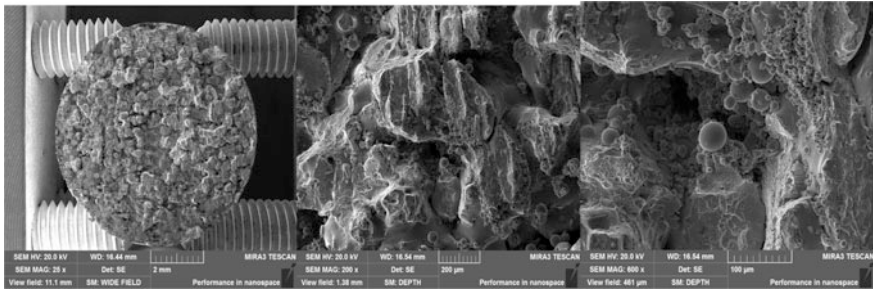


Fig. 16 The strong de-cohesion of the C2 specimen—many of non-sintered particles and intercrystalline cracks

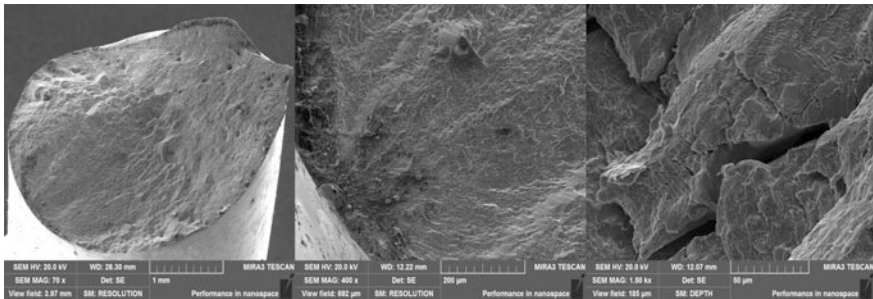


Fig. 17 The A2 specimen (a surface nucleation of the crack, regular striations)

- inner nucleation, initialized mainly in the places of non-melted zones—as-built series *F*, *G*—Fig. 19,
- a combined mechanism—series *B*, *E*.

For specimens built with higher hatch spacing 0.1050 mm (*A*, *B*, *C* and *F* (as-built)) many striations and intercrystalline cracks were observed what proved a good resistance of the material to the dynamic loading. In general, the better unions of material particles were observed, the higher similarity to mechanical loading of wrought steels was found in the view of crack propagation, formation of striations and symmetry of the fractured surfaces.

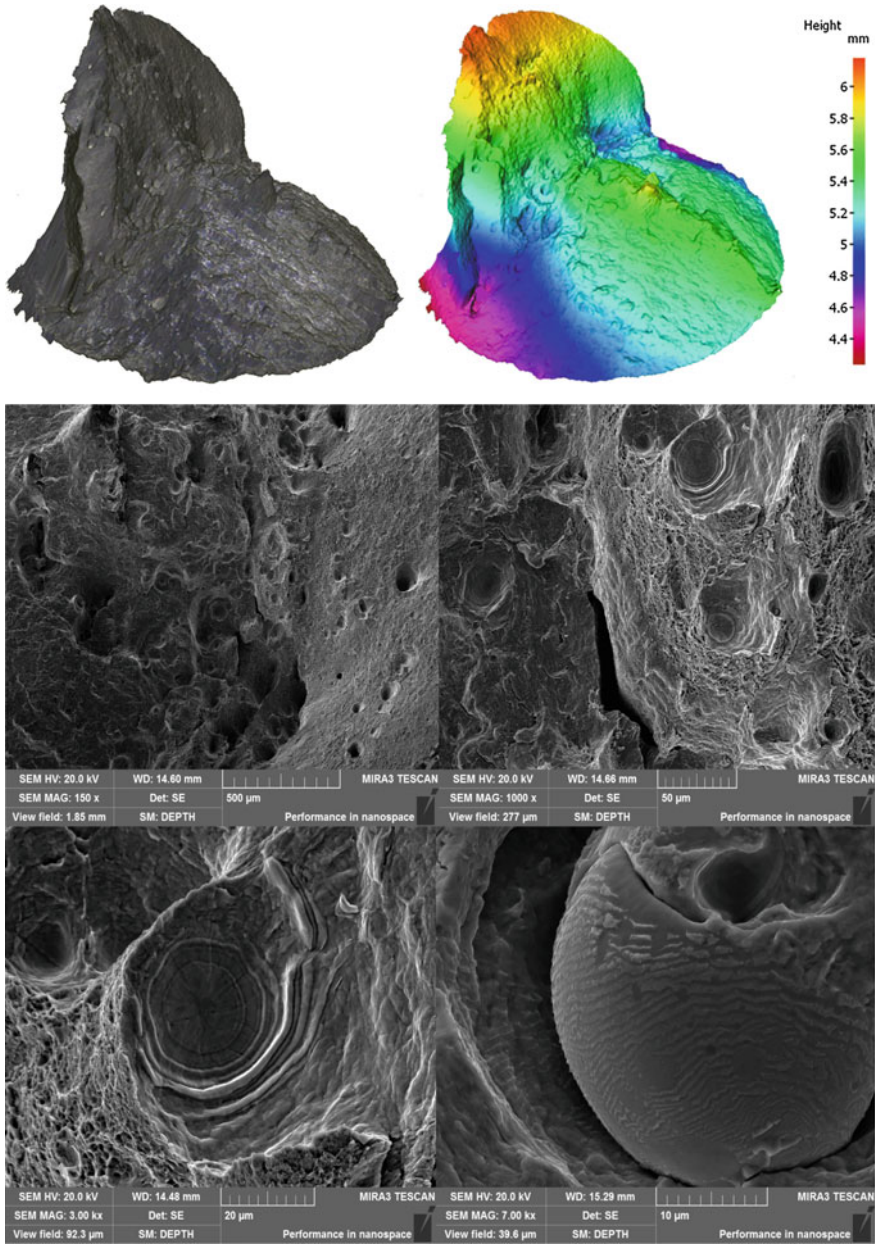


Fig. 18 The D2 specimen (a surface nucleation, striations on the powder grain borders)

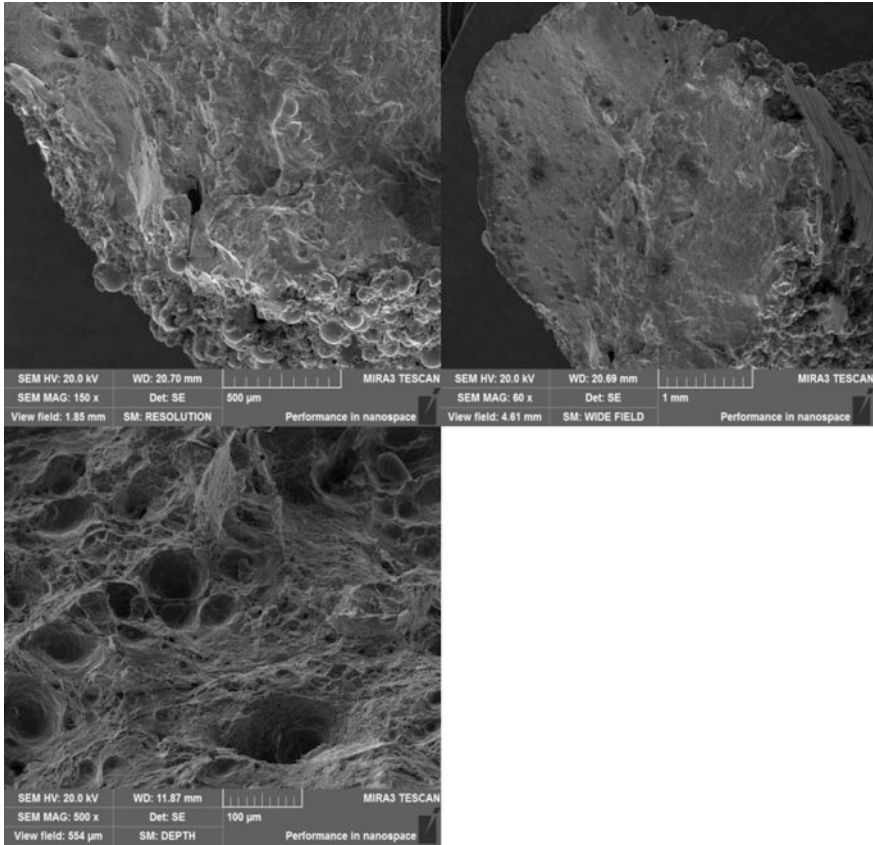


Fig. 19 The G2 specimen—a surface crack nucleation, interior craters and non-sintered powder grains

4 Discussion

The density and total amount of inserted energy showed to have an important impact on the material properties. With a higher energy density of laser beam (reached via lower hatch spacing) acting onto fabricated surface the quality of the material expressed in the fatigue values increases. However, the reduction of hatch spacing on the surface quality reflected in the significant deterioration of the surface of the raw (as-built) specimens (about ten times in average roughness), so a machining and polishing of the dynamically loaded parts is necessary. In this work the CNC machining and mechanical polishing significantly improved the quality of the surfaces and it resulted in the superior fatigue properties. However, all the polished samples showed higher fatigue lives compared to the as-built specimens but no statistically significant difference of the laser beam orientation to the

specimens have been found. The number of the specimens should be taken in considerations also.

5 Conclusions

In general, the research confirmed that the PBF process is a challenging additive manufacturing technology today. With the optimized technological strategy a material having very good mechanical and fatigue properties can be made. The machinability tests can be enhanced with a more precise specification of the surface layer (thickness, extent of deformation hardening). Next research will be devoted to a refinement of the structure with the advanced *CNC* control of the laser navigation and optimization of its power with regard to the fatigue and expected part loading.

Acknowledgments This research work was supported by the BUT, Faculty of Mechanical Engineering, Brno, Specific research 2013, with the grant “Research of advanced technologies for competitive machinery”, FSI-S-13-2138, ID 2138 and technical support of Intemac Solutions, Ltd., Kurim.

References

1. Cronskaar, M.: The use of Additive Manufacturing in the Custom Design of Orthopedic Implants, Department of engineering and sustainable development, Mid Sweden University, SE—851 70 Sundsvall, Sweden ISSN 1652–8948, Mid Sweden University Licentiate Thesis 63, ISBN 978-91-86694-42-5 (2011)
2. Vandebroucke, B., Kruth, J.P.: Selective laser melting of biocompatible metals for rapid manufacturing of medical parts. *Rapid Prototyping J.* **13**(4), 196–203. ISSN: 1355-2546
3. Boivie, K., Karlsen, R., Van der Eijk, C.: Material Issues of the Metal Printing Process. Department of Production and Quality Engineering, Norwegian University of Science and Technology, NTNU, Trondheim, Norway SINTEF Technology and Society, Product and Production, Trondheim, Norway SINTEF Materials and Chemistry, Metallurgy, Trondheim, Norway, 2011. [2.1.2014] <http://utwired.engr.utexas.edu/lff/symposium/proceedingsArchive/pubs/Manuscripts/2006/2006-19-Boivie.pdf>
4. Levy, G.N., Schindel, R., Kruth J.P.: Rapid manufacturing and rapid tooling with layer manufacturing (LM) technologies, states of the art and future perspectives. In: *Annals of the CIRP*. Elsevier Vol. 52/2/2003. pp. 589–609. ISSN: 0007-8506
5. Catalog of LaserConcept, Misan s r. o. Obráběcí stroje a nástroje, 2013. <http://www.misan.cz/pdf/-souhrny-katalog-concept-laser/>. Accessed 21 Nov 2013
6. Sherekar, R.M., Pawar, A.N.: Design and manufacturing of customized anatomical implants by using Rapid Prototyping technique, August 12, 2011, *BIOINFO Mechanical Engineering*, vol. 1, Issue 1, 2011, pp. 01–05, <http://www.bioinfo.in/contents.php?id=180>
7. Leuders, S., Thone, M., Riemer, A., Niendorf, T., Troster, T., Richard, H., Maier, J.: On the mechanical behaviour of titanium alloy Ti-al6-v4 manufacture by selective laser melting: fatigue resistance and crack growth performance. *Int. J. Fatigue* **48**, 300–307 (2013)
8. Boivie, K.: An overview of processe and materials. Dagen Kista. <http://3dp.se/wp-content/uploads/2013/09/Klas-Boivie-Sintef.pdf>. Accessed 19 Sep 2013

9. Hunt, J., Derguti, F., Todd I.: Selection of steels suitable for additive layer manufacturing. Institute of Materials, Minerals and Mining Published by Maney on behalf of the Institute, Ironmaking and Steelmaking. 2014, vol. 41, No 4, p. 255 doi:10.1179/0301923314Z.00000000269
10. Slotwinski, J.A., Garboczi, E.J., Stutzman, P.E., Ferraris, C.F., Watson, S.S., Peltz, M.A.: Characterization of Metal Powders Used for Additive Manufacturing. National Institute of Standards and Technology Gaithersburg MD 20899. *J. Res. Nat. Inst. Stand. Technol.* **119** (2014)
11. Kruth, J.-P., Badrossamay, M., Yasa, E., Deckers, E., Thijs, L., Van Humbeeck, J: Part and material properties in selective laser melting of metals. In: 16th International Symposium of Electromachining
12. Read, N., Wang, W., Essa, K., Attallah, M.M.: Selective laser melting of AlSi10 Mg alloy: process optimisation and mechanical properties development. *Mater. Des.* **65**, 417–442 (2015)
13. Dai, D., Gu, D.: Tailoring surface quality through mass and momentum transfer modeling using a volume of fluid method in selective laser melting of TiC/AlSi10 Mg powder. *Int. J. Mach. Tools* **88**(0), 95–107, 2015. ISSN: 0890-6955
14. Vaithilingam, J., Kilsby, S., Goodridge, R.D., Christie, D.R., Edmondson, S., Hague, R.J.M.: Functionalisation of Ti6Al4 V components fabricated using selective laser melting with a bioactive compound. *Mater. Sci. Eng., C* **46**, 52–61 (2015)
15. Wang, T., Zhu, Y.Y., Zhang, S.Q., Tang, H.B., Wang, H.M.: Grain morphology evolution behavior of titanium alloy components during laser melting deposition additive manufacturing. *J. Alloy. Compd.* **632**, 505–513 (2015)
16. Zhu, Y., Tian, X., Li, J., Wang, H.: Microstructure evolution and layer bands of laser melting deposition Ti–6.5Al–3.5Mo–1.5Zr–0.3Si titanium alloy. *J. Alloy. Compd.* **616**, 468–474 (2014)
17. Luo, J., Pan, H., Kinzel, E.C.: Additive manufacturing of glass. *J. Manuf. Sci. Eng.* **136** (2014). doi:10.1115/1.4028531
18. Dai, D., Gu, D.: Thermal behavior and densification mechanism during selective laser melting of copper matrix composites: simulation and experiments. *Mater. Des.* **55**, 482–491 (2014)
19. Luecke, W.E., Slotwinski, J.A.: Mechanical Properties of Austenitic Stainless Steel Made by Additive Manufacturing. National Institute of Standards and Technology, vol. 119. 2014
20. Hunt, J., Derguti, F., Todd, I., Institute of Materials, Minerals and Mining Published by Maney on behalf of the Institute, Ironmaking and Steelmaking, vol. 41. 2014. doi:10.1179/0301923314Z.00000000269
21. Furumoto, T., Koizumi, A., Alkahari, M.R., Anayama, R., Hosokawa, A., Tanaka, R., Ueda, T.: Permeability and strength of a porous metal structure fabricated by additive manufacturing. *J. Mater. Process. Technol.* **219**, 10–16 (2015)
22. Kempena, K., Yasaa, E., Thijsb, L., Kruth, J.-P., Van Humbeeck, J.: Microstructure and mechanical properties of Selective Laser Melted 18Ni-300 steel. *Sci. Dir. Phys. Procedia* **12**, 255–263 (2011)
23. Jamshidinia, M., Sadek, A., Wang, W., Kally, S.: Additive manufacturing of steel alloys using laser powder-bed fusion. *Adv. Manuf. Adv. Mater. Process.* (2015)
24. Chery, J.A., Davies, H.M., Mehmood, S., Lavery, N.P., Brown, S.G.R., Sienz, J.: Investigation into the effect of process parameters on microstructural and physical properties of 316L stainless steel parts by selective laser melting. *Int. J. Adv. Manuf. Technol.* **76**, 869–879 (2015). doi:10.1007/s00170-014-6297-2
25. Ziolkowski, G., Chlebus, E., Szymczyk, P., Kurzac, J.: Application of X-ray CT method for discontinuity and porosity detection in 316L stainless steel parts produced with SLM technology. *Arch. Civil Mech. Eng.* **14**, 608–614 (2014)
26. Gu, H., Gong, H., Pal, D., Rafi, K., Starr, T., Stucker, B.: Influences of Energy Density on Porosity and Microstructure of Selective Laser Melted 17-4PH Stainless Steel. Department of Industrial Engineering, Department of Chemical Engineering, J. B. Speed School of Engineering, University of Louisville, Louisville, KY 40292. <http://utwired.engr.utexas.edu/fff/symposium/proceedingsArchive/pubs/Manuscripts/2013/2013-37-Gu.pdf>

27. Mahamood, R.M., Akinlabi, E.T., Shukla, M., Pityana, S.: Characterizing the effect of laser power density on microstructure, microhardness, and surface finish of laser deposited titanium alloy. *J. Manuf. Sci. Eng.* **135**(064502-1). <http://manufacturingscience.asmedigitalcollection.asme.org/>
28. Edwards, P., O'Conner, A., Ramulu, M.: Electron beam additive manufacturing of titanium components: properties and performance. *J. Manuf. Sci. Eng.* **135**(061016-7), ISSN: 1087-1357. <http://manufacturingscience.asmedigitalcollection.asme.org/>. Accessed 27 Jan 2014
29. Stamp, R., Sutcliffe, C., Fox, P., O'Neill, W., Jones, E.: *The development of a Scanning Strategy for the Manufacture of Porous Biomaterials by Selective Laser Melting*. Springer Science + Business Media, LLC 2009, Published online: 18 June 2009. ISSN 1573-4838
30. Verhaeghe, L.T.F., Craeghs, T., Humbeeck, J.V., Kruth, J.-P.: A study of the microstructural evolution during selective laser melting of Ti-6Al-4 V, Katholieke Universiteit Leuven, Department of Metallurgy and Materials Engineering, Department of Mechanical Engineering, Leuven, Belgium, [26.02.2014]. file:///C:/Users/Pav1%20C3 %20ADna/Documents/BAKALARKA/Bovie%20Klas/A%20study%20of%20the%20microstructural%20evolution%20during%20selective%20laser%20melting.pdf. Accessed Mar 16 2010
31. Marlok Metso Powdermet, Material Technology Solution. [http://www.metso.com/MEP/info.nsf/WebWID/WTB-051025-22570-3FF66/\\$File/Marlok%20brochure%202005.pdf](http://www.metso.com/MEP/info.nsf/WebWID/WTB-051025-22570-3FF66/$File/Marlok%20brochure%202005.pdf)
32. Loeber, L., Biamino, S., Ackelid, U., Sabbadini, S., Epicoco, P., Fino, P., Eckert, J.: Comparison of Selective Laser and Electron Beam Melted Titanium. In: *Solid freeform fabrication proceedings*. Austin: University of Texas, 2011. pp. 547–556, ISSN 1053-2153
33. Casalino, G., Campanelli, S.L., Contuzzi, N., Ludovico, A.D., Experimental investigation and statistical optimisation of the selective laser melting process of a maraging steel. *Optics Laser Technol.* **65**, 151–158 (2015)

Transferability of Fracture Toughness with Constraint

Guy Pluinage, Julien Capelle and Mohamed Hadj Meliani

Abstract Constraint approaches to transferability of fracture toughness are examined. The different constraint parameters are defined and discussed. Special attention is given to the actual trends to use the plastic constraint in the Material Failure Master Curve (MFMC) and the Material Transition Temperature Master Curve (MTTMC).

1 Introduction

Mechanical properties are not intrinsic to material but depend on geometrical factors such as the specimen geometry, thickness, surface roughness and length, defect geometry such as the relative length, radius, or opening angle, loading mode, and environment.

Material properties available from data banks are therefore to be considered as reference material properties, as results from standard tests. To use these reference properties for a structure and component which differ in terms of geometry and loading mode, a correction needs to be made, which is called transferability.

The properties to be used in a structure P_{struct} are deduced from the reference properties $f(p)$ and the transferability function $f(p)$, where p is the transferability parameter.

$$P_{struct} = P_{ref} \cdot f(p) \tag{1}$$

G. Pluinage (✉)
FM.C 57530 Silly Sur-Nied, France
e-mail: pluinage@cegetel.net

J. Capelle
LaBPS – ENIM, 1 route d’Ars Laquenexy, CS, 65820, 57078 Metz, France

M. Hadj Meliani
LPTPM, FT, Hassiba BenBouali University of Chlef, Esalem City, 02000 Chlef, Algeria

For fractures emanating from a defect where fracture mechanics can be applied, the transferability is sometimes treated with the concept of characteristic length or scale factor [1] but more often by using the stress constraint or the relative stress gradient. These transferability parameters emanate from the defect tip distribution (notch or crack). If we compare the stress distribution obtained in a reference situation (generally small scale yielding) with another general one, the stress distribution is modified in two ways: there is a shift of the stress distribution and a small rotation. These modifications of the stress distribution are considered as transferability problems. The shift of the stress distribution is introduced into the plastic constraint, which is used as the transferability parameter. In the literature, we can note the following constraint parameters: the plastic constraint factor L [2], the stress triaxiality β [3], the Q parameter [4], T stress [5] and A_2 [6].

In this paper, the different constraint parameters are defined and discussed. Special attention is given to the plastic constraint in the Material Failure Master Curve (*MFMC*) and the Transition Temperature Master Curve (*TTMC*).

2 Constraints at Defect Tip

Constraint is considered as a modification of the defect tip distribution under the effects of specimen or defect geometries or loading mode. Different constraint parameters are defined and associated with the defect type or stress-strain behaviour.

2.1 Singular Elastic Stress Distribution

For a notch with infinite acuity, Williams [7] has given a solution for elastic stress distribution as the following series:

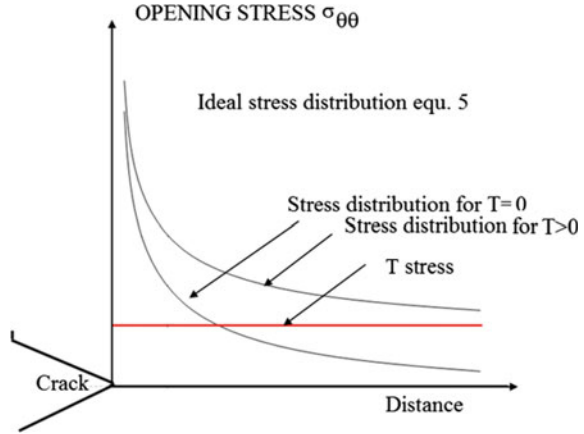
$$\sigma_{ij} = \sum_{n=1}^{\infty} R_e [A_n r^{\lambda_n - 1} f_{ij}(\lambda_n, \theta)]_{i,j} = r, \theta \quad (2)$$

For a crack, Larson et al. [8] have suggested describing the elastic stress field at the crack tip by three terms and introduce for the first time the T term as the second one of the series:

$$\sigma_{ij} = \frac{K_{ij}}{\sqrt{2\pi r}} f_{ij}(\theta) + T \delta_{1i} \delta_{1j} + O\sqrt{r} \quad (3)$$

Therefore, ideally T stress is a constant stress which acts along the crack direction and shifts the opening stress distribution according to the sign of this

Fig. 1 Ideal T stress distribution and shift of opening stress distribution by T stress



stress (Fig. 1). For stress distribution emanating from a blunted crack or notch, T stress is not constant along the ligament. This leads to consider a conventional value defined as the effective T stress.

2.2 Singular Elastic-Plastic Stress Distribution

The power-law expansion of the elastic-plastic *HRR* [8] field if higher-order singular or non-singular terms are considered is represented by:

$$\sigma_{ij}(r, \theta) = \hat{A}_1 \left[\left(\frac{r}{l}\right)^{s_1} : f_{ij}^{(1)}(\theta) + \hat{A}_2 \left(\frac{r}{l}\right)^{s_2} : f_{ij}^{(2)}(\theta) + \hat{A}_2^2 \left(\frac{r}{l}\right)^{2s_2-s_1} : f_{ij}^{(3)}(\theta) \right] + \dots \quad (4)$$

with $s_1 = -1/(N + 1)$ and $\hat{A}_1 \sim J^{1/(N+1)}$, where N is the hardening exponent according to the Ramberg-Osgood constitutive equation, s_2 is the exponent of the second singular or non-singular term, J is a path integral, and l is a reference length.

O’Dowd and Shih [9] have simplified this formula. Considering strain hardening exponent values in the range $5 \leq N \leq 20$, the angular functions $f_{\theta\theta}$ and f_{rr} are equivalent and constant $f_{\theta\theta} \approx f_{rr} \approx \text{constant}$, and the value of $f_{r\theta}$ is negligible when compared with $f_{\theta\theta}$ ($f_{\theta\theta} \gg f_{r\theta}$) for $|\theta| < \pi/2$. The stress field is therefore described by:

$$\sigma_{ij} = \left(\frac{J}{B_0 I_n r} \right)^{\frac{1}{n+1}} f_{ij}(\theta, n) + Q \left[\frac{r}{J/\sigma_0} \right]^q f_{ij}(\theta, n) + \dots \quad (5)$$

B_0 and I_n are constants for fixed values of $f(\theta, n)$ and n , q is a parameter close to zero ($q \approx 0$) and σ_0 is the reference stress. The Q parameter is called the amplitude factor of the second-order field or simply Q .

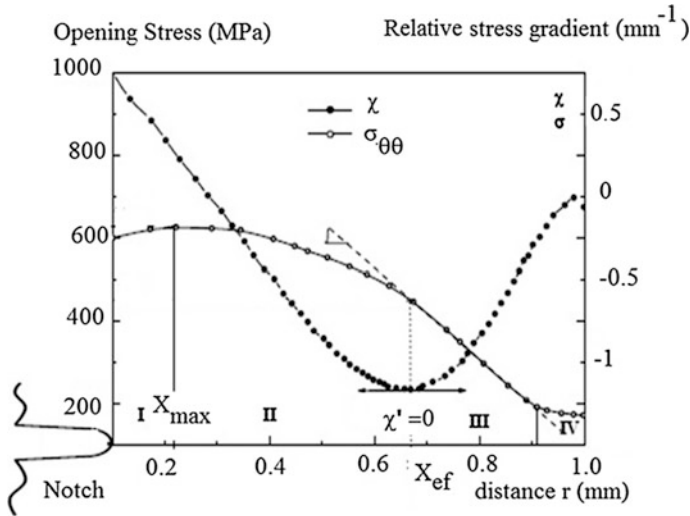


Fig. 2 Elastic-plastic stress distribution and definition of the effective distance from the minimum of the relative stress gradient

2.3 Non-singular Elastic and Elastic Plastic Stress Distribution

The opening stress at the notch tip exhibits a more complex distribution. The stress increases until it reaches a maximum, which occurs behind the notch tip at distance X_{max} . At distance X_{ef} (the effective distance), the distribution is governed by a power law with an exponent close to those given by the elastic stress distribution of Williams [7]. In Fig. 2, zone III represents precisely this zone, where the stress distribution exhibits a linear behaviour in the bi-logarithmic diagram and is governed by the notch stress intensity factor. In zone IV, the stress distribution decreases until it reaches the gross stress level. The effective distance X_{ef} corresponds to the minimum of the relative stress gradient.

3 The Different Constraint Parameters

To assess the effect of geometry and loading mode on fracture toughness, different two-parameter concepts are applied as $K - T$ stress- and $J - A_2$ -concepts based on a rigorous description of the asymptotic fields as well as the phenomenological $J - Q$ and $J - \beta$ concepts using the Q parameter and the stress triaxiality β as secondary fracture parameters.

3.1 T Stress

The stress distribution ahead of a crack tip depends on the polar angle θ , as we can see in Eq. (2). However for some particular θ angles, the T stress is given by particular values of the difference between the opening stress σ_{yy} and the stress parallel to the crack σ_{xx} (see Table 1).

Particularly for $\theta = 0$, the T stress is given by:

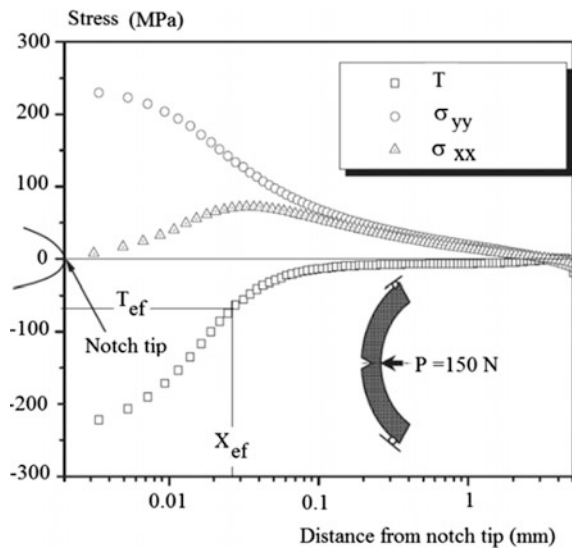
$$T = (\sigma_{xx} - \sigma_{yy})_{\theta=0} \tag{6}$$

Equation (8) is the basis of the so-called stress difference method, which was proposed by Yang et al. [10]. The stress distribution in the direction $\theta = 0$ is generally computed by the finite element method. An example of the computed T stress distribution along the ligament for a Roman tile specimen with a notch is given in Fig. 3. It can be seen that T is not really constant as it is in theory. For short cracks, distribution of the T stress is stabilized after some distance. For long cracks, T increases linearly with the ligament except in a region close to the crack tip. To avoid this dependence of the T stress on distance, it is attractive to use a conventional definition of the effective T stress.

Table 1 T stress values according to polar direction θ

$\theta = 0$	$\theta = \pm \frac{\pi}{2}$	$\theta = \pm \frac{\pi}{3}$	$\theta = \pm \frac{\pi}{2}$	$\theta = \pm \frac{2\pi}{3}$
$T = \sigma_{xx} - \sigma_{yy}$	$T = \sigma_{xx}$	$T = \frac{\sigma_{xx} - \sigma_{yy}}{3}$	$T = \frac{\sigma_{xx} - \sigma_{yy}}{3}$	$T = \sigma_{xx} - \sigma_{yy}$

Fig. 3 T stress evolution with distance for a Roman tile specimen. Values of T_{ef} parameter obtained by extrapolation or volumetric methods



Using the volumetric method, Hadj Meliani et al. [5], suggested defining the effective Tstress as the corresponding value in the Tstress distribution for a distance equal to the effective distance X_{ef} . Figure 5 gives the Tstress evolution with distance for a Roman tile specimen and the definition of T_{ef} . One notes that in these cases the values of T_{ef} obtained by extrapolation or the volumetric method is relatively close. In the following, the T_{ef} parameter obtained from the critical stress distribution is called $T_{ef,c}$.

3.2 Q Parameter

In Eq. (5) the J -integral sets the size scale over which high stresses develop while the second parameter, Q , quantifies the level of some stress shift at distances of a few $CTODs$ ahead of the crack tip; such a dimension defines the physically relevant length scale of the fracture process zone X_{ef} .

The constraint has been defined by Dodds et al. [11] using the Q parameter. This parameter is defined as the difference between the opening stress level for a given geometry or loading mode and a reference situation with generally small scale yielding (ssy) divided by the reference stress σ_0 .

$$Q = \frac{\sigma_{\theta\theta} - (\sigma_{\theta\theta})_{ssy}}{\sigma_0} \quad (7)$$

O'Dowd and Shih [12] showed that Q corresponds effectively to a spatially uniform hydrostatic stress and represents the relative difference between the high triaxiality reference stress field and that of the fracture specimen. Q is defined at a non-dimensional distance of $(\sigma_0 \cdot r)/J = 2$. In order to fulfil the condition of a spatially uniform Q , it is necessary that the reference and the studied stress field be homothetic. The following conditions are added for a correct determination of Q :

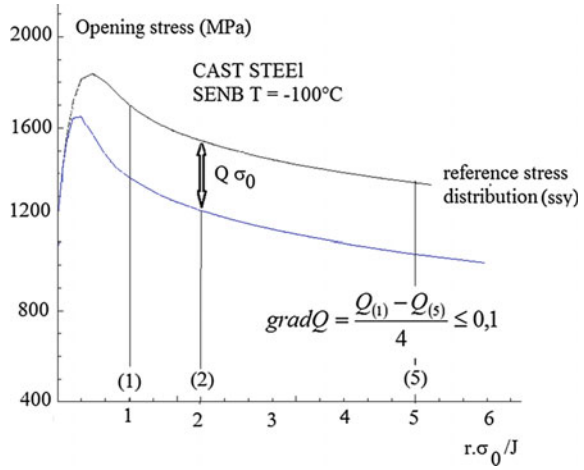
$$gradQ = \frac{Q_{(1)} - Q_{(5)}}{4} \leq 0, 1 \quad (8)$$

where $Q_{(1)}$ and $Q_{(5)}$ are Q values determined respectively at the non-dimensional distances 1 and 5 (Fig. 4).

3.3 Stress Triaxiality

The stress triaxiality β is also used as a measure of the constraint and leads to the two-parameter fracture mechanics approach $K - \beta$ or $J - \beta$. Stress triaxiality is chosen as a transferability parameter because ductile fracture is sensitive to this parameter through void growth [13] as well as cleavage stress for brittle fracture

Fig. 4 Definition of Q parameter and validity condition



[14]. This parameter is defined as the ratio of the hydrostatic stress over the equivalent von Mises stress.

$$\beta = \frac{\sigma_h}{\sigma_{VM}} \tag{9}$$

where:

$$\sigma_h = \frac{\sigma_{xx} + \sigma_{yy} + \sigma_{zz}}{3} \tag{10}$$

and:

$$\sigma_{VM} = \frac{1}{\sqrt{2}} \sqrt{(\sigma_1 - \sigma_3)^2 + (\sigma_1 - \sigma_2)^2 + (\sigma_2 - \sigma_3)^2} \tag{11}$$

The critical stress triaxiality distribution at the notch tip increases until it reaches a maximum, which for the critical event is called $\beta_{max,c}$ and corresponds to the distance $X_{\beta_{max,c}}$. After that, it decreases, then sometimes increases again, and finally falls to zero when the distance is far from the notch tip.

The maximum critical stress triaxiality is sensitive to the notch radius and ligament size. It decreases practically linearly with the notch radius and increases with relative notch depth [15]. It has been noted that the maximum triaxiality always occurs inside the fracture process zone since $X_{\beta_{max,c}}^{\beta_c}$ remains lower than or equal to the critical effective distance $X_{ef,c}$ [15].

With an increase of the relative notch depth, the position of maximum stress triaxiality approaches or reaches the limit of the fracture process zone. According to [15], the maximum stress triaxiality parameter is not the most suitable constraint parameter to explain the modification of fracture toughness with ligament size or

thickness. An improvement has been made using the effective critical stress triaxiality $\beta_{ef,c}$. This parameter is defined as the average value of the critical stress triaxiality over the critical effective distance $X_{ef,c}$.

$$\beta_{ef,c} = \frac{1}{X_{ef,c}} \int_0^{X_{ef,c}} \beta(x) dx \tag{12}$$

4 Influence of Constraint on Fracture Toughness

Eisele et al. [16] pointed out that the fracture toughness K_c or J_c increases with the loss of constraint T stress or Q .

This can be seen in Fig. 5, where the $J_c - Q$ locus of a low carbon manganese cast steel is plotted [17]. Three-point bending tests were used for fracture behaviour determination. Fracture toughness was determined using three test specimen geometries. The first one was the standard three point bend specimen $25 \times 50 \times 220$ mm with a ratio $a/W = 0.5$. The other ones were selected to receive shallow cracks (specimen 1: $a/W = 0.1$; $25 \times 30 \times 130$ mm; specimen 2: $a/W = 0.2$; $25 \times 27 \times 120$ mm). The stress distribution using the standard method for Q -parameter determination was computed by the finite element method at load level corresponding to the fracture force.

One notes that the fracture toughness decreases when the constraint increases; that is, the Q -parameter increases (Fig. 6).

Fig. 5 J_c - Q locus of a low carbon manganese cast steel [17]

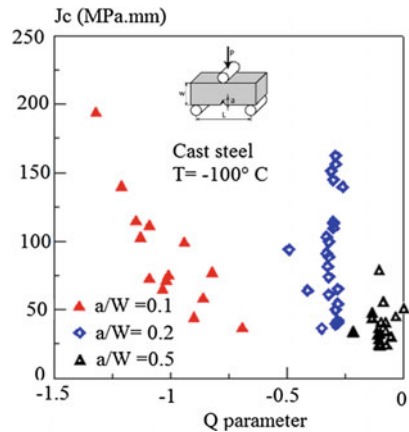
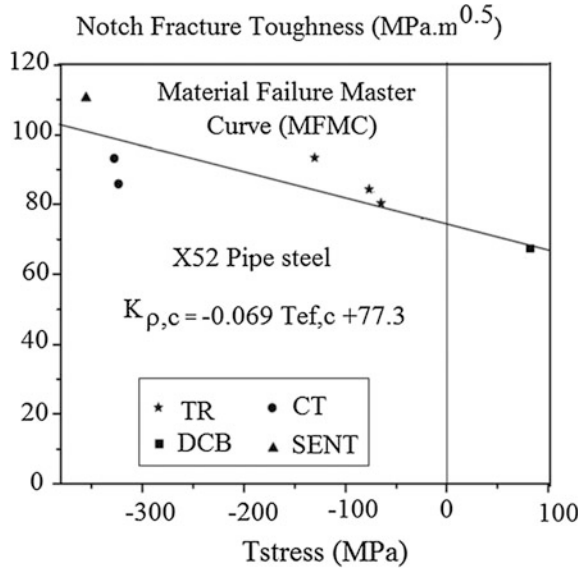


Fig. 6 $K_{\rho,c}$ - $T_{ef,c}$ locus of a low carbon manganese cast steel [5]



Hadj Meliani et al. [5] have also pointed out this effect on the notch fracture toughness $K_{\rho,c}$ with the critical constraint described by the T_{ef} -parameter. The material used in this study is API X52 steel.

Several specimens of four types, namely *CT*, *DCB*, *SENT*, and *RT*, were extracted from a steel pipe of diameter 610 mm. The geometries of these specimens were as follows:

- *SENT* specimen: thickness = 5.8 mm, width = 58.40 mm;
- *CT* specimen: thickness = 5.8 mm, width = 63.80 mm, height = 61 mm;
- *DCB* specimen: thickness = 5.8 mm, height = 45.70 mm;
- *RT* specimen: thickness = 5.8 mm, width = 40 mm, length = 280 mm.

The specimens have a notch with a notch angle $\psi = 0$, a notch radius $\rho = 0.25$ mm and a/W ratio in the range 0.3–0.6. The stress distribution used was computed by the finite element method at a load level corresponding to the fracture force. $T_{ef,c}$ was determined by the volumetric method. It can be noted in Fig. 6 that the fracture toughness decreases linearly with the constraint according to:

$$K_{\rho,c} = aT_{ef,c} + K_{\rho,c}^0 \tag{13}$$

where $K_{\rho,c}^0$ is the fracture toughness corresponding to $T_{ef,c} = 0$, which is considered as a reference. $a = -0.069$ and $K_{\rho,c}^0 = 77.2 \text{ MPa}\sqrt{\text{m}}$ for the API X52 pipe steel.

5 Influence of Constraint on Transition Temperature

Wallin [18] has established a new *MFMC*, where the fracture toughness K_c is a function of the temperature T and the T stress. The standard master curve K_0 corresponding to a reference temperature T_0 has the form:

$$K_0 = 31 + 77 \exp(0.019 \cdot [T - T_0]) \quad (14)$$

T_0 is the transition temperature corresponding to a conventional value of fracture toughness of $100 \text{ MPa}\sqrt{\text{m}}$. Materials that have a similar exponential evolution of fracture toughness with temperature T are characterized by a single parameter T_0 .

In order to account for the constraint effect in the *MFMC*, Wallin [18] assumed that the reference temperature is constraint dependent. A linear relation was found between the reference temperature T_0 and the T_{stress} .

$$T_0(T_{stress}) = T_{0,ref} + \frac{T_{stress}}{10} \cdot \frac{^{\circ}\text{C}}{\text{MPa}} \quad \text{for } T_{stress} > 0 \quad (15)$$

$T_{0,ref}$ is the reference temperature for a reference constraint as obtained for small scale yielding or for $T_{stress} = 0$.

More generally, Wallin [19] proposed:

$$T_0 = T_{0,T=0} + \frac{AT_{stress}}{\sigma_y} \quad (16)$$

A is a new parameter, T_0 assess the validity of Eq. (31), Hohe et al. [20] presented the results of fracture resistance of nuclear grade 22 *NiMoCr 3-7* pressure vessel steel as a linear regression analysis of both the fracture toughness K_{Ic} and the respective secondary fracture parameter Y (T_{stress}/σ_0 , Q , A_2 or β respectively).

$$T_0 = c \cdot Y + d \quad (17)$$

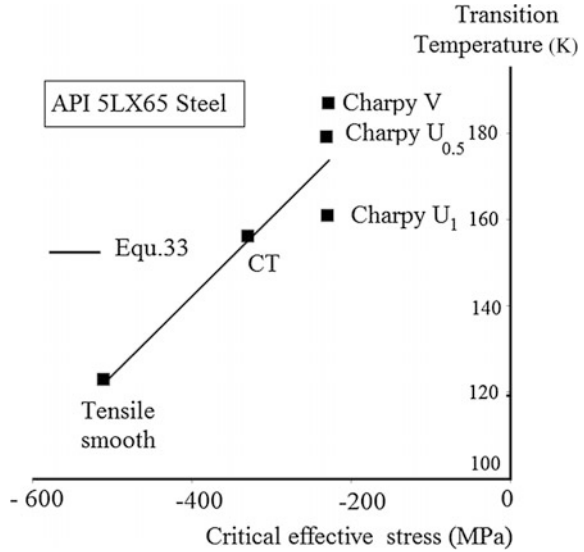
A similar relation was found for *X65* pipe steel by Coseru et al. [21] between various transition temperatures T_t ($T_{t,tensile}$, T_0 , and $T_{K1/2}$) and the critical effective T stress, $T_{ef,c}$.

$$T_t = T_{t,T_{ef,c}=0} + 0.14 T_{ef,c} \quad (18)$$

This equation represents the Material Transition Temperature Master Curve (*MTTMC*) $T_t = f(T_{ef,c})$, which is the key to determining the appropriate reference transition temperature by comparison with the structure transition temperature.

In Fig. 7, the determination of the *MTTMC* of *API X65* pipe steel was done using three specimen types (tensile, *CT*, and Charpy) [21]. Different Charpy specimens were used: Charpy V specimens (V notch, notch radius $\rho = 0.25 \text{ mm}$, notch depth $a = 2 \text{ mm}$), Charpy U_1 (U notch, notch radius $\rho = 1 \text{ mm}$, notch depth $a = 5 \text{ mm}$),

Fig. 7 The MTTMC of API X65 pipe steel [21]



and Charpy $U_{0.5}$ (U notch, notch radius $\rho = 0.5$ mm, notch depth $a = 5$ mm), and the transition temperatures of the Charpy specimens were corrected to take into account the influence of the loading rate.

The *MFMC* was modified by Wallin. By combining (14) with (15), he obtains:

$$K_0 = 31 + 77 \exp\left(0.019 \left[T - T_{0, T_{stress}=0} - \frac{T_{stress}}{12 \text{ MPa } / ^\circ\text{C}} \right] \right) \quad (19)$$

6 Conclusion

Most of the problems of transferability in fracture toughness can be treated with the help of a constraint parameter or a characteristic length.

T stress according to its definition is only used for elastic situations but is often extended to elastic plastic fracture.

Q is used only for elastic plastic fracture. We have seen that for pure brittle fracture, the Q parameter reduces to a relative difference of fracture toughness K_{Ic} (Eq. 15).

L is used strictly for plastic collapse in order to calculate limit load. Stress triaxiality β is used for any stress strain behaviour.

Determination of T stress needs only a single fracture test. This is an advantage compared with the Q parameter. A second advantage is that it can be determined numerically or experimentally. This is particularly interesting in the case of a complex part of a structure. The major difficulty with the T stress concept is that

T stress is not constant along a ligament ahead of a defect. Therefore a conventional value is needed. It has been proposed to use the effective distance [10] or extrapolation of the T stress evolution to origin but these two definitions are not always in agreement.

The distance where the Q parameter is determined, depends on an idea of the relative shift of the opening stress distribution at defect tip. It suffers from the following problems:

its definition is purely conventional at a non-dimensional distance of $(\sigma_0 \cdot r/J = 2)$ which rarely corresponds to the characteristic or the effective distance.

Q is valid with a condition of homothety of the stress distribution given by Eq. 13. For low strength steels, this condition is not generally fulfilled. Q determination needs two tests, the second as reference, which has to be performed according to small-scale yielding conditions. This is not easy to realise if the material does not have the required thickness.

References

1. Chechulin, B.B.: Influence of specimen size on the characteristic mechanical value of plastic fracture (in Russian). *Zhur. Tekh. Fiz.* **24**, 1093–1100 (1954)
2. Mouwakeh, M., Pluvinage, G., Masri, S.: Failure of water pipes containing surface cracks using limit analysis notions. *Res. J. Aleppo. Univ. Eng. Sci. Ser.* **63** (2011)
3. Henry, B.S., Luxmore, A.R.: The stress triaxiality constraint and the Q-value as a ductile fracture parameter. *Eng. Fract. Mech.* **57**, 375–390 (1997)
4. Ruggieri, C., Gao, X., Dodds, R.H.: Transferability of elastic–plastic fracture toughness using the Weibull stress approach: significance of parameter calibration. *Eng. Fract. Mech.* **67**, 101–117 (2000)
5. Hadj Meliani, M., Matvienko, Y.G., Pluvinage, G.: Two-parameter fracture criterion (K_p, χ - $T_{ef,c}$) based on notch fracture mechanics. *Inter. J. Fract.* **167**, 173–182 (2011)
6. Williams, M.L.: On the stress distribution at the base of stationary Crack. *ASME J. Appl. Mech.* **24**, 109–114 (1957)
7. Larsson, S.G., Carlsson, A.J.: Influence of non-singular stress terms and specimen geometry on small-scale yielding at crack tips in elastic–plastic materials. *J. Mech. Phys. Solids* **1(21)**, 263–277 (1973)
8. Hutchinson, J.W.: Singular behavior at the end of a tensile crack in a hardening material. *J. Mech. Phys. Solids* **16**, 13–31 (1968)
9. O’Dowd, N.P., Shih, C.F.: Family of crack-tip fields characterized by a triaxiality parameter: Part I—Structure of fields. *J. Mech. Phys. Solids* **39**, 989–1015 (1991)
10. Yang, B., Ravichandar, K.: Evaluation of T stress by stress difference method. *Eng. Fract. Mech.* **64**, 589–605 (2001)
11. Dodds, R., Ruggieri, C., Koppenhefer, K.: 3D Constraint effects on models for transferrability of cleavage fracture toughness. *ASTM* **1321**, 179–197 (1997)
12. O’Dowd, N.P., Shih, C.F.: Family of crack-tip fields characterized by a triaxiality parameter: Part II—Fracture applications. *J. Mech. Phys. Solids* **40**, 939–963 (1992)
13. Rice, J.R., Tracey, D.M.: on the ductile enlargement of voids in triaxial stress field. *J. Mech. Phys. Solids* **26**, 163–186 (1969)
14. Kaechele, L.E., Tetelman, A.S.: A statistical investigation of microcrack formation. *Acta Metall.* **17**, 463–475 (1969)

15. Akourri, O., Elayachi, I., Pluvinage, G.: Stress triaxiality as fracture toughness transferability parameter for notched specimens. *Int. Rev. Mech. Eng. (I.R.E.M.E.)* **1**(6) (2007)
16. Eisele, U., Roos, E.: Evaluation of different fracture-mechanical J-integral initiation values with regard to their usability in the safety assessment of components. *Nucl. Eng. Des.* **130**, 237–247 (1990)
17. Dlouhy, I., Holzmann, M., Chlup, Z.: Fracture resistance of cast ferritic C Mn steel for container of spent nuclear fuel in transferability of fracture mechanical characteristics. *Edito Dlouhy, NATO Sciences Series*, pp. 47–64 (2001)
18. Wallin, K.: Quantifying T-stress controlled constraint by the master curve transition temperature T_0 . *Eng. Fract. Mech.* **68**, 303–328 (2001)
19. Wallin, K.: Structural integrity assessment aspects of the Master Curve methodology. *Eng. Fract. Mech.* **77**, 285–292 (2010)
20. Hohe, J., Hebel, I., Friedmann, V., Siegele, D.: Probabilistic failure assessment of ferritic steels using the master curve approach including constraint effects. *Eng. Fract. Mech.* **74**, 1274–1292 (2007)
21. Coseru, A., Capelle, J., Pluvinage, G.: On the use of charpy transition temperature as reference temperature for the choice of a pipe steel. *Eng. Fail. Anal.* **37**, 110–119 (2014)

Crack Path Stabilisation and T-Stress Estimation in Connection with the Global Approach for Inclined Notches

Mohammed Hadj Meliani, Omar Bouledroua,
Mohamed Ould-M'beirick, Khled Elmiloudi,
Mohamed Sadou and Guy Pluvinage

Abstract In this paper, we investigate the effects of non-singular stress (T-stress) on the mixed mode loading (I + II) near notch-tip field's elastic compression-sensitive under plane stress and small scale yielding conditions. The crack path is estimated for three different shapes of notches using the Maximum Tangential Stress (MTS) approach. Constraint induced by the notch depth, shape of defaults and the notch-tip stress field in laboratory specimens is examined by Finite Element Analysis, and the effect of the deformation on modified (HRR) singularity stress field are discussed. The Volumetric Method (VM) criterion for compression and/or tension sensitive materials is described by a linear combination of the effective stress and the Notch Stress Intensity Factor. The results of our finite element computations based on a two-parameter fracture mechanics formulation show that the T stress has significant effects on the sizes, the shapes of the plastic zones and the crack path.

Keywords T-stress · Mixed mode · Notch stress intensity factor · Volumetric method · Constraint

1 Introduction

Recently, authors and research groups takes more discussed and observations an increasing number of papers, were working on the topic of characterization of crack tip stresses using more than one fracture mechanics parameter in mixed mode. Risk of mixed-mode fracture appears when a preexisting defect is load by a multiaxial

M. Hadj Meliani (✉) · O. Bouledroua · M. Ould-M'beirick · K. Elmiloudi · M. Sadou
LPTPM, FT, Hassiba Benbouali University of Chlef,
Salem City. BO. Box 151, 02000 Chlef, Algeria
e-mail: hadjmeliani@univ-chlef.dz; hadjmeliani@univ-metz.fr

M. Hadj Meliani · G. Pluvinage
LaBPS-ENIM, Université Paul Verlaine de Metz, île de Saulcy,
57045 Metz, France

loading or uniaxial load in a direction different to the normal direction to defect line. Prediction of this risk needs to answer to the following questions:

- What is the fracture load knowing fracture toughness according to each elementary fracture mode?
- What is the direction of fracture path?
- For a blunt notch what is the fracture initiation point?

For a crack like defect, the problem of mixed mode of fracture has received a large attention. Several criteria are proposed in literature and can be classified in several families: local stress criteria, local strain energy density, equivalent notch stress intensity factor, local strain criteria, maximum energy release rate in local direction or local crack opening displacement criterion. A review of these different criteria is given in [1]. Validity of these criteria depends on fracture behavior of materials (brittle or ductile), level of mode mixity ratio M^e (predominant opening mode or not) and constraint.

$$M^e = \frac{2}{\pi} \tan^{-1} \left(\frac{K_I}{K_{II}} \right) \quad (1)$$

When restricting our interest to brittle materials and low mode mixity ratio, the maximum tangential stress (MTS) criterion, originally proposed by Erdogan and Sih [2] and the strain energy density factor by Sih [3]. Mixed mode fracture emanating from notch has recently received increasing attention [4, 5]. El Minor et al. [6] have proposed an approach based on equivalent notch stress intensity factor. Ayatollahi et al. [7] have developed a criterion based on the maximum tangential stress (MTS) criterion. The critical tangential stress is expressed in terms of mode I and II notch stress intensity factors. Berto et al. [8] have proposed two fracture criteria and applied to blunt-notched components made of brittle materials loaded under mixed mode; the former is based on the averaged strain energy density over a given control volume, the latter on the cohesive crack zone model. These authors have studied brittle materials and received some success when using the maximum tangential stress (MTS) criterion and the strain energy density factor by Sih.

However for mixed mode of fracture emanating from notch, initiation point and influence of constraint needs particular attention. In mode I, fracture systematically initiates from the notch tip located on the notch bisector line; this is the point where the main principal stress is at a maximum, as well as the maximum shear stress and the strain energy density. Conversely, the point where fracture starts in mixed mode varies from case to case, because it depends on the geometry of the notch and loading mode mixicity ratio. Ayatollahi et al. [9] have taken into account the constraint in mixed mode of fracture emanating from notch by introducing the biaxiality ratio B and found that the mode mixicity ratio is affected by B .

$$B = T \cdot \frac{(\pi a)^{0.5}}{(K_I^2 + K_{II}^2)^{0.5}} \quad (2)$$

Kim et al. [10] have shown that the biaxiality ratio B have some influence on bifurcation angle. This paper is focus on initiation point on fracture emanating from notch using *MTS* criterion. A comparison between U and V notches is made. Influence of T-stress on fracture load for Brazilian disc made in bio-ceramics is also study.

2 Material and Specimen

One of the key differences between metals and bioceramics is the “brittle” character of bioceramics. They may have to adapt to a deformation of more than a few microns. Unlike metals, bioceramics have no plasticity. They are characterized by a purely elastic behavior with a high Young’s modulus (Table 1) and until the failure stress is reached. Although bioceramics have a brittle fracture type, some of them can withstand very high compressive stresses, is the case of Zirconia, even if their total lack of plasticity does not allow them to accommodate deformation under the effect of stress concentrations. The study of compression behavior of bioceramics was performed on disk Brazilian loaded in mode I ($\beta = 0^\circ$), mode II ($\beta = 90^\circ$), and mixed mode ($I + II$). Two notches in V and U have been chosen. Dimensions are in millimeters, Fig. 1, for more details see Ref. [1]. The specimen thickness t is 4 mm and the values of length notch for U and V are 12 mm. Eleven different notch inclination $\theta = 10, 20, 30, 40, 50, 60, 70, 80$ and 90° , were considered. Figure 2 represent some numerical results about Brazilian disk in compression loading (mixed mode). We present two types of notches: U and V in different angles from 0° (*simple mode I*) to 90° (*simple mode II*).

Table 1 Mechanic’s characterization of materil study

Mechanics characterization	Alumina (Al_2O_3)	Zirconia (ZrO_3)
Compression strength (MPa)	4000	6000
Bending strength (MPa)	550	2200
Young modulus (GPa)	380	220
Poisson coefficient (γ)	0.18	0.31
average grain size (μm)	1.3	0.35
Hardness HV (MPa)	2017	1750
Density (g/cm^3)	3.9	6.1
Static Toughness, $K_{I,c}$ ($MP.m^{0.5}$)	3.5	6

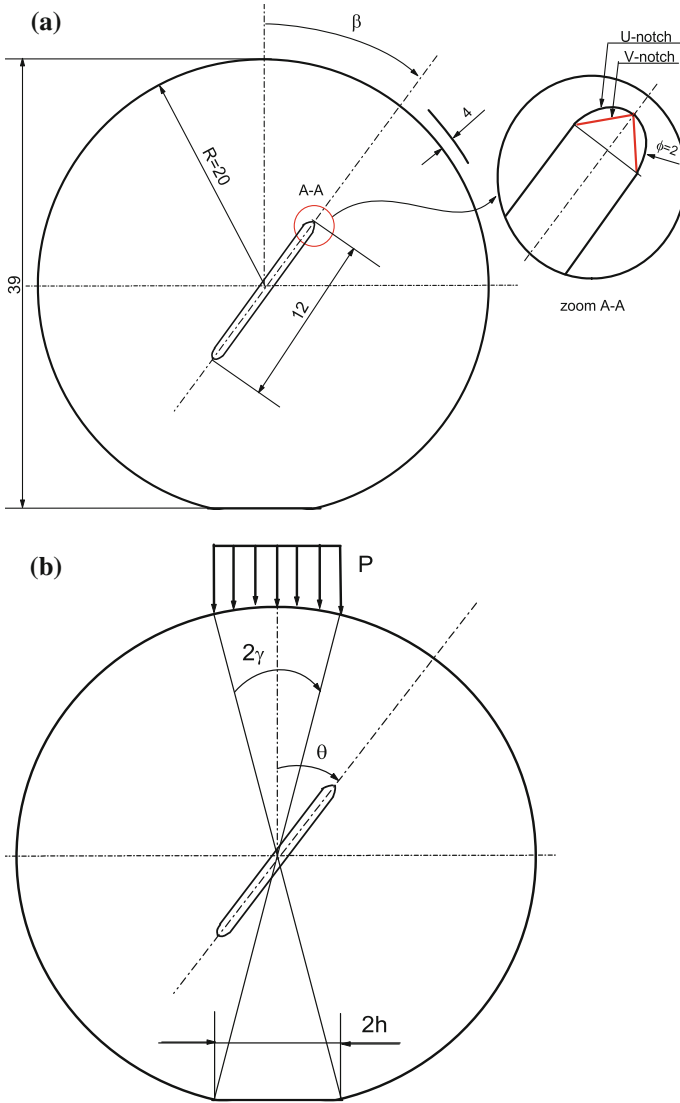


Fig. 1 **a** dimensions of the Brazilian disk specimen with U and V-notch and **b** the applied loading position, all dimensions are in mm

Two different materials are used, Alumina and Zirconia. The specimens were loaded diametrically using a 100 kN capacity universal testing machine with a crosshead speed of 0.02 mm/min at ambient air. At first, loading was continued till failure at the different notch (*U* and *V*) and different inclination angle from (*simple mode I*) to *simple mode II* with respect to the loading direction to confirm a fracture

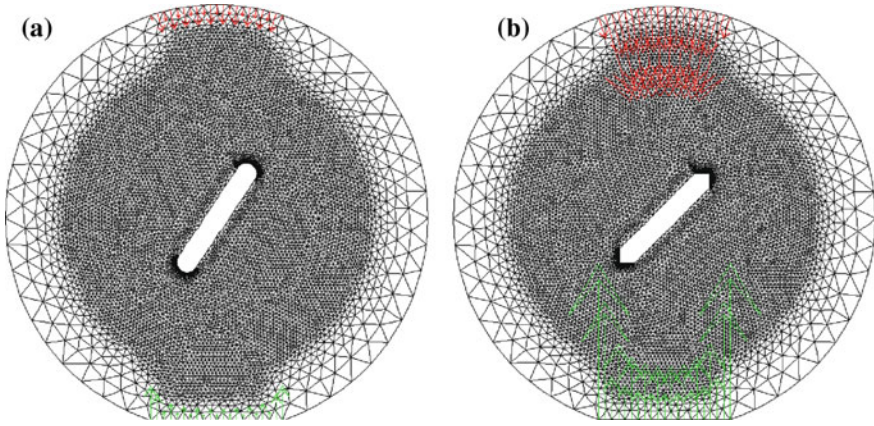


Fig. 2 Example Meshing of the Brazilian disk in compression with the action forces (red color) and reaction forces in (green color) contain **a** U-notch at 30°, **b** V-notch, at 45°

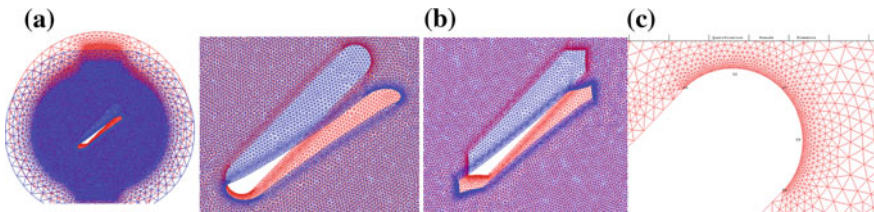


Fig. 3 **a** Deformation of the disk before and after loading; **b** zoom of the U-notch deformation and the V-notch and **c** mesh near the notch-tip and the contour of stresses ($L_6 + L_5$)

load for each notch angle condition. Results of the maximum values of loading, for each shape and inclination on the two specimens, are presented in the Table 2.

Isoperimetric triangular elements were used with six nodes with a dense network in the vicinity of notches. The same mesh style was retained for all samples of Alumina and Zirconia in mode *I* and mode *I + II* to eliminate any influence of change of the mesh on the results. The material is assumed to have an isotropic elastic behavior. The Brazilian disk, before and after loading, is presented in Fig. 3a with red and blue color, respectively. Zoom of the affected zone is detailed in the Fig. 3b. The distributions of the principal stresses are given in the lines ($L_6 + L_5$) (see Fig. 3c).

Examples of the tangential stress distributions for simple mode *I* (0°), simple mode *II* (90°) and mixed mode *I-II* (45°) are shown in Fig. 4. The tangential stress was formed along the notch line and was concentrated at the notch tip regardless of the notch inclination angle. Although the applied load for the pure mode *I* (212 N) was less than that for the mixed mode *I + II* (606 N), the tangential stress was much lower under the mixed mode *I + II* loading than the simple mode *I* loading. The

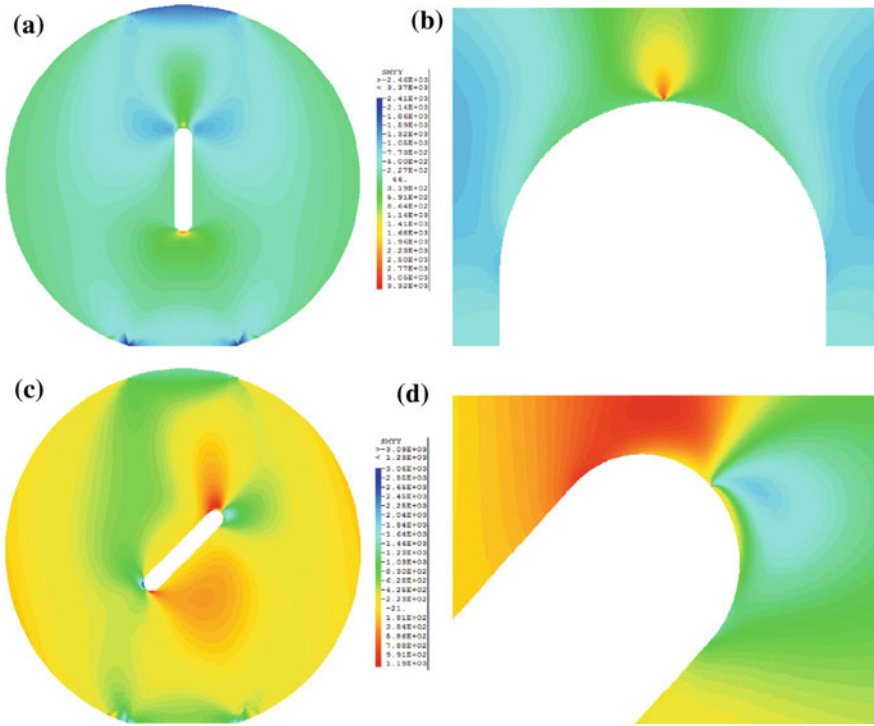


Fig. 4 Some results of tangential stress with U-notch for Alumina and Zirconia specimen for mode I (0°) and mixed mode (I + II) (45°)

simple mode II $\theta = 0^\circ$ gives the higher values of loading for the two specimens with U and V notches.

3 Determination of Bifurcation Angle

The calculations of numerical results are based on the maximum tangential stress (MTS) criterion was first proposed by Erdogan and Sih [2] for brittle fracture in mixed mode *I/II* crack problems. This criterion will be extended to the notches problems. According to this, crack growth from notch, initiates radially from the notch tip along the direction of maximum tangential stress $\sigma_{\theta\theta,max}$. The tangential stresses distribution along the contour (P6P7P8) are presented in the Fig. 5, for different angle, from pure mode I in compression ($\theta = 0^\circ$) to the simple mode II ($\theta = 90^\circ$). The contour (P6P7P8) is represented in radius. Figure 6 shows the principal stress distribution $\sigma_{\theta\theta}$, σ_{rr} and $\sigma_{\theta r}$ along of the contour (P6P7P8) for Alumina specimen with U-notch. Important difference on the tangential stress is observed for inclination angles θ and the two notches U and V. We assume that the

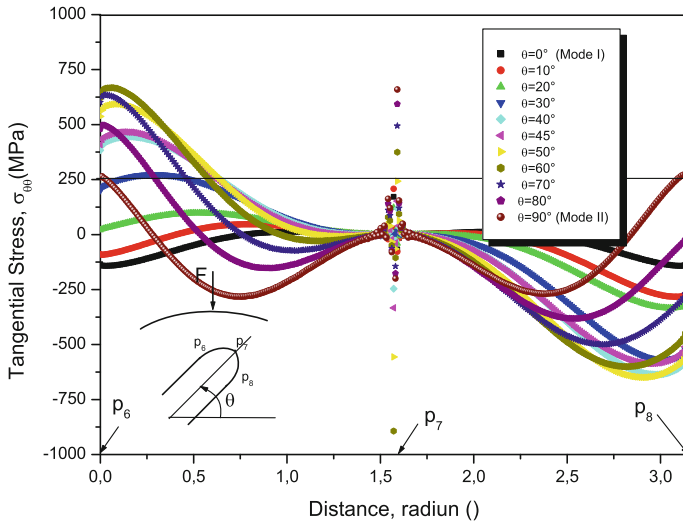


Fig. 5 Tangential stress evolution along of ligament ($P_6P_7P_8$)

mixed-mode ($I + II$) notch-initiated fracture is governed by the tangential stress (while $\sigma_{\theta\theta}$ plays the major role in the cracking process).

Further, we have studied this stress distribution according to the maximum tangential stress direction.

In the Fig. 7, the determination of the point of the bifurcation are focus on the contour $P_6P_7P_8$ in the aim to identified and localized the condition of failure of structure emaning from U and V notches. The different situations of bifurcation are determined for the two materials Alumina and Zirconia for different orientation angle. The criterion assumes that in mixed-mode ($I + II$) fracture crack initiation from notches is governed.

By the tangential stress, is proposed, so called the Equivalent Notch Stress Intensity Factor, $ENSIF$. For the two materials with U and V notches shape, Alumina and zirconia, and inclination angles we have determined the maximum tangential stress points over the notch contour, Fig. 8a, b. The distributions of tangential stresses at the notch tip are analyzed according to this approach. The curves of maximum tangential stress distribution gives a minimum values in an orientation of $\theta = 20^\circ$ for the U-notches and $\theta = 30^\circ$ for the V-notches.

Figure 9a represent the numerical results of the maximum tangential stress for different orientation of loading θ^* on the Alumina Brazilian disk with V-notch, coupled with the bifurcation orientation β^* . A sudden drop of the maximum

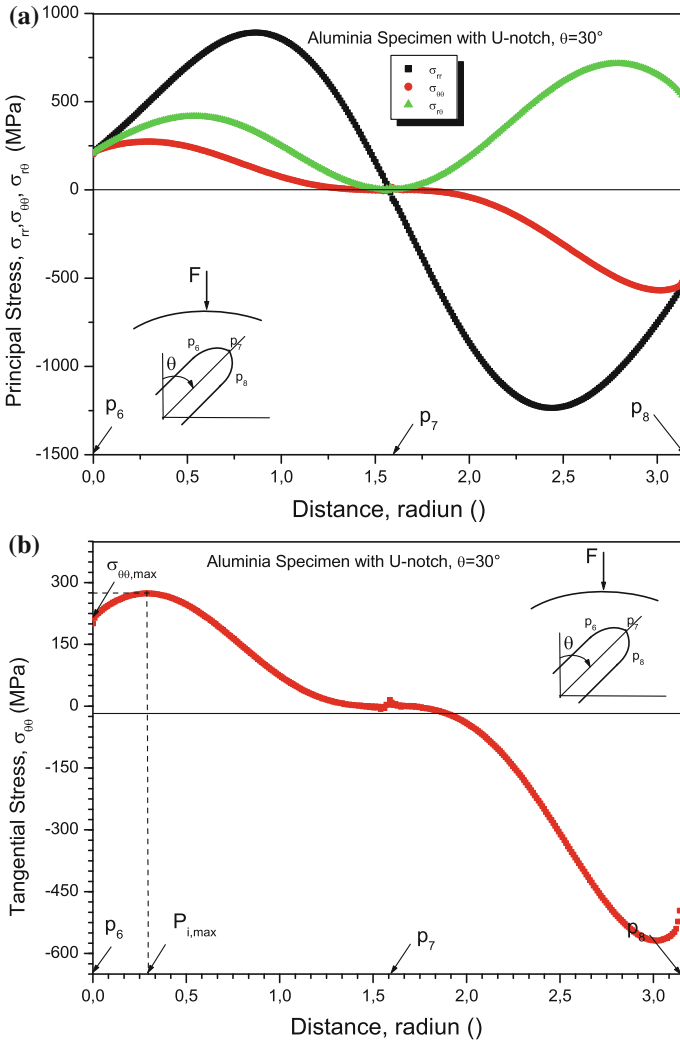


Fig. 6 **a** Example of the principal stress distribution for Alumina with U-notch on the 30° of orientation. **b** Example of determination of the distance with the maximum tangential stress

tangential stress is noticed for a $\theta = 30^\circ$, orientation with the change in deviation propagation is taken from 90° to 0° .

The predicted directions of initial crack propagation are compared in Fig. 9b at the notch tip for *U* and *V* shape using the MTS fracture criteria. Numerical tests have shown that the series term has significant influence on the prediction of initial crack propagation direction β^* with different shape of the notch. For the both shapes *U* and *V* notches, and in the margin of 0° – 20° , they are deflected in the same way at the point *P7*. On the other side, when to move in the direction between 30° – 60° ,

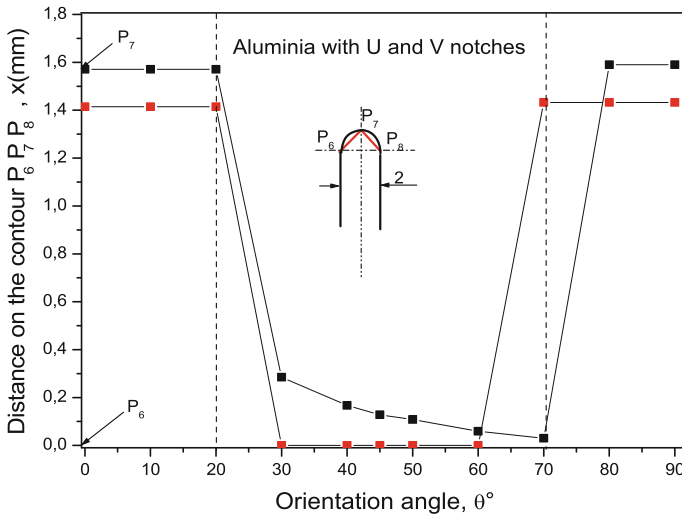


Fig. 7 Determination of the point of bifurcation along of the contour $P_6P_7P_8$ for U and V notches

the *U*-shaped deflected quickly compared to the *V* shape. The two notches returns to point *P7* guidelines that exceed 70° .

4 Determination of the Equivalent Notch Stress Intensity Factor

In the local mode I criterion, the magnitude of the elastic stress field can be described by a single parameter, K_{eq} , designated the Equivalent Notch Stress Intensity factor, *ENSIF*. The applied stress, the crack shape, size, and orientation, and the structural configuration of structural components subjected to this type of deformation affect the value of the *NSIF*. This allows translating laboratory results directly into practical design information. The Equivalent Toughness, or the Equivalent Notch Stress Intensity Factor in mixed mode, *ENSIF*, is described and defines as a function of effective distance and effective stress given by relationship:

$$K_{eq,\rho} = \sigma_{eq} \sqrt{2\pi X_{ef}} \tag{3}$$

The *ENSIF* is considered as a value of fracture toughness in the mixed mode, with units $\text{MPa}\sqrt{\text{m}}$, and the minimum effective distance corresponds to the abscissa of the upper limit of zone II and its distance from notch rot was suggested to be the effective distance X_{ef} . It is a principle of fracture mechanics that unstable fracture occurs when the notch stress intensity factor at the notch tip reaches a critical value

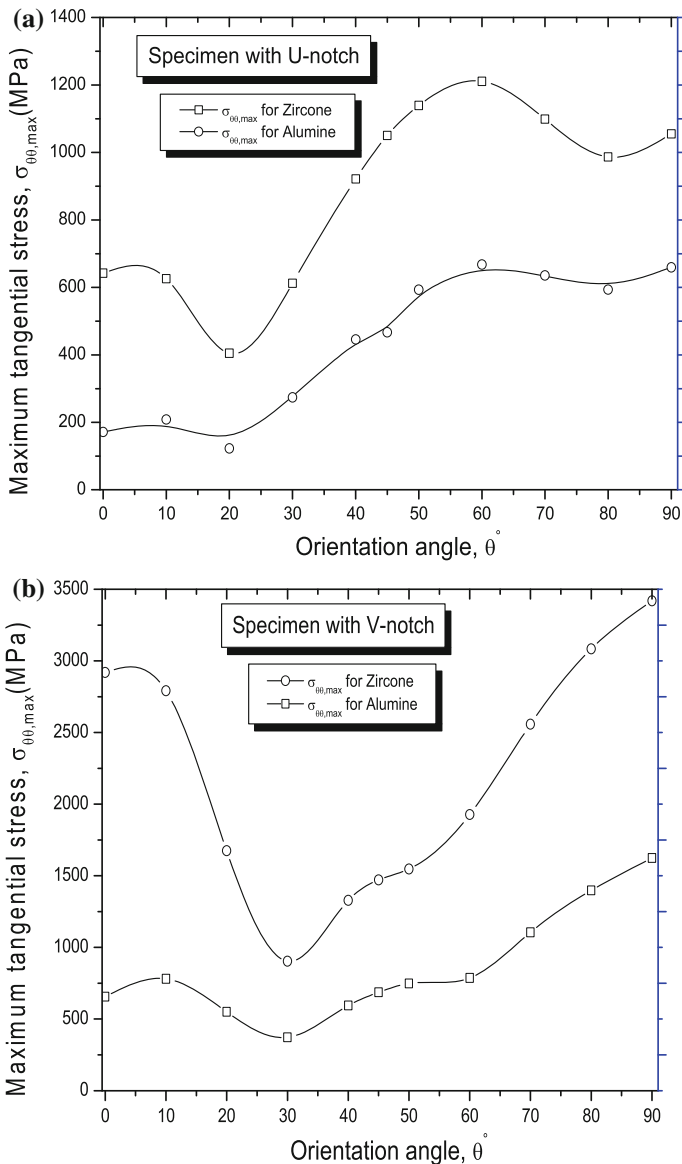


Fig. 8 Evolution of the maximum tangential stress for different inclination angle on Alumina and Zirconia specimens with **a** U-notches and **b** specimens with V-notches

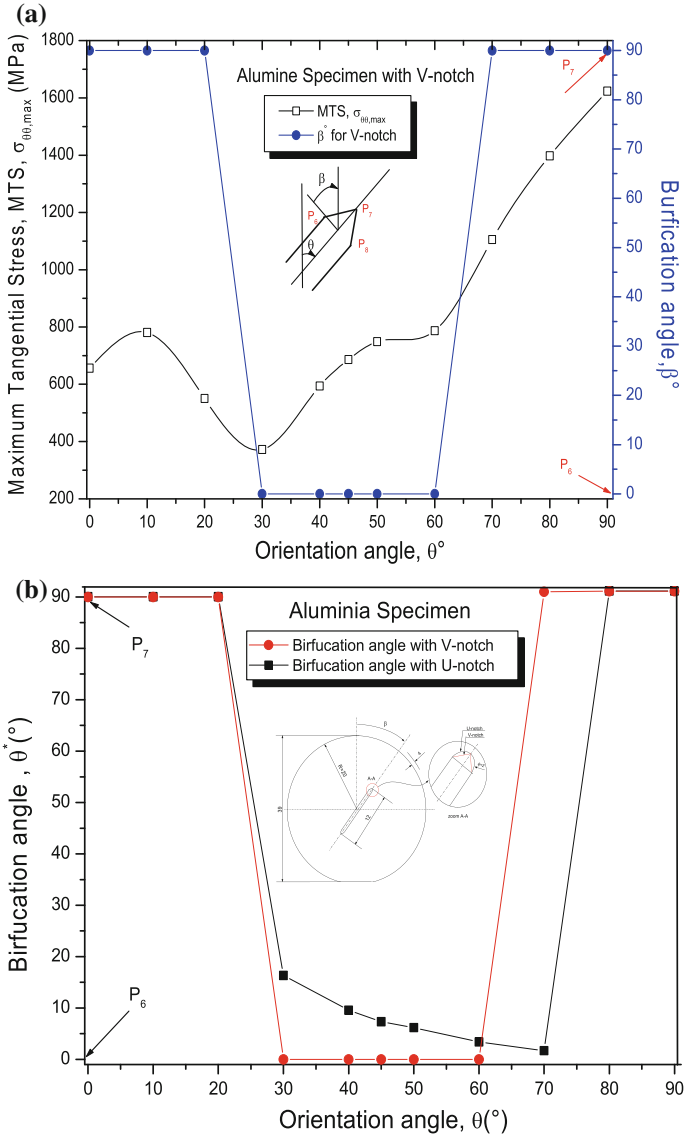


Fig. 9 Bifurcation angle on the Alumina with the maximum tangential stress specimen for the **a** V-notch and **b** U and V-notch

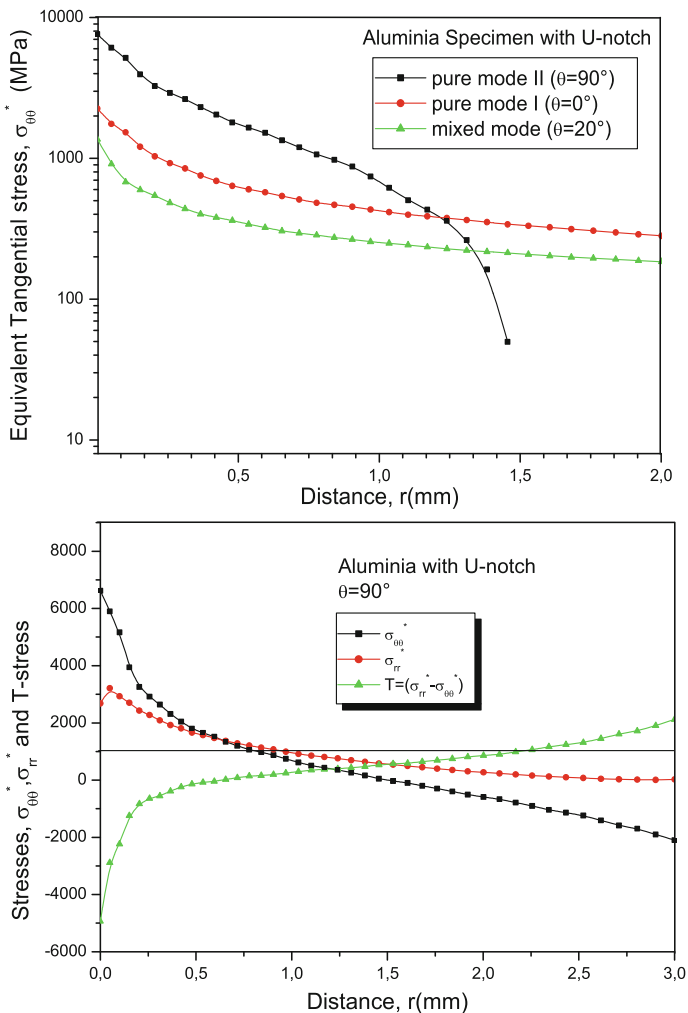


Fig. 10 Equivalent tangential stress distribution along of the ligament (r) for $\theta = 0, 60$ and 90° for U-notch

$K_{\theta\theta}$. For the local mode I deformation and for small crack tip plastic deformation, i.e. plane strain conditions, the critical notch stress intensity factor for fracture instability is $K_{eq,\rho,c}$. The value $K_{eq,\rho,c}$ represents the fracture toughness of the material. A simple fracture criterion is obtained by using the critical notch stress intensity factor $K_{eq,\rho,c}$ and write:

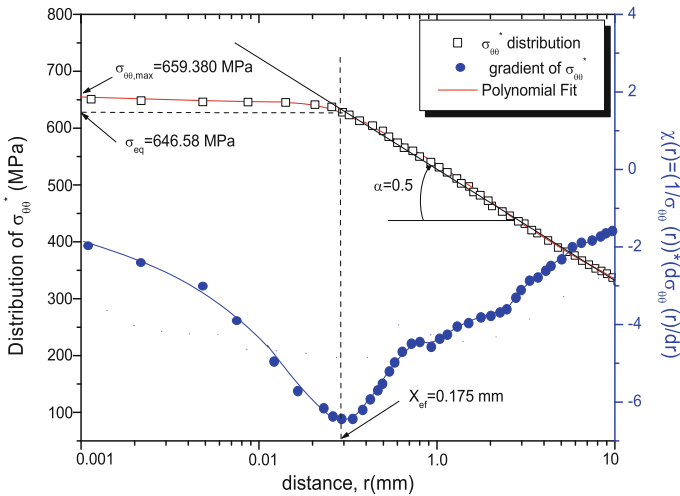


Fig. 11 Tangential stress distribution at the notch tip. Relative tangential stress gradient versus the distance. Determination of the effective tangential distance

$$K_{eq,\rho} = K_{eq,\rho,c} \tag{4}$$

The critical equivalent notch stress intensity factor is a fracture toughness values with units $\text{MPa}\sqrt{\text{m}}$, if the notch has parallel side (notch angle equal to zero) and for elastic behaviour.

The tangential stress component value occurring along the notch-tip is plotted in Fig. 10 as a function of the distance r . The inclined path is perpendicular to the notch-tip and starts from the point of the maximum of ($P6P7P8$) stress component along the notch profile. The finite element results are compared with the pure mode I ($\theta = 0^\circ$), pure mode II ($\theta = 90^\circ$) and mixed mode ($I + II$) ($\theta = 20^\circ$).

By definition, the effective tangential distance is the diameter of the process volume assuming it has a cylindrical shape. A typical example of the tangential stress distribution is presented in Fig. 11. The relative tangential stress has also been plotted versus distance r for Alumina with U -notch at $\theta = 90^\circ$. All results for different notches and orientation of the two materials are recapitulated in the Table 2.

Figure 12a shows typical equivalent notch stress intensity factor curves for various notch inclination angles for Alumina and Zirconia. The $ENSIF$ values decreased as the notch inclination angle increased in the range of $0 < \theta \leq 20^\circ$. The Zirconia material gives the high values. The dependence of the fracture toughness on the notch inclination angle in the mixed mode loading condition can be understood by examining the stress distribution of notch tip formulated by Atkinson. For pure mode I $\theta = 0^\circ$, the maximum tangential stress is in tension but the shear stress tend to zero so that the crack propagates only under the influence of the tangential stress. However, for mixed mode $I-II$ $0 < \theta \leq 20^\circ$, the shear stress

Table 2 Recapitulative of the different results for Alumina and Zirconia specimen with U and V notch

θ	Alumina with U-notch	Zirconia with U-notch								
	P_c	$\sigma_{\theta\theta,max}$	σ_{eq}	x_{ef}	$K_{eq,c}$	P_c	$\sigma_{\theta\theta,max}$	σ_{eq}	x_{ef}	$K_{eq,c}$
0	2.12	171.38	160.00	0.12	4.39	7.94	641.91	629.58	0.21	22.75
10	2.35	208.20	198.54	0.13	5.84	8.10	625.38	610.65	0.20	21.69
20	2.85	122.66	112.69	0.157	3.53	8.40	404.58	489.65	0.18	16.55
30	4.79	273.79	265.00	0.18	8.91	10.70	611.99	596.54	0.19	20.76
40	5.60	445.50	437.56	0.195	15.31	11.58	921.42	912.65	0.22	34.30
45	6.06	466.67	456.40	0.21	16.57	12.04	1050.30	1042.15	0.23	39.60
50	6.48	593.03	580.24	0.228	21.95	12.43	1139.20	1130.86	0.24	44.35
60	7.39	667.65	667.12	0.24	25.89	13.40	1210.50	1204.96	0.25	48.12
70	8.23	635.20	628.40	0.210	22.82	14.22	1098.80	1079.24	0.23	41.37
80	9.11	593.39	575.45	0.20	20.84	15.15	986.75	872.56	0.22	33.01
90	10.	659.38	646.58	0.17	21.43	16.00	1055.00	1038.67	0.23	39.56
θ	Alumina with V-notch	Zirconia with V-notch								
0	–	656.21	647.21	0.18	22.06	–	2919.00	2900.00	0.43	150.70
10	–	780.71	772.56	0.20	27.85	–	2791.40	2781.00	0.38	136.56
20	–	550.31	539.45	0.17	17.88	–	1674.50	1662.58	0.30	72.16
30	–	371.93	363.45	0.16	11.55	–	903.86	895.32	0.23	34.39
40	–	594.02	579.18	0.19	20.42	–	1328.40	1319.67	0.26	53.42
45	–	686.32	675.45	0.19	23.33	–	1471.60	1463.47	0.26	60.15
50	–	748.94	738.12	0.19	26.09	–	1547.50	1536.95	0.27	64.21
60	–	786.87	777.67	0.20	27.63	–	1927.60	1912.62	0.32	86.14
70	–	1105.30	1091.64	0.24	42.46	–	2557.90	2536.64	0.36	121.28
80	–	1397.60	1375.65	0.27	56.96	–	3083.40	3062.45	0.44	162.43
90	–	1623.70	1608.98	0.29	69.13	–	3419.40	3398.54	0.48	187.75

increase with increasing on θ , take positive value with a maximum at around. $\theta = 20^\circ$, the tangential stress is decreasing and tend to minimum value on tensile. In this range, crack initiated from notch by the shear deformation at the notch tip might intensify the tangential stress so that the crack could be propagated at relatively low fracture toughness with increasing the notch inclination angle. Chandra Rao et al. [11] show, for modified compact tension specimen, the total fracture toughness remains more or less unchanged when the inclination of θ increases from 0 to 30° and subsequently increases when θ increases from 30 to 45° .

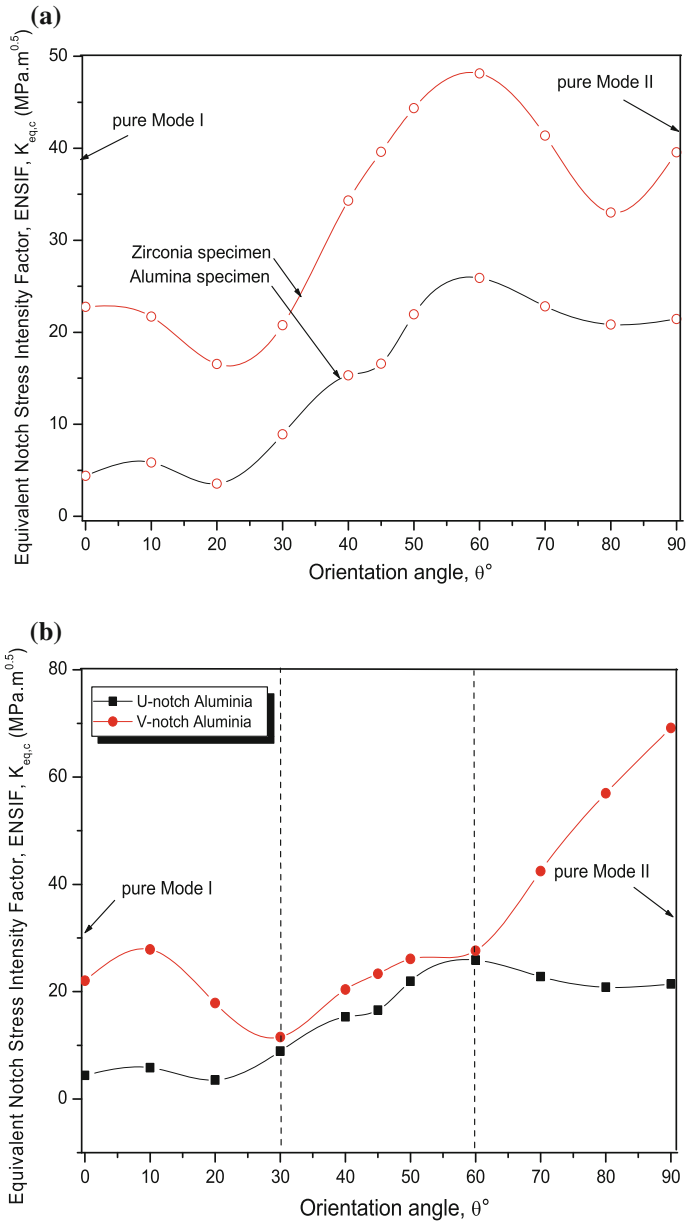


Fig. 12 Evolution of the equivalent notch stress intensity factor for Alumina and Zirconia specimen with a U-notch and b comparison between U and V notches for Alumina

5 Conclusion

Mixed mode of fracture criteria predicts generally loading conditions of fracture and direction of bifurcation. In this paper, using the maximum tangential stress (MTS) criterion, in addition we are looking for position of fracture initiation emanating from notches. The criterion assumes crack initiation from notches is governed by the maximum tangential stress, introduced in the Equivalent Notch Stress Intensity Factor, ENSIF. This problem has been studied for the two ceramics (alumina and zircona) on Brazilian disks with U and V notches shape. Numerical results indicate that in fracture initiation location move by discrete values from center of the notch for low and high loading angle values to end of notch for intermediate values corresponding to some seldom experimental results in steel specimens. Evolution of computed equivalent notch stress intensity factor confirms existence of these three domains of fracture behavior with limits independent of notch geometry and material behavior.

References

1. Louah, M.: Fissuration en Fatigue en mode mixte I + II à l'aide du disque brésilien. Thèse de doctorat, Université de Metz (1986)
2. Erdogan, F., Sih, G.C.: On the crack extension in plates under plane loading and transverse shear. *J. Basic Engng. Trans. ASME* **85**, 525–527 (1963)
3. Sih, G.C.: Strain-energy-density factor applied to mixed mode crack problems. *Int. J. Fract.* **10**, 305–321 (1974)
4. Papadopoulos, G.A., Paniridis, P.I.: Crack initiation from blunt notches under biaxial loading. *Eng. Fract. Mech.* **31**(1), 65–78 (1988)
5. Priel, E., Bussiba, A., Gilad, I., Yosibash, Z.: Mixed mode failure criteria for brittle elastic V-notched structure. *Int. J. Fract.* **144**, 247–265 (2007)
6. El Minor, H., Louah, M., Azari, Z., Pluvinage, G., Kifani, A.: Brittle Mixed Mode Fracture I + II-Application of Equivalent Notch Stress Intensity Factor to the Cracks Emanating From Notches, *Problems of strenght*, No. 6, pp. 61–71. Décembre (2002)
7. Ayatollahi, M.R., Torabi, A.R.: Investigation of mixed mode brittle fracture in rounded-tip V-notched components. *Eng. Fract. Mech.*
8. Berto, F., Lazzarin, P., Gómez, F.J., Elices, M.: Mixed mode loading two procedures based on the equivalent local mode I concept. *Int. J. Fract.* **148**, 415–433 (2007)
9. Smith, D.J., Ayatollahi, M.R., Pavier, M.J.: The role of T-stress in brittle fracture for linear elastic materials under mixed-mode loading. *Fatigue Fract. Eng. Mater. Struct.* **24**, 137–150 (2001)
10. Kim, J.H., Paulino, G.H.: T-stress, mixed mode stress intensity factors and crack initiation angles in functionally graded materials: a unified approach using the interaction integral method. *Comp. Meth. Appl. Mech. Eng.* **192**, 1463–1494 (2003)
11. Chandra Rao, B.S.S., et al.: *Mater. Sci. Eng.* **A476**, 162–168 (2008)

Measuring of Strain and Displacements in Welded Joints Subjected to Tensile Load Using Stereometric Methods

Branislav Djordjevic, Simon A. Sedmak, Uros Tatic, Milos Milosevic and Filip Vucetic

Abstract During the experimental testing of a welded joint, made of steel P460NL1, complete strain and displacement fields, which provide full insight into the behaviour of a welded joint under tensile load, were obtained using an optical stereometric measuring method. Optical stereometric method involved the application of digital image correlation. Presented in this paper are the strain and displacement for various load levels are shown, along with the behaviour of the welded joint as a whole. As a result of this approach, concrete and accurate values of the observed strain field as a whole can be compared directly, rather than as chosen representative parts that would be tested using a strain gauge in a single position, and provide a more detailed insight into the behaviour of the tested joint. With the aid of images obtained using cameras, the development of strain over time can be monitored, while pointing out the critical parts of a welded joint, allowing the determining of potential locations with increased stress intensity factor.

1 Introduction

Systems for stereometric optical measuring of strain and displacement consist of a special set of cameras and lenses, as well as commercial software ARAMIS (GOM mbH, Braunschweig, Germany) [1] which records pairs of digital images in defined time intervals. This optical measuring technique is known as Digital Image Correlation technique (*DIC*) and has found wide application in various fields of experimental mechanics. The monitoring system uses two cameras which provide a synchronous stereo view of the simple or complex object. Other components of the

B. Djordjevic (✉) · S.A. Sedmak · U. Tatic · M. Milosevic · F. Vucetic
Innovation Centre of Faculty of Mechanical Engineering, Belgrade, Serbia
e-mail: djordjevic88@gmail.com

system include a stand which provides stability to the working of sensors, control and power supply unit, the unit for storage of recorded images and the system for data processing (computer).

This system can be, among other things, applied in structural integrity analysis, determining of material properties and used for verifying or improving of numerical calculations, by comparing to them to results obtained by conventional test methods and/or finite element method. More often than not, all three methods are used simultaneously in order to relate and verify obtained results in a best way possible.

2 Digital Image Correlation

A Digital Image Correlation system records the surface structure of a non-deformed measured object in form of digital images, and then assigns coordinates to every pixel in the image. Additional images are made while the load is being applied (or afterwards) and are then compared with the first one and calculates displacement and strain of characteristic points or parts of the object. In this way, it is possible to measure very small strain with high accuracy. Calculations are limited to local level displacements that are tangent to the surface.

As additional information, data about displacements perpendicular to the surface are missing and it is impossible to determine the $3D$ strain tensor, hence it is assumed that the third dimension of the observed value is constant during loading. Graphical representation of strain in a unit square, containing points $(0/0)$, $(0/1)$, $(1/0)$, $(1/1)$, can be seen in Fig. 1.

Displacement and strain measuring can be monitored in both $2D$ and $3D$, by using one or two cameras, respectively, wherein the latter case is also known as stereometric measuring, whose application was described in the previous section. Main advantage of this method is that it is a non-contact method, and that these tests can be performed using standard specimens, non-standard specimens, cracked

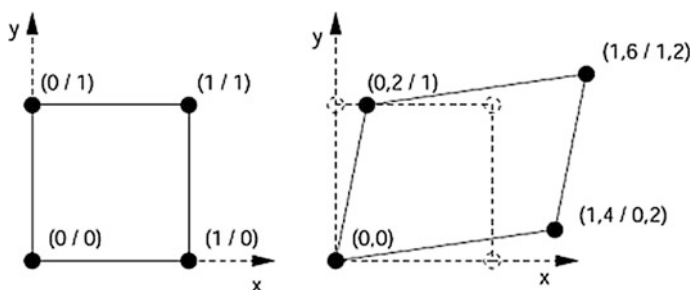


Fig. 1 An example of a unit square in **a** non-deformed state, **b** deformed state [2]

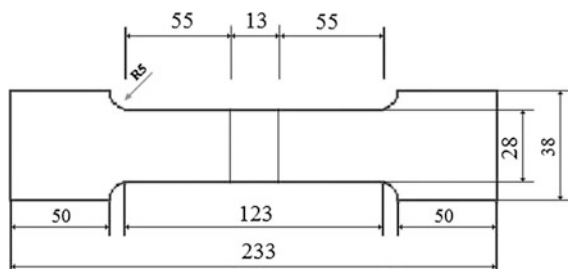
beams or doubled cracked beams in order to obtain a detailed image of strain or displacement distribution. The fact that this method can be applied to cracked beams is of particular importance, since it can be used to determine the behaviour around the crack tip [3], and thus can be used in determining of fracture mechanic parameters. Presented in the following section are the results of welded joint tests, along with explanations of results and possibilities of application of non-contact method. Even though this method has numerous advantages and exceptional accuracy, it is necessary to check the results, since, like every other method, it is subjected to errors which may sometimes be minor, and sometimes significant [3].

3 Welding Procedure

Specimens were taken out of a welded plate made of two micro alloyed steel plates *P460NLI* that were welded together. Each plate was 14 mm thick. *P460NLI* steel is developed for working at temperatures down to $-60\text{ }^{\circ}\text{C}$ and has a wide application in tanks in use nowadays. Test plates were welded using the MAG procedure, in 12 % Ar + 82 % CO_2 shielding atmosphere. VAC65 wires with a diameter of 1.6 mm, made in Zelezarna Jesenice, were used as additional material.

Taking into account the characteristic of parent metal weldability, preheating temperature was calculated using the Ito-Bessyo method [4], and versus carbon equivalent and other parameters, this temperature was determined to be $200\text{ }^{\circ}\text{C}$. Welded plates were then cut into specimens that were subjected to tensile testing. Two specimens were tested: one was subjected to a load which lead to fracture, and the other was loaded until plastic strain reached 5 %. Shown in Fig. 2 is the geometry of the specimens that were used.

Fig. 2 Shape and dimensions of specimens used for tensile tests [4]



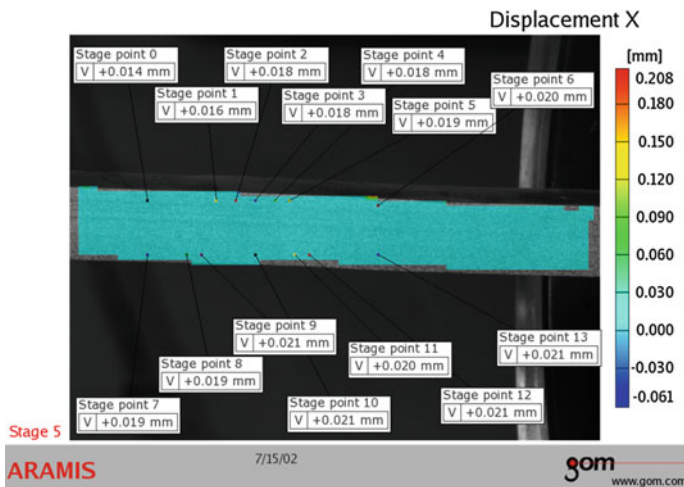


Fig. 3 Displacement field for a tested specimen at the beginning of the test

Prior to the testing, every specimen was separately prepared and appropriate measuring system calibration was performed, along with corresponding adjustments of parameters of stereometric testing. Two cameras were used. Testing was performed on a test machine SCHENCK TREBL RM 400, using static load. First recorded image of the non-deformed specimen represents the initial image, based on which strain and displacement are determined by mutual comparison (Fig. 3), as was described previously.

4 Results

Shown in this section are the results of testing of welded joints made of steel *P460NL1* subjected to tensile load for the purpose of determining the displacement and strain field. For the purpose of performing optical analysis, optical system GOM and ARAMIS GOM mbH software were used. Stage points 0–13 denote the points where we want to see accurate strain values. Displacement of points was monitored along the x direction.

First specimen was loaded until fracture. During the increase of load, as well as while maintaining it, the whole weld is deformed and the optical system records the images during many separate stages of deformation, based on which ARAMIS software calculates the coordinates of points or pixels and compares them to the initial (non-deformed) image. Diagram of dependence between measuring point's

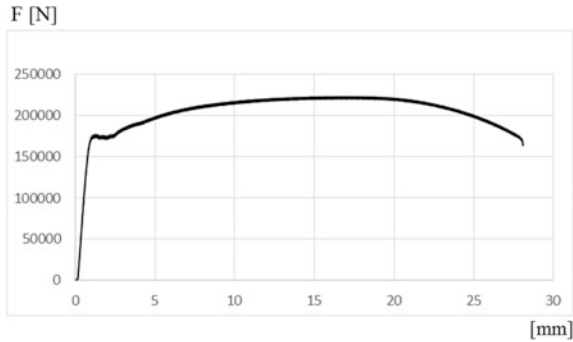


Fig. 4 Force-displacement of first specimen dependence diagram

displacement and the force is shown in Fig. 4. It can be noticed that due to different properties of parent metal and weld metal, the measuring part of the specimen was deformed unequally under the effect of a tensile force. The load increased linearly until a certain value.

Given in Fig. 5 is the displacement field of all points in an observed part of the first specimen at the moment of fracture. Shown in points 0–7 are the concrete values of displacement and strain in the welded joint zone. The change in cross-section contraction is smallest in the weld metal area. A clearly formed neck in the parent metal indicates significant plastic strain in that part. As complete illustration of the total strain of the whole specimen, Fig. 6 shows the strain field for the whole specimen obtained by ARAMIS software calculations.

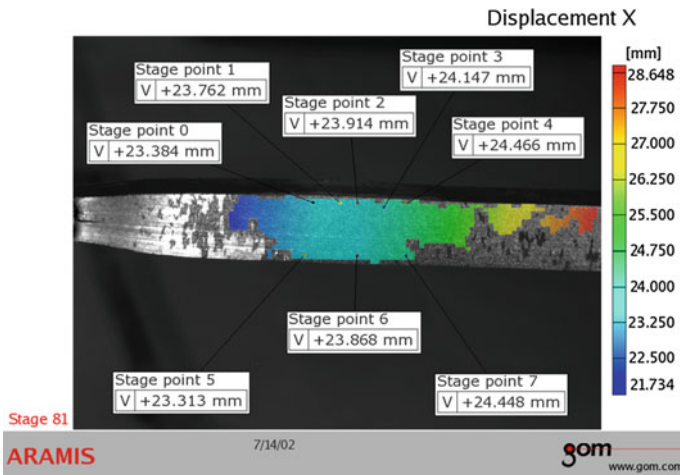


Fig. 5 Displacement field along the x direction for the first specimen

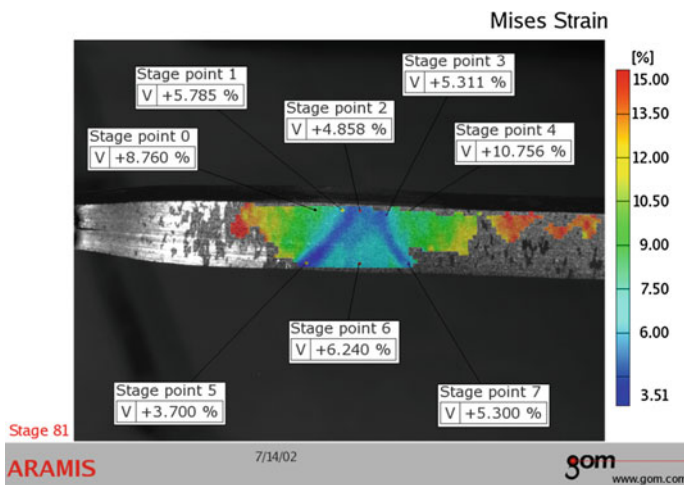


Fig. 6 Strain field of the first tested specimen

Sections denote the lines which include the parts of the deformed surface (Fig. 7). Section 0 includes the parent metal, heat affected zone (*HAZ*) and the root of the weld, and section 1 includes the part of the parent metal adjacent to the *HAZ*, *HAZ* and weld metal. Shown in Fig. 7 is the display of strain according to the given sections of the first specimen, and here it can be accurately seen that the *HAZ* had the smallest strain (a bit over 3.5 %).

Second specimen was subjected to a load that did not lead to fracture, resulting in small displacement and strain. Dependence of force and displacement for the second specimen can be seen in Fig. 8. The load was increased until the plastic strain of 5 %. Displacement field of points for the second specimen is shown in Fig. 9. Accurate values of displacement and strain are shown for stage points 0–17. Small tensile force resulted in small strain and shown in Fig. 10 is the strain field for the second specimen.

In Fig. 11, section 0 includes areas of the parent metal which is further away from the weld metal and the area closer to the weld metal, *HAZ* and weld root, whereas section 1 includes a part of the parent metal, *HAZ* and weld metal. The diagram in Fig. 11 represents the comparison of strain levels along the welded joints.

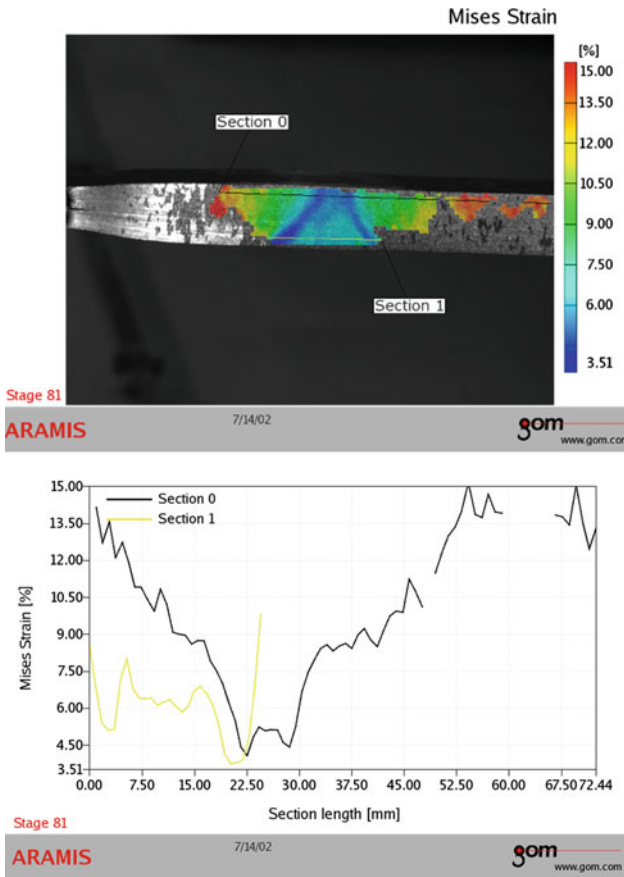


Fig. 7 Display of sections and diagram of strain distribution according to the sections of the first specimen

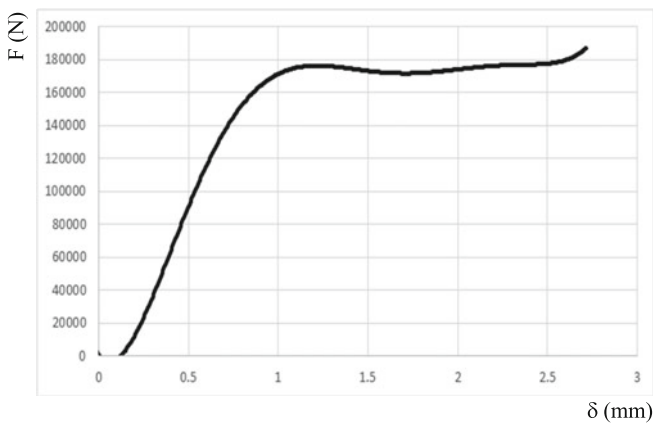


Fig. 8 Force-displacement diagram for the second specimen

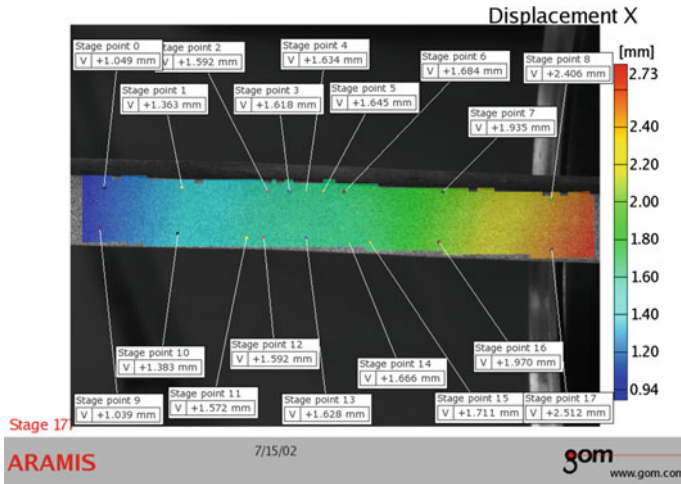


Fig. 9 Displacement field along the x direction of the second specimen

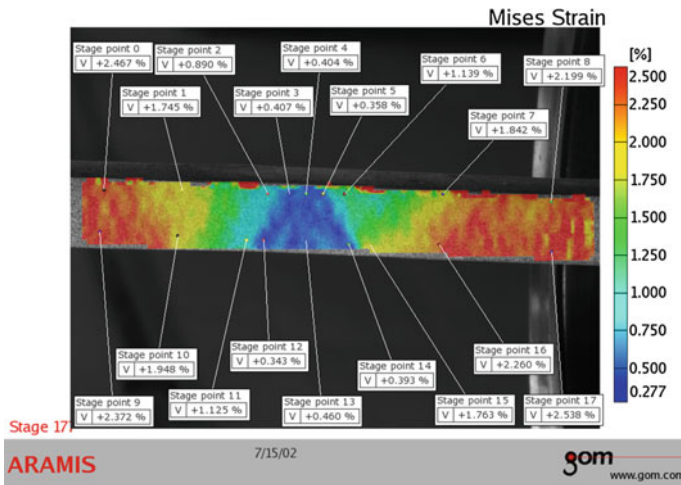


Fig. 10 Strain field for the second test specimen

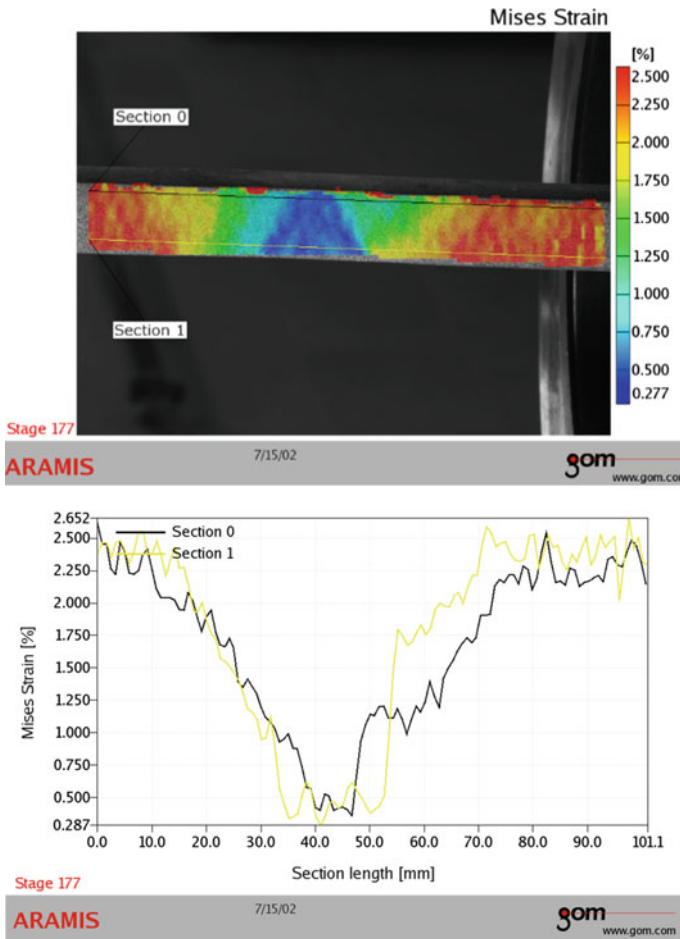


Fig. 11 Display of sections 0 and 1 and diagram of strain distribution in second specimen sections

5 Discussion and Conclusions

General research involving welded joints is related to studying of behaviour of cracks in welded joints, i.e. their behaviour during the exploitation and the influence it has on their work life [5]. Welding represents a complex process, during which physical, chemical and metallurgical processes take place, especially in a case that weld metal and parent metal do not have the same chemical and mechanical properties. Hence, cracks are an unavoidable part of the process, and need to be taken into account when considering the behaviour of pressure vessels from the standpoint of fracture mechanics. Strain and displacement field aid in the total

understanding of materials and provide complete insight into the behaviour of a deformed welded joint, i.e. weld metal, fusion line, *HAZ* and the parent metal as well, whereas concrete values in all points make the whole image of deforming much more accurate and clear and may be used for further analysis.

Results of testing of the first specimen have shown the extent to which the welded joint (including the parent metal and weld metal) deforms during fracture and indicated which parts of the weld were critical. In addition, these results have also determined the difference in strength between weld and parent metal, i.e. how much the weld metal is stronger than the parent metal. Results of the first tested specimen have amount of deformation of the tested welded joint (and parent metal and weld metal) during fracture and have indicated areas that are critical as well as the difference in the strength between weld metal and parent metal. Strength of weld metal is higher than that of the parent metal, since the fracture has occurred in the parent material. Strain in *HAZ* and weld root are the smallest, implying that these areas of the welded joint have the highest strength. Cross-section contraction of the specimen is smallest in area where the weld metal is located.

Second specimen was subjected to load that has lead to a total plastic strain of 5 %. Results of the second test specimen have pointed out the possibility of non-uniform strain distribution and peaks in strain value in the weld metal, which are the consequence of small strain. Results of the second specimen indicate that the ARAMIS system has difficulties with calculating small strain, hence peaks that may give the wrong impression about the welded joint and indicate errors in the welded joints and the parent metal alike, can occur. These experiments were used to show a direct application and significance of the stereometric testing method which replaces all traditional measuring devices which were necessary for performing experiments.

The fact that the accuracy stereometric optical measuring of strain via *DIC* is much higher with increased load (which lead to fracture) suggests that this method could be effectively and efficiently applied to fracture mechanics as well, since cracks typically occur and grow at higher levels of load. Further goals of this research should focus on determining of fracture mechanics parameters and combining such analysis with numerical methods in order to develop efficient and accurate methods for determining the behaviour of cracks in welded joints, particularly in case of pressure vessels.

References

1. GOM mbH: Optical Measuring Techniques. <http://www.gom.com>
2. ARAMIS User Manual—Software: ARAMIS v6.1 and higher
3. Dorđević, B., Sedmak, A., Sedmak, S., Tatić, U., Pavišić, M., Perović, J., Milošević, M.: The use of non-contact optical systems for determination of fracture mechanics parameters. *Weld. Mater. Test.* (2), 9–12 (2014)

4. Jovičić, R.: Analysis of crack influence on the integrity of ferrite-austenite welded joints. Doctoral thesis, Belgrade (2007)
5. Sedmak, S., Tatic, U., Mitrovic, N., Jovicic, R., Maneski, T., Sedmak, A., Milosevic, M.: Modern approach experimental verification of numerical models for tensile testes of welded specimens. In: Danubia-Adria Symposium on Advances in Experimental Mechanics (2013)

Experimental and Numerical Investigations of Friction Stir Welding of Aluminum to Copper

Gihad Kerrar, Nesar Merah, Abdelrahman Nasr Shuaib,
Fadi AL-Badour and Abdelaziz Bazoune

Abstract In this paper, results of performing successful butt-welding of aluminum grade Al6061-T6 to commercial pure copper using the relatively new friction stir welding (FSW) process are presented and discussed in conjunction with finite element results. A sound weld joint between these dissimilar materials has been achieved only when the pin tool was offset a certain distance from the center of the weld line and the harder material (copper) was placed at the advancing side of the FSW tool. On the other hand, the tool offset was not required when joining the similar materials of aluminum to aluminum and of copper to copper. A combined use of temperature distribution of the aluminum to copper weld nugget determined by a finite element model, the elemental concentration of copper and aluminum in the weld nugget from EDS analysis, and aluminum-copper phase diagram have been used to identify the phases present in the different weldment zones. The aluminum-copper joint was found to consist of several single and two phase intermetallic compounds such as Al_2Cu , Al_4Cu_9 , and $(Al + Al_2Cu)$. The results revealed higher hardness values for the weld nugget compared with the two base metals.

Keywords Welding dissimilar metals and alloys · Friction stir welding · Sound weld joint · Joining aluminum to copper

1 Introduction

It is possible to partially or completely replace copper with aluminum for several engineering applications because aluminum shares with copper some similar physical properties, e.g. electrical conductivity and because aluminum has lower price and lower density. Therefore, researchers are striving to join these two metals

G. Kerrar · N. Merah (✉) · A.N. Shuaib · F. AL-Badour · A. Bazoune
Mechanical Engineering Department, King Fahd University of Petroleum
and Minerals (KFUPM), Dhahran 31261, Saudi Arabia
e-mail: nesar@kfupm.edu.sa

together, while facing many challenges, including differences in chemical compositions and physical and mechanical properties. Based on its relative advantages against conventional fusion welding processes, researchers investigated the possibility of using *FSW* technique to replace the conventional joining methods of dissimilar metals and alloys, such as aluminum to copper, and achieve better quality weld joints [1–3]. Galvao et al. [4, 5] and Xue et al. [5, 6] analyzed the effects of tool design and working conditions on the material flow during *FSW* of aluminum grade *AA5083-H11* to copper. They reported that the relative location of material with respect to the advancing side of the tool as well as the tool geometry have significant effects on the shape of Al–Cu interaction regions and the intermetallic compounds formation. Shin et al. [7] performed an experimental study for dissimilar welding of *BMG* alloy to lightweight crystalline alloys, and studied the influences of tool geometry having round and triangular shaped pins. They concluded that the triangular pin tool produced more chips, and its cutting effect resulted in lowering the tool axial load and workpiece temperature in the early stage of the process as compared to the round pin case. Sun et al. [8] who analyzed flat *FSSW* for dissimilar metals, *Al 6061-T6* to mild steel succeeded to remove the keyhole produced by *FSSW* using a dent in the back plate and rotating pinless flat shoulder. However, they relied on physical bonding which resulted in weak joint strength.

This paper presents the results of performing successful butt-welding of aluminum grade *Al6061-T6* to commercial pure copper using friction stir welding (*FSW*) process. A finite element model was developed based on earlier work by Al-Badour et al. [9] to estimate the temperature distributions in the dissimilar materials and help explain the observed nuggets structures.

2 Experimental Procedure

Pure commercial copper and *Al6061-T6* plates measuring 100 mm × 50 mm × 4 mm were butt jointed using *FSW* process. The *FSW* tool used in this investigation was manufactured from tool steel (*H13 RC 50–55*), with 5 mm threaded pin diameter, 3.8 mm length, and had a scrolled shoulder of 11.52 mm diameter. Table 1 illustrates the welding conditions used in the investigation. The rotational speed of the tool was maintained at 900 rpm for all test conditions. All tests were

Table 1 Welding parameters and conditions

Condition	Welding speed (mm/min)	Tool offset (mm)	Advancing side material
1	150	0	Al6061-T6
2	20	0	Cu
3	40	0	Cu
4	40	2	Al6061-T6
5	40	2	Cu

performed on a fully instrumented experimental model *RM-1* friction stir welder manufactured by *MTI*. The weld beads were cross-sectioned, polished, and etched using a solution of 1 g of FeCl_3 , 10 ml HCl , and 100 ml distilled water to reveal copper side microstructure first and then using a solution of 3 ml HNO_3 , 6 ml HCl , 6 ml HF and 150 ml of distilled water to reveal the *Al6061-T6* side microstructure. The weld joints quality was evaluated by examining the optical microscope images of their cross sections to identify the presence or lack of voids, cracks and discontinuities. Using 300 g load and 10 s dwell time, Vicker’s hardness readings were taken across the weld joint at two locations, 1.5 mm and 3.00 mm below the top surface of the plate. Energy dispersive spectroscopy (*EDS*) analysis was performed at various locations of the weld joint to identify the elemental distribution of copper and aluminum.

3 Finite Element Model

A modified coupled Eulerian Lagrangian (*CEL*) finite element model that was developed by Al-Badour et al. [9], was used to simulate the *FSW* process of joining aluminum grade *Al6061-T6* to pure copper. The modified model, which is implemented and solved in Abaqus environment using Explicit Solver [10], considers a full geometrical model with threaded feature for the pin tool. Johnson-Cook’s-empirical law [11] in Eq. (1), is used to represent the plastic flow stress, σ_0 , of copper and Aluminum *6061-T6*.

$$\sigma_0 = \left(A + B\bar{\epsilon}_{pl}^n \right) \cdot \left(1 + \frac{c \ln \bar{\dot{\epsilon}}_{pl}}{\dot{\epsilon}_0} \right) \cdot \left[1 - \left(\frac{T - T_{ref}}{T_{melt} - T_{ref}} \right)^m \right] \quad (1)$$

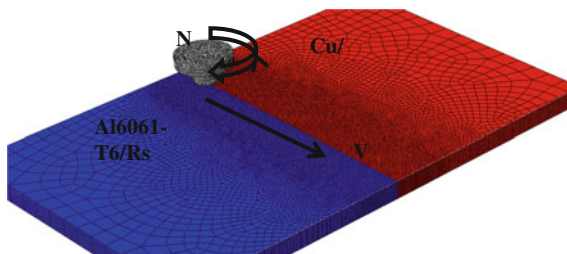
where $\bar{\epsilon}_{pl}$ is the effective plastic strain, $\bar{\dot{\epsilon}}_{pl}$ the effective plastic strain rate, $\dot{\epsilon}_0$ normalizing strain rate (typically 1.0 s^{-1}), A , B , C are material constants, n parameter takes into account the effect of strain hardening, m models the thermal softening effect and c represents the strain rate sensitivity. T_{ref} is the temperature where A , B and n are evaluated while T_{melt} is the material solidus temperature. Johnson-Cook’s-empirical law constants for copper and aluminum are given in Table 2.

Coulomb’s friction Law with an average coefficient of friction $\mu = 0.5$ was used to represent the interaction between the Eulerian (aluminum and copper) and Lagrangian (tool) domains [12]. As the Eulerian mesh is rigid, velocity constrains around the Eulerian domain were applied to avoid material escape. The tool

Table 2 Copper Johnson-Cook’s parameters [10]

Material	A (MPa)	B (MPa)	C	n	m	T_m (K)	T_0 (K)
Copper	90	292	0.025	0.31	1.09	1356	298
Al 6061-T6	324	114	0.002	0.42	1.34	855	298

Fig. 1 Al6061-T6/Cu CEL model materials locations and mesh generation



rotational speed and welding speed were 900 rpm and 40 mm/min, respectively. Moreover, the effect of tool offset on the weld joint quality was studied using 2 mm offset value to the retreating side. Figure 1 shows a typical model mesh of the Eulerian and Lagrangian domains.

4 Results and Discussions

4.1 Optimizing Welding Parameters

This section covers the procedure for finding the friction stir welding conditions that produce defect free weldments of aluminum to copper butt joint. Welding tests were first conducted to identify the *FSW* parameters that produced sound weld joints for each of Aluminum grade *Al6061-T6* to aluminum grade *Al6061-T6* and welding copper to copper. The goal is to use the results of these tests to find starting process parameters for welding aluminum to copper. Defect free weld joints of *Al6061-T6* to *Al6061-T6* were obtained when welding was performed at tool rotation speed of 900 rpm, welding speed of 175 mm/min, plunging depth of 3.8 mm, and tool tilt angle of 3°. Likewise, the welding parameters for obtaining sound Cu to Cu weldments were found to be 900 rpm rotational speed, 125 mm/min welding speed, 3.8 mm plunging depth, and 3° tool tilt angle. These optimum process parameters of welding copper to copper and aluminum to aluminum have been used as initial trial parameters for welding aluminum to copper.

The first trial test for welding aluminum to copper used the test condition 1 of Table 1. The 150 mm/min welding speed of this condition is the average value of the welding speeds used in joining copper-to-copper and aluminum-to-aluminum. No welding was achieved during the first test condition and the tool pin failed by fracture after travelling a distance of 50 mm only. The tool failure is attributed to an excessive cross feed (traverse) force of 7 kN that overloaded the tool. This high level of traverse force at the relatively fast welding speed of 150 mm/min was caused by a stronger weld bead that was subjected to faster cooling rate. In order to avoid tool failure and to obtain sound weld quality, several trials were performed under lower welding speed conditions of 80, 40, and 20 mm/min. Furthermore, the effect of having the softer material (aluminum) or the harder material (copper) at the

advancing side of the tool and of using tool offset relative to the center of the weld bead was explored at these welding speeds. The conditions which resulted in lower welding forces and acceptable weldment quality are: using lower welding speed, placing the hard material on the advancing side, and using a 2 mm offset of the tool. However, placing copper at the retreating side resulted in higher forces, even with the presence of an offset.

4.2 Quality of the Friction Stir Welded Al6061-T6 to Cu Joint

The effects of test conditions on the quality of the friction stir welded Al6061-T6 to Cu joints, with respect to the presence or lack of discontinuities, in the cross sections of the joints are revealed in the optical microscope images of the sectioned, polished, and etched weldments shown in Fig. 2. The two dissimilar material joints in Fig. 2a, b were both made using 900 rpm tool rotation, no tool offset, 3.78 mm

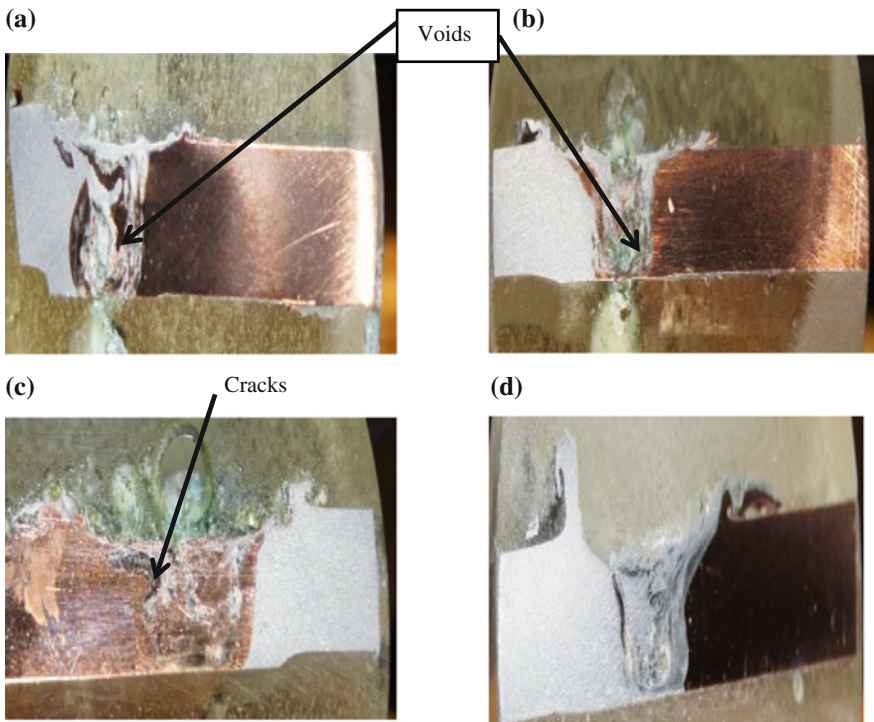


Fig. 2 Cross sections of the friction stir welded Al6061-T6 to Cu joint at different welding conditions, a condition 2, b condition 3, c condition 4, d condition 5

penetration depth, 3° tilt angle, and with copper placed at the advancing side of the pin tool. However, the joint of Fig. 2a was performed at 20 mm/min and that of Fig. 2b at 40 mm/min. The lack of tool offset under these two conditions appears to be the reason for the presence of voids in the *Al6061-T6-Cu* joint.

Evidence of presence of cracks appeared in a magnified image of the weldment of Fig. 2c which was made under condition 3 in Table 1. This weldment was performed under the conditions of Fig. 2b, except for the fact that the weld illustrated in Fig. 2c is made using 2 mm tool offset and the softer *Al60-T6* was placed on the advancing side. This lead to the conclusion that placing the softer material on the advancing side produces cracks. Figure 2d shows aluminum to copper weldment with no defects. This weldment was produced at the same welding conditions of weldment in Fig. 2c, except that the harder copper material was placed at the advancing side of the tool where more heat is generated by the tool compared with the retreating side. This provided copper with enough heat to soften and at the same time compensated for the heat loss arising from the higher thermal conductivity of copper. The relatively lower amount of heat generation when *Al6061-T6* was placed on the retreating side allowed it to be softened below melting point. These results are supported by those of the finite element analysis. It can now be concluded from the preceding that it is possible to weld copper to *Al6061-T6* and obtain sound weldments with relatively low welding force when copper is placed at the advancing side of the tool and by using tool offset of 2 mm towards the retreating side. The results of *EDS* analysis performed on the interface of the sound weld revealed the presence of Al_2Cu intermetallic compound of composition 71.0 wt% of Al and 29.0 wt% of Cu.

4.3 Phases in the Copper-to-Aluminum Weld Nugget

The approach to identifying the phases present in the aluminum-to-copper weld joint nugget is to simultaneously utilize the following:

- Elemental composition and relative concentrations of aluminum and copper at various locations of the nugget using *EDS* analysis.
- The temperature distribution of the weld nugget obtained from the finite element model.
- Phases and intermetallic compounds from Cu–Al phase diagram at various compositions and temperatures.

For example, to identify the phase or intermetallic compound present at a certain location of the nugget, find the concentration of Cu and its ratio to aluminum using *EDS* analysis, determine the temperature at the location, and then use the phase diagram of Al–Cu to identify the phase at that location. This process is repeated for all points of interest. Figure 3 shows the temperature distribution within the weld

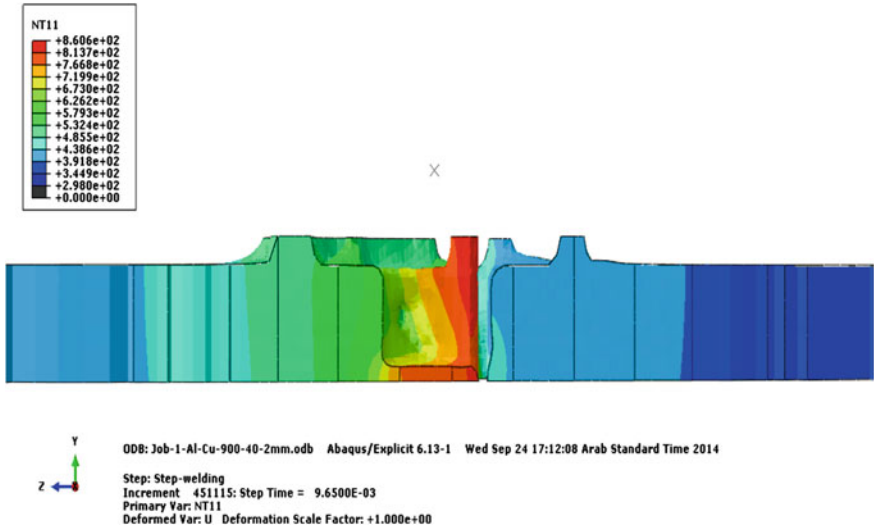
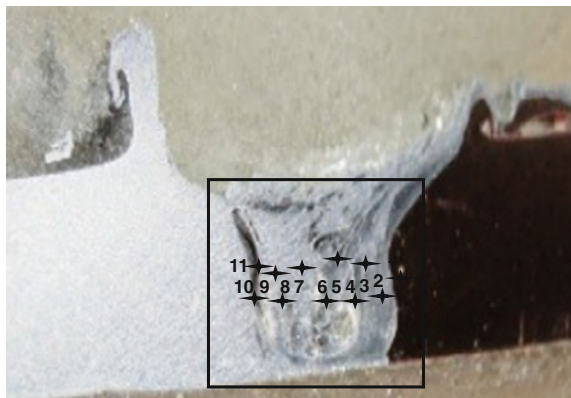


Fig. 3 CEL model temperature distributions, condition 3

Fig. 4 Aluminium to copper weld joint and EDS analysis locations, condition 3



joint obtained from the finite element analysis and Fig. 4 shows the sound aluminium to copper weld joint together with some of the locations where *EDS* analysis was performed. The aluminium copper phase diagram is shown in reference [13]. The concentrations of copper and aluminium where *EDS* analyses were performed are illustrated in Table 3, together with the corresponding intermetallic phases present in the copper side of the sound aluminium to copper weld nugget; and Table 4 is for the aluminium side. The elements and phases present on the copper side of the nugget include single phases of Al_2Cu , $AlCu$, Al_4Cu_9 , and Solid Solution $Al(Cu)$ in addition to a two phase ($Al + Al_2Cu$). Similar phases were also identified on the aluminium side of the sound nugget as shown in Table 4. The presence of intermetallic

Table 3 Spectrum analysis toward the Cu side

Al wt%	Cu wt%	Spectrum	Phase presents
69.55	30.45	1	Al ₂ Cu
76.17	23.14	2	Al ₂ Cu
92.87	6.36	3	Solid solution Al (Cu)
86.74	12.46	4	Al + Al ₂ Cu
84.31	14.95	5	Al + Al ₂ Cu
75.23	24.04	6	Al ₂ Cu
67.1	32.05	7	Al ₂ Cu
72.05	27.23	8	Al ₂ Cu
82.33	16.89	9	Al + Al ₂ Cu
52.66	46.75	10	AlCu
29.78	70.22	11	Al ₄ Cu ₉

Table 4 Spectrum analysis toward the Al6061-T6 side

Spectrum	Al wt%	Cu wt%	Phase presents
1	94.44	4.75	Solid solution Al (Cu)
2	19.05	80.95	Al ₄ Cu ₉
3	90.89	6.78	Solid solution Al (Cu)
4	93.54	5.65	Solid solution Al (Cu)
5	64.32	34.96	Al ₂ Cu
6	93.72	5.35	Solid solution Al (Cu)
7	71.71	27.62	Al ₂ Cu
8	61.30	37.85	Al ₂ Cu
9	55.38	44.62	AlCu

compounds and grain size refinement in the weld nugget caused the measured hardness values in the stir zone and surrounding areas to reach values of 200–250 HV. Note that the base metal hardness values vary between 47.8–68 HV for aluminum and 78.4–97 HV for copper.

5 Conclusion

The friction stir welding of aluminum grade *Al6061-T6* to pure copper was investigated using experimental and numerical approaches and the conditions that resulted in sound weld quality were identified. The following specific conclusions are drawn from the results of the present combined experimental and numerical study:

- A sound weld joint between these dissimilar materials has been achieved at lower welding speeds only when the pin tool was offset by 2 mm from the center of the weld line and the harder material (copper) was placed at the advancing side of the tool.

- A combined use of temperature distribution of the aluminum to copper weld nugget determined by a finite element model, the elemental concentration of copper and aluminum in the weld nugget from *EDS* analysis, and aluminum-copper phase diagram have been used to identify the phases present in the weldment.
- The aluminum-copper joint was found to consist of several single and two phase intermetallic compounds such as Al_2Cu , Al_4Cu_9 , $\text{Al} + \text{Al}_2\text{Cu}$.
- The presence of intermetallic compounds and grain size refinement in the weld nugget caused hardness values in the stir zone and surrounding areas to reach more than twice the hardness values of the base metals.

Acknowledgments The authors acknowledge the support provided by King Abdulaziz City for Science and Technology (KACST) through the Science and Technology Unit at King Fahd University of Petroleum and Minerals (KFUPM) for funding this work through project No. NSTP11-ADV2130-04 as part of the National Science, Technology and Innovation Plan.

References

1. Li, X., Zhang, D., Qiu, C., Zhang, W.: Microstructure and mechanical properties of dissimilar pure copper/1350 aluminum alloy butt joints by friction stir welding. *Trans. Nonferrous Met. Soc. China* **22**(6), 1298–1306 (2012)
2. Galvão, I., Verdera, D., Gesto, D., Loureiro, A., Rodrigues, D.M.: Influence of aluminum alloy type on dissimilar friction stir lap welding of aluminium to copper. *J. Mater. Process. Technol.* **213**(11), 1920–1928 (2013)
3. Ouyang, J., Yarrapareddy, E., Kovacevic, R.: Microstructural evolution in the friction stir welded 6061 aluminum alloy (T6-temper condition) to copper. *J. Mater. Process. Technol.* **172**(1), 110–122 (2006)
4. Galvão, I., Leal, R.M., Loureiro, A., Rodrigues, D.M.: Material flow in heterogeneous friction stir welding of aluminium and copper thin sheets. *Sci. Technol. Weld. Join.* **15**(8), 654–660 (2010)
5. Xue, P., Ni, D.R., Wang, D., Xiao, B.L., Ma, Z.Y.: Effect of friction stir welding parameters on the microstructure and mechanical properties of the dissimilar Al–Cu joints. *Mater. Sci. Eng. A* **528**(13–14), 4683–4689 (2011)
6. Galvão, I., Loureiro, A., Verdera, D., Gesto, D., Rodrigues, D.M.: Influence of tool offsetting on the structure and morphology of dissimilar aluminum to copper friction-stir welds. *Metall. Mater. Trans. A* **43**(13), 5096–5105 (2012)
7. Shin, H.-S.: Tool geometry effect on the characteristics of dissimilar friction stir spot-welded bulk metallic glass to lightweight alloys. *J. Alloys Compd.* **586**, S50–S55 (2014)
8. Sun, Y.F., Fujii, H., Takaki, N., Okitsu, Y.: Microstructure and mechanical properties of dissimilar Al alloy/steel joints prepared by a flat spot friction stir welding technique. *Mater. Des.* (2012)
9. Al-Badour, F., Merah, N., Shuaib, A., Bazoune, A.: Coupled Eulerian Lagrangian finite element modeling of friction stir welding processes. *J. Mater. Process. Technol.* **213**(8), 1433–1439
10. Abaqus ‘software’ **6**(11–2) (2011)
11. Johnson, G.R., Cook, W.H.: A constitutive model and data for metals subjected to large strains, high strain rates and high temperatures. In: 7th International Symposium on Ballistics, Netherlands, pp. 541–547 (1983)

12. Al-Badour, F., Merah, N., Shuaib, A., Bazoune, A.: Thermo-mechanical finite element model of friction stir welding of dissimilar alloys. *Int. J. Adv. Manuf. Technol.* **72**(5–8), 607–617 (2014)
13. Kutz, M. (ed.): *Mechanical Engineers Handbook*, 2nd edn. Wiley (1998)

Heat-Affected Zone as Critical Location in Pressure Equipment

Ljubica Milović

Abstract The majority of pressure equipment is made from joining by welding parts or sub-assemblies. Welded structure should be produced by spending minimum of cost, assuring in the same time required function and safety. By proper selection of welded joint and material, designer determines the properties of final product, and also possibility of its fabrication. The greatest attention during designing and fabrication of pressure equipment should be paid to the most vulnerable part of a welded joint, its heat-affected zone. In current paper, an approach in solving the problem of cylindrical vessel under internal pressure containing an axial crack is presented.

Keywords Heat-affected zone • Residual stresses • Surface crack • Elastic-plastic fracture mechanics

1 Introduction

Frequent failures of equipment operating at high pressure during their operating life time may cause catastrophic consequences in human life losses and great material damage.

Pressure equipment is in general a welded structure because of high speed and low costs during fabrication. Microstructural inhomogeneity of weldments makes them susceptible to material discontinuities, flaws and residual stresses which may lead to life time reduction and failure.

The experience, built-in into developed standards, indicates that cracks are not allowed imperfections in welded joints (*ISO 5817*), except cracks in crater of low quality welded joints and microcracks whose cross section is less than 1 mm^2 . It is not always possible to detect reliably cracks of that size. Therefore, welded joints

L. Milović (✉)

University of Belgrade, Faculty of Technology and Metallurgy,
Karnegijeva 4, 11120 Belgrade, Serbia
e-mail: acibulj@tmf.bg.ac.rs

can contain crack-like defects, so welded structures containing crack can be used in service in real loading conditions, what is in conflict with valid requirements. Cracks can also be initiated from locations of stress concentration and developed under operational loading and environment effects by different mechanisms (fatigue, creep, corrosion and stress corrosion).

In order to avoid failure of pressure equipment the defects and heterogeneities have to be under strict control and inspection.

Pressure equipment includes different constructions, from simple units, like gas holder for household use, up to components in very complex systems, like oil refinery or power generation plant. They are exposed to different pressure levels, from low, somewhat above atmospheric pressure, up to several hundred bars, and they are operating in different environments. The consequences of failure of pressure equipment can be from negligible till catastrophic, with human loss and great material damage, depending on the risk level [1].

Stress analysis is the determination of the relationship between external forces applied to a pressure vessel or related equipment and the corresponding stress. In order to get a safe, reliable and economical design it is not necessary to find every stress, but rather to be aware of the governing stresses and how they relate to the construction or its parts [2].

2 Materials for Pressure Vessels Manufacturing

The rapid development of the steel production technology of the 21st century is challenged by global climate changes and environmental pollution. A significant influence on economy of the own weight of heavily loaded steel constructions such as pressure vessels or penstocks, should not be neglected neither. Scientists and engineers worldwide are faced with the necessity of developing modern high strength steels which will have excellent toughness, favorable cold forming properties and good welding capacity which shall not contradict their high strength. For example, if the steel strength was increased from 400 to 800 MPa, the steel consumption would be reduced greatly, which will contribute to energy conservation and emission reduction of greenhouse gases.

In order to fulfill the requirements for lightweight heavily loaded constructions with reduction of the own weight without a loss of the load capacity and reduction of the operation costs, modern metallic materials need to poses good weldability for reduce limitations of preheating, decrease bead and length of repair welding. The high resistance of those advanced steels to brittle fracture is also required. Nowadays the leading steel-producing companies and suppliers provide high-grade weldable, quenched and tempered, fine-grained structural steel products with yield stress up to 1100 MPa and ultimate tensile strength varying from 1200 to 1500 MPa. Those contemporary advanced materials are high-strength low-alloyed (*HSLA*) fine-grained steels with a fine martensitic/bainitic microstructure possessing

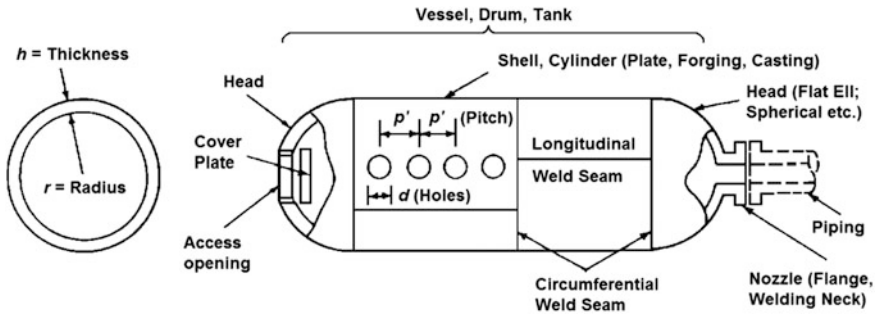


Fig. 1 Pressure vessel main components [1]

appropriate combination of high strength, excellent toughness and high fatigue resistance [3].

The plastic mechanical properties of a material are those which measure its ability to resist rupture, undergo deformation, and absorb energy. These are obtained from the same stress-strain diagram of the material as the elastic mechanical properties.

The steel plates used to fabricate the shells and heads of the vessels, Fig. 1, must have sufficient strength and ductility to permit them to be bent from a flat plate to their final curvatures without cracking. It is often necessary to heat the material to high temperatures to increase its ductility during the forming operation.

The increasing use of vessels for processing, storage and power generation under unusual conditions of pressure, temperature and environment requires better analytical and experimental methods for determining their operating stresses and understanding of their significance.

Detailed knowledge of material behavior is required not only to avoid failures, but also to enable optimal choice of material from economical point of view. If the stresses or strains in a structure are overly low, its size becomes larger than necessary and the economic potential of the material is not reached. Developments in the nuclear and chemical industries have placed additional demands on materials suitable for extremes in temperature, impact and fatigue. Sometimes these applications also require consideration of other environmental effects, such as corrosion and hydrogen embrittlement.

3 Welded Joints of High-Strength Steels

Cracks in components subjected to static and cycle loads, for a certain operation period can grow stable (subcritical) after when they become unstable (critical). Safety assessment of detected/supposed flaws in welded structure, i.e. conservative assessment if those flaws will become critical in an observed operating interval, is

based on linear elastic or elastic-plastic fracture mechanics. Therefore, the Leak-Before-Break concept (*LBB*) is generally accepted as a method for determination of pressurized components susceptibility to unstable crack growth fracture. The *LBB* concept comprises the phenomenon that the stable crack growth through the wall causes leak that could be easily detected long before the global fracture of component occurs, so the ‘through wall’ fracture is considered as safe.

The fatigue life of a welded structure depends on the fatigue strength of its welded joints. The shape of those joints and the quality of the welds are much more important than material fatigue strength. Thus the welds have to be considered as areas where fatigue cracks initiate and propagate. The use of *HSLA* steels in the case of predominant fatigue loading is considerably limited due to their notch sensitivity. The high static strength value of the parent material (*PM*) can result in higher fatigue strength value of welded joints if the welds are of very good profile and almost without imperfections [4–10].

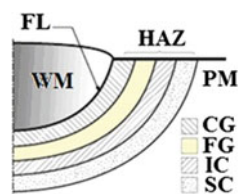
Usually the most critical region of a welded joint is its heat-affected zone (*HAZ*). Generally speaking the term *HAZ* comprises the *PM* underlying the weld which has been heated to peak temperatures (T_p) above A_1 temperature (typically 723 °C) but below the solidus temperature which is around 1495 °C. Steel microstructure in *HAZ* depends on the heat input during welding and varies depending on the distance from the fusion line (*FL*): as the distance from the *FL* increases, T_p that the *PM* microstructure is exposed to, decreases. Because of welds microstructure inhomogeneity and diversity, susceptible zones which are either more strong and brittle or more weak and ductile than the *PM*, exists in welds and/or their *HAZ*.

Certain microstructures that may occur in *HAZ* are susceptible to brittle fracture. These regions called *Local Brittle Zones* (*LBZ*) must be studied in details because brittle fracture is a weak-link process that is triggered by a local cleavage event [11].

Welding thermal cycle is the most suitable described by the maximal heating temperature T_p and the cooling time between the temperature interval from 800 to 500 °C, $\Delta t_{8/5}$.

Typical *HAZ* of high-strength steels consists of four regions: coarse-grained, fine-grained, intercritical and subcritical [11–16]. In Fig. 2 typical microstructure manifested during single pass welding of high-strength quenched-and-tempered steel are presented, where:

Fig. 2 Schematic view of single-pass heat-affected zone region of a high-strength quenched-and-tempered steel



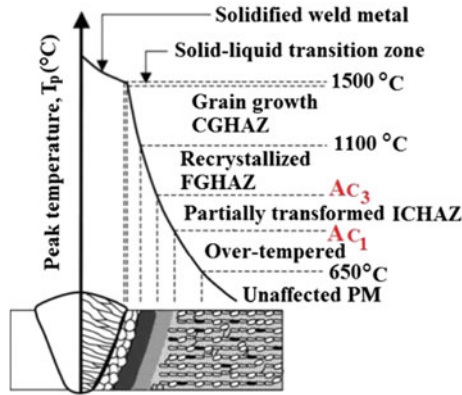


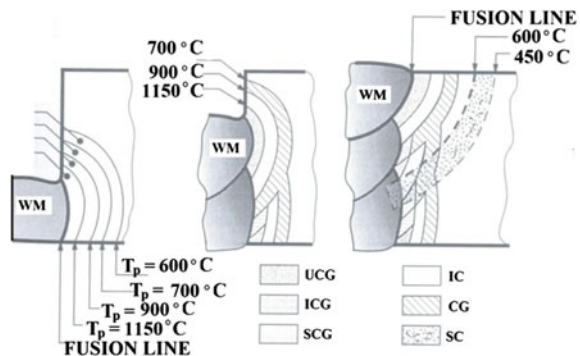
Fig. 3 Typical microstructures in the HAZ of high strength steels formed during welding: $T_{PCGHAZ} \sim (1100 \div 1400) \text{ } ^\circ\text{C}$; $T_{PFGHAZ} \sim (900 \div 1100) \text{ } ^\circ\text{C}$; $T_{PICHAZ} \sim (700 \div 900) \text{ } ^\circ\text{C}$; $T_{PSCHAZ} \sim (<700) \text{ } ^\circ\text{C}$

- *FL* denotes *fusion line*, region of fusion or partial melting;
- *CG* denotes *course grain* region. During welding metal close to the *FL* reaches the temperature above A_{c3} point; all carbides presenting the major obstacle to austenite grains growth are dissolved, and as a consequence, course austenite grains are formed;
- *FG* denotes *fine grain* region. Away from *FL* this is the region of normalization, i.e. of grain refinement;
- *IC* denotes *intercritical* region, i.e. region of partial austenitization and
- *SC* denotes annealing region called *subcritical* region.

The T_p temperature defines the width of each region. The approximate T_p ranges for each of the four characteristic regions of HAZ shown in Fig. 2 are presented in Fig. 3 (Fig. 4).

Usually, *CGHAZ* and sometimes *ICHAZ* have the lowest toughness. In a multipass welds, parts of the *CGHAZ* are subjected to the same range of T_p , i.e. part is

Fig. 4 Schematic view of HAZ microstructure during single-pass, double-pass and three-pass welding



melted, part reforms as *CGHAZ*, part is refined and part is modified by exposure to lower temperatures. The later parts, which retain the coarse grain structure, are identified as the intercritical *CGHAZ* (*ICCGHAZ*) and the subcritical *CGHAZ* (*SCCGHAZ*). The entire CG region, which includes the unaltered plus the *ICCGHAZ* and *SCCGHAZ*, is potentially in *LBZ* [11–17].

4 Influence of Residual Stresses Induced by Welding on Behavior of Pressure Vessels Containing Cracks

Generally speaking, residual stresses are mechanical stresses which can act alone or in addition to applied loading in materials and components.

Due to local heating during welding, the joints made by fusion of materials are exposed to the influence of residual stresses induced by welding thermal process. As welded joints are formed in complex shapes and groove geometries, the residual stresses have complex three-dimensional distributions. Residual stresses arisen as a result of welding thermal cycles are difficult to measure and to estimate theoretically, but they are significant when comparing with service stresses on which they superimpose [18].

As the design of engineering components becomes less conservative, there is increasing interest in how residual stress affects their mechanical properties [19]. High tensile residual stresses gradients in the vicinity of welds may generate brittle fracture, fatigue or stress corrosion cracking, while compressive residual stresses may reduce buckling strength. If the *PM* is brittle, residual stresses may remarkably reduce the fracture strength of the weldment. In case that *PM* is ductile, the effects of residual stresses can be neglected.

Under the influence of residual stresses caused by welding thermal cycles, material yield strength can be reached slowly or rapidly which depends on stress multi-axiality, local changing in hardness, increasing risk of brittle fracture, susceptibility to stress corrosion cracking induced by surface tensile stresses and distortion of components.

Occurring of residual stresses is always associated with inhomogeneous line or volume deformation of certain areas of material wherein this deformation does not necessarily have to be mechanical.

Residual stresses in a body are those which are not necessary to maintain equilibrium between the body and its environment. They may be categorized by cause (thermal or elastic mismatch), by the scale over which they self-equilibrate, or according to the method by which they are measured [20]. There are three types of residual stresses in accordance with volume of material that they cover, e.g. a length scale perspective (from a few nanometers to few millimeters):

First order residual stresses (Type I), also called macro residual stresses containing several grains and equilibrate with all surrounding volume of material. They

may originate from mechanical, thermal, chemical treatment operations or their combined effect.

Second order residual stresses (Type II), also called intergranular stresses or homogenous micro residual stresses, are almost homogeneous over the grain scale (inside one grain or even part of one grain) and equilibrate in areas of sufficient number of grains. *Type II* residual stresses develop rarely, for example in the individual grains of a homogenous material with pronounced yield stress anisotropy, after being subjected to elastic-plastic deformation, because of the fact that the elastic and thermal properties of differently oriented neighboring grains are different.

Third order residual stresses (Type III), also called inhomogeneous micro residual stresses are inhomogeneous in submicroscopic dimensions of material, e.g. in several interatomic distances in the small grain area. They may originate from:

- vacancies, substitutional and interstitial atoms, edge dislocations, low angle grain boundaries, twin boundaries;
- groups of vacancies, foreign atoms zones, grain boundaries, phase boundaries;
- precipitates, inclusions, microcracks, voids.

Residual stresses always occur during welding. In case of multilayer welded joints of thick components like pressure vessels, it is extremely important to know the possible effect that residual stresses can make on the structural behavior and integrity. Distributions of residual stress field at the plate surface and over the thickness of the pressure vessel wall are equally important. It is important to measure values of residual stresses in both weld directions (longitudinal and transverse) in order to make their distribution.

5 Pressure Vessel Design by Application of Allowed Damage on the Basis of Nonlinear Fracture Mechanics

Within the study of dissipative environments fracture, various forms of asymptotic stress and strain fields around the crack tip were suggested. The most widely accepted solution is the one given independently by Hutchinson and Rice and Rosengren, e.g. field near the crack tip where $r \rightarrow 0$, named after the three of them the *HRR* singularity.

$$\sigma_{ij} = \sigma_0 \cdot \left(\frac{E \cdot J}{\alpha \cdot \sigma_0^2 \cdot I_n \cdot r} \right)^{\frac{1}{n+1}} \cdot \tilde{\sigma}_{ij}(n, \theta) \quad (1a)$$

$$\varepsilon_{ij} = \alpha \cdot \varepsilon_0 \cdot \left(\frac{E \cdot J}{\alpha \cdot \sigma_0^2 \cdot I_n \cdot r} \right)^{\frac{n}{n+1}} \cdot \tilde{\varepsilon}_{ij}(n, \theta) \quad (1b)$$

where n , $\varepsilon_0 = \frac{\sigma_0}{E}$ and α are constants that exists in constitutive equation $\frac{\varepsilon}{\varepsilon_0} = \frac{\sigma}{\sigma_0} + \alpha \cdot \left(\frac{\sigma}{\sigma_0}\right)^n$, whereas I_n is an integration constant that depends on strain hardening exponent n and $\tilde{\sigma}_{ij}$ and $\tilde{\varepsilon}_{ij}$ are dimensionless functions of n and θ [21]. From Eq. (1a, 1b) Rice-integral:

$$J = \int_{\Gamma} \left[W dy - \sigma_{ij} \cdot n_j \cdot \frac{\partial u_i}{\partial x} ds \right] \quad (2)$$

Plays the role of amplitude of *HRR* singularity so that the one-parameter characterization of fracture is extended to elastic-plastic domain.

However, numerous limitations in which this asymptotic approach is valid exist. First of all the applied load must be proportional with the strain. It means that a growing crack or crack induced by cyclic load can not be considered within the *HRR* field. *HRR* analysis is valid at the distances very close to the crack tip, completely inside the plastic zone where the elastic strains are small comparing to the total strain.

Single parameter fracture mechanics, e.g. K , J or $CTOD$ is no more valid under large-scale yielding (*LSY*) because critical J value is no more constant with crack growth but depends on the size and geometry of the test specimen.

Additional parameter will be added to this analysis. This is the value of the *process zone* (*PZ*) near the crack tip ($0 \leq r \leq \Delta$). Bearing in mind that within this zone *HRR* singularity is no longer valid, *PZ* can be considered as a kind of “black hole” which is covered by fields described by continuum mechanics. However it is possible, by introducing such extremely nonlinear (but not singular!) zone in analysis, take into account material behavior under disproportionate loading as cyclic loading, no matter if small-scale yielding (*SSY*) or *LSY* is considered.

Symbol Δ denotes the extent of small region next to the crack tip so-called *process zone* which enters into the theory through a criterion of quasi-static crack extension, such as Wnuk’s final stretch criterion [22].

$$\frac{d\zeta}{dQ} = \frac{2 \cdot \zeta \cdot Q}{\ln\left(\frac{j}{\zeta \cdot Q^2}\right) - Q^2} \quad (3)$$

where j designates the quotient of the R-curve upper limit (stationary state) and its initial value, i.e. $j = \frac{J_{SS}}{J_{Ic}}$. By integration of Eq. (3) per one cycle the corresponding increment of crack length can be determined as:

$$\Delta\zeta_{one\ cycle} = \frac{\Delta\zeta}{\Delta N} = \int_{Q_{min}}^{Q_{max}} \left[\frac{2 \cdot \zeta \cdot Q \cdot dQ}{\ln\left(\frac{j}{\zeta \cdot Q^2}\right) - Q^2} \right]_{\zeta \cong const} \quad (4)$$

In general case the integral in Eq. (4) is evaluated numerically. However if some simplifications are taken into account, it is possible to get the closed-form solution as:

$$\frac{da}{dN} = \alpha_1 \cdot \left(\frac{E}{\sigma_0^2} \right) \cdot \frac{dJ}{T_0} \cdot \frac{j - \frac{J_m}{J_{fc}}}{j - 1} \quad (5)$$

where α_1 is an empirical constant and T_0 is dimensionless tearing modulus. T_0 is defined by the initial slope of resistant curve J_R in function of Δa ,

$$T_0 = \frac{E}{\sigma_0^2} \cdot \left(\frac{dJ_R}{da} \right)_{ini} \quad (6)$$

The other variables are:

$\Delta J = J_{\max} - J_{\min}$, J -integral range;

$J_m = \frac{J_{\min} + J_{\max}}{2} = \frac{J_{\max} \cdot (1 + r^2)}{2}$, J -integral arithmetic mean expressed also by the r-ratio $r = \frac{J_{\min}}{J_{\max}}$;

$j = \frac{J_{SS}}{J_{fc}}$, quotient of toughness increasing.

In case of relatively simple material behavior ($n = \infty$), resistant curve is given by Wnuk equation [23, 24]:

$$\frac{dR}{da} = M - \frac{\ln\left(\frac{4 \cdot e \cdot R}{\Delta}\right)}{2} \quad (7)$$

where R linearly depends on J_R as:

$$R = \left(\frac{\pi \cdot E}{8 \cdot \sigma_0^2} \right) \cdot J_R \quad (8)$$

In order that the crack growth is stable, the value of tearing modulus $M = \frac{\dot{K}}{\Delta}$ must be between the lower (M_{\min}) and upper (M_{\max}) bound:

$$\frac{1}{2} + \frac{1}{2} \cdot \ln(4 \cdot \rho_i) < M \leq \rho_i \quad (9)$$

If the value of tearing modulus defined by Paris from Eq. (6) is known, then modulus M can be determined as:

$$M = \frac{\pi}{8} \cdot \eta \cdot T_0 + 0.5 \cdot \ln(4 \cdot e \cdot \rho_i) \quad (10)$$

$\eta = 1$ for plain stress conditions and $\eta = 1 - \nu^2$ for plain strain conditions. Finally, if the ductility parameter ρ_i and the tearing modulus M are known, then quotient of toughness increasing j can be determined from

$$j = \frac{1}{4 \cdot \rho_i} e^{(2M-1)} \quad (11)$$

The ductility parameter ρ_i is defined as quotient of nonlinear zone length at the beginning of crack growth R_{mi} and value of the process zone Δ

$$\rho_i = \frac{R_{mi}}{\Delta} \cong \frac{\varepsilon_f^{pl}}{\varepsilon_0} \quad (12)$$

It is observed that ρ_i has a direct impact on all values that describes fatigue crack growth as it is given by Eq. (5).

Using Ramberg-Osgood constitutive equation for the hardening material:

$$\varepsilon_{ij}^{pl} = \frac{3}{2} \cdot \alpha \cdot \left(\frac{\sigma_e}{\sigma_0} \right)^{n-1} \cdot \frac{s_{ij}}{E} \quad (13)$$

where $\sigma_e = \frac{1}{\sqrt{2}} \cdot [(\sigma_1 - \sigma_2)^2 + (\sigma_1 - \sigma_3)^2 + (\sigma_2 - \sigma_3)^2]^{\frac{1}{2}}$ denotes effective von Mises stress and $(\sigma_1, \sigma_2, \sigma_3)$ are the three principal normal stresses. Hunsacharoonroj and Wnuk [25] derived following expression for R -curve

$$\frac{dR}{da} = M_n - \frac{1}{2} \cdot \left(\frac{R}{\Delta} \right)^\beta - \frac{1}{2} \cdot \left(\frac{R}{\Delta} \right)^\beta \cdot \ln^{1-0.5\beta} \left[4 \cdot \left(\frac{R}{\Delta} \right)^{1-\beta} \right] \quad (14)$$

where M_n denotes tearing modulus for hardening material, $\varepsilon^{pl} = \alpha \cdot \left(\frac{\sigma}{\sigma_0} \right)^{n-1} \cdot \left(\frac{\sigma}{E} \right)$, and $\beta = \frac{1}{n+1}$.

5.1 Application of Elastic-Plastic Fracture Mechanics on Fail-Safe Pressure Vessel Design

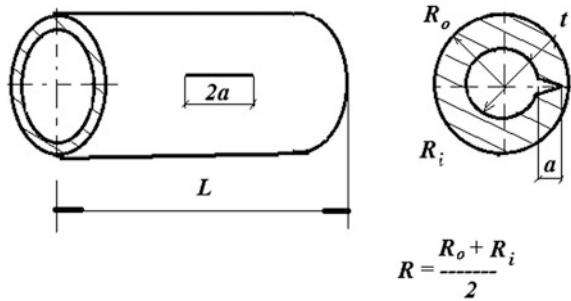
Problem of cylindrical vessel under internal pressure containing an axial crack, taking account material plasticity and strain hardening, will be considered by using two methods: $R6$ procedure e.g. Failure Assessment Diagram (FAD) and assessment by $EPRI$.

The design methodology will be illustrated on the example of thick-walled pressurized cylindrical vessel with axial crack on the inner side, Fig. 5.

The example will be done with following data which correspond to $A533B$ steel [26, 27].

$R_i = 500$ mm, $R_o = 600$ mm, $t = 100$ mm, $a = 25$ mm, $\sigma_0 = 414$ MPa, $E = 207$ GPa, $\nu = 0.3$, $\alpha = 1.12$, $\varepsilon_0 = 0.002$, $n = 10$.

Fig. 5 Geometry of cylindrical vessel under internal pressure with axial crack



Besides listed data, analytically obtained J_R curve is also used [27]. Boundary value J_{IC} is about $350 \text{ kN/m} = 0.350 \text{ MPa} \cdot \text{m}$. Equivalent value for K_{IC} , e.g. K_{Jc} is:

$$K_{Jc} = \sqrt{\frac{J_{IC} \cdot E}{1 - \nu^2}} = \left[\frac{(0.350 \cdot 207000)}{1 - 0.3^2} \right]^{\frac{1}{2}} = 282 \text{ MPa}\sqrt{\text{m}} \quad (15)$$

For strain hardening material, flow stress σ_{flow} can better describe material behavior than usual yield stress σ_0 . By incorporating value $N = \frac{1}{n} = 0.1$ and σ_0 :

$$\sigma_{\text{flow}} = \frac{\sigma_0}{2} \cdot \left[1 + \frac{\left(\frac{N}{\varepsilon_0}\right)^N}{e^N} \right] = 484 \text{ MPa} \quad (16)$$

It is now possible to apply *FAD* defined by intersection of critical parameters $K_r = \frac{K_I}{K_{IC}}$ and $S_r = \frac{\sigma}{\sigma_c}$ based on strip yield model [21]:

$$K_r = S_r \cdot \left[\frac{8}{\pi^2} \cdot \ln \sec\left(\frac{\pi}{2} \cdot S_r\right) \right]^{-\frac{1}{2}} \quad (17)$$

The curve resulting from the Eq. (17) is shown on Fig. 6.

Critical value of fracture stress σ_c can be determined for the pressure for complete elastic deformation of the cylinder without crack,

$$p_L^{(0)} = \frac{2}{\sqrt{3}} \cdot \sigma_{\text{flow}} \cdot \ln \frac{R_o}{R_i} = 102 \text{ MPa} \quad (18)$$

or for the cylinder containing crack as

$$p_L^{(1)} = \frac{2}{\sqrt{3}} \cdot \sigma_{\text{flow}} \cdot \ln \frac{R_o}{R_i + a} = 74.6 \text{ MPa} \quad (19)$$

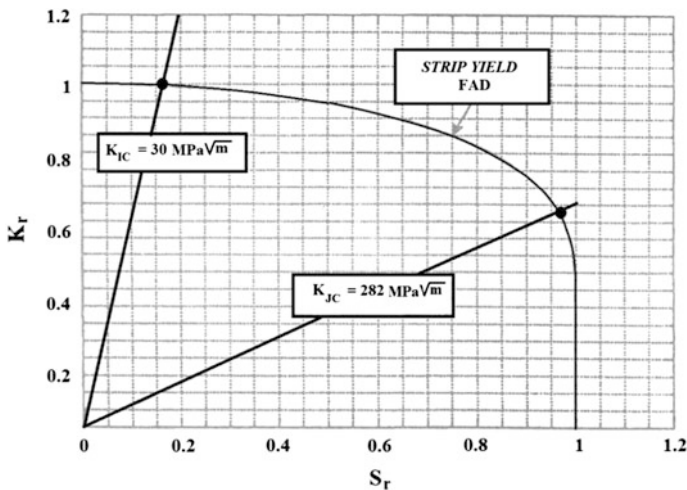


Fig. 6 Failure assessment diagram according to Eq. (17)

This value represents limit pressure for cracked cylinder made of material with infinite fracture toughness. The value of $p_L^{(1)}$ will be used for approximate determination of σ_c . Now the dimensionless variable S_r in Eq. (17) becomes:

$$S_r = \frac{p}{74.6} \tag{20}$$

From the handbook [28] for given geometry in Fig. 5:

$$K_I = \frac{2 \cdot p \cdot R_o^2}{R_o^2 - R_i^2} \cdot \sqrt{\pi \cdot a} \cdot F\left(\frac{a}{t}\right) \tag{21}$$

$$F\left(\frac{a}{t}\right) = 1.1 + A \cdot \left[4.951 \cdot \left(\frac{a}{t}\right)^2 + 1.092 \cdot \left(\frac{a}{t}\right)^4 \right] \tag{22a}$$

$$A = \left(0.125 \cdot \frac{R_i}{t} - 0.25 \right)^{\frac{1}{4}} = 0.78254 \tag{22b}$$

For the starting value of crack depth $\frac{a}{t} = 0.25$ it is obtained $F(0.25) = 1.345486$ and $K_I(0.25, p) = 2.468 \cdot p$. Second dimensionless variable in Eq. (17) becomes:

$$K_r = \frac{2.468 \cdot p}{K_{IC}} \tag{23}$$

Taking into account:

$$K_{IC} = \begin{cases} 30 \text{ MPa}\sqrt{m}, & \text{lower toughness limit} \\ 282 \text{ MPa}\sqrt{m}, & \text{upper toughness limit} \end{cases} \quad (24)$$

we get two solutions of Eq. (17): $S_r = \frac{p}{74.6}$ and $K_r = \frac{2.468 \cdot p}{K_{IC}}$.

Those solutions are:

$$\begin{aligned} p_f^L &= 12.10 \text{ MPa} && \text{for lower toughness limit} \\ p_f^U &= 71.97 \text{ MPa} && \text{for upper toughness limit} \end{aligned} \quad (25)$$

We will now go on *EPRI* assessment in order to analyze in details ascertainment that ductile material such as *A533B* can stand a certain crack growth, and *EPRI* assessment methodology covers instabilities during ductile deformation process around the crack tip. Elastic value of J_{el} integral is:

$$J_{el} = \frac{K_I^2 \cdot (1 - \nu^2)}{E} = 0.02678 \cdot p^2 \quad (26)$$

Fully plastic deformation of the cracked ligament is given as plastic value of J_{pl} integral

$$J_{pl} = \alpha \cdot \varepsilon_0 \cdot \sigma_0 \cdot \frac{b \cdot a}{t} \cdot h_1 \left(\frac{a}{t} \right) \cdot \left(\frac{p}{p_0} \right)^{n+1} \quad (27)$$

Auxiliary function h_1 value for $\frac{a}{t} = 0.25$ is $h_1(0.25) = 9.45$ and:

$$p_0 = \frac{2 \cdot b \cdot \sigma_0}{\sqrt{3} \cdot (R_i + a)} \quad (28)$$

$$J_{pl}|_{a=0.25} = 164.3166 \cdot \left(\frac{p}{p_0} \right)^{11} \quad (29)$$

The referent loading is now:

$$p_0 = \frac{2 \cdot 75 \cdot 10^{-3} \cdot 414 \cdot 10^6}{\sqrt{3} \cdot (500 + 25) \cdot 10^{-3}} = 68.292 \text{ MPa} \quad (30)$$

Total value of J integral in the beginning of the ductile crack growth (tearing fracture):

$$(J_{el} + J_{pl})_{a=25\text{mm}} = J_{IC} \quad (31a)$$

or:

$$0.02678 \cdot p^2 + 164.3166 \cdot \left(\frac{P}{68.292}\right)^{11} = 350 \quad (31b)$$

Solution of above equation is:

$$p_{mi} = 70.084 \text{ MPa} \quad (32)$$

represents the loading value at the beginning of ductile crack growth. Obviously there is good agreement with result of $R6$ curve (71.97 MPa, Eq. (25)), specially if we have in mind that in that case strain hardening was neglected.

Now we will compare crack driving forces values

$$J(X, p) = J_{el}(X, p) + J_{pl}(X, p) \quad (33)$$

with J_R material resistant curve $J_R = J_R(X - X_0) = J_R(\Delta X)$, where $X = \frac{a}{t}$ is dimensionless crack length.

For steel $A533B$ a lot of experimental data about $J_R - \Delta a$ curve exists. Combining data taken from *EPRI* with Wnuk Mura method for curve fitting [29].

$$\frac{dJ_R}{da} = \frac{A \cdot J_{IC}}{J_R} - B \quad (34)$$

It is possible to present analytically empirical *EPRI* data. For the value $J_{IC} = 350$ kN/m and $A = 44000$ and $B = -1000$ kPa, Eq. (34) can be integrated. What we need is only the first segment of J_R curve [30]. For the ligament of the cylinder with crack of 75 mm length and initial crack depth 25 mm, it is possible to conclude that increase of crack length Δa will not exceed 20 % of initial crack depth. Confirmation of this estimation is shown in Fig. 7. Intersection point in Fig. 7b denotes transition from stable to unstable fracture. Values for T_{appl} and T_R are determined from relations:

$$T_{appl} = \frac{\partial J(X, p)}{\partial X} \text{ and } T_R = \frac{dJ_R}{dX} \quad (35)$$

5.2 Discussion

As it can be seen on Fig. 7a, b, both approaches give the same result. For the example demonstrated in Sect. 5.1, coordinates of critical point are: $\Delta X_f = 0.036997$ or $a_f = 28.7$ mm and $J_f = 1150$ kPa · m for $p_f = 76.09$ MPa.

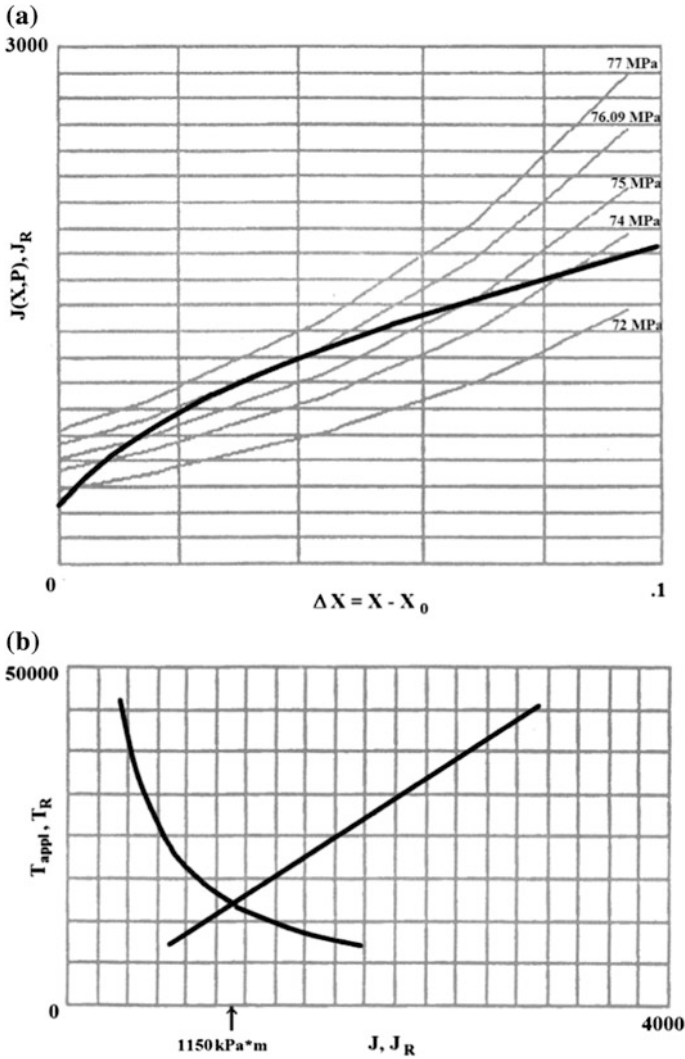


Fig. 7 Structural integrity analysis, **a** crack driving force versus dimensionless crack length for given loadings, **b** stability estimation diagram

Those values indicate around 15 % of slow stable crack growth followed by increasing of the limit load of 8.6 %. Having in mind that the whole process takes place in quite steep slope segment of the J_R curve, increasing of apparent material toughness measured by J_R integral is 214 % (or 146 % if K_R is taken for measure of fracture toughness).

6 Conclusion Remarks

Concept of the existing fracture like defect which must be taken into account during designing by appropriate methodology, form the fundamental nature of fail-safe pressure vessel design. Material fracture toughness determination is only one aspect of fracture mechanics. In order to apply the fail-safe-with-allowed-defects design for structures like aircrafts, thermal and nuclear power plants, spacecrafts and space stations, the latest technologies should be established in the industry. It is necessary to know mathematical relations between toughness, stress and crack length.

References

1. Sedmak, A., Sedmak, S., Milović, Lj.: Pressure Equipment Integrity Assessment by Elastic-Plastic Fracture Mechanics Methods DIVK (2011)
2. Dennis, R.M.: Pressure Vessel Design Manual. Elsevier (2004)
3. Tschersich, H.-J., Kern, A., Schriever, U.: Modern high-strength structural steels with high component reliability, pp. 3–10. In: Neumann, P., Allen, D., Teuckhoff, E. (eds.) Steels and Materials for Power Plants, EUROMAT 99-vol. 7. Wiley-Vch (2000)
4. Gliha, V., Toplak, D.: Fatigue strength of a butt welded HSLA structural steel with backing. In: Sedmak, S. (ed.) The Application of Fracture Mechanics to Life Estimation of Power Plant Components, pp. 255–270. EMAS (1990)
5. Zrilić, M., Rakin, M., Milović, Lj., Burzić, Z., Grabulov, V.: Experimental and numerical evaluation of a steamline behaviour using local approach. *Metalurgija* **46**(2), 87–92 (2007)
6. Manjgo, M., Medo, B., Milović, Lj., Rakin, M., Burzić, Z., Sedmak, A.: Analysis of welded tensile plates with a surface notch in the weld metal and heat affected zone. *Eng. Fract. Mech.* **77**(15), 2958–2970 (2010)
7. Milović, Lj., Vuherer, T., Zrilić, M., Momčilović, D., Jaković, D.: Structural integrity assessment of welded pressure vessel produced of HSLA steel. *J. Iron Steel Res. Int.* **18**(1–2), 888–892 (2011)
8. Vuherer, T., Milović, Lj., Gliha, V.: Behaviour of small cracks during their propagation from Vickers indentations in coarse-grain steel: an experimental investigation. *Int. J. Fatigue* **33**(12), 1505–1513 (2011)
9. Bulatović, S., Milović, Lj., Sedmak, A., Samardžić, I.: Identification of low cycle fatigue parameters of high strength low-alloy (HSLA) steel at room temperature. *Metalurgija* **53**(4), str. 466–468 (2014)
10. Bulatović, S., Burzić, Z., Aleksić, V., Sedmak, A., Milović, Lj.: Impact of choice of stabilized hysteresis loop on the end result of investigation of high-strength low-alloy (HSLA) steel on low cycle fatigue. *METALURGIJA* **53**(4), str. 477–480 (2014)
11. McHenry, H.I., Denys, R.M.: Measurement of HAZ toughness in steel weldments. In: Sedmak, S. (ed.) The Application of Fracture Mechanics to Life Estimation of Power Plant Components, pp. 211–222, EMAS (1990)
12. Gerić, K.: Crack initiation and growth in high strength steel welded joints, Doctoral Thesis, Faculty of Technology and Metallurgy, University of Belgrade (1997)
13. Milović, Lj., Vuherer, T., Zrilić, M., Sedmak, A., Putić, S.: Study of the simulated heat affected zone of creep resistant 9–12 % advanced chromium steel. *Mater. Manuf. Process.* **23**(6), 597–602. ISSN 1042-6914 (IF/2009: 0,968) M22 (2008)
14. Milović, Lj.: Microstructural investigations of the simulated heat affected zone of the creep resistant steel P91. *Mater. High Temperatures* **27**(3), 233–242 (2010)

15. Milović, Lj., Vuherer, T., Blačić, I., Vrhovac, M., Stanković, M.: Microstructures and mechanical properties of creep resistant steel for application at elevated temperatures. *J. Mater. Design* **46**, 660–667 (2013)
16. Vuherer, T., Dunder, M., Milović, Lj., Zrilić, M., Samardžić, I.: Microstructural investigation of the heat-affected zone of simulated welded joint of P91 steel. *Metalurgija* **52**(3), 317–320 (2013)
17. Devillers, L., Kaplan, D., Testard, P.: An Approach for Predicting Microstructure and Toughness Properties in Heat Affected Zones of Multipass Welds of Structural Steels. IRSID (1991)
18. Vuherer, T., Milović, Lj., Samardžić, I., Zrilić, M.: Acceptability of residual stresses measurement methods of butt weldments and repairs. *Strojarstvo* **51**(4), 323–331 (2009)
19. Withers, P.J., Bhadeshia, H.K.D.H.: Residual stress part 2-Nature and origins. *Mater. Sci. Technol.* **17**, 366–375 (2001)
20. Withers, P.J., Bhadeshia, H.K.D.H.: Residual stress part 1-Measurement techniques. *Mater. Sci. Technol.* **17**, 355–365 (2001)
21. Anderson, T.L.: *Fracture Mechanics, Fundamentals and application*, 2nd edn. CRC Press (1995)
22. Feng, H., Lasky, M.S., Wnuk, M.P., Model of fatigue crack growth based on energy dissipated within the process zone. In: Salama, K., Ravi-Chandar, K., Taplin, D.M.R., Rama Rao, P. (eds.) *Advances in Fracture Research, Proceedings of the 7th International Conference on Fracture (ICF7)*, Houston, Texas, 20–24 March 1989, vol. 1. Pergamon Press, pp. 1121–1132
23. Wnuk, M.P.: Quasi-static extension of a tensile crack contained in a viscoelastic-plastic solid. *ASME Trans. J. Appl. Mechanics* **41**, 234–242 (1974)
24. Rice, J.R., Drugan, W.J., Sham, T.L.: *ASTM STP 700*, 189–221 (1980)
25. Hunsacharoonroj, I.: *Quasi-static Crack Extension in Ramberg-strain Hardening Solids*. Ph.D. Dissertation. University of Wisconsin, Milwaukee (1987)
26. Wnuk, M.P.: *Projektovanje posuda pod pritiskom primenom dozvoljenog oštećenja na osnovu nelinearne mehanike loma. Eksploatacijske prsline u posudama pod pritiskom i rezervoarima*, pp. 170–191. TMF-ECPD-GOŠA, Beograd (1994)
27. Kumar, V., et al.: *Advances in Elastic-Plastic Fracture Analysis*”, EPRI Report NP-3607. Electric Power Research Institute, Palo Alto, CA (1985)
28. Tada, H., Paris, P.C., Irwin, G.R.: *The Stress Analysis of Cracks Handbook*. Del Research Corp, Hellertown, Penn, USA (1973)
29. Wnuk, M.P., Mura, T.: Effect of microstructure on the upper and lower limits of material toughness in elastic-plastic fracture. *Mech. Mater.* **2**, 33–46 (1983)
30. Milović, Lj., Vuherer, T., Zrilić, M., Momčilović, D., Jaković, D.: Structural integrity assessment of welded pressure vessel produced of HSLA steel. *J. Iron Steel Res. Int.* **18**(1–2), 888–892. ISSN 1006-706X, Gangtie Yanjiu Xuebao (2011)

Mixed Mode Static and Dynamic Modeling in Fracture Mechanics for Plane Composite Materials by X-FEM

Sadam Houcine Habib, Brahim Elkhalil Hachi, Mohamed Guesmi and Mohamed Haboussi

Abstract In this paper, static and dynamic fracture behaviors of cracked orthotropic structure are modeled using extended finite element method (X-FEM). In this approach, the finite element method model is first created and then enriched by special orthotropic crack tip enrichments and Heaviside functions in the framework of partition of unity. The mixed mode stress intensity factor (SIF) is computed using the interaction integral technique based on J-integral in order to predict cracking behavior of the structure. The developments of these procedures are programmed and introduced in a self-software platform code. To assess the accuracy of the developed code, results obtained by the proposed method are compared with those of literature.

1 Introduction

Due to their hardness, lightness, super elasticity and life duration, orthotropic materials have a major interest in modern industrial applications as in aeronautic, aerospace, mechanical and civil engineering and biomechanics. However, these materials may be subject to sever static, cyclic or dynamic loads which lead to crack initiation then brittle or crack-propagating fracture.

The growing development of composites employed in new structures requires establishing tools for modeling their mechanical behavior with taking into account

S.H. Habib · B.E. Hachi (✉) · M. Guesmi
LDMM, University of Djelfa, PB 3117, Djelfa 17000, Algeria
e-mail: br_khalil@yahoo.fr

S.H. Habib
e-mail: hb_houcine@yahoo.fr

M. Guesmi
e-mail: guesmi.mohamed@yahoo.fr

M. Haboussi
LSPM, University of Paris13, 99 Av. J-B Clément, 93430 Villetaneuse, France
e-mail: haboussi@univ-paris13.fr

the effect of the eventually crack presence. The classical finite element, recognized by their popularity due to their high ability to model a variety of physical problems, shows some limitations in fracture mechanics due to the obligation of mesh refinement at the crack tip as well as of remeshing during propagation. That may conduct to increase the computing time and affect the accuracy of results. The extended finite element method (*X-FEM*), developed in 1999 [1], offers a promising alternative and is currently the subject of numerous studies in different applications dealing with discontinuities (cracks, interfaces, voids ...) such as the fracture mechanics. The main characteristic of this method is to represent discontinuities independently of the mesh by enriching the finite element approximation with appropriate functions.

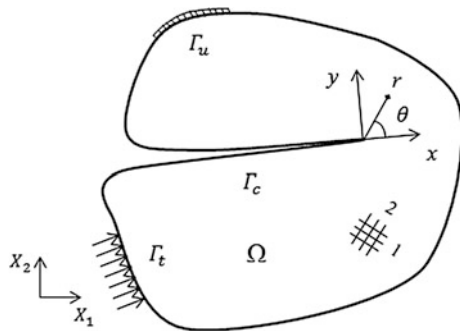
In this paper, *X-FEM* is presented for analyzing orthotropic plane crack problems, in static and dynamic cases. Orthotropic crack-tip enrichment functions [2] are implemented to accurately calculate the displacement and stress fields. Mixed mode stress intensity factors (*SIF*) are numerically evaluated by using the interaction integral technique based essentially on J-integral concept. Two practical applications with different configurations are treated, for which the orientations of crack and orthotropic axes are discussed. The results given by the proposed method implanted in a software code are compared with other numerical methods of literature.

2 Governing Equations

Consider a cracked elastic orthotropic body Ω subjected to traction forces f_i applied at Γ_t and displacement conditions applied at Γ_u in the absence of body forces, as shown in Fig. 1. The partial differential equation of the stress functions of this problem can be obtained using equilibrium and compatibility conditions [3].

$$c_{22} \frac{\partial^4 \phi}{\partial x^4} - 2c_{26} \frac{\partial^4 \phi}{\partial x^3 \partial y} + (2c_{12} + c_{66}) \frac{\partial^4 \phi}{\partial x^2 \partial y^2} - 2c_{16} \frac{\partial^4 \phi}{\partial x \partial y^3} + c_{11} \frac{\partial^4 \phi}{\partial y^4} = 0 \quad (1)$$

Fig. 1 An arbitrary orthotropic cracked body with boundary conditions



where (x, y) is local Cartesian coordinate, φ is the stress function and c_{ij} is the components of the compliance matrix which is computed in terms of Young moduli (E), Poisson ratios (ν) and shear modulus (μ) as follow:

$$c = \begin{bmatrix} 1/E_1 & -\nu_{12}/E_1 & -\nu_{13}/E_1 & 0 & 0 & 0 \\ -\nu_{12}/E_1 & 1/E_2 & -\nu_{23}/E_2 & 0 & 0 & 0 \\ -\nu_{13}/E_1 & -\nu_{23}/E_2 & 1/E_3 & 0 & 0 & 0 \\ 0 & 0 & 0 & 1/\mu_{23} & 0 & 0 \\ 0 & 0 & 0 & 0 & 1/\mu_{13} & 0 \\ 0 & 0 & 0 & 0 & 0 & 1/\mu_{12} \end{bmatrix} \quad (2)$$

The general characteristic equation of the partial differential equation is:

$$c_{11}s^4 - 2c_{16}s^3 + (2c_{12} + c_{66})s^2 - 2c_{26}s + c_{22} = 0 \quad (3)$$

The four roots of this characteristic equation are complex and conjugate two-two [3], these roots were used by Sih et al. [4] to derive the displacement and the stress fields in the vicinity of the crack tip for an infinite domain.

The stress components for pure mode I are:

$$\sigma_{xx}^I = \frac{K_I}{\sqrt{2\pi r}} \operatorname{Re} \left[\frac{s_1 s_2}{s_1 - s_2} \left(\frac{s_2}{(\cos \theta + s_2 \sin \theta)^{\frac{1}{2}}} - \frac{s_1}{(\cos \theta + s_1 \sin \theta)^{\frac{1}{2}}} \right) \right] \quad (4a)$$

$$\sigma_{yy}^I = \frac{K_I}{\sqrt{2\pi r}} \operatorname{Re} \left[\frac{1}{s_1 - s_2} \left(\frac{s_1}{(\cos \theta + s_2 \sin \theta)^{\frac{1}{2}}} - \frac{s_2}{(\cos \theta + s_1 \sin \theta)^{\frac{1}{2}}} \right) \right] \quad (4b)$$

$$\sigma_{xy}^I = \frac{K_I}{\sqrt{2\pi r}} \operatorname{Re} \left[\frac{s_1 s_2}{s_1 - s_2} \left(\frac{1}{(\cos \theta + s_1 \sin \theta)^{\frac{1}{2}}} - \frac{1}{(\cos \theta + s_2 \sin \theta)^{\frac{1}{2}}} \right) \right] \quad (4c)$$

and for pure mode-II are:

$$\sigma_{xx}^{II} = \frac{K_{II}}{\sqrt{2\pi r}} \operatorname{Re} \left[\frac{1}{s_1 - s_2} \left(\frac{s_2^2}{(\cos \theta + s_2 \sin \theta)^{\frac{1}{2}}} - \frac{s_1^2}{(\cos \theta + s_1 \sin \theta)^{\frac{1}{2}}} \right) \right] \quad (5a)$$

$$\sigma_{yy}^{II} = \frac{K_{II}}{\sqrt{2\pi r}} \operatorname{Re} \left[\frac{1}{s_1 - s_2} \left(\frac{1}{(\cos \theta + s_2 \sin \theta)^{\frac{1}{2}}} - \frac{1}{(\cos \theta + s_1 \sin \theta)^{\frac{1}{2}}} \right) \right] \quad (5b)$$

$$\sigma_{xy}^{II} = \frac{K_{II}}{\sqrt{2\pi r}} \operatorname{Re} \left[\frac{1}{s_1 - s_2} \left(\frac{s_1}{(\cos \theta + s_1 \sin \theta)^{\frac{1}{2}}} - \frac{s_2}{(\cos \theta + s_2 \sin \theta)^{\frac{1}{2}}} \right) \right] \quad (5c)$$

The displacements for pure mode-I are:

$$u_x^I = K_I \sqrt{\frac{2r}{\pi}} Re \left\{ \frac{1}{s_1 - s_2} \left[s_1 d_2 (\cos \theta + s_2 \sin \theta)^{\frac{1}{2}} - s_2 d_1 (\cos \theta + s_1 \sin \theta)^{\frac{1}{2}} \right] \right\} \quad (6a)$$

$$u_y^I = K_I \sqrt{\frac{2r}{\pi}} Re \left\{ \frac{1}{s_1 - s_2} \left[s_1 e_2 (\cos \theta + s_2 \sin \theta)^{\frac{1}{2}} - s_2 e_1 (\cos \theta + s_1 \sin \theta)^{\frac{1}{2}} \right] \right\} \quad (6b)$$

and for pure mode-II are:

$$u_x^{II} = K_{II} \sqrt{\frac{2r}{\pi}} Re \left\{ \frac{1}{s_1 - s_2} \left[d_2 (\cos \theta + s_2 \sin \theta)^{\frac{1}{2}} - d_1 (\cos \theta + s_1 \sin \theta)^{\frac{1}{2}} \right] \right\} \quad (7b)$$

$$u_y^{II} = K_{II} \sqrt{\frac{2r}{\pi}} Re \left\{ \frac{1}{s_1 - s_2} \left[e_2 (\cos \theta + s_2 \sin \theta)^{\frac{1}{2}} - e_1 (\cos \theta + s_1 \sin \theta)^{\frac{1}{2}} \right] \right\} \quad (7b)$$

where (r, θ) are local crack tip polar coordinates, K_I and K_{II} are the stress intensity factors for mode I and mode II, respectively, and the constant values of d_i and e_i are computed as:

$$d_i = c_{11}s_1^2 + c_{12} - c_{16}s_i \quad i = 1, 2 \quad (8)$$

$$e_i = c_{12}s_i + \frac{c_{22}}{s_i} - c_{26} \quad i = 1, 2 \quad (9)$$

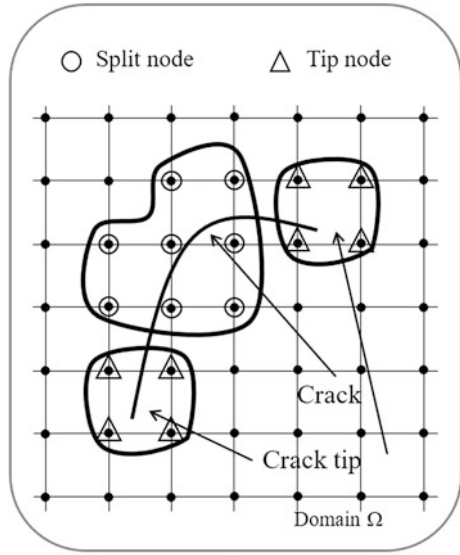
3 Extended Finite Element Method Modeling

The *X-FEM* method differs from the *FEM* method by the fact that some selected nodes are enriched in order to describe displacement discontinuities. Consequently, few degrees of freedom are added to points near the location of a crack (Fig. 2). The generalized Heaviside and crack-tip enrichment functions are utilized by using extra degrees of freedom to model discontinuous and singular fields near a crack. The displacement approximation $u(\zeta)$ for an arbitrary point of the medium $\zeta = (x, y)$ can be written in a generalized form as:

$$u(\zeta) = \sum_{i=1}^{n_{en}} N_i u_i + \sum_{j=1}^{n_{cf}} N_j H(\zeta) a_j + \sum_{k=1}^{n_{ct}} N_k \left(\sum_{\alpha=1}^4 F_\alpha(\zeta) b_k^\alpha \right) \quad (10)$$

where N_i is the classical function, u_i is the conventional displacement vector, H and F_α are the Heaviside function and crack tip enrichment functions respectively. The additional degrees of freedom related to the crack face and crack tip modeling are represented by a_j and b_k^α respectively. The n_{cf} is the number of nodes corresponding

Fig. 2 Split and tip enriched nodes of the meshed domain



to elements that have crack face and n_{ct} is the number of nodes corresponding to elements associated with crack tip. The Heaviside function is defined as “+1” above the crack and “-1” otherwise.

4 Orthotropic Enrichment Function

Based on asymptotic form of the displacement field near to the crack tip for orthotropic materials, new special crack-tip enrichment functions have been recently derived by Asadpoure and Mohammadi [2]:

$$\{F_i(r, \theta)\} = \left\{ \begin{array}{l} \sqrt{r} \cos\left(\frac{\theta_1}{2}\right) \sqrt{g_1(\theta)} \sqrt{r} \cos\left(\frac{\theta_2}{2}\right) \sqrt{g_2(\theta)} \\ \sqrt{r} \sin\left(\frac{\theta_1}{2}\right) \sqrt{g_1(\theta)} \sqrt{r} \sin\left(\frac{\theta_2}{2}\right) \sqrt{g_2(\theta)} \end{array} \right\} \quad (11)$$

were $g_k(\theta)$ and θ_k are defined as:

$$g_k(\theta) = \sqrt{(\cos \theta + s_{kx} \sin \theta)^2 + (s_{ky} \sin \theta)^2}; \quad k = 1, 2 \quad (12)$$

$$\theta_k = \arctan\left(\frac{s_{ky} \sin \theta}{\cos \theta + s_{kx} \sin \theta}\right); \quad k = 1, 2 \quad (13)$$

and s_{kx} , s_{ky} are the real and the imaginary parts of characteristic roots of Eq. (3), respectively.

5 Stress Intensity Factor Computation

For approximating the stress intensity factor, there are several numerical techniques available in the literature. In this study, we use the interaction Integral technique based on the J integral concept. This method uses the definition of an auxiliary state to extract mixed mode SIF for the actual state by the combination:

$$J = J^{act} + J^{aux} + M \quad (14)$$

where J^{act} and J^{aux} are the actual and auxiliary states J integrals, and J is the J -integral value for the superposition state. Its general form is written as [5]:

$$J = \int_{\Gamma} \left(w_s \cdot \delta_{1j} - \sigma_{ij} \frac{\partial u_i}{\partial x_1} \right) n_j d\Gamma \quad (15)$$

and M is the interaction integral defined as:

$$M = \int_A \left[\sigma_{ij} \frac{\partial u_i^{aux}}{\partial x_1} + \sigma_{ij}^{aux} \frac{\partial u_i}{\partial x_1} - w_s \delta_{ij} \right] \frac{\partial q}{\partial x_i} d\Gamma \quad (16)$$

where $w_s = \frac{(\sigma_{ij} \cdot \epsilon_{ij}^{aux} + \sigma_{ij}^{aux} \cdot \epsilon_{ij})}{2}$ is the strain energy density for linear elastic material, Γ is an arbitrary contour surrounding the crack tip, n_j is the j th component of the outward unit normal to Γ , δ_{ij} is the Kronecker delta, q is a smoothly varying function from 1 on the crack-tip to zero on the boundary of the domain, and A is the area inside Γ .

After developing Eq. (16), the interaction integral can be written in the following form [2]:

$$M = 2t_{11}K_I K_I^{aux} t_{12} (K_{II} K_{II}^{aux} + K_{II} K_I^{aux}) + 2t_{22}K_{II} K_{II}^{aux} \quad (17)$$

where:

$$t_{11} = -\frac{c_{22}}{2} \text{Im} \left(\frac{s_1 + s_2}{s_1 s_2} \right) \quad (18)$$

$$t_{12} = -\frac{c_{22}}{2} \text{Im} \left(\frac{1}{s_1 s_2} \right) + \frac{c_{11}}{2} \text{Im}(s_1 s_2) \quad (19)$$

$$t_{22} = \frac{c_{11}}{2} \text{Im}(s_1 + s_2) \quad (20)$$

With considering the two states and calculating M from both Eqs. (16) and (17), the mixed mode stress intensity factor can be obtained by solving the following system of linear algebraic equations:

$$M^{(1)} = 2t_{11}K_I + t_{12}K_{II} \quad (21)$$

$$M^{(2)} = t_{12}K_I + 2t_{22}K_{II} \quad (22)$$

where state 1 and state 2 defined as $(K_I^{aux} = 1, K_{II}^{aux} = 0)$ and $(K_I^{aux} = 0, K_{II}^{aux} = 1)$, respectively.

6 Applications

All of the above theoretical developments are programed on a self-platform software code (previously carried out) based on *X-FEM* in the aim to extend its using to the orthotropic behavior modeling. In order to validate the proposed approach and show the good working of the developed code, two practical problems of composites subject to mixed mode static and dynamic loadings are treated below.

6.1 Static Problem

A finite orthotropic plate of dimension $h = 2w$ with a central crack of length $2a = (2\sqrt{2}/10) \cdot w$ loaded by a unitary tensile stress along the top and bottom edges, in a plane stress state, is considered as shown in Fig. 3. To investigate the effect of the crack inclination on the SIF value, several crack angles are treated. For the sake of validation of the present approach, the orthotropic properties of the plate are taken from the Ref. [6] as follows: $E_1 = 3.5$ GPa, $E_2 = 12$ GPa, $G_{12} = 3$ GPa, $\nu_{12} = 0.7$.

A uniform meshing of 4543 elements is used. Figure 4a shows split and tip enriched nodes near of the crack. The contour surrounding the crack tip includes 7×7 .

Gauss quadrature integrates points for each concerned element. Sub-triangle technique is used for split elements with 7×7 Gauss quadrature points for each sub-element (Fig. 4b). The rest of elements include 3×3 Gauss quadrature points each one.

Figure 5 presents the obtained results of the normalized mixed-mode *SIF* with those of other studies reported by Asadpoure and Mohammadi [2] using the *X-FEM* method, and Ghorashi et al. [6] using the enriched Element Free of Galerkin (*XEFG*) method.

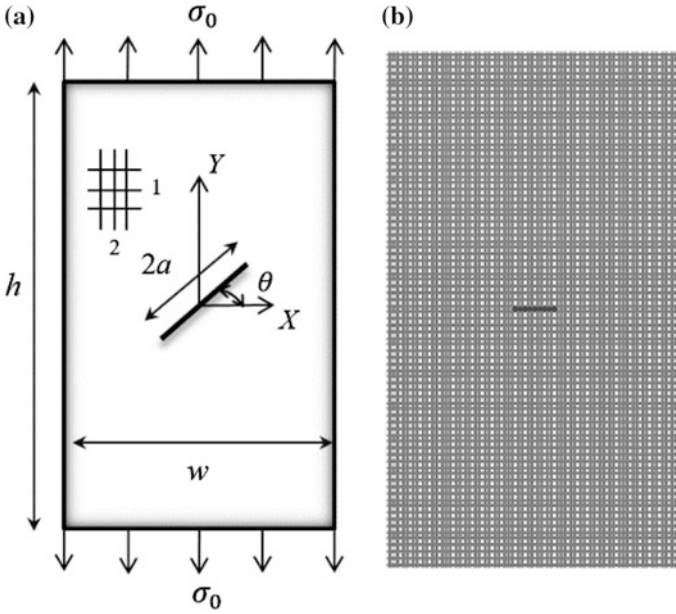


Fig. 3 a Geometry and b mesh of an orthotropic plate with a central crack

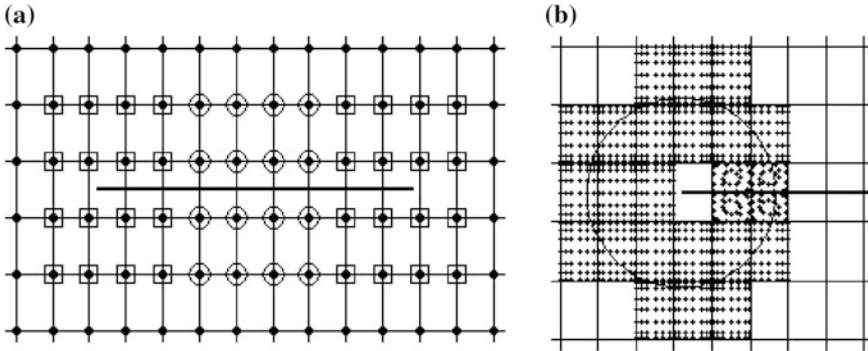


Fig. 4 a Enriched nodes and b Gauss points within its support domain

According to Fig. 5, some remarks can be made:

- The agreement of the present results with those of literature is very clear for both modes of fracture.
- As expected, the critical state (corresponding to the max of *SIF*) is observed at $\theta = 0^\circ$ in mode I. However, in mode II, the critical situation is observed at $\theta = 45^\circ$ for which the shear stress is maximal.

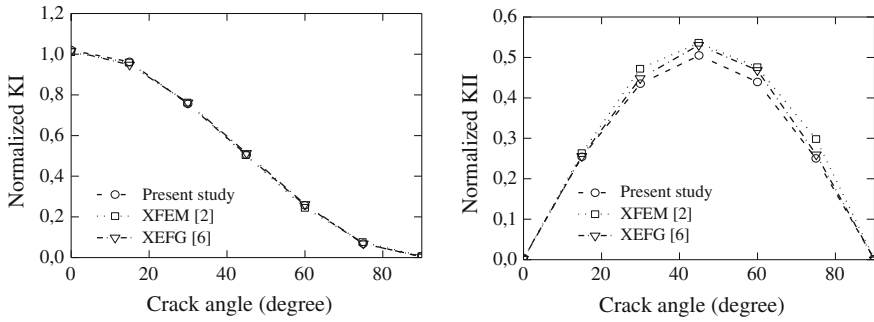


Fig. 5 Evolution of the normalized mode I and II SIF with respect to different crack angles

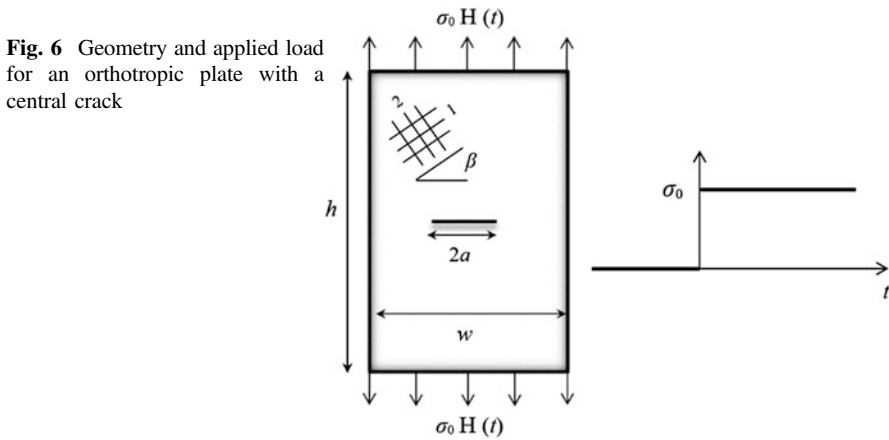


Fig. 6 Geometry and applied load for an orthotropic plate with a central crack

According to previous remarks, the orthotropic behavior has not significant effect on the *SIF* evolution.

6.2 Plate with a Stationary Central Crack (Dynamic)

In this part, a dynamic Heaviside-step loading is applied on a graphite epoxy composite plate (Fig. 6). The effect of the orientation angle β of the orthotropic axes is discussed for the case of horizontal central crack. The geometrical configuration of the plate is taken as: $h = 2w$, $2a = 0.48w$ and $\beta = 0^\circ, 15^\circ, 30^\circ$ and 45° . In the aim of comparison, the material properties are those of [7], given as follow: $E_1 = 118.3$ GPa, $E_2 = 54.8$ GPa, $G_{12} = 8.79$ GPa, $\nu_{12} = 0.083$. A uniform meshing of 5000 elements is used for the same numerical configuration as the previous problem. Figure 7 shows the evolution of the mixed mode dynamic SIF with

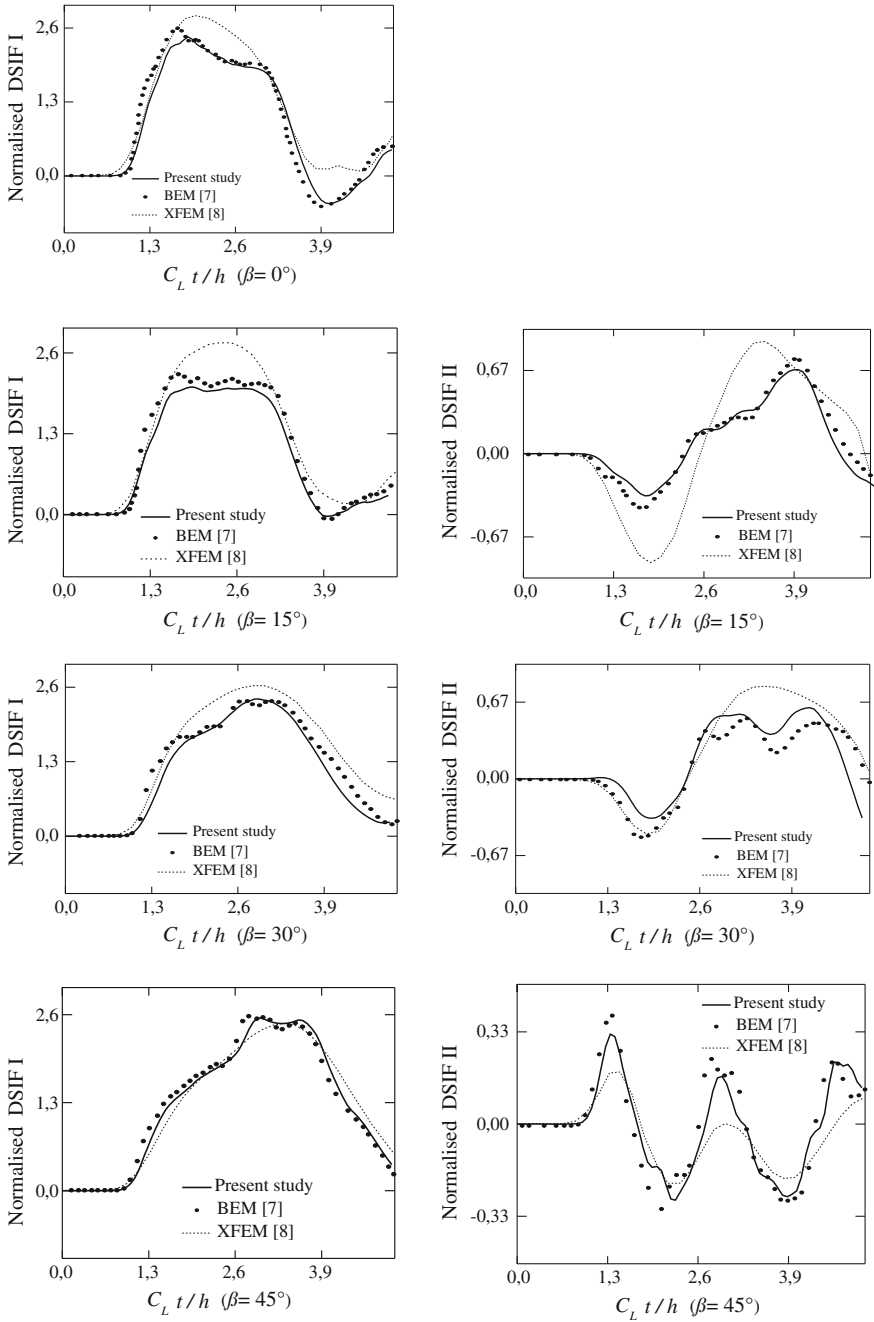


Fig. 7 DSIFs with different orientations of the orthotropic axes

respect to the dimensionless time parameter c_{Lt}/h . c_L is the wave velocity along the principal material axis 2. d_{22} is a component of elasticity matrix (inverse of compliance matrix). The obtained results are compared to those reported by García-Sánchez et al. [8], Motamedi and Mohammadi [7] using BEM and XFEM approaches, respectively (Fig. 7).

According to graphs, some observations can be made:

- The obtained *DSIF* evolutions are in good agreement with other results of literature for all the treated configurations.
- Even when the loadings are perpendicular to the crack, the orthotropic behavior of the material generates a mode II Dynamic *SIF* when orthotropic axes are inclined.
- For all graphs, the present approach based on *X-FEM* gives results closer to those of García-Sánchez et al. [8] using *BEM* than those of Motamedi and Mohammadi [7] using *X-FEM*. This can be explained by the difference in the programming details between the present developed code and that of Motamedi and Mohammadi [7], especially the techniques used for the J-integral evaluation and those of the subdivision of crack-tip elements and gauss points repartition.
- For mode I *SIF*, the amplitude of the response (time evolution of *SIF*) still globally invariant with the inclination angle of the orthotropic axes. However, the period of this response slightly increases with β .
- For the mode II *SIF*, the amplitude and the period decrease with β .

7 Conclusions

The quality of the obtained results regarding their good agreement with the results of literature demonstrates the accuracy of the present approach and the robustness of the developed code. As expected, the inclination angle of the crack with respect to static tensile loads generates and affects the values of the mixed mode *SIF*. Similarly, the inclination angle of the orthotropic axes generates and affects the evolution in time of the dynamic mixed mode *SIF* for Heaviside step tensile loading even when the crack still perpendicular to load.

References

1. Moes, N., Dolbow, J., Belytschko, T.: *Int. J. Numer. Meth. Eng.* **46**, 131–150 (1999)
2. Asadpoure, A., Mohammadi, S.: *Int. J. Numer. Meth. Eng.* **69**, 2150–2172 (2007)
3. Lekhnitskii, S.G.: *Anisotropic Plates*. Gordon and Breach Science Publishers, New York (1968)
4. Sih, G.C., Paris, P.C., Irwin, G.R.: *Int. J. Fract. Mech.* **1**, 189–203 (1965)
5. Rice, J.R.: *J. Appl. Mech.* **35**, 379–386 (1968)
6. Ghorashi, S.S., Mohammadi, S., Sabbagh-Yazdi, S.R.: *Eng. Fract. Mech.* **78**, 1906–1927 (2011)
7. Motamedi, D., Mohammadi, S.: *Eng. Fract. Mech.* **77**, 3373–3393 (2010)
8. García-Sánchez, F., Zhang, C., Sáez, A.: *Eng. Fract. Mech.* **75**, 1412–1430 (2008)

The Preheating Temperature Effects on the Residual Stresses of the Welded Rails Sections

Oussama Bouazaoui and Abdelkrim Chouaf

Abstract Aluminothermy welding is one of the most common processes in the railway industry. Nevertheless, this process leaves, locally, significant residual stresses that may, eventually, be responsible of the potential damaging process. These residual stresses depend highly of the preheating temperature. Failure of an efficient application of this preheating temperature is often pinpointed with the occurrence of significant internal defects and sometimes exposed cracks. In this study, we intend to highlight the correlation that bound the preheating temperature and the residual stress, and discuss the potential damaging risks.

Keywords Simulation · Aluminothermy · Temperature · Preheating · Residual stresses

1 Introduction

As known, rail junctions are connected by through thermite welding. Both rail ends are joined by a metal casting [1, 2]. This procedure is the main practice of the rail system in Morocco. The quality of this joining depends on the conditions of the realization generally not observed [3, 4]. However, this process generates significant residual stresses as seen on every permanent joining process [5, 6]. Adding these constraints to the cyclic external stresses, affecting the rails behavior [7–9]. Depending on their levels, these constraints may decrease the resistance of rail [10, 11]. Consequently, it is important to identify the origin of these constraints and the involved parameters.

Most studies of the rail thermite welds stress the analysis of fatigue cracks spread. However, the welding process parameters are generally overlooked, although it

O. Bouazaoui · A. Chouaf (✉)

Laboratory of Control and Mechanical Characterization of Materials and of Structures, National School of Electrical and Mechanical, Hassan II University, El Jadida Road, Oasis Casablanca, Morocco
e-mail: a.chouaf.ensem@gmail.com

raises significant issues being addressed, for example by Skattebol [6, 11]. That acts on the rail behavior and reduce its resistance to cyclic external loading. At the end, therefore ensuring the safety of railway traffic, it seems necessary to determine these constraints and to highlight the effect of preheating temperature on their severity and take the necessary precautions. So in order to ensure the safety of railway traffic, it seems necessary to highlight these constraints and to stress out the effect of preheating temperature on their seriousness, and take the necessary precautions.

2 Modelling

We have conducted a numerical simulation of the finite element method using the calculation code (*ABAQUS*) to describe the thermo-mechanical stresses evolution on the rails welded area. For this, we have considered a thermal loading. In this loading, we have given the temperature difference between the final state ($T_f = 20^\circ\text{C}$), the molten zone $T_{MZ} = 600^\circ\text{C}$ and the heat affected zone $T_{HAT} = 579^\circ\text{C}$ [12, 13].

Based on the formula, [6, 7], many studies have been conducted to stress out the thermoplastic origin of the residual stresses.

$$\sigma = \alpha E (T_f - T_{MZ}) \quad (1)$$

with:

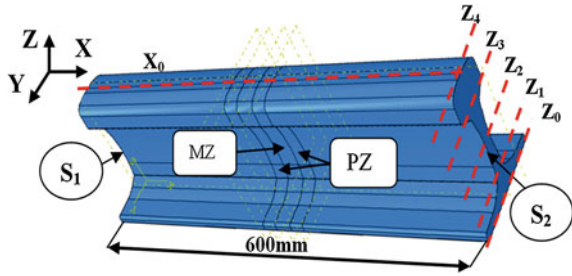
- σ Residual stress,
- α Thermal expansion coefficient,
- E Young's modulus,
- T_f Final state temperature,
- T_{MZ} Molten zone temperature

2.1 Geometry

Our case study has considered a 600 mm long rail *UIC60* profile type [3]. This latter is defined by the standard *NF A 45-317* [14]. This section includes the welding zone of a 25 mm wide and two preheating zones.

The boundary conditions are taken into account: the displacements and rotations according to axes X , Y and Z are zero on the surface (S_1) and only the displacement along the axis X which is free on the surface (S_2) as shown in Fig. 1.

Fig. 1 Portion of the rail having a weld junction with the identification of different zones [Molten Zone (MZ) Preheating Zones (PZ), the axes (Z_0, Z_1, Z_2, Z_3, Z_4)]



2.2 Mesh

For the mesh structure and particularly in the weld joint, we used solid elements type Hex code *ABAQUS* (Fig. 2). The number of items considered is 50.661, of which 30 % was allocated to the welding joint area. Indeed, the mesh refinement at that particular area will allow us to develop our analysis from accurate result.

2.3 Materials

The material is considered as the steel with Young’s modulus 200–243 GPa and rail for welding [5]. Poisson’s ratio is taken to be 0.3 and the coefficient of thermal expansion for the 1.33×10^{-5} rail and 1.2×10^{-5} to the welded zone [6, 7].

2.4 Residual Stress Determination According to the Preheat Temperature

To study the residual stress, we considered six noted preheating temperature cases T_{pc_i} ($T_{pc_1} = 20 \text{ }^\circ\text{C}$; $T_{pc_2} = 200 \text{ }^\circ\text{C}$; $T_{pc_3} = 400 \text{ }^\circ\text{C}$; $T_{pc_4} = 500 \text{ }^\circ\text{C}$; $T_{pc_5} = 550 \text{ }^\circ\text{C}$; $T_{pc_6} = 600 \text{ }^\circ\text{C}$) placed in the preheating zones (Fig. 1), and in the molten zone an initial temperature of $600 \text{ }^\circ\text{C}$ is considered. For its various cases we initially determined the temperature’s field distribution when considering a $20 \text{ }^\circ\text{C}$ final temperature.

Fig. 2 Mesh structure studied by solid elements type Hex (*ABAQUS*)



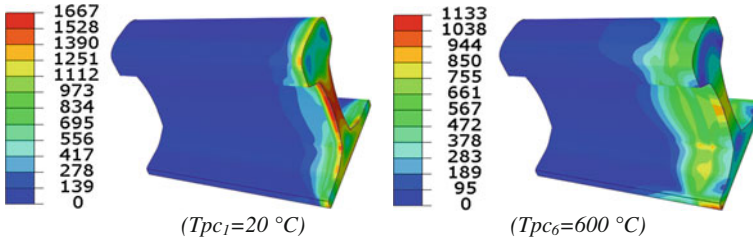


Fig. 3 Von Mises stress Cartography of preheating temperature (20 and 600 °C) extreme cases

From a thermal analysis, we determined residual stresses generated throughout the rail. Among the results we have got, in Fig. 3 we have represented the Von Mises stresses map for the most extreme cases (T_{pc1} and T_{pc6}).

According to these two maps, we can see preheating temperature extreme cases, a significant difference between the residual stresses values and distributions. In all cases, this difference is clearly demonstrated through the graph of Fig. 4. The critical values of these stresses can be observed in the central portion of the rail. Overall, these results, we can see that the higher the preheating temperature increases the higher the stress decreases.

According to Von Mises stresses distributions, we can notice that the maximum stress is concentrated in the weld zone. In this zone, the value of the Von Mises stress is from 833 MPa for a $T_{pc6} = 600$ °C preheating temperature at a value of 1533 MPa value for the case without preheating ($T_{pc1} = 20$ °C). As a result, the weld zone may be a very critical zone as the relevant preheat temperature. It is this particular area that draws our attention to locally develop our analysis.

In this analysis, we introduced the weld zone vicinity, the σ_{xx} stress on the surface and along the X axis for different cases (Fig. 5).

The results showed that the residual compressive stresses occur in the molten zone (MZ) of the rail weld, while the residual tensile stresses appear in the zone

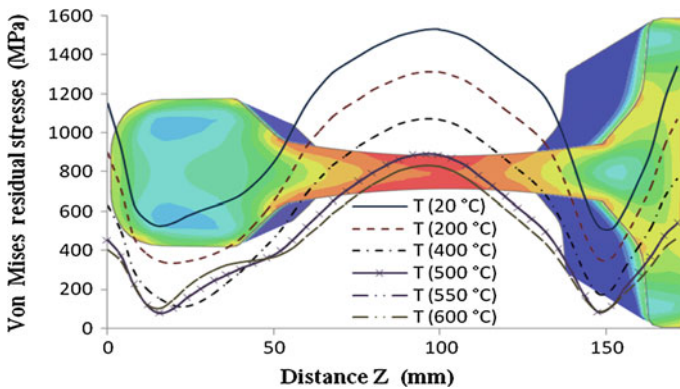


Fig. 4 Von Mises stresses distribution on the rail for the different cases of preheats temperatures

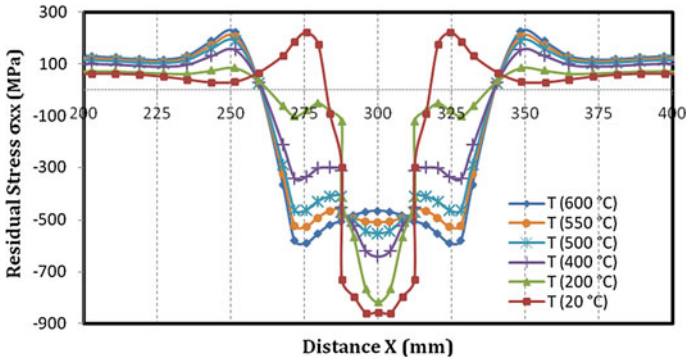


Fig. 5 σ_{XX} distribution on the surface stresses on the molten zone vicinity

(HAZ), with a relatively high level related to the rest of the rail. The central part of the weld (molten zone) has the highest value of stress, it is of the order of -464 MPa for a preheating temperature $T_{pc6} = 600$ °C. It reaches a value of -856 MPa for this case without preheating. For the heat affected zone (HAZ), the stress is in the range of -594 MPa to $T_{pc6} = 600$ °C and 230 MPa for $T_{cp1} = 20$ °C. However, on the metal base, the stress moves gradually away from the weld zone tending to zero [15, 16]. For each of these particular areas (MZ: Molten Zone, HAZ: Heat Affected Zone and BM: metal base), we have shown the effect of the preheating temperature on residual stress Fig. 6.

From this local stress analysis, we can see, that when the preheating temperature reaches a value of about 550 °C, the stresses on the zones (MZ) and (HAZ) are similar. Therefore, with this temperature valve, stress discontinuities are reduced at the interface (MZ/HAZ) which often contains defects.

Having showing the correlation between the surface residual stresses and the preheating temperature, we have developed our analysis on the rail volume. With respect to a normal section to the axis X and passing through the center of the welded zone, we analyzed the distribution of residual stresses. Our first results show

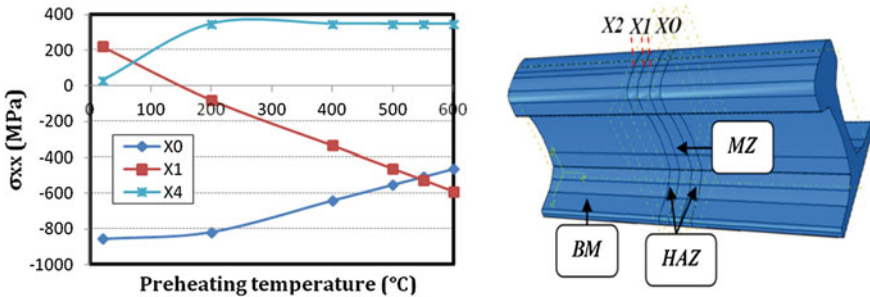


Fig. 6 Evolution of the residual stress as a function of the preheating temperature in the MZ areas HAZ and BM

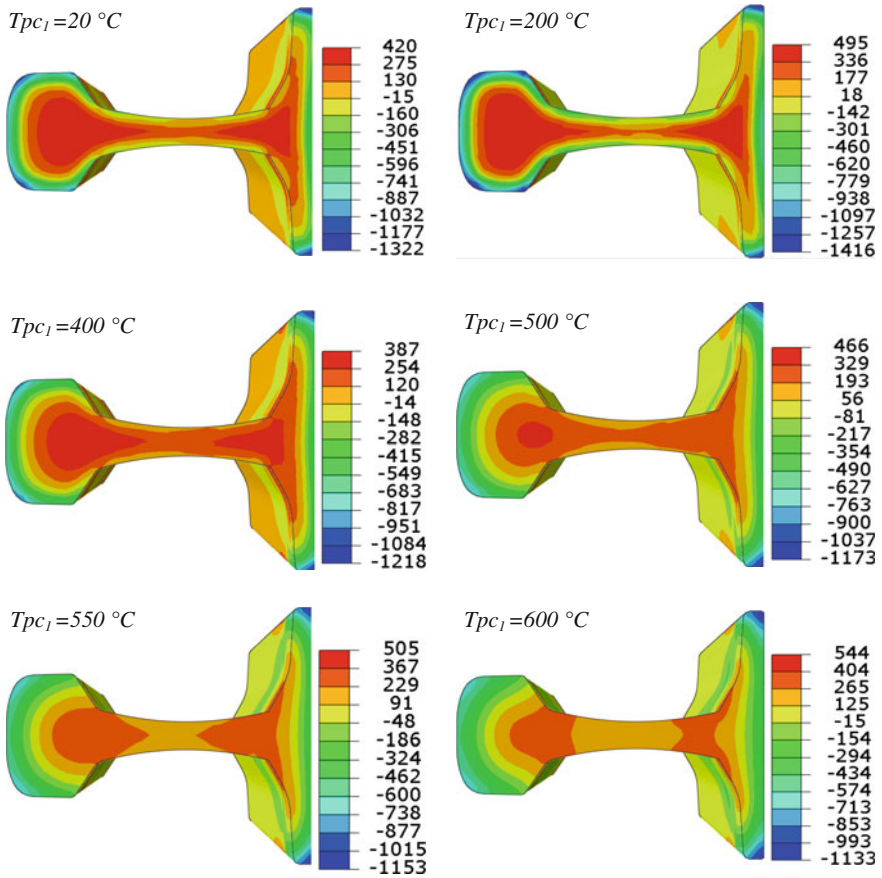


Fig. 7 σ_{XX} stress component cartography for the different cases of preheats temperature

a very significant difference on the equivalent Von Mises stresses between the different preheating temperatures Fig. 7.

To illustrate this difference in the evolution of the stresses on the rail by volume and especially from one case to another, we have drawn the most significant component σ_{XX} along the Z axis (Fig. 8).

In this distribution, we can distinguish three areas; head web and foot. Indeed, at the head to the preheat temperature ($T_{cp6} = 600\text{ }^\circ\text{C}$), the stress changes from compression -464 MPa free surface at a voltage of 291 MPa at a depth of 20 mm . In contrast to the preheating temperature ($T_{cp1} = 20\text{ }^\circ\text{C}$), the stress of 870 MPa passes free surface to 534 MPa at the same depth of 2 mm . In the head, these constraints by annulling about ten mm of the free surface. This same trend was observed in the other cases, at the foot, but the stress level remains lower than that of the head. For the central portion (web), the stress remains on tension and has an average value of the order of 221 MPa due to its small area. All of these orders of

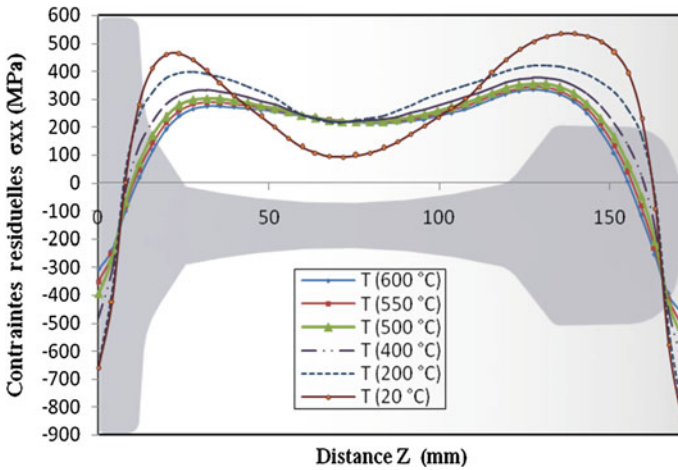


Fig. 8 σ_{XX} constraints distribution depending on the distance following the Z axis

magnitude and the distribution of stresses that we obtained are comparable to those obtained experimentally by Skyttebol et al. [6, 11]. In contrast, with the other components, the effect of the preheating temperature is marked as shown in Fig. 9. In this figure, we have shown at the weld zone, the stress σ_{YY} along the Z axis.

In this σ_{YY} distribution, we can distinguish three areas; head, web and web/foot off. Indeed, at the head stress reaches the maximum values for the temperature case ranging from 20 to 550 °C. In this area the most critical values were noted for the case of 20 and 200 °C.

The same findings were observed on the area leave web/foot but with higher level. In contrast, on the central zone the web, σ_{YY} stresses tend to negligible values.

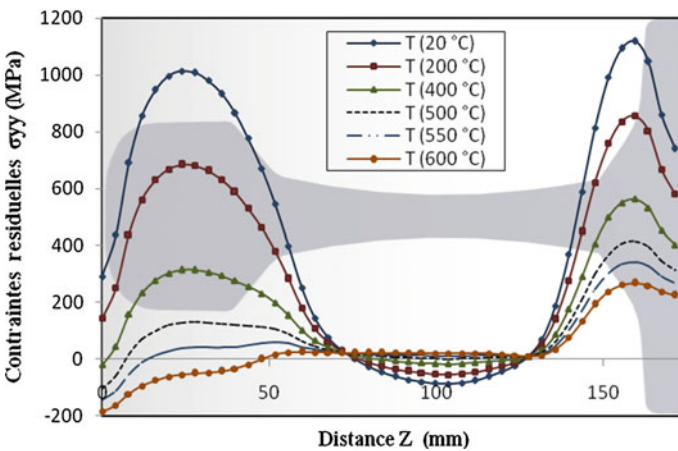


Fig. 9 σ_{YY} stress distribution as a function of the distance along the Z axis

Unlike the σ_{YY} component, the σ_{ZZ} component is predominant on the central zone (web). Locally, it reaches very high values and become increasingly singular with the preheating temperature decrease. According to these distributions we obtained, we can distinguish five specific areas of the rail section defined by different Z_i positions ($Z_0 = 0$ mm; $Z_1 = 20$ mm; $Z_2 = 71$ mm; $Z_3 = 140$ mm; $Z_4 = 172$ mm), see Fig. 10. In the next section we will clarify these areas from the one with the most critical cases.

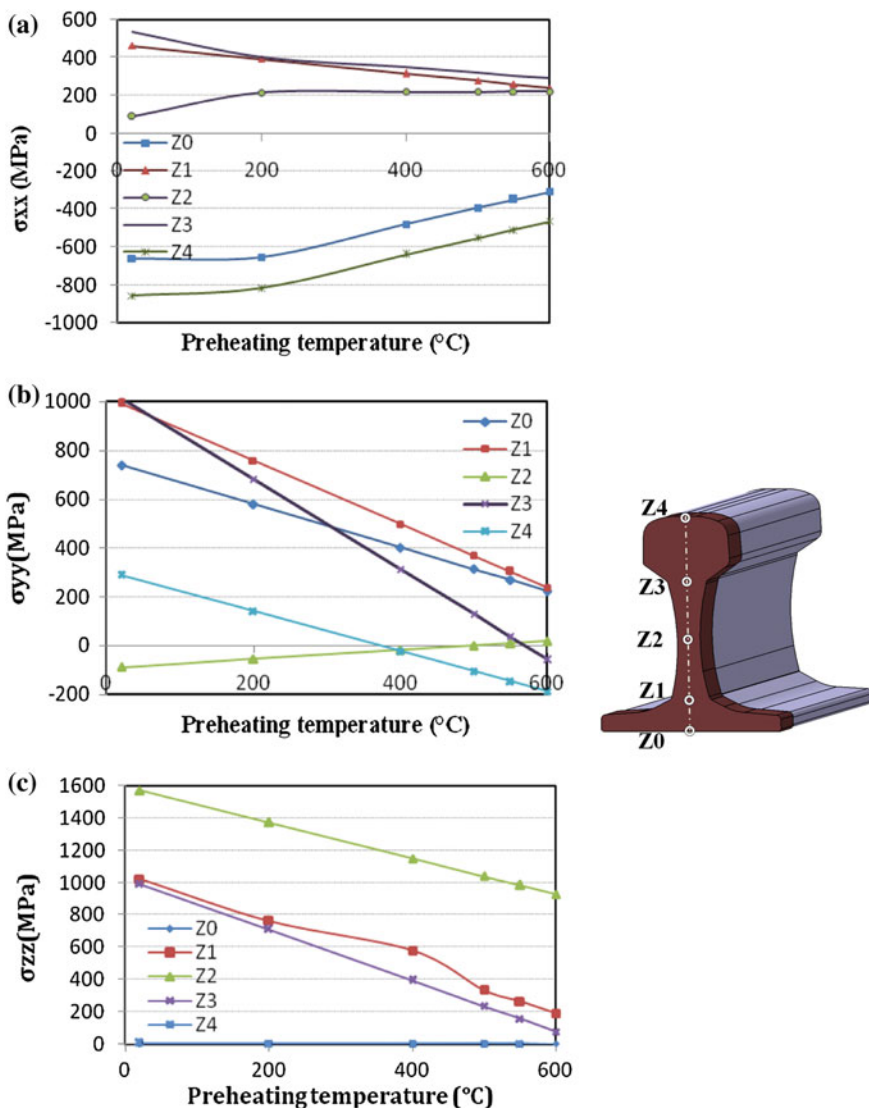


Fig. 10 Stress distribution **a** σ_{XX} , **b** σ_{YY} and **c** σ_{ZZ} as a function of the preheating temperature following the Z_0 ; Z_1 ; Z_2 ; Z_3 and Z_4 sections

3 Critical Areas Determination

In order to specify the most critical area, we will compare the associated residual stresses according to the preheating temperature. To do this, we have shown in Fig. 10, the evolution of the stress (σ_{XX} , σ_{YY} , σ_{ZZ}) for the different considered areas.

From these developments, we can distinguish two types of behavior. Indeed, for the Z_0 and Z_4 a section corresponding to free surfaces, the compressive stress is in contrast with the sections Z_1 , Z_2 and Z_3 , it is in tension to σ_{YY} . For both cases, the constraint decreases in absolute value as a function of the preheating temperature and approaches a value of approximately 250 MPa for the portions (Z_1 , Z_2 , Z_3) and of 500–300 MPa for sections Z_0 and Z_4 . Overall, these two sections (Z_0 and Z_4) generate higher stress levels compared to the others. Moreover, they are very sensitive to the preheating temperature. Indeed, once you go below 500 °C, the stress increases rapidly for these sections (Z_0 , Z_4). By contrast for the other sections, the stress becomes sensitive below 400 °C.

For the σ_{YY} component, we can observe the same behavior for the sections Z_0 , Z_1 , Z_3 and Z_4 . The stress decreases in value as a function of the preheating temperature and approaches an approximately 250 MPa value for the sections (Z_0 , Z_1) and to 78–200 MPa for Z_3 and Z_4 sections. This component σ_{YY} is in compression for Z_2 sections which corresponds to the central section of the web, in contrast it is in tension to the sections Z_1 , Z_2 and Z_3 . For σ_{ZZ} component, we notice a significant decrease with the function of preheat temperature. Both sections (Z_0 and Z_4), corresponding to the two free surfaces σ_{YY} and σ_{ZZ} stresses, are zero.

4 Conclusion

Following the connection by rail thermite welding, these have residual stress that can sometimes cause local damage. These damages could be one of the consequences of poor preheating. To highlight the relationship that binds the residual stress field and the preheating temperature, we performed a series of numerical simulations by finite element after confirming the initial results of our model in the literature. Through these results, clearly we have shown that when the preheating temperature is below 500 °C, the residual stress increases. They can become very critical below 400 °C. The residual stress criticality is often associated with the occurrence of damage. As an example, for the case without pre-heating, there may be a high density of porosity defects in the junction of the rail. It seems, therefore necessary to respect the preheat temperatures which must be of the order of 600 °C. With this temperature, the stress is about 400 MPa and without defects.

References

1. Schroeder, L.C., Poirier, D.R.: The mechanical properties of thermite welds in premium alloy rails. *Mater. Sci. Eng.* **63**, 1–21 (1984)
2. Jezzini-Aouad, M., Flahaut, P., Hariri, S., Winiar, L.: Optimisation des soudures aluminothermiques: Aspects mécaniques, métallurgiques et fiabilité. *Revue de Mécanique Appliquée et Théorique* **2**(2), 163–172 (2010)
3. Mouallif, I., Chouaf, A., El Amri, A., Benali, A.: Effects of alumino-thermic welding defects on the rails mechanical behavior. *Mécanique & Industries* **12**(5), 343–351 (2011)
4. Webster, P.J., Wang, X., Mills, G., Kamg, W., Webster, G.A.: Residual stress measurements on ORE railway rails by neutron diffraction. UIC, Final Report BRSUIC02/91 (1991)
5. Lennart Josefson, B., Jonas Ringsberg, W.: Assessment of uncertainties in life prediction of fatigue crack initiation and propagation in welded rails. *Int. J. Fatigue* **31**, 1413–1421 (2009)
6. Skyttebol, A., Josefson, B.L., Ringsberg, J.W.: Fatigue crack growth in a welded rail under the influence of residual stresses. *Eng. Fract. Mech.* **72**, 271–285 (2005)
7. Zerbst, U., Lundén, R., Edel, K.O., Smith, R.A.: Introduction to the damage tolerance behaviour of railway rails a review. *Eng. Fract. Mech.* **76**, 2563–2601 (2009)
8. Desimone, H., Beretta, S.: Mechanisms of mixed mode fatigue crack propagation at rail butt-welds. *Int. J. Fatigue* **28**(5–6), 635–642 (2006)
9. Mutton, P.J., Alvarez, E.F.: Failure modes in aluminothermic rail welds under high axle load conditions. *Eng. Fail. Anal.* **11**(2), 151–166 (2004)
10. Salehi, I., Kapoor, A., Mutton, P.: Multi-axial fatigue analysis of aluminothermic rail welds under high axle load conditions. *Int. J. Fatigue* **33**, 1324–1336 (2011)
11. Skyttebol, A., Josefson, B.L.: Numerical simulation of flash-butt-welding of railway rails. In: Cerjak, H. (ed.) *Mathematical Modelling of Weld Phenomena*. Graz, Austria
12. Bouazaoui, O., Chouaf, A.: Distribution of residual stresses in welded rails. ICMCSF, 17–22 May 2015, Lille, France (2015)
13. Bouazaoui, O., Chouaf, A.: Sévérité des contraintes résiduelles en fonction de la largeur de soudure dans les rails. 22^{ème} Congrès Français de Mécanique Lyon, 24 au 28 Août 2015 (2015)
14. NF A 45-317 Produits sidérurgiques laminés a chaud, Rail Vignole type 60 kg/m et éclisse, Profil: caractéristiques et tolérance
15. Webster, P.J., Mills, G., Wang, X.D., Kang, W.P., Holden, T.M.: Residual stresses in alumino-thermic welded rails. *J. Strain. Anal.* **32**, 389–400 (1997)
16. ERRI: Rail rolling contact fatigue. Residual stress measurements on naturally hard and two head-hardened rails by neutron diffraction, Utrecht Committee D 173/RP42 (1993)

Dynamic Analysis of Fiber Reinforced Composite Beam Containing a Transverse Crack

Yassine Adjal, Rachid Benzidane and Zouaoui Sereir

Abstract The present research article investigates the effect of a transverse crack on the flexural vibration of fiber reinforced composite beam based on Euler-Bernoulli beam theory. The presence of a crack in structural elements leads to an energy concentration near to crack's region and introduce a local flexibility which affect its dynamic response. Linear fracture mechanic theory has been used for crack modeling by using the stress intensity factors expressions. A parametric study has carried out in order to investigate the influence of fiber orientation, crack depth and crack location on the natural frequencies and theirs corresponding shape modes.

Keywords Flexural vibration · Cracks · Composite beam · Natural frequency

1 Introduction

The Fiber-Reinforced composite materials have been attracted many engineering industry, such as aerospace, naval construction and civil building. The increasing of its using, due mainly to excellent various properties, including high stiffness, good resistance to environmental conditions and high fatigue strength. The Fiber-reinforced composite beams have used in the many structural elements, such as robot arms, rotating machine parts, and turbine blades.

The presence of a crack in structural elements may affect its mechanical behavior and leads to damage failures. Due to this fact, many researchers have focused their investigations in the improvement of mechanical proprieties of these structures based on the study of cracks. Thus, the presence of cracks can introduce a local flexibility which has an influence on their dynamic characteristics. However, the evaluation of dynamical behavior of cracked structures can be used as indicator

Y. Adjal (✉) · R. Benzidane · Z. Sereir
Laboratoire Structure en Composite et Matériaux Innovants – LSCMI,
Faculté de Génie Mécanique, BP 1505, El M'Naouer, UST-MB, Oran, Algeria
e-mail: adjaleng@gmail.com

in the predicting of cracks. This research topic has been tackled in many research papers available at literature.

The deriving of crack formulation was based on fracture mechanic theory including the stress intensity factors which considered as important parameters for identifying the flexibility matrix. Krawczuk [7] has determined the flexibility coefficients matrix of composite beam containing a single crack. According to literature, it can be found a range of analytical and numerical methods for studying the influence of cracks on dynamic characteristic of composite beam. Concerning the analytical methods, the works have done by Wang et al. [10] focused in the developing of a new mathematical model for evaluating the natural frequencies and theirs corresponding mode shapes of unidirectional cracked composite beam under coupled flexural–torsion vibrations. Semi-analytical method titled Generalized Differential Quadrature, used by Daneshmehr et al. [4] for free vibration analysis of cracked composite beam, based on first order shear theory. Ghoneam [5] proposed a new analytical model to study the effect of fiber orientation and various boundary conditions in dynamic behavior of cracked and uncracked laminate composite beam. A transfer matrix method related to state vector has been used by Mostafa [9] for free vibration analysis and crack identification of stepped beams with multiple edge cracks and different boundary conditions.

Many researchers have interested in the using of numerical method like finite element method, for example. Krawczuk [8] has proposed new finite element for identification the dynamical characteristic of cracked composite beam. Behera et al. [3] used finite element method for free vibration of laminate composite beam with a transverse crack, based on first shear deformation. Kisa [6] studied the effect of crack on natural frequencies and their corresponding modes shapes of a cantilever composite beam, using finite element associated with component mode synthesis methods. Other authors interested in the using of finite element analysis by means a numerical code [1] investigated the variations in the eigen-nature of cracked composite beams due to different crack depths and locations using numerical and experimental investigation.

This present paper is devoted for studying the effect of an edge crack on the flexural vibration of unidirectional composite beam. A Parametric study has carried out in order to investigate the influence of fiber orientation, crack depth and crack location on the natural frequencies and theirs corresponding shape modes. The dynamic analysis of cracked composite beam used as technique for prediction the fatigue damage.

2 Crack Formulation Theory

Considering a composite beam containing a transversal edge crack, shown in Fig. 1, the beam is subjected to pure bending load P .

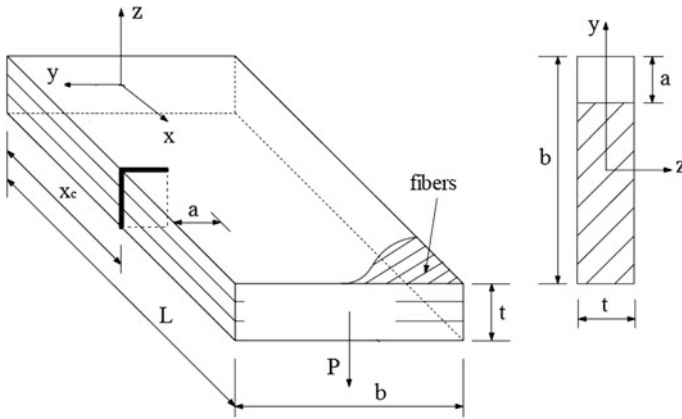


Fig. 1 Geometry of cracked composite beam [10]

Based on linear fracture mechanic theory, the crack formulation have been derived in which, the flexibility coefficients are expressed as a function of stress intensity factors and crack geometry.

The additional displacement due to presence of a crack in rectangular cross section, under the acting of load P , determined by the Castigliano's theorem.

$$u_i = \frac{\partial U}{\partial P_i} \tag{1}$$

where U is the strain energy of a cracked structure, defined as follows:

$$U = \int_A \left(D_{11} \sum_{i=1}^{i=N} K_{Ii}^2 + D_{12} \sum_{i=1}^{i=N} K_{Ii} \sum_{i=1}^{i=N} K_{IIi} + D_{22} \sum_{i=1}^{i=N} K_{IIi}^2 \right) dA \tag{2}$$

where A denotes the cracked surface, K_I and K_{II} are the stress intensity factors for fracture mode I, II respectively, these factors were used to evaluate the stress field around the cracks region, D_{11} , D_{22} and D_{12} are coefficients depending on the materials parameters, are taken from [7]. The stress intensity factors for cracked composite beam, given as [2]:

$$K_{ij} = \sigma_n \sqrt{\pi a} Y_j(\zeta) \cdot F_{jm} \left(\frac{a}{b} \right) \tag{3}$$

where σ_n is the stress of cracked area which relating to corresponding fracture mode, is the correction function dependent in geometry, $Y_j(\zeta)$ is the correction factor for the anisotropic material [10], a is the crack depth and, L and b are the

length and the breadth of beam respectively. The stress intensity factor corresponding to cracked beam under bending loading about z-axis, given as follows:

$$K_I = \sigma \sqrt{\pi a} Y_1(\zeta) \cdot F\left(\frac{a}{b}\right); \quad \sigma = \frac{12P}{bh^3} z \quad (4)$$

where:

$$F\left(\frac{a}{b}\right) = \frac{\sqrt{\frac{\tan \lambda}{\zeta}} [0.752 + 2.02\left(\frac{a}{b}\right) + 0.37(1 - \sin \lambda^3)]}{\cos \lambda}; \quad \lambda = \frac{\pi a}{2b}$$

$$Y_1(\zeta) = 1 + 0.1(\zeta - 1) - 0.016(\zeta - 1)^2 + 0.002(\zeta - 1)^3$$

The flexibility coefficients of cracked composite beam under loading are expressed in the following form:

$$c_{ij} = \frac{\partial^2}{\partial P_i \partial P_j} \int_{-h/2}^{h/2} \int_0^a j(\alpha) d\alpha dz \quad (5)$$

where $j(\alpha) = \frac{\partial U}{\partial \alpha}$ is the elastic strain energy release rate j and a is the crack depth. The coefficient flexibly parameter used in the case of pure bending load, considered herein, is c and given as:

$$c = \frac{24\pi D_1}{b^2 h^3} \int_0^a \alpha \left[F_1\left(\frac{\alpha}{b}\right) \right]^2 d\alpha \quad (6)$$

3 Equation of Motion for Flexural Vibration

The free flexural vibration of an Euler-Bernoulli beam with constant cross-section is expressed in the following differential equation:

$$EI \frac{\partial^4 h}{\partial y^4} - m \frac{\partial^2 h}{\partial t^2} = 0 \quad (7)$$

where EI represents the flexural rigidity of unidirectional composite beam and m is the mass per unit length, given as [10]:

$$EI = b \cdot \left(D_{22} - \frac{D_{12}^2}{D_{11}} \right) \quad (8)$$

$$m = b \cdot \rho h \quad (9)$$

By using the separation of variable $h(y, t) = H(y) \cdot e^{i\omega t}$, the Eq. 7 yield:

$$EI \cdot H^{iv} - m\omega^2 H = 0 \tag{10}$$

where: $\lambda = \left(\frac{m\omega^2 L^4}{EI}\right)^{\frac{1}{4}}$

The general solution of the above equation is:

$$H(x) = A_{K1} \cosh \lambda x + A_{K2} \sinh \lambda x + A_{K3} \cos \lambda x + A_{K4} \sin \lambda x \tag{11}$$

The expressions for cross-sectional rotation $\Theta(x)$ the bending moment $M(x)$ and the shear force $S(x)$ become:

$$\Theta(x) = \frac{1}{L} [A_{K1} \lambda \sinh \lambda x + A_{K2} \eta \cosh \lambda x - A_{K3} \eta \sin \lambda x + A_{K4} \eta \cos \lambda x] \tag{12}$$

$$M(x) = \frac{EI}{L^2} [A_{K1} \lambda^2 \cosh \lambda x + A_{K2} \lambda^2 \sinh \lambda x - A_{K3} \lambda^2 \cos \lambda x - A_{K4} \lambda^2 \sin \lambda x] \tag{13}$$

$$S(x) = -\frac{EI}{L^3} [A_{K1} \lambda^3 \sinh \lambda x + A_{K2} \lambda^3 \cosh \lambda x + A_{K3} \lambda^3 \sin \lambda x + A_{K4} \lambda^3 \cos \lambda x] \tag{14}$$

The cracked composite is divided in two sub-beams at cracked section. Thus, the continuity conditions for an edge crack located at distance $x = x_c$ can be expressed as:

$$M_i(x_c) = M_{i+1}(x_c) \tag{15}$$

$$S_i(x_c) = S_{i+1}(x_c) \tag{16}$$

$$H_i(x_c) = H_{i+1}(x_c) \tag{17}$$

Moreover, a discontinuity cross-sectional rotation due to an existing crack can be expressed as follows:

$$\Theta_i(x_c) = \Theta_{i+1}(x_c) - c_{44} M_i(x_c) \tag{18}$$

where c_{44} is the crack-sectional flexibility coefficient parameter; using in the case of cracked beam under bending load in vertical direction. The subscript (i) and ($i + 1$) in Eqs. 15–18 refers to left and right of sub-beam at cracked section.

The boundary conditions of clamped composite beam are:

- at fixed end:

$$H_i(0) = \Theta_i(0) = 0 \tag{19}$$

- at free end:

$$M_{i+1}(1) = S_i(1) = 0 \tag{20}$$

Substitution of Eqs. 11–14 into Eqs. 15–20 will yield the characteristic equation of the cracked composite beam.

$$[B]\{A\} = \{0\} \tag{21}$$

where:

$\{A\} = \{A_{11}, A_{12}, A_{13}, A_{14}, A_{21}, A_{22}, A_{23}, A_{24}\}^T$ is a vector composed of 8 unknowns and $[B]$ represents a characteristic matrix given as function of natural frequency. Setting the determinant $\det[B(w)] = B(w) = 0$ yields the natural frequencies. The corresponding mode shapes are obtained by substituting each natural frequency back into Eq. 11. The characteristic matrix $[B]$ is given as:

$$[B] = \begin{bmatrix} 1 & 0 & 1 & 0 & 0 & 0 & 0 & 0 \\ 0 & 1 & 0 & 1 & 0 & 0 & 0 & 0 \\ 0 & 0 & 0 & 0 & ch(\lambda) & sh(\lambda) & -c(\lambda) & s(\lambda) \\ 0 & 0 & 0 & 0 & -sh(\lambda) & -ch(\lambda) & -s(\lambda) & c(\lambda) \\ ch(\lambda x) & sh(\lambda x) & -c(\lambda x) & -s(\lambda x) & -ch(\lambda x) & -sh(\lambda x) & c(\lambda x) & s(\lambda x) \\ -s(\lambda x) & -ch(\lambda x) & -s(\lambda x) & c(\lambda x) & sh(\lambda x) & ch(\lambda x) & s(\lambda x) & -c(\lambda x) \\ -ch(\lambda x) & -sh(\lambda x) & -c(\lambda x) & -s(\lambda x) & ch(\lambda x) & sh(\lambda x) & c(\lambda x) & s(\lambda x) \\ \frac{-ish(\lambda x)L - c_{44}EI\lambda^2 ch(\lambda x)}{L^2} & \frac{-ich(\lambda x)L - c_{44}EI\lambda^2 sh(\lambda x)}{L^2} & \frac{-is(\lambda x)L - c_{44}EI\lambda^2 c(\lambda x)}{L^2} & \frac{-ic(\lambda x)L - c_{44}EI\lambda^2 s(\lambda x)}{L^2} & \frac{ish(\lambda x)}{L} & \frac{ich(\lambda x)}{L} & \frac{is(\lambda x)}{L} & \frac{ich(\lambda x)}{L} \end{bmatrix} \tag{22}$$

where: $sh = \sinh$; $ch = \cosh$; $s = \sin$; $c = \cos$.

4 Numerical Example and Discussion

Consider a cracked composite beam clamped at left end and free at right end, having length L , height t and width b , containing an edge crack located at a distance x from the left end, as shown in Fig. 2. The composite beam considered herein is made of unidirectional graphite fiber-reinforced, where its physical and geometrical characteristics are chosen similarly to [7].

The material properties of the graphite fiber-reinforced composite beam are given in Table 1. The geometrical characteristics involve the length (L), height (t) and width (b) of the composite beam, are taken as 0.5, 0.005 and 0.1 m respectively.

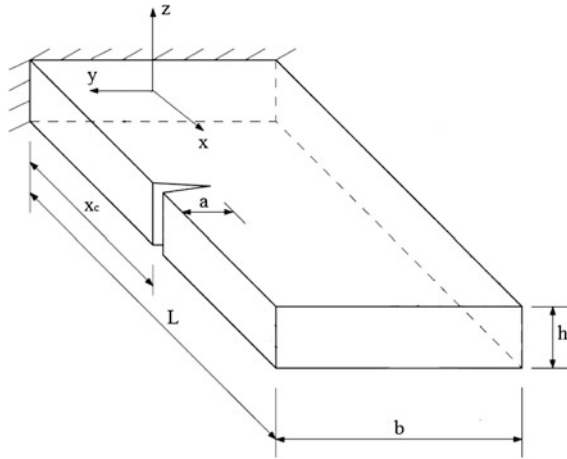


Fig. 2 A cantilever cracked composite beam [10]

Table 1 The material properties of the graphite fiber-reinforced composite beam

E_f (GPa)	E_m (GPa)	G_f (GPa)	G_m (GPa)	ρ_f (kg/m ³)	ρ_m (kg/m ³)	ν_f	ν_m
275.6	2.76	114.8	1.036	1900	1600	0.2	0.33

The numerical results have been adopted for evaluating the effect of fiber fraction volume, crack depth ration and crack locations on the dynamic characteristic of a cracked composite beam, which are presented graphically. The influence of the fiber orientation on flexural rigidity of composite beam for different values of the fiber volume fraction ($a/b = 0.2, 0.4, 0.6$ and 0.8) shown is in Fig. 3. As can be observed, the bending stiffness with higher values occurs when the angle of fiber is greater than 45° . In the same figure, the increasing of fiber volume fraction affects considerably the bending stiffness of composite beam. Therefore, it can be concluded that the rigidity of composite beam is a function of fiber volume fraction and fiber orientation.

Figure 4 shows the effect of fiber orientation on fundamental natural frequency for various crack depth ($a/b = 0.2, 0.4, 0.6$ and 0.8) the fiber volume fraction considered herein is ($V = 0.5$) and the crack is located at a distance ($x/L = 0.3$). Based on graphically results shown in this figure, the changes in fundamental natural frequency are appeared due to the variation of fiber angle from 0° to 90° , when the fiber angle is greater than 45° , these changes become more sensitive, this due to fact that the change in flexural rigidity which is a function of fiber angle. In

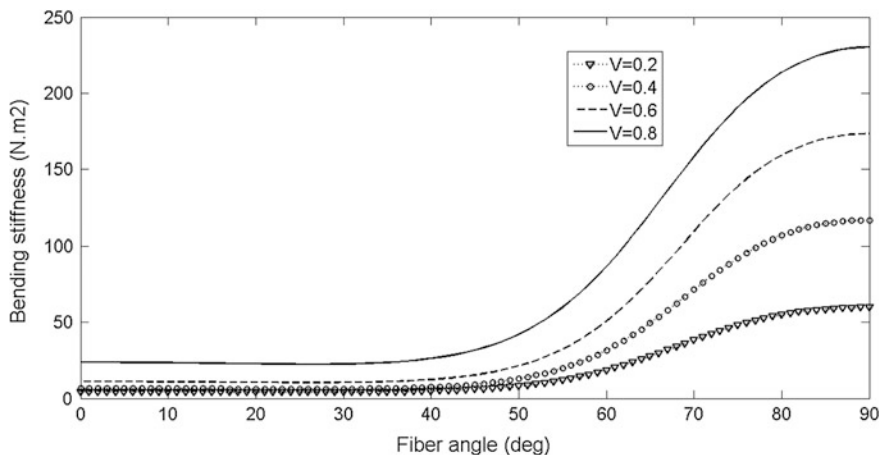


Fig. 3 Variation of bending stiffness of composite beam for different values of fiber volume fraction $V = 0.2, 0.4, 0.6, 0.8$

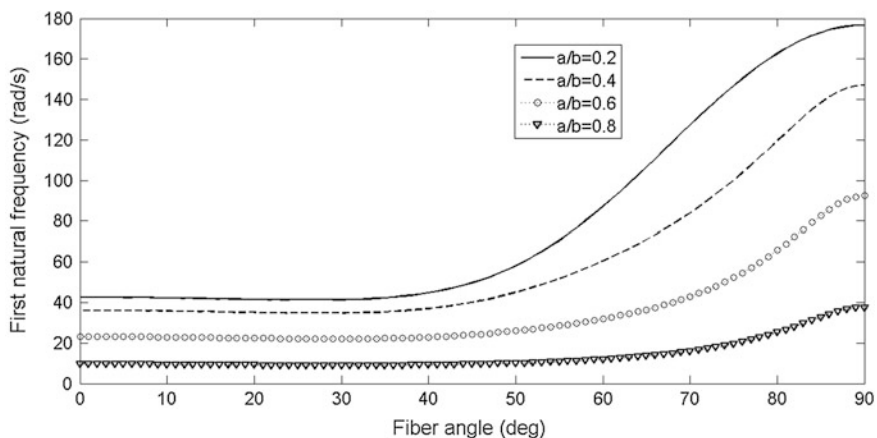


Fig. 4 Effect of angle of fiber on fundamental natural frequency of the cracked composite beam for different crack depth ($a/b = 0.2, 0.4, 0.6$ and 0.8)

Fig. 5, it is noticeable also the increasing in crack depth led to reduction in fundamental natural frequencies.

The variation of first natural frequency of cracked composite beam for range of crack position is illustrated in Fig. 6. As observed from results that, these changes due to variation of fiber angle for a crack located at distance ($x/L = 0.3$) from the

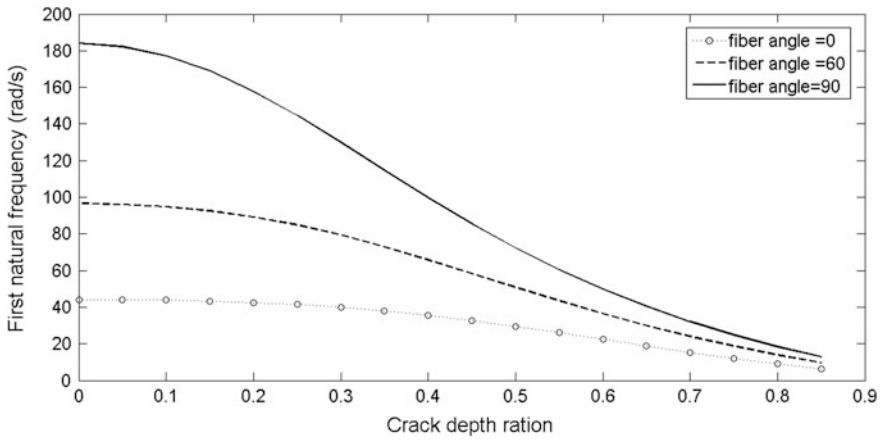


Fig. 5 Effect of crack depth on fundamental natural frequency of the cracked composite beam for different angle of fiber

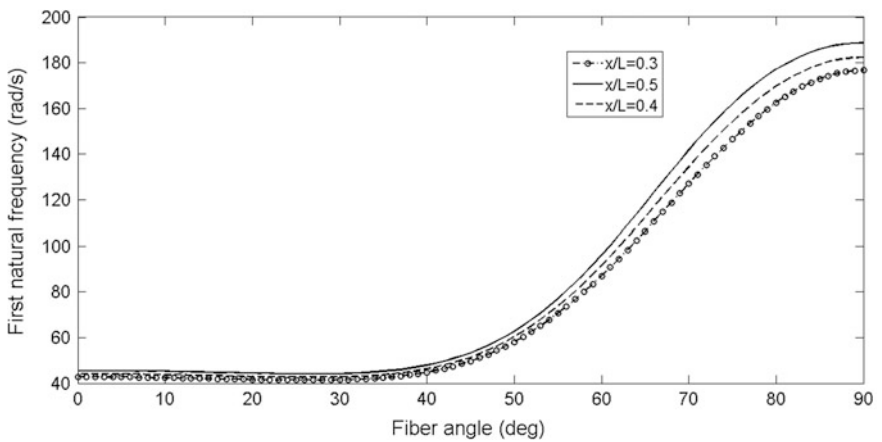


Fig. 6 Effect of angle of fiber on fundamental natural frequency of the cracked composite beam for different crack location $x/L = 0.3, 0.4$ and 0.6

fixed end of composite beam is lower compared to those located at 0.4 and 0.5 therefore, the crack position has also affect the variation of natural frequencies.

The Fig. 7 shows the variation of the first natural frequency as a function of crack depth ration for different values of fiber volume fraction ($V = 0.2, 0.4, 0.6$ and 0.8).

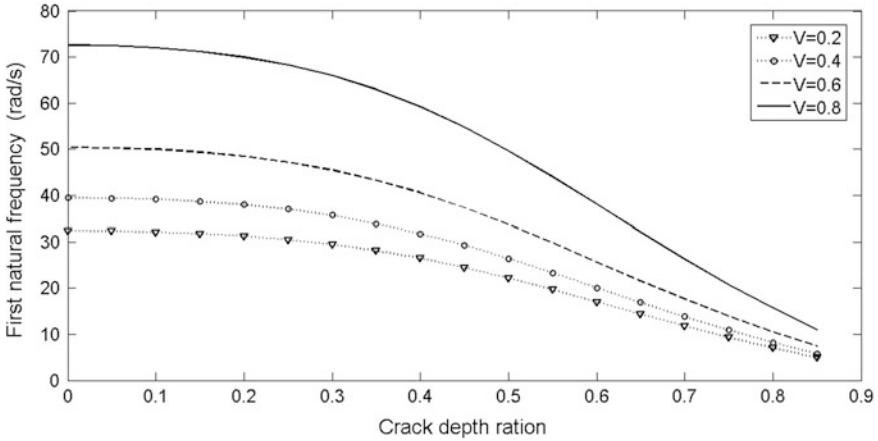


Fig. 7 Effect of crack depth on fundamental natural frequency of the cracked composite beam for different crack location ration $x/L = 0.2, 0.4, 0.6$ and 0.8

It can be seen that the reduction in the natural frequency is caused by the increasing of crack depth, it is also observed from this figure, that the natural frequencies having higher values when the fiber volume fraction is ($V = 0.8$).

In Fig. 8 demonstrates the variation of fundamental natural frequency as a function of crack depth ration, the increasing of crack depth reduces the first natural frequency. The results show also that these variations of natural frequency to crack position at a distance ($x/L = 0.2$) from the fixed end are less sensitive compared to other crack positions ($x/L = 0.4$ and 0.6).

The effect of crack location on first natural frequency of cracked composite beam for various values of crack depth ration is illustrated in Fig. 9. The angle of fiber is assumed to be zero degree, As can be seen, the changes in crack positions have a considerable effect on natural frequency variation, the crack located near to fixed end of composite beam has a smaller effect.

The effect of crack depth on first, second and third mode shape is illustrated in Fig. 10. As observed in this figure, it is evident that the changes in mode shape are caused by the presence of a crack, these changes are more significant, when the crack depth is greater than ($a/b = 0.8$) for the first mode shape, therefore, it can be concluded that the modification in mode shape will be used as a technique for predicting the damage in structures.

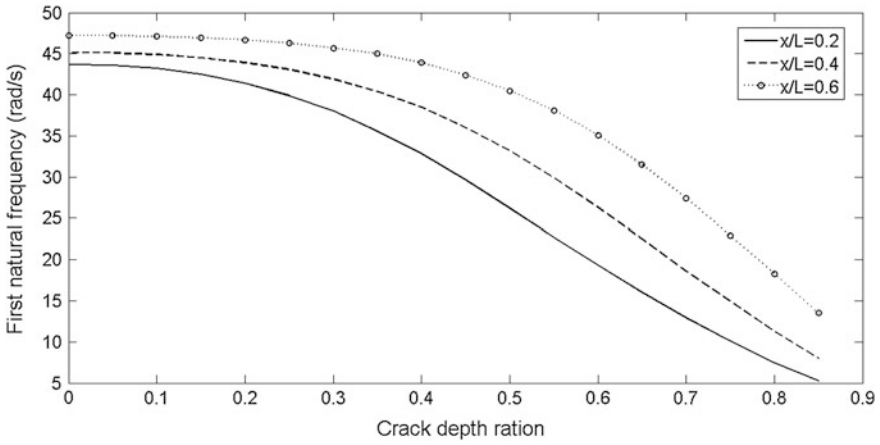


Fig. 8 Effect of crack depth on fundamental natural frequency of the cracked composite beam for different crack location ratio $x/L = 0.2, 0.4$ and 0.6

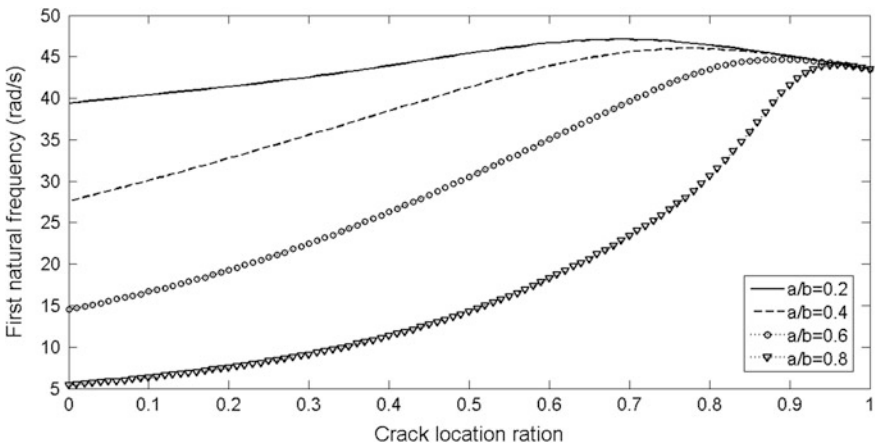


Fig. 9 Effect of crack location on fundamental natural frequency of the cracked composite beam for different crack depth ratio $a/b = 0.2, 0.4, 0.6,$ and 0.8

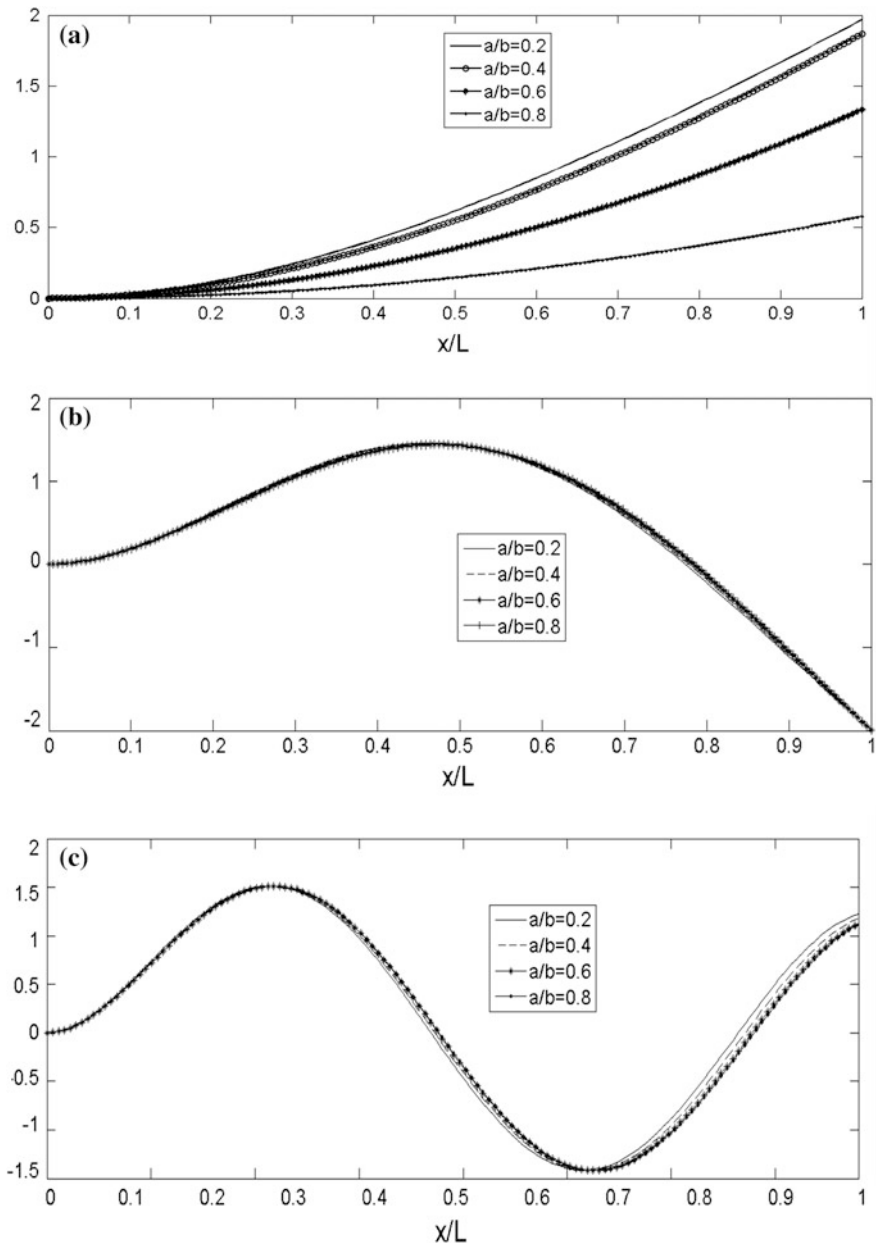


Fig. 10 The mode shapes of vibration for a crack located at ($x_c = 0.5$) and fiber angle 60° as a function of crack depth ratio changes. **a** First mode shape of flexural vibration. **b** Second mode shape of flexural vibration. **c** Third mode shape of flexural vibration

5 Conclusion

The flexural vibration of fiber reinforced composite containing an edge crack, based on Euler-Bernoulli theory is studied. The obtained results show the influence of several parameters, such as fiber angle, crack depth ration and crack positions on natural frequencies; however, the reduction in natural frequency values is more sensitive when the crack depth increase. Also, the dynamic behavior of unidirectional cracked composite beam with a lower flexural rigidity is more sensitive to presence of a crack. In addition to these numerical results, the natural frequencies variation is more significantly affected when the crack is located at middle of beam, due to fact, that the bending moment is higher at this position. Finally, the evaluation of dynamical behavior of cracked composite beam can be used as robust technique in predicting a presence of crack.

References

1. Abd El-Hamid, : An investigation into the Eigen-nature of cracked composite beams. *Compos. Struct.* **38**(1-4), 45-55 (1998)
2. Bao and Suo: The role of material orthotropy in fracture specimens for composites. *J. Appl. Mech.* **29**, 1105-1116 (1992)
3. Behera, S., Sahu, S.K., Asha, A.V.: Vibration analysis of laminated composite beam with transverse cracks. *Adv. Struct. Eng.* pp. 67-75 (2015)
4. Daneshmehr, A.R., Nateghi, A., Inman, D.J.: Free vibration analysis of cracked composite beams subjected to coupled bending-torsion loads based on a first order shear deformation theory. *Appl. Math. Model.* **37**, 10074-10091 (2013)
5. Ghoneam, S.M.: Dynamic analysis of open cracked laminated composite beams. *Compos. Struct.* **32**, 3-11 (1995)
6. Kisa, : Free vibration analysis of a cantilever composite beam with multiple cracks. *Compos. Sci. Technol.* **64**(2004), 1391-1402 (2003)
7. Krawczuk, M., Ostachowicz, W.M.: Modeling and vibration analysis of a cantilever composite beam with a transverse open crack. *J. Sound Vib.* **183**(1), 69-89 (1995)
8. Krawczuk, M., Ostachowicz, W., Zak, A.: Dynamics of cracked composite material structures. *Comput. Mech.* **20**, 79-83 (1997)
9. Mostafa, A.: A transfer matrix method for free vibration analysis and crack identification of stepped beams with multiple edge cracks and different boundary conditions. *Int. J. Mech. Sci.* **57**, 19-33 (2012)
10. Wang, K., Inman, D.J., Farrar, C.R.: Modeling and analysis of a cracked composite cantilever beam vibrating in coupled bending and torsion. *J. Sound Vib.* **284**, 23-49 (2005)

Determination of Elastic-Plastic Parameters of Inconel Arc Sprayed Coating

Yamina Mebdoua, Yazid Fizi and Hadj Lahmar

Abstract Various approaches have been proposed to determine the mechanical properties of power law materials using dimensionless analysis and the concept of a representative strain based on the forward and reverse algorithms. This work introduces an inverse analysis procedure to determine the elastic-plastic properties of an arc-sprayed inconel coating, using indentation test. The Levenberg-Marquardt optimization method was used to extract the elastic modulus, yield strength and strain-hardening exponent from the indentation load-depth curve. The optimization of the elastic-plastic behavior of the material allows the simulation of the tensile test using finite element model.

Keywords Wire arc sprayed coating · Inconel 625 · Elastic-Plastic properties · Inverse analyses

1 Introduction

Thermal sprayed coatings are extensively used to protect components against wear and corrosion. Twin wire arc spraying method is one of the less expensive thermal spraying processes able to produce coatings with a wide rate of material deposition [1]. Wire arc spraying is a well-developed technology capable to deposit thick coating layers up to a few millimeters in thickness. Wire arc spraying makes use of wire electrodes made of the desired coating material. An electric arc is created between the wires tips, liquid droplets are then propelled toward the treated surface

Y. Mebdoua (✉) · Y. Fizi · H. Lahmar
Centre de Développement des Technologies Avancées «CDTA»,
Algiers, Baba Hassen, Algeria
e-mail: ymebdoua@cdta.dz

Y. Fizi
e-mail: yfizi@cdta.dz

H. Lahmar
e-mail: hlahmar@cdta.dz

using an atomizing gas [2]. The spraying rate depends mainly on the material properties, on the wire diameter and on the process parameters. Thick coatings can be built up by stacking the propelled particles onto the substrate. Wire arc spraying requires minimal facilities and is a versatile, portable, and easily automated thermal spray technique [3, 4]. Since the 1940s, super alloys have been developed to protect surfaces in corrosive environment and high service temperatures. Such extreme conditions commonly exist in gas turbines used in aircraft and electrical generators. Nickel-based alloys are a good example of such class of high temperature materials that exhibits significant resistance to various applied loads at harsh environments [5–7]. Nickel based alloys such as Inconel 625, 600, or 718 outperform iron alloys and other high temperature materials like ceramics, because they are known for exceptional oxidation resistance at high temperatures, exceptional toughness, and ductility [7–9]. Numerous works were focused on the measure of thermal spray coating properties using instrumented indentation as a non-destructive tool in material characterization field [10–12]. This technique becomes increasingly used thanks to its simplicity and versatility. Instrumented indentation involves an indenter being pressed down on a sample of a material to a certain depth and then withdrawn back. The whole process is typically treated as quasi-static. However, rate-effects can also be investigated under dynamic indentation conditions. Monitoring the indentation load P as a function of indentation depth h , into a substrate during both loading and unloading yields a Load-displacement (P - h) curve. Because of the high cost of Ni-base alloys compared to stainless steels, Nickel alloys coatings are reserved for particular cases where the stainless steels are not suitable or when purity or safety are critically important [13]; that is why Ni alloys are deposited to protect surfaces of cheaper materials. However, due to coating microstructure, losses in performance could be occurred compared to bulk material performance [14]. In the present study, the mechanical properties of arc sprayed Inconel 625 coating were investigated. A number of methods based on both experimental and numerical studies have been proposed to extract the elastic-plastic properties from the indentation data (Fizi et al. [15], Luo [16, 17], Chaiwutand and Esteban [18]). In this study, a mechanistic approach was proposed to extract the mechanical properties of inconel coating; the approach is based on the combination of micro-indentation experiment, finite element and inverse analysis techniques.

2 Experimental Measurements

Wire arc spray gun ARCSPRAY 234 (Metallization Company) was employed to spray Sulzer Metco SM8625 (Ni 21Cr 9Mo 4(Ta + Nb)). The deposited material is introduced in the form of two consumable wires electrodes. The diameter of these two wires is 1.6 mm. Inconel 625 was deposited onto C35 substrate with cylindrical form of 25 mm in diameter and 5 mm in thickness. Table 1 lists the nominal composition of the Inconel 625 coating and that of the substrate used in this study.

Table 1 Chemical composition of Inconel 625 coating and substrate (mass fraction %)

Elements	Cr	Ni	Fe	Mo	Mn	Nb	Cu	Ti
SM8625	21.04	65.4	0.34	9.25	–	3.89	–	–
C35	0.17	0.19	98.4	–	0.79	–	0.16	0.16

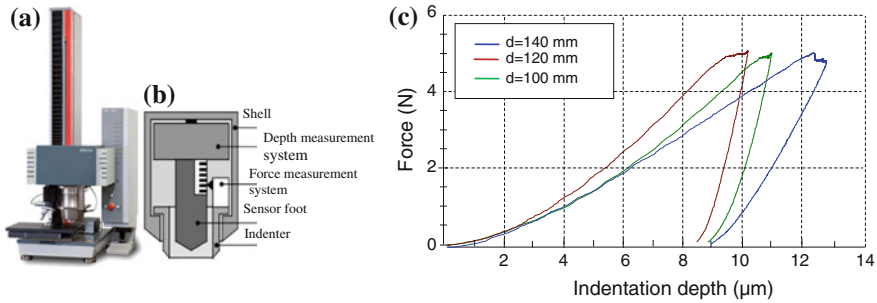


Fig. 1 Z2.5 Zwick indentation device: **a** View of the machine, **b** Hardness measurement head, **c** Indentation curves of three samples elaborated with different spray distances

The sprayed coating was sectioned parallel to the spraying direction, polished prior to optical microscopy, and micro-indentation.

Elastic modulus and hardness of the coatings were obtained by micro-indentation instrumented tests. Zwick/Roell equipment, with a resolution of $\pm 0.01\%$ in force and $0.02\ \mu\text{m}$ in displacement, was used as shown in Fig. 1a. The experiment was displacement controlled with an indentation velocity of $8.3\ \mu\text{m/s}$. When the maximum available depth was reached, the indenter was held for 15 s, and then moved back with the same velocity. A Vickers indenter with a maximum load of 5N was used. The Inconel coating hardness elaborated with different distance spray values: 100, 120 and 140 mm, are $HV_{0.5} = 289.5 \pm 4$, $HV_{0.5} = 333 \pm 12$, $HV_{0.5} = 248.5 \pm 30$, respectively. The variation of the three indentation curves of the above specimens are shown in Fig. 1c.

An example of the impression by an indentation made across the coating thickness is shown in Fig. 2. A cross sectional microscopic observation shows the inhomogeneity of the coating explained by the presence of pores, oxides and unmelted particles. The coating microhardness exhibits a declining and upward trend with the spray distance ratio of 0.8. It increases from $286.1HV_{0.5}$ to $341.6HV_{0.5}$ then decreases from $341.6HV_{0.5}$ to $254.9HV_{0.5}$.

Combining with the coating microstructure and deposition efficiency, the variation of coating microhardness with the spray distance could be attributed to the variation of oxides inclusion and inhomogeneity of the *Inconel 625* coating. The post-impact oxidation may be the key factor increasing and decreasing the coating oxide inclusions. The microstructures of the three samples are almost similar; the

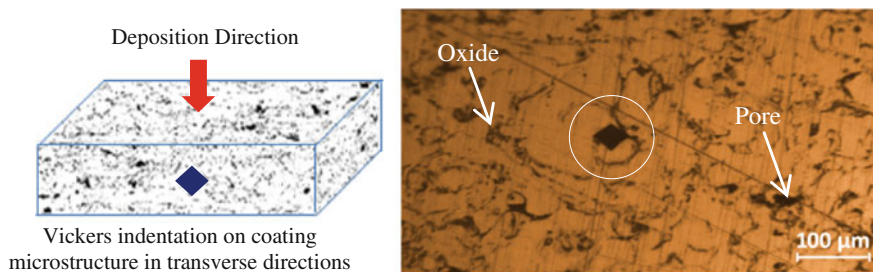


Fig. 2 Indentation across the thickness of the Inconel 625 coating

sample elaborated with spray distance of 120 mm is characterized by higher hardness compared to the other samples. The indentation curve corresponding to this test is used to determine the mechanical properties of the coating.

3 Finite Element Analysis

The finite elements code ABAQUS[®], is used to simulate the sharp indentation test. The indenter is modeled as a rigid conical shape body with half apex angle of 68° . Overall 1818 axisymmetric four node elements with reduced integration (CAX4R) are used to make the model discrete. The friction coefficients at the contact surfaces between the indenter and the top surface of the bulk material are assumed to be zero, since friction has a negligible effect on the indentation process [19].

The presence of the substrate material was ignored in the analysis as the indentation depth is shallow enough to neglect the influence of the substrate material. Furthermore, a downward displacement of $9.015 \mu\text{m}$ (experimental value of the specimen elaborated with a distance spray of 120 mm) was applied to the rigid indenter. Displacement-controlled condition is preferred to a load-controlled loading because of its stable numerical convergence in contact simulations.

The equivalent reaction force is reported as the indentation load and the indentation depth is obtained from the vertical displacement of the node directly underneath the indenter tip. It is noted that the small amount of porosity which is inherent in all arc sprayed coatings was not considered. Moreover, any micro-cracks, which may occur during indentation, were not considered in the analysis.

3.1 Application of Inverse Analysis in Indentation Problem

There are four material parameters, namely, E , σ_y , n and ν , to be defined for an elastic–plastic material. For simplicity, the value of Poisson’s ratio of the coating was taken from the literature as 0.275 [20]. Three elastic–plastic parameters

(Young’s modulus E , Yield stress σ_y and Work hardening exponent n) are extracted, in a non-linear optimization approach, fully integrated with FE analysis, using results from a single indentation curve.

In this study, the inverse analysis based on Levenberg–Marquardt (LM) method is used to estimate these two material properties. The LM method is described extensively in [21] and its use within the context of this work is illustrated by the flow chart shown in Fig. 3.

Essentially, it processes the experimental data and attempts to obtain the best estimate for unknown state variables based on least-squares theory. The theory of the LM method is based on minimizing an error function, ϕ with respect to the parameter p , as:

$$\phi(p) = \frac{1}{2} \sum_{i=1}^m [r_i(p)]^2 = \frac{1}{2} r^t r \tag{1}$$

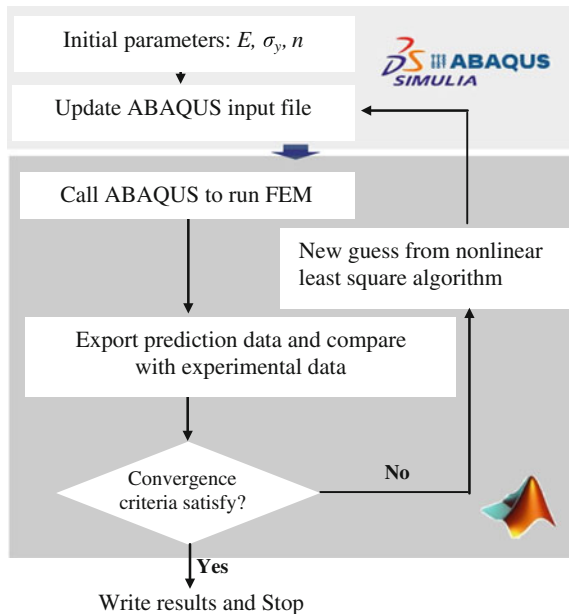
where p is a vector which contains the unknown parameters and m is the number of measurements.

The vector r is defined as:

$$r = p_i - p_{oi} \tag{2}$$

where p_i and p_{oi} are the numerically generated and measured indentation load, respectively, at the specified indenter displacement values. Starting with initial guess values of E , σ_y and n , a FE analysis of the indentation problem was

Fig. 3 Flowchart of the inverse FEM



performed to obtain the indentation loading response p_i . This resulting curve is subsequently compared with the measured one p_{oi} , through “Eq. 2”. The problem is iteratively solved through the inverse procedure until the convergence of the problem is obtained. The computations were conducted using the *FE* code ABAQUS®.

3.2 Material Model

Since the initial guess values for E , σ_y , n are provided, the optimization procedure is carried out in several steps with MATLAB®. In terms of pre-processing of FE analysis, the material properties in the ABAQUS® input file are replaced by new elastic–plastic material properties. In ABAQUS®, these are Young’s modulus, Poisson’s ratio, and discrete points on the post yielding true stress–true strain curve. In this study, a power law strain hardening curve has been used to simulate the indentation experiments. The assumptions as used by several authors [19, 22, 23, 24]. The stress and strain of elastic–plastic material obeying a power law description are given by:

$$\sigma = \begin{cases} E\varepsilon & \text{for } \sigma \leq \sigma_n \\ R\varepsilon^n & \text{for } \sigma > \sigma_y \end{cases} \quad (3)$$

For continuity:

$$\sigma_y = E\varepsilon = R\varepsilon^n \quad (4)$$

In the plastic region the strains are split into elastic and plastic parts:

$$\varepsilon_{Total} = \varepsilon_{el} + \varepsilon_{pl} \quad (5)$$

The plastic part can be rewritten as:

$$\sigma = \sigma_y \left(1 + \frac{E}{\sigma_y} \varepsilon_{pl} \right)^n \quad (6)$$

Since finite element codes such as ABAQUS®, require all plastic strains to be given as true strains, the relation [25], can be converted into a relation involving true stresses and true strains, as follow:

$$\sigma_{true} = R\varepsilon_{nor}^n (1 + \varepsilon_{nor}) \quad (7)$$

$$\varepsilon_{true}^{pl} = \ln(1 + \varepsilon_{nor}) - \frac{R\varepsilon_{nor}^n (1 + \varepsilon_{nor})}{E} \quad (8)$$

In the plastic part of “Eq. 3”, where σ_{true} and ϵ_{true} are the input data in the FE program, which could be consistent with “Eq. 3” if it is assumed to be given in terms of nominal quantities. R in “Eq. 7” and “Eq. 8” is obtained from continuity.

3.3 Identification of the Material Properties

Three parameters should be optimized E , σ_y and n . The material parameters that lead to the best fitting between simulated and experimental indentation curves were considered to represent the constitutive behavior of the coating. The initial values of σ_{yy} and n have been chosen as arbitrary ones, whereas young’s modulus $E = 94.527$ GPa was determined experimentally. The initial and optimization results are summarized in Table 2 where the sensitivity of the proposed algorithm is demonstrated by matching simultaneously three parameters. This simulation result was observed after 9 iterations with an error less than 1.7 %.

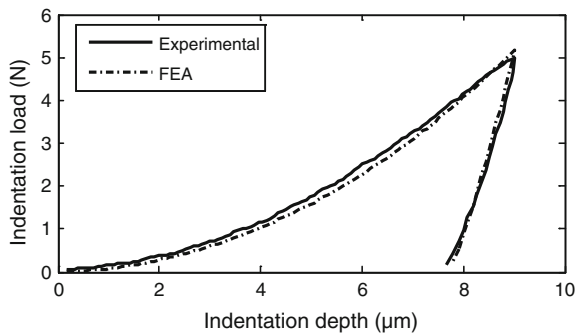
As shown in Fig. 4, there is a good agreement between the *FE* modeling and experimental results. It is worth mentioning that the result obtained by considering optimized Young’s modulus and those obtained using Young’s modulus extracted directly from the indentation records using the Oliver and Pharr method [26] shows a standard deviation of ± 1 GPa.

This is explained by the fact that the quantity of porosity was not considered. Moreover, any micro-cracks, which may occur during indentation, were not considered in the analysis.

Table 2 Three parameter optimization for a Vickers indenter

Parameters	Initial values	Final optimized values
E (MPa)	9.4527000E + 04	9.2793093E + 04
σ_y (MPa)	5.5000000E + 02	5.0818970E + 02
n	3.0000000E-01	3.8018646E-01

Fig. 4 Comparison between experimental and simulation data of indentation curves



4 The Tensile Adhesive Test

The tensile adhesive test is one of the few standardized tests to determine interface strength. The European *EN582* (*ČSN EN 582 1995*) and American *ASTM C633* (*ASTM C633-01 2001*) standards are the most diffused, this test is largely used in industrial and scientific laboratories. A three-dimensional finite elements model of this test was developed using ABAQUS[®] code (Fig. 5). Materials of the coating are elastic-plastic corresponding to optimized behavior in Sect. 3.2. *Inconel 625* coating was simulated onto a cylindrical substrate (radius $R_0 = 12.7$ mm and height = 50 mm). The coating thickness was about 400 μm . The substrate is modeled with the properties of steel (*AISI 1018*). The mechanical properties are: Young's modulus 205 GPa, Poisson's ratio 0.29; Density 7870 kg/m^3 . Yield tensile 370 MPa, ultimate tensile 440 MPa [27]. The adhesive had a Young's modulus of 3500 MPa, Density 870 kg/m^3 , Tensile Strength 69 MPa. The tensile test simulated was controlled by a displacement velocity of 0.015 mm/s.

Finite element analysis has been found to be a useful tool for evaluating the stress distribution at the interface between coating and substrate. Figure 6 shows the stress variation with time at the coating. We note that the used velocity, responsible stress at coating fracture is characterized by a maximum amplitude value of 59.8 MPa (Fig. 6c). In this case, with the value of bond strength (<69 MPa) a fracture at the interface coating-substrate can occur.

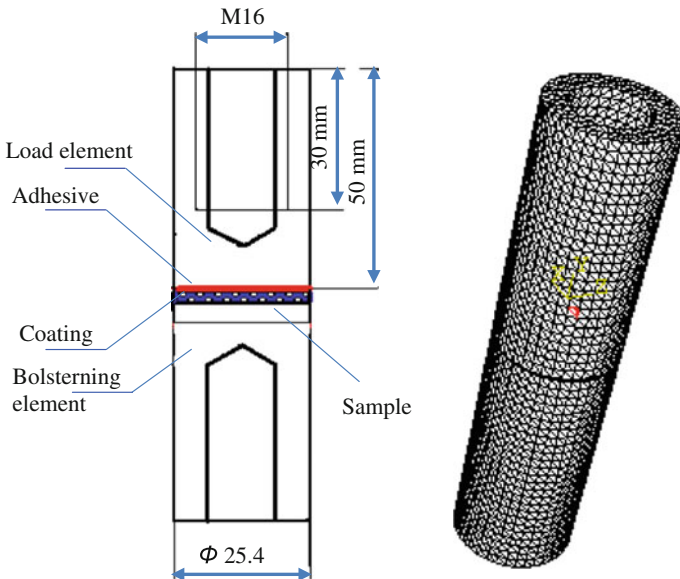


Fig. 5 Evaluation of the adhesive strength and FE model used in our simulation

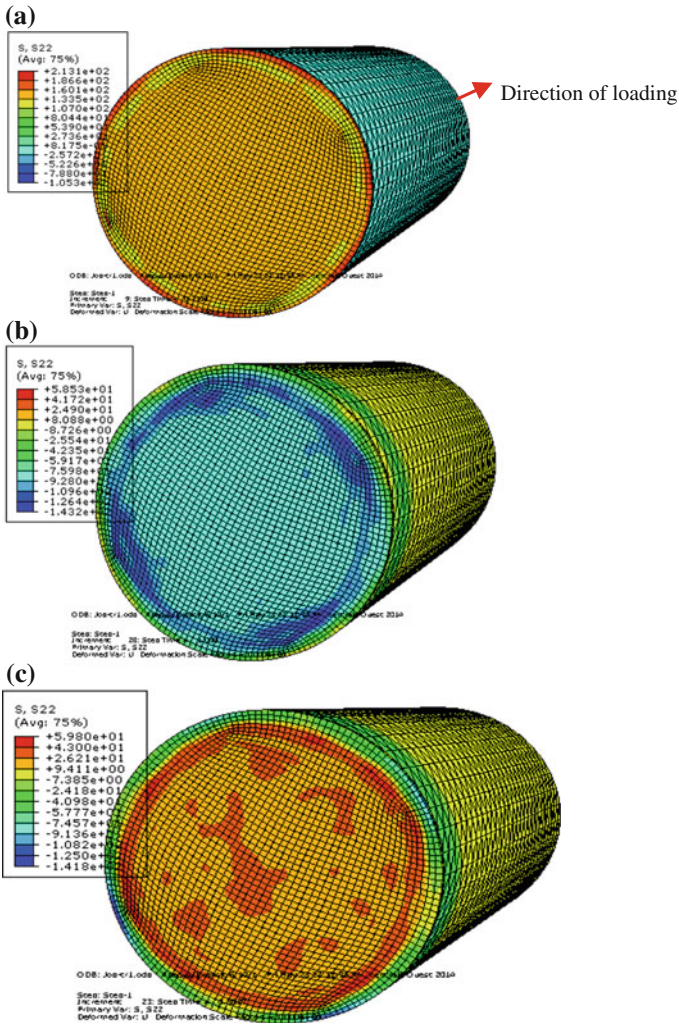


Fig. 6 Time evolution of stress at the coating. a Initial time. b Final time. c Instant of fracture

5 Conclusion

The results obtained in this study indicate that instrumented indentation test can be a fast and easy technique to estimate the elastic-plastic properties of arc sprayed Inconel coating.

The unknown material properties are identified using inverse finite element analysis method by fitting the simulation results to the experimentally obtained load-displacement curves.

The results show that the maximum gap between the experimental applied load and calculated one is about 3.52 %. Due to the difficulty of conducting tensile test when the glue is not strong enough for example, the optimized behavior law is used to simulate the adhesive test of the coating. The test controlled by a displacement velocity of the order of 0.01 mm/s demonstrated the possibility to estimate the adhesion value.

References

1. Thorpe, M.L.: Thermal spray: Industry in transition. *Adv. Mater. Process* **143**(5), 50–60 (1993)
2. Pawłowski, L.: *The Science and Engineering of Thermal Spray Coatings*. Wiley, Chichester, England, New York (2008)
3. Gedzevicius, I., Valiulis, A.V.: Influence of the particles velocity on the arc spraying coating adhesion. *Mater. Sci.* **9**, 334–337 (2003)
4. Jandin, G., et al.: Correlations between operating conditions, microstructure and mechanical properties of twin wire arc sprayed steel coatings. *Mater. Sci. Eng. A* **349**, 298–305 (2003)
5. Betteridge, W., Shaw, S.: Temperature capability of Alloys Versus Year of Introduction. *Mater. Sci. Technol.* **3**, 682–694 (1987)
6. Chester, T., Sims, N.S.: *Superalloys II*. Wiley, New York (1987)
7. Reed, R.C.: *The Superalloys: Fundamentals and Applications*. Cambridge University Press, New York (2006)
8. Smith, G., Shoemaker, L.: Advanced nickel alloys for coal-fired boiler tubing. *Adv. Mater. Process.* **162**, 23–26 (2004)
9. Williams, J.C., Starke, E.A.: Progress in structural materials for aerospace systems. *Acta Mater.* **51**, 5775–5799 (2003)
10. Goldbaum, D.: Mechanical behavior of Ti cold spray coatings determined by a multi-scale indentation method. *Mater. Sci. Eng. A* **530**, 253–265 (2011)
11. Kalkhoran, S.M., et al.: Estimation of plastic anisotropy in Ni–5 % Al coatings via spherical indentation. *Acta Mater.* **60**, 803–810 (2012)
12. Rico, A.: Mechanical properties of thermal barrier coatings after isothermal oxidation. Depth sensing indentation analysis. *Surf. Coat. Technol.* **203**, 2307–2314 (2009)
13. Revie, R.: *Uhlig H, Corrosion and Corrosion Control*. Wiley, United States of America (2008)
14. Ahmed, N., et al.: The effects of microstructural features on the performance gap in corrosion resistance between bulk and HVOF sprayed Inconel 625 *Surf. Coat. Technol.* **204**, 2294–2301 (2010)
15. Fizi Y., et al. (2013) Experimental study and numerical simulation of the indentation test of a coating prepared by thermal spraying before and after annealing treatment. 21^{ème} Congrès Français de Mécanique. Bordeaux, 26–30 Août (2013)
16. Luo, J., et al. (2006) Study on the determination of mechanical properties of a power law material by its indentation force–depth curve. *Philos. Mag.* **86**, 2881–2905
17. Luo, J., Lin, J.A.: Study on the determination of plastic properties of metals by instrumented indentation using two sharp indenters. *Int. J. Solids Struct.* **44**, 5803–5817 (2007)
18. Chaiwut, G., Esteban, P.B.: Characterization of elastoplastic properties based on inverse analysis and finite element modeling of two separate indenters. *J. Eng. Mater. Technol.* **129**, 603–608 (2007)
19. Bucaille, J.L., et al.: Determination of plastic properties of metals by instrumented indentation using different sharp indenters. *Acta Mater.* **51**, 1663–1678 (2003)

20. Leither, C., et al.: Determination of the elastic modulus of wire arc sprayed alloy 625 using experimental, analytical, and numerical simulations. *Surf. Coat. Technol.* **235**, 611–619 (2013)
21. Schnur, D.S., Zabarar, N.: An inverse method for determining elastic material properties and a material interface. *Int. J. Numer. Methods Eng.* **33**, 2039–2057 (1992)
22. Antunes, J.M., et al.: A new approach for reverse analysis in depth-sensing indentation using numerical simulation. *Acta Mater.* **55**, 69–81 (2007)
23. Chollacoop, N., et al.: Depth-sensing instrumented indentation with dual sharp indenters. *Acta Mater.* **51**, 3713–3729 (2003)
24. Dao, M., et al.: Computational modelling of the forward and reverse problems in instrumented sharp indentation. *Acta Mater.* **49**, 3899–3918 (2001)
25. ASTM C633-01 (2001) Standard method of test for adhesion or cohesive strength of thermal spray coatings. American Society for Testing and Materials, Philadelphia (Pennsylvania, USA)
26. Oliver, W.C., Pharr, G.M.: An improved technique for determining hardness and elastic modulus using load and displacement sensing indentation experiments. *J. Mater. Res.* **7**, 1564–1583 (1992)
27. Howard, E. B., Timothy, L. G. (eds.) American Society for Metals, Materials Park, OH (1985)

Study of Noise Inside a Mechanical Shovel Cabin Using a Sound Perception Approach

Nacer Hamzaoui

Abstract The use of perceptive and sound quality approaches in the mechanical field, in which it is necessary to establish the link between the conception (taking an interest in the object producing noise) of the mechanical system and the auditory perception (taking an interest in the noise emitted), is still considered as rather new. Perceptive analysis allows extracting information making it possible to use well-adapted physical analysis methods and metrics so as to better choose the technical responses to a noise problem [1, 2]. In the case of a mechanical shovel (Volvo Compact), perceptive tests of comparisons by pairs have been used to define only the necessary frequency bands of the noise studied and classifying their participation as a function of subjective (annoyance, etc.) and objective (global level) terms [3]. The utility of modeling adapted to low frequencies (BEM or FEM) has been shown when simulating structural modifications and assessing their effects on the interior noise of a mechanical shovel cabin. Manufacturers need a predictive model of sound annoyance for a complete machine and identify those of its elements which contribute to annoyance, so as to implement a hierarchical noise reduction approach inside the cabin. A prediction model of sound preference that can be used to identify the procedure for improving sound annoyance from simulations has been built and validated [4].

1 Introduction

Nowadays, sound image is an important element of product appreciation; the mere quantification of the acoustic level (in decibels A) is not always enough to reproduce the sound perception of users. Acoustic annoyance, often a motive for com-

N. Hamzaoui (✉)

Laboratory of Vibration-Acoustics, University of Lyon, INSA of Lyon, Bâtiment A. St. Exupéry, 25 bis Avenue Jean Capelle, 69621 Villeurbanne Cedex, France
e-mail: nacer.hamzaoui@insa-lyon.fr

plaints, leads manufacturers to focus on reducing the noise of their products. Acoustic studies usually consist in carrying out either experimental diagnostics or vibro-acoustic computations to understand the physical functioning of the noise source, and then in making modifications to conform to a specification developed by specialists. The share taken by perceptive analysis, which includes the users of the product, still remains rather small in these studies. Perceptive approaches can usefully complete physical studies, making it possible to reach the target expected by customers more quickly [5–7].

The psychophysics techniques currently used allow assessing the perception of a product more accurately, as they question a large number of users. Questionnaires on the problem are defined. They are more especially developed in view to obtaining good resolution linked to the physical approach. Subjectively assessed noises are obtained from recorded sound samples and then listened to through headphones with the aim of obtaining a faithful reproduction of the real noise. This has already become an important aspect of current research. The advantage of numerical sound synthesis is clear: noises recorded from several different products can be compared with each other more easily and the physical modifications made to the signal processing can be simulated. A classification of sound preference scores can for instance be extracted from a pairwise comparative analysis [8] of a set of sound samples. This subjective result can be linked to physical phenomena in order to correlate it with one or several indicators representing the processed signals. This correlation then allows identifying the physical parameters characterizing the noise annoyance studied, and thus identifying annoying frequencies and annoying sources. Thus it makes the resolution of the problem formulated more efficient.

In this paper, the application of a global sound perception process to an industrial object is presented in view to reaching physical objectives. This research is part of a study carried out in the framework of collaboration with Volvo Compact Excavators, a manufacturer of mechanical shovels. The objectives determined within this collaboration were:

- On a complete machine, the manufacturer wanted to obtain a predictive model of sound annoyance and to identify the elements of the machine contributing to annoyance so as to establish a hierarchical approach to noise reduction inside the cabin.
- The definition of frequency bands assumed to be useful, which intervene in sound perception and thus allow choosing a physical modeling method adapted to the problem.

This paper summarizes the process used and the results obtained to reach these two objectives.

2 Analysis of a Complete Mechanical Shovel

The process applied to a complete mechanical shovel is presented in two steps in this part:

1. The first step is the formulation of a preference model on the basis of a dissimilarity and preference test;
2. The second step includes both the validation and the use of the preference model to identify the elements of the machine participating in sound perception.

2.1 Formulation of a Preference Model

Several configurations to be studied from 2 different machines (Fig. 1) were chosen with the collaboration of Volvo Compact's engineers, with the aim of building a predictive model of sound preference.

The analysis parameters used are:

1. The rotation velocity of the engine: low speed (≈ 920 rpm), maximum speed (≈ 2300 rpm) and 2000 rpm,
2. The hydraulic load: 1 and 2 movements,
3. The cabin configuration: completely closed, and completely opened (windows and door).

Sound recordings were made with 2 types of tipper cache for the EC20 model: the old one and a new one assumed to reduce the sound level. The combination of all these parameters generated a set of 42 sound recordings for both models. It was decided to use a dissimilarity test to establish a perceptive space and a preference test using the pairwise comparison method in order to determine the preference model. The number of sound samples had to be reduced to 10 sound files to ensure that the maximum duration of these tests did not exceed 1 h. Indeed, 45 pairs for comparison can thus be constituted by adding both repeated pairs and equivalent



Fig. 1 The two models of mechanical shovel used: (EC20) a 2-ton mechanical shovel with a three cylinder engine; (EC45) a 4.5-ton mechanical shovel with a four cylinder engine

Table 1 Selected sounds for dissimilarity and preference tests

Rotational speed	Cabin configuration	Load	
Slow running	Open	None	
Slow running	Closed	None	
2000 rpm	Closed	None	
2000 rpm	Closed	2 movements	
2000 rpm	Open	None	
Maximum	Open	None	Old tipper cache
Maximum	Closed	None	
Maximum	Closed	2 movements	
Maximum	Open	None	
Maximum	Open	2 movements	

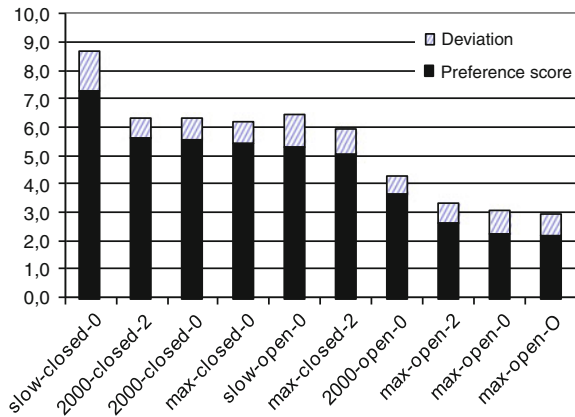
pairs to assess both the mistakes made by listeners and the difficulty of the test conducted with these ten files. A two-step process was used to reduce the number of files from 42 down to 10:

1. The comparison between sound levels (in *dBA*) made between all the measurements performed on both models allowed led to choosing the *EC20* model, because its sound levels were higher than those of the *EC45* model.
2. The choice between the 28 remaining files was made possible by a preliminary dissimilarity test (reduced number of listeners), to assess the influence of several parameters: open or closed cabin, 1 or 2 movement hydraulic load, maximum engine speed or 2000 rpm, and old or new tipper cache. The difference of perception between the former/new rocker arm cache files and 1/2 movement was insignificant, whereas the effects of both the rotation rating and the opening of windows and doors of the cabin were clearly perceived.

Thus ten sounds were obtained for analysis (Table 1), of which 9 were configurations acquired with both the new rocker arm cache and a sound emitted with the former rocker arm cache.

Three repeated pairs (the three pairs used at the beginning of the process were reintroduced at the end of the test) and three equivalent pairs (2 similar sounds) were added to the 45 pairs of the 10 selected sounds, constituted with the Ross series. About thirty listeners participated in both tests (dissimilarity and preference). Attention was given to the confidence that could be given to them before presenting the global results obtained. The average error could be computed for each listener, for both repeated and equivalent pairs regarding dissimilarity and the preference score. The global error was quite small for equivalent pairs, except for dissimilarity for which the error rate of three listeners was 50 %, apparently due to confusions in the positioning of the cursor between dissimilarity (the cursor was placed completely on the left) and preference (the cursor was placed in the middle) after the examination of individual answers. For repeated pairs in the preference test, the majority of the listeners (90 %) remained faithful to the choice they made at the

Fig. 2 Preference score according to the configurations studied



beginning. An assessment could be performed on the number of circular errors made by listeners regarding the preference scores; a circular error was made when A was preferred to B, followed by B preferred to C and lastly C preferred to A. The average number of circular errors was 5.1, which is rather low, since the maximum number of circular errors could reach 120.

The results appeared correct and no listener warranted exclusion from the tests, which did not seem to involve any great difficulty. It was observed from the average preference score obtained (Fig. 2) that closing the mechanical shovel passenger compartment increased sound annoyance and that increasing the rotation velocity decreased it. The difference of assessment between a slow running sound with respect to the other two ratings was significant, but it became very small between the sound at 2000 rpm and the maximum rating. It was obvious that the new rocker arm cache was not very efficient regarding sound annoyance.

Only one of all the other listeners assessed both the slow running sounds in the opposite way, thus it did not seem necessary to establish two categories of listeners. About twenty metrics were computed in parallel, using the MTS Sound Quality software, and their possible correlation with the preference scores was sought directly in the first step.

The correlation of a preference score with a linear relation of one of the parameters computed did not give a satisfactory result ($R^2_{maxi} = 0.53$). Intuitively, the sound level (loudness or level in dB_A) seemed preponderant. However, this first result showed that sound annoyance was not influenced by a parameter linked to sound level. A correlation of this annoyance was then sought with a linear combination of two metrics. The best correlation obtained corresponded to a linear correlation with both the dB_B level and intelligibility; the latter parameter played an important role as it was found several times in the 5 best combinations.

It should be borne in mind that intelligibility was initially created to measure the comprehension of a verbal message between two persons. In fact, this parameter has turned out to be very useful for assessing estimations of preference regarding sounds having nothing to do with conversations between two persons. The Sound

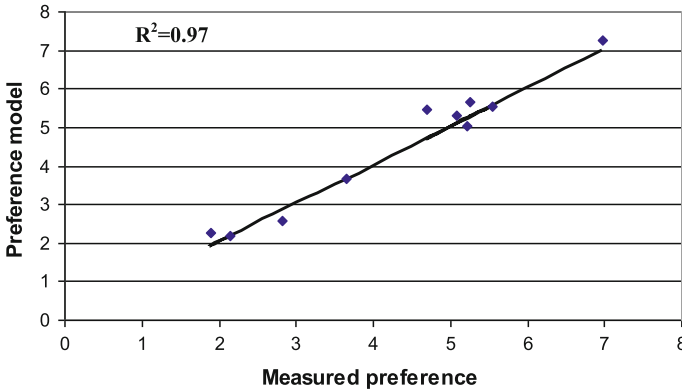


Fig. 3 Computed preference score according to measured preference scores

Quality software computed intelligibility according to the *ANSI S3.5* standard: pressure levels in dB_{in} by one-third octave between 160 and 6300 Hz were calculated first. They were located in a chart defining the percentage of intelligibility of each one-third octave. This percentage, reduced to a value included between 0 and 1, was multiplied by a weighting coefficient to obtain the articulation index by a third of an octave. The sum of these indices from the one-third octaves between 160 and 6300 Hz gives the intelligibility in %.

As planned, the dissimilarity test results were also used to define a perceptive space whose dimensions were represented by parameters computed previously, and then to search a correlation between these dimensions and the preference score compared with the previous model. A principal component analysis (*PCA*), which provided the coordinates of each sound in this space, was used to build this perceptive space. The search of a correlation between each dimension and one of the computed parameters did not give satisfactory results ($R^2 < 0.6$). The first dimension was well correlated ($R^2 = 0.96$) with both the dB_B level and the intelligibility and the second dimension were correlated ($R^2 = 0.9$) using a combination of two parameters with a linear combination of the dB_B and dB_A levels. Both the dissimilarity and preference tests allowed building a preference model ruled by dB_B and intelligibility (Fig. 3).

$$\text{Preference} = 0.81(dB) + 0.41(\text{intelligib}) - 69.8 \quad (1)$$

These two parameters (dB_B level and intelligibility) have the same importance at the level of the preference model. However, it seemed paradoxical that the increase in the dB_B level improves sound annoyance. In fact, these two parameters are linked (in a non linear way), and boundary values are required at the dB_B level beyond which the model is no longer valid. This is the purpose of the following paragraph which is dedicated to both the validation and the use of this model to identify the elements of the mechanical shovel participating in noise annoyance.

2.2 Validation and Use of the Preference Model to Characterize the Different Sound Sources Present in the Mechanical Shovel

Three sound sources participating in the contribution of noise inside the cabin were identified:

1. the heat engine,
2. the hydraulic pump,
3. and the hydraulic distribution.

Five configurations of acoustic measurements were used while proceeding with the hydraulic coupling between two machines: engine alone, engine coupled to the pump (without any distribution), engine with the distribution (without the pump), and distribution alone and, lastly, normal operation (engine + pump + distribution). The parameters of the study were: engine rotational speed (slow or max. running speed), cabin opened or closed, and with or without hydraulic load. All these configurations and variations of parameters resulted in about thirty sound files from which twelve were extracted and used to assess the validity of the preference model (1). These files are presented in Table 2, the distribution operates without any hydraulic load when in stand-by.

A preference test performed with about thirty listeners provided the preference score measurement of these 12 sounds. This test was slightly different from that used to establish the preference model. In this test all the sounds are presented to the listener who assesses them according to sound annoyance. Another study [9] showed that this type of test is much quicker and globally gives the same preference scores as a pair-wise comparison test. The dB_B level, the intelligibility and the preference score (I) were computed for each sound. The comparison between the

Table 2 Configurations used to assess the validity of the preference model

Sounds	Configuration	Engine speed	Cabin	Distribution
Test 01	Normal	Slow running	Open	Stand-by
Test 02	Normal	At top speed	Open	Stand-by
Test 03	Engine alone	At top speed	Open	None
Test 04	Engine alone	At top speed	Closed	None
Test 05	Engine + distrib.	At top speed	Closed	Stand-by
Test 06	Engine + distrib.	At top speed	Closed	1 Movement
Test 07	Engine + pump	At top speed	Closed	1 Movement
Test 08	Normal	Slow running	Closed	Stand-by
Test 09	Engine alone	Slow running	Closed	None
Test 10	Engine + distrib.	Slow running	Closed	Stand-by
Test 11	Engine + pump	Slow running	Closed	Stand-by
Test 12	Former (E + P)	At top speed	Open	1 Movement

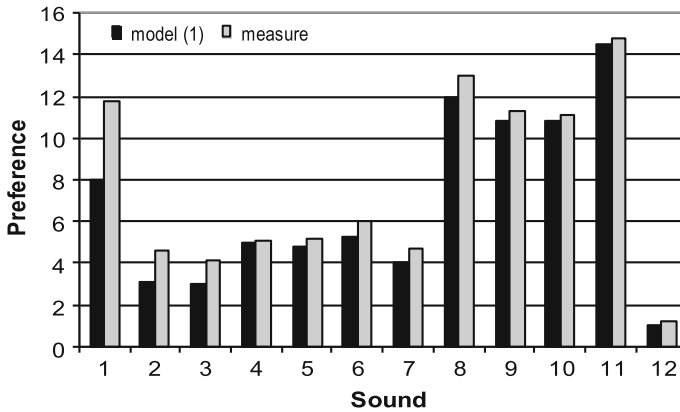


Fig. 4 Comparison (1) between computed and measured preference scores

computed and measured preference scores is shown in Fig. 4. Very good correlation between the prediction and the model can be observed, except for sound 1 which seems to be under-assessed by the preference model (1).

The analysis of measured preference scores shows the importance of the intelligibility parameter associated with the dB_B level, since sounds $n^{\circ}11$ and 8 with respective levels of 81.2 and 78.7 dB_B and with respective intelligibilities of 45.3 and 45.7 %, were predicted by the preference model 1, whereas sound $n^{\circ}1$ (75.1 dB_B and 42.7 %) was not correctly predicted. 11 sound files obtained by filtering sound $n^{\circ}12$ were constituted to define the validation boundaries of this model. This filtering based on the domains of definition of the B weighting of the ear and intelligibility can vary the level in dB_B without overly affecting intelligibility, but the contrary can occur. These twelve sounds were submitted to about twenty listeners through a preference test: sound $n^{\circ}1$ was the original one, and sounds from 2 to 12 were filtered.

The comparison between both the measured and computed preference scores (Fig. 5) shows that the model was different from the subjective measurement for both sounds $n^{\circ}11$ and 12.

The model is valid for sounds of which the dB_B level is higher than 75.5 dB_B ; they are systematically preferred when the level of this value is lower, contrary to what the model predicted. It can thus be concluded that the model is valid for the dB_B sounds between 75.5 and 86.4 dB_B . One of the aims of this model was to study the contribution of mechanical shovel elements (engine, pump, distribution) to sound annoyance. The value of the preference score of each sound can be obtained and the correlation between the parameters of the model and the different configurations measured can be assessed by computing both the dB_B level and the intelligibility of the thirty sounds or so observed at the beginning of the experiment. The main results obtained are summarized hereunder:

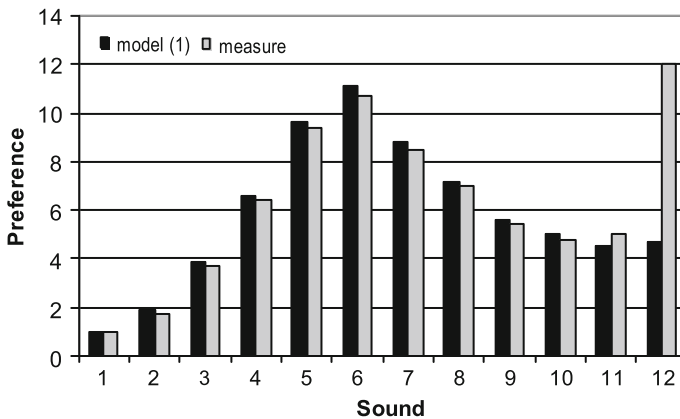


Fig. 5 Comparison between both computed and measured preference scores

- The engine + pump configuration was that most appreciated regarding the parameters: slow engine rotation speed, closed cabin and the presence of a movement constituted the basic preference of listeners.
- With the engine, the presence of the distribution had almost no influence on the intelligibility of the overall structure, but considerably increased the dB_B level, whereas the presence of the pump determined the intelligibility and had almost no influence on the dB_B level.

The sound files of the three separated sources were acquired while using filtering, making it possible to extract the noise of the pump from the engine + pump structure. This very difficult manipulation was validated while assessing the reconstituted noise by grouping the three sources with the real measured noise in a perceptive way. Some manipulations could be simulated from the sources to estimate their effects on sound annoyance. For instance, it was interesting to simulate a casing for the pump (-3 dBlin), which permitted increasing the intelligibility of the assembly by 5 %, without affecting the dB_B level, and increasing sound quality.

3 (Engine + Chassis + Cabin) System in the Laboratory

The structure of the mechanical shovel studied is composed of a cabin linked by four mounts to a chassis excited by an engine (Fig. 6a). The physical studies performed on this machine emphasized the importance of the vibroacoustic transmission between the chassis and the cabin through the mounts. Modeling the cabin excited by the mounts was suggested in order to assess the acoustic contribution of certain modifications. The model was built using a finite and frontier element approach (Fig. 6b), to obtain the interior noise from a vibratory computation of the cabin subjected to mechanical excitation transmitted through the mounts.

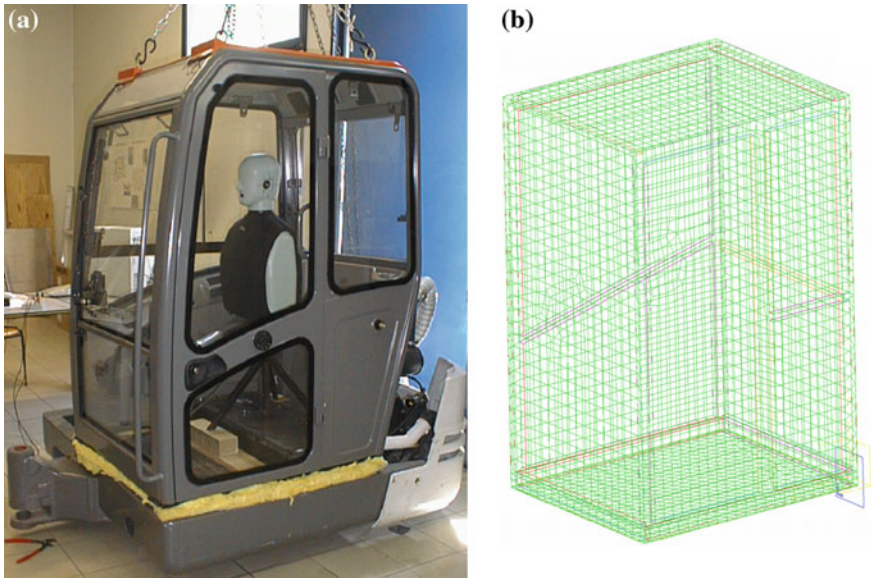


Fig. 6 **a** The cabin studied, **b** the Model of physical analysis

This kind of approach limits the study to low frequencies, because it requires too much memory and computation time. In this case, the contribution of the subjective approach to the physical analysis concerned the definition of useful frequency bands, in which all the modifications were sensitive at the level of sound perception. Thus the interest of such modeling can be assessed.

The effect of different experimental configurations regarding the (stiff/smooth) nature of the mounts, the participation of the floor, the windows and the door were also analyzed subjectively.

The acoustic pressure developed from different engine rotational speeds was measured via the dummy head to seek the definition of useful frequency bands. The basic measurement was determined by a synthetic file, the sampling frequency of which corresponded to with a frequency field reaching up to. This synthetic file was then filtered through low and high frequency filters and generated several sound files which were characterized in *dBA* (see Figs. 7 and 8).

The *dBA* level becomes invariable from 3200 Hz, which shows the importance of frequencies lower than or equal to 3200 Hz in the participation of the *dBA* level.

The participation of frequency becomes significant from with high frequency filters. The most influential frequency band can be identified from the sound level in *dBA* when both the frequency fields defined from both filters are grouped. This concerns the (-) interval.

A dissimilarity (see Figs. 9 and 10) and preference test was performed between all the filtered sounds in comparison to the original sound. The form of the

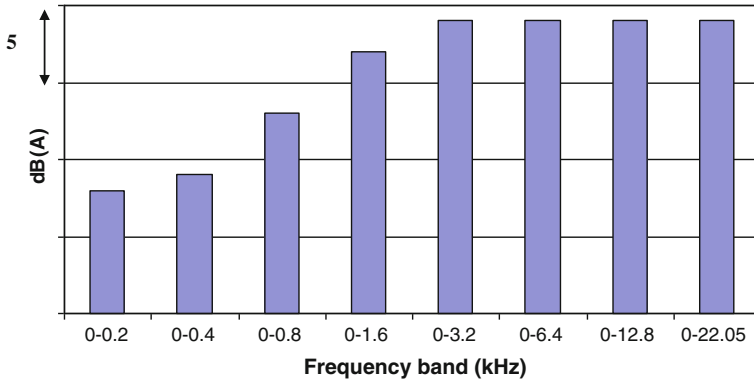


Fig. 7 Pressure level in dB_A for different sound files from the low frequency filtered original sound (0–22.05 kHz)

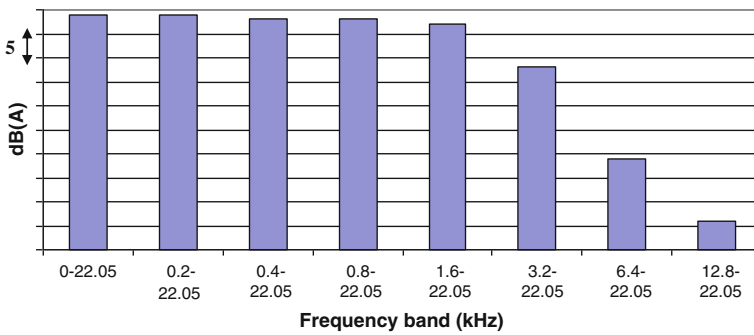


Fig. 8 Pressure level in dB_A for different sound files from the high frequency filtered original sound (0–22.05 kHz)

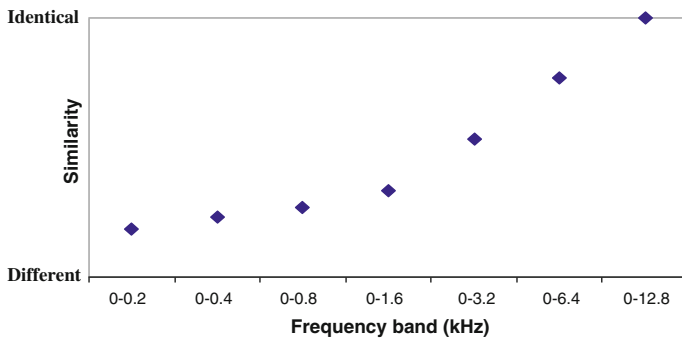


Fig. 9 Similarity between different sound files from the low frequency filtered original sound and the original sound

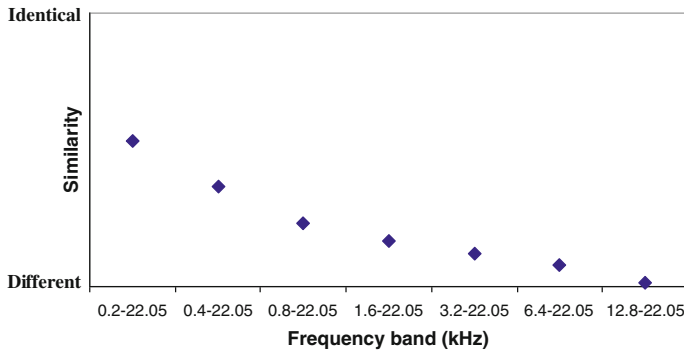


Fig. 10 Dissimilarity between different sound files from the high frequency filtered original sound and the original sound

dissimilarity test was similar to that used for hair plucking devices; a linear scale, similar to that of the dissimilarity test, was used for preference.

The overall frequencies lower than 3200 Hz had to be taken into account so that the similarity of sounds from filtered synthetic files were correct with respect to the original sound; low frequencies are important in this case. An analysis similar to the previous one showed that the participation of low frequencies (<400 Hz) is of major importance in the assessment of acoustic annoyance, using the results of the preference test. It can thus be concluded that the analysis of dissimilarity and preference results between filtered sound samples (low frequency and high frequency) and the original sounds for different configurations integrating engine rotation speed emphasizes:

- the importance of low frequencies, the absence of which is enough to make the noise unrecognizable, even without showing any drop in dB_A ;
- the definition of a frequency range (0–3200 Hz), including the overall physical and perceptive sound information;

the contribution of low frequencies in the assessment of sound annoyance.

BEM physical modeling is thus very useful at the level of sound perception when dedicated to low frequencies, even though the global level in dB_A does not remain very sensitive. Synthetic sound files from configurations with two engine rotation speeds and three different links between the chassis and the cabin were recorded via the dummy head and the influence of link mounts between the cabin and the chassis:

Configuration 1: suspended cabin, without any mechanical link with the chassis while maintaining acoustic airtightness between the interior and the exterior of the cabin.

Configuration 2: stiff link between the cabin and the chassis.

Configuration 3: mount of origin between the cabin and the chassis.

A preference test (*30 listeners*) emphasized the importance of the mechanical link between the chassis and the cabin through a pairwise comparison between these three configurations. The mount of origin was almost considered in the same way as the stiff link for sound annoyance. Some flexibility would improve sound perception inside the cabin. It must also remain compatible with the use of the mechanical shovel on uneven terrain. *FEM/BEM* modeling can thus be used to optimize this link.

4 Conclusions

Sound perception tools were used in this example to identify frequency bands participating in both the perceptive and quantitative contribution of noise inside a cabin of a mechanical shovel on the one hand, and to build a preference model to simulate technological modifications to predict sound annoyance on the other hand. It was possible to perform an in-depth study with respect to the first example while assessing the difficulty of both dissimilarity and preference tests correctly thanks to several uncertainty computations made by the listeners, and by performing other types of assessment of sound preference.

The identification of useful frequency bands confirmed the interest of *FEM/BEM* modeling at low frequencies to simulate the influence on sound of vibro-isolation mounts located, for instance, between the cabin and the chassis. The good quality of the preference model obtained from both the dissimilarity and preference results was validated by the application conditions (boundary values of the dB_B level). Lastly, it was possible to show that this type of approach may allow identifying sound sources contributing to noise annoyance, and that the use of the predictive preference model may simulate the effect of several technological modifications.

References

1. Susini, P., Mcadams, S., Winsberg, S.: A multidimensional technique for sound quality assessment. *ACUSTICA Acta Acustica* **85**, 650–6561 (1999)
2. Hamzaoui, N., Guyader, J.L., Parizet, E.: Mixing of perception and physical analyses for the study of acoustic radiation issues. *Euronoise 2001*, Patra 14–17 Janvier 2001
3. Daval, J.: Définition des critères de confort acoustique au sein d'une pelle mécanique. Rapport de DEA, LVA (2001)
4. Koehl, V.: Contribution des différentes sources sonores à l'agrément lié au bruit à l'intérieur d'une pelle mécanique. Rapport de DEA, LVA (2002)
5. Parizet, E., Hamzaoui, N.: Contribution des études perceptives au développement d'un produit". *First European Forum Cetim*, Senlis Juillet (2001)
6. Hamzaoui, N., Sandier, C., Parizet, E., Wetta, P., Besseyrias C.: Subjective assessments of the acoustic radiation from steel structures: some effects of a few parametric variations. *Forum Acusticum*, Séville 16–20 Septembre 2002

7. Charasse, B.: Maîtrise de la qualité sonore d'un épileur. Rapport de D.E.A au Laboratoire Vibrations Acoustique de l'INSA Lyon, Juin (2000)
8. David H.A.: The method of paired comparison. Oxford University Press (1988)
9. Parizet, E, Hamzaoui, N, Sabatie, G.: Comparison of some listening test methods: a case study. *Acustica United Acta Acustica* **91**, 356–364 (2005)

Perceptual Study of Simple and Combined Gear Defects

Ramdane Younes, Nouredine Ouelaa, Nacer Hamzaoui
and Abderrazek Djebala

Abstract This work is devoted to the vibro-acoustic analysis of the gear teeth defect sounds. The tests have been realized at the acoustic vibration laboratory (LVA), INSA of Lyon, France. From the obtained results, a correlation of sound perception with the vibration indicators is established. In conclusion, the results allowed the definition of the most representative vibration indicators of the sound perception, such as the Spectral Center of Gravity SCG, Overall Level OL and Kurtosis. On another hand according to the coordinated MDS method results, the sounds are in perfect agreement with the gear deterioration degree, namely without defect, single, double and triple defects.

1 Introduction

Gears are a mean of transmitting and changing the rate of machinery shaft rotation. They can also change the direction of the rotation axis and can change rotary motion to linear motion; they have existed since the invention of rotating machinery. Because of their force-multiplying properties, early engineers used them for hoisting heavy loads such as building materials. However, dedicated for high-speed machinery such as an automobile transmission, gears are the optimal technological solution for low energy loss, high accuracy and low play. Gears are of several categories, and can be combined in a multitude of ways. As vibration and acoustic have the same generation

R. Younes (✉) · N. Ouelaa · A. Djebala
Mechanics and Structures Laboratory, University of Guelma, B.P. 401
Guelma, Algeria
e-mail: ramdane_ys@yahoo.com

N. Hamzaoui
Laboratory of Vibration-Acoustics, INSA of Lyon, Bâtiment A. St. Exupéry,
25 bis Avenue Jean Capelle, 69621 Villeurbanne Cedex, France
e-mail: nacer.hamzaoui@insa-lyon.fr

R. Younes
Mechanical Engineering Department, Badji Mokhtar University, P.O. Box 12, 23000
Annaba, Algeria

mechanism, acoustic noise can also be used for machinery condition monitoring combined with effective signal processing methods, such as the sound perception method. Perceptual tests can be used to analyze various characteristics of the sounds, and discover the perceptive dimensions used by listeners to differentiate these audio stimuli. The perceptive approach of sounds has been used in several domains; for example in automobile for the study of the sounds produced by the air conditioning systems, and in railways for the perception of the interior noise in a high-speed train, to improve comfort to meet the consumers' expectations [1, 2]. Many researchers investigated the comparison of the listening tests and explain the benefits of the paired comparison method [3]. Other researchers studied a serious problem in the paired comparison method; it is the important listening tests duration when the number of stimuli is rather large which lead to auditive fatigue.

The search for a test allowing the evaluation of a great stimuli number leads adapting a new method inspired from the visual perception called comparison with reference method, the task consists to assess the similarity of a stimuli group compared to a Ref. [4]. Kanzari [5] carried out a vibro-acoustic analysis of sounds resulting from gears teeth anomalies. From the obtained results, she established a correlation with the scalar indicators. These results showed that the scalar indicators such as vibratory speed, the spectral center of gravity, and the peak to peak value well explain the preference judgments for gears sounds in the rotating machines.

2 Multidimensional Scaling Method

The multidimensional scaling method allows the representation of objects in a space starting from the proximity relationship existing between each objects couple. Each object can then be represented in this space. There exist many algorithms, starting from the distances between objects that allow determining the coordinates of these last in a space. Some of these algorithms allow taking into account specificities of the various subjects or groups of subjects of the various stimuli, even of both of them at the same time. In our case the items are sounds, and the proximity between the sounds is evaluated using dissimilarity judgments. The principle of this analysis is to match the measured dissimilarities between stimuli distances between points representing these stimuli in a Euclidean space. The dimensions of this space are continuous, i.e. all stimuli may be classified according to these dimensions.

3 Experimental Setup

3.1 Test Rig

In order to be closer with real gear defects, an experimental setup has been designed in the vibration-acoustic laboratory of the INSA of Lyon—France. The test rig contains two gear transmissions normally lubricated. The first transmission consists

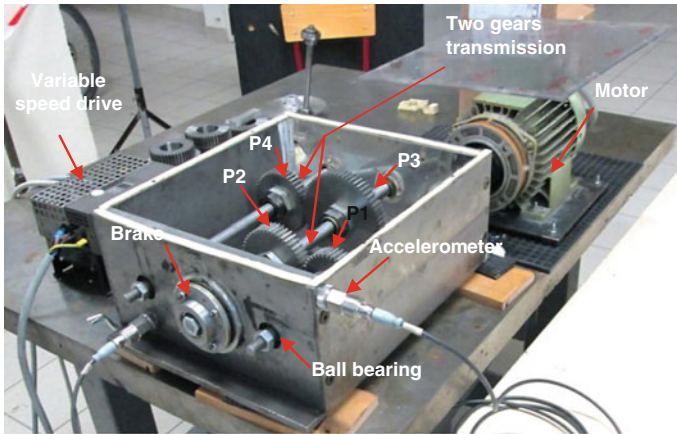


Fig. 1 Experimental setup

of a pinion of 42 teeth mounted in the input shaft and a wheel of 50 teeth. The second transmission consists of a wheel of 65 teeth and a pinion of 45 teeth mounted in the output shaft. The test rig contains also a brake to simulate a variable load (Fig. 1).

3.2 Experiments Conduct

Simple and multiple defects, with different severity, are simulated on the gears teeth using a mini grinder. The corresponding sounds were then acquired to perform a sound base representative of the gear defects diversity. For the sound measurements, resulting from our testing device, the recordings base will be formed by the vibration signals from the accelerometer which, using the acquisition and vibratory analysis software “DynamX V.7”, will be saved as “wav” format. This is possible, since when transmissions are enclosed in a casing, like in the case of a gearbox, the radiated noise is mainly due to the vibrations of this one [6].

4 Sound Perception Tests

4.1 Stimuli

In this part, the objective is to study the ability of listeners to identify different defect type, ranging from a small single defect to a combination of defects. To do this, we simulated several faults with different degrees of degradation as follow:

- Healthy Gears *HG*
- Small Defect on Pinion1 *SDP1*
- Average Defect on Pinion 1 *ADP1*
- Great Defect on Pinion 1 *GDP1*
- Great Defect on Pinion 1 & Small Defect on Pinion 2 *GDP1SDP2*
- Great Defect on Pinion 1 & Average Defect on Pinion 2 *GDP1ADP2*
- Great Defect on pinion 1 & Great Defect on Pinion 2 *GDP1GDP2*
- Great Defect on pinion 1, Great Defect on Pinion 2 & Great Defect on Pinion 3 *GDP1GDP2GDP3*.

After each combination of simulated defects, the corresponding signal is performed. At the end, we will have a database from which it may possible to perform several analyzes. The recording database consists of 22 sounds for a given rotational speed. A preliminary listening was used to select the most different sounds between them, a second selection is carried out leading to obtain 8 sounds on which the paired comparison method was performed.

4.2 Sounds Restitution

The evaluation dissimilarities tests were carried out in an ordinary room of the mechanics and structures laboratory (*LMS*) of the University of Guelma, Algeria. The sounds reproduction was done through stereo headphone. The reproduction chain is composed of a PC with I5 Dell processor, tests interface under Matlab environment, and a Sennheiser *HD201* headphone.

4.3 Tests Interface and Subjects

The interface of the tests is programmed in MATLAB language, it contains two phases: the first is called training phase in which the sounds are subjected to the listening of auditors. Listeners can become familiar with the sounds of running test. The second is a dissimilarity pair comparison phase. 30 listeners (07 women and 23 men), aged from 22 to 50 years, are taken to realize these two tests.

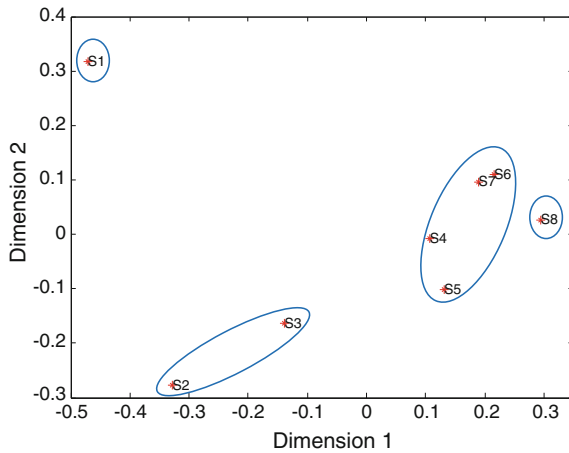
4.4 Results Analysis

We present in Table 1 the coordinates of the simulated sounds in two dimensions space (*DIM1* and *DIM2*). Where *DIM1* represents the evolution of the defect degradation, and *DIM2* represents the difference in severity of each sound compared to other sounds, according to the paired comparison test (see Fig. 2). One

Table 1 Sounds coordinates in two dimensions perceptual space

Sounds	DIM1	DIM2	Type of defect
Sound ₁	-0.4714	0.3165	Without defect
Sound ₂	-0.3281	-0.2775	Simple defect
Sound ₃	-0.1394	-0.1631	
Sound ₄	0.1073	-0.0068	
Sound ₅	0.1323	-0.1010	Double defect
Sound ₆	0.2158	0.1105	
Sound ₇	0.1887	0.0956	
Sound ₈	0.2949	0.0259	Triple defect

Fig. 2 Perceptual space



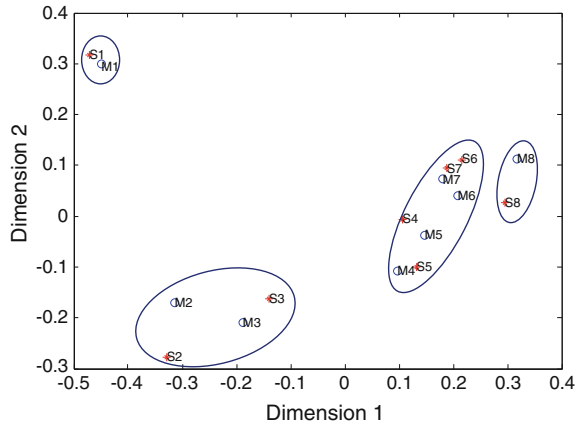
note that the coordinates results are in good agreement with the gear deterioration degrees, namely without defect (S_1), single (S_2, S_3), double (S_5, S_6, S_7) and triple defects (S_8). Nevertheless, it is noted that the great defect (S_4) was perceived near to the double defects that those of the simple defects.

4.5 Correlations Between Scalar Indicators and Dimensions

The correlation obtained for *DIMI* with two physical parameters. Shows the presence of *OL* and *K* in the mathematical model (1) confirms the previous *DIMI* analysis, since these two indicators are directly related to the defect degradation level. The correlation factor is $R^2 = 0.97 \cdot (P < 0.001)$.

$$DIM1 = 1.5981 \cdot OL + 0.013647 K - 0.7405 \tag{1}$$

Fig. 3 Sounds classed by listeners (S_i), and those calculated by mathematical models (M_i)



Equation 2 presents the correlation obtained for $DIM2$ with two physical parameters. The model of this dimension is characterized by the OL and the SCG related to the spectral balance. The correlation factor is $R^2 = 0.82$ ($P < 0.002$).

$$DIM2 = 1.4118 \cdot OL + 0.0026603 SCG - 1.8297 \quad (2)$$

4.6 Application of the Mathematical Correlations Models

Figure 3 presents, in the sound proximity space, the classification coordinate values of the 8 sounds obtained by the perception tests S_i and the two models M_i obtained previously from Eqs. 1 and 2. This figure shows good agreement, therefore the models obtained are reliable with a correlation coefficient $R_2 = 0.97$ for $DIM1$ and $R_2 = 0.82$ for $DIM2$.

5 Conclusion

The aim of this work is to study the evolution of gears defects using sound perception approach. For that, several defects were simulated on gears assembled on laboratory test rig. Perceptual study based on the paired comparison and the *MDS* methods was carried out to study gear sounds for different degradation levels. This study allowed identifying the vibration parameters for establishing a vibro-acoustic relationship in rotating machinery namely gears transmission.

In this work, we studied the capacity of the listeners to identify different type of defect, ranging from a small simple defect until the combination of several defects. For that, we simulated several defects with various degradation degrees.

According to the results obtained in this work one shows that:

- Coordinates sounds in the proximity space are in good agreement with the gears degradation degrees.
- The scalar indicators; Spectral Center of Gravity, Overall Level, Kurtosis and the K-factor well explain the dissimilarity judgments for the gears sounds in the case of a simulated defect.
- The correlations between the objective and subjective aspects helped to highlight the important relationship between the vibration indicators and the distances between gear sounds in proximity space.
- The mathematical correlations models obtained for dimensions 1 and 2 can be used as a follow-up tool of the gears' degradation evolution without repeating perceptions tests.

References

1. Vincent, H.: Etude de la qualité sonore d'appareils de soufflage et de climatisation. M.Sc thesis, Pierre & Marie Curie University, Paris (2005)
2. Parizet, E., Hamzaoui, N., Jacquemoud, J.: Noise assessment in a high-speed train. *Appl. Acoust.* **63**, 1109–1124 (2002)
3. Parizet, E., Hamzaoui, N., Sabatie, G.: Comparison of some listening test methods: a case study. *Acta Acust. United Acust.* **91**, 356–364 (2005)
4. Michaud, P.Y., Meunier, S., Herzog, P., Aubigny, G.D., Lavandier, M.: Méthode de test adaptée à l'évaluation perceptive d'un grand nombre de stimuli audio Application aux enceintes acoustiques. In: 10th French congress of Acoustics, CFA2010. Lyon, France (2010)
5. Kenzari, M.: Vibroacoustic diagnosis of gears defects: sound perception approach analysis. M.Sc thesis, INSA of Lyon, France (2009)
6. Reboul, E.: Vibroacoustique of high frequencies mechanisms: application to gears transmissions. Ph.D., thesis, Central School of Lyon, France (2005)

Natural Frequencies of Composite Cylindrical Helical Springs

Sami Ayadi and Ezzeddine Haj Taïeb

Abstract This study presents a method for calculating the natural frequencies of a Carbon-Epoxy helical spring. The mathematical formulation presented describes the linear dynamic behavior of composite excited helical springs. The governing mathematical model of such behavior is formed by a system of four partial differential equations of first order of hyperbolic type. This system describes the axial and rotational wave propagation of strains and velocities, which are the primary dependent variables. They depend on time and the space coordinate along the spring axis. These waves propagate in the spring with two speeds; the speed of slow axial waves and the speed of the fast rotational waves. To simplify mathematical model, the spring is assumed to be homogeneous. The mechanical and geometrical characteristics of the spring are obtained by a weighted average of those of its two components. The area fraction is used as weights. The impedance method is then applied to determine the natural frequencies of the spring. The results show the existence of two sets of resonance frequencies, the frequencies of slow axial waves and those of rapid rotational waves. They correspond to the fundamental and odd harmonics of the system. Each resonant frequency is separated in the impedance diagram by an anti-resonance frequency, the impedance at which the module is zero. The results clearly show the influence of the area fraction on the evolution of the natural frequencies of composite helical springs.

Keywords Helical spring · Composite · Impedance method · Natural frequency

S. Ayadi (✉) · E. Haj Taïeb
Laboratory of Applied Fluid Mechanics, Process Engineering
and Environment, ENIS, BP 1173, 3038 Sfax, Tunisia
e-mail: Sami.ayadi@issatgb.rnu.tn

E. Haj Taïeb
e-mail: e_hajtaieb@yahoo.fr

1 Introduction

Helical springs are important mechanical components in many industrial applications [14, 15]. They allow maintaining tensions or forces in a mechanical system absorb shocks, control expenses and couples, reduce vibrations. However, resonant vibrations of the helical springs were observed for some frequencies and a number of incidents have been explained by different forms of resonance oscillations (vehicles traveling on undulating slopes). In many research papers, evaluation of natural frequencies of elastic springs is carried out using various methods. In these methods, the equations of motion of the helical springs are developed based on the theory of Timoshenko beam. Among them, one can mention the method of the transfer matrix to determine the stiffness matrix [11, 16, 19] and the pseudo spectral method to calculate the root of the determinant of this matrix [10]. Becker et al. [6] determined the resonance frequency of a helical spring subject to axial loading of static compression. For this, they conducted a numerical solution of the linearized equations of motion using the method of the transfer matrix.

However, using composites instead of metal materials created new problems in the design and manufacture of helical springs. As these springs have some advantages over those metals (vibration insulation, energy storage and power transmission when the weight and chemical resistance are concerned, viscous damping...). Several studies have been developed to analyze their frequency spectrum. These include, for example, the work of Yildirim [17] based on the method of transfer matrix, Temel et al. [13] by applying the inverse Laplace transform, Chiu et al. [7] studying the effects of the rubber core and the braided exterior layer on the mechanical properties of composite springs. The springs are considered leaf springs formed of composite laminates folds transversely. Beadmore et al. [4, 5] evaluated the potential for the use of composite auto parts and the ability to reduce the weight of automobiles to save energy. Moris [12] has devoted its work to the integration of composites in the rear suspension system of automobiles and Daugherty [8] developed the composite leaf springs for heavy-duty trucks. In fact, Audi is the first automaker to integrate composite springs for the suspension system of its vehicles. Therefore, to improve the quality of these composite helical springs, problems regarding the manufacture and the design must be carefully reviewed.

In this paper, we numerically study the frequency composite helical springs following a sinusoidal excitation of the axial velocity. The considered spring consists of carbon-epoxy. The fibers in epoxy, of number n , have a section s . The composite material is assumed elastic homogeneous of section S . It can be assumed that the area fraction $\gamma = ns/S$ of the fibers is preserved during the deformation of the spring. The dynamic working generates waves of rotational and axial deformations that propagate along the spring. The aim of this study is to present a method for determining the resonance frequencies of an excited composite helical spring. A mathematical formulation is presented to describe the linear dynamic response of composite helical springs.

The governing equations for such a movement form a system of four partial differential equations of hyperbolic type. Axial and rotational strains and velocities are the main dependent variables. The mechanical impedance is expressed at every point of the spring and especially the extreme points which are the most stressed points. Frequency spectra are shown in the impedance diagram.

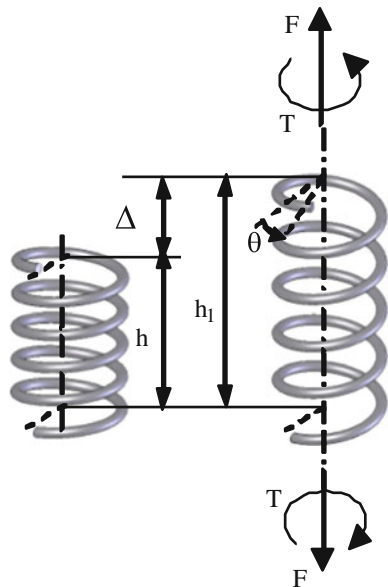
2 Mathematical Formulation

2.1 Equations of Motion

The mathematical model represents the equations of wave propagation of axial and rotational strains and velocities in the helical springs. It is obtained by applying the theory of dimensional analysis, the general theory of bending and twisting of thin rods and the elementary strength of materials formulas to an element of the spring between two sections x and $x + dx$ submitted to axial force F and torque T (Fig. 1). This model can be written in the following matrix form [2]:

$$\frac{\partial Y}{\partial t} + \frac{\partial G(Y)}{\partial x} = 0 \tag{1}$$

Fig. 1 Static deflection of helical spring



where: $G(Y)$ is a vector function of the unknown vector Y :

$$Y = \begin{pmatrix} u_x \\ v_x \\ u_t \\ v_t \end{pmatrix}, G(Y) = - \begin{pmatrix} u_t \\ v_t \\ a u_x + b v_x \\ b u_x + c v_x \end{pmatrix} = -BY = - \begin{pmatrix} 0 & 0 & 1 & 0 \\ 0 & 0 & 0 & 1 \\ a & b & 0 & 0 \\ b & c & 0 & 0 \end{pmatrix} Y \quad (2)$$

This model is a system of four partial differential equations of first order of hyperbolic type. It takes into account of the four unknown variables: u_x the axial strain, v_x the rotational strain, u_t the axial velocity and v_t the rotational velocity. It includes dynamic coupling between the axial and rotational waves using the Poisson's ratio ν contained in the constants a , b and c defined by:

$$a = \frac{Eh \sin \alpha}{Mr^2} \left(1 - \frac{\nu}{1+\nu} \cos^2 \alpha \right) \quad (3a)$$

$$b = - \frac{Eh \sin \alpha}{Mr^2} \frac{\nu}{1+\nu} \sin \alpha \cos \alpha \quad (3b)$$

$$c = \frac{Eh \sin \alpha}{Mr^2} \left(1 - \frac{\nu}{1+\nu} \sin^2 \alpha \right) \quad (3c)$$

where h is the length of the spring in the unstretched position, E is the Young modulus of the spring material, ν is Poisson's ratio of the spring material, M is the total mass of the spring, α is the helix angle of the spring in the unstretched position, r is the radius of the spring helix in the unstretched position and $I = \pi r_f^2 / 4$ is the moment of inertia of the wire cross section.

The application of the theory of characteristics [1] shows the presence of slow axial waves (u_x, u_t) and fast rotational one (v_x, v_t) which propagate in the spring with two velocities:

$$c_s = \sqrt{\frac{Eh \sin \alpha}{Mr^2} \frac{1}{1+\nu}}, c_f = \sqrt{\frac{Eh}{Mr^2} \sin \alpha} \quad (4)$$

Under these conditions, Eq. (1) and the expressions (2), (3a–3c) and (4) describe the linear dynamic behavior of the spring.

To these equations we associate the initial conditions defined by:

$$u_t(x, 0) = 0, u_x(x, 0) = \frac{\Delta}{h}, v_t(x, 0) = 0, v_x(x, 0) = \frac{r\theta}{h}, 0 \leq x \leq h \quad (5)$$

2.2 Characteristic of the Composite Spring

The Fig. 2 shows the section of a unidirectional composite helical spring [18]. This study examines the effect of the properties of composite materials on the natural frequencies of the spring. The spring is assumed to be homogeneous. The area fraction γ defined by $\gamma = ns/S$, where s is the section of the n fibers and S is the total section of the wire spring, is assumed constant.

According to the theory of structural mechanics, the characteristics of the composite spring (Young’s modulus, Poisson’s ratio and density ρ) can be expressed, with those of its constituents, by the following relationships:

$$\begin{aligned}
 E &= \gamma E_f + (1 - \gamma)E_m, & v &= \gamma v_f + (1 - \gamma) \cdot v_m \\
 M &= \rho \vartheta = [\gamma \rho_f + (1 - \gamma)\rho_m] \cdot S \frac{h}{\sin \alpha}
 \end{aligned}
 \tag{6}$$

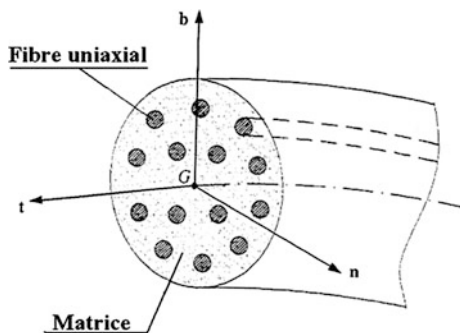
2.3 Impedance Method

This method evaluates the dynamic characteristics of the spring: frequency response, transfer function, etc. The instantaneous variables in Eq. (1) are written as a sum of two terms: the mean variables and the oscillatory variables $Y = \bar{Y} + Y'$. The equations of motion are linear, the terms of fluctuations Y' obey the same system of Eq. (1) where $\Delta' = 0$ and $\theta' = 0$.

Solving these equations is performed by the variable separation method $Y(x, t) = X(x) \cdot T(t)$ which $X^t(x) = (U_x \ V_x \ U_t \ V_t)$ is a vector of one variable x and T is a function only of the variable t .

By limiting the study to the particular case of the harmonic oscillation pulse regime $T(t) = Ce^{i\omega t}$, where ω is the angular frequency and after substituting and rearranging:

Fig. 2 Section of a helical spring in uniaxial composite



$$\frac{dX}{dx} = i\omega B^{-1}X \quad (7)$$

Applying the Cayley Hamilton [18], the solution of Eq. (7) is written [9]:

$$X(x) = e^{i\omega x B^{-1}} X(0) = [A(x)]X(0) \quad (8)$$

The eigenvalues of the matrix B are $\{-c_f \quad -c_s \quad c_s \quad c_f\}$ and those of the matrix $i\omega B^{-1}$ are $\{\lambda_1 = -i\omega x/c_s \quad \lambda_2 = -i\omega x/c_f \quad \lambda_3 = i\omega x/c_f \quad \lambda_4 = i\omega x/c_s\}$. By using of Mathematica 4 processing software, the following coefficients of the matrix $[A(x)]$, depending on ω , c_f , c_s , and x [3], are obtained:

$$A_{11} = A_{33} = \sin^2 \alpha \cos\left(\frac{\omega x}{c_f}\right) + \cos^2 \alpha \cos\left(\frac{\omega x}{c_s}\right) \quad (9a)$$

$$A_{12} = A_{21} = A_{34} = A_{43} = \sin \alpha \cos \alpha \left[\cos\left(\frac{\omega x}{c_s}\right) - \cos\left(\frac{\omega x}{c_f}\right) \right] \quad (9b)$$

$$A_{13} = i \frac{\sin^2 \alpha}{c_f} \sin\left(\frac{\omega x}{c_f}\right) + i \frac{\cos^2 \alpha}{c_s} \sin\left(\frac{\omega x}{c_s}\right) \quad (9c)$$

$$A_{14} = A_{23} = -i \sin \alpha \cos \alpha \left[\frac{1}{c_f} \sin\left(\frac{\omega x}{c_f}\right) - \frac{1}{c_s} \sin\left(\frac{\omega x}{c_s}\right) \right] \quad (9d)$$

$$A_{22} = A_{44} = \cos^2 \alpha \cos\left(\frac{\omega x}{c_f}\right) + \sin^2 \alpha \cos\left(\frac{\omega x}{c_s}\right) \quad (9e)$$

$$A_{24} = i \frac{\cos^2 \alpha}{c_f} \sin\left(\frac{\omega x}{c_f}\right) + i \frac{\sin^2 \alpha}{c_s} \sin\left(\frac{\omega x}{c_s}\right) \quad (9f)$$

$$A_{31} = ic_f \sin^2 \alpha \sin\left(\frac{\omega x}{c_f}\right) + ic_s \cos^2 \alpha \sin\left(\frac{\omega x}{c_s}\right) \quad (9g)$$

$$A_{32} = A_{41} = i \cos \alpha \sin \alpha \left[c_s \sin\left(\frac{\omega x}{c_s}\right) - c_f \sin\left(\frac{\omega x}{c_f}\right) \right] \quad (9h)$$

$$A_{42} = ic_f \cos^2 \alpha \sin\left(\frac{\omega x}{c_f}\right) + ic_s \sin^2 \alpha \sin\left(\frac{\omega x}{c_s}\right) \quad (9i)$$

And the complex strains and velocities, as functions of position x in helical spring, indicated in the relation (8), result:

$$\begin{aligned}
 U_x(x) &= A_{11}(x) \cdot U_x(0) + A_{12}(x) \cdot V_x(0) + A_{13}(x) \cdot U_t(0) + A_{14}(x) \cdot V_t(0) \\
 V_x(x) &= A_{21}(x) \cdot U_x(0) + A_{22}(x) \cdot V_x(0) + A_{23}(x) \cdot U_t(0) + A_{24}(x) \cdot V_t(0) \\
 U_t(x) &= A_{31}(x) \cdot U_x(0) + A_{32}(x) \cdot V_x(0) + A_{33}(x) \cdot U_t(0) + A_{34}(x) \cdot V_t(0) \\
 V_t(x) &= A_{41}(x) \cdot U_x(0) + A_{42}(x) \cdot V_x(0) + A_{43}(x) \cdot U_t(0) + A_{44}(x) \cdot V_t(0)
 \end{aligned}
 \tag{10}$$

The mechanical impedances in the helical spring are defined as the ratio of complex axial and rotational strains to the complex axial and rotational velocities as follows:

$$\begin{aligned}
 Z_1(x) &= \frac{u'_x}{u'_t} = \frac{U_x}{U_t} & Z_2(x) &= \frac{v'_x}{v'_t} = \frac{V_x}{V_t} \\
 Z'_1(x) &= \frac{u'_x}{v'_t} = \frac{U_x}{V_t} & Z'_2(x) &= \frac{v'_x}{u'_t} = \frac{V_x}{U_t}
 \end{aligned}
 \tag{11}$$

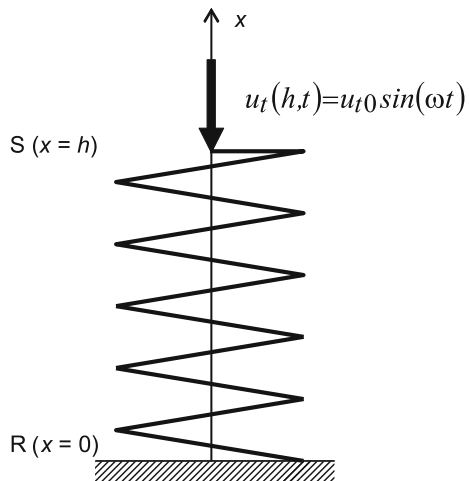
In the case where the spring is clamped at the extremity $R(x = 0)$ and axially loaded at the extremity $S(x = h)$ of the spring as indicated on Fig. 3, the boundary conditions can be expressed:

$$U_t(0) = 0 \quad V_t(0) = 0 \quad U_t(h) \neq 0 \quad V_t(h) = 0
 \tag{12}$$

In these conditions, the terms of impedances, at $x = h$ is simplified:

$$\begin{aligned}
 Z_1(h) &= \frac{A_{11}(h) \cdot A_{42}(h) - A_{41}(h) \cdot A_{12}(h)}{A_{31}(h) \cdot A_{42}(h) - A_{41}(h) \cdot A_{32}(h)} \\
 Z_2(h) &= \frac{A_{21}(h) \cdot A_{42}(h) - A_{41}(h) \cdot A_{22}(h)}{A_{31}(h) \cdot A_{42}(h) - A_{41}(h) \cdot A_{32}(h)}
 \end{aligned}
 \tag{13}$$

Fig. 3 Spring fitted at R ($x = 0$) and loaded at ($x = h$)



For against, in the case where the spring is excited efficiently through $S(x = h)$, the boundary conditions are expressed by:

$$U_t(0) = 0 \quad V_t(0) = 0 \quad U_t(h) = 0 \quad V_t(h) \neq 0 \quad (14)$$

and the expressions of the impedances at $x = h$, are written:

$$\begin{aligned} Z'_1(h) &= \frac{A_{11}(h) \cdot A_{32}(h) - A_{31}(h) \cdot A_{12}(h)}{A_{41}(h) \cdot A_{32}(h) - A_{31}(h) \cdot A_{42}(h)} \\ Z'_2(h) &= \frac{A_{21}(h) \cdot A_{32}(h) - A_{31}(h) \cdot A_{22}(h)}{A_{41}(h) \cdot A_{32}(h) - A_{31}(h) \cdot A_{42}(h)} \end{aligned} \quad (15)$$

The impedances (12) and (14) vary with frequency and are maximum for a certain infinite number of frequencies called natural frequencies of the spring. They correspond to the zeros of the following expression:

$$A_{41}(h) \cdot A_{32}(h) - A_{31}(h) \cdot A_{42}(h) = c_f c_s \sin\left(\frac{\omega h}{c_f}\right) \cdot \sin\left(\frac{\omega h}{c_s}\right) \quad (16)$$

That is the zeros of the function:

$$D(\omega) = \sin(\omega h/c_f) \cdot \sin(\omega h/c_s) \quad (17)$$

Thus, the own pulsation resonance (k odd) and anti-resonance (k even) are expressed by:

$$\omega_{sk} = k \frac{\pi c_s}{h}, \omega_{fk} = k \frac{\pi c_f}{h}, \quad k = 0 \quad 1 \quad 2 \quad \dots \quad (18)$$

3 Application and Results

Consider a helical spring whose characteristics are: the height of the spring $h = 1.1938$ m, the angle of helix $\alpha = 0.198281$ rd, the radius of the coils $r = 0.157607$ m, number of turns $n = 6$, the wire radius $r_f = 0.007$ m. In this study, the spring is considered Composite Carbon-Epoxy (AS4/3501-6) with the same Poisson's ratio $\nu_m = \nu_f = 0.3$ and the same density $\rho_m = \rho_f = 1389$ Kg/m³. The Carbon Young's modulus is $E_m = 144.8$ GPa. That of Epoxy is $E_f = 9.65$ GPa. The properties of the composite material are given in Table 1 for two values and the area fraction $\gamma = 0.25$ and $\gamma = 0.75$.

Software written in FORTRAN language was developed to calculate the mechanical impedance for a frequency range $f \in [0.500]$. In general, the impedances at the ends of the composite spring are complex numbers that can be expressed:

Table 1 Mechanical properties of the considered springs

Young's modulus (GPa)			Celerities (m/s)		Frequencies (Hz)	
			Slow	Fast	Slow	Fast
Material	$\gamma = 0.25$	111	34.30	39.11	14.36	16.38
Composite spring	$\gamma = 0.75$	43.4	21.46	24.46	8.99	10.25

$$\begin{aligned} Z_1(h) &= Z_{1R} + iZ_{1I} = |Z_1|e^{i\psi_1} & Z'_1(h) &= Z'_{1R} + iZ'_{1I} = |Z'_1|e^{i\psi'_1} \\ Z_2(h) &= Z_{2R} + iZ_{2I} = |Z_2|e^{i\psi_2} & Z'_2(h) &= Z'_{2R} + iZ'_{2I} = |Z'_2|e^{i\psi'_2} \end{aligned} \tag{19}$$

Thus, resonant natural frequencies (k odd) and anti-resonance (k even) are expressed by:

$$f_{sk} = \frac{\omega_{sk}}{2\pi} = k \frac{c_s}{2h} = 14.36k, f_{fk} = \frac{\omega_{fk}}{2\pi} = k \frac{c_f}{2h} = 16.38k \quad k = 0123 \tag{20}$$

These frequencies are shown in Fig. 4 for two values of the area fraction. An expansion function $D(f)$ is shown in Fig. 5 for $\gamma = 0.25$. This figure shows the axial and rotational frequencies.

The amplitudes of the two impedances (12) are shown in the impedance diagram in Fig. 6 as a function of the rotational frequency ω for two values of the area fraction $\gamma = 0.25$ and $\gamma = 0.75$.

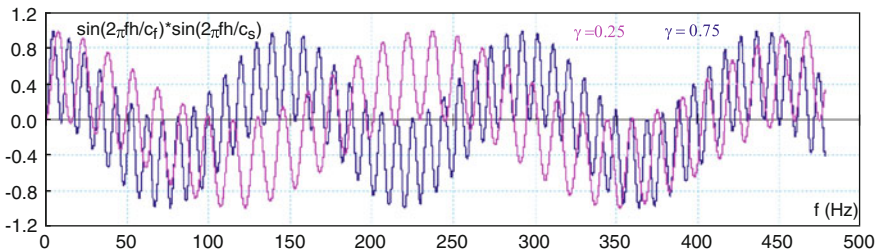


Fig. 4 Natural frequencies of waves for two values of the area fraction

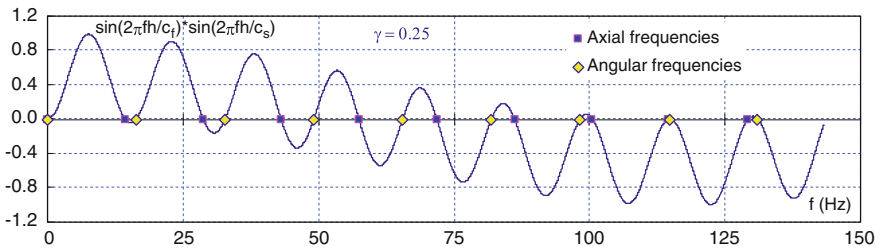


Fig. 5 Axial and rotational frequencies

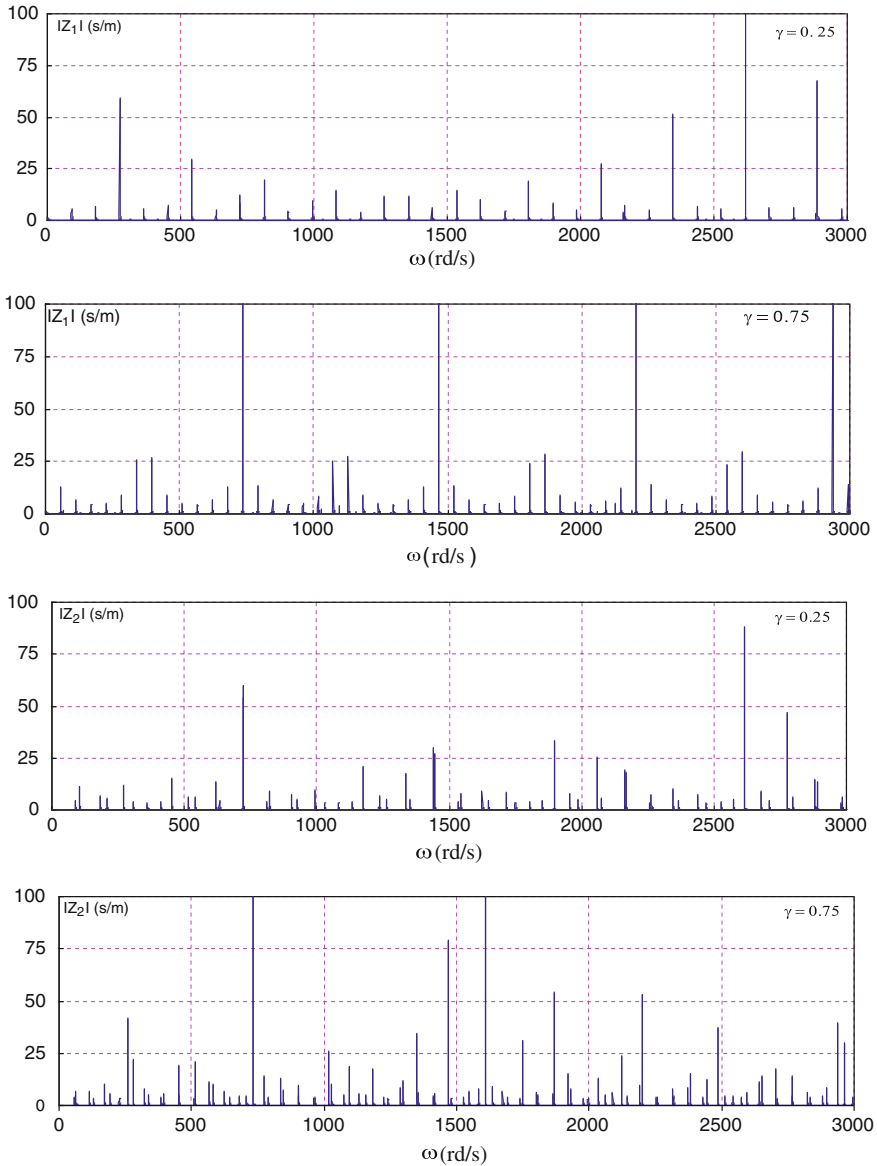


Fig. 6 Diagrams impedances $|Z_1|$ and $|Z_2|$

The highest values of the spectrum are related to the resonant frequencies; while the minimum values corresponding to the antiresonance one.

When the pulse disturbances in the composite spring coincide with the resonance pulse, changes in strains and velocities are amplified and can lead to the rupture of the spring.

4 Conclusion

In this study, the natural frequencies of a composite cylindrical helical spring subjected at the end to a sinusoidal excitation of the axial velocity, were numerically simulated. The mathematical formulation is presented by adopting the area fraction of fiber. Therefore, we have obtained a simple and credible formulation that combines the behavior of the matrix with that of the fibers. The approach of the impedance was used, limiting solution for the stationary-oscillatory cases by assuming harmonic oscillations. In this case, the behavior of axial and rotational strains and velocities is governed by a system of four linear partial differential equations. The separation of variables technique was used to develop the mechanical impedances of the composite spring. These impedances vary with frequency and are maximum for the infinite number of resonating frequencies corresponding to the fundamental and odd harmonics. The results are used to analyze the evolution of the impedance at the end of the loaded composite spring. They show that the natural frequencies are proportional to the velocity of propagation of slow axial waves and to the velocity of propagation of rapid rotational waves.

References

1. Ayadi, S., Hadj-Taïeb, E.: Influence des caractéristiques mécaniques sur la propagation des ondes de déformations linéaires dans les ressorts hélicoïdaux. *Mécanique et Industrie* **7**, 551–563 (2006)
2. Ayadi, S., Hadj-Taïeb, E.: Finite element solution of dynamic response of helical springs. *Int. J. Simul. Model.* **7**(1), 17–28 (2008)
3. Ayadi, S., Hadj-Taïeb, E.: Evaluation of the natural frequencies of cylindrical helical springs by the impedance method, ICSAAM, September 7–10. Tarbes, France (2009)
4. Beadmore, P.: Composite structures of automobiles. *Comput. Struct.* 163–176 (1986)
5. Beadmore, P., Johnson, C.F.: The potential for composites structural automotive applications. *Compos. Sci. Technol.* **26**, 251–281 (1986)
6. Becker, L.E., Chassie, G.G., Cleghorn, W.L.: On the natural frequencies of helical compression springs. *Int. J. Mech. Sci.* **44**, 825–841 (2002)
7. Chiu, H.C., Hwan, C.L., Tsai, H.S., Lee, W.P.: An experimental investigation into the mechanical behaviors of helical composite springs. *Compos. Struct.* (2005)
8. Daugherty, R.L.: Composite leaf springs in heavy truck applications. In: *Proceedings of Japon-US Conference Composite Materials*, Tokyo, pp. 529–538 (1986)
9. Fröberg, C.E.: *Introduction to Numerical Analysis*. Adison-Wesley Publishing Company, USA (1979)
10. Lee, J.: Free, vibration analysis of cylindrical helical springs by the pseudospectral method. *J. Sound Vib.* **302**, 187–196 (2007)
11. Lee, J., Thompson, D.J.: Dynamic stiffness formulation, free vibration and wave motion of helical springs. *J. Sound Vib.* **239**(2), 297–320 (2001)
12. Moris, C.J.: Composite integrated rear suspension. *Comput. Struct.* 233–242 (1986)
13. Temel, B., Çalim, F.F., Tütüncü, N.: Forced vibration of composite cylindrical helical rods. *Int. J. Mech. Sci.* **47**, 998–1022 (2005)
14. Wahl, A.M.: *Mechanical Springs* Penton Publishing Co. Cleveland, Ohio (1963)

15. Wittrick, W.H.: On elastic wave propagation in helical springs. *Int. J. Mech. Sci.* **8**, 25–47 (1966)
16. Yildirim, V.: An efficient numerical method for predicting the natural frequencies of cylindrical helical springs. *Int. J. Mech. Sci.* **41**, 919–939 (1999)
17. Yildirim, V.: Free vibration of uniaxial composite cylindrical helical springs with circular section. *J. Sound Vib.* **239**(2), 321–333 (2001)
18. Yildirim, V.: Numerical buckling analysis of cylindrical helical springs in dynamic manner. *Int. J. Eng. Appl. Sci.* **1**, 20–32 (2009)
19. Yildirim, V., Sancaktar, E.: Linear free vibration analysis of crossply laminated cylindrical helical springs. *Int. J. Mech. Sci.* **42**, 321–333 (2000)

Improvement of the Sensitivity of the Scalar Indicators Using a Denoising Method by Wavelet Transform

Mustapha Merzoug, Khalid Ait Shgir, Abdelhamid Miloudi
and Jean Paul Dron

Abstract Gears are main components in the industrial machines and considered among the most critical elements. Therefore their diagnosis is vital to avoid failure and prevent catastrophic failure of the machinery. The vibration analysis is the most used approach for the gears diagnosis. However the vibration signal captured from a gear mesh with faulty gears is in general non-stationary and noisy in nature. In this frame, this work addresses the gears diagnosis by the combination of the classical indicators with a denoising method. For this a gear dynamic model, including the evolution of a localized tooth defect, is developed. The model consists of a spur gear pair, two inertias which incorporate the effects of time-varying mesh stiffness and damping, excitation due to the gear errors. The Newmark integration scheme is used to calculate a dynamic model. Then, the obtained simulation signals were drawn in a random noise which simulates the vibration background noise. For the simulation signals, the temporal and the frequency indicators were proposed for the early detection of the crack evolution. By using the wavelet technique these indicators were improved and the comparison of its performance was made. Several types of wavelet functions were used for this purpose and it was seen that the most appropriate is the adaptive wavelet function. The simulation results are validated with experimental signals which consist in a test rig with gear transmissions.

M. Merzoug (✉) · A. Miloudi
Laboratoire de Mécanique Avancée, USTHB, Algiers, Algeria
e-mail: moustapha_merzoug@yahoo.fr

A. Miloudi
e-mail: amiloudi@yahoo.fr

K. Ait Shgir · J.P. Dron
GRESPI, Université Champagne Ardène, Reims, France
e-mail: khalid.ait-sghir@univ-reims.fr

J.P. Dron
e-mail: jp.dron@univreims.fr

1 Introduction

The gear transmission is an essential part on most machinery for changing the shaft speed, the torque and the power. Therefore, their diagnosis is vital to prevent catastrophic failure of the machinery. There are several techniques available for the early detection of failure, and one of the most useful is vibration analysis. A popular technique of vibration analysis has been spectral analysis. Spectral analysis is a particularly powerful technique because the different elements of a mechanical system in general produce vibration at different frequencies.

The impact produced by the faulty gear can generate a non-stationary signal, which contains a wealth of information about faults; therefore, it is indispensable to analyze the non-stationary signals using the time-frequency techniques, which allow viewing the temporal evolution of the frequency content of the signal [1, 2]. The non-stationary nature of the signal may be analyzed by the Wavelet Transform (*WT*), which provides powerful multi-resolution analysis in both domains of time and frequency. The time and frequency signal analysis makes the *WT* as a preferred tool to extract the transient characteristics of non-stationary vibration signals over *FFT* spectrum [3, 4]. For some time, the wavelet transform is used because it is capable of providing both the time-domain and frequency-domain information simultaneously, has been successfully used in non-stationary vibration signal processing and fault diagnosis.

Djebala [5] proposed an approach that benefits the local nature of wavelet analysis and its ability to detect transients. They first calculated the Hilbert transform of the signal then calculate an envelope of the signal will be processed by wavelet analysis. It then extracts the detail covering the rotation frequency of the defective wheel. The examination of the envelope technique for defect identification is found unsatisfactory in measuring the angle between two faulty teeth Jena [6] proposes another technique that consists in undecimated wavelet transform (*UWT*), which is used to denoise the signal. The analytic wavelet transform (*AWT*) has been implemented on approximation signal followed by a time marginal integration (*TMI*) of the *AWT* scalogram.

Merainani [7] used the Empirical Wavelet Transform (*EWT*) which designs an appropriate wavelet filter bank fully depends on the processed signal with Hilbert Transform in the early detection and condition monitoring of tooth crack fault. Results of analyzing the pinion's vibration displacement show that the proposed approach denoted (*HEWT*) successfully detect the tooth crack at a much earlier stage of damage development even though in noisy environment.

The most vital step in wavelet analysis is the selection of the mother wavelet function as well as the decomposition level of signal. In the context of the use of discrete wavelet transform, orthogonal wavelets have been applied in this research; among them Daubechies and Symlets wavelets have been widely implemented as it matches the transient components in vibration signals.

The aim of this chapter is to show the interest the wavelet transforms in improving the sensitivity of the scalar indicators (kurtosis and crest factor) in the

context of conditional maintenance by vibratory analysis of gear transmissions. When the gear is damaged, the appearance of a crack on the gear tooth disturbs signal. This change is due to the presence of periodic pulses. Nevertheless, the presence of noise induced by the random excitation can have an influence on the values of these time indicators. Denoising of these signals by wavelet transform allows improve the sensitivity of these indicators and to increase the reliability of diagnosis. To simulate the signal to be analyzed, we voluntarily introduced a crack default gear tooth. We selected wavelet of Symlets type that is well suited to this type of problem.

The purpose is to try to master the various parameters related to the wavelet analysis for reliable and inexpensive detection, namely, the order of the wavelet and the level of decomposition. The approach is to observe the kurtosis and the crest factor for several wavelet orders depending on the gravity of the fault.

2 Analytical Model

The analytical model used in the present paper is available in literature and the corresponding graphical representation is shown in Fig. 1.

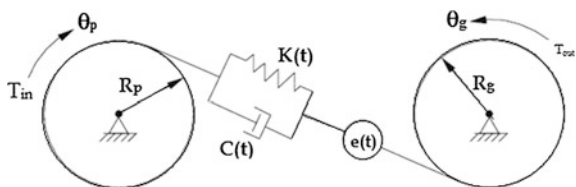
$$M \frac{d^2x}{dt^2} + C(t) \frac{dx}{dt} + K(t)x = F \tag{1}$$

where x variable is the analyzed degree of freedom, named dynamic transmission error, and it is defined as:

$$x = R_p \cdot \theta_p - R_g \cdot \theta_g - e(t) \tag{2}$$

where, R_p and R_g are the base radius, θ_p et θ_g the rotations, respectively, of input and output gears. Further, M is an equivalent mass that will be described in Eq. 4; the stiffness term $K(t)$ is mathematically treated by means of a Fourier development. F is the contact force between teeth and the last term is the second derivative of static transmission error, treated as an external input acting on the system. The force is calculated as the rapport between the torque T and the corresponding base radius R :

Fig. 1 Model for gear dynamic behavior



$$F = \frac{T_{in}}{R_p} = \frac{T_{out}}{R_g} \quad (3)$$

$$M = \frac{I_p I_g}{I_g R_p^2 + I_p R_g^2} \quad (4)$$

M , it is a function of the two gears moments of inertia, I_p and I_g , and of the corresponding base radius, R_p and R_g .

2.1 Influence of the Gear Mesh Stiffness Calculating Model on the Simulated Signal

The time-varying mesh stiffness $K(t)$ is obtained as [8]:

$$K(t) = k_0 + \sum_{r=1}^R k_r \cos(2\pi r f_m t - \Phi_r) \quad (5)$$

The values of K_r and Φ_r are obtained using following formulate:

$$\frac{k_0}{k_s} = ICR \quad (6)$$

$$\frac{k_r}{k_s} = \frac{\sqrt{2 - 2 \cos(2\pi r(ICR - 1))}}{\pi r} \quad (7)$$

$$\Phi_r = \frac{1 - \cos(2\pi r(ICR - 1))}{\sin(2\pi r(ICR - 1))} \quad (8)$$

where, k_0 : Average mesh stiffness, ICR : Involute Contact Ratio, k_s : Gear mesh stiffness during single tooth contact, k_s and Φ_r : r th Fourier Coefficient and phase angle of $k(t)$.

Gear tooth crack is a defect that has severe impact on healthy machine functioning. Detecting this defect as soon as possible has an extreme importance. In tooth root crack modeling, most of the studies consider some modifications in meshing stiffness profile [9]. For instance, faulty tooth stiffness decreases and it is repeated once per contact cycle of this tooth. Therefore, the authors proposed to model a localized crack on a tooth taking into account its angular position on the base circle. On this position, meshing stiffness decrease is considered and this phenomenon is repeated at each time the cracked tooth enters in contact with the teeth of the opposed gear. In this case, the condition that governs the stiffness expression in the presence of a localized fault on a tooth is as follows:

- If the contact is between two healthy teeth, the meshing stiffness is given by $k(t)$.
- If the contact is between the cracked tooth and the tooth of the opposed gear, the stiffness is given by $k(t) \cdot [1 - D(t)]$, with $0 < D(t) < 1$.

where $D(t)$ is a periodic function representing the amount of stiffness degradation expressed as:

$$D(t) = \alpha \delta \left[1 + \sum_n \frac{\sin(n\alpha\pi)}{(n\alpha\pi)} \cos(n\Omega_i t) \right] \tag{9}$$

where: $\Omega_i = 2\pi \cdot f_i$ and f_i represents the rotation frequency of the gear affected by the crack. δ is the amplitude of the function $D(t)$, it represents the amount of stiffness degradation or the crack evolution $\alpha = \frac{1}{Z_i}$ represents the cyclic ratio.

2.2 Simulated Analysis

The vibration signal of the gearbox contains amplitude and phase modulations, which is periodic with the rotational frequency of the gear. The modulation of meshing frequency from the faulty gear generates the sidebands. The sidebands are either the shaft rotational speed or one of its multiples. An analysis of the spectrogram (Fig. 2) shows a line around the meshing frequency. We also note a high-energy frequency band which represents the natural frequency of the system.

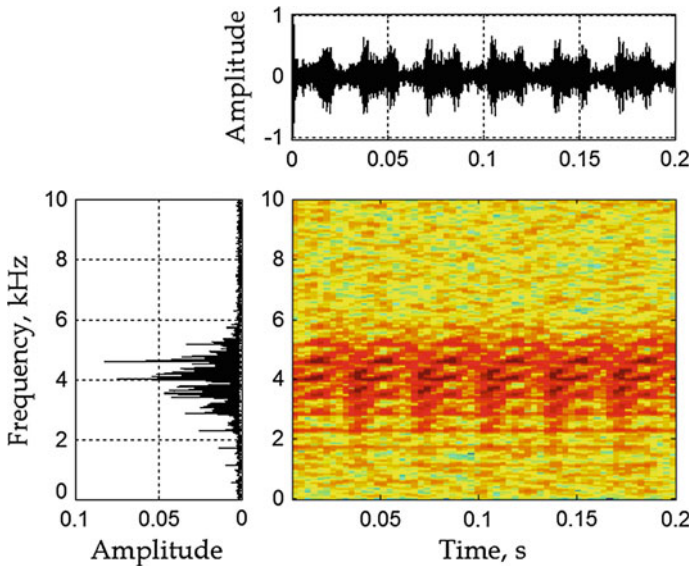


Fig. 2 Spectrogram of the simulated signal

3 Optimization of Multi-resolution Wavelet Analysis

For a long time FFT was the tool of choice to address this problem, except that it was always difficult to avoid altering the signal by reducing a large amount of noise. Methods based on thresholding wavelet transform have emerged to fill the gaps [10–13]. Their strength resides in their ease of implementation and their effectiveness. Therefore the main idea is to remove the small coefficients responsible for the noise in the signal. The denoising of the noisy signal using wavelet transform is obtained in three basic steps [14]:

- Signal decomposition: Signal is decomposed into j level of wavelet transform and coefficients are calculated.
- Thresholding: Then the threshold is selected and the detail parts through wavelet transform are compared with the threshold and the detail parts are set to zero if they are less than the threshold.
- Signal reconstruction: Finally the signal is reconstructed using the original approximation coefficients of level j and modified detail coefficients.

Soft and Hard thresholding In the literature there are two types of thresholding techniques applicable to signal processing which are Hard thresholding and Soft thresholding. Hard thresholding can be described as the usual process of setting to zero the elements whose absolute values are lower than the threshold. Soft thresholding is an extension of hard thresholding, first setting to zero the elements whose absolute values are lower than the threshold, and then shrinking the nonzero coefficients towards zero. The drawbacks of the Hard and Soft thresholding are that the Hard threshold is not continuous at threshold whereas the Soft threshold is not differentiable at this value; a pre-requisite for any optimization problem [15].

If denotes λ the given threshold, the Soft threshold can be defined by [11]:

$$T_{doux}(x) = \begin{cases} \text{sign}(x)(|x| - \lambda) & |x| \geq \lambda \\ 0 & \text{otherwise} \end{cases} \quad (10)$$

and Hard thresholding can be written as:

$$T_{dur}(x) = \begin{cases} x & |x| \geq \lambda \\ 0 & \text{otherwise} \end{cases} \quad (11)$$

With the above thresholding methods in place the obvious question is how to set an appropriate value of λ . A widely adopted approach, introduced by Donoho [12], is to use the universal threshold. For a series of length n the universal threshold is given by:

$$\lambda = \sigma\sqrt{2 \log(N)} \quad (12)$$

where λ is the threshold value? N is the length of the noisy signal. In threshold selection, we should not ignore the detail coefficients in every level that probably influence the robustness of the threshold estimating. So we have to rescale a selected threshold in some level. In this paper, the threshold is dependent on the detail coefficients at every level. The standard deviation σ is thus estimated by:

$$\sigma = \frac{\text{mediane}(|d_1|)}{0.6745} \quad (13)$$

3.1 Methodology for Performance Evaluation

To evaluate the performance of our approach several assessment tests such as *SNR* and *RMSE* are employed.

3.1.1 Signal to Noise Ratio

Signal to noise ratio (abbreviated *SNR*) is a measure used in science and engineering that compares the level of a desired *signal* to the level of background noise. It is defined as the ratio of signal power to the *noise* power, often expressed in *decibels*. The global *SNR* values are determined by the following equation:

$$SNR_{dB} = 10 \log_{10} \left(\frac{\sum_n x^2(n)}{\sum_n [x(n) - \hat{x}(n)]^2} \right) \quad (14)$$

3.1.2 Root Mean Square Error

Root Mean Square Error will be used as a performance measure. The *RMSE* is defined as:

$$RMSE = \sqrt{\frac{1}{N} \sum_n [x(n) - \hat{x}(n)]^2} \quad (15)$$

where, $x(n)$ is the original signal, $\hat{x}(n)$ is the denoised signal and n is the number of the samples.

3.2 The Choice of Analyzing Wavelet

The study of the choice of analyzing wavelet will be conducted on the basis of a test of several wavelets. This will be on the study of *SNR* between the original signal and the signal after reconstruction. The analyzing wavelet chosen will be the one who will present the value of the highest *SNR*. We apply Mallat algorithm multiresolution analysis using the analyzing wavelet for different orders. The most analysands wavelets used are Daubechies (*db*) and Symelet (*sym*). White Gaussian noise is added to the simulated signals. The noisy signal is represented in Fig. 3, for *SNR* value.

Firstly, this signal is denoised using wavelet transform with the methods of soft and hard thresholding. For comparison with the same conditions, the parameters of the wavelet transform are set for both cases. The wavelet decomposition family is the *db3* and level 8 is selected.

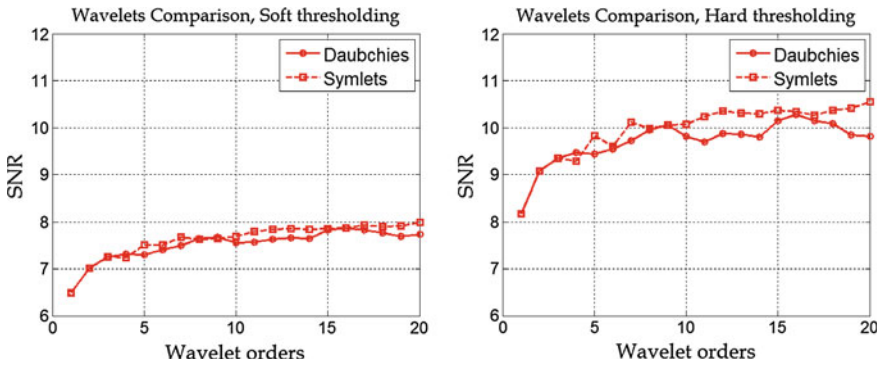


Fig. 3 SNR versus different wavelet orders

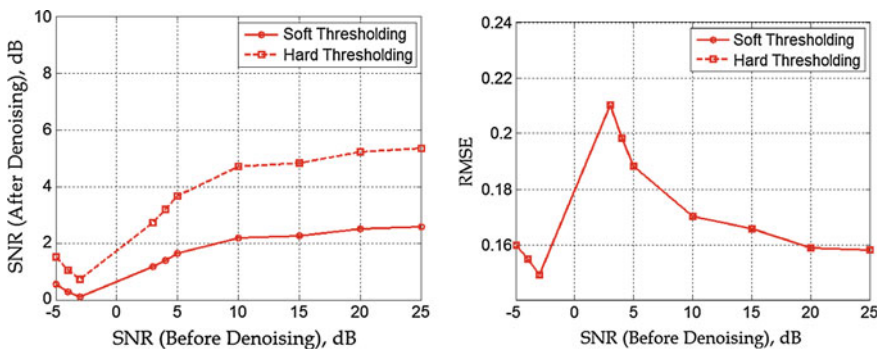


Fig. 4 SNR and RMSE versus different noisy signal

In order to illustrate performance of the proposed threshold selection, the signal is corrupted by noise at different level of signal to noise ration (*SNR*). These noisy signals are denoised using wavelet transform with universal thresholds. Root Mean Square Error (*RMSE*) and *SNR* out are used as performance measure for denoising. The Hard thresholding method clearly has the best performance for these white noise conditions. The output *SNR* of the hard thresholding method shows the linear *SNR* improvement as compared with soft thresholding (Fig. 4).

3.3 Statistical Parameters

To obtain useful information from the time-domain acoustic and vibration signals various statistical techniques have been developed over the years. One of the parameters, namely, the crest factor, which is defined as the ratio of maximum absolute value to the *RMS* value of the vibration signal, gives an idea about the occurrence of impulse in the time-domain signal. In real-time condition monitoring, an increased value of the crest factor over a period of time indicates the presence of wear or pitting. Another powerful parameter called kurtosis measures the degree of peakiness of a distribution compared to a normal distribution [16].

Mathematically, crest factor and kurtosis for signal $x(n)$ with N number of samples in the time domain can be expressed as the Root Mean Square (*RMS*) of the acceleration. It is defined by:

$$A_{RMS} = \sqrt{\frac{1}{N} \sum_{n=0}^{N-1} [x(n) - \bar{x}]^2} \quad (16)$$

with \bar{x} the mean of the time series $x(n)$. Kurtosis is a statistical parameter allowing the analysis of the distribution of the vibratory magnitudes contained in a time domain signal. It corresponds to the moment of fourth order divided the square of the standard deviation:

$$Kurtosis = \frac{\frac{1}{N} \sum_{n=0}^{N-1} [x(n) - \bar{x}]^4}{\left[\frac{1}{N} \sum_{n=0}^{N-1} [x(n) - \bar{x}]^2 \right]^2} \quad (17)$$

The Crest Factor is another time domain criterion consisting in the ratio between maximum magnitude of the time signal and A_{RMS} :

$$Crest\ factor = \frac{\max[x(n)]}{A_{RMS}} \quad (18)$$

4 Application to the Early Detection of Gear Defect

It is clear from Fig. 5 that in the case of the original signals, the statistical indicators increase considerably, implying a dramatic decrease in the gear mesh stiffness. The kurtosis and the crest factor thus evolve always increasingly as a function of increasing crack length. From a degradation rate of 6 %, the kurtosis and the crest factor begin to be higher and their progression is practically proportional to the length of the crack.

An improvement of the kurtosis and of the crest factor sensibility can be noticed. It can also be noticed that those two indicators (crest factor and kurtosis) do not vary in a linear manner when the size of the defect is very important [17]. Indeed, when the size of the defect is very important, the time space between two successive shocks becomes inferior to the relaxation time and the hypotheses on which the application validity lies on are not any more confirmed [18]. The crest factor

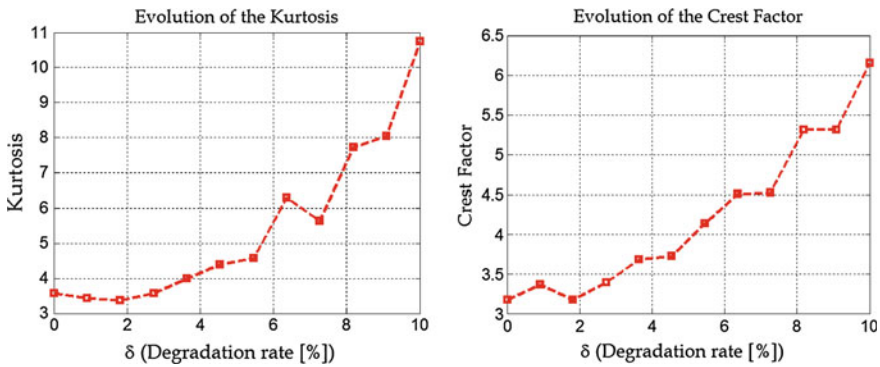


Fig. 5 Kurtosis and Crest Factor evolution versus the degradation rate

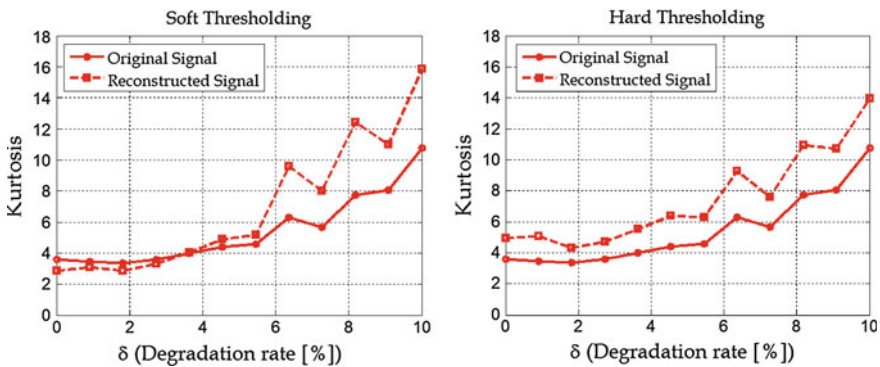


Fig. 6 Kurtosis comparison of original and reconstructed signals

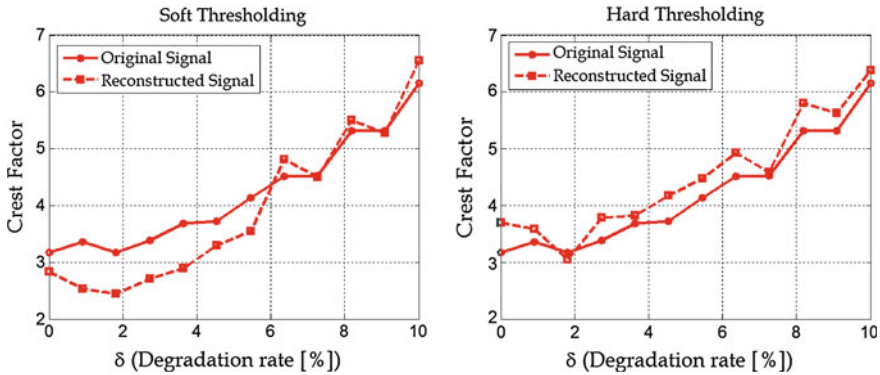


Fig. 7 Crest Factor comparison of original and reconstructed signals

and the kurtosis value become inferior or equal to three and are not anymore characteristic of an impulsive signal [19]. A comparison between the values of Kurtosis and Crest factor before and after the signal decomposition (Figs. 6 and 7) shows the contribution of wavelet transforms in improving the sensitivity of these indicators with respect to the conventional case.

5 Conclusion

The wavelet transform is widely used for analyzing non-stationary vibration signals from rotating machines. The approach just described can trace the origin of some defects after decomposition of the original signal details and approximations. It allows removing the time invariant noise of a signal. This method improves the sensibility of temporal indicators such as the kurtosis and the crest factor which are often used in conditional maintenance by vibratory analysis.

This study also shows that the kurtosis is a better indicator than the crest factor for the detection of an impulsive defect in the case of hard thresholding.

References

1. Dalpiaz, G., Rivola, A., Rubini, R.: Gear fault monitoring: comparison of vibration analysis techniques. In: Proceedings of the 3rd International Conference on Acoustical and Vibratory Surveillance Methods and Diagnostic Techniques, vol. 13, pp. 623–637 (1998)
2. Randall, R.B.: A new method of modeling gear faults. *J. Mech. Des.* **104**, 259–267 (1982)
3. Peng, Z.K., Chu, F.L.: Application of the wavelet transform in machine condition monitoring and fault diagnostics: a review with bibliography. *Mech. Syst. Signal Process.* **18**(2), 199–221 (2004)

4. Shi, D.F., Wang, W.J., Qu, L.S.: Defect detection for bearing using envelope spectra of wavelet transform. *ASME J. Vib. Acoust.* **120**, 567–574 (2004)
5. Djebala, A., Ouleaa, A., Kebbabsa, T., Ramdane, Y.: Détection des défauts non stationnaires de dentures d'engrenages par application de l'analyse en ondelettes et la transforme de Hilbert, Congrès Algérien de Mécanique, 27–29 November, Mascara (2013)
6. Jena, D.P., Panigrahi, S.N., Kumar, R.: Gear fault identification and localization using analytic wavelet transform of vibration signal. *Measurement* **46**, 1115–1124 (2013)
7. Merainani, B., Benazzouz, D., Rahmoune, C.: Early detection of tooth crack damage in gearbox using empirical wavelet transform combined by Hilbert transform. *J. Vib. Control* (1077546315597820, first published on August 25) (2015)
8. Kahraman, A., Blankenship, G.W.: Effect of involute contact ratio on spur gear dynamics. *ASME J. Mech. Des.* **121**, 112–118 (1999)
9. Abbes, M.S., Trigui, M., Chaari, F., Fakhfakh, T., Haddar, M.: Dynamic behaviour modelling of a flexible gear system by the elastic foundation theory in presence of defects. *Eur. J. Mech. A. Solids* **29**, 887–896 (2010)
10. Donoho, D.L.: De-noising by soft thresholding. *IEEE Trans. Inf. Theory* **41**, 613–627 (1995)
11. Donoho, D.L., Johnstone, L.M.: Ideal spatial adaptation by wavelet shrinkage. *Biometrika* **81** (3), 425–455 (1994)
12. Johnstone, I.M., Silverman, B.W.: Wavelet threshold estimators for data with correlated noise. *J. Roy. Statist. Soc. B* **59**, 319–351 (1997)
13. Chang, S., Kwon, Y., Yang, S., Kim, I.-J.: Speech enhancement for non-stationary noise environment by adaptive wavelet packet. In: *Proceedings of IEEE International Conference on Acoustics, Speech, and Signal Processing (ICASSP '02)*, vol. 1, pp. 561–564 (2002)
14. Kulkarni, P.G., Sahasrabudhe, A.D.: Application of wavelet transform for fault diagnosis of rolling element bearings. *Int. J. Sci. Technol. Res.* **2**(4) (2013)
15. Kumar, R., Pate, P.: Signal denoising with interval dependent thresholding using DWT and SWT. *Int. J. Innovative Technol. Explor. Eng. (IJITEE)* **1**(6) (2012). ISSN: 2278-3075
16. Jena, P.D., Panigrahi, S.N.: Gear fault diagnosis using bispectrum analysis of active noise cancellation-based filtered sound and vibration signals. *Int. J. Acoust. Vib.* **18**(2), 59–70 (2013)
17. Tandon, N.: A comparison of some vibration parameters for the condition monitoring of rolling element bearings. *Measurement* **12**, 285–289 (1994)
18. Pachaud, C.: Crest factor and kurtosis contributions to identify defects inducing periodical impulsive forces. *Mech. Syst. Signal Process.* **11**(6), 903–916 (1997)
19. Dron, J.P., Bolaers, F., Rasolofondraibe, I.: Improvement of the sensitivity of the scalar indicators (crest factor, kurtosis) using a de-noising method by spectral subtraction: application to the detection of defects in ball bearings. *J. Sound Vib.* **270**, 61–73 (2004)

Fault Diagnosis Through the Application of Cyclostationarity to Signals Measured

Tarek Kebabsa, Nouredine Ouelaa, Jerome Antoni,
Mohamed Cherif Djamaa, Raid Khettabi and Abderrazek Djebala

Abstract In this paper we have used a frequency modulation method for detecting faults in the plain bearings and the gear teeth defects. This method is based mainly on the analysis of some cyclostationarity non-stationary signals. Indeed, a cyclostationary signal has hidden periodicities; that is to say, it is not periodic in the strict sense but some statistical properties of the signal are periodic. This frequency is used to identify the spectral correlation which has the advantage of being a function of a single variable frequency instead of two. The experimental validation is performed on the basis of signals measured in an industrial environment (turbogenerator). The application of this method to non stationary signals has helped to highlight very clearly the presence of defects in the bearings of the gearbox, which has been difficult to demonstrate by spectral analysis.

T. Kebabsa (✉) · N. Ouelaa · M.C. Djamaa · R. Khettabi · A. Djebala
Mechanics and Structures Laboratory, University 8 May 1945, Po Box 401, 24000 Guelma,
Algeria
e-mail: kebabsa.tarek@yahoo.fr

N. Ouelaa
e-mail: n_ouelaa@yahoo.fr

M.C. Djamaa
e-mail: mc_djamaa@yahoo.fr

R. Khettabi
e-mail: khettabi@uqtr.ca

A. Djebala
e-mail: djebala_abderrazek@yahoo.fr

T. Kebabsa
Mechanical Engineering Department, University of Badji Mokhtar, Po Box 12,
23000 Annaba, Algeria

J. Antoni
Laboratory of Vibration-Acoustics, INSA of Lyon, Bâtiment A. St. Exupéry, 25 bis Avenue
Jean Capelle, 69621 Villeurbanne Cedex, France
e-mail: jerom.antoni@insa-lyon.fr

Keywords Spectral analysis · Cyclostationarity · Intensity modulation distribution · Spectral correlation density · Spectral coherence density · Turbo-Alternator

1 Introduction

Monitoring of vibration analysis machines, has grown significantly due to the evolution of such systems maintenance concepts, to minimize downtime and revision time, the maintenance method adopted is that of conditional preventative maintenance [1, 2]. Reducing production costs and increasing the availability of production tools have indeed become issues that needed to detect and identify any defects at an early stage. Currently, the challenge is more to demonstrate the value of using vibration analysis in the field of maintenance of rotating machines, but to assimilate the basics and know the limitations of each technique of choice. It becomes clear that the failures cannot be tolerated because of the complexity of the machine and its criticality in the process [3, 4]. For effective conditional preventative maintenance, reliable and accurate measurements of the state of the machine must be carried out. The “revolution” in the field of vibration diagnostic of machines is probably using periodic methods that allowed the development of more reliable methods based on cyclostationarity [5, 6] and on the separation of cyclical component of the signal [7, 8]. Cyclostationarity formulation has several advantages for the analysis of such signals over conventional approaches. First of all it allows to grasp with the same tools a wide range of behaviors, from simple deterministic frequency (unbalance phenomena, misalignment, eccentricity, inversion strength, meshing default, etc....) to the non-stationary random (fluid movement, friction forces, grab, ...) [9, 10]. Then she explicitly incorporates a time dimension that tracks the evolution of non-stationarity of the systems studied. This analysis allows discovering the amplitude modulations present in the vibration signals [11, 12]. This modulation varies as a function of the signal components. These can often provide valuable data. An error occurs when the measuring time is insufficient [13]. Several studies have shown that the presence of modulations confirms the existence of defects in rolling bearings and gears [14–16].

2 Principle of the Method

Statically, in signal processing, it is customary to distinguish two main families of signals; stationary signals, whose moment's statistics the probability density are independent of time, and the non-stationary signals, the statistical moments depend on time. In the latter family, there is a particular class of signals that are cyclostationary signals. A process is said cyclostationary to order n , if all its statistical moments up to order n are time-dependent periodically with the period

T. A stationary signal has the peculiarity of only contain frequency components uncorrelated, the fact that its self correlation does not depend on time.

The first application of the theory of cyclostationarity for diagnosing gear was proposed by C. Capdessus in 1992 and is followed by Sidahmed and Lacoume in 1995 [17]. Other authors such as Rubini, Marcomick in 1997 and in 1998 [18] have discussed the application process cyclostationarity in diagnosing [19, 20] rotating machines.

3 Cyclostationarity Order a “Synchronous Average”

A cyclic order a statistical process $n = I$, can be represented by the first order of time expressed as:

$$m(t) = E[m(t)] = m(t + T) \tag{1}$$

with: $E[m(t)]$ s the expected, in English “the mathematical expectation” or “the statistical expectation operator”.

Cyclostationarity of the order is operated in the condition monitoring applications through the use of the synchronous average [18]. By applying this method the vibration signal $S(t)$ is averaged for a single period of rotation by calculating the average of the measured samples to a number of rotations N_r separated by a time interval T corresponds to a rotation period, Eq. 1, is written:

$$m(t) = \frac{1}{N - 1} \sum_{K=0}^{N-1} S(t + KT) \tag{2}$$

4 Order Two Cyclostationarity “Autocorrelation”

As we had said earlier, stationary or cyclostationarity a signal can be identified from the state of its autocorrelation. From a mathematical point of view it is expressed as follows [17]:

$$R_s(t, \tau) = E \left[S \left(t + \frac{\tau}{2} \right) S \left(t - \frac{\tau}{2} \right) \right] \tag{3}$$

τ : The gap between two observations

A signal $S(t)$ is stationary second order if $R_s(t, \tau) = R_s(\tau)$ i.e. d independent of t

A signal $S(t)$ is cyclostationary second order, where: $\exists t : R_s(t, \tau) = R_s(t + T, \tau)$ where T is the cyclic period, and $\alpha = \frac{1}{T}$ the basic cyclic frequency or frequency separation

A signal $S(t)$ is cyclostationary at large, if $R_s(t, \tau)$ present several intervals with respect to t

The autocorrelation function is periodic; it can be expressed as a Fourier series:

$$R_s^\alpha(\tau, s) = \sum_{\alpha} R_s^\alpha(\tau) \cdot e^{-2j\pi\alpha t} \tag{4}$$

$R_s^\alpha(\tau)$: Fourier coefficients define the cyclic autocorrelation function

$R_s^0(\tau)$: Fourier coefficients define the stationary autocorrelation function for $\alpha = 0$

The Fourier transforms, with respect to t , and gives the function of the spectral correlation density (Spectral Correlation Density Function “CSFE”) or the spectral correlation.

$$SC_s^c(f) = \int_{-\infty}^{+\infty} R_s^\alpha(\tau) \cdot e^{-2j\pi\alpha t} d\tau \tag{5}$$

Note that for we obtain the spectral power density “Power Spectral Density”, noted PSD of the signal $S(t)$. The spectral correlation can be expressed by:

$$SC_s^c(f) = TF_{t, \tau}[R_s(t, \tau)] = E\left[S_f\left(f + \frac{\tau}{2}\right) \cdot S_f\left(f - \frac{\tau}{2}\right)\right] \tag{6}$$

When the $SCDF$ is zero everywhere except the signal $S(t)$ is stationary, if it is not zero for a finite number of value is said that the signal is cyclostationary.

It is possible to compound other functions help to estimate the degree of cyclostationarity of the signal. The first is the spectral coherence function (Spectral Coherence Function “CAF”) given by:

$$C_s^\alpha(f) = \frac{SC_s^\alpha(f)}{\sqrt{|S_f(f + \frac{\alpha}{2})|} \cdot \sqrt{|S_f(f - \frac{\alpha}{2})|}} \tag{7}$$

with signal S_f of the power spectrum

The second is called the degree of cyclostationarity which was proposed by Zivanovic and Gardner (1991) mathematically given by the expression:

$$DSC^\alpha = \frac{\int |R_s^\alpha(\tau)|^2 d\tau}{\int |R_s^0(\tau)|^2 d\tau} \tag{8}$$

This is the ratio between the energy and for a stationary signal, with $DCS = 1$. Equation (8) can be written using the spectral correlation:

$$DSC^\alpha = \frac{\int |SC_s^\alpha(\tau)|^2 df}{\int |SC_s^0(\tau)|^2 df} \tag{9}$$

The modulation function spectral coherence distribution density is obtained by:

$$MID_{\Delta f}^{PSCoh}(f, \alpha) = \frac{SC_x^\alpha(f + \frac{\alpha}{2})}{\sqrt{SC_x^0(f + \frac{\alpha}{2})SC_x^0(f)}} \cdot \frac{SC_x^\alpha(f - \frac{\alpha}{2})}{\sqrt{SC_x^0(f - \frac{\alpha}{2})SC_x^0(f)}} \tag{10}$$

The denominator of “Eq. (10)” represents normalization by the power of the signals used for the spectral correlation measure. This property may be particularly critical in protecting the state of rotors of rotating machines.

The *MID* distribution integration represents the spectral correlation density, expressed by different sources is called *IMID*. This integration will be selected over the entire band carrier frequencies defined by:

$$IMID_{f_1}^{f_2}(\alpha; \Delta f) = \int_{f_1}^{f_2} MID_{\Delta f}(f; \alpha) df \tag{11}$$

where: $MID_{\Delta f}(f; \alpha)$ is a vector calculated in the carrier frequency band from f_1 to f_2 . In what follows, we will *IMID* applied to the diagnosis of turbo generator.

5 Experimental Study

5.1 Facility Description

The operating principle of the turbo-alternator *GZ1164* comprises introducing superheated vapor at an elevated pressure, commonly called admission vapor, via inlet pipe of the turbine. The latter comprises 16 wheels, each one comprising a number of blades *NB* (see Table 1). Each wheel is composed by plurality of eight fixed vanes. The setup comprises a turbine which converts the kinetic energy into mechanical energy that rotates the turbine rotor, a speed reducer in one stage with herringbone teeth, an alternator that rotates at the same output speed of reducer (whatever the load producing electricity) [21], and other accessories Fig. 1.

5.2 Frequency Characteristics of the Reducer

Table 2 shows the technical data of the reducer and its characteristic frequencies. According to the ISO standard 2372 (*ISO 2372, 1974*), the studied mechanism is

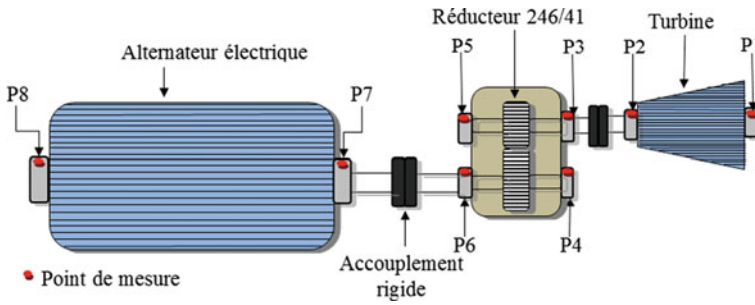


Fig. 1 Kinematic diagram of the turbo-alternator GZ1164 (Enterprise FERTIAL)

Table 1 Characteristic frequencies of blades passage defects

Number of gear	Number of blade (NP)	Fault frequency (FPA) (Hz)
1	40	5976
2	48	71.712
3	48	71.712
4	56	83.664
5	64	95.616
6	88	131.472
7	88	131.472
8	88	131.472
9	88	131.472
10	88	131.472
11	88	131.472
12	88	131.472
13	88	131.472
14	80	11.952
15	112	167.328

Table 2 Reducer’s specifications and its characteristic frequencies

Model/dimension	GVAB420
Nominal power	8300 kW
Transmission performance	0.18
Input speed (N_1)	9000 RPM say $F_{r1} = 150$ Hz
Output speed (N_2)	1500 RPM say $F_{r2} = 25$ Hz
Number of pinion’s teeth Z_1	41
Number of wheel’s teeth Z_2	246
Transmission ratio I	6
Meshing frequency $F_m = F_{r1} Z_1 = F_{r2} Z_2$	6125 Hz

classified in group 3, i.e. high power machines (>300kW) and mounted on a rigid foundation.

5.3 *Equipment Acquisition and Processing of Measurements*

Vibration measurements were collected on the eight bearings P_1 to P_8 of the turbo-alternator in the three directions. Two accelerometers were used; a mono axial accelerometer B&K type 4511-001 and another triaxial one B&K 4524B-001 (Fig. 2a). For the collection and processing of measurements, the analyzer B&K PULSE 16.1 has been used (Fig. 2b).

5.4 *Data of the Different Sets of Measurements*

Because of the importance of the turbo-alternator *GZ1164* in the production process of the electrical energy, it requires continuous monitoring. In this study, it was found that this mechanism is simply monitored by periodic tests based on the overall values of the *RMS* of speed and, time to time, of spectral analysis of speed and of displacement at low and medium frequency respectively (0–200 Hz) and (0–1000 Hz). The purpose of the spectral measurements is the detection of any shock into the mechanism, such as shock in gears, shaft friction, bearing wear, etc. Unfortunately, these frequency bands used by the maintenance department of the company do not allow identifying the defects mentioned above; since they are phenomena that mostly occur at high frequency.

Based on *RMS* overall levels of vibration of measured speed by the company and which show very high levels of vibration up to 14 mm/s, we was asked to carry out

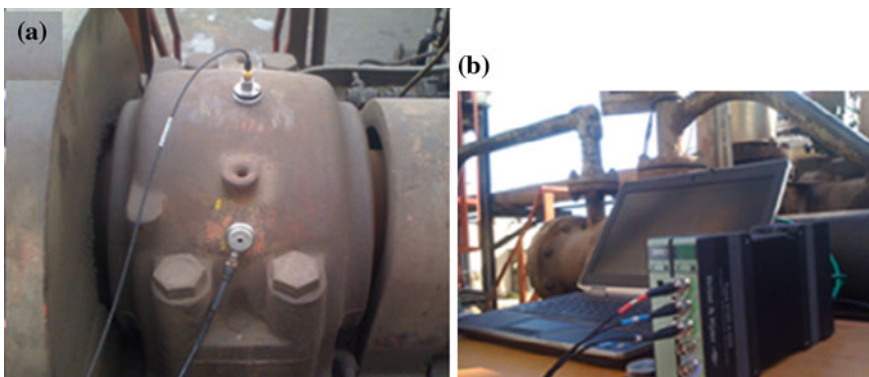


Fig. 2 a Industrial accelerometer (1) triaxial accelerometer (2), b analyzer Pulse 16.1

a global diagnosis of the turbo-alternator. On this basis, it was necessary to launch a series of tests in different frequency bands in order to try to establish a diagnosis of potential defects that cause this increase in the vibration level.

6 Low Frequency Analysis of the Reducer

6.1 Input Bearing of Reducer

The Fig. 3 shows the spectrum of the acceleration signal measured on the bearing 3 in the oblique direction with a mono-axial sensor in the frequency band (0–200 Hz).

In addition to the peaks corresponding to the frequencies of input and output of the reducer approximately ($Fr_1 = 150$ Hz and $Fr_2 = 25$ Hz) respectively, the spectrum analysis highlights other peaks corresponding to the frequencies of 54.88 and 104.9 Hz. According to the document of Brüel and Kjær [22], the frequency of oil whirl in the journal bearing is in relation to the frequency of the reducer's input-shaft

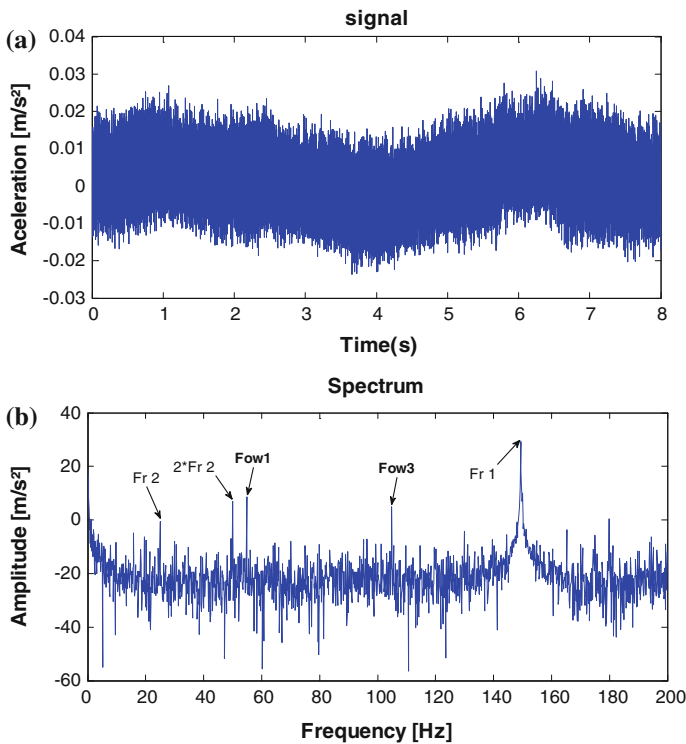


Fig. 3 Spectrum of measured acceleration signal on the bearing 4 in the frequency band (0–200 Hz)

$F_{ow} = kFr_1$ with $k = 0.3 \div 0.5$ for the general case and 0.7 for industrial installations. Indeed, the ratios $k_1 = 54.88/150 = 0.36$ and $k_2 = 104.9/150 = 0.7$ mean that two frequencies F_{ow1} and F_{ow2} which appear on the spectrum indicate the presence of the oil whirl defects on the journal bearing of the input shaft of the reducer.

6.2 Output Bearing of the Reducer

The Fig. 4 shows the spectrum of the acceleration signal measured on the bearing 4 in the oblique direction with a mono-axial sensor in the frequency band (0–200 Hz). The analysis highlights the peaks corresponding to the reducer’s input frequency of 149.4 Hz and output frequency of 25 Hz and its harmonics. The spectral analysis did not highlight the presence of the defect in the journal bearing.

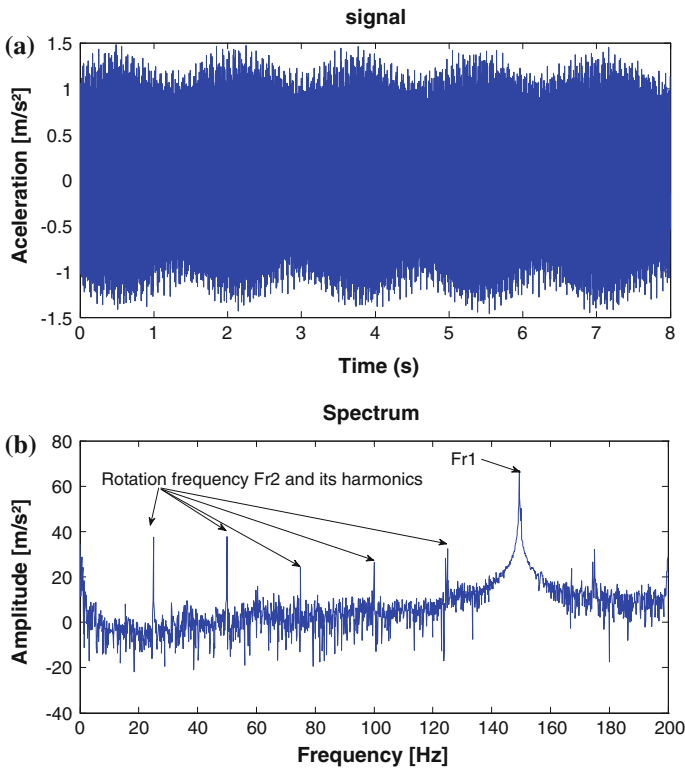


Fig. 4 Measured acceleration signal of one the bearing 3 in the frequency band (0–25.600 Hz)

6.3 High Frequency Analysis of the Reducer

The Fig. 5a, b represent the acceleration signal measured on the bearing 3 in the oblique direction with a mono-axial sensor and its spectrum respectively in the frequency band (0–25.600 Hz).

The spectrum shows the appearance of the meshing frequency $F_m = 6125$ Hz and its harmonics $2F_m = 12.250$ Hz, $3F_m = 18.375$ Hz and $4F_m = 24.500$ Hz. The decay of the amplitudes of the meshing frequency and its harmonics confirms the existence of a generalized wear of the reducer’s wheels tooth.

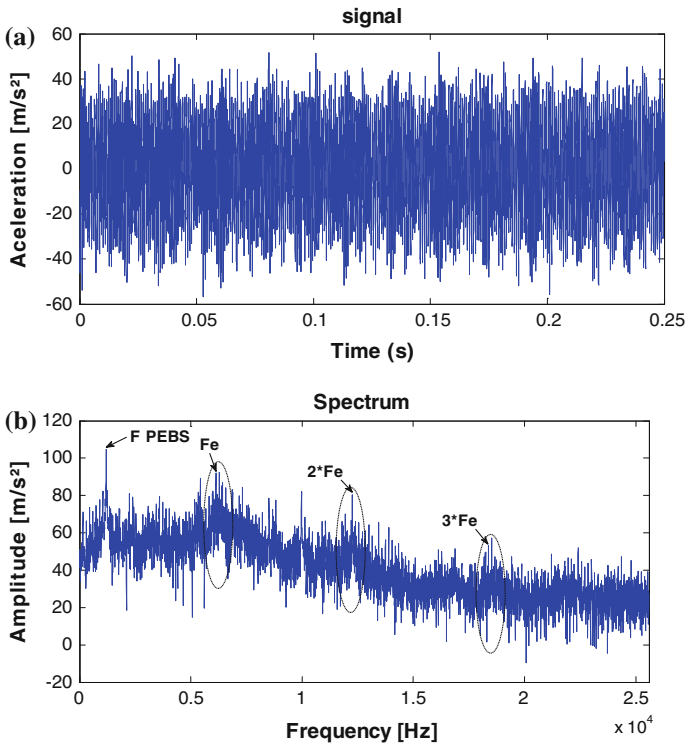


Fig. 5 Acceleration signal measured on the bearing 3 in the band (0–25.600 Hz) (a), and its spectrum (b)

7 Application of the Cyclostationarity on the Signals Measured on the Reducer's Bearings

7.1 Analysis of the Reducer in Low Frequency

In the previous section, it has been shown that the spectral analysis was used to highlight the wear defects on the teeth of the input and output wheel. However, the latter method does not allow localizing, by a clear way, the presence of defects in the journal bearings of the reducer. For that reason, the method of cyclostationarity is used to allow searching in very efficient way the modulations that may be present in the measured signals.

7.2 Input Bearing of the Reducer

The application of the analysis of modulation intensity distribution of the coherence spectral power (with $f_s = 4096$ Hz) for each frequency variation $MID_{\Delta f}^{PSCoh}$ of the acceleration signal measured on the bearing 3 Fig. 6 shows the appearance of two

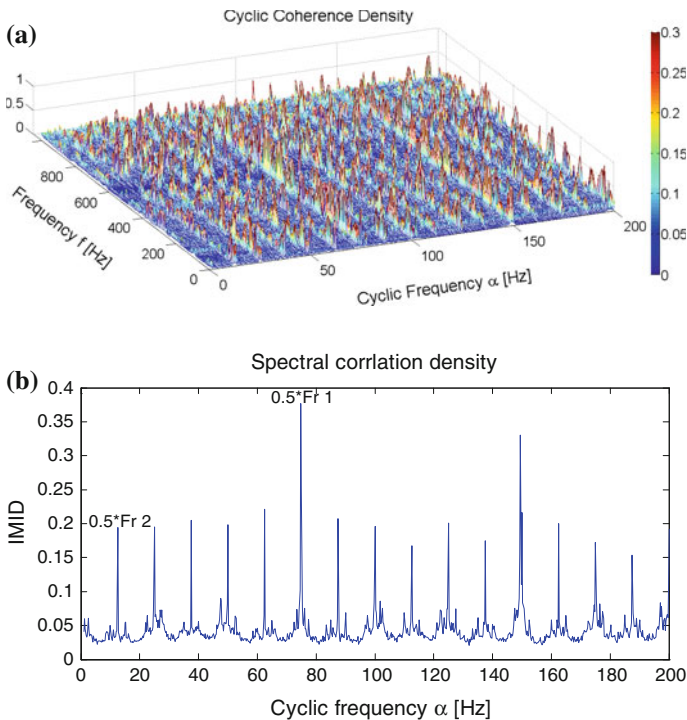


Fig. 6 a Spectral correlation (MID) with the corresponding (IMID) (b) of the signal of Fig. 3

cyclic frequencies: the first $\alpha_2 = 3 \times 10^{-3}f_s \approx 12.5$ Hz, corresponding to $\frac{1}{2}$ times the rotation frequency of the reducer’s output shaft, and the second, with a very important amplitude, at $\alpha_1 = 18.22 \times 10^{-3}f_s \approx 74.75$ Hz corresponding to $\frac{1}{2}$ times the rotation frequency of the reducer’s input shaft (see Fig. 6a).

This phenomenon is explained by the presence of an oil whirl defect on the journal bearings. We can note also in (Fig. 6b) that the use of the integration of the modulation intensity distribution (IMID) allows identifying by a very clear manner the two cyclic frequencies and their modulations.

7.3 Output Bearing of the Reducer

The application of the method *MID* on the signal measured on the output bearing 4 see Fig. 19, gives a spectrum similar to the typical spectrum corresponding to the friction defect in the rotor [22] Fig. 8. It shows the appearance of a fundamental cyclic frequency $\alpha = 2.4 \times 10^{-2}f_s \approx 12.5$ Hz (with $f_s = 512$ Hz), and its harmonic corresponding to $\frac{1}{2}$ times the rotation frequency of the reducer’s output shaft 25 Hz shown on (Fig. 7a).

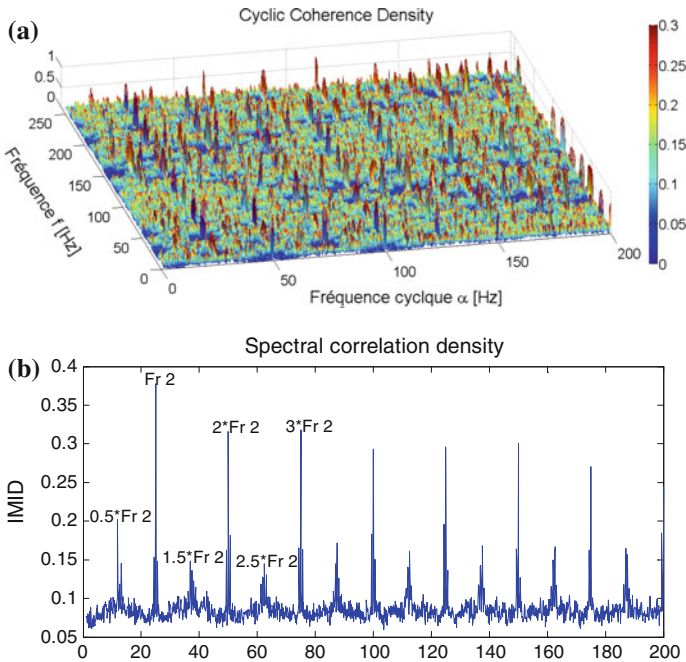


Fig. 7 a Spectral Correlation (MID) with the corresponding (IMID) (b) of the signal of Fig. 4

The application of *IMID* (Fig. 7b), allows identifying more clearly the fundamental cyclic frequency = 12.5 Hz and its harmonic. According to the typical spectrum of the defect (Fig. 8), the phenomenon presented in (Fig. 7b) corresponds to a friction defect in the journal bearing (Photo 1).

7.4 Analysis of the Reducer at High Frequency

The treatment of the signals measured on the reducer’s bearings at high frequency bands by the spectral analysis allowed highlighting the presence of wear on a large number of teeth of the wheels. We wanted to confirm this result by applying the cyclostationarity. The application of the *MID* on a signal measured in the frequency band (0–25.600 Hz) on the bearing 3 of the reducer, see Fig. 5, shows the appearance of two cyclic frequencies: the first for $\alpha_1 = 3.81 \times 10^{-4} f_s \approx 25$ Hz corresponding to the rotation frequency of the output shaft and the second one for $\alpha_2 = 2.28 \times 10^{-3} f_s \approx 150$ Hz (with $f_s \approx 65.536$ Hz) with very high amplitude corresponding to the rotation frequency of the input shaft.

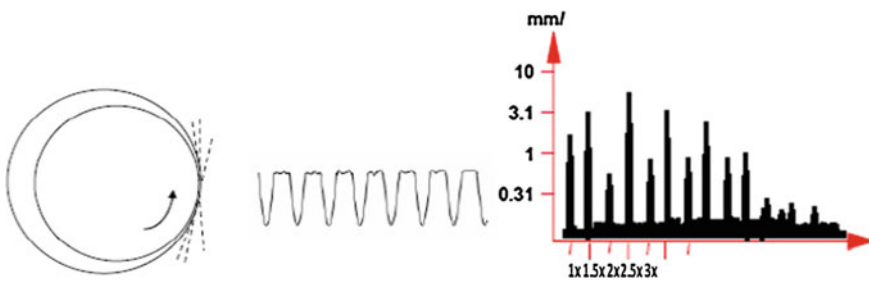


Fig. 8 Typical spectrum of oil whirl defect (Brüel and Kjør Vibro)

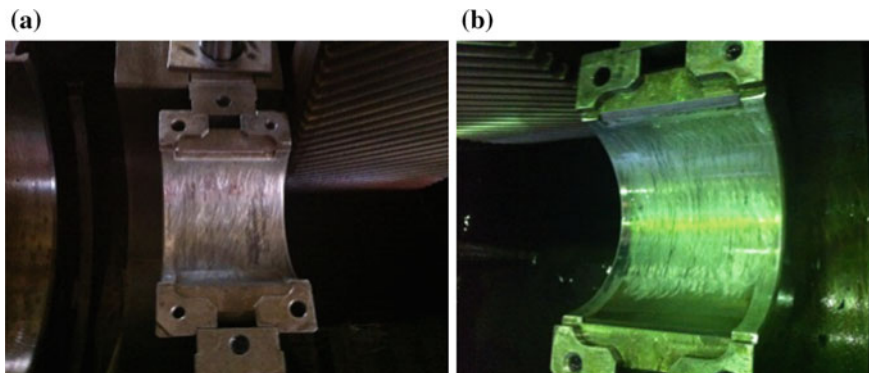


Photo 1 a Wear in the bearing 3. b Wear in the bearing 4

The modulation of these two cyclical frequencies explains the presence of generalized tooth wear on both wheels, (see Fig. 10a). The application of *IMID* allowed to highlight, by a very clear and visible way, the both cyclic frequencies and its modulations, (see Fig. 10b).

There is also the appearance of a carrier frequency at 1196 Hz, which corresponds to the passage frequency of fixed blades sets and the fifth and sixth harmonics at 5980 and 7176 Hz respectively. These two latter frequencies correspond to the passage frequencies of wheel blades 1 and 2 of the turbine, (see Fig. 10a).

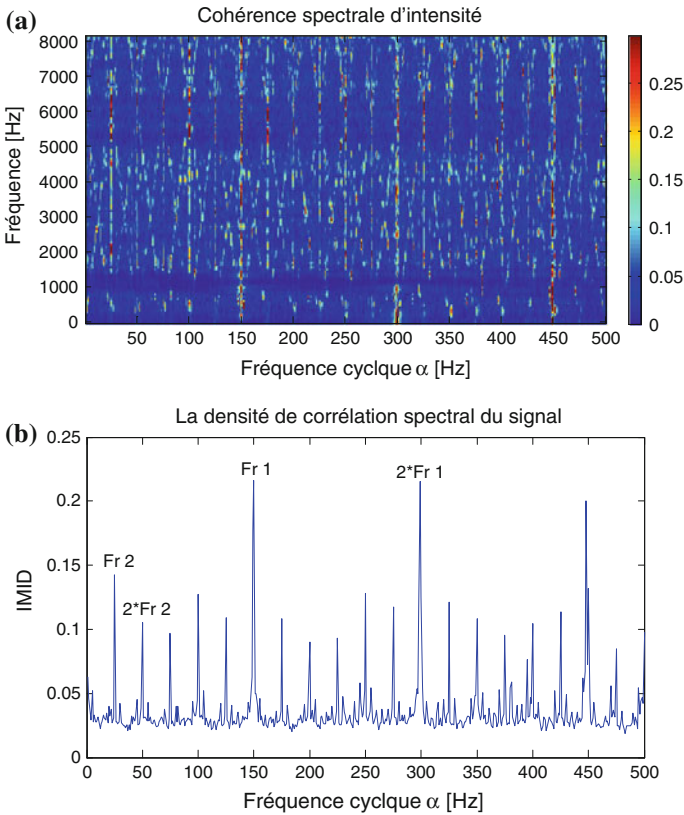


Fig. 10 a Spectral correlation (MID) with the corresponding (IMID) (b) of the signal of Fig. 5

8 Conclusions

In this work, we have shown that diagnosis turbo generator by conventional signal processing methods showed limitations in identifying defects that appear base frequency. To remedy this problem, we used the method of cyclostationarity that has a great location modulations power present in the non-stationary signals.

Any time the spectral analysis was used to identify the defects of wear on the teeth of two toothed wheels of the gear by the appearance of a large number of peaks corresponding to two frequencies of rotations of the input and output shafts the gear in addition to the meshing frequency and its harmonics. It also showed the clear appearance of the pass frequency of the fixed assemblies of *FPEFA* blades where their amplitudes have been heavily influenced by the decrease in the electrical load. Unfortunately, spectral analysis failed to locate defects in plain bearings.

References

1. Boulenger, A., Pachaud, C., et al.: Vibratory diagnosis in maintenance préventive, pp. 239–295. Dunod, Paris (1998) ISBN 2100041053
2. Heng, J.: Practical of the preventive maintenance, 1st edn. Mechanics-Tire-Hydraulics-Electricity-cold. Dunod, Paris (2002)
3. Heng, J.: Practical of the preventive maintenance, 3rd edn. Mechanics-Tire-Hydraulics-Electricity-Cold. Dunod, Paris (2005)
4. Muller, A.: Contribution to the proactive maintenance of manufacturing system: formalisation of the prognosis process. Ph.D. Thesis, IAEM & Lorraine University. Henri Poincare (2005)
5. Heng, J.: Practical of the preventive maintenance, 3rd edn. Mechanics Tire-Hydraulics-Electricity-cold. Dunod, Paris (2011)
6. Estoque, P.: A methodological approach numerical and experimental support for the detection and monitoring of vibration fault chipping ball bearing. Ph.D. Thesis, University of Lille (2004)
7. Antoni, J.: Cyclostationarity by examples. *Mech. Syst. Sig. Process.* **23**, 987–1036 (2009)
8. Boustany, R., Antoni, J.: A subspace method for the blind extraction of a cyclostationarity source: application to rolling element bearing diagnostics. *Mech. Syst. Sig. Process.* **19**, 1245–1259 (2005)
9. Urbanek, J., Barszcz, T., Zimroz, R., Antoni, J.: Application of averaged instantaneous power spectrum for diagnostics of machinery operating under non-stationary operational conditions. *Measurement* **45**, 1782–1791 (2012)
10. Urbanek, J., Barszcz, T., Sawalhi, N., Randall, R.B.: Comparison of amplitude based and phase based methods for speed tracking in application to wind turbines. *Metrol. Measur. Syst.* **XVIII**(2) (2011)
11. Gellermann, T.: Requirements for condition monitoring systems for wind turbines. AZT Expertentage, 10-11.11.2003, Allianz (2003)
12. Antoni, J.: Cyclic spectral analysis of rolling-element bearing signals: facts and fictions. *Sound Vib* **304**, 497–529 (2007)
13. Gardner, W.A., Spooner, C.M.: Cyclic spectral analysis for signal detection and modulation recognition. In: *Proceedings—IEEE Military Communications Conference*, vol. 2, pp. 419–424 (1988)

14. Makowski, R., Zimroz, R.: Adaptive bearings vibration modeling for diagnosis. *Lect. Notes Artif. Intell.* **943**, 248–259 (2011)
15. Randall, R.B., Antoni, J.: Rolling element bearing diagnostics—a tutorial. *Mech. Syst. Sig. Process.* **25**(2), 485–520 (2011)
16. Antoni, J., Bonnardot, F., Raad, A., El Badaoui, M.: Cyclostationary modelling of rotating machine vibration signals. *Mech. Syst. Sig. Process.* **18**(6), 1285–1314 (2004)
17. Taher, F., Fakher, C., Mohamed, H.: Numerical and experimental analysis of a gear system with teeth defects. *Int. J. Adv. Manuf. Technol.* **71**, 809–816 (2005)
18. D'Elia, G., Delvecchio, S., Cocconcelli, M., Dalpiaz, G.L.: Combining blind separation and cyclostationarity techniques for monitoring distributed wear in gearbox rolling bearings. In: *Proc. of surveillance, Compiegne, France* (2011)
19. Urbanek, J., Barszcz, T., Antoni, J.: Time–frequency approach to extraction of selected second-order cyclostationary vibration components for varying operational conditions. *Measurement* **46**, 1454–1463 (2013)
20. Bonnardot, F., Randall, R.B., Guillet, F.: Extraction of second-order cyclostationary sources application to vibration analysis. *Mech. Syst. Sig. Process.* **19**(6), 1230–1244 (2005)
21. Technical document, group turbo-alternator GZ1164, Department maintenance FERTIAL
22. Brüel & Kjær vibro: Analyse des vibrations maintenance conditionnelle des machines tournantes. Brüel & Kjær vibro copyright 0906 v.1-B site www.bkvibro.com (2005)
23. Roger, B., Antoni, J.: A subspace methode for the blind extraction of a cyclostationary source: Application to rolling element bearing diagnostics. *Mech. Syst. Sig. Process.* **19**, 1245–1259 (2005)
24. Urbanek, J., Barszcz, T., Zimroz, R., Antoni, J.: Integrated modulation intensity distribution as a practical tool for condition monitoring. *Appl. Acoust.* **77**, 184–194 (2014)
25. Presentation of the standard ISO 2372, (1974) International standard ISO 10816 (1995) replaces the standard ISO 2372

Experimental Study of Real Gear Transmission Defects Using Sound Perception

Nouredine Ouelaa, Ramdane Younes, Nacer Hamzaoui
and Abderrazek Djebala

Abstract The aim of this paper is to study gear defects able to appear on rotating machines using sound perception. To assimilate a real gear defect, the experimental setup was left operating under given load during several days. Measurements have been taken each 2 h on the input and output shafts. Acoustic sounds are performed using the processing software «DynamX V.7». These sounds are analyzed with the paired comparison method to find a correlation between the sounds perception and the scalar indicators. The results show that perception tests allowed classifying gear defect sounds in degradation order. The correlation between objective and subjective aspects highlights an important relationship between scalar indicators (kurtosis, Crest Factor, the spectral center of gravity SCG and the root mean square RMS) and the difference between gear sounds characterized by the sounds distance in the proximity space. Vibratory analysis is also performed to follow up the gear degradation state and to confirm sound perception results obtained from the proposed approach.

Keywords Sound perception · Real gear defects · Classifying gear defect · Scalar indicators

N. Ouelaa (✉) · R. Younes · A. Djebala
Mechanics and Structures Laboratory, University of Guelma, B.P. 401, Guelma, Algeria
e-mail: n_ouelaa@yahoo.fr

R. Younes
e-mail: ramdane_ys@yahoo.com

A. Djebala
e-mail: djebala_abderrazek@yahoo.com

N. Hamzaoui
Laboratory of Vibration-Acoustics, INSA of Lyon, Bâtiment A. St. Exupéry,
25 bis Avenue Jean Capelle, 69621 Villeurbanne Cedex, France
e-mail: nacer.hamzaoui@insa-lyon.fr

1 Introduction

The monitoring and the diagnosis of the defects of rotating machines belong to the programs of conditional maintenance, and are 75 % based on vibration analysis. Regarding the procedures of maintenance, one can classify the stages of intervention in two levels:

- the first level devoted to the monitoring, uses scalar indicators (total level, Peak factor, Kurtosis, Factor K , etc.) to announce the defect presence,
- the second level characterized by the diagnosis, intervenes after the stage of monitoring and uses much more detailed indicators (Spectrum, Zoom, Envelope, Cepstrum, etc.), in order to more precisely locate the nature and the position of the defect.

The use of these indicators still encounters some difficulties of interpretation in the case of complex industrial machines which have several defects. Many researchers still work on the improvement or the development of the indicators resulting from vibratory or acoustic signals. The experience feedback is based mainly on the competence of the maintenance man and especially to acoustical and vibratory perception related to mechanical defects. We use an acoustic approach of perception in order to propose an optimization of the indicators of monitoring to improve detection of the defects.

The perceptive approach of sounds has been used in several domains; for example in automobile for the study of the sounds produced by the air conditioning systems, and in railways for the perception of the interior noise in a high-speed train, to improve comfort to meet the consumers' expectations [1, 2]. Many researchers investigated the comparison of the listening tests and explain the benefits of the paired comparison method [3]. Other researchers studied a serious problem in the paired comparison method; it is the important listening tests duration when the number of stimuli is rather large which lead to auditive fatigue. The search for a test allowing the evaluation of a great stimuli number leads adapting a new method inspired from the visual perception called comparison with reference method, the task consists to assess the similarity of a stimuli group compared to a reference [4].

2 Multidimensional Scaling Method

The multidimensional scaling analysis is a technique used to represent an ensemble of similarities between items as points in a Euclidean space. In our case the items are sounds, and the proximity between the sounds is evaluated using dissimilarity judgments. The principle of this analysis is to match the measured dissimilarities between stimuli distances between points representing these stimuli in a Euclidean

space. The dimensions of this space are continuous, i.e. all stimuli may be classified according to these dimensions.

There exist many algorithms, starting from the distances between objects that allow determining the coordinates of these last in a space. Some of these algorithms allow taking into account specificities of the various subjects or groups of subjects of the various stimuli, even of both of them at the same time.

3 INDSCAL Algorithm

The Multidimensional Scaling algorithms used in the literature are: Winsberg et al. [5], Winsberg et al. [6], Koehl [7], Torgerson [8], and INDSCAL. In this article the INDSCAL algorithm is considered for the results processing. INDSCAL Algorithm (INDividual Differences SCALing) was proposed by Carroll and Chang (Carroll et al. [9]) and allows, unlike MDSCAL, to allot for each subject a different scale. Like MDSCAL, it assumes that all the listeners use the same dimensions but not with the same weighing. These weightings appear in the Eq. (1) in the form of W_{kr} factor representing the weight which the listener k allots to perceptive dimension R of perceptive space.

$$d_{ij,k} = \left[\sum_{r=1}^R W_{kr} (X_{ir} - X_{jr})^2 \right]^{\frac{1}{2}} \quad (1)$$

where $d_{ij,k}$ is the distance between the objects i and j according to subject k . X_{jr} and X_{ir} are the coordinates of these objects on the dimension R of the perceptual space.

4 Experimental Setup

4.1 Test Rig

In order to be closer with real gear defects, an experimental setup has been designed in the vibration-acoustic laboratory of the INSA of Lyon- France. The test rig contains two gear transmissions normally lubricated. The first transmission consists of a pinion of 42 teeth mounted in the input shaft and a wheel of 50 teeth. The second transmission consists of a wheel of 65 teeth and a pinion of 45 teeth mounted in the output shaft. The test rig contains also a brake to simulate a variable load.

Fig. 1 Gears photos: **a** with defect, **b** without defect



4.2 Experiments Conduct

To simulate real gear defects, the setup is left operating under load during several days. Vibratory acceleration signals have been measured on the input and output shafts each 2 h. When transmissions are enclosed in a casing, like in the case of a gearbox, the radiated noise is mainly due to the vibrations of this one [10], that why we have used Dynae IEPE (Integral Electronic PiezoElectric) accelerometers with sensitivity of 100 mV/g for signals acquisition. Vibration signals are then directly converted to acoustic sounds using the Dynam X software. These sounds are analyzed by sound perception tests. The following figures present photos of healthy gears (Fig. 1a), and damaged gears (Fig. 1b).

5 Sound Perception Tests

5.1 Stimuli

At the end of the experience we visually noted the appearance of a generalized wear on all the pinions teeth mounted on the input and the intermediate shafts. This observation confirms the vibratory analysis results reported previously.

Among the 46 measured sounds, a first selection based on a preliminary listening allowed selecting 8 sounds the most different between them. They will be the subject of the listening test. Note that the DynamX software allows calculating several scalar indicators, in addition of the kurtosis, such as Crest Factor (*CF*), Spectral Center of Gravity (*SCG*), Peak-to-Peak, etc.

The evaluation dissimilarities tests were carried out in an ordinary room of the mechanics and structures laboratory (*LMS*) of the University of Guelma, Algeria. The sounds restitution was done through stereo headphone. The restitution chain is composed of a PC with I5 Dell processor, tests interface under Matlab environment, and a Sennheiser *HD201* headphone.

5.2 Tests Interface and Subjects

The interface of the tests is programed in MATLAB language, it contains two phases: the first is called training phase in which the sounds are subjected to the listening of auditors. Listeners can become familiar with the sounds of running test. The second is a dissimilarity pair comparison phase. 26 listeners (11 women and 15 men), aged from 22 to 50 years, are taken to realize these two tests.

5.3 Results Analysis

We present in Table 1 the sounds coordinates in a two dimensions space (DIM_1 and DIM_2), where DIM_1 represents the evolution of the defect degradation. One note that the coordinates results are in perfect agreement with the chronology of the sounds collect, starting from sound 1 (S_1) corresponding to the case without defect until sound 8 (S_8) corresponding to the more degraded gear.

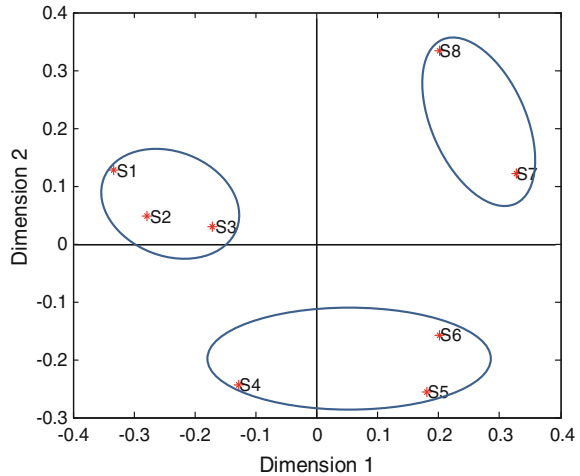
5.4 Proximity Space

Despite the low wear that appeared on the tested gears teeth, perception tests allowed to classify the sounds in degradation order from least degraded sound (S_1) to the most degraded sound (S_8) (see Fig. 2). S_1 is measured at the test beginning

Table 1 Sounds coordinates in two dimensions perceptual space

Sounds	Dim ₁	Dim ₂
S ₁	-0.333	0.127
S ₂	-0.279	0.047
S ₃	-0.171	0.029
S ₄	-0.128	-0.244
S ₅	0.181	-0.256
S ₆	0.201	-0.159
S ₇	0.327	0.122
S ₈	0.202	0.333

Fig. 2 Perceptual space



(healthy teeth case), S_2 is measured after approximately 4 operating hours, and then S_3 is measured at the end of the first day. The listeners classified the three sounds in the first quarter of the sounds proximity space, corresponding to similar sounds (close severity). Sounds S_4 , S_5 and S_6 are measured during the second day of operation at different time intervals. Listeners have classified S_4 in the second quarter of proximity space. The shock caused by the teeth degradation is perceived by the listeners and confirmed by kurtosis values, which passes from 6.6 for S_3 to 9.6 for S_4 . For S_5 and S_6 the teeth degradation becomes more important (wear phenomenon thus low kurtosis [11]), the listeners classified these two sounds in the third quarter of the proximity space corresponding to sounds different to the initial state S_1 . Finally the sounds S_7 and S_8 , measured during the third day, are classified in the fourth quarter of the proximity space corresponding to sounds very different compared to S_1 .

5.5 Correlations Between Scalar Indicators and Dimensions

Since these dimensions perfectly describe the sound dispersion in the proximity space, and in order to relate the vibration indicators to acoustic perception, we look for a correlation between this dispersion and the calculated scalar indicators: Kurtosis K , Crest Factor CF , Spectral Center of Gravity SCG , RMS , Peak-to-Peak, overall level OL , the peak value and the K-factor. So the dimensions of this space will be a linear function of different indicators.

To this end we conducted an ascending linear regression, having for entry the vibratory indicators. Selected dimension will be that which presents the best score of similarity, so a better alignment of clouds point on the regression line.

The correlation between these dimensions and the metric scalar indicators used previously gives a dimensions 2 is correlated with the:

- kurtosis and the crest factor with a correlation coefficient $R_2 = 0.95$,
- spectral centre of gravity and *RMS* with a correlation coefficient $R_2 = 0.96$.

6 Conclusion

The objective of this article is the application of the sound perception approach in the study and the detection of teeth gears defects. First, vibratory analysis is carried out to follow up the degradation state of the tested gears. Perceptual study based on the paired comparison and the *MDS* methods is carried out to study gear's sounds for different degradation levels. This study allowed identifying the vibration parameters for establishing a vibro-acoustic relationship in rotating machinery namely gears transmission.

The obtained results in this work showed that:

- The proposed sounds selection method, based on the kurtosis values, gives more important correlation coefficient than those obtained by listening methods mentioned in the literature.
- Perception tests allowed classifying the sounds in degradation order from least degraded sound R_a to the most degraded sound S_8 .
- The correlations between the objective and subjective aspects helped to highlight the important relationship between the vibration indicators and the distances between gear sounds in proximity space.
- Scalar indicators: kurtosis, Crest Factor, the *SCG* and the *RMS* factors best explains the preference judgments for gear's sounds in the case of a real defect.

References

1. Vincent, H.: Etude de la qualité sonore d'appareils de soufflage et de climatisation. M. Sc Thesis, Pierre & Marie Curie University, Paris (2005)
2. Parizet, E., Hamzaoui, N., Jacquemoud, J.: Noise assessment in a high-speed train. *Appl. Acoust.* **63**, 1109–1124 (2002)
3. Parizet, E., Hamzaoui, N., Sabatie, G.: Comparison of some listening test methods: a case study. *Acta Acust United Ac* **91**, 356–364 (2005)
4. Michaud, P.Y., Meunier, S., Herzog, P., Aubigny, GD, Lavandier, M.: Méthode de test adaptée à l'évaluation perceptive d'un grand nombre de stimuli audio Application aux enceintes acoustiques. In: 10th French congress of Acoustics, CFA2010. Lyon, France (2010)
5. Winsberg, S., Carroll, J.D.: A quasi-nonmetric method to multidimensional scaling via an extended euclidean model. *Psychometrika* **54**, 217–229 (1989)
6. Winsberg, S., De Soete, G.: A latent class approach to fitting the weighted euclidean model. *CLASCAL. Psychometrika* **58**(2), 315–330 (1993)

7. Koehl, V.: Influence of structure dispersions on sound perception. Ph.D. Thesis, INSA of Lyon. France (2005)
8. Torgerson, W.S.: Multidimensional scaling: I. theory and method. *Psychometrika* **17**(4), 401–419 (1952)
9. Carroll, J.D., Chang, J.J.: Analysis of individual differences in multidimensional scaling via an n-way generalization of “eckart-young” decomposition. *Psychometrika* **35**, 283–319 (1970)
10. Reboul, E.: Vibroacoustique of high frequencies mechanisms: application to gears transmissions. Ph.D., Thesis Central School of Lyon. France (2005)
11. Djebala, A.: Application of the wavelet transform to the study and the vibratory analysis of the mechanical systems. Ph.D. Thesis, Badji Mokhtar University, Annaba, Algeria (2008)

Taguchi Design of Experiments for Optimization and Modeling of Surface Roughness When Dry Turning X210Cr12 Steel

Oussama Zerti, Mohamed Athmane Yallese, Salim Belhadi and Lakhdar Bouzid

Abstract The surface roughness is a widely used index of product quality in terms of precision fit of mating surfaces, fatigue life improvement, corrosion resistance, aesthetics, etc. This paper presents an approach for determining the optimum machining parameters leading to minimum surface roughness by Taguchi method. The turning operations were performed based on the Taguchi design of experiment method using $L_{18}(2^1 \times 3^4)$ a mixed orthogonal array. The signal to noise ratio (S/N) based on the “smaller-is-the better” approach was calculated to determine the optimum levels of the machining parameters. The results of optimization showed that the best surface roughness is obtained by using small feed rate and large nose radius. The application of the analysis of variance (ANOVA) is used to study the effects of the machining parameters on the surface roughness. The results of this study indicate that the feed rate (f) and the nose radius (r) have the most significant effect followed by the interaction (f × ap) on surface roughness. Mathematical models in function of machining parameters and these interactions were developed by regression analysis for the prediction of surface roughness. The results obtained have shown that the Taguchi method is very reliable in optimizing the machining parameters for improved surface roughness.

Keywords Optimization · Modeling · Taguchi method · Surface roughness · S/N ratio · ANOVA

O. Zerti (✉) · M.A. Yallese · S. Belhadi · L. Bouzid
Mechanics and Structures Research Laboratory (LMS), May 8th 1945 University of Guelma,
P.O. Box 401, Guelma 24000, Algeria
e-mail: oussama_zerti@yahoo.fr

M.A. Yallese
e-mail: yallese.m@gmail.com

S. Belhadi
e-mail: belhadi23@yahoo.fr

L. Bouzid
e-mail: issam.bouzid@yahoo.fr

1 Introduction

The surface quality of machined parts is one of the most important indicators of the quality of products and one of the requirements of the most frequent guests. It is a key factor in assessing the quality of a product and has a great influence on the functional behavior of parts machined operations and manufacturing costs. The desired surface quality is a major constraint in the choice of the optimum of the cutting conditions and the tool geometry in the production process. It also influences the tribological characteristics, fatigue resistance, the corrosion resistance and aesthetic appearance of the machined parts. During machining it is mainly influenced by the feed rate, the cutting speed, the tool geometry, the material characteristics, the stability and the rigidity of the machine tool, the cutting tool, fluid cut etc. In another hand, quantify the relationship between surface roughness and machining parameters is a very important task for the estimation of responses.

A numerous researches were carried out to modeling and optimization of cutting conditions and tool geometry to obtain minimum surface roughness. Nalbant et al. [1] used the Taguchi method in the optimization of cutting parameters (f , ap , t) when the turning *AISI1030* steel by carbide inserts coated with TiN. They found from the analysis of variance (*ANOVA*) as the tool nose radius and the feed rate have a great influence on the surface roughness with a contribution of 48.54 and 46.95 % respectively. The authors recommended that the use of a large nose radius and a small feed rate and depth of cut gives a better roughness. In the work of Süleyman Neşçeli et al. [2], the tool geometry (r , χr , γ) was optimized when turning *AISI1040* steel by the response surface methodology (*RSM*). They developed a mathematical prediction model related to the surface roughness (R_a). From the *ANOVA* table the authors found that the tool nose radius is the most important factor that influences the surface roughness with a contribution of 51.45 %. In addition, the major cutting edge angle and the inclination angle are significant factors on the surface roughness with a contribution of 18.24 and 17.74 % respectively. In addition of the cutting conditions (V_c, f, ap), Emre Yucel et al. [3] considered cutting materials in his study as a variable factor for investigate their influence on the surface roughness (R_a) and the cutting force (F_c) during turning on the cast Ni-Hard. They applied the Taguchi method to determine the optimal levels by calculating the ratio (S/N) for (R_a) and (F_c) by the approach 'the smaller, the better'. They found after the *ANOVA* table that the depth of cut is the significant factor on the cutting force with a contribution of 74.5 % and the feed rate has a very important effect on the surface roughness with a contribution of 75.78 %. Ashoc and Swastik [4] selected the optimal values of cutting conditions (V_c, f, ap) by Taguchi approach to minimize the surface roughness (R_a) and flank wear (VBC) during dry turning on composite metal matrix (*Al/SiCp*). The same technique was used by Ilhan and Harun [5] to optimize cutting conditions when hard turning of *4140* steel (*51HRC*) for obtained minimum roughness criterions (R_a) and (R_z). They observed that the feed rate has the most significant effect on R_a and R_z . Similarly, Yang and Tarn [6] chosed the optimal cutting parameters (V_c, f, ap) by the Taguchi method to reduce the roughness (R_a)

and the tool life, when turning of *S45C* steel bars using tungsten carbide cutting tools. Yaltese et al. [7] predicted the effect of feed rate on surface roughness by a power model deduced from experimental data and compared it with a theoretical model in turning of *X210Cr12* steel. Horng et al. [8] interested by the effect of tool nose radius and cutting parameters on surface roughness of Hadfield steel hard turned with mixed ceramic insert. The *ANOVA* revealed that the cutting speed and the tool nose radius influenced significantly the surface roughness.

2 Optimization of Taguchi

Quality engineering method known as Taguchi method is an experimental strategy in which Taguchi created a number of special orthogonal arrays; the main idea is to focus only on some experiences that are essential for the analysis. He introduced the use of the signal to noise ratio (*S/N*) to measure the quality of results. The *S/N* ratio is defined as the desired signal relative to the undesired random noise value and has the characteristics of quality of experimental data. There are three categories of performance characteristic analysis in the *S/N* ratio which are: Nominal is the best, Larger-is-the better, Smaller-is-the better. For each of these categories, the optimal level of a process parameter is the level which results in the largest value of *S/N* ratio. The results obtained cannot be optimal, but when these results are implemented, the process is improved. Therefore, less money and time are spent when the Taguchi method is used.

The *S/N* ratio used in this work is calculated on the basis of the ‘Smaller-is-the better’ (formula 1) because the purpose of this experiment is to find the cutting parameters that minimize the surface roughness.

$$\frac{S}{N} = -10 \log\left(\frac{1}{n} \sum_{i=1}^n y_i^2\right) \quad (1)$$

where y_i are the results observed in the experiments and n is the number of trials. The use of the Taguchi method to optimize a cutting process comprises the following steps [1]:

- Identify performance characteristics and select process parameters to evaluate.
- Determine the number of levels to the process parameters and possible interactions between process parameters.
- Select the appropriate orthogonal array and complete the process parameters in this table.
- Carry out the experiments based on the order of the orthogonal array.
- Calculate the *S/N* ratio.
- Analyze experimental results by using the *S/N* ratio and *ANOVA*.
- Select the optimum levels of process parameters.
- Check optimum process parameters through the confirmation experience.

3 Experimental Procedure

In this study a conventional lathe of check company “TOS TRENCIN” *SN40* model, with a power of 6.6 KW on the spindle was used for carrying out the turning operations in dry working conditions. These operations were performed on a round work-piece *X210Cr12* steel, of diameter 70 mm and length 400 mm. Due to its high wear resistance, the steel *X210Cr12* (afnor *X200Cr12*) also known under the name of *AISI D3* steel with a high chromium tool with minimum risk of deformation and alteration of the dimensions thermal treatment. It has excellent wear resistance (high wear resistance), used for the manufacture of dies and cutting punches and stamping, profilers shingle, wheels, woodworking tools, roll comb, nets [9]. The chemical composition of the *X210Cr12* steel is as follows 2 %C, 0.30 %Mn, 0.25 %Si, 12 %Cr, 0.70 %W. All turning operations were made by three mixed ceramic inserts *CC650* Sandvik Coromant with chemical composition $Al_2O_3(70\%) + TiC(30\%)$. Each insert is characterized by a nose radius $r = 0.80, 0.12, 0.16$ mm, with geometric designation; *SNGA120408T01020*, *SNGA120412T01020*, *SNGA120416T01020* respectively. These are removable, square form with mechanical fixation by central hole and each has eight cutting edges. They are mainly recommended for finish machining of hardened steels and refractory super-alloys, requiring good wear resistance combined with good thermal properties. Figure 1 illustrates the cutting inserts with different nose radius.

Two tool holders are used, in which the inserts are fixed mechanically with central hole. Their geometry of the active part is the same for the following angles: $\alpha = 6, \gamma = -6$ and $\lambda = -6$, but it differs for the angle: $\chi_r = 45^\circ$ and 75° respectively. Measuring roughness criteria (R_a, R_z, R_t) was performed using a *2D* Surf-roughness test *SJ-201* (Mitutoyo). The measurements were repeated at three equally spaced locations around the circumference of the work-piece and the result is an average of these values for a given machining pass. Figure 2 shows the method of measuring roughness criteria. To study the impact of various cutting parameters (V_c, f, ap) and tool geometry (χ_r, r) on the surface roughness, we chose a mixed factorial Taguchi design L_{18} as experimental design with 5 factors. Factors (V_c, f, ap, r) varies at three levels (3^4) and the factor (χ_r) varies at two levels (2^1).

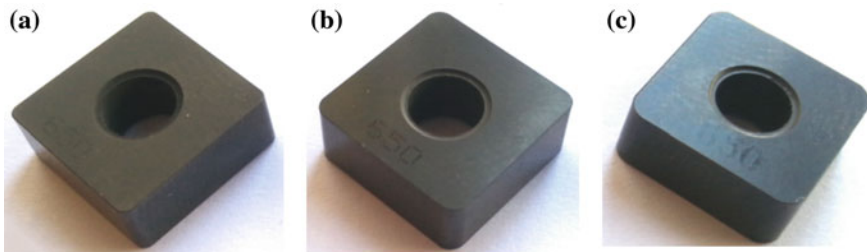


Fig. 1 Mixed ceramic cutting inserts CC650. **a** $r = 0.8$ mm, **b** $r = 1.2$ mm and **c** $r = 1.6$ mm

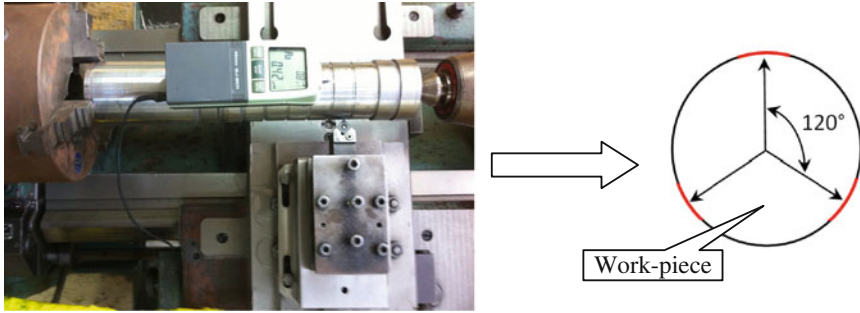


Fig. 2 Method of measurement of roughness criteria (Ra , Rz and Rt)

Table 1 Factors and their levels

Levels	χ_r (°)	r (mm)	Vc (m/min)	f (mm/rev)	ap (mm)
1	45	0.8	220	0.08	0.15
2	75	1.2	307	0.12	0.3
3	–	1.6	440	0.16	0.45

The parameter levels were chosen in the intervals recommended by the manufacturer of cutting tool. The parameters to be studied and respective levels attribution are shown in Table 1.

4 Results and Discussion

Roughness criteria values showed in Table 2 were obtained following the different combinations of cutting parameters levels. Formula (1) was used to calculate the S/N ratio for each criterion which aims to minimize the surface roughness.

4.1 Analysis of Variance (ANOVA)

The results of the ANOVA analysis of S/N ratios corresponds to the criteria roughness (Ra , Rz , Rt) are reported in Tables 3, 4 and 5 respectively. This analysis is performed to a level of significance $\alpha = 0.05$ (i.e. for a confidence level of 95 %). This analysis classifies the machining parameters in order of influence on various roughness criteria. It can be seen that the feed rate comes in the first position of influence on surface roughness; because its increase generates a grooves resulting from machining kinetics which are parallel to the cutting speed direction. These grooves are deeper and broader as the feed rate increases; with a contribution of 50.22 % on Ra , 39.53 % on Rz and 40.24 % on Rt . This is a good agreement with the previous research work of Ilhan and Harun [5]. The tool nose radius comes in second position with an impact of 20.26 % on Ra , 36.52 % on Rz , and 31.46 % on

Table 2 Results of the roughness criteria in function of cutting parameters

Trials no.	χ_r (°)	r (mm)	V_c (m/min)	f (mm/rev)	ap (mm)	Ra (μm)	S/N (dB)	Rz (μm)	S/N (dB)	Rt (μm)	S/N (dB)
1	45	0.8	220	0.08	0.15	0.47	6.55	2.83	-9.02	3.02	-9.59
2	45	0.8	307	0.12	0.3	0.59	4.63	3.85	-11.70	4.20	-12.45
3	45	0.8	440	0.16	0.45	0.63	3.96	3.93	-11.88	4.57	-13.20
4	45	1.2	220	0.08	0.3	0.43	7.26	2.46	-7.80	2.72	-8.70
5	45	1.2	307	0.12	0.45	0.55	5.14	2.86	-9.12	3.07	-9.74
6	45	1.2	440	0.16	0.15	0.78	2.19	4.01	-12.05	4.34	-12.74
7	45	1.6	220	0.12	0.15	0.39	8.10	2.47	-7.86	2.72	-8.69
8	45	1.6	307	0.16	0.3	0.57	4.83	3.36	-10.53	3.79	-11.57
9	45	1.6	440	0.08	0.45	0.40	8.03	2.62	-8.35	3.19	-10.07
10	75	0.8	220	0.16	0.45	1.01	-0.08	4.54	-13.14	4.89	-13.78
11	75	0.8	307	0.08	0.15	0.43	7.39	3.09	-9.80	3.42	-10.68
12	75	0.8	440	0.12	0.3	0.65	3.69	3.85	-11.70	4.25	-12.57
13	75	1.2	220	0.12	0.45	0.39	8.17	2.36	-7.45	2.68	-8.56
14	75	1.2	307	0.16	0.15	0.54	5.35	3.16	-9.98	3.60	-11.11
15	75	1.2	440	0.08	0.3	0.33	9.71	2.34	-7.39	2.58	-8.22
16	75	1.6	220	0.16	0.3	0.51	5.79	2.86	-9.11	3.16	-10
17	75	1.6	307	0.08	0.45	0.41	7.74	2.38	-7.51	2.68	-8.55
18	75	1.6	440	0.12	0.15	0.43	7.33	2.43	-7.72	2.73	-8.71

Table 3 Analysis of variance for *S/N* of *Ra*

Source	DF	SS	MS	F-value	Cont %
<i>Xr</i>	1	1.0755	1.0755	116.9	1.06
<i>r</i>	1	20.4583	20.4583	2223.73	20.26
<i>Vc</i>	1	0.0569	0.0569	6.18	0.04
<i>f</i>	1	50.6817	50.6817	5508.88	50.22
<i>ap</i>	1	1.3091	1.3091	142.29	1.28
$\chi r \times r$	1	1.3651	1.3651	148.38	1.34
$\chi r \times Vc$	1	0.0179	0.0179	1.95	0.009
$\chi r \times f$	1	1.1715	1.1715	127.34	1.15
$\chi r \times ap$	1	3.8569	3.8569	419.23	3.81
$r \times Vc$	1	2.7503	2.7503	298.95	2.72
$r \times f$	1	0.1536	0.1536	16.7	0.14
$r \times ap$	1	2.9522	2.9522	320.89	2.92
$Vc \times f$	1	0.3393	0.3393	36.88	0.32
$Vc \times ap$	1	1.9258	1.9258	209.33	1.9
$f \times ap$	1	12.8056	12.8056	1391.91	12.68
Error	2	0.0183	0.0092		0.009
Total	17	100.938			100

Table 4 Analysis of variance for *S/N* of *Rz*

Source	DF	SS	MS	F-value	Cont %
χr	1	1.13	1.13	1.52	1.90
<i>r</i>	1	21.75	21.75	29.39	36.52
<i>Vc</i>	1	1.62	1.62	2.18	2.72
<i>f</i>	1	23.55	23.55	31.82	39.53
<i>ap</i>	1	0.09	0.09	0.12	0.15
$\chi r \times r$	1	1.63	1.63	2.20	2.74
$\chi r \times Vc$	1	0.40	0.40	0.54	0.67
$\chi r \times f$	1	0.01	0.01	0.01	0.01
$\chi r \times ap$	1	0.60	0.60	0.81	1.00
$r \times Vc$	1	0.25	0.25	0.33	0.42
$r \times f$	1	0.00	0.00	0.00	0.00
$r \times ap$	1	1.76	1.76	2.37	2.96
$Vc \times f$	1	0.58	0.58	0.78	0.97
$Vc \times ap$	1	0.18	0.18	0.24	0.30
$f \times ap$	1	4.55	4.55	6.14	7.64
Error	2	1.47	0.74		2.47
Total	17	59.57			100

Rt. Similarly, Makadia and Nanavati [10] found that the feed rate is the main factor followed by tool nose radius influences the surface roughness. The interaction $f \times ap$ comes in third position with effect of 12.68 % on *Ra*, 7.64 % on *Rz*, and 5.58 % on *Rt*.

Table 5 Analysis of variance for S/N of R_t

Source	DF	SS	MS	F-value	Cont %
χr	1	1.16	1.16	0.9	2.04
r	1	17.97	17.97	14.03	31.46
V_c	1	2.92	2.92	2.28	5.12
f	1	22.99	22.99	17.96	40.24
ap	1	0.47	0.47	0.36	0.83
$\chi r \times r$	1	1.96	1.96	1.53	3.45
$\chi r \times V_c$	1	1.01	1.01	0.78	1.77
$\chi r \times f$	1	0.11	0.11	0.08	0.20
$\chi r \times ap$	1	0.22	0.22	0.17	0.40
$r \times V_c$	1	0.1	0.1	0.07	0.17
$r \times f$	1	0.03	0.03	0.02	0.06
$r \times ap$	1	1.85	1.85	1.44	3.25
$V_c \times f$	1	0.40	0.40	0.31	0.70
$V_c \times ap$	1	0.002	0.002	0.001	0.00
$f \times ap$	1	3.33	3.33	2.6	5.83
Error	2	2.56	1.28		4.48
Total	17	57.14			100

4.2 Regression Analysis

Regression analysis is used for modeling and analysis of multivariate where there is a relationship between the dependent variable and one or more independent variables. In this study, the dependent variables are the criteria for surface roughness (R_a , R_z , R_t), while the independent variables are the Major cutting edge angle (χr), the tool nose radius (r), cutting speed (V_c), feed rate (f) and depth of cut (ap). The predictive equations of R_a , R_z and R_t in function of the cutting conditions, tool geometry and these interactions of which were obtained by the multiple linear regression model of the surface roughness are given below with respective coefficients of determination R^2 of 99.72; 97.47 and 95.63 %. Figure 3 shows the comparison between the predicted and measured values of surface roughness criteria, R_a , R_z and R_t . The predicted values of the surface roughness criteria are closer to those readings recorded experimentally; we notice a superposition between the measurement values and estimated. Therefore, the obtained response equation can be used to successfully forecast the surface roughness values for any combination of the cutting parameters within the range of the performed experimentation.

$$\begin{aligned}
 Ra = & -0.751523 - 0.0390656 \cdot \chi r + 2.11283 \cdot r + 0.00839753 \cdot V_c \\
 & + 20.5609 \cdot f - 9.98742 \cdot ap - 0.00225299 \cdot \chi r \cdot r + 5.98103 \cdot \chi r \cdot V_c \\
 & + 0.116648 \cdot \chi r \cdot f + 0.00051299 \cdot \chi r \cdot ap - 0.00318008 \cdot r \cdot V_c \\
 & - 23.6922 \cdot r \cdot f + 6.56501 \cdot r \cdot ap - 0.0255462 \cdot V_c \cdot f \\
 & - 0.0163664 \cdot V_c \cdot ap + 53.2321 \cdot f \cdot ap
 \end{aligned} \tag{2)$$

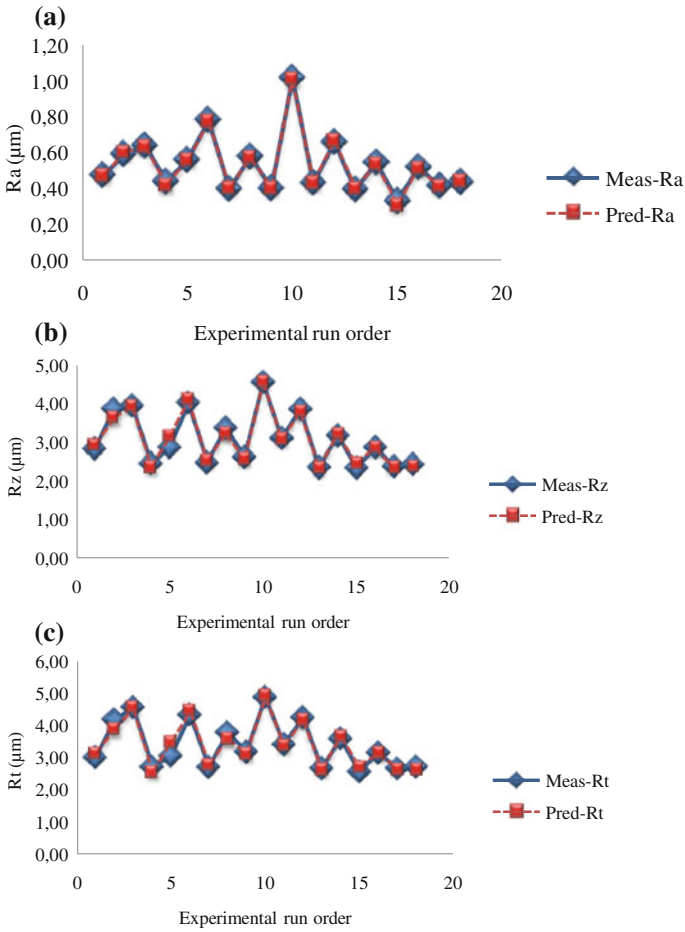


Fig. 3 Comparison between the predicted and measured values for the three surface roughness criterions

$$\begin{aligned}
 R_z = & -3.40388 - 0.105012 \cdot \chi r + 6.52961 \cdot r + 0.0337345 \cdot V_c + 95.2966 \cdot f \\
 & - 35.7346 \cdot ap - 0.00474198 \cdot \chi r \cdot r + 0.000180011 \cdot \chi r \cdot V_c \\
 & + 0.204126 \cdot \chi r \cdot f - 0.0143024 \cdot \chi r \cdot ap - 0.0122216 \cdot r \cdot V_c \\
 & + 80.1372 \cdot r \cdot f + 23.1535 \cdot r \cdot ap - 0.117315 \cdot V_c \cdot f \\
 & - 0.0489721 \cdot V_c \cdot ap + 172.507 \cdot f \cdot ap
 \end{aligned} \tag{3}$$

$$\begin{aligned}
 Rt = & -3.13886 - 0.0819587 \cdot \chi r + 6.42643 \cdot r + 0.0299867 \cdot V_c + 90.4691 \cdot f \\
 & - 35.44 \cdot ap - 0.0108477 \cdot \chi r \cdot r + 0.000147321 \cdot \chi r \cdot V_c + 0.205393 \cdot \chi r \cdot f \\
 & - 0.0204319 \cdot \chi r \cdot ap - 0.0108953 \cdot r \cdot V_c + 77.688 \cdot r \cdot f + 22.2094 \cdot r \cdot ap \\
 & - 0.0997738 \cdot V_c \cdot f - 0.040557 \cdot V_c \cdot ap + 163.399 \cdot f \cdot ap \quad ((4))
 \end{aligned}$$

4.3 Optimization of Cutting Parameters

The Taguchi method was used to determine the optimal levels of factors depending on the *S/N* ratio which is the most important criterion in this method for the analysis of experimental data. The mean values of *S/N* ratios for each level of factors are given in Tables 6, 7 and 8 for each criterion roughness (*Ra*, *Rz*, *Rt*), respectively. Figures 4, 5 and 6 also show the graph of the values given in the above tables.

Whatever the performance characteristic category the maximum value of *S/N* ratio corresponding to better performance by the Taguchi method. Consequently, the optimal level of cutting parameters that gives the best roughness is the level corresponding to the maximum value of the *S/N* ratio. Therefore, it found after Tables 6, 7, 8 and Figs. 4, 5, 6 that the optimum machining parameters to minimize roughness criteria (*Ra*, *Rz*, *Rt*) are the following: $\chi r = 75^\circ$, $r = 1.6$ mm, $V_c = 220$ m/min, $f = 0.08$ mm/rev, $ap = 0.15$ mm. Similar results were reported by Makadia and Nanavati [10], they recommended that the use of higher insert radius, low feed rate and low depth of cut provides better surface finish in turning operation.

Table 6 *S/N* response table for *Ra*

Level	χr	r	V_c	f	ap
1	5.636	4.361	5.968	7.786	6.157
2	6.125	6.308	5.85	6.181	5.989
3	–	6.973	5.823	3.675	5.496

Table 7 *S/N* response table for *Rz*

Level	χr	r	V_c	f	ap
1	–9.819	–11.21	–9.069	–8.319	–9.411
2	–9.317	–8.972	–9.781	–9.264	–9.711
3	–	–8.519	–9.853	–11.12	–9.581

Table 8 *S/N* response table for *Rt*

Level	χr	r	V_c	f	ap
1	–10.75	–12.04	–9.889	–9.304	–10.25
2	–10.24	–9.849	–10.68	–10.12	–10.58
3	–	–9.601	–10.92	–12.07	–10.65

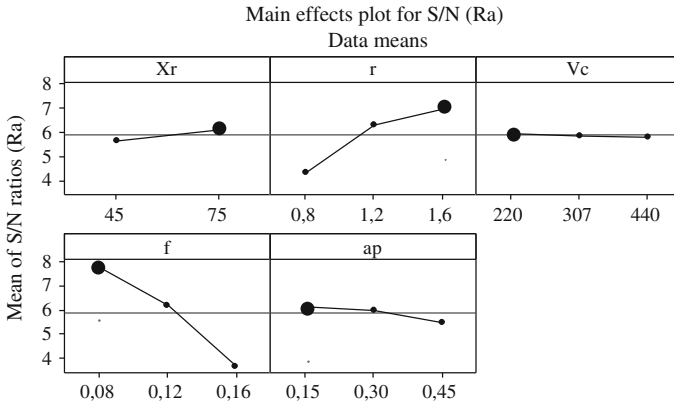


Fig. 4 Graph of the main effects of S/N for Ra

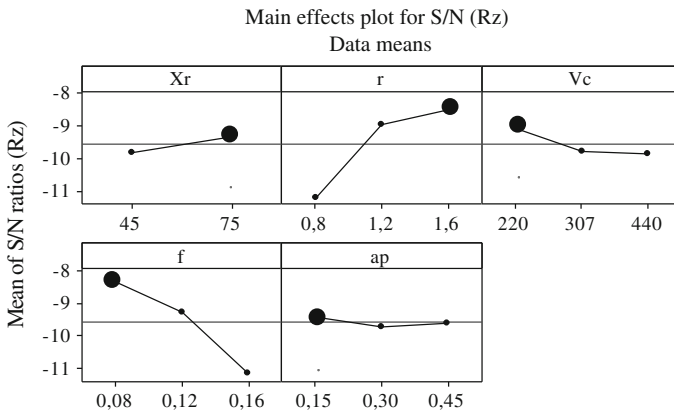


Fig. 5 Graph of the main effects of S/N for Rz

4.4 Confirmation Tests

Once the optimal level of process parameters is selected. The final step is the confirmation test which consists to carrying out an experiment with the optimal level of cutting parameters. Then the use of the formula (1) for calculating the S/N of the obtained results. The results should be compared to those predicted by the Eq. (5) [1]:

$$\hat{\eta} = \eta_m + \sum_{i=1}^q (\bar{\eta}_i - \eta_m) \tag{5}$$

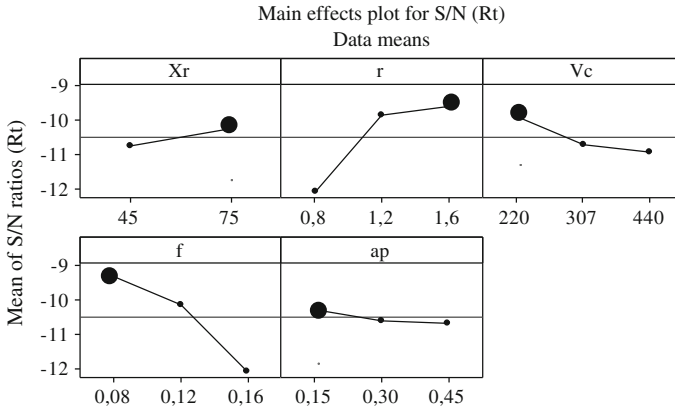


Fig. 6 Graph of the main effects of S/N for Rt

- $\hat{\eta}$ Expected value of the response in the optimum conditions
- $\bar{\eta}_i$ Average S/N ratios at the optimum level of the factors
- η_m Average sum of all test responses
- q Number of significant factors

The values of S/N ratios of the surface roughness criteria (R_a , R_z , R_t) obtained by confirmatory tests and predicted by Eq. (5) are shown in Tables 9, 10 and 11. Good agreement between the predicted machining performance and actual machining performance is shown. The increase of the S/N ratio from the initial cutting parameters to the optimal cutting parameters for criteria of roughness is as

Table 9 Experimental validation for R_a

	Initial trial	Optimal cutting parameters	
		Prediction	Experiment
Level	$\chi r2$ r2 Vc2 f2 ap2	$\chi r2$ r3 Vc1 f1 ap1	$\chi r2$ r3 Vc1 f1 ap1
Roughness criterion (R_a)	0.50	–	0.39
S/N ratio	6.02	8.88	8.17
Improvement of S/N ratio	2.15		

Table 10 Experimental validation for R_z

	Initial trial	Optimal cutting parameters	
		Prediction	Experiment
Level	$\chi r2$ r2 Vc2 f2 ap2	$\chi r2$ r3 Vc1 f1 ap1	$\chi r2$ r3 Vc1 f1 ap1
Roughness criterion (R_z)	2.84	–	2.37
S/N ratio	–9.06	–7.27	–7.49
Improvement of S/N ratio	1.57		

Table 11 Experimental validation for *Rt*

	Initial trial	Optimal cutting parameters	
		Prediction	Experiment
Level	$\chi r_2 r_2 V_{c2} f_2 ap_2$	$\chi r_2 r_3 V_{c1} f_1 ap_1$	$\chi r_2 r_3 V_{c1} f_1 ap_1$
Roughness criterion (<i>Rt</i>)	2.84	–	2.50
S/N ratio	–10.34	–8.40	–7.95
Improvement of S/N ratio	2.39		

following: 2.15 for *Ra*, 1.57 for *Rz*, 2.39 for *Rt*, which means also that the surface roughness is decreased by about 1.28 times for *Ra*, 1.19 times for *Rz*, and 1.13 times for *Rt*.

5 Conclusion

This article presented an application of the Taguchi method in the optimization of the cutting conditions and tool geometry. The following conclusions can be drawn based on the experimental results of this study:

- The statistical analysis based on the technique of ANOVA has confirmed that the feed rate (*f*) has the highest influence on the surface roughness criteria. The influences are about (50.22, 39.53, 40.24 %) for roughness *Ra*, *Rz* and *Rt* respectively. Followed by tool nose radius *r* and the interaction (*f* × *ap*) with (20.26, 12.68 %), (36.52, 7.64 %), (31.46, 5.58 %) contribution for roughness *Ra*, *Rz* and *Rt*, respectively.
- Mathematical models of *Ra*, *Rz* and *Rt* with correlation coefficient *R*² of 99.72; 97.47 and 95.63 %, respectively, represent a significant industrial interest since they help in the predictions of the surface roughness.
- The optimum values obtained from the Taguchi optimization to minimize roughness criteria are identical and they given as follow: $\chi r = 75^\circ$, *r* = 1.6 mm, *V_c* = 220 m/min, *f* = 0.08 mm/rev, *ap* = 0.15 mm.
- The improvement of S/N ratio from initial parameter level to optimal parameter level is found to be 2.15 for *Ra*, 1.57 for *Rz*, 2.39 for *Rt*. Based on the result of the confirmation test, the roughness criterions (*Ra*, *Rz* and *Rt*) are decreased by about 1.28 times, 1.19 times, and 1.13 times, respectively.
- The Taguchi method is very suitable for optimizing the cutting process; the S/N ratio is the most important criterion in the Taguchi method.

References

1. Nalbant, M., Gökkaya, H., Sur, G.: Application of Taguchi method in the optimization of cutting parameters for surface roughness in turning. *Mater. Des.* **28**, 1379–1385 (2007)
2. Süleyman, N., Süleyman, Y., Erol, T.: Optimization of tool geometry parameters for turning operations based on the response surface methodology. *Measurement* **44**, 580–587 (2011)
3. Emre, Y., Mustafa, G.: Modelling and optimisation of the cutting conditions in hard turning of high-alloy white cast iron (Ni-Hard). *J. Mech. Eng. Sci.* **0**(0), 1–11 (2012)
4. Ashok, K.S., Swastik, P.: Modeling and optimization of Al/SiCp MMC machining using Taguchi approach. *Measurement* **46**, 3064–3072 (2013)
5. Ilhan, A., Harun, A.: Determining the effect of cutting parameters on surface roughness in hard turning using the Taguchi method. *Measurement* **44**, 1697–1704 (2011)
6. Yang, W.H., Tarn, Y.S.: Design optimization of cutting parameters for turning operations based on the Taguchi method. *J. Mater. Process. Technol.* **84**, 122–129 (1998)
7. Yallese, M.A., Rigal, J.F., Chaoui, K., et al.: The effects of cutting conditions on mixed ceramic and cubic boron nitride tool wear and on surface roughness during machining of X200Cr12 steel (60 HRC). *Proc. IMechE. Part B J. Eng. Manuf.* **219**, 35–55 (2005)
8. Horng, J.T., Liu, N.M., Chiang, K.T.: Investigating the machinability evaluation of Hadfield steel in the hard turning with Al₂O₃/TiC mixed ceramic tool based on the response surface methodology. *J. Mater. Process. Technol.* (2008)
9. Dureja, J.S., Gupta, V.K., Sharma, V.S., Dogra, M.: Wear mechanisms of coated mixed-ceramic tool during finish hard turning of hot tool die steel. *J. Mech. Eng. Sci.* **223**, 1–11 (2009)
10. Makadia, A.J., Nanavati, J.I.: Optimisation of machining parameters for turning operations based on response surface methodology. *Measurement* **46**, 1521–1529 (2013)

Study Contribution of Surface Quality Parts Machined by Turning Using Hard Materials

Razika Aouad and Idriss Amara

Abstract The white ceramic to zirconia based (Al_2O_3 and ZrO_2) and of titanium carbide ($\text{Al}_2\text{O}_3 + \text{TiC}$) cutting tools as well as the ceramic mixed and the titanium carbonitride are widely coveted for the machining operations of relatively hard materials, used within hard cutting conditions. In this paper, are exposed the results of an experimental study relative for the machining of the steel after annealing 42CrMo_4 with having a Brinell hardness HB 174, machined by three tools separately, white ceramic to zirconia based (Al_2O_3 and ZrO_2), the ceramic mixed (CC650) as well as the metallic carbide coated (GC3015). The testing series is devoted to the roughness main criteria of the cutting conditions influence of the machined surfaces. To do this we have made plain factorial trials and based on multifactorial the method of experimental design, the variable parameters: cutting speed, feed per revolution and the cutting depth. The results, to which we arrived, show that the white ceramic is comparable to that of rectified surfaces after the machining operation classic. The results comparison show that the machined steel by mixed ceramic give a very good surface states with high cutting speeds (180; 250 m/min) in relation to others cutting tools. The mathematical models expressing the relation between the studied parameters and the parameters used while the experiments have made the comparison object (Gilbert type, Taylor generalized model) as well as a comparison of theoretical and practical results has been made to the nuance C650.

Keywords Carbide · Roughness · Ceramics · Ceramic mixed · Surface roughness

R. Aouad (✉) · I. Amara

Laboratory of Transportation Engineering and Environment, Faculty of Technology Sciences,
University of Brothers Mentouri Constantine, Constantine, Algeria
e-mail: aouadrazika@yahoo.fr

I. Amara

e-mail: a.idriss.2011@gmail.com

1 Introduction

The hard steels machining of knew it's primarily development with the new development cutting materials such as cermets, ceramics and cubic boron nitride. This last is distinguished by a high hardness [1–4] and a large hot strength. It is to emphasize that hard turning may substituted or be complementary to the grinding [5–7]. We have realized of the tests based on the experiments planning method, where the variable parameters are: the cutting speed, feed and cutting depth. It's in this context the work has been done and presented the experimental results of the influence of cutting conditions study on the surface condition product during machined steel $42CrMo_4$ with tools Al_2O_3 and ZrO_2 , *CC 650* and *GC 3015*.

2 Experimental Procedure

The equipments used and the cutting conditions are:

2.1 Machine Tool

Parallel lathe having a power of 6.6 kW with the rotational speeds of the spindle ranges from 80 to 200 rev/min.

2.2 Platelets Holder and Platelets

For the tests realization, we used two tool holders. Platelets used are removable, of shape square, with two types of platelets SPK and Sandvik coromant:

- Pure ceramic Al_2O_3 and ZrO_2 : ENGN 13.04.08. [8]: Oxide ceramics are aluminium oxide based (Al_2O_3), with added zirconia (ZrO_2) for crack inhibition. This generates a material that is chemically very stable, but which lacks thermal shock resistance.
- Coated carbide *GC 3015(K10)*: SNGN 12.04.08. [9]: GC3015 has a thick, 14 μm , CVD TiCN- Al_2O_3 -TiN coating optimized for high wear resistance in cast iron machining. The hard substrate withstands high temperatures without being deformed. GC3015 is an excellent general purpose grade for roughing to finishing of cast irons at moderate to high cutting speeds.
- Mixed ceramic *CC650*: SNGN 12.04.08. [8]: Mixed ceramic for high speed finishing of grey cast irons and hardened materials.

Table 1 Characteristics of the used material

42 Cr Mo ₄	The chemical compositions (mass%)							
	Fe	C	Si	Mn	Cr	Mo	P	S
	96.719	0.396	0.282	0.895	1.085	0.272	0.015	0.018
	The mechanical characteristics							
	A (%)	Re (N/mm ²)		Rm (N/mm ²)	HB		Kcu (J/cm ²)	
10	832.96		921.57	285.174 after annealing		50		

Platelets holder serving to the testing:

- CEGNR 3225 P13 [10]
- PSBNR 2525 M12 [11]

2.2.1 Machined Matter

The test piece in low alloy steel *42CrMo4* is used in the automotive industry for the manufacture of connecting rods, whose dimensions are 48 mm in diameter and 120 mm in length (Table 1).

2.2.2 Measurement Setup

For the measurement criteria of different roughness (*Ra*, *Rt* and *Rz*) we used a roughness (2D) *MITUTOYO SURFTEST SJ 301*. It consists of a diamond tip, with a tip radius of 5 μm moving linearly on the measured surface.

2.2.3 Cutting Conditions

The tests on the effect of cutting conditions on the roughness of machined surfaces were made operations Roughing, without lubrication within the cutting conditions following: $0.08 \leq f \leq 0.02$ mm/rev; $0.1 \leq ap \leq 1$ mm et $60 \leq Vc \leq 350$ m/mm.

3 Results

3.1 Cutting Speed Evolution

Figure 1a–c represents the results of the effect of cutting speed on the roughness. In the Fig. 1a, we observe the increase of the cutting speed up to 220 m/min, but for

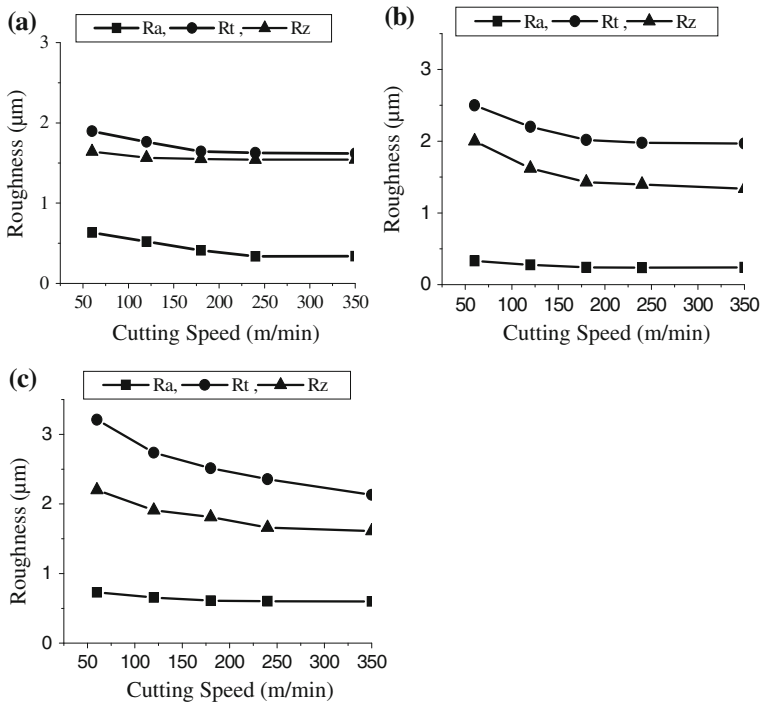


Fig. 1 Effect of the cutting speed on the roughness at $f = 0.08$ mm/rev and $a_p = 0.1$ mm with **a** composite ceramic, **b** mixed ceramic and **c** carbide

Fig. (1b, c) the cutting speed go up to 180 m/min, beyond these limits, they are stabilizing slightly. However the roughness criteria for the composite ceramic ($Ra = 0.51 \mu\text{m}$, $Rt = 1.86 \mu\text{m}$, $Rz = 1.67 \mu\text{m}$) but for mixed ceramic ($Ra = 0.28 \mu\text{m}$, $Rt = 2.52 \mu\text{m}$, $Rz = 2.00 \mu\text{m}$) and to carbide ($Ra = 0.63 \mu\text{m}$, $Rt = 3.25 \mu\text{m}$, $Rz = 2.25 \mu\text{m}$) decrease.

3.2 Advance Evolution

Figure 2a–c represent the results of the effect of the advance on the roughness. It is noticed that the roughness criteria (Ra , Rt and Rz) increased with the increasing advance. For the value $f = 0.08$ mm/rev we found the results for the composite ceramic ($Ra = 0.36 \mu\text{m}$, $Rt = 1.21 \mu\text{m}$, $Rz = 1.12 \mu\text{m}$), but for mixed ceramic ($Ra = 0.27 \mu\text{m}$, $Rt = 1.19 \mu\text{m}$, $Rz = 1.09 \mu\text{m}$) and for the carbide ($Ra = 0.60 \mu\text{m}$, $Rt = 3.37 \mu\text{m}$, $Rz = 1.90 \mu\text{m}$). For the value $f = 0.18$ mm/rev we found the results for the composite ceramic ($Ra = 0.80 \mu\text{m}$, $Rt = 1.78 \mu\text{m}$, $Rz = 1.48 \mu\text{m}$), but for

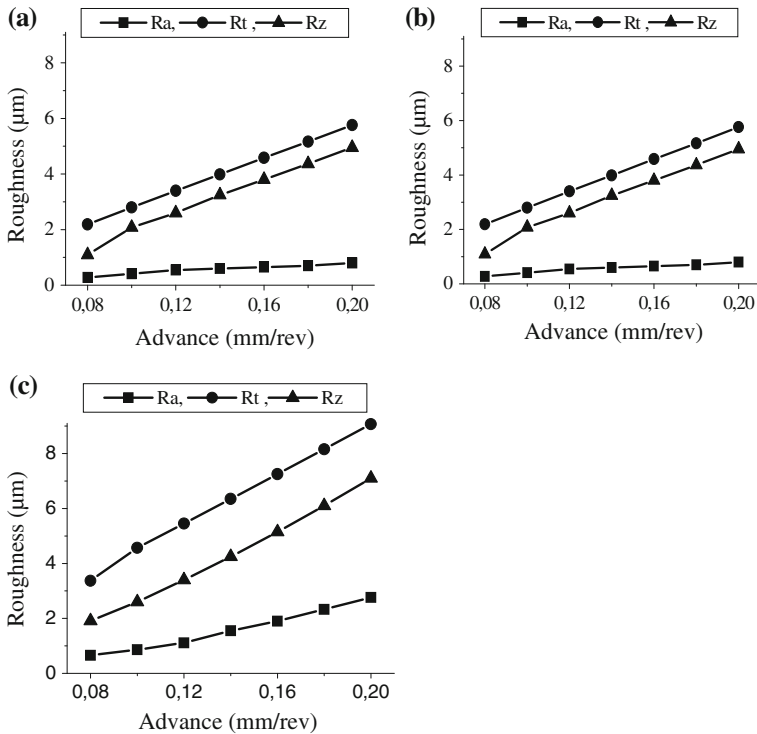


Fig. 2 Effect of the advance on the roughness at $V_c = 180 \text{ m/min}$ and $a_p = 0.1 \text{ mm}$ with **a** composite ceramic, **b** mixed ceramic and **c** carbide

the mixed ceramics ($R_a = 0.7 \mu\text{m}$, $R_t = 5.16 \mu\text{m}$, $R_z = 4.36 \mu\text{m}$) and for the carbide ($R_a = 1.5 \mu\text{m}$, $R_t = 7.84 \mu\text{m}$, $R_z = 5.71 \mu\text{m}$).

3.3 Cutting Depth Evolution

Figure 3a–c represent the results of the effect the cutting depth on the roughness. It is noticed that the criteria of roughness (R_a , R_t and R_z) increased with the increase depth of cutting. In the value $a_p = 0.2 \text{ mm}$ we find the results for composite ceramic ($R_a = 0.35 \mu\text{m}$, $R_t = 2.6 \mu\text{m}$, $R_z = 1.75 \mu\text{m}$), but for mixed ceramic ($R_a = 0.26 \mu\text{m}$, $R_t = 2.27 \mu\text{m}$, $R_z = 1.62 \mu\text{m}$) and for the carbide ($R_a = 0.56 \mu\text{m}$, $R_t = 3.51 \mu\text{m}$, $R_z = 2.12 \mu\text{m}$). In the value $a_p = 0.4 \text{ mm}$ we find the results for composite ceramic ($R_a = 0.4 \mu\text{m}$, $R_t = 2.65 \mu\text{m}$, $R_z = 1.85 \mu\text{m}$), but for mixed ceramic ($R_a = 0.35 \mu\text{m}$, $R_t = 2.42 \mu\text{m}$, $R_z = 1.75 \mu\text{m}$) and for the carbide ($R_a = 0.68 \mu\text{m}$, $R_t = 3.53 \mu\text{m}$, $R_z = 2.25 \mu\text{m}$) beyond these limits, they are stabilized slightly in this case we can say that the cutting depth does not play a paramount role on roughness (R_a).

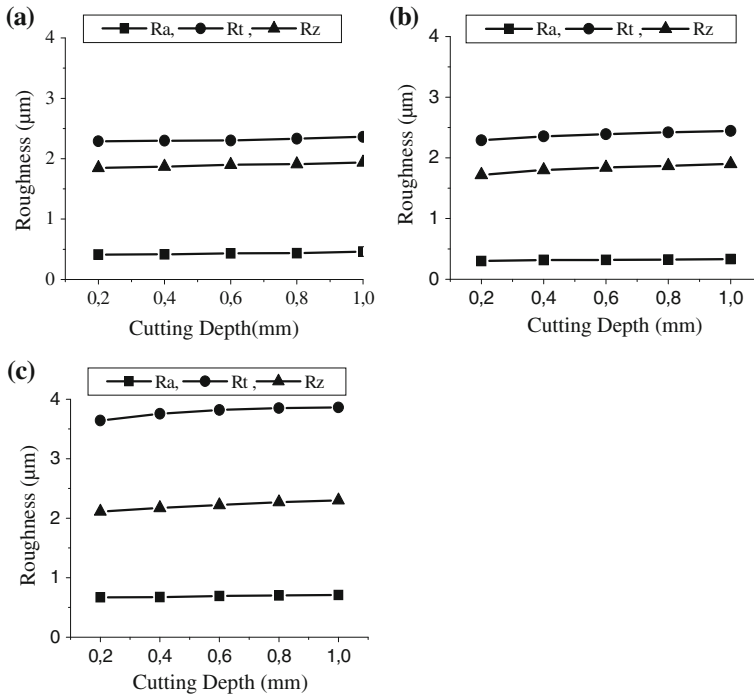


Fig. 3 Effect of the cutting depth on the roughness at $V_c = 180$ m/min and $f = 0.08$ mm/rev with **a** composite ceramic, **b** mixed ceramic and **c** carbide

4 Discussion of Results

The characterization of the machined surface quality was limited to the total roughness criteria R_t , Arithmetic mean roughness R_a and Mean depth of roughness R_z . The Figs. 1, 2 and 3a-c illustrate the influence of the cutting mode elements (V_c, f and ap) on the roughness of surface of steel $42CrMo4$, machined by pure ceramics, mixed ceramic $CC650$ and carbide $GC3015$. The Fig. (1a-c), express the evolution of the roughness criteria according to the cutting speed. The analysis of these curves shows that during machining, roughness decreases slightly with the increase cutting speed for the three cutting nuances; we noticed that the surface quality improves with the increase the cutting speed until the limit of 180 m/min. We record a light increase in roughness because of the wear accelerated of the tool at the high cutting speeds. Beyond this value, we recorded a stabilization of roughness for the nuance carburizes covered $GC3015$, and an increase for pure ceramic Al_2O_3 and ZrO_2 , mixed ceramic $CC650$. By comparing the values of the roughness are obtained for three materials of cut used, we notice clearly that tool $CC650$ is more powerful than the two other nuances.

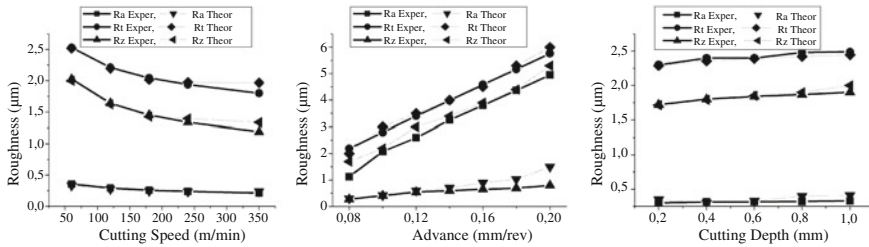


Fig. 4 Comparison of theoretical and experimental values for CC650 in function of the cutting parameters (V_c , f and ap)

Figure 2a–c show a clear influence of the advance on the roughness, with the increase of this last; the surface quality obtained is degraded in a significant way. Consequently the advance is one of the parameters of which the effect is most sensitive on the roughness of the machined surfaces. A multiplication by two of the values of the advance 0.08 to 0.16 mm/rev, led to an increase in roughness R_a of 3.09 times for *CC650*, 2.89 times for *GC3015* and 1.75 times for pure ceramic. Lastly, if we base our results only on roughness, we notice clearly that the *CC650* is more performer than the others.

Figure 3a–c illustrate the evolution of the roughness criteria according to the cutting depth. Roughness varies very little especially for the low cutting depth values. Indeed with the increase the cutting depth from 0.2 to 0.6 mm, roughness R_a increases by 1.05 times. But, when the cutting depth varies from 0.2 to 1 mm, the roughness R_a increases by 1.10 times.

The analysis of the results shows that this parameter is less important than the advance. We record a stabilization of the roughness criteria for the plates. The Fig. 4 represents the comparison of the theoretical and experimental results between the cutting conditions V_c , f and ap for mixed ceramic *CC650*.

5 Roughness Models in Function of the Cutting Conditions

According to the plan of experiments, a series of tests was carried out for various combinations of cutting conditions V_c , f and ap .

Criteria of roughness considered, as it is defined higher, are R_a , R_t and R_z . The goal is to develop correlations between these criteria and the parameters of machining in the same form of the following equation:

$$R_i = C \cdot V_c^\alpha \cdot f^\beta \cdot ap^\gamma \quad (i = R_a, R_z, R_t) \tag{1}$$

Table 2 Models mathematics of the roughness obtained

Cutting material	Parameters	Models mathematics	R ²
Pure ceramic	f (mm/rev) ap (mm) Vc (m/min)	$Ra = e^{4.814} Vc^{-0.936} f^{-0.054} a_p^{0.0538}$	0.987
		$Rt = e^{3.631} Vc^{-0.705} f^{-1.741} a_p^{0.706}$	0.977
		$Rz = e^{5.456} Vc^{-0.814} f^{-0.015} a_p^{0.008}$	0.988
Mixed ceramic (CC650)		$Ra = e^{4.097} Vc^{-0.287} f^{-1.521} a_p^{0.03}$	0.980
		$Rt = e^{4.456} Vc^{-0.192} f^{-1.038} a_p^{0.041}$	0.990
		$Rz = e^{5.107} Vc^{-0.299} f^{-1.187} a_p^{0.062}$	0.970
Coated carbide (GC3015)		$Ra = e^{4.71} Vc^{-0.198} f^{1.625} a_p^{0.05}$	0.960
		$Rt = e^{4.687} Vc^{-0.232} f^{0.987} a_p^{0.028}$	0.970
		$Rz = e^{5.456} Vc^{-0.200} f^{1.441} a_p^{0.086}$	0.950

with the coefficients α , β , and γ which respectively indicates the influence of each parameter (Vc, f and ap) on roughness. The given mathematical models show that the advance is the most influencing factor the various roughness criteria.

The statistical processing by the method of least squares with the Coefficient of determination R², allowed us the determination of the following models (Table 2):

6 Conclusion

From this experimental study and the follow-up results of the roughness evolution according to the cutting conditions and the machining time, we can conclude that the found roughnesses by mixed ceramics are comparable to those obtained by grinding.

This gives the opportunity of carrying out operations (roughing, 1/2 finishing, finishing) on the same machine, which influences advantageously the cycle of production, the manufacturing costs and the precision.

Also the machining conditions Vc, f and ap have a considerable influence on the machined surface quality. Indeed, the most relevant influence on the roughness is attributed in advance, followed by the cutting speed and finally the cutting depth. The roughness which has found by mixed ceramics are also comparable with those obtained by grinding.

The analysis of the tests results shows that the cutting depth does not have a significant influence on the roughness. However, if we want to obtain a good finishing state of machined surfaces, we must always decrease the advance, and increase the cutting speed.

Moreover, the models found are very useful for predictions for optimization studies of the cutting process.

References

1. Poulachon, G.: Phenomenological aspects, mechanical and metallurgical in turning CBN hardened steels. Doctoral thesis from ENSAM of cluny, déc (1999)
2. Pastor, H.: The evolution of cutting tool materials. Bulletin from Circle studies of the Metals, N° = 13 (1996)
3. Luo, S.Y, Lia, Y.S., Tsai, Y.Y.: Wear Characteristics in Turning High Hardness Alloy Steel by Ceramic and CBN Tools, pp. 114–121, PII:S0924-0136(98)00376-8 (1999)
4. Kevin, Y., Evans, Chris J.: Cubic boron nitride tool wear in interrupted hard cutting. *Wear* **225–229**:234–245 (1999)
5. Hug, J.L.: Turning of the hard metal. *Production machine*, pp. 17–19 (1995)
6. Kaufeld, M., Torbaty, S.: Rationalization of machining very high speed. SOFETEC (1999)
7. Yallese, M.A., Boulanouar, L., Belhadi, S.: Study the damage of cutting tools in black ceramic and in CBN during the filming of a hardened steel. *J. Appl. Mech. Theor.* **1**(5) (2003)
8. <http://www.sandvik.coromant.com/sitecollectiondocuments/downloads/global/brochures/en-gb/c-2929-61.pdf>
9. <http://www2.coromant.sandvik.com/coromant/pdf/smallparts/catalogue/P127-132.pdf>
10. Ceram Tec. SPK tools catalogue for turning. IKS tools for turning. *Innovation Ceramic Engineering*. Germany, pp. 10–48 (2000)
11. Directindustry. Turning tools catalogue from Sandvik Coromant—general turning. pp. 109/529 (2012)

Prediction of Cutting Tool's Optimal Lifespan Based on the Scalar Indicators and the Wavelet Multi-resolution Analysis

Mohamed Khemissi Babouri, Nouredine Ouelaa,
Abderrazek Djebala, Mohamed Cherif Djamaa and Septi Boucherit

Abstract The objective of this article is to propose Wavelet Multi-Resolution Analysis as an effective tool allowing the improvement of the sensitivity of the scalar indicators for the identification of cutting tool's degradation state during the machining of X200Cr12 steel. Indeed, these indicators are very sensitive to the variations in the temporal signal related directly to the vibrations induced during turning operation. Nevertheless, their reliability is immediately limited in the presence of intense levels of random noise and other machine components. In addition to the Wavelet Multi-Resolution Analysis (WMRA) which brought a solution to this problem, one proposes a new spectral indicator, which one called overall level, to separate the phases characterizing the tool's wear. The results obtained from this article made it possible to study the phenomena of vibration associated with machining, and to locate the transition point from the normal wear period to the accelerated wear period.

Keywords Flank wear · Wavelet multi-resolution analysis · Overall level

1 Introduction

An improvement of the productivity and quality of the parts leads to significant cumulated profits which are closely related to the lifespan of the cutting tools. Although several scientists tried to propose monitoring systems of the cutting process to improve the productivity and quality of the product, the realization of such industrial system encounters many difficulties. Such a system utilized a great

M.K. Babouri (✉)

University of Sciences and Technology Houari Boumediene, USTHB, BP 32,
El-Alia, Bab-Ezzouar, 16111 Algiers, Algeria
e-mail: babouri_bmk@yahoo.fr

M.K. Babouri · N. Ouelaa · A. Djebala · M.C. Djamaa · S. Boucherit
Mechanics and Structures Laboratory (LMS), 8 May University of Guelma,
24000 Guelma, Algeria

number of parameters, generally dependent between them according to the type of machining, the nature of machined materials, the nature of the operation, and many other factors such as the cutting parameters. Recently, many works have been developed for the tool wear monitoring in real time by measuring the vibratory signals, the cutting forces, and the noise of machining which are directly correlated with the tool wear [3, 7, 8, 12].

Several authors concentrated their efforts on the detection of the cutting tool's rupture which is usually indicated by an abrupt change of the tendencies of the measured parameters whose values exceed a preset threshold. Ravindra et al. [9] developed a method to detect the flank wear through the variation of the Root Mean Square and the acoustic signal spectrum. This study showed that the Root Mean Square of the acoustic signal decreases in the phase of break-in, remains stable in the normal wear phase and increases significantly in the phase of accelerated wear. Dimla et al. [4] summarized several works which highlight the relation between the vibrations emitted during machining and the degree of tool's wear. They also expose some results obtained from the vibration analysis during turning operation. In a recent study [1] we proposed a monitoring method based on the temporal and frequential analysis of the vibratory signals in order to identify the cutting tool wear. The results obtained confirm the effectiveness of these promising techniques for the control of flank wear of a turning tool.

In the current work, we propose a technique of tool's wear follow-up based on the analysis of the vibratory signals measured during cutting process in order to predict its lifespan before its final degradation. The adopted strategy consists in using Wavelet Multi-Resolution Analysis to improve the sensitivity of scalar indicators. The final objective is to distinguish the transition points between the Break-in phase, the stabilization phase, and especially the acceleration wear phase synonymous of cutting edge rupture.

2 Lifespan of Cutting Tools

All the cutting tools wear progressively with use until the end of their lifespan. The lifespan represents the productive time during which the cutting edge keeps its cutting capacity in order to provide acceptable results taking into account the specific parameters of roughness and dimensional accuracy [10].

Several works established mathematical models allowing the calculation of the cutting tool's lifespan according to the cutting parameters. Taylor was the first researcher who proposed in 1907 a mathematical model connecting the tool's effective cutting duration to the cutting parameters. This model, considered to be sufficiently representative, is usually employed to evaluate the cutting tools life [6]. In 1950, Gilbert proposed the generalization of Taylor's model by taking into account the cutting tool geometry, the feed rate, and depth of cut. Koning-Deperieux, in 1969, proposed an exponential type model allowing correct representation of the wear law in agreement with experimental curves.

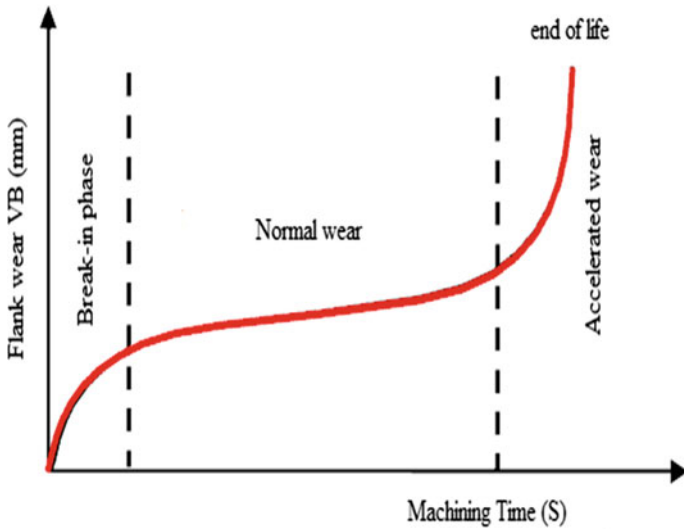


Fig. 1 Tool wear

In practice, flank wear VB is the most used mean to evaluate the cutting tool life. The evolution of wear according of the machining time passes by three phases during the tool life: break-in phase, normal wear and accelerated wear (Fig. 1).

3 Experimental Setup

3.1 Experimental Conditions and Acquisition of the Vibratory Responses

The tests of long duration of straight turning on $X200Cr12$ steel were carried out. The purpose of these operations was to determine the wear curves as a function of machining time and therefore the tool life of various cutting materials used. Figure 1 shows the evolution of the flank wear VB versus machining time at $f = 0.08$ mm/rev, $ap = 0.2$ mm and $V_c = 280$ m/min. The machining experiments were realized under dry conditions using a conventional lathe type $SN 40C$ with 6.6 kW spindle power. The material used in this study is steel $AISI D3$ applied for the manufacture of matrices, punches for cutting and stamping, profiling rollers, mollettes and combs rolling nets because of its excellent behaviour to wear. Its chemical composition is given as follows: 2 %C, 11.50 %Cr, 0.30 %Mn, 0.25 %Si and 0.70 %W.

The workpieces are used in the form of round bars having 80 mm in diameter and 400 mm in length. All the tests were carried out under the following conditions: $V_c = 120$ m/min, $f = 0.12$ mm/rev, and $ap = 0.2$ mm. The cutting insert employed have geometry SNMG 432-MF 2015 and having a coating multilayer of TiCN/ Al_2O_3 /TiN formed on a cemented carbide substrate. The tool holder, of reference *PSDNN 2525 M12*, has the following geometry: $\chi = 75^\circ$, $\alpha = 6^\circ$, $\gamma = -6^\circ$ and $\lambda = -6^\circ$ [11].

The acquisition of vibratory signals was carried out during machining by using piezoelectric accelerometers Brüel & Kjaer type 4524B. The acceleration signals, of 16384 samples, were measured in the three principal directions in the frequency band (0–12,800 Hz). The results were stored directly on the PC hard drive by using an acquisition and analysis system working under pulse Lab shop[®] Brüel & Kjaer software (Fig. 2).

After each test, the cutting insert is dismantled from the tool holder, cleaned then placed on the table of the microscope to measure flank wear using an optical microscope Standard Gage type—Visual 250. A 2D roughness meter type surf test 301 Mitutoyo was used to measure the various criteria of roughness of the machined surfaces without disassembling the work piece in order to reduce uncertainties due to the resumption operations. The measurements are repeated

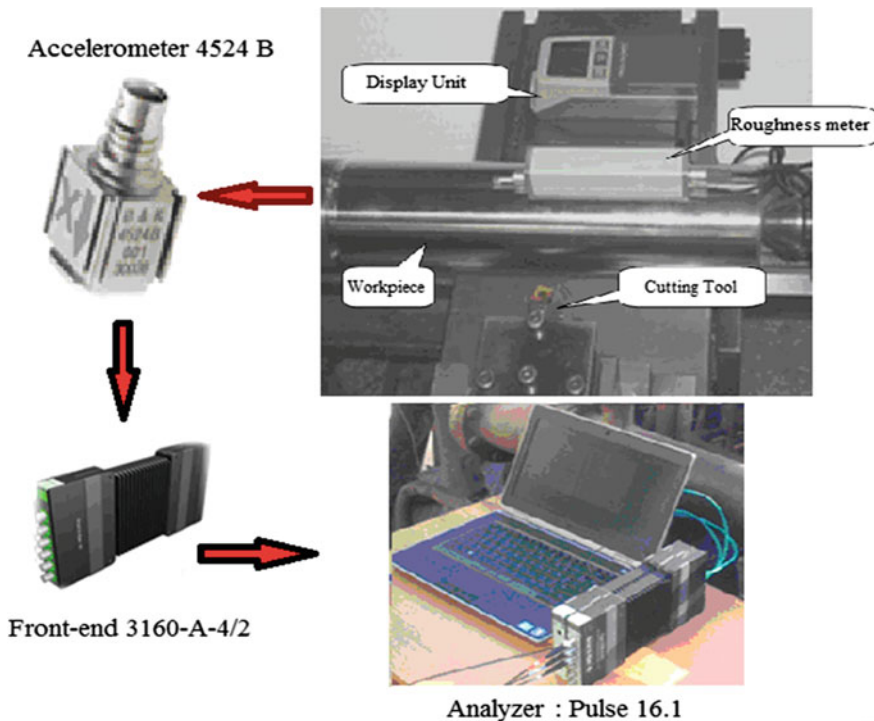


Fig. 2 Experimental installation and measuring equipment

Table 1 Experimental results

Run N°	Machining time cumulated	Flank wear	Roughness		
	t (s)	VB (mm)	R _a (μm)	R _t (μm)	R _z (μm)
1	240	0.041	0.50	5.15	4.87
2	480	0.090	0.66	5.66	5.42
3	720	0.118	0.87	5.67	5.33
4	1200	0.154	1.08	6.66	5.67
5	1440	0.180	1.25	6.35	5.87
6	1680	0.202	1.56	6.79	6.70
7	1920	0.215	1.87	9.14	8.73
8	2400	0.257	2.20	11.38	10.34
9	2640	0.280	2.27	10.48	10.04
10	2880	0.292	2.55	11.16	10.62
11	3360	0.323	2.97	14.18	13.62
12	3600	0.345	2.99	15.09	14.59
13	3840	0.360	3.20	15.40	14.61
14	4080	0.377	3.26	16.09	14.67
15	4320	0.396	3.51	16.81	16.12
16	4560	0.403	3.62	17.01	16.15

three times on the work piece surface at three reference lines equally positioned at 120°, and the average of these values is taken as final result. The experimental results are given in Table 1.

3.2 Vibratory Signals and Wear Characterization

The exploitation of the vibratory signals acquired during machining makes it possible to follow the evolution of the cutting tool wear. These signals are recorded at the end of each test. The machining stop when the width of flank wear (VB) exceeds the value of 0.3 mm, which is synonymous of the tool life [10]. The experimental procedure allows preserving the same conditions of signals’ measurement so that to detect any variation closely related to the change of the state of cutting insert.

Figure 3 shows the concatenation of 16 vibration acceleration signals measured during the cutting tool life. In all acquisitions it is interesting to note that the radial acceleration is the most significant component than axial and tangential ones, which is in agreement with the results obtained in the case of the treated steel machining [2]. Three principal phases were observed and summarize the tool’s life. The objective of the proposed analysis tends to allow the detection of the transition point from the stabilization phase to the accelerated wear phase which is basically related to the beginning of the catastrophic wear of the cutting tool before its total collapse.

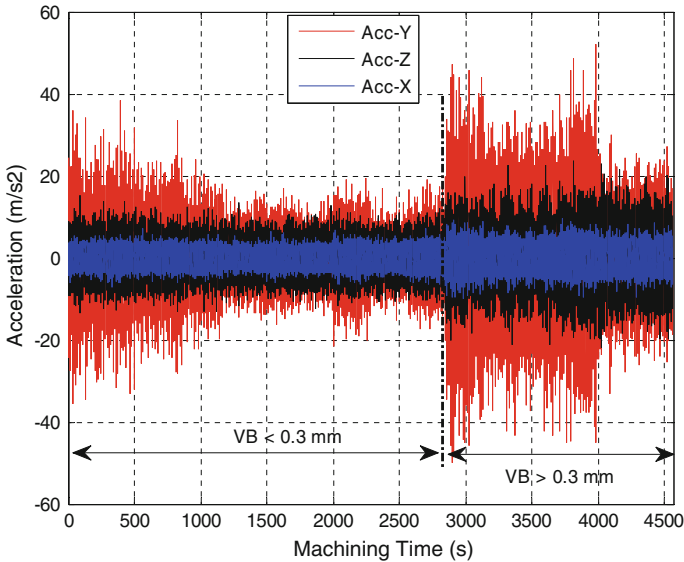


Fig. 3 Concatenation of the measured signals

4 Results and Discussions

4.1 Statistical Analysis of Wear

For the statistical analysis of the tool's wear two scalar indicators are used in this study; the energy E and the Root Mean Square RMS . These indicators were calculated from the vibratory signals acquired during the tool life (From the first use of the tool until its last use) according to three directions x , y , z using a slipping window whose size is of 1024 samples. Figure 4 shows the evolution of the energy and the RMS according to the machining time for the three directions.

The analysis of the evolution of the scalar indicators presented in Fig. 4 shows that the radial component well indicates the three phases of the tool's life. The principal result is the detection of the transition point from the wear stabilization phase to the wear acceleration phase. From this transition point the scalar indicators undergo an abrupt change characterized by significant increase of their values with machining time.

4.2 Spectral Analysis

The spectral analysis is certainly one of the most significant techniques used in industry. Before the analysis of the spectra measured during the machining and covering the entire tool life, modal analysis has first been carried out. Figure 5

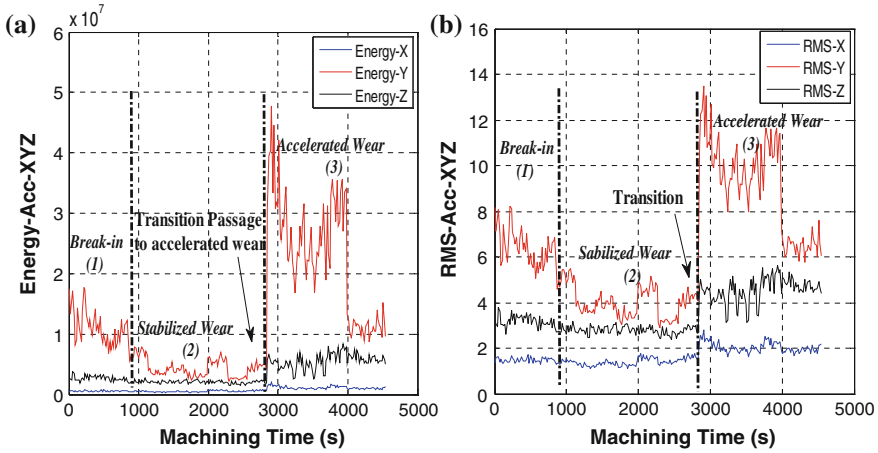


Fig. 4 Evolution of the scalar indicators according to machining time for the three directions X, Y and Z: **a** energy, **b** RMS

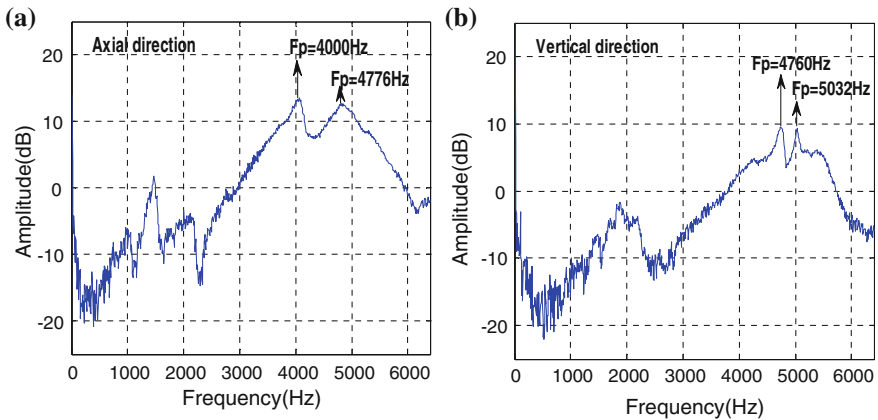


Fig. 5 Natural frequencies of the cutting tool. **a** Axial direction, **b** vertical direction

shows the natural frequencies of the cutting tool according to the axial and vertical directions. We distinguish the tool natural frequency represented in the frequency band 4000–5100 Hz. Also can note the bending mode in the axial direction which appears around 4100 Hz, the torsion mode between 4700 and 4800 Hz in the two directions, and finally the bending mode in the tangential direction around 5032 Hz.

Figure 6a represents the acceleration spectrum obtained according to the three directions during the test 12. We distinguish the tool natural frequency which appears in the frequency band 4000–5100 Hz identical to that identified by modal analysis of Fig. 5. The amplitudes of the tool natural frequency of the radial component are very remarkable compared to those of the axial and tangential

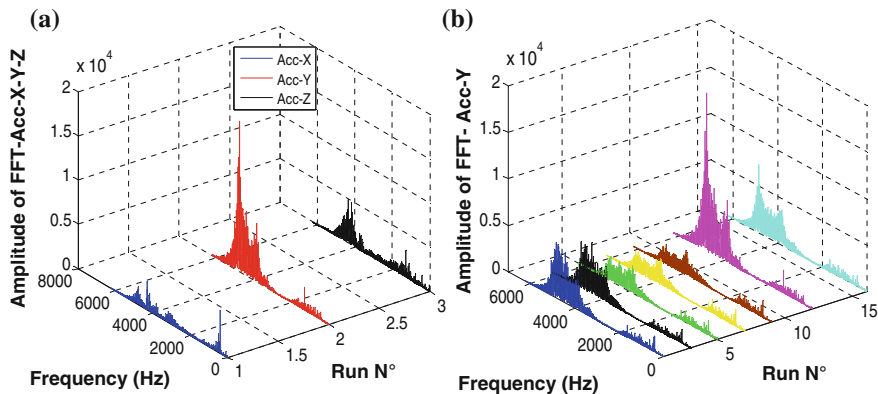


Fig. 6 Spectrum obtained from: **a** test 12, **b** radial direction

directions. This finding is the same obtained in the case of hard machining [2]. In addition, Fig. 6b shows the spectrum of the signals measured in the radial direction according to the tool state for some tests. One note, after the break-in period, a stability of the tool's natural frequency amplitudes. When wear exceeds its allowable value, the amplitudes of the natural frequency increase abruptly. From this result one conclude that the evolution of the tool's natural frequency in the radial direction well summarize the three principal phases of the tool life and can then be considered as a good frequential indicator which can be integrated in an on-line monitoring system.

5 Tool Wears Prediction Using Wavelet Analysis

5.1 Theory of the Wavelet Multi Resolution Analysis

The wavelet transform is a mathematical transformation which represents a signal $s(t)$ in term of shifted and dilated version of singular function called wavelet mother $\psi(t)$.

A practical version of this transform, called Wavelet Multi-Resolution Analysis (WMRA), was introduced for the first time by Mallat in 1989, and which consists to introduce the signal $s(t)$ in two low-pass (L) and high-pass (H) filters. In this level, two vectors will be obtained, cA_1 and cD_1 . The elements of the vector cA_1 are called approximation coefficients, they correspond to the low frequencies of the signal, while the elements of the vector cD_1 are called detail coefficients, and they correspond to highest of them. The procedure can be repeated with the elements of the vector cA_1 and successively with each new vector cA_j obtained. The process of decomposition can be repeated n time, with n the maximum number of levels. During the decomposition, the signal $s(t)$ and vectors cA_j undergo a downsampling

and this is why the approximation cA_j and detail cD_j coefficients pass again through two reconstruction filters (LR) and (HR). Two vectors result: A_j called approximations and cD_j called details [5].

5.2 Results Obtained

The Wavelet Multi-Resolution Analysis is applied on the acceleration signals measured in radial direction using the Daubechies 5 ($db5$) wavelet. Six levels of decomposition are calculated allowing different details and approximations. The RMS and the energy of the various details, since it represent the high frequencies, are calculated. It seems obvious from Fig. 7, that the detail 1 (D_1) has the highest values and can be taken as a reconstructed signal.

To demonstrate the validity of this finding, spectral analysis of the reconstructed signals obtained from different tests covering the entire tool life has been carried out in Fig. 8. The variation of the tool's natural frequency well explains the tool's wear evolution. In the Break-in phase, the contact tool-workpiece is very small from where the vibration amplitudes are significant following a weak damping of the cutting tool (test 1). In the phase of wear stabilization, the surface of contact tool-workpiece becomes larger and regular which damps out the vibration of the cutting tool by provoking a reduction in the amplitudes of its natural frequency and become almost constant (tests 5 and 9).

The third phase corresponds to accelerated wear, characterized by the irregularity of the surface of contact tool-workpiece and the change of the geometry of the cutting tool. These modifications enormously reduce the crossing capacity of the cutting tool and support friction, which results in an increase in the vibrations amplitudes of the cutting tool's natural frequency (test 16).

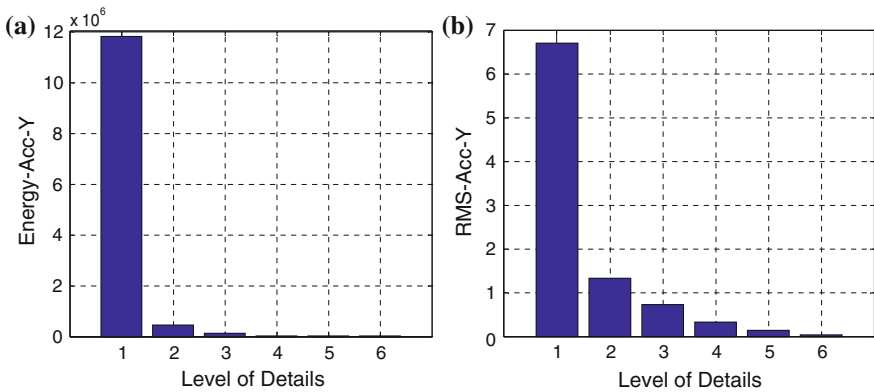


Fig. 7 Evolution of the scalar indicators according to the level of details for test 1: **a** energy, **b** RMS

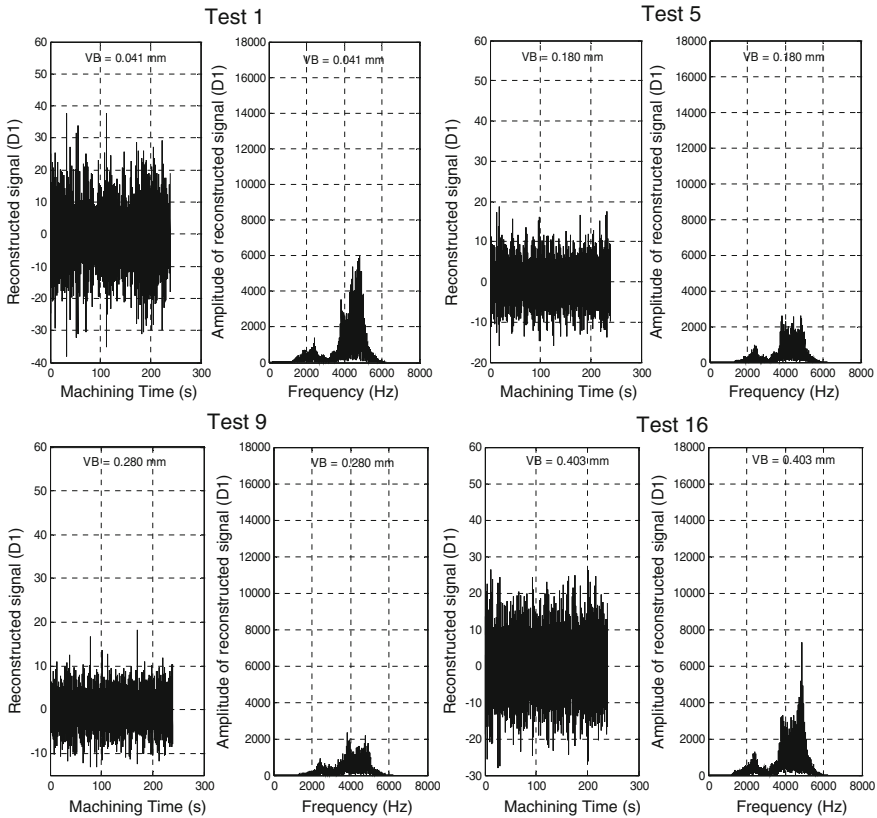


Fig. 8 Reconstructed signal (D_1) and its spectrum for different tests

5.3 Frequency Indicator

In this section we propose a frequency indicator, that we called overall level, calculated starting from the spectrum of the reconstructed signals in the frequency band covering the tool natural frequency, by the following expression:

$$OL = \sqrt{\frac{2}{3} \sum_{F_{min}}^{F_{max}} (N_i)^2} \tag{1}$$

with F_{min} and F_{max} the limits of the tool’s natural frequency band and N_i the number of spectrum lines in the same band.

Figure 9 represents the evolution of the proposed frequency indicator (overall level) over the entire tool life. The variation of this indicator is marked by two main phases. The normal tool wears phase until approximately 2800 s of machining, and

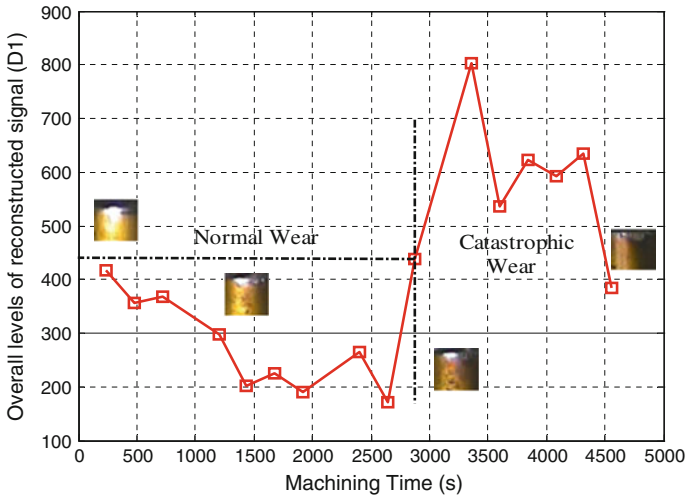


Fig. 9 Overall level of reconstructed signal over the entire tool life

the catastrophic wear phase characterized by an abrupt increase in the overall level values. The transition point from these two phases is clearly detectable which makes it possible to avoid consequently the tool breakage and the machining fall.

6 Conclusion

In this work, we proposed the application of the scalar indicators and the Wavelet Multi-Resolution Analysis for the prediction of tool's wear in turning operation. A new frequencial indicator, named Overall Level, has been proposed to follow-up the evolution of the wear over the entire tool life. These indicators will have a major importance if they will be exploited to develop a monitoring system of the tool's wear in real time thus making it possible to increase the profitability of machining. The first conclusions which can be drawn are as follows:

- Abrasion and chipping are the principal mechanisms of flank wear which are observed during machining.
- The evolution of the amplitude of the tool's natural frequency well summarize the three wear phases and allows locating the transition point from the normal wear to the accelerated wear phase. Consequently it can be used as a reliable indicator integrated in an on-line tool's wear monitoring system.
- The proposed new indicator, the Overall Level, proved its capacity to predict the transition from the normal wear to the catastrophic wear.
- All the indicators proposed in this study are very easy to implement in an on-line monitoring system, and require a computing time similar to a simple *FFT* spectrum.

References

1. Babouri, M.K., Ouelaa, N., Djebala, A.: Temporal and frequential analysis of the tools wear evolution. *Mechanika* **20**(2), 205–2012 (2014)
2. Bouacha, K.: Comportement du couple outil-matière lors de l'usinage des matériaux durs. Thesis University of Guelma, Algeria (2011)
3. Dimla, D.E., Lister, P.M.: On-line metal cutting tool condition monitoring. I: Force and vibration analyses. *Mach. Tools Manufact.* **40**, 739–768 (2000)
4. Dimla, D.E.: Multivariate tool condition monitoring in a metal cutting operation using neural networks. Ph.D. thesis, School of Engineering and Built Environment, The University of Wolverhampton, UK (1998)
5. Djebala, A., Ouelaa, N., Benchaabane, C., Laefer, D.F.: Application of the wavelet multiresolution analysis and Hilbert transform for the prediction of gear tooth defects. *Meccanica* **47**, 1601–1612 (2012)
6. Kiouss, M., Boudraa, M., Ouahabi, A., Serra, R.: Influence of machining cycle of horizontal milling on the quality of cutting force measurement for the cutting tool wear monitoring. *Prod. Eng. Res. Dev.* **2**, 443–449 (2008)
7. Li, X.: A brief review: acoustic emission method for tool wear monitoring during turning. *Mach. Tools Manufact.* **42**, 157–165 (2000)
8. Li, D., Mathew, J.: Tool wear and failure monitoring techniques for turning—a review. *Int. J. Mach. Tools Manufact.* **30**(4), 579–598 (1990)
9. Ravindra, H.V., Srinivasa, Y.G., Krishnamurthy, R.: Acoustic emission for tool condition monitoring in metal cutting. *Wear* **212**, 78–84 (1997)
10. Rmili, W.: Analyse vibratoire pour l'étude de l'usure des outils de coupe en tournage. Thesis University François Rabelais of Tours, France (2007)
11. SANDVIK Coromant: Catalogue Général, Outils de coupe Sandvik Coromant, Tournage – Fraisage – Perçage – Alésage – Attachements (2009)
12. Scheffer, C., Heyns, P.S.: Wear monitoring in turning operations using vibration and strain measurements. *Mech. Syst. Signal Process.* **15**, 1185–1202 (2001)

Diffusion Modelling of Composite with Permeable Fiber

Djelloul Gueribiz, Frédéric Jacquemin, Hocine Bourenane and Silvain Fréour

Abstract In order to predict the long-term durability of composite materials subjected to humid environments, the diffusing behavior has to be regarded. The knowledge of the effective diffusivity is actually required for estimating the moisture content of polymer based fiber reinforced materials following a Fick's law. In this work, the effective diffusivity is determined by solving unit cell problems on representative volume elements with several multi-scale approaches. Composite materials with permeable fibers are studied. The proposed approaches are extended to the practical case of composite materials containing voids.

1 Introduction

Composite materials absorb moisture during service principally through the resin but also through the fibers when they are permeable [1]. In numerous cases, the moisture kinetic follows a Fick's law [2] and the knowledge of the moisture diffusivity with the appropriate boundary conditions allow to calculate the moisture content in the composite material. The objective of this paper is to determine the effective moisture diffusivity, by using several multi-scale models, of polymeric composite materials with impermeable or permeable fibers. The effective diffusivity is obtained by solving a unit cell problem on a Representative Volume Element (RVE). The defined RVE is submitted to a macroscopic moisture gradient inducing local fields and gradients. The effective diffusivity is calculated by considering between constituents discontinuity of the moisture contents and continuity of the moisture flux. At the interface between two materials with different diffusing

D. Gueribiz (✉) · H. Bourenane
Laboratoire de Génie des Procédés, Université de Laghouat, Laghouat, Algeria
e-mail: gueribm@yahoo.com

F. Jacquemin · S. Fréour
Institut de Recherche en Génie Civil et Mécanique (UMR CNRS 6183),
LUNAM Université de Nantes, Ecole Centrale de Nantes, Bd de l'Université,
BP 406, 44602 Saint-Nazaire, France

behaviors, only the continuity of the chemical potentials is assumed [3]. Thus, a parameter representative of the moisture content jump between the constituents is introduced in the unit cell problem to be solved. In the case of permeable fibers, an inverse approach allowing the determination of the moisture diffusivity of the fibers is proposed. Finally, the presented multi-scale approaches are extended to composite materials containing voids and the influence of the void contents on the effective diffusivity is discussed.

2 Effective Moisture Diffusivity

The multi-scale approaches are based on the resolution of the unit cell problem on a representative volume element (Fig. 1). The RVE is composed of the fiber, radius r_f and volume V_f , the matrix, radius r_m and volume V_m , and of the equivalent homogeneous medium with the properties to be determined. In this configuration, the application of a moisture content flux \vec{G} on the RVE permits to obtain the equivalent diffusing behavior.

The unit cell problem is defined with the following system of equations:

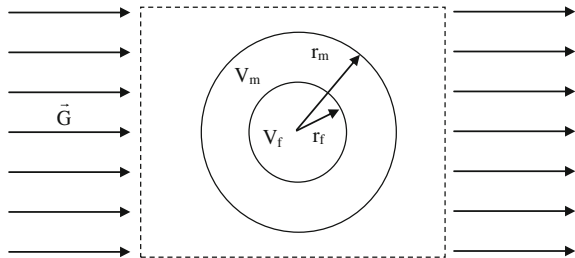
$$\begin{cases} \text{div}\vec{q}(y) = 0 \\ \vec{q}(y) = -D(y)\overrightarrow{\text{grad}} C(y) \\ \|\vec{q} \cdot \vec{n}\| = 0 \text{ at the interfaces} \\ \|C\| \neq 0 \text{ at the interface fibre/matrix} \end{cases} \quad (1)$$

The sign $\| \|$ stands for the jump of moisture contents and flux at the interfaces. For cylindrical constituents, the moisture content field solution of the unit cell problem Eq. 1 is:

$$\begin{cases} C(r, \theta) = A_f \cdot r \cos \theta \\ C(r, \theta) = (A_m \cdot r + \frac{B_m}{r}) \cos \theta \\ C(r, \theta) = G \cdot r \cos \theta \end{cases} \begin{cases} \text{in the fibre} \\ \text{in the matrix} \\ \text{in the equivalent medium} \end{cases} \quad (2)$$

where A_f , A_m and B_m are unknown constants.

Fig. 1 Representative Volume Element (RVE)



Let us considering, the boundary conditions, the continuity and discontinuity conditions at the interfaces and the permeability of the fibers.

2.1 At $r = r_m$

The continuity of the moisture contents between the equivalent medium and the matrix is considered:

$$A_m r_m^2 + B_m - G r_m^2 = 0 \tag{3}$$

The moisture content flux in the matrix is equal to the moisture content flux in the equivalent medium:

$$D_m A_m r_m^2 + D_m B_m - D_{eff} G r_m^2 = 0 \tag{4}$$

where D_m and D_{eff} are the diffusion coefficients respectively of the matrix and equivalent medium.

2.2 At $r = r_f$

The continuity of the flux between fiber and matrix is considered ($D_f \frac{\partial C}{\partial r} |_{r_f} = D_m \frac{\partial C}{\partial r} |_{r_f}$):

$$D_m A_m r_f^2 + D_m B_m - D_f r_f^2 = 0 \tag{5}$$

where D_f is the diffusion coefficient of the fiber.

The discontinuity of the moisture contents between fiber and matrix involves a moisture content jump $C_f = \alpha C_m$:

$$\alpha A_m r_f^2 + \alpha B_m - A_f r_f^2 = 0 \tag{6}$$

where α is a constant representative to the moisture content jump between fiber and matrix.

Equations 3, 4, 5 and 6 constitute a system of four equations with four unknown constants (A_m, B_m, A_f, G):

$$\begin{bmatrix} r_m^2 & 1 & -r_m^2 & 0 \\ D_m r_f^2 & -D_m & 0 & -D_f r_f^2 \\ D_m r_m^2 & -D_m & D_{eff} r_m^2 & 0 \\ \alpha r_f^2 & \alpha & 0 & -r_f^2 \end{bmatrix} \begin{bmatrix} A_m \\ B_m \\ G \\ A_f \end{bmatrix} = 0 \tag{7}$$

Thus, making the determinant equal to zero we obtain the effective diffusion coefficient:

$$D_{eff} = D_m \frac{D_m \left(1 - \frac{r_f^2}{r_m^2}\right) + \alpha D_f \left(1 + \frac{r_f^2}{r_m^2}\right)}{D_m \left(1 + \frac{r_f^2}{r_m^2}\right) + \alpha D_f \left(1 - \frac{r_f^2}{r_m^2}\right)} \quad (8)$$

For a cylindrical geometry the ratio $\frac{r_f^2}{r_m^2}$ corresponds to the fiber volume fraction v_f and Eq. 8 can be expressed as follows:

$$\frac{D_{eff}}{D_m} = \frac{(1 - v_f) + \alpha \frac{D_f}{D_m} (1 + v_f)}{(1 + v_f) + \alpha \frac{D_f}{D_m} (1 - v_f)} \quad (9)$$

By introducing the parameter $\psi = \alpha \frac{D_f}{D_m}$, the expression (9) becomes:

$$\frac{D_{eff}}{D_m} = \frac{(1 - v_f) + \psi(1 + v_f)}{(1 + v_f) + \psi(1 - v_f)} \quad (10)$$

For $\psi = 0$, we get the Hashin's expression [4] for composite materials with impermeable fibers:

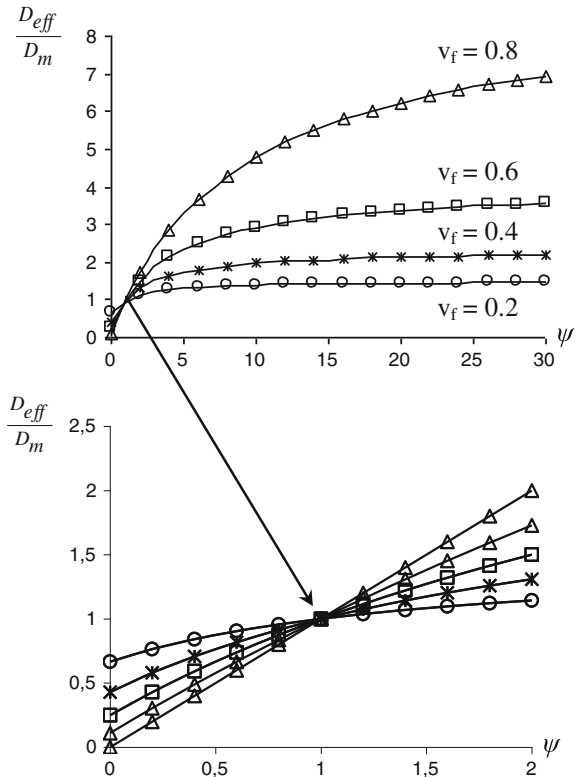
$$\frac{D_{eff}^{impr}}{D_m} = \frac{1 - v_f}{1 + v_f} \quad (11)$$

Figure 2 shows the evolution of the effective diffusion coefficient, obtained by Eq. 10 as a function of the parameter ψ for different fiber volume fractions. The diffusion coefficient increase with the parameter ψ , then it becomes constant for a value of ψ depending on the fiber volume fraction v_f . The intersection of curves observed at $\psi = 1$ corresponds to $D_{eff} = D_m$. The regions with $\psi < 1$ and $D_{eff} < D_m$ characterize composite materials with fibers of weak permeability. The fact that the curves with high volume fractions are below those with weak volume fractions reveals the amortization effect of fibers on the diffusion process. In this model, the parameter ψ can be assimilated to a fiber permeability index. A fiber permeability index lower than one involves that the fibers reduce the velocity of the diffusion process in the composite material.

Eq. 10 can be expressed as:

$$\frac{D_{eff}}{D_m} = \frac{\frac{1-v_f}{1+v_f} + \psi}{1 + \psi \frac{1-v_f}{1+v_f}} \quad (12)$$

Fig. 2 Dimensionless effective diffusivity as a function of ψ



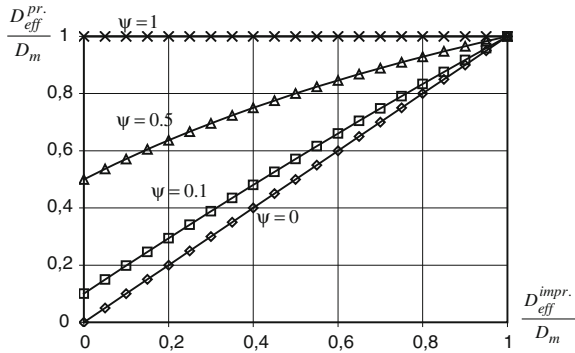
By considering Eqs. 11 and 12, we get:

$$\frac{D_{eff}^{pr}}{D_m} = \frac{\frac{D_{eff}^{impr}}{D_m} + \psi}{1 + \psi \frac{D_{eff}^{impr}}{D_m}} \tag{13}$$

where D_{eff}^{impr} and D_{eff}^{pr} are respectively the effective diffusion coefficients for composites with impermeable and permeable fibers.

Figure 3 presents the evolution of the effective diffusion coefficient for a composite material with permeable fibers as function of the effective diffusion coefficient for a composite with impermeable fibers for different values of the parameter ψ . The diffusion coefficient increase with the diffusion coefficient of the composite with impermeable fibers. The diffusion coefficient of the matrix represents an upper bound, and ψ a lower bound for composites reinforced with fibers of weak or negligible permeability. Contrary for values of ψ superiors to 1 the matrix diffusion coefficient.

Fig. 3 Dimensionless effective moisture diffusivity with permeable fibers as a function of dimensionless effective moisture diffusivity with impermeable fibers



3 Identification of Fiber Diffusion Parameters

In case of a permeable fiber, a concentration jump is imposed on both sides of the fiber/matrix interface. At saturation, the average concentration in the composite C_c is given by the fiber average concentrations C_f of fiber and of the matrix C_m as:

$$C_c = (1 - v_f)C_m + v_f C_f \tag{14}$$

By considering the jump $C_f = \alpha C_m$, (14) becomes:

$$\frac{C_c}{C_m} = 1 + v_f(\alpha - 1) \tag{15}$$

by writing: $\omega = \frac{C_c}{C_m} = \frac{M_c \rho_{csec}}{M_m \rho_{msec}}$

where $M_c, M_m, \rho_{csec}, \rho_{msec}$, are the moisture contents, dry composite and matrix densities respectively? The jump parameter is expressed by:

$$\alpha = \frac{\omega - 1 + v_f}{v_f} \tag{16}$$

For a composite with permeable fibers if hygroscopic data is available (moisture content and diffusivity of matrix and the composite), one can identify the fiber diffusivity and moisture content. First the moisture content is determined from Eq. 17 using Eq. 16 and diffusivity by Eq. 18 using Eq. 10 in witch:

$$M_f = \alpha \frac{M_m \rho_{msec}}{\rho_{fsec}} \tag{17}$$

$$D_f = D_m \frac{\psi}{\alpha} \tag{18}$$

where ρ_{fdry} dry fiber density.

Table 1 Diffusion data and identification results for composite Jute Fiber-Epoxy

Diffusion data (T = 298°K)	Epoxy matrix (LY556HT972)	Composite Jute fiber-/ Epoxy ($v_f = 0.7$)	Permeability parameter ψ Calculated	Fiber Jute Diffusivity D_f Calculated	Fiber Jute moisture content M_f Calculated	Jump Parameter α Calculated
Moisture content M (%)	3.2	8.5	79.43	17.3161×10^{-7}	10.44	3.808
diffusivity (mm^2/s)	8.3×10^{-8}	4.4×10^{-7}				

Table 1 summarised the data of the test immersion in distilled water for composite Jute–Epoxy (Rao and Chanda 1984) at room temperature $T = 298$ K and the results of identification for the Jute fiber. For fiber diffusivity we get the value $D_f = 17.3161 \times 10^{-7}$ mm²/s, that found in literature is 17.7430×10^{-7} mm²/s, the Aditya Sinha (1996) the difference between the two values is about 2.4 %.

4 Effective Moisture Diffusivity of Porous Composite Materials

Three phases approach: fiber, void, matrix. In this approach the void is modeled as a thin layer located between the fiber and the matrix (Fig. 4).

In this case, the cellular diffusion problem through every layer is expressed as follows:

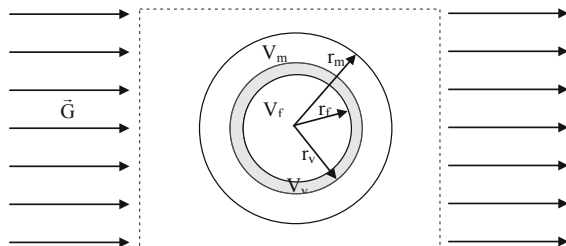
$$\begin{cases} \operatorname{div} \vec{q}(y) = 0 & \text{in each phase } V_\alpha \\ \vec{q}(y) = -D(y) \overrightarrow{\operatorname{grad}} C(y) & \text{in each phase } V_\alpha \\ \|\vec{q} \cdot \vec{n}\| = 0 \text{ at the interfaces} & \text{at interfaces} \\ \|C\| \neq 0 \text{ at the interface fibre/matrix} & \text{at interfaces} \end{cases} \quad (19)$$

The solution field takes then the form:

$$\begin{cases} C(r, \theta) = A_f r \cos(\theta) & \text{in the fibre} \\ C(r, \theta) = (A_v r + \frac{B_v}{r}) \cos(\theta) & \text{in the voids} \\ C(r, \theta) = (A_m r + \frac{B_m}{r}) \cos(\theta) & \text{in the matrix} \\ C(r, \theta) = Gr \cos(\theta) & \text{in the equivalent medium} \end{cases} \quad (20)$$

The conditions of flux continuities and moisture content discontinuities at interfaces involve the following set of equations:

Fig. 4 RVE of the three phases approach



$$\begin{bmatrix} 0 & 0 & \alpha_{fv} r_f^2 & \alpha_{fv} & -r_f^2 & 0 \\ 0 & 0 & D_v r_f^2 & -D_v & -D_f r_f^2 & 0 \\ \alpha_{mv} r_v^2 & \alpha_{mv} & -r_v^2 & -1 & 0 & 0 \\ D_m r_v^2 & -D_m & -D_v r_v^2 & D_v & 0 & 0 \\ r_m^2 & 1 & 0 & 0 & 0 & -r_m^2 \\ D_m r_m^2 & -D_m & 0 & 0 & 0 & -D_{eff} r_m^2 \end{bmatrix} \begin{bmatrix} A_m \\ B_m \\ A_v \\ B_v \\ A_f \\ G \end{bmatrix} = \begin{bmatrix} 0 \\ 0 \\ 0 \\ 0 \\ 0 \\ 0 \end{bmatrix} \quad (21)$$

α_{fv} and α_{mv} are the jump parameters corresponding to the interfaces voids/fiber and voids/matrix respectively. The knowledge of saturation mass of different constituents leads to the determination of jump parameters. By making the determinant equal to zero, we obtain the expression of the effective diffusivity:

$$D_{eff} = D_m \frac{D_m(1 - kv_f)[D_v(1 + k) + \alpha_{fv}D_f(k - 1)] + \alpha_{mv}D_v(1 + kv_f)[D_v(k - 1) + \alpha_{fv}D_f(1 + k)]}{D_m(1 + kv_f)[D_v(1 + k) + \alpha_{fv}D_f(k - 1)] + \alpha_{mv}D_v(kv_f - 1)[D_v(1 - k) - \alpha_{fv}D_f(k + 1)]} \quad (22)$$

where, $k = \frac{v_v + v_f}{v_f}$, v_v and v_f are respectively the void and fiber volume fractions. Finally:

$$\frac{D_{eff}}{D_m} = \frac{(1 - kv_f)[1 + k + \alpha_{fv} \frac{D_f}{D_v}(k - 1)] + \alpha_{mv}(1 + kv_f)[\frac{D_v}{D_m}(k - 1) + \alpha_{fv} \frac{D_f}{D_m}(1 + k)]}{(1 + kv_f)[1 + k + \alpha_{fv} \frac{D_f}{D_v}(k - 1)] + \alpha_{mv}(kv_f - 1)[\frac{D_v}{D_m}(1 - k) - \alpha_{fv} \frac{D_f}{D_m}(1 + k)]} \quad (23)$$

By introducing $\phi = \frac{D_v}{D_m}$ and $\xi = \alpha_{fv} \frac{D_f}{D_m}$ Eq. (23) becomes:

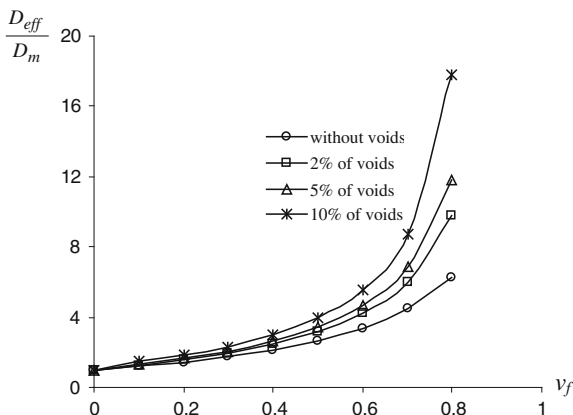
$$\frac{D_{eff}}{D_m} = \frac{(1 - kv_f)[1 + k + \frac{\xi}{\phi}(k - 1)] + \alpha_{mv}(1 + kv_f)[\phi(k - 1) + \xi(1 + k)]}{(1 + kv_f)[1 + k + \frac{\xi}{\phi}(k - 1)] + \alpha_{mv}(kv_f - 1)[\phi(1 - k) - \xi(1 + k)]} \quad (24)$$

Assuming that moisture diffusion in void is faster than in any other constituents, we choose $\alpha_{fv} < 1$ and $\alpha_{mv} > 1$. $\alpha_{fv} = 0.2$ ($\xi = 4.18$) corresponds to an interface jute fiber/voids [5].

Figure 5 shows the evolution of the effective diffusivity of a composite material with permeable fibers for values $\xi = 4.18$ and $\phi = 10$ and different void volume fractions. We note a large increase of the diffusivity with the rate of voids.

For 2 % of voids and a fiber volume fraction equal to 70 %, an increase of about 35 % is observed. For 10 % of voids and the same fiber volume fraction, the increase in diffusivity is about 100 %. These values reveal the strong sensitivity of the effective diffusivity to the void volume fraction. We get the expression of the effective diffusion coefficient for composite with impermeable fibers by considering $D_f = 0$ ($\xi = 0$) in Eq. (24):

Fig. 5 Void effects on the composite diffusivity in the case of permeable fibers ($\phi = 10, \xi = 4.18, \alpha_{fv} = 0.2, \alpha_{mv} = 15$)

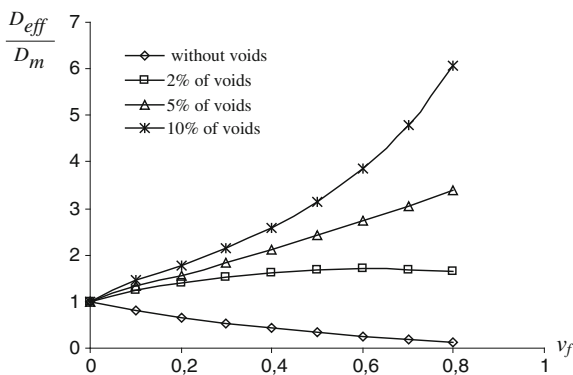


$$\frac{D_{eff}}{D_m} = \frac{(1 - kv_f)(1 + k) + \alpha_{mv} \frac{D_v}{D_m} (1 + kv_f)(k - 1)}{(1 + kv_f)(1 + k) + \alpha_{mv} \frac{D_v}{D_m} (kv_f - 1)(1 - k)} \tag{25}$$

In case of impermeable fibers Fig. 6 shows, that the difference between the diffusion coefficients is proportional to the void volume fraction. The difference observed between the effective diffusivities for non-porous and porous materials is more important than in the case of permeable fiber: for the volume fractions of fibers and voids equal respectively to 10 and 70 %, the effective diffusion coefficient is 26 times more important than that of composite without void.

A decrease in the effective diffusion coefficient as a function of v_f in the case of a non porous material, is observed. The presence of voids with impermeable fibers not only tends to reduce the damping effect of the fibers but also undertakes the influence of the matrix on diffusive behavior of the composite. This behavior is not presented when the effective diffusivity of the composite material is calculated by using the effective diffusivity of porous matrix deduced with the diluted approach.

Fig. 6 Void effects on the composite diffusivity in the case of impermeable fibers ($\phi = 10, \alpha_{mv} = 15$)



5 Conclusion

Closed-form solutions are proposed for calculating the effective diffusivities as functions of diffusivities of the constituents, volume fraction of the constituents and, when permeable fibers are considered, to a representative parameter of the moisture content jump between the constituents. These solutions also allow estimating the moisture diffusivity of a constituent, from the knowledge of the effective moisture diffusivity, through inverse approaches. A special attention is devoted to the determination of the effective moisture diffusivity for composite materials containing voids, which are often met in practice in such materials.

References

1. Tsai, S.W., Hahn, H.T.: Introduction to Composite Materials, Technomic (1980)
2. Springer, G.S., Shen, C.H.: Moisture absorption and desorption of composite materials. *J. Compos. Mater.* 2–20 (1976)
3. Stastna, J., De Kee, D.: Transport Properties in Polymers, Technomic (1995)
4. Hashin, S.: Theory of Fiber Reinforced Materials, NASA CR-1974 (1972)
5. Rao, R.M., Chanda, M., Balsubramanian, A.: Factors affecting moisture absorption in polymer composites part II: influence of external factors. *J. Reinforced Plastic Compos.* 246–251 (1984)

Elastic Buckling at the Scale of a Bone Trabecula: The Influence of the Boundary Conditions

Hamza Bennaceur, Salah Ramtani and Toufik Outtas

Abstract Trabecular fatigue fractures are observed as compressive stress fractures in the proximal femur, vertebrae, calcaneus and tibia. These fractures are often preceded by buckling and bending of microstructural elements. But the etiology of these bone fractures is still poorly understood in biomechanical perspective. In the present work, it comes to predicting the buckling mechanism trabeculae in progress remodeling bone and in function of the boundary conditions without experimental data.

Keywords Adaptive elasticity · Bone remodeling · Beam buckling theory · Boundary conditions

1 Introduction

The study of the physiology of bone tissue usually develops through its two fundamental roles within our organization: inorganic elements tank (calcium, phosphorus, magnesium) and mechanical support to the soft tissue. This last function allows movement and locomotion using the combined action of muscles, tendons and ligaments within the locomotive apparatus. These two functions are based on architectural organization of bone tissue particularly developed, and the existence of an adaptability of its structure (architectural adaptation to changing mechanical conditions) due to the modeling and remodeling mechanism themselves linked to the activity of specialized bone coupled cell populations [1–3, 8].

H. Bennaceur · T. Outtas

Laboratoire de Mécanique des Structures et Matériaux, Université de Batna, 05000 Batna, Algeria

e-mail: ben.hamza86@yahoo.fr

S. Ramtani (✉)

Laboratoire CSPBAT – Biomatériaux pour la Santé, UMR 7244 CNRS, Université Paris-Nord, Villetaneuse, France

e-mail: ramtani@univ-paris13.fr

Our daily activities, submitting certain bones of our skeleton to cyclic loading which may result an increased risk of fracture [4, 11]. Trabecular bone, a spongy and porous type of bone tissue made of a lattice of interconnected rods and/or plates, plays an important role in the load transmission in major joints such as the hip, knee and spine [3, 7, 8]. It is affected by many metabolic bone diseases, such as osteoporosis, which cause bone loss and result directly in decreased bone strength and an increased risk of bone fracture [4, 11].

Three abnormalities that can account for skeletal fragility disproportional to the degree of bone loss have been described [5, 11]:

- a loss of trabecular connectivity such that vertical weight-bearing bars lose their cross attachments with each other, thus becoming susceptible to buckling;
- an inefficient and prolonged microdamage repair due to periods of pause in the formation phase of remodeling;
- an accumulation of unpaired microdamage in unremodeled bone tissue in the central part of trabeculae due to reduced osteon wall thickness coupled with the maintenance of trabecular thickness.

The knowledge of the mechanisms of interaction between the remodeling process and the appearance of elastic instabilities is important to better understand the potential mechanisms involved in microfractures associated with certain bone diseases like osteoporosis. The interest of a theoretical framework for understanding the process of buckling at the local level of trabeculae proves to be more than necessary and was the subject of recent work [10]. As part of work, we have opted for the theory of elastic adaptation implemented by Cowin [2, 6]. Here we focus our efforts on the study of the influence of boundary conditions on the stability of deflection and the critical load of Euler buckling influenced by the spatiotemporal evolution of the bulk density of bone tissue. Readers are encouraged to consult the reference documents for more details [2, 9, 10].

2 Equation Model

2.1 Equilibrium Equation

We recently established a new specific buckling equilibrium equation of straight beams, adaptive elastic across the trabecula. Under certain simplifying conditions, it is written [10]:

$$\left(1 + \eta \frac{\bar{e}}{\xi_0}\right) \frac{d^4 \bar{w}(\bar{x})}{d\bar{x}^4} + \frac{P}{\xi_0 E^0 I_{Oy}} \frac{d^2 \bar{w}(\bar{x})}{d\bar{x}^2} = 0 \quad (1)$$

With L is the length of the beam, $\bar{x} = \frac{x}{L}$ is the current position of a point of the beam, P is the compressive load at the end of the beam, $\eta = \frac{E^1}{E^0}$ represents a characteristic parameter of the material, E^0 and E^1 is respectively the primary and secondary elastic modulus.

2.2 Modeling/Bone Remodeling Law

The internal remodeling process concerning the change of the elastic properties (physical) of the bone takes place in the following four phases:

- An activation phase characterized by a deposit of osteoclasts and osteoblasts along remodeling service. For example, the increased number of osteoblasts is a consequence of the stimulation of cell division, their precursors (osteoprogenitor cells) and activation.
- Resorption phase reflecting the activity of osteoclasts that destroy existing bone. At the quiescent state, the surface of the extracellular matrix of the bone is covered by an edge of osteoblasts that prevent access of osteoclasts. Under the action of bone resorbing factors, osteoblasts retract and leave the place for the osteoclasts which can adhere to the matrix.
- A phase inversion during which the osteoclasts are replaced by mononuclear cells.
- On the same site which just happen resorption, neighborhood osteoblasts start to secrete new bone matrix which is then mineralized (reconstruction). During this phase, some osteoblasts remain trapped in the newly created matrix and become osteocytes whose function, among others, is to ensure that trade between the bone matrix and blood plasma (mechanosensors).

For simplicity, we voluntarily ignore the aspect multi-physics coupling related to the complexity of the process modeling/bone remodeling.

We denote $\xi(x, y, z, t)$ the volume fraction of bone matrix and by ξ_0 its reference value. The variation in the volume fraction of bone matrix is defined by $e(x, y, z, t) = \xi(x, y, z, t) - \xi_0$ and its average $\bar{e} = \bar{e}(x, t)$ on a cross section Σ_0 by [10]:

$$\bar{e}(x, t) = \int_{\Sigma_0} e(x, y, z, t) dy dz \quad (2)$$

The simplified law of bone modeling/remodeling is written [2, 9, 10]:

$$\frac{d}{dt} \bar{e}(x, t) = a_0 + a_1 \bar{e} + a_2 \bar{e}^2 - A(1 + \bar{e}) \frac{d^2 w(x)}{dx^2} \quad (3)$$

The expression (3) connects the rate of modeling/remodeling of the deformation state of the beam characterized by the deflection $w(x)$. a_0 , a_1 , a_2 and A are parameters of the model, in s^{-1} , Hypothetical values for which experimental data are missing. In its undeformed state, the beam is assumed to be in an equilibrium state which results in the relationship $a_0 + a_1 \bar{e} + a_2 \bar{e}^2 = 0$, and one of whose initial values $e_0 = 0.1$ is one of the roots of trinomial.

3 Numerical Results and Discussion

3.1 Boundary Conditions

Spongy bone is composed of a network of beams and/or plates interconnected, playing an important role in the transmission of loads supported by the skeleton. In this case we want to explore the influence of boundary conditions on the critical buckling load of slender beams is known on conventional beams. The nature of the boundary conditions determines the buckling mode and the distance between the deformed points of the beam. Two boundary conditions are considered and shown in Fig. 1 and indicated in Table 1.

The two beams are chosen rectangular cross-section, under constant compression load $N = -P$, ($L; b, h$), are the dimensions of the beam representing respectively the length, width and height. The resolution of the balance equation (Eq. 1) is carried out by the finite difference method associated to the Inverse power method for research eigenvalues (Euler critical load) and eigenvectors (beam deflection) while the remodeling law is determined by the numerical scheme Euler [13]. The hypothetical values of model parameters, extracted from the literature [9, 10], are reported in Table 2.

Fig. 1 Boundary conditions of the bone beam, **a** Bi clamped beam, **b** simple-pinned beam [12, 14]

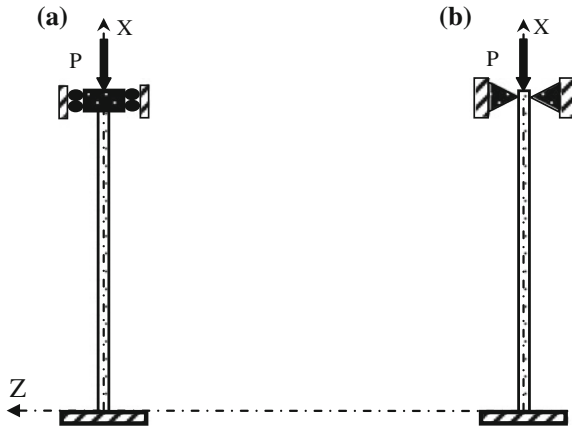


Table 1 The boundary conditions

Liaison	X = 0	X = 1
(CC) Bi clamped	$\bar{w}(\bar{x}) = 0 \quad \frac{d\bar{w}(\bar{x})}{d\bar{x}} = 0$	$\bar{w}(\bar{x}) = 0 \quad \frac{d\bar{w}(\bar{x})}{d\bar{x}} = 0$
(SP) Simple-pinned	$\bar{w}(\bar{x}) = 0 \quad \frac{d^2\bar{w}(\bar{x})}{d\bar{x}^2} = 0$	$\bar{w}(\bar{x}) = 0 \quad \frac{d^2\bar{w}(\bar{x})}{d\bar{x}^2} = 0$

Table 2 Hypothetical remodeling rate coefficients [10]

Bone remodeling parameters	a_0 (s^{-1})	a_1 (s^{-1})	a_2 (s^{-1})	A (s^{-1})	ξ_0
		10^{-8}	$-2.50 \cdot 10^{-7}$	$-1.50 \cdot 10^{-6}$	0.50
Geometrical and elastic parameters	L	b	h	E^0 (GPa)	n
	1.00	0.10	0.10	18.40	35

3.2 Evolution of Buckling Modes $\bar{w}(x, t)$

In the first time we start with the analysis of spatio-temporal of deflection evolution $\bar{w}(x, t)$ in respect to each boundary condition type. Concerning the beam with connection (CC), we see Fig. 2 that the evolution over time of the deflection (mode I) is unstable because is disrupted by the birth of a reverse mode I at $t = 42.08$ days and will be stabilized until the remodeling process. It also notes the absence of a mode II buckling. For the beam with connection (SP), the deflection mode I in Fig. 3 remained stable until the end of the adaptation process.

3.3 Evolution of the Bone Volume Fraction $\bar{e}(x, t)$

Secondly, we focus on the analysis of spatio-temporal evolution of the bone volume fraction $\bar{e}(x, t)$ for each type of connection. As shown in Fig. 4, the evolution of the volume fraction of bone material is very strongly affected by the type of connection (CC) with the appearance of two stationary points at $\bar{x} \approx 0.25$ and $\bar{x} \approx 0.85$. An initial apposition activity (formation) is noted in the central part of the beam and resorption activity in the other two beam sections.

This scenario still until the appearance of the elastic instability Fig. 2 after a few days, remodeling activities are reversed, and we can mark the resorption in the central part and bone material apposition outside of the central section.

The beam with the connection (SP) Fig. 5 has no singular point, because of the stability of its deflection, and it is in the continuous reinforcement of a volume fraction (apposition).

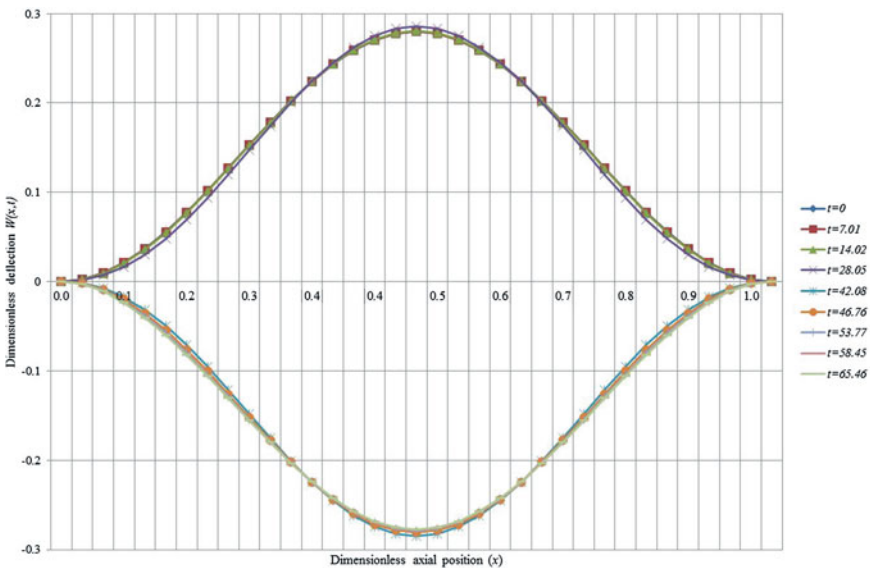


Fig. 2 Deflection evolution with the connection (CC) for $\eta = 0.85$

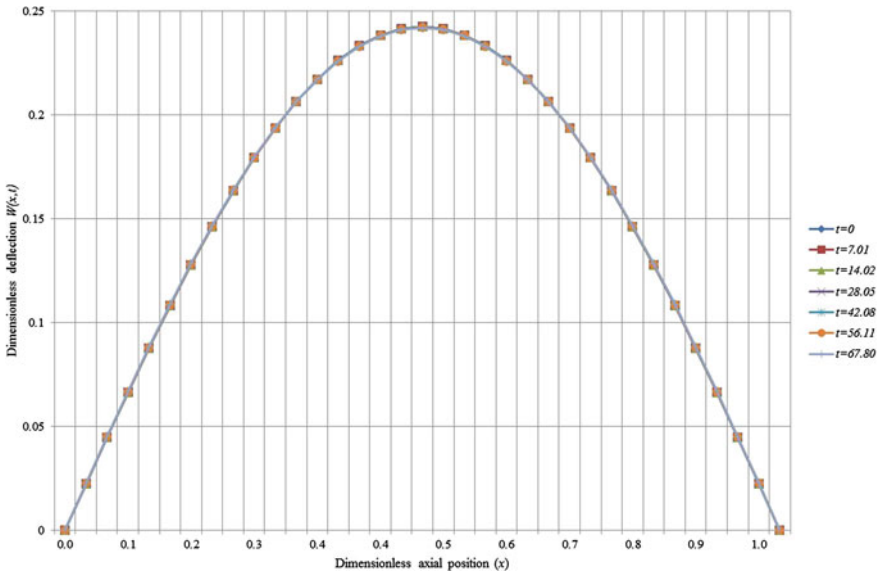


Fig. 3 Deflection evolution with the connection (SP) for $\eta = 0.85$

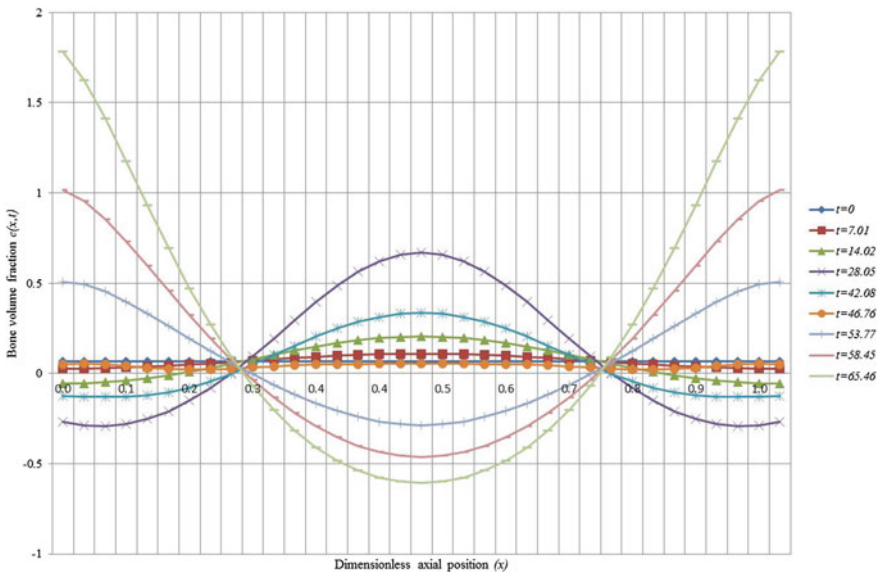


Fig. 4 Evolution of the bone volume fraction with the connection (CC) for $\eta = 0.85$

The evolution of the critical buckling load is different for each type of connection Fig. 6. Firstly, there is a nonlinear evolution and intensity of the largest critical load for the connection (CC) and the lowest for the connection (SP).

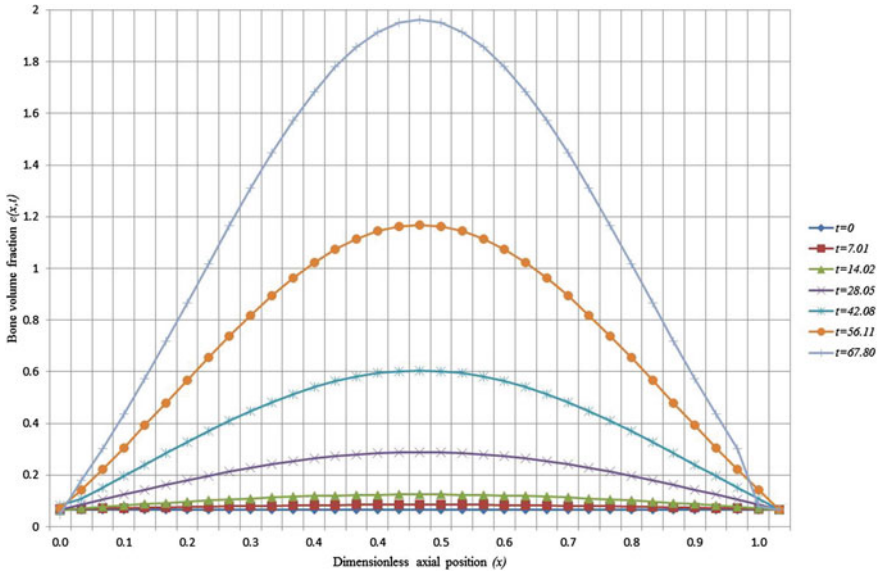


Fig. 5 Evolution of the bone volume fraction with the connection (SP) for $\eta = 0.85$

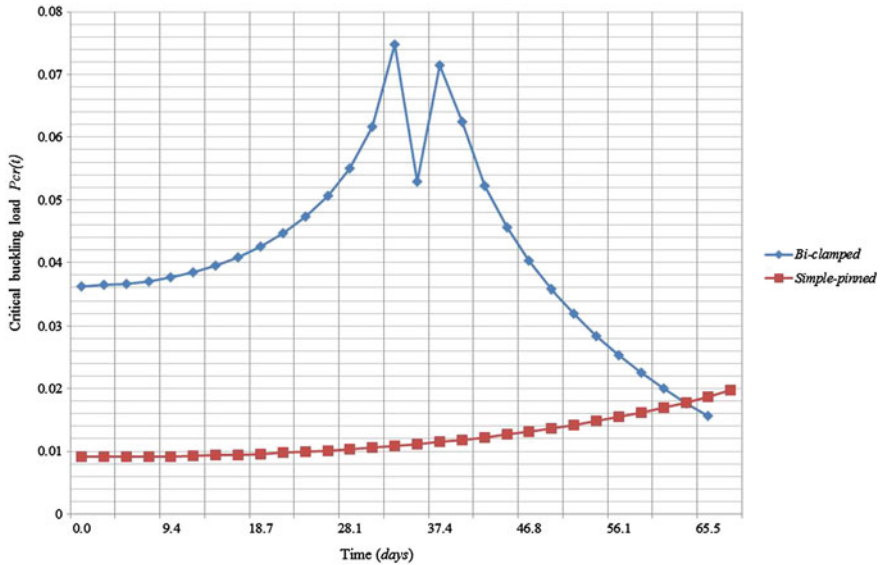


Fig. 6 Critical buckling load for the two boundary conditions

The observed dropout Fig. 6 corresponds to the appearance of elastic instability favoring the reversal of remodeling activity in the case (CC). The stable case (SP) does not present elastic instability, so no dropout.

4 Conclusions

The adaptive elasticity theory proves to be an appropriate tool for the study of microstructural elements buckling mechanisms of trabecular bone tissue. In this contribution based on recent work we have established, at least from a theoretical and numerical view point, the whole point of the boundary conditions on elastic stability of the element and cell activity in the bone tissue formation and resorption. We also observed a link between the appearance of new buckling modes (reverse mode I) and dropout of the Euler critical load during the time course. This work encouraging, promising and original, which has no equivalent in the current literature, provides a new basis for reflection for the development of experimental protocols to other hypotheses that will help us to understand better local buckling fracture mechanisms related to patients with osteoporosis. The main difficulty is the absence, at the scale of trabeculae, experimental data for validation.

References

1. Ciarelli, T.E., Fyhrie, D.P., Parfitt, A.M.: Effects of vertebral bone fragility and bone formation rate on the mineralization levels of cancellous bone from white females. *Bone* **32**, 311–315 (2003)
2. Cowin, S.C., Hegedus, D.M.: Bone remodeling I: theory of adaptive elasticity. *J. Elast.* **6**, 313–325 (1976)
3. Fung, Y.C.: *Biomechanics: Mechanical Properties of Living Tissue*. Springer, Berlin Heidelberg New York (1993)
4. Gomberg, B.R., Saha, P.K., Song, H.K., Hwang, S.N., Wehrli, F.W.: Topological analysis of trabecular bone MR images. *IEEE Trans. Med. Imaging* **19**, 166–174 (2000)
5. Hasegawa, K., Turner, C.H., Recker, R.R., Wu, E., Burr, D.B.: Elastic properties of osteoporotic bone measured by scanning acoustic microscopy. *Bone* **16**, 85–90 (1995)
6. Hegedus, D.H., Cowin, S.C.: Bone remodeling II: small strain adaptive elasticity. *J. Elast.* **6**, 337–352 (1976)
7. Muller, R., Gerber, S.C., Hayes, W.C.: Micro compression: a novel method for the non-destructive assessment of bone failure. *J. Biomech.* **31**, 150 (1998)
8. Ramtani, S.: *Biomécanique-Mécanobiologie des systèmes complexes*, Habilitation à diriger des recherches (HDR), Université Paris 12 (2003)
9. Ramtani, S., Abdi, M.: Buckling of adaptive elastic bone-plate: theoretical and numerical investigation. *Biomech. Model. Mechanobiol.* **3**, 200–208 (2005)
10. Ramtani, S., Bennaceur, H., Outtas, T.: A simplified theory of adaptive bone elastic beam buckling. *Adv. Biomech. Appl.* **1**(3), 211–225 (2014)
11. Recker, R.R.: Low bone mass may not be the only cause of skeletal fragility in osteoporosis. *ProcSocExpBiol Med* **191**(3), 272–274 (1989)
12. Reismann H., P.S., Pawlik, *Elasticity: theory and applications*, New York: Wiley, 1980
13. Richtmyer, R.D., Morton, K.W.: *Difference Methods for Initial Value Problems*. Inter Science Publishers, Wiley, New York (1967)
14. Vinson, J.R.: *The Behavior of Thin Walled Structures-Beams, Plates, and Shells*. Kluwer Academic Publishers, Dordrecht etc. (1989)

Dynamic Characterization of MR Damper and Experimental Adjustment of Numerical Model

Said Boukerroum and Nacer Hamzaoui

Abstract In this present work, we analyze through the hysteresis loops the modified Bouc-Wen model performance governing the internal dynamics of a Magneto-Rheological (MR) damper. The analysis of the energy dissipated per cycle of vibration is made by a MR damper dynamic characterization on a dynamic testing machine in order to examine the effect of the frequency, the amplitude of the displacement and of the excitation current on the dissipated energy and therefore the equivalent damping coefficient. The dynamic responses of the modified Bouc-Wen numerical model will be compared with experimental responses and then recalibrated on the latter, while performing an adjustment of the influence parameters model.

Keywords MR damper · Dynamic characterization · Modified Bouc-Wen model · Hysteresis curve · Dissipated energy · Control law

1 Introduction

Magneto-rheological dampers (*MR*) are subject in recent years of special attention because of their characteristics including mechanical simplicity, high dynamic range, low power, high capacity power and robustness. However, and early 2000s, researchers began to consider the development and use of these dampers in several areas, especially where other technologies have begun to emerge to make their practical use possible. Microprocessors, sensors and controllers to increase the processing speed control have created opportunities that did not exist before.

S. Boukerroum (✉)

USTHB/FGMGP, LMA, BP 32, El Allia, 16111 Bab Ezouar, Alger, Algeria
e-mail: sboukerroum@yahoo.fr

N. Hamzaoui

INSA de Lyon, LVA, Bâtiment a de St. Exupéry, 25 bis avenue Jean Capelle,
69621 Villeurbanne, France
e-mail: Nacer.hamzaoui@insa-lyon.fr

A large range of use of *MR* dampers allowed the researchers to improve their performance, focusing their internal dynamics. Indeed several mathematical models highlighting the physical and energy characteristics (electric current, magnetic fields, flow, viscosity) of fluids *MR*, have enabled the development of several digital models governing the internal dynamics of these dampers such as models of Bingham, Gamota and Filisko, Bouc-Wen and modified Bouc-Wen [1]. To validate the performance of these models, researchers are mostly oriented to experimental studies often very complex and expensive, whose interest is to adjust these models. In order to have a model of the *MR* damper more representative, may substitute for experimentation in other developments and analyzes schemes and control laws, it is necessary to validate it through confrontation “computing-test” to better analyze response times and allow to perform recalibration (adjusting), the main objective of this confrontation for a better representation of the digital model [2].

2 Magneto Rheological Damper

The *RD-1005-3* (Fig. 1), is a small, compact monotube damper of Lord Corporation [3]. With a length of 208 mm in the extended position, it incorporates an electromagnet at the piston, fed a low voltage of 12 V (*DC*) and a small electrical current which can be varied in a range from 0 to 2 A. The resistance of the coil at ambient temperature is 5 Ω . Its stroke is equal at 25 mm and develops a maximum load intensity of 4448 N [3]. The current adjustment via its controller, allows varied the magnetic field at the piston coil and change accordingly in real-time the damping coefficient, and therefore the damping force. The response time of this damper does not exceed 25 ms (time to reach 90 % of the maximum level during a step entry of 0–1 A at a speed of 51 mm/s) [4].

The advantage of *MR* damper is associated with its ability to provide a continuous modification of damping characteristics during the period of control.

2.1 Characterization of the MR Damper

The characterization of the damper (*RD-1005-3*) is a necessary step to obtain the dynamic data for its functioning, such as the ratio force/displacement and force/velocity and the saturation current. The *MR* damper was tested on a dynamic

Fig. 1 MR structure of a monotube damper (*RD-1005-3*) [3]

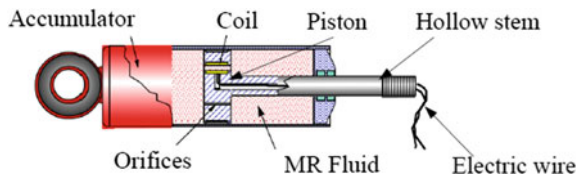


Fig. 2 Characterization of the MR damper (RD-1005-3) on fatigue machine 'MTS 810'



tensile testing machine capable of generating the sinusoidal cyclic inputs, adjustable in frequency and amplitude (Fig. 2). The performance of this damper measured by the input current are the evolution of the damping force versus time, the ratio force/displacement and force/speed that highlight the hysteretic behavior (visco-plastic behavior of *MR* fluid). The excitation of the damper is a sinusoidal displacement to the frequency 1, 5 and 2.5 Hz during twenty cycles for three different displacement amplitudes of the damper piston. To prevent its damage, we set the three amplitudes of peak to peak displacement at 15, 20 and 25 mm. The control of the electric current supplied to the damper, is made with a controller via an amperemeter to measure the input current. The intensities of the current supplied to the damper during testing are: 0, 0.2, 0.4, 0.6, 0.8, 1 and 1.6 A.

Figure 3, shows the time evolution of the damping force depending on the intensity of the current supplied to the damper for a peak displacement to peak amplitude equal to 15 mm and imposed on the piston at the frequency of 2.5 Hz. With the increase of the electric current delivered to the damper, the average magnitude of the damping force increases conspicuously to 1350 N for a current equal to 0.8 A (Fig. 3). However, when the applied current exceeds this intensity, increasing the damping force becomes insignificant (Fig. 4). This means that under

Fig. 3 Time evolution of the damping force measured, according to the current

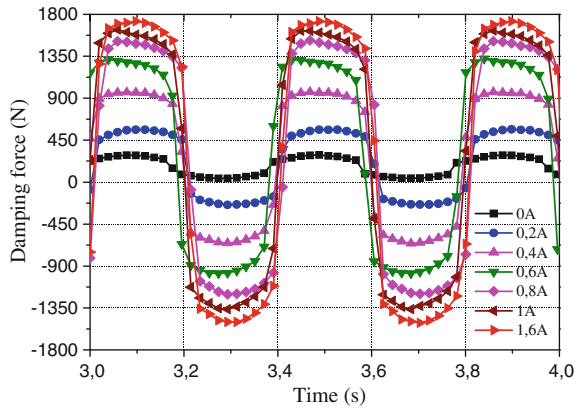
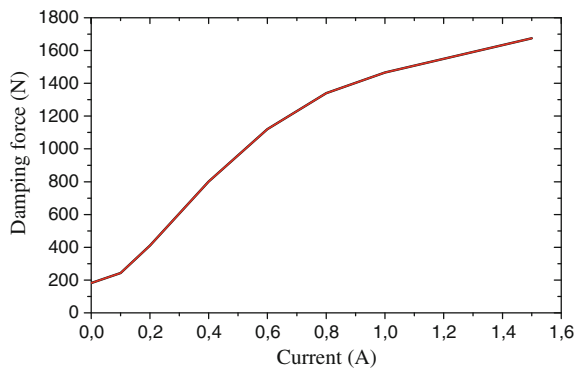


Fig. 4 Average peak value damping force measured, according to the current

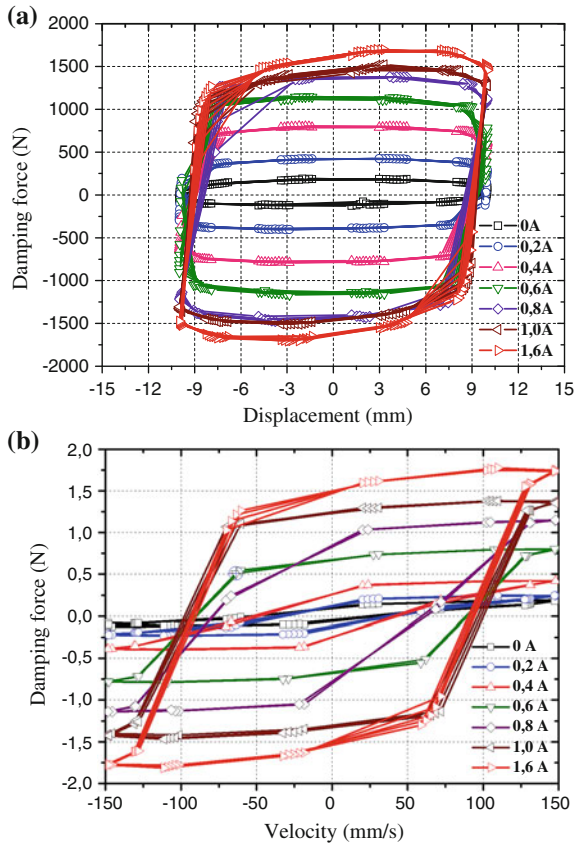


the conditions of the measurements, the saturation of the magnetorheological effect occurs at a current between and 0.8 A [5, 6]. It is also noted that the force produced by the *MR* damper is not exactly centered at zero, as can be seen in Fig. 3.

This is due in part to the presence of the accumulator in the *MR* damper filled with compressed gas which prevents the piston in its compression phase finish its stroke. The force developed by the damper with a current of 1 A is approximately eight times greater than that obtained without magnetic field ($I = 0$ A).

Figure 5a, b, which represent respectively the ratio force/displacement and force/velocity for different values of the electric current supplied to the *MR* damper, confirm this nonlinear behavior of *MR* fluids, where the increase of electric current is grown the damping force significantly from 0 to 0.8 A. The ratio force/velocity shown in Fig. 5b shows an increase in the damping force depending on the speed calculated by differentiation of the measured displacement. A significant increase of the damping force according to the electric current is observed, until the value of 0.8 A, from which begins the saturation phenomenon. The area of the different loops hysteresis which represents the energy dissipated per cycle of the *MR* damper, obeys perfectly visco-plastic behavior of the *MR* fluids. Indeed this area increases

Fig. 5 Experimental responses force/displacement (a) and force/velocity (b)

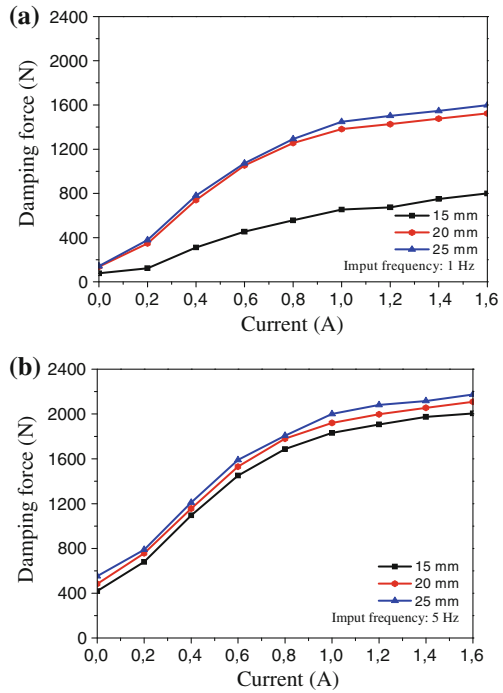


with the increase in fluid viscosity due to the increase of the magnetic field with the electric current [4].

The damping force is not only a function of current supplied to the damper, but also a function of the excitation frequency and the amplitude of displacement imposed to the piston of the MR damper. Figure 6 show, in fact, the influence of the excitation frequency and the amplitude of the displacement of the damping force intensity. Firstly for a given frequency, the damping force increases with the displacement imposed to the piston and the electric current. On the other hand, for a given displacement the intensity of the damping force increases as a function of the frequency and the electric current. It is therefore clear that the damping coefficient equivalent to an MR damper is a function of the three input parameters are the frequency, the displacement and the excitation current.

This increase of the damping force as a function of the excitation frequency for a peak to peak displacement of 15 mm and a current of 1 A is also followed by an

Fig. 6 Variation of the damping force of the shock absorber in function of the displacement and the excitation current at a frequency of 1 Hz (a) and 5 Hz (b)



increase of the hysteresis loops area force/displacement (Fig. 7a) and force/velocity (Fig. 7b) that reflect well the energy dissipated per cycle of operation of the MR damper.

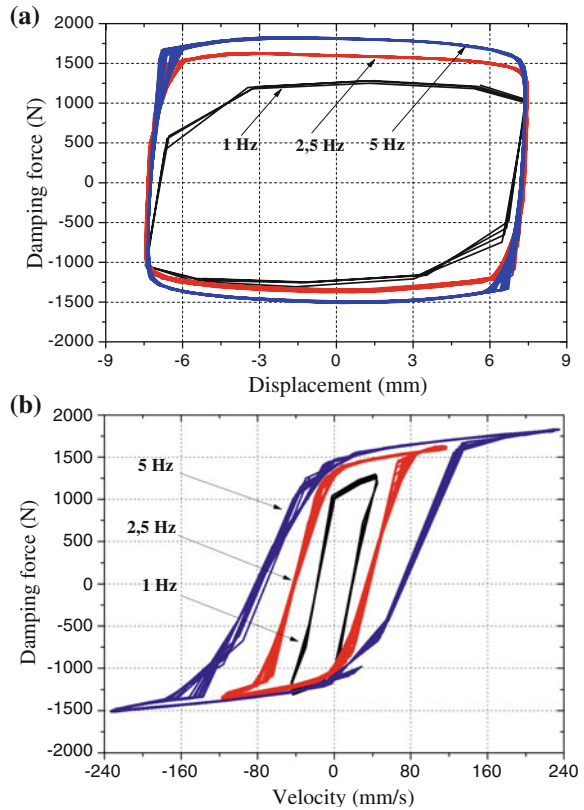
2.2 Determination of the Equivalent Damping Coefficient

The equivalent damping coefficient may be determined according to the times of the input current, frequency and amplitude of excitation [7]. Assuming that this is a passive linear damper with an ideal damping of each condition, we can determine, by integrating the energy E dissipated by the MR damper during a cycle of vibration.

The equivalent damping coefficient may be determined according to the times of the input current, frequency and amplitude of excitation [7]. Assuming that this is a passive linear damper with an ideal damping of each condition, we can determine, by integrating the energy E dissipated by the MR damper during a cycle of vibration.

$$E = \int_0^{T=1/f} F_{MR} dx = \int_0^{2\pi/\omega_e} F_{MR} dx = \int_0^{2\pi/\omega_e} c_{eq} \dot{x} dx \quad (1)$$

Fig. 7 Ratios force/ displacement (a) and force/ velocity (b) of the damper according to the excitation frequency of a 15 mm displacement and a current of 1A



where ω_e (rad/s) is the angular frequency of the excitation frequency f (Hz), \dot{x} (mm/s) is the relative velocity of the damper stem and F_{MR} (N), the measured damping force.

The expression (1) of the dissipated energy E expressed in the field time is written:

$$E = \int_0^{2\pi/\omega_e} c_{eq}(\dot{x})^2 dt \tag{2}$$

By adopting a simple harmonic excitation, of sinusoidal type: $x(t) = X_0 \sin \omega_e t$ with X_0 is the maximum amplitude of relative displacement MR damper piston, the expression (2) becomes:

$$E = \int_0^{2\pi/\omega_e} c_{eq} (\omega_e X_0 \cos \omega_e t)^2 dt = \pi c_{eq} \omega_e X_0^2 \tag{3}$$

Hence the expression of the calculated equivalent damping coefficient:

$$c_{eq} = \frac{E}{\pi\omega_e X_0} \tag{4}$$

The curve of the energy dissipated per cycle drawn from the expression (4), actually shows an increase in this energy as a function of the excitation frequency of the induced current and for a given displacement (Fig. 8a, b). Whichever the excitation frequency this increase in the dissipated energy is more pronounced for the currents supplied to the MR damper below 0.8 A.

For a given displacement and frequency of oscillation or fix, the equivalent damping coefficient increases with the current induced in the MR damper (Fig. 9a), by against this coefficient decreases with the excitation frequency for displacement and a current fixed (Fig. 9b). These two results validate the expression (4) of the equivalent damping coefficient calculated, where the increase in dissipated energy and therefore current grown this coefficient, while for a current fixed in advance, an increase in the frequency excitation or displacement amplitude imposed on the damper piston, made decreasing the damping coefficient.

Fig. 8 Dissipated energy variation of the damper according the amplitude displacement and excitation current for 1 Hz (a) and 5 Hz (b)

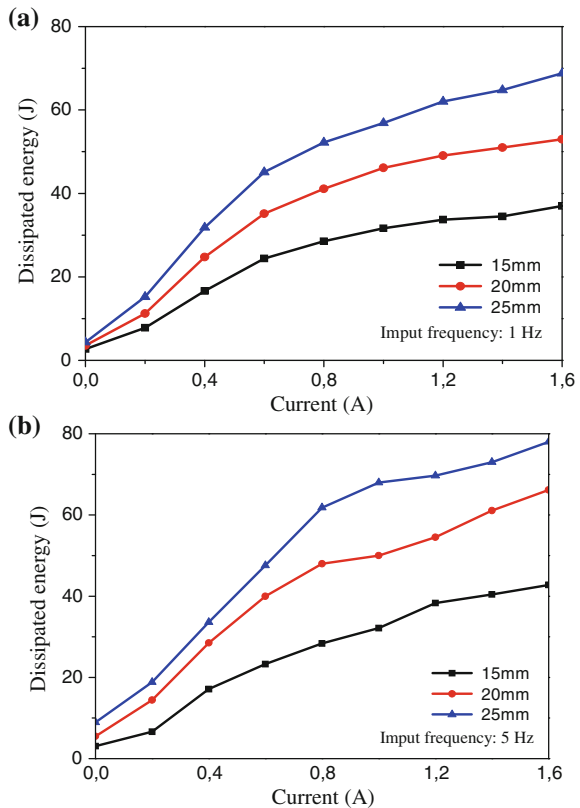
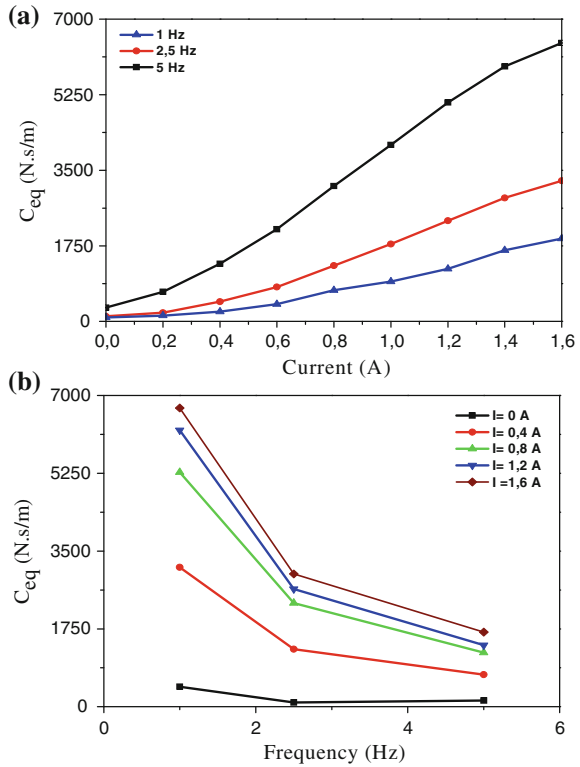


Fig. 9 Equivalent damping coefficient variation of MR damper according the current (a) and frequency (b), for 20 mm of displacement



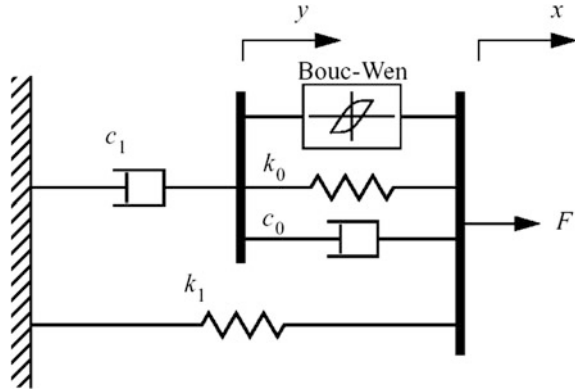
3 Numerical Modified Bouc-Wen Model

The Bouc-Wen model proposed by Wen [8] in 1976 does provide the behavior force/displacement of the MR damper, and has a force/velocity behavior that more closely resembles the experimental data with resulting hysteresis loops that translate better nonlinearities of MR fluids. However, similar to the Bingham model [9, 10], the nonlinear response of the report force/velocity of Bouc-Wen model does not decay in the region where the acceleration and velocity have opposite signs during transitions [1].

To better predict the behavior of the MR damper at low velocities and in cases where the acceleration and velocity have opposite signs, a model based on the Bouc-Wen proposed by Spencer et al. [1]. In this model named modified Bouc-Wen model or phenomenological model (Fig. 10), the rigidity of the accumulator, not existing element in the other models mentioned, is represented by k_1 .

A damping coefficient c_1 is also included in this model to produce the decrease was observed in the experimental data at low velocities. Stiffness k_0 is introduced for controlling the stiffness at high velocities and the viscous attenuation observed for these higher velocities is represented by c_0 . The initial displacement x_0 of the stiffness spring k_1 is related to the nominal force damper due to the accumulator.

Fig. 10 Modified Bouc-Wen model by Spencer et al. [1]



To obtain the equations governing the movement of the model, consider the upper half model of Fig. 10. The forces on either side of the rigid middle bar are equivalent, therefore:

$$c_1 \dot{y} = \alpha z + k_0(x - y) + c_0(\dot{x} - \dot{y}) \tag{5}$$

Evolutionary variable is written as [9]:

$$z = -\gamma |z_2 - z_3| \cdot z \cdot |z|^{n-1} - \beta(z_2 - z_3)|z|^n + A(z_2 - z_3) \tag{6}$$

Where β , γ , n and A are the parameters characteristic of the *Bouc-Wen* model that can be controlled to adjust the linearity and smoothing the transition periods in the pre and post-stress threshold. From (5), the velocity is:

$$\dot{y} = \frac{1}{(c_0 + c_1)} \cdot [\alpha z + c_0 \dot{x} + k_0(x - y)] \tag{7}$$

The total force generated by the system is then the sum of the forces of the upper and lower sections of the model of Fig. 10:

$$F = \alpha z + k_0(x - y) + c_0(\dot{x} - \dot{y}) + k_1(x - x_0) \tag{8}$$

or:

$$F = c_1 \dot{y} + k_1(x - x_0) \tag{9}$$

For zero intensity of the current supplied to the *MR* damper, stiffness $\alpha = 38.24$ N/mm and damping coefficients $c_0 = 0.59$ Ns/mm and $c_1 = 4.73$ Ns/mm are introduced by the modified Bouc-Wen model, and the coefficient of z hysteresis function such that: $n = 2$, $A = 10.013$, $\beta = 3.044 \text{ mm}^{-2}$, $\gamma = 0.103 \text{ mm}^{-2}$ and $k_0 = 1.121$ N/mm. The stiffness K_1 of the accumulator is fixed to 0.84 N/mm, with an initial displacement $x_0 = 2.5$ mm. The parameters α , c_0 and c_1 , depending on the

current supplied to the *MR* damper, were deduced from the polynomial functions below, expressed in terms of the input current intensity I [11, 12].

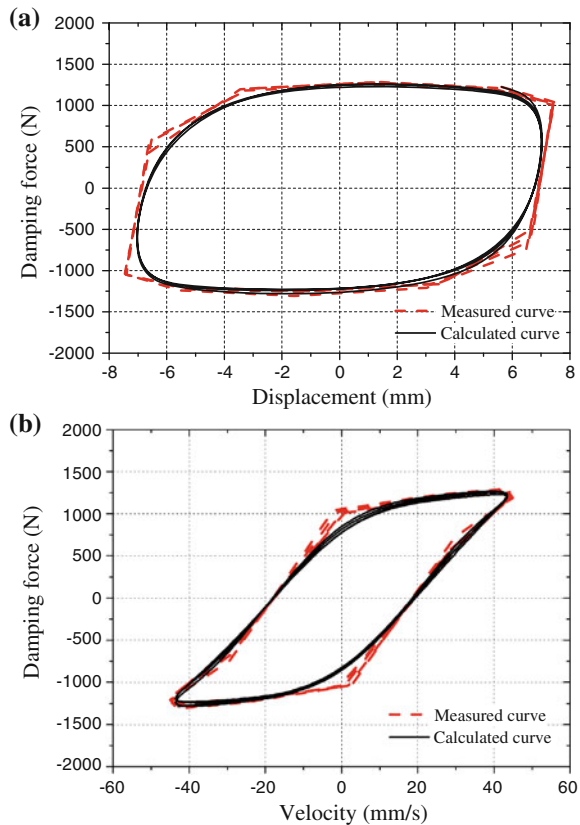
$$\alpha(I) = -826.67I^3 + 905.14I^2 + 412.521I + 38.24 \tag{10}$$

$$c_0(I) = -1173I^3 + 10.51I^2 + 11.02I + 0.59 \tag{11}$$

$$c_1(I) = -54.40I^3 + 57.03I^2 + 64.57I + 4.73 \tag{12}$$

These parameters are adapted to the experimentally measured response of the *MR* damper (*RD-1005-3*) shown in Fig. 1 and the amplitude of the sinusoidal displacement be submitted to the piston damper at a frequency of 1 Hz, is 15 mm, with an applied voltage of 5.5 V and an current intensity of 1 A. A comparison of the responses calculated from the numerical model (Fig. 10) and experimentally measured responses is presented in Fig. 11. The model of modified Bouc-Wen proposed, provides very well the behavior of the MR damper in all regions including the area where the acceleration and velocity are of opposite sign and when the velocity

Fig. 11 Hysteresis curves force/displacement (a) and force/velocity (b) calculated and measured for a 15 mm displacement imposed on the frequency of 1 Hz and a current of 1 A



amplitude is low during the transition between the compression and expansion of the damper. The hysteresis curves relationships force/displacement (Fig. 11a) and force/velocity (Fig. 11b) of the numerical model were obtained after adjustment of the most influential parameters of evolutionary variable z given by the expression (6). Thus, after an analysis of the influence of the variable parameters, the coefficients A , β and k_0 were brought respectively to the values at 22.5, 8.25 mm⁻² and 3.55 N/mm. The disadvantage of this model is linked to the large number of parameters involved in the procedure for its adjustment or recalibration of the real behavior of an *MR* damper, and by any mathematical or experimental approach used, which increases the necessary calculation time.

4 Conclusion

From this study we can see first through the characterization of the *MR* damper, the equivalent damping coefficient experimentally obtained is a factor very complex, difficult to quantify because it depends on several parameters which are the frequency and amplitude of oscillation supplied thereto as well as the intensity of current issued to it. However, this will allow us to better approximate the parameters of the internal dynamics of the *MR* damper polynomial functions that take into account the effect of the excitation frequency also.

Finally this work allowed through confrontation hysteresis curves force/displacement and force/velocity, obtained by experimental measurements and calculations on the modified Bouc-Wen model, readjust the responses calculated from the experimentation for a representative numerical model for real damper. The readjustment of the numerical model made on the basis of the experimental curves is possible by adjusting the most influential for the same working conditions of the *MR* damper settings. This allows through this present study to analyze and validate the performance of a control scheme of a semi-active suspension incorporating an *MR* damper, making only content with the simulation results obtained with modified Bouc-Wen model adopted as internal dynamics of the *MR* damper was previously adjusted and readjusted.

References

1. Spencer, B.F., Dyke, S.J., Sain, S.J., Carlson, J.D.: Phenomenological model of a magneto-rheological damper. *J. Eng. Mech.* **123**, 230–238 (1997)
2. Boada, M.J.L., Calvo, J.A., Boada, B.L., Diaz, V.: Modeling of a magnetorheological damper by recursive lazy learning. *Int. J. Non-Linear Mech.* **46**, 479–485 (2011)
3. Rheonetic RD-1005-3 MR damper, Lord Corporation product bulletin (2001). www.lord.com
4. Lord Rheonetic Magnetically Responsive Technology: Hydrocarbon-Based MR Fluid MRF-132DG. Rapport technique, Product Bulletin (2006)

5. Yao, G.Z., Yap, F.F., Chen, G., Li, V., Yeo, S.H.: MR damper and its application for semi-active control of vehicle suspension system. *Mechatronics* **12**, 963–973 (2002)
6. Dua, H., Sze, K.Y., Lam, J.: Semi-active ∞ H control of vehicle suspension with magneto-rheological dampers. *JSV* **283**, 981–996 (2005)
7. Ang, W.L., Li, W.H., Du, H.: Experimental and modelling approaches of a MR damper performance under harmonic loading. *J. Inst. Eng. Singapore* **44**(4), 358–372 (2004)
8. Wen, Y.: Method for random vibration of hysteretic systems. *J. Eng. Mech. Div.* **102**(2), 249–263 (1976)
9. Stanway, R., Sproston, J.L., Stenens, N.G.: Non-linear modelling of an electro-rheological vibration damper. *J. Electrostat.* **20**, 167–184 (1987)
10. Honga, S.R., Wereleya, N.M., Choia, Y.T., Choib, S.B.: Analytical and experimental validation of a nondimensional Bingham model for mixed-mode magnetorheological dampers. *J. Sound Vib.* **312**, 399–417 (2008)
11. Braz-Cézar, M.T., Barros, R.C.: Experimental and numerical analysis of MR dampers. In: 4th ECCOMAS, Thematic Conference on Computational Methods in Structural Dynamics and Earthquake Engineering, Kos Island, Greece, 12–14 June 2013
12. Boukerroum, S., Hamzaoui, N., Ouali, N.: Experimental validation and adjustment of the semi-active suspension numerical model incorporating a MR damper. *Appl. Mech. Mater.* **232**, 828–835 (2012)

Evaluation of Nonlinear Seismic Response of Reinforced Concrete Structures

Samira Bouyakoub and Taïeb Branci

Abstract The seismic response of a building structure is generally evaluated using simplified methods based on elastic response spectra which pass by a linear elastic analysis still takes no account of the true behavior of the structure which may be the both linear and non-linear. To consider the problem of non-linearity, non-linear methods have emerged as static methods (Pushover) and nonlinear temporal dynamics. The purpose of this communication is to use these two methods to evaluate the seismic response of two types of structures: (1) mixed (web + frame) and (2) freestanding gantry, both located in a zone of high seismicity. The dynamic analysis is conducted from two known accelerograms: El Centro 1940 Kobe 1995. The results show that the mixed structure has a better performance vis-à-vis the seismic actions.

1 Introduction

In seismic regulations, the study of the response of building structures to the effects of earthquakes is conducted using simplified methods based on response spectra. These methods allow engineers to use either a linear analysis for the calculation of forces and displacements, but conventional linear elastic methods are not generally consistent, so we had to find nonlinear methods to determine the design of a structure, for example the method of nonlinear static analysis “Pushover” and the non-linear temporal method based on accelerograms. The recent earthquakes such as earthquakes (El Centro 1940 Boumerdes 2003; Kobe 1995) where

S. Bouyakoub (✉) · T. Branci (✉)
Département of Civil Engineering, University Hassiba Benbouali, Chlef, Algeria
e-mail: bouyakoubsamira@hotmail.com

T. Branci
e-mail: brancit@yahoo.fr

the majority of reinforced concrete structures were damaged or destroyed have indicated the need to assess the actual seismic behavior of existing buildings. In particular, the seismic rehabilitation of reinforced concrete structures in areas with strong sismicités. The main objective of this study is to apply the application of Pushover method on two types of reinforced concrete structures ($R + 5$): one consists of a mixed bracing system (*web + frame*) and the other consists of a freestanding system in both directions located in a high seismic zone and dimensioned according to the Algerian seismic regulations *RPA 99/2003* [1]. The 2nd structure are used as a reference used for comparison by the structure *1st* specifically calculating the capacity curve, the point of seismic performance, check the vulnerability and the state of damage that can occur in the structure of an upcoming earthquake terre. Egalement, for comparison a direct non-linear dynamic analysis was conducted on the specific structures based on two chosen accelerograms (El Centro 1940 and Kobe 1995) to assess the dynamic response of structures themselves considered in terms maximum relative displacement, lateral displacement and maximum floor shear and check the results obtained with the Algerian seismic regulations *RPA99 2003* [1] version.

2 Nonlinear Static Method

The Pushover method is based on the assumption that the response of the structure which can be likened to the response of a system with a single degree of freedom equivalent, which means that the response is basically controlled by a single mode of vibration and the form of this mode, remains constant during the duration of the quake. As part of the analysis “Pushover”, we considered a modal distribution of applied forces established by *FEMA 450 code*:

$$F_i = C_{v,i}V \quad C_{v,i} = \frac{w_i h_i^k}{\sum_{j=1}^n w_j h_j^k} \quad (1)$$

where:

$C_{v,i}$ the coefficient of distribution of forces.

V the total lateral force.

w_j the weight of the level j .

h_j the height of the level j (measured from the base).

3 Evaluation of the Seismic Response of Structures Considered by the Nonlinear Static Method (Pushover)

The methodology of the nonlinear static method on structure considered for obtaining the capacity curve and the performance point, and determining lateral displacements at each stage and the distribution of shearing forces at the floors, and to highlight what level of damage can be classified structures.

3.1 Mixed Structure (Web + Frame)

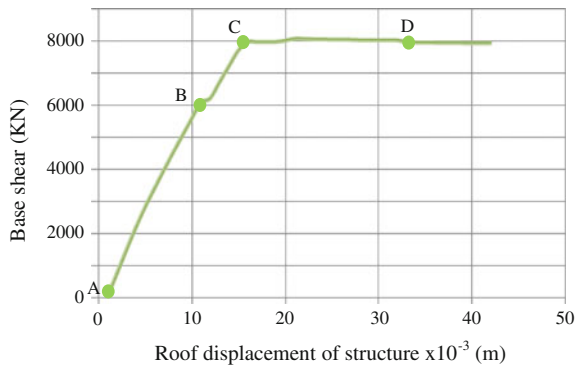
The non-linear calculation provides a structure capacity curve. This curve represents the horizontal force to the base of a function building movement there of (Fig. 1). The capacity curve is generally formed by a linear elastic nature phase followed by a nonlinear phase corresponding to the formation of plastic hinges, features elastic limits (shear-displacement) show that the structure has a greater margin plastic.

Several reference points were placed on the curve to show the different states of the building when loading.

- Point A: corresponds to the point of origin.
- Point B: is the elastic behavior of the structure and represents the normal level of seismic design. It therefore indicates a state of surface damage (or non damage).
- Point C: We continue loading, the appearance of plastic hinge type B at the left of the inner ends of the beams line C.
- Point D: With the increased loading capacity curve and reached the maximum at this level is moderate lamination type IO and LS at the beams so the building is considered damaged.

Following transformation of the screen capacity curve (D-T) format (S_d-S_a) (Fig. 2), and after changing the seismic coefficients C_v and C_a , the intersection

Fig. 1 Shear force to the base according to the movement of the roof of the structure



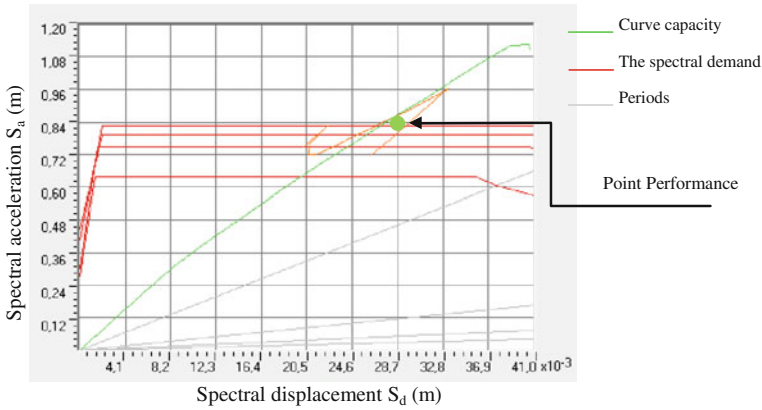


Fig. 2 Curve capacity of the mixed structure (web + frame)

between the curve and capacity of the response spectrum gives the performance point at coordinates $(S_d-S_a) = (0.865; 0.028)$ this corresponds to a lateral force to the base of the structure 6 162.820 Kn for 4.00 cm displacement of the stage gravity center roof. The appearance of the plastic phase is numerically very divergence.

3.2 Freestanding Structure

Figure 3 illustrates the size capacity curve (*D-T*) is generally formed by a linear elastic nature phase followed by a nonlinear phase corresponding to the formation of plastic hinges, features elastic limits (*shear-displacement*) show that the structure has a larger plastic margin.

- Point A: corresponds to the point of origin.
- Point B: corresponds to the appearance of the first plasticity in the building (points on the structural elements). The first points of plasticity appear in the beams of the *RDC* (axis 1) reaches its elastic limit (type of plastification *B*) and is localized at their ends and the shear force is still lower than that of Algerian

Fig. 3 Shear force to the base according to the movement of the roof of the freestanding structure

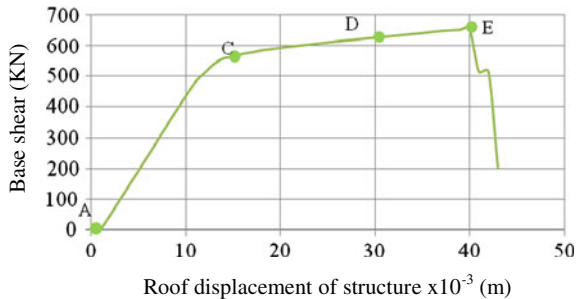
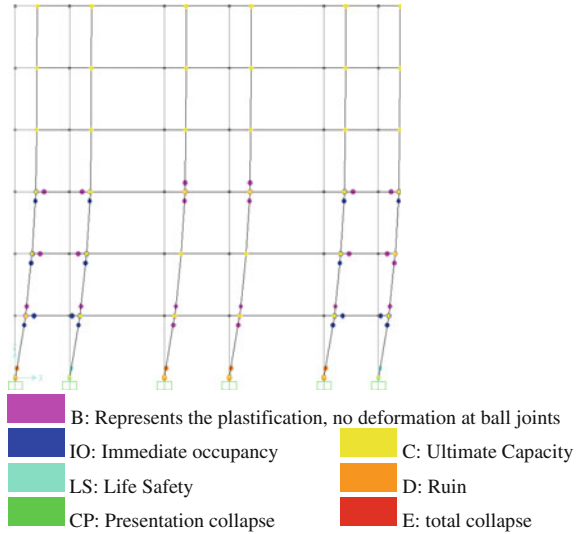


Fig. 4 Formation plastic hinges just before the ruin



regulation, after appearance ball joints at the columns of the *DRC* (1 file axis *A*, *B*, *C* and *D*) due to the axial force required to balance the time dictated by the lateral force, and also under the effect of the weight of the upper floors. These elements verify the real behavior of the structure.

- Point *C*: we continue loading, the appearance of plastic hinges *IO* type and capacity curve reaches the maximum level at which the building is considered damaged.
- Point *D*: The maximum shear force is obtained approximately at this point and plasticizing to moderate type *LS*, beyond this value the system is no longer able to support the load and shear force that remains constant the displacement increases.
- Point *E*: shear takes the maximum value to the maximum displacement after a rapid decrease in the value of the shear force and the appearance of various important plastification (*CP*, *C* and *D*) so the collapse of structure.

Figure 4 shows the formation of plastic hinges to the type “*D*” corresponding to the ruins at the columns, especially those in the *RDC* because of the significant efforts submitted to them and at the level of the beams.

The coordinates point of the performance $(S_w, S_d) = (0.126, 0.104)$ corresponding to a lateral force to the base of the structure of 619.541 kN to 12.5 cm of displacement at the center of gravity of the roof floor (Fig. 5).

- A comparison of the responses is conducted for both types of structure in terms of maximum lateral and shear forces to the base. From Fig. 6 it is found that:
- The maximum lateral movement of the free-standing structure is more important. For example it is noted for the last stage a shift of 0.19 m for the free-standing structure and a displacement of 0.07 m for the mixed structure.

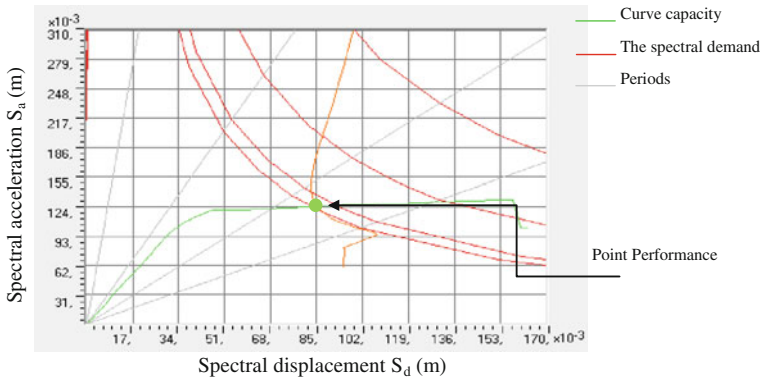


Fig. 5 Curve capacity of the freestanding structure

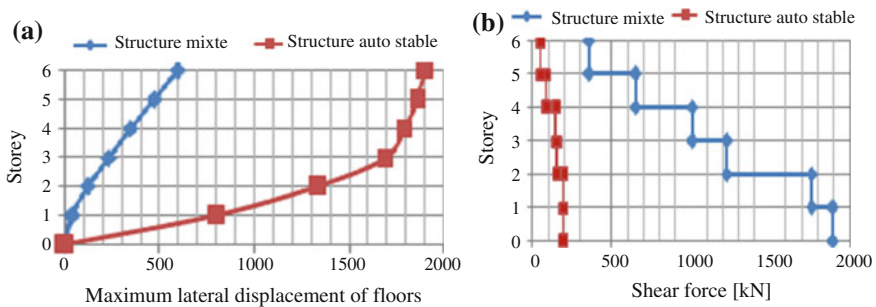


Fig. 6 Maximum lateral displacements **a** and sharp Efforts **b** of the analyzed structures obtained by nonlinear static analysis

- The values of the shear force at the base of the mixed structure is greater than a value of 1900 kN contrary to the freestanding structure equal to 200 kN.

4 Evaluation of the Response Structures Considered by the Nonlinear Dynamic Analysis

Under this method the results will be more accurate, because it sets the actual behavior of a structure facing an earthquake in presenting the response directly as displacement, velocity and acceleration versus time. However, in this type of method, the difficulty is in the choice of the earthquake and in particular its accelerogram. Indeed, the study should be based on either a measured natural earthquake or an artificial accelerogram. The characteristics of two accelerograms

Table 1 Features seismic accelerograms considered

Earthquake	Date	Component	Site	Max Acceleration (g)	Total duration (s)
El Centro (USA)	18/05/1940	180°	Californie	0.313	40.00
Kobé (Japon)	16/01/1995	00°	Japon	0.509	40.96

considered in this research, in this case El Centro (USA) and Kobe (Japan), are shown in Table 1 given below, and graphs in Fig. 7.

Analyzes are performed on the two structures considered previously (mixed and freestanding) to evaluate their dynamic response in terms of lateral displacement, relative movements and shear forces of floors under the effect of the selected

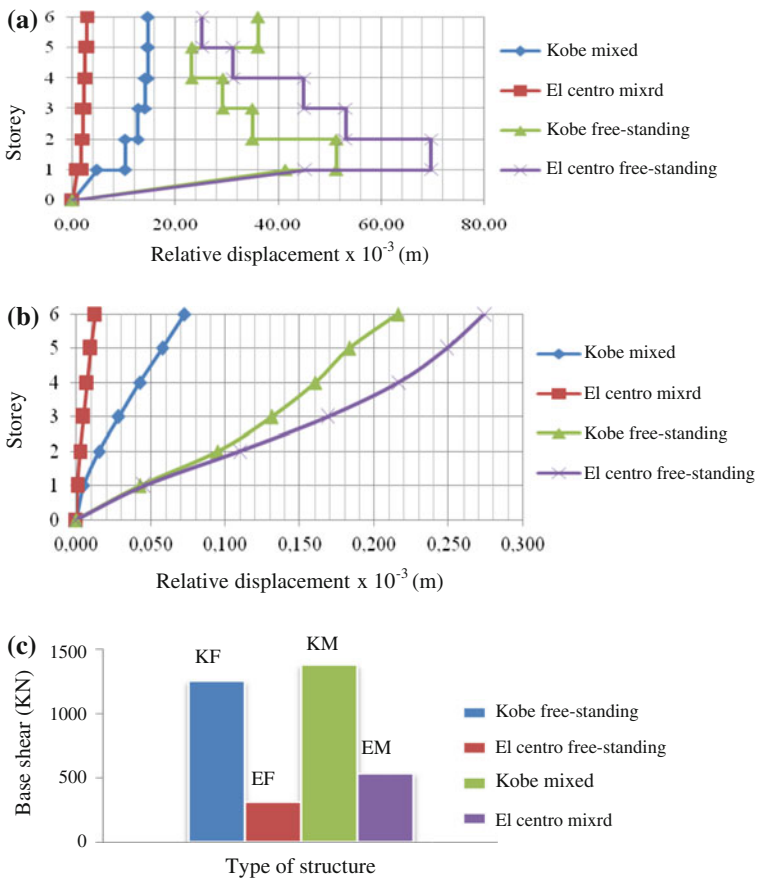


Fig. 7 Structures analyzed responses comparison obtained under the accelerograms of El Centro and Kobe **a** relative displacements, **b** lateral displacements and **c** shearing forces

acceleration time. This evaluation aims to situate the previous results obtained by nonlinear static method with those obtained by nonlinear dynamic method.

From this figure we see that:

- The maximum relative displacement of the free-standing structure is always greater than that of the mixed structure but we note that there is a large gap displacement between floors as opposed to the mixed structure; this is due to the difference in rigidity between levels.
- The level where the reinforcement and section columns are reduced inter-floor relative displacement also decreases for freestanding structure.
- The maximum lateral displacement of the freestanding portico floors are larger than those of the portico reinforced concrete walls reinforced especially on the top floors, this is due to the flexibility of the freestanding portico in which the lateral stiffness is lower.
- The freestanding structure has a larger distance along the structure (0.045, 0.274) in contrast to the composite structure which are respectively (0.00092; 0.0126).
- The lateral movement of the freestanding structure beyond the elastic limit contrary to the mixed structures is always lower.
- The mixed structure braced by reinforced concrete sails presents Room shear stresses higher compared to freestanding structure.
- Little variation between the efforts of the summit and the base of the portico.
- By against, a large difference is registered between the force of the top and that of the base structure (wall + frame) due to the variation in the rigidity of the structural elements along the structural height.

For a better comparison of the results under the two acceleration time to the maximum lateral displacements, displacement interstage relative ETAGS buildings considered is given in Fig. 7a–c. The figure clearly shows the difference of non-linear dynamic responses of structures considered under the action of accelerograms used the El Centro and Kobe. On the basis of these comparisons it is found that:

- Structures subject to accelerogram Kobe have a greater deformation and are superior in terms of maximum lateral displacements, displacement stage relative compared to those obtained under the action of the accelerogram El Centro, except in the case of lateral movement of the free-standing structure. This difference is of normal character because of the type of accelerograms Played. Particularly as regards the duration and magnitude.
- The movements of joint structures in accordance with the movement calculated by the code RPA99 ($1\% h_e = 0.0306$ m) by two accelerograms contrary to the freestanding structure where the displacement exceeds the limit required by the code RPA99.
- Compared to shear forces at the base is observed that the mixed structure (wall + frame) has a gap of 39 % under the Kobe earthquake compared to the earthquake in El Centro and a gap of 25 % for freestanding structure.

5 Conclusion

According to the study the most important results are summarized as follows: structure braced by webs has a greater elastic range than the plastic phase because of the distribution of the webs in the two directions which increases the rigidity of the structure where the damage is probably acceptable with respect to the freestanding structure having a greater elastic phase to the total collapse of the structure and the addition of walls increases the resistance of the structure.

The non-linear static calculation is able to assess the seismic vulnerability of existing structures and study the condition of the structure under the effect of an earthquake. The Pushover analysis is a powerful and very useful method that can allow studying several reinforcement schemes of existing buildings and propose new structures that will perform adequately during future earthquakes. Moreover, despite nonlinear dynamics produced all the desired results (effort and moving every moment of the earthquake), but it is very costly in time compared to the nonlinear static method is therefore proof of promoting static method nonlinear its speed diagnose structures.

Reference

1. RPA: Règles Parasismiques Algériennes RPA99/Version 2003. Centre de Recherche Appliquée en Génie Parasismique, Alger (2003)

A Finite Element Approach for Predicting the Flexural Response of Light Weight FRP-Concrete Beams Under Cyclic Loading

Abdelmadjid Si Salem, Souad Ait Taleb and Kamal Ait Tahar

Abstract The main objective of this study is to predict the flexural and the shear response of light weight beams designed by embedded triangular FRP/Polymer member under cyclic loading. A local approach based on 3D finite element modeling is carried out to assess the most adequate parameters influencing the ultimate behavior of the new beam and also to evaluate the contribution of the FRP-Jacket comparing to conventional reinforced concrete beams. Concrete is modeled according to a damageable elastic-plastic model, which makes it possible to visualize the damages evolution at the local level and to determine the ultimate response and failure mechanism of the simulated beams. However, an elastic-orthotropic model is used to describe the FRP/Polymer behavior. Results comparison in terms of damage, stress, deformation and stiffness recovery highlight the performances of the FRP-Concrete beam.

1 Introduction

The ultimate response of concrete members under static and dynamic loading depends mainly on the evolution of their main materials proprieties during their lifetime; and cracks caused by dead loads due to the structure own weight and accidental stresses due to the seismic effect represent the starting point for all kinds of failure sources [1]. In this respect, the vulnerability studies led towards the use of composite materials as an attractive solution to substitute the use of steel sheets as reinforcement ensuring an increasing of strength and ductility [2]. Currently,

A. Si Salem (✉) · S. Ait Taleb · K. Ait Tahar
Laboratory LaMoMS, University Mouloud Mammeri of Tizi Ouzou,
Tizi Ouzou, Algeria
e-mail: sisalemabdelmadjid@yahoo.fr

S. Ait Taleb
e-mail: aittalebsouad@yahoo.fr

K. Ait Tahar
e-mail: aittaharK@yahoo.fr

Polymer and *FRP* are considered as multifunctional materials, leading to their applications in the repair and the confining of *RC* structures. Such materials have some unique features compared to traditional ones: i.e. high strength and stiffness to weight ratio, attractive corrosion resistance and ease of handling. Some of these features offer the ability for manufacturers and designers to combine function and form; new design processes, industrialization and manufacturing can resolve technical and economic problems [3].

The mechanical behavior of civil building under cyclic loading is conditioned by their wind bracing elements, which have the ability to scatter energy that confers to the structure a relatively ductile behavior [4]. Considering the high mechanical properties of composites combined with their reasonable cost and lightness, it becomes alternative to associate them in the composition of these members, to better resist applied external loading. In order to ensure satisfactory energy dissipation under statical and dynamic rules, new fully concrete composite based beams, in which the strained concrete was partially substituted by integrated cylindrical and rectangular Polymer/*FRP* members, were designed by Si Salem et al. [5–7]. Moreover, our contribution in the present study is focused on the first stage investigation of structural behavior of composite based beams with a new shape of the polymer member under imposed cyclic loads. In order to assess the new beam performances, a finite element approach based on non linear finite element analysis is carried out on simply supported beams under increased monotonic cyclic loading until failure. The modeling of the specimens is conducted in a full *3D* space to predict the failure modes and the corresponding flexural and shear capacity. The used numerical concrete model takes account their asymmetry behavior in compression and in tension, and also a coupling with the damage evolution. In this connection, the numerical modeling results in terms of flexural performances to weight ratio compared to classical beams with traditional reinforcement are emphasized and analyzed.

2 Beam System Equilibrium

Nonlinear studies carried out on classical reinforced concrete beams under cyclic loading have showed that the concrete strained zones are mechanically ineffective, [5, 8].

In this connection, an encased triangular GFRP/Polymer member, as shown in Fig. 1 is introduced to reduce the structure mass ratio and to preserve external and esthetic aspect of concrete-composite works.

Taking into account all the constitutive materials, the ultimate resistance moment of the considered section located at the mid-span of the light weight beam, relatively to the application point of the concrete compressive strength f_b , is assessed by the Eq. 1 as follows:

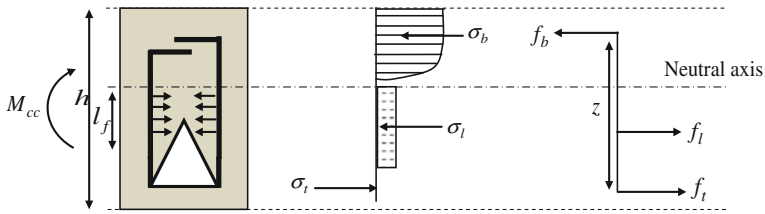


Fig. 1 Proposed system and cross section equilibrium

$$M_{cc} = f_t z + f_i (l_f/2 + h/3) \tag{1}$$

In which z and l_f are respectively the neutral axis position and the length of the tensile FRP to this axis l_f is the resultant lateral force of the confining pressure. While, f_t is the GFRP flexural strength through the polymer member.

2.1 Finite Element Approach

In this section, we emphasize the improvement in flexural capacity of light weight composite beams due to the FRP/Polymer jacketing. In addition, a numerical model based on finite element analysis was developed and validated to predict the full response of the new beam under imposed cyclic loading. This analysis model takes into account the contribution of the composite jacket to prevent the deformation of the polymer member, and also to determine the failure mode and the corresponding load level compared to tested RC beams with the same geometrical characteristics (see details in Ref. [5]).

2.2 Materials Models

Concrete is usually described as brittle material, due to their unstable behavior resulting in the cracks apparition and asymmetrical behavior in tensile and compression.

In this respect, an elasto-plastic damage model is used to describe the nonlinear cyclic material properties of concrete [9–11]. It bases on the classical continuum damage theory assuming geometric linearity [12]. In addition, Fig. 2 shows the stress-strain relation and linear unloading path for the compressive and tensile loads of the used numerical model.

Three stepwise defined material functions describe the stress-strain behavior under uniaxial compressive loading (Fig. 2a). The compressive damage value given in Eq. (2) is linked to the plastic strain. For cyclic tests, a value $b_c = 0.7$ fits well with experimental data [12]. Similarly, for the tensile damage given in Eq. (3), an experimentally determined parameter was found to be $b_t = 0.1$ [12].

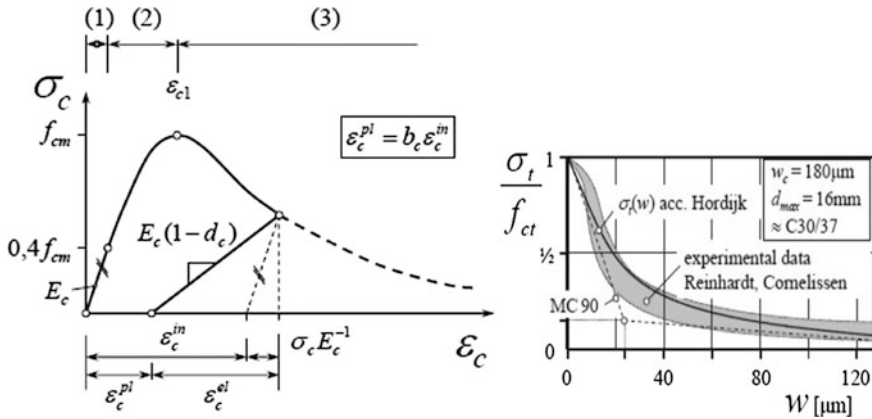


Fig. 2 Stress-strain relation and unloading path for the compressive and tensile loading of the used concrete model [12]

$$d_c = 1 - \frac{\sigma_c E_c^{-1}}{\epsilon_c^{pl} \left(\frac{1}{b_c} - 1 \right) + \sigma_c E_c^{-1}} \quad \text{and} \quad d_t = 1 - \frac{\sigma_t E_c^{-1}}{\epsilon_t^{pl} \left(\frac{1}{b_t} - 1 \right) + \sigma_t E_t^{-1}} \quad (2)$$

The elastic behavior of *GFRP* composites assuming orthotropic plane stresses is described by introducing the constants stiffness summarized in Table 1. The failure stresses measured by tensile, compressive, and shear tests are given in Table 2. They were modeled according to the Hill-Tsai failure criterion in the case of an anisotropic material.

2.3 Meshes and Loading Setup

The summary of the simulated beam geometry and the boundary conditions as well as the imposed loading setup are shown in Fig. 3. As regards the *FE* models, the mesh for concrete is the same in both cases with linear solid elements (*HEX8*,

Table 1 The elastic orthotropic model parameters [3]

E_1 (MPa)	E_2 (MPa)	ν_{12}	ν_{13}	G_{12} (MPa)
72000	13600	0.31	0.33	4700

Table 2 The ultimate failure stresses of the used *GFRP* [3]

X_t Longitudinal ultimate tensile strength (MPa)	1400
X_c Longitudinal ultimate compressive strength (MPa)	910
Y_t Transverse ultimate tensile strength (MPa)	35
Y_c Transverse ultimate compressive strength (MPa)	110
S Ultimate shear strength (MPa)	70

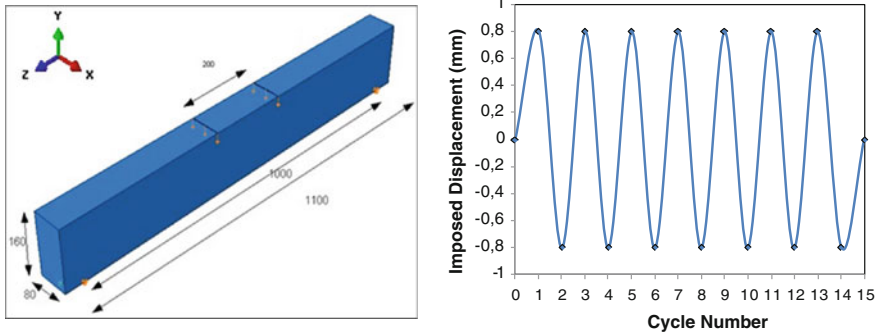


Fig. 3 Boundary condition and imposed cyclic displacement

C3D8/C3D8R elements). Whereas, quadratic finite elements models (*2D*) are used to mesh the FRP/Polymer member. The quadratic *FEMs* are coupled with the solid ones with the embedded elements function. With such hypothesis, the nodes of beam finite element are kinematically constrained to those of the solid one, which it is located in. The imposed cyclic displacement applied to the load-time function given by Eq. (3) for both simulated beams namely: the light weight *FRP* based beam referred to as (*CCBB*) and the reference one made with conventional reinforced concrete referred to as (*CRCB*) is depicted in Fig. 3b.

$$F(t) = A \cos(\varpi t) + B \sin(\varpi t) \tag{3}$$

In the used software, the angular frequency ϖ , the periodic amplitude as well as the initial stiffness parameters (*A*) and (*B*) defining the loading function versus time $F(t)$ are input point by point.

3 Results Comparison and Analyses

In order to check the numerical procedure reliability, qualitative and quantitative predictions about the behavior of the simulated beams are established. The qualitative aspect of the confrontation includes the visualization of the damaged concrete zones and the depiction of the evolution of shear damage according to the periodic time. As regards the quantitative aspect of this investigation, the evolution of bearing capacity as function of the mid-span deflection is reported.

The average simulation results as well as the final discussion illustrate the aforementioned advantages of the proposed finite element approach.

3.1 Load-Time Response

In this section, numerical results in terms of cyclic response at ultimate limit state were presented. Therefore, the evolution of the applied external loading as a function of the periodic time until failure is shown in Fig. 4. The curves confrontation shows the positive contribution of the light weight *FRP* based beam in terms of bearing capacity and damages rate reduction, which are respectively around of 30 and 15 % compared to the reference one. For more clarity, Table 3 presents the details of average ultimate load, tensile and shear damages corresponding to the ultimate and the first crack loads.

The ultimate bearing capacity of the composite based beam generated under cyclic loading is around of 4.9 kN corresponding to 1 s periodic time. However, the loading rate of the control beam made with reinforced concrete, the simulated value of the same parameter is lower than the *CCBB* one, which is in the order of 3.7 kN. In the other hand, the tensile and shear damage varies of zero and unit values. The first shear crack occurs for an external load of 1.31 kN for the reference *CRCB*, while the same parameter of the developed *CCBB* comes around of 1.62 kN. These

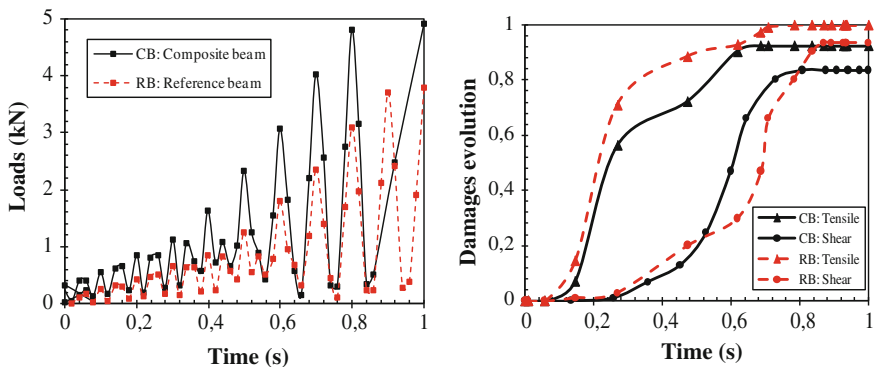


Fig. 4 Ultimate loads and damages versus time comparison

Table 3 Summary of simulation results comparison

Simulated beams	CCBB	CRCB
Initial damage load (kN)	0.98	0.32
Initial damage time (s)	0.11	0.14
Ultimate load (kN)	4.92	3.78
Ultimate shear damage value	0.834	0.932
Ultimate tensile damage value	0.924	0.998

results showed that with reduced own weight, the average shear damage rate is improved by nearly 25 % due to GFRP/Polymer jacketing effects.

3.2 Stresses and Deflections Distribution

Figure 5 shows the global vertical deflection, for both simulated beams. These cartographies show that the composite based beam exhibits better behavior in terms of displacement field distribution. In addition, a reduction around of 45 % in terms of ultimate deflection compared to the reference beam is recorded. The distribution of the ultimate Mises and Tsai stresses within the FRP/Polymer member is depicted in Fig. 6. It is concluded that the lateral deformations of the polymer member are prevented by the mobilization of the lateral confinement pressure due to the difference in flexural stiffness between the constitutive compatible materials namely: concrete and composites. In conclusion, the mechanical performances of the GFRP/Polymer jacketing provide an acceptable strength and ductility level.

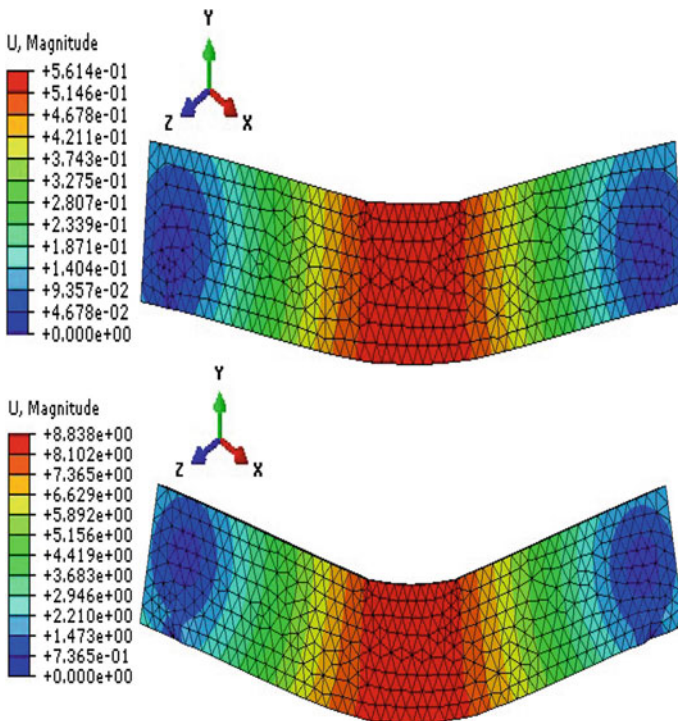


Fig. 5 Ultimate deflections of both simulated beams

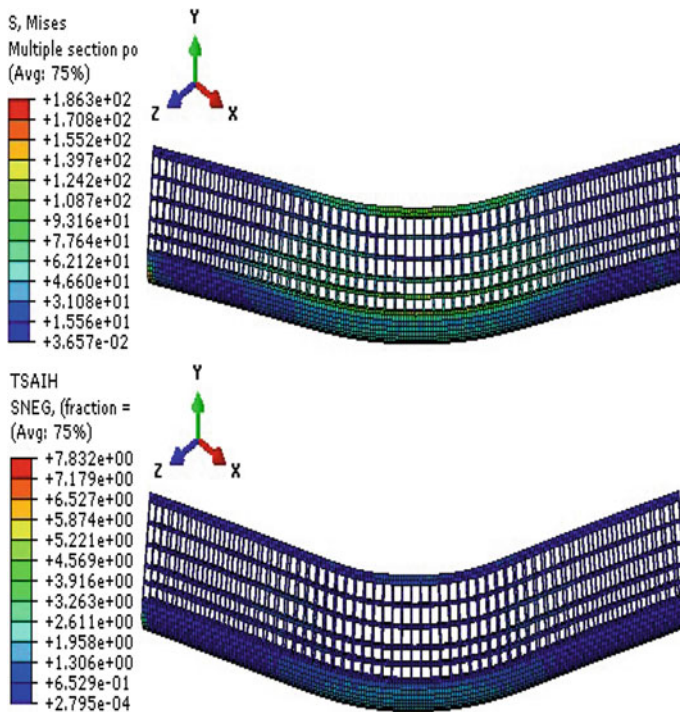


Fig. 6 Mises and Tsai stress distribution within the FRP/Polymer member

4 Conclusion

The different average results based on finite element modeling highlight clearly the enhancement in terms of dynamic performances of the new beam compared to classical reinforced concrete ones. The various recorded positive inputs of our contribution are summarized as follows:

- With the same geometrical characteristics, the average own weight is reduced by nearly 15 % due to the polymer member incorporation. Such reduction leads to an increasing in ductility and a reduction of the seismic stresses, which is very important for safety reasons.
- A significant improvement in terms of first crack appearance and bearing capacity generated under cyclic loads is recorded due to the conjugation of the high performances the FRP/Polymer jacketing.
- The composite based beam presents a relatively ductile behavior. Also, a reduction around of 45 % in terms of ultimate vertical displacement, hence, allows the building evacuation which can be possible to save human fatalities.

Results analysis suggests the interest of the proposed light weight FRP-concrete beam; however, further studies should be conducted to validate the obtained numerical results. Therefore, further simulation works including bond slip models are necessary to take account of the bonding adhesion between the various components of the proposed beam design.

References

1. AFPS–Parasismic French Association: The seism of May 21, 2003 in Algeria. Preliminary report of the AFPS mission, Ministry for ecology and the durable development, 8 July (2003)
2. Fernandes, C., et al.: Importance of the bond–slip mechanism in the numerical simulation of the cyclic response of RC elements with plain reinforcing bars. *Eng. Struct.* **56**, 396–406 (2013)
3. Berthelot J.M.: *Matériaux composites, comportement mécanique et analyse des structures*, pp. 172 & 245. Edition Lavoisier, ISBN: 2-7430-0771-0 (2005)
4. Shafaei, J., et al.: Effects of joint flexibility on lateral response of reinforced concrete frames. *Eng. Struct.* **81**, 412–431 (2014)
5. Si Salem, A., et al.: Experimental and statistical investigation of a new concrete-composite beam with encased polymer tube wrapped by FRP. *Front. Struct. Civil Eng.* **9**(2), 154–162 (2015)
6. Si Salem, A., Ait Taleb, S., Ait Tahar, K.: Static and dynamic behavior of composite concrete-based beams with embedded Polymer/FRP Components. *Procedia Eng.* **114**(C), 173–180 (2015)
7. Ait Tahar, K., Si Salem, A.: Development and analysis of a new design concrete composite beam. In: 5th International Symposium on Aircraft Materials, Marrakech (2014)
8. Harajli, M.H.: Cyclic response of concrete members with bond-damaged zones repaired using concrete confinement. *Constr. Build. Mater.* **21**, 937–951 (2007)
9. Lubliner, J., Oliver, J., Oller, S., Onate, E.: A plastic-damage model for concrete. *Int. J. Solids Struct.* **25**(3), 299–326 (1989)
10. Oller, S., Onate, E., Oliver, J., Lubliner, J.: Finite element nonlinear analysis of concrete structure using a plastic-damage model. *Eng. Fract. Mech.* **35**, 219–231 (2001)
11. Lee, J., Fenves, G.L.: Plastic-damage model for cyclic loading of concrete structures. *J. Eng. Mech.* **124**(8), 892–900 (1998)
12. Mark, P., Bender, M.: Computational modeling of failure mechanisms in reinforced concrete structures. *Archit. Civil Eng.* **8**(1) (2010)

Study of Composite with Metallic Matrix WC/W₂C–20W–20Ni Realized by Spontaneous Infiltration of the Bronze Alloy Cu–30Mn–3P

Mokrane Gousmine, Djamel Miroud, Mohamed Farid Benlamnour,
Boualeme Demri and Abderrahmane Younes

Abstract The improved efficiency and lifetime of an impregnated tool for the mineral drilling, requires thorough understanding of the mechanisms involved in the consolidation of powder mixtures in the liquid phase sintering cycle (FPL). The elements used for the manufacture of the active parts of these tools are usually made from mixtures of loose powders based on WC/W–Ni. The spontaneous infiltration process is the most appropriate method, it offers a long possibilities to shape due to molding, and lets to have much density of the metal matrix composite (MMC) constituting the active head and increase its resistance to erosion and abrasion. This work consists to develop a metal matrix composite which can constitute the active part of a drilling tool impregnated by infiltrated industrial process SILP (Sintering by Infiltration of an appropriate mixture of Loose Powders). The mixture of loose powders (WC/W₂C–W–Ni) is infiltrated by a manganese bronze (Cu-30Mn-3P) under hydrogen and then characterized by DTA, optical microscopy, SEM coupled with EDS, HRA hardness and micro-hardness Hv0.1.

M. Gousmine (✉) · M.F. Benlamnour (✉) · A. Younes (✉)
Research Center in Industrial Technologies CRTI, P.O.Box 64,
Cheraga 16014, Algiers, Algeria
e-mail: m.gousmine@csc.dz; mokrane.goss@gmail.com

M.F. Benlamnour
e-mail: f.benlamnour@csc.dz

A. Younes
e-mail: a.younes@csc.dz

M. Gousmine · B. Demri (✉)
Metallurgical Laboratory, National Polytechnic School,
10 Rue des Frères OUDEK, 16200 Algiers, Algeria
e-mail: demrib@yahoo.fr

D. Miroud (✉)
Materials Science and Process Engineering Laboratory (LSGM),
Department of Mechanical Engineering & Process Engineering,
USTHB, BP. 32 El Alia, 16111 Bab Ezzouar, Algiers, Algeria
e-mail: jamelart@yahoo.fr

1 Introduction

The exploitation of hydrocarbon deposits requires a hard-performance drilling tools, resistant to abrasion and erosion. These tools work by grinding and abrading rock. They are composed of a tungsten carbide matrix infiltrated by SILP infiltration process *SILP* (Sintering by Infiltration of an appropriate mixture of Loose Powders), then covered by a crust formed by a mixture of diamond and tungsten carbide [1], or a sintered segments embedded in the matrix. This process is similar to liquid phase sintering, in which one of the constituents of the powder melts and spreads by capillarity throughout the compacted. The Pores are filled by the volume shrinkage and rearrangement of grains. During infiltration, the liquid (molten metal of different composition of the porous body) comes from outside to fill, under the effect capillary forces, the interconnected pore system of the powder mixture. The reduction of the total energy of the system is pre required during infiltration [1, 2].

2 Experimental Method

2.1 Materials Used

The success of the consolidation of the metal matrix composite depends on the thermal cycle infiltration and reaction of the binder-metal powder, The composite will be made of a bronze alloy matrix (Cu–30Mn–3P) which ensures cohesion between the reinforcements so as to distribute the mechanical stresses, and to infiltrate the mixture of powders (WC–20Ni–20W).

2.2 Study of the Infiltrate

The properties of the infiltrate (binder metal) are very important in the selection of the thermal cycle of infiltration, its composition defines the practice infiltration temperature. The duration of infiltration depends on, its qualities of wettability. The metallic binder (Cu–30Mn–3P) used, belongs to the class of copper-manganese, It is usually used in the drilling industry. Figure 1 illustrates the block form (Raw of casting). The chemical composition is shown in Table 1.

2.2.1 Determining the Infiltration Temperature

The liquidus temperature of this alloy is determined by the heat flow measuring absorbed or released by the alloy when a temperature variation is to be undergo. Figure 2 shows the *DTA* of infiltrating Cu–30Mn–3P performed on device brand

Fig. 1 Appearance of the binder in the raw state of delivery



Table 1 Chemical composition of the infiltrating (Cu-30MN-3P) [3]

The infiltrant	Chemical composition (Weight %)		
	Cu	Mn	P
	67	30	3

SETARAM LABSYSATD-DSC ($T_{max} = 1,600\text{ }^{\circ}\text{C/ref. Water}$) shows an endothermic peak which corresponds to a mean temperature of $860\text{ }^{\circ}\text{C}$.

2.2.2 Choice of Infiltration Temperature

The practical area to ensure the uniform distribution of the liquid in the mixture of loose powders, corresponds to a range of $100\text{--}140\text{ }^{\circ}\text{C}$ [3, 4]. The infiltration temperature is imposed by the starting point of melting of infiltrant determined by DTA. In our case, we chose the applied infiltration temperature is in the order of $1030\text{ }^{\circ}\text{C}$ above the melting temperature of our binder [3]. It is at $860\text{ }^{\circ}\text{C}$ (Fig. 2), and a holding time is 20 min.

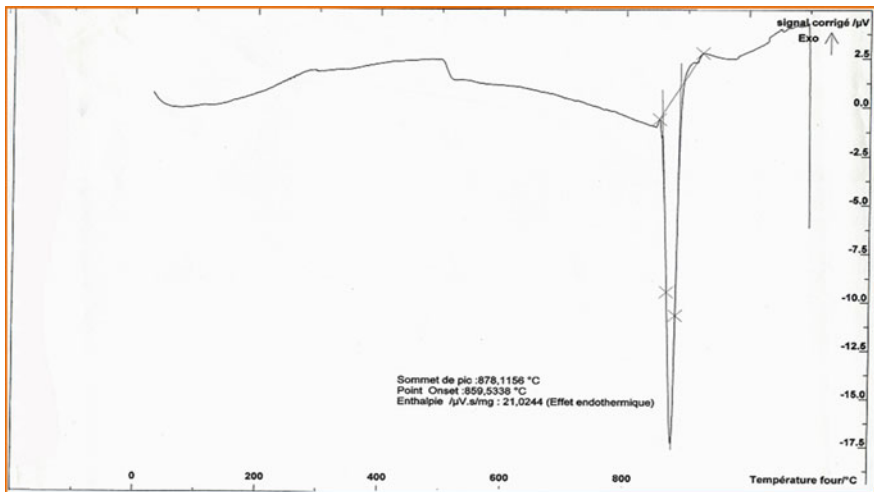


Fig. 2 Thermographs of the Differential Thermal Analysis (DTA) of the binder (Cu-30MN-3P)

Table 2 Elementary analysis of the basic powders [3]

powder	Element (Weight %)											
	W	Ni	Ca	Cr	Fe	Ga	Zn	Mo	Co	Si	S	C
W	99.5	0.172	0.103	0.098	0.085	0.029	0.026	–	–	–	–	0.055
WC	95.2	0.069	0.126	–	0.332	0.037	–	0.17	–	–	–	3.5
Ni	–	99.7	0.027	–	0.013	–	–	–	0.017	0.080	0.037	0.063

3 Study of the Mixture Powder (WC–20 20W–Ni)

3.1 Chemical Analyses of the Powder Mixture

An elementary analysis of the base powders, using the X technic is given in Table 2. The carbon and sulfur analysis performed with automatic analyzer carbon/sulfur; the purity of the Ni powder is about 99.7 %. It presents low proportion of cobalt, iron and silicon. These impurities are naturally present in the Ni ore and after carbonyl decomposition (following Sherritt's method).

The presence of impurities such as Fe, Ni, Cr and Co in the W powder probably result by the sources contamination of the reduction furnace [5].

The impurities present in the WC powder are principally carbon used in the manufacture corresponding to carburization of W in the presence of graphite in high frequency furnace sub hydrogen [5]. The concentration of volatile components such as Ca, Si and Ga depends essentially on the carburization temperature.

3.2 Preparation of Mixture Powder ($W_2C/WC-20W-20Ni$)

The Preparation of our mix in the laboratory “LSGM” consists to carry out sampling of the basic powders supplied by ENSP-Direction fabrication “ALDIM”, weighed, carefully stored in labeled vials Fig. 3a, and stored in a steamed room at 60 °C, by following the standard *NFA95-101 (ISO 3954-1977)* [6]. The powders are then mixed in a TURBULA 3D to get a good homogeneity of the mixture Fig. 3b.

3.3 Characterization of the Mixture ($W_2C/WC-20W-20-Ni$)

The characterization of the powder mixture of Ni, W and WC allowed us to highlight the effect of the composition of the metal binder on the final densification of the compound. The SEM microstructure of the powder mixture $W_2C/WC-20W-20-Ni$ represented in Fig. 4. Shows the morphology of WC/ W_2C powder, W and Ni namely:

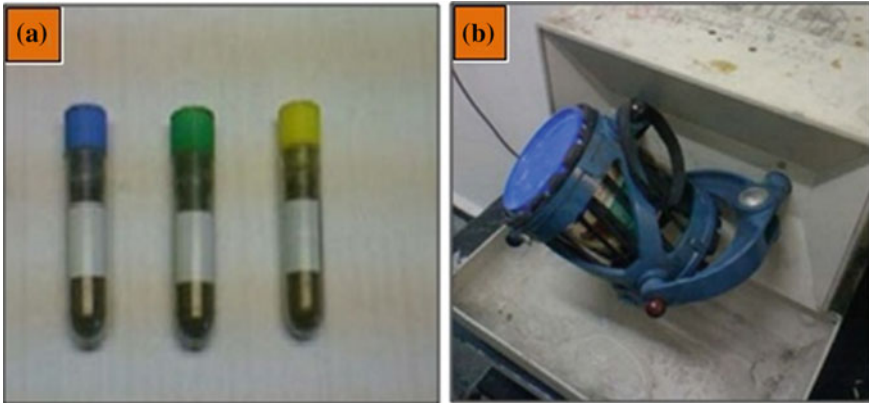
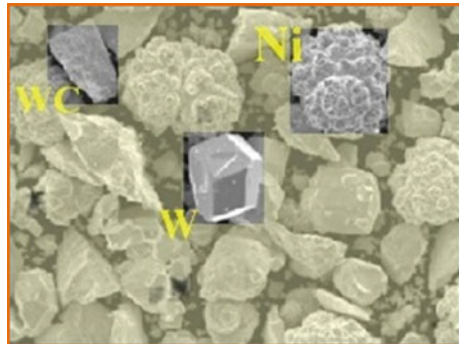


Fig. 3 Equipment used for mixing powders; **a** powder flasks, **b** Mixer TURBULA 3D

- The spherical-granular appearance ‘cauliflower’ shaped of Nickel Ni particles.
- Faceted polygonal shape with varied distribution of grain size. A small amount of W powder is grouped into agglomerate (cluster) probably formed under conditions of high temperature reduction [3].
- The particular powder morphology of WC/W₂C, are irregularly shaped with sharp angles and have uneven rough surfaces.

The gap in stoichiometry of WC and W₂C phases were identified by XRD peaks (Fig. 5), the latter is in substantial proportions.

Fig. 4 Micrographic showing WC/W₂C, W and Ni particle aspect of the W₂C/WC–20W–20Ni mixture



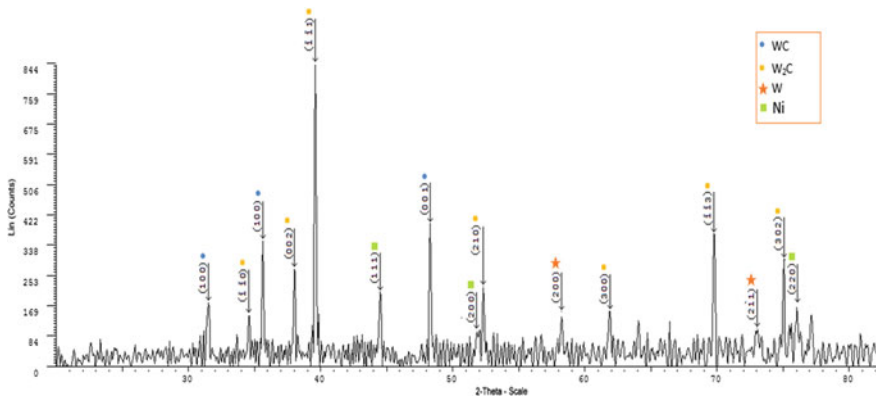


Fig. 5 X-ray diffraction spectrum of the ($W_2C/WC-20W-20Ni$) powder mixture

4 Elaboration of the Composite by Infiltration

To elaborate our sample, we planned the preparation of two graphite half mold. The first will serve as a mold which will be occupied by the mixture of loose powders in cubic packed imprints $10 \times 10 \times 10$ mm dimensions. The second will be fitted into the mold. It will serve to contain granular of the binder that will feed the loose powders into liquid metal at the time of merger through vertical channels or fingerprints linking attacks with sufficient amounts of liquid.

5 Result and Interpretation

5.1 Characterization of ($W_2C/WC-20W-20Ni$) Mixture Infiltrated by the Binder ($Cu-30Mn-3P$)

Figure 6 shows the particular aspect of the consolidated obtained by the back-scattered electron micrograph and the distribution of chemical elements in the middle of the sample performed by the EDS mapping, from the infiltration of the $WC-20W20Ni$ mixture by the $Cu-30Mn-3P$ binder at $1030^\circ C$ during 20 min. The examination of the sample by scanning electronic microscopy gives the following results:

- Presence a good cohesion of the composite and Homogeneous distribution of WC/W_2C and W particles.
- Presence of the phase rich in Mn-P, especially in the region of the WC/W_2C and/or W particles.
- Full dissolution of Nickel.

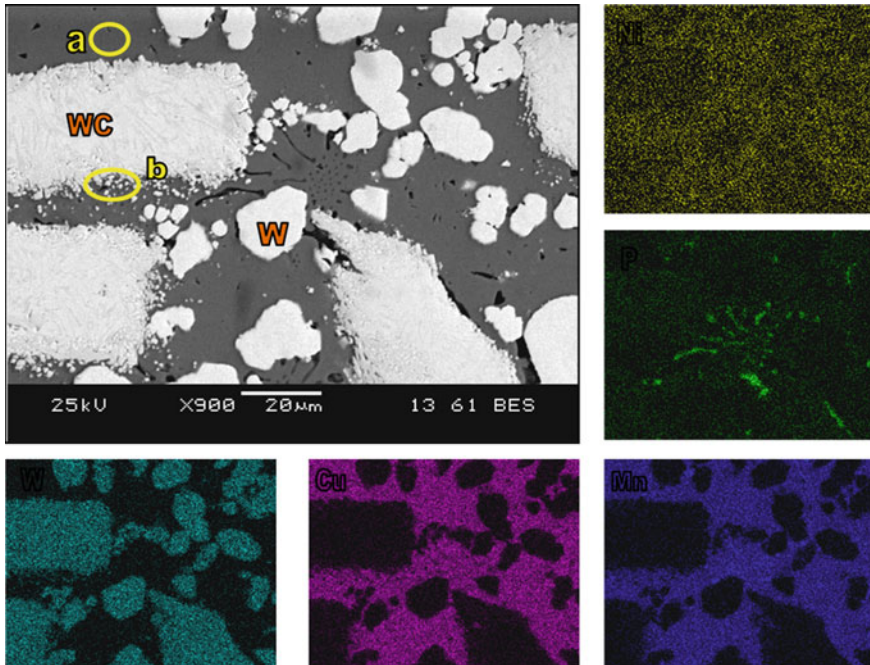


Fig. 6 Backscattered electrons micrograph showing the particular aspect of the consolidated and EDS mapping showing the distribution of chemical elements in the center of the sample from the infiltration of the mixture powder WC/W₂C–20Ni–20W by the Cu–30Mn–3P binder at 1030 °C during 20 min, **a** rich phase in copper, **b** Particle of WC

- Advanced decomposition of boundaries of WC/W₂C particles (Fig. 5b) causing the solution treatment of micrometric particle, see the submicrometre in the binder phase.

The identification of the X-ray diffractogram (Fig. 7) of the compound from the infiltration of the WC/W₂C–20Ni–20W mixture with the Cu–30Mn–3p binder, shows that the full dissolution of nickel doesn't give a ternary solid solution, but a binary solid solution (Cu–Mn) of substitution (Fig. 6a).

5.2 Micro-hardness Study

The levels of hardness histogram are given in the direction of consolidate infiltration. Figure 8 show that the full dissolution of nickel in the Cu–Mn binary phase has no influence on the hardening (average 140 Hv0.1).

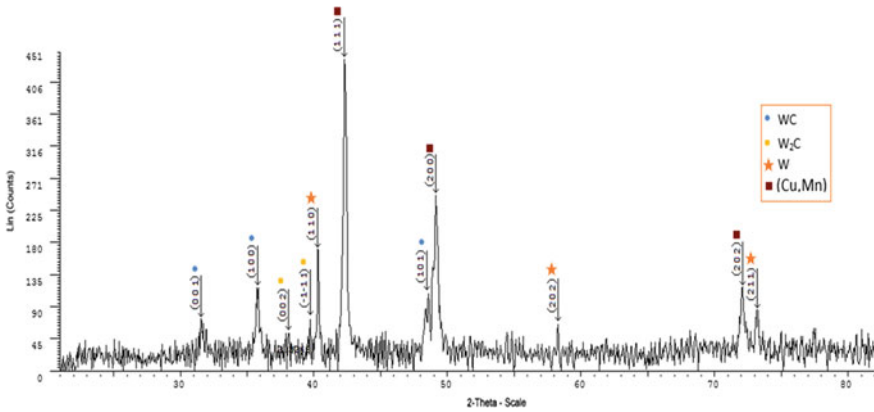


Fig. 7 X-ray diffraction spectrum of the WC/W₂C–20W–20Ni powders mixture infiltrated by the copper manganese (Cu–30Mn–3P) at 1030 °C during 20 min

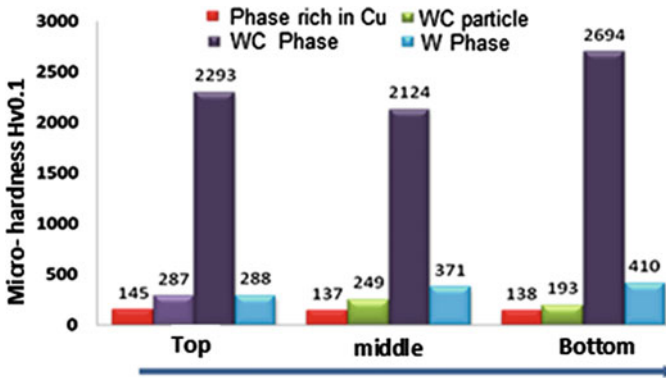


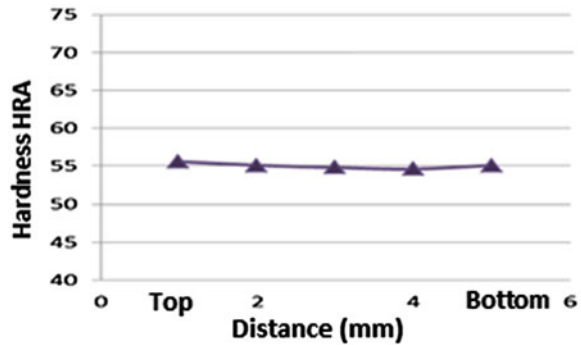
Fig. 8 Average levels of Microhardness Hv0.1 established in the direction of infiltration (*vertical*) of the composite

However, the decomposition of WC/W₂C particles (edge) gives a hardness of (240 Hv0.1). This result confirms the decomposition of WC, knowing that the average hardness of WC is 2370 Hv0.1 and that correspond to W is about 356 Hv0.1.

5.3 Hardness Study

Figure 9, corresponds to the hardness profile in the infiltration direction of the WC/W₂C–20W–20Ni compound infiltrated by the Cu–30Mn–3p binder.

Fig. 9 HRA hardness of WC/W₂C–20W–Ni composite infiltrated by the Cu–30Mn–3P binder



The average value is about 55 HRA registered in the direction of infiltration seems to confirm the excellent densification despite of the settling effect of refractory WC and W particles.

6 Conclusions

The consolidates realized from different powders, have permitted to highlight the effect of the interaction of solid particles in maintaining at optimal infiltration temperature. The choice of the binder composition (effect of addition elements) appears to depend on the Ni dissolution rate into the liquid. The final structure obtained consolidated under the same cooling kinetic conditions can have a major consequence on the level of hardness. In fact the total dissolution of Nickel in our composite does not seem to give a ternary solid solution. However, it contributes to the hardening of the binder phase by the decomposition phenomenon of the WC/W₂C carbides. This decomposition is probably accentuated by the decarburization of the eutectic phenomenon WC/W₂C under conditions of infiltration in the presence of the liquid phase rich of nickel.

The binder hardness (Cu–30Mn–3p) therefore has a better regularity in the direction of the infiltration in a practical point of view, so we can conclude that the proportions of solid particles of Ni in industrial mixtures dissolved in the binder liquid can contribute significantly to reduce the overall shrinkage of the matrix constituting the head of a drilling tool. This behavior in the liquid phase and during solidification can improve the design of the tool.

References

1. Domsa, S., Orban, R.: New developments in wear resistant hard materials processing by the powdered matrix infiltration with molten binder alloy. 199–204 (1999)

2. German, R.M.: Liquid Phase Sintering. Plenum Press, pp. 5–10, 119–122, 160–162 (1985)
3. Miroud, D., Tata, M., Caractérisation physico-chimique des poudres industriels utilisées pour ALDIM dans la fabrication des outils de forages. Rapport ALDIM (2005)
4. Orban, R., Domsa, S.: Metallic binder for diamond tool production using synthetic diamond. In: Proceedings, Euro PM 99 European Conference on Advances in Hard Materials Production, Italie, November 1999, pp. 65–70
5. Lassner, E., Schubert, W.D.: Tungsten, Properties, Chemistry, Technology of the Element, Alloys and Chemical Compounds, pp. 215–263. Plenum Publishes (1999)
6. Métallurgie des poudres, poudres et produits frittés, échantillonnage. NF. A95–101, Edition AFNOR tome 1, p. 63 (1990)

Investigations on the Residual Shear Properties of a Composite Subjected to Impact Fatigue Loading

Said Mouhoubi and Krime Azouaoui

Abstract The main object of this experimental study is to understand the effects of the damages induced in laminated composites by impact fatigue loading on mechanical properties. Therefore, in this paper, the shear residual properties of composite plates subject to impact fatigue loading are experimentally investigated. The effects of impact parameters such as energy level and number of impacts on the post-impact behavior are identified. The glass woven/polyester plates of 280 mm × 180 mm are subjected to impact-fatigue using a specially designed machine, at two different energy levels (3 and 5 J). Coupons are cut from the impacted plates and subjected to static tests in order to investigate the residual shear properties. For that, an Iosipescu device is manufactured. The results show that the energy level and the number of impacts influenced significantly the degradation of residual strength and the loss of stiffness for the impacted plates. It was found that the rate of reduction of the shear residual stiffness is close to 45.74, 57.66 and 63.67 %, respectively for 50, 100 and 150 impacts. The residual strength reductions are of the order of 15.15, 28.70 and 34.21 %, respectively for 50, 100 and 150 impacts.

1 Introduction

Understanding the damage phenomena of composite structures subjected to impacts is of particular interest. Many works have shown the dangers and risks related to the deterioration of mechanical properties due to the multiplication of low-energy impacts. Many researchers have been interested in the evolution of damage in composite materials subjected to repeated impact load. One example is the work of Wu and Wang [1]; in this study the behavior of stitched and unstitched glass/epoxy

S. Mouhoubi (✉) · K. Azouaoui
Laboratoire de Mécanique Avancée, USTHB, BP32 El-Alia Bab-Ezzouar,
16111 Alger, Algeria
e-mail: said.mouhoubi@gmail.com

K. Azouaoui
e-mail: kazououi@gmail.com

laminated composites, subjected to impacts was analyzed. Test specimens were impacted repeatedly in order to investigate the growth of damages, including delamination and transverse cracking. However, these measures do not allow to have an overall estimate of materials behavior and to estimate the damage tolerance and also measure the residual strength after low-energy impacts. In addition to non-destructive testing, an effective way to characterize the degree of damage resulting from the repetition of impacts is to quantify the residual properties of composite laminates subjected to repeated impacts. A majority of research works have used Compression-After-Impact testing to measure the residual strength for low velocity impact [2–5]. This is understandable, because of the high sensitivity of compression property of composites to impact, mainly because of delamination (induced by impacts) that creates inter-ply separation zones. The multiplication of low-energy impacts may indeed lead to a severe decrease in residual strength of composite structures [6–14], including compressive strength as well as tensile or shear strengths.

In order to design a composite structure tolerant to impact, it is important to study its damage under impact fatigue, the effect of this damage on its residual strength and the permanent damage caused by the impacts to rule on its possible detectability.

The objective of this experimental work is to analyze the damages and to follow their evolution according to impacts of low-energy, and to measure the shear residual strength and stiffness. For the post-impact characterization, a specific device (Iosipescu) was designed and manufactured [11, 12].

2 Experimental Procedure

2.1 Material

The studied material is 2 mm thickness composite laminate, constituted of polyester matrix reinforced with woven (*δHS*) E-glass fiber. The composite plates are manufactured by the airline company “Air-Algérie”, using the vacuum molding Process. Table 1 shows the material mechanical properties.

Table 1 Mechanical properties (tensile and shear)

Material	Tension ultimate stress σ (MPa)	Young's modulus E (GPa)	Shear ultimate stress τ (MPa)	Shear modulus G (GPa)
Glass/Polyester	353.13	23.87	42.85	5.82

2.2 Impact Fatigue Testing

The machine of impact fatigue produces repeated impacts due to a crank-connecting rod system (Fig. 1) [7]. The plates of 280 × 180 mm are embedded on two edges, and impacted repeatedly in their center by a cylindrical projectile of 5.7 kg and hemispherical head of 20 mm in diameter. The impact energy represents, in fact, the kinetic energy of the projectile calculated at the moment of impact. Either v_i the incident velocity measured just before that the impact takes place, and either (m) the mass of the projectile, the kinetic energy is given by the equation (Eq. 1).

$$E_i = \frac{1}{2}mv_i^2 \tag{1}$$

2.3 Post-impacts Shear Test

The shear testing is based on the principles of Iosipescu device (ASTM D5379-93) which uses specimens of 180 × 50 mm cross section with “V” notch; these specimens are called “butterfly-shaped”, taken on the impacted plates, so as to have all of the damaged area in the center of the shear specimen (Fig. 2). An Iosipescu shearing

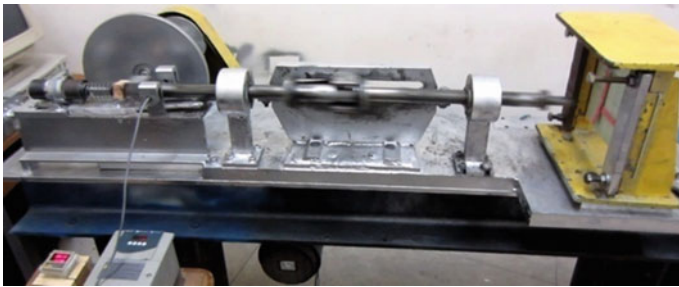


Fig. 1 Impact fatigue machine

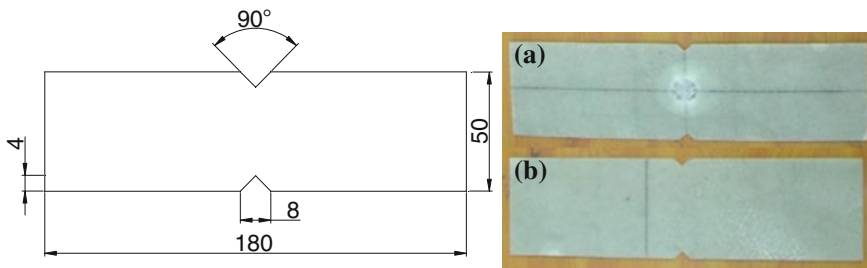
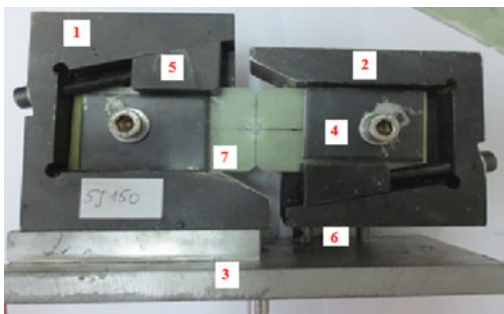


Fig. 2 Dimension of shear specimens, a impacted specimen, b virgin specimen

device [11] is designed to hold the shear specimens (Fig. 3), so as to avoid buckling, while ensuring a localized breakage at the damaged area. For this use is made of clamping wedges to ensure a perfect adhesion of the test specimens to the device. The tests are performed on a MTS 810 machine with a speed 2 mm/min (Fig. 4).

2.4 Test Parameters

To implement the experimental protocol, shock fatigue tests are carried out, until perforation occurs, in order to estimate the number of impacts to failure for each impact energy (Table 2). The impact energies selected are 3 and 5 J. It was agreed to submit the specimens to the number of following impacts: 50, 100, 150, for post-impact shear tests. For the measurement of damage, impact fatigue testing is stopped at regular intervals (*every 25 impacts*) to measure the dimensions of the crater and the delaminated surface.




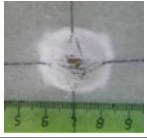

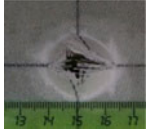
- 1: Fixed Jaw.
- 2: Mobile jaw.
- 3: Base.
- 4: A clamping wedge.
- 5: Adjusting shim
- 6: Guide rods.
- 7: Specimen.

Fig. 3 Iosipescu shear device



Fig. 4 Iosipescu device mounted on a MTS 810 machine

Table 2 Number of impacts to rupture and damage induced

Energy	Number of impacts to failure	Front face (after perforation)	Rear face (after perforation)
3 J	11970 Impacts		
5 J	235 Impacts		

The laminate being translucent, it is opacified by delaminating, making easy the measurement of damage. Photos are taken on both sides of the impacted plate, and we can easily monitor the delamination surface and the diameter of the crater resulting from impact fatigue testing.

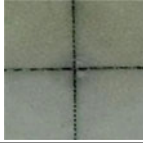




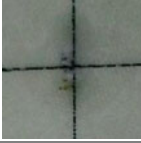


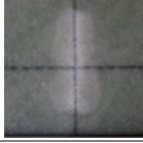



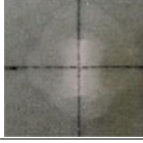
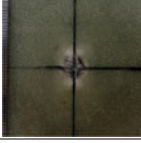


3 Results and Discussions

3.1 Damage Induced by Impact Fatigue Testing

During impact fatigue tests, we observed from the 1st impacts a whitish area surrounding the point of impact, this area can be explained by the delamination which occurs at the first impact. The delamination surface grows until it reaches a threshold corresponding to a slowing of the propagation. This propagation is done by a more pronounced manner for energy of 5 J. Also, a remarkable darkening of the plates at the impact point is observed and increases gradually as the number of impact increases, it is probably due to the heat induced by the impact repetition that burns the resin in this point. The delamination surface and the crater diameter tend to increase with the number of impacts (Table 3). Thus, one can state unequivocally that there is an intimate relationship between the number of impacts and the evolution of the damage (delamination and crater). After the analysis of the graph of Fig. 5 it can be seen that for the same energy level, the delamination increases with the number of impacts. Also, for the same number of impacts, the delaminated surface is larger for energy 5 J compared to 3 J. From Fig. 6 it can be easily noted that the crater diameter increases with the number of impacts and this for both energies (5 and 3 J). It should be noted that growth of the crater diameter is the same type as the delamination surface.

We clearly see an evolution in two phases: a much larger growth in the first phase and a slowdown in the second phase.

Table 3 Damage induced by impacts on front and rear faces (3 and 5 J)

Number of impacts	Impact energy			
	5 J		3 J	
	Rear face	Front face	Rear face	Front face
25				
50				
100				
150				

3.2 Post-impact Properties and Residual Shear Tests

Following the post-impact shear tests, it has been necessary to estimate the angular distortion γ to plot the shear stress curves (τ)—angular distortion (γ). For this, the determination of angular distortion was done by calculating the ratio of the cross sliding displacement (δ) by the distance between restraints Δx . The transverse displacement (δ) is taken from the sensor to the moving crosshead of the testing machine (Fig. 7).

An example of stress–strain curves is given in Fig. 8.

By analyzing Fig. 8, the curve increases until a maximum value followed by the fracture of the specimen by shearing. From there, we can take the shear stress to failure τ_0 of the virgin specimen and τ_i of damaged specimens. The curves of impacted specimens show a drop in tensile strength as and when the number of impacts increases. Photos of 5 J specimens (50, 100 and 150 impacts) and the 3 J (5000 impacts) show shear failure of the specimens (Fig. 9).

Fig. 5 Evolution of delamination according to number of impacts (3 and 5 J)

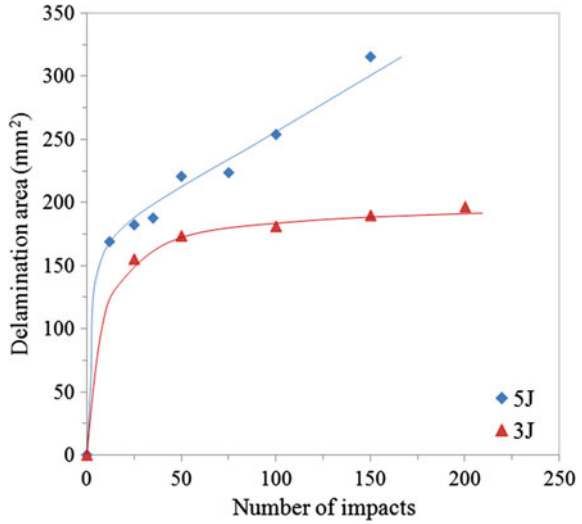


Fig. 6 Crater diameter evolution according to number of impacts (3 and 5 J)

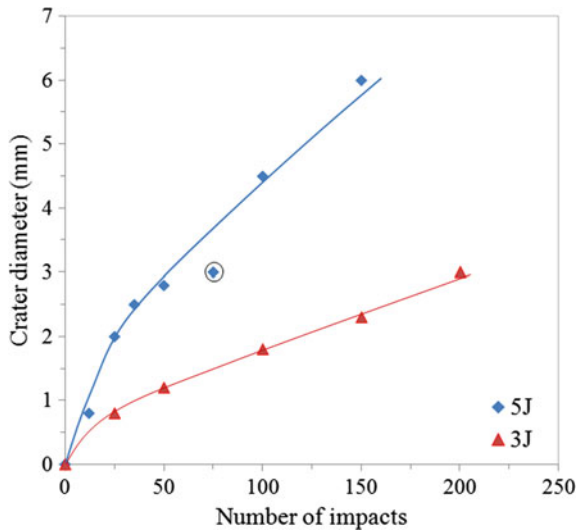


Figure 10 shows the evolution of residual strength of the impacted specimens at energy of 5 J according to impact number. In Fig. 11, we note an undeniable stiffness loss of plates with number of impacts.

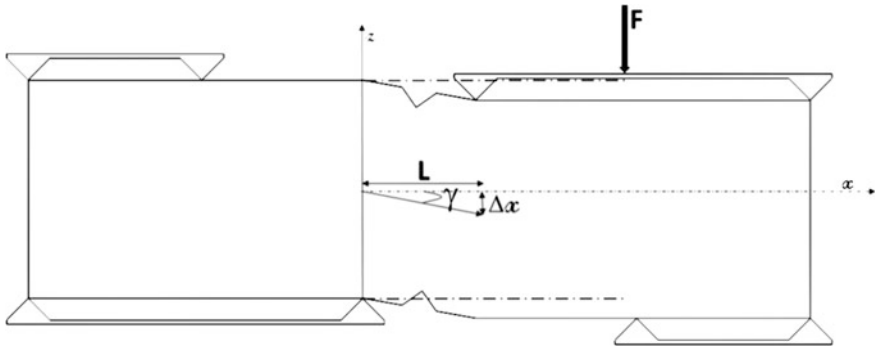


Fig. 7 Estimation of angular distortion γ

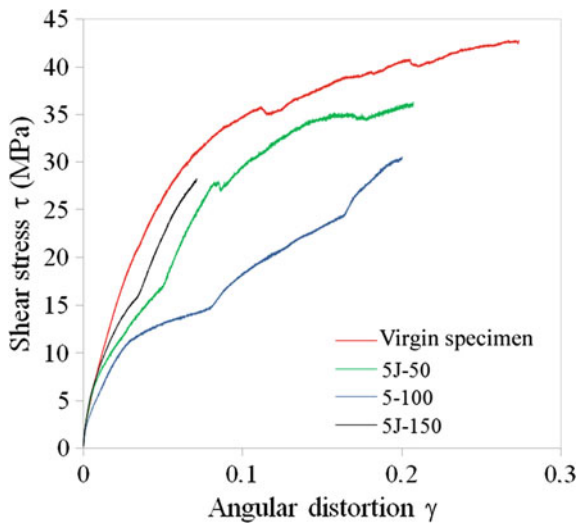


Fig. 8 Stress (τ) –strain (γ) diagrams (for 5 J: 50, 100 and 150 impacts)

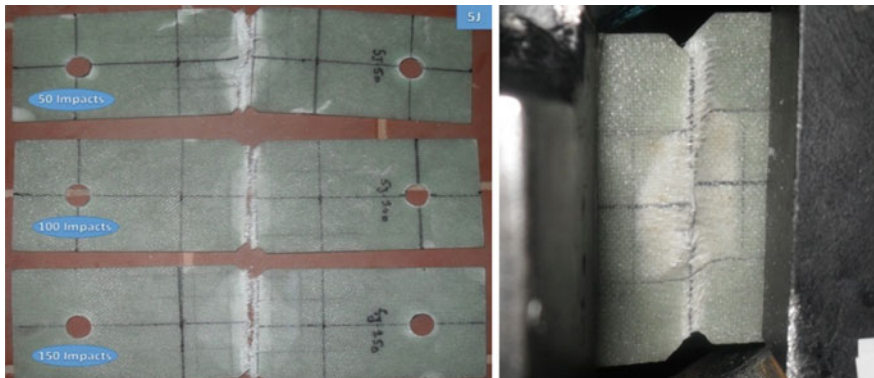


Fig. 9 Photos of specimens broken in shear

Fig. 10 Evolution of residual strength according to impact number (energy of 5 J)

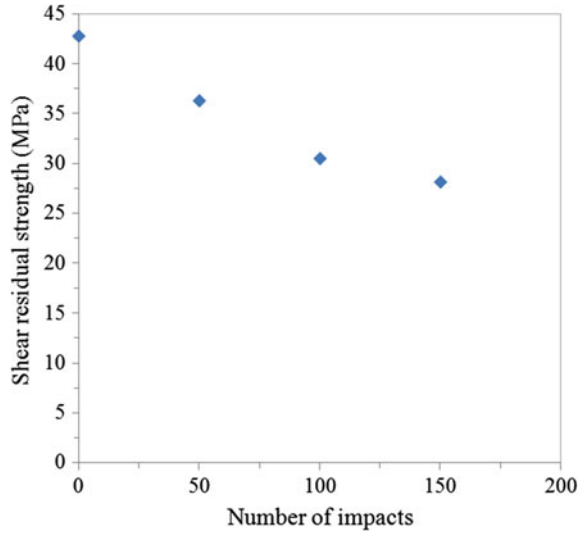
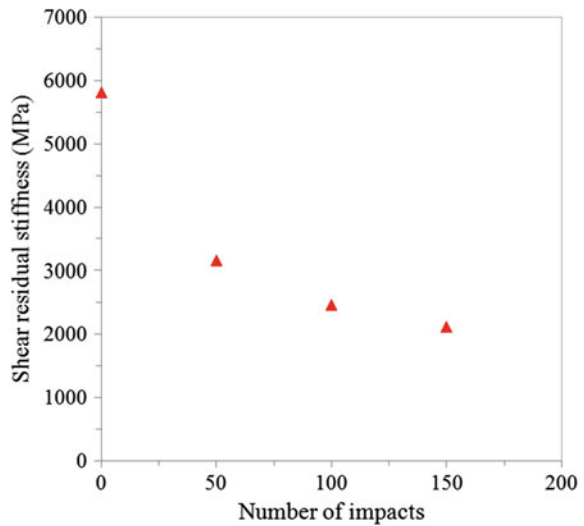


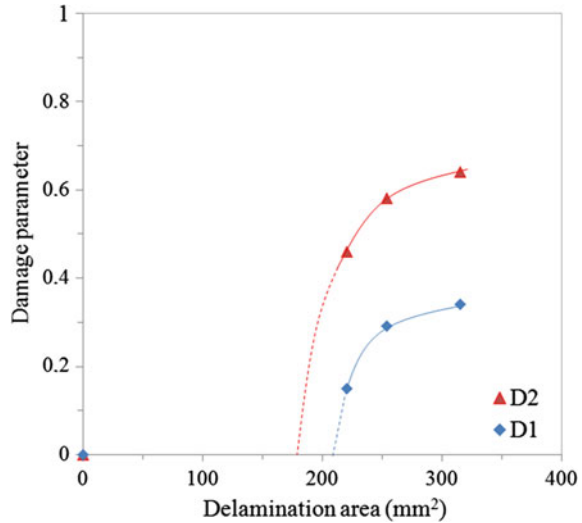
Fig. 11 Evolution of residual shear stiffness depending on number of impacts (energy of 5 J)



3.3 Damage Parameters D_i

To better describe the strength loss depending on number of impacts, a damage parameter D_I is established (Eq. 2). It is defined as the ratio between the strength loss ($\Delta\tau = \tau_0 - \tau_i$), τ_i being the residual shear stress for a number of impact (n_i), and the ultimate shear stress of a virgin specimen (τ_0).

Fig. 12 Evolution of damage parameters D_1 and D_2 with delamination area (energy of 5 J)



$$D_1 = 1 - \frac{\tau_i}{\tau_0} \tag{2}$$

Similarly a second definition of the damage variable is proposed, to better understand the loss of rigidity observed. For this we first measured the shear modulus of the virgin specimen (not impacted) G_0 , then the shear module G_i for each impacted specimen. The shear modulus was determined from Eq. 3 [15].

$$G = \frac{\tau}{\gamma} \tag{3}$$

D_2 damage parameter is calculated from Eq. 4.

$$D_2 = 1 - \frac{G_i}{G_0} \tag{4}$$

To highlight the losses of strength and stiffness with the size of the delaminated surface, we plotted the evolution of damage variables depending on delamination surface. Figure 12 shows in fact the losses of strength and stiffness which result in the growth of damage parameters with the growth of the delamination surface.

The extrapolation of trend of experimental curves corresponding to $D_i = 0$ (discontinuous lines in Fig. 12), give threshold values, which are likely to think of thresholds below which the strength and residual strength are not affected by impacts. At these area values corresponds the threshold number of impacts taken from Fig. 5. Hence it is probably easy to assume that the paces of strength and stiffness curves are as shown in Fig. 13a, b.

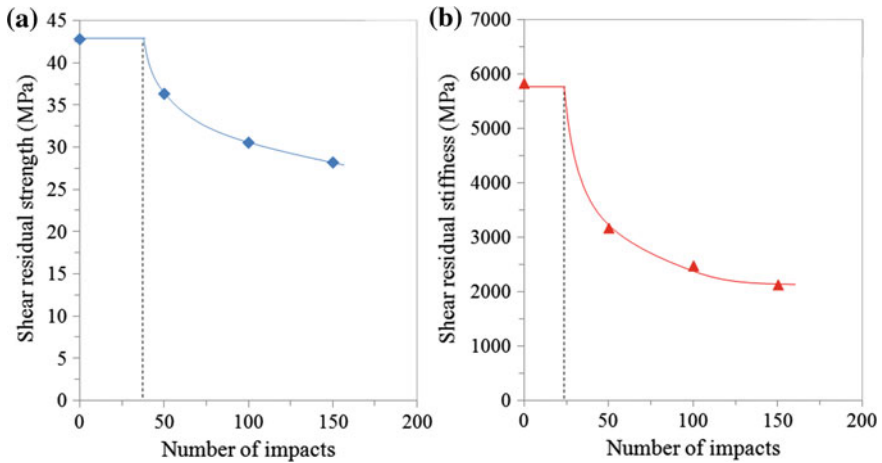


Fig. 13 Correction of strength (a) and stiffness (b) curves

4 Conclusion

The results of impact fatigue tests and those of post-impact shear tests have better clarify the evolution of the damage according to number of impacts and impact energy. Delamination and crater diameter exhibit changes in two stages depending on number of impacts. The first is an initiation phase (mainly delamination), the second is a phase where the propagation slowed due to the elastic response of the plates as well as the energy absorbed by the heat dissipation at the impacted area. The damage induced by impact at energy of 5 J is largest than damage induced by energy of 3 J, at same number of impacts.

Residual strength and residual stiffness significantly decrease with increasing number of impacts; the reduction rate of residual stiffness in shear of impacted plates are close to 45.74, 57.66 and 63.67 %, respectively for 50, 100 and 150 impacts. The residual strength shows lesser reductions of the order of 15.15, 28.70 and 34.21 %, respectively for 50, 100 and 150 impacts. Also, the D_1 and D_2 damage parameters unambiguously show losses of residual strength and stiffness with impact numbers. It is found that below a threshold number of impacts (around 40 impacts for D_2 , and 25 for D_1) the residual strength and stiffness are not affected by impacts.

References

1. Wu, E., Wang, J.: J. Compos. Mater. **29**(17), 2254–2279 (1995)
2. Cantwell, W., Curtis, P., Morton, J.: Composites **14**(3), 301–305 (1983)
3. Liu, D., Raju, B.B., Dang, X.: Int. J. Impact Eng **21**(10), 837–854 (1998)
4. Mahfuz, H., Saha, M., Biggs, R., Jeelani, S.: Key Eng. Mater. **141–143**, 209–234 (1998)

5. Zhou, G.: *Key Eng. Mater.* **141–143**, 305–334 (1998)
6. Amaro, A.M., Reis, P.N.B., De Moura, M.F.S.F., Neto, M.A.: *Compos. B* **52**, 93–99 (2013)
7. Azouaoui, K., Azari, Z., Pluinage, G.: *Int. J. Fatigue* **32**, 443–452 (2010)
8. Hou, J.P., Jeronimidis, G.: *Compos. A* **31**, 121–132 (2000)
9. Guades, E., Aravinthan, T.: *Compos. Struct.* **95**, 354–365 (2013)
10. Ray, V., Sakar, B.K., Bose, N.R.: *Compos. A* **33**, 233–241 (2002)
11. Iosipescu, N.: *J. Mater.* **2**(3), 537–566 (1967)
12. Adams, D.F., Walrath, D.E.: *J. Compos. Mater.* **21**(6), 494–507 (1987)
13. Odegard, G., Kumosa, M.: *Compos. Sci. Technol.* **60**, 2917–2943 (2000)
14. Niklas, M.L.: *Composite Structures* **76**, 106–115 (2006)
15. Chiang, M.Y.M., Jianmei, H.: *Compos. B* **33**, 461–470 (2002)

Development of a Reliability-Mechanical: Numerical Model of Mechanical Behavior of a Multilayer Composite Plate

Abdelhakim Maizia, Abdelkader Hocine, Hocine Dehmous
and David Chapelle

Abstract Due to the design of uncertainty caused by manufacturing processes and measures, that may affect composite structures, mechanical reliability analysis of a multilayer composite plate, using the finite element method, been the subject of this paper. To that end, we propose a reliability-mechanical numerical model, conditioned by Tsai-Wu failure criterion. This model was developed in two steps, first, the development of a deterministic model, afterwards, a probabilistic computation. To get to our lens, a probabilistic study was carried out to highlight the influence of design parameters on random damage to composite structures, using the Monte Carlo simulation method, which made it possible to estimate the failure P_f probability of the studied structure. The results obtained show that the uncertainties loading and winding angle are the first two responsible for the composite structure failure.

A. Maizia (✉) · A. Hocine
Controls, Testing, Measurement and Mechanical Simulations Laboratory,
Hassiba Benbouali University, Hay Salem, National Road No. 19,
Chlef 02000, Algeria
e-mail: maiziamaster2012@gmail.com

A. Hocine
e-mail: hocineak.dz@gmail.com

H. Dehmous
Department of Civil Engineering, University Mouloud Mammeri,
Campus Hasnaoua, Tizi-Ouzou, CP 15000, Algeria
e-mail: hocine_dehmous@ummto.dz

D. Chapelle
Département de Mécanique Appliquée, FEMTO ST,
Université de Franche Comté, Besançon, France
e-mail: david.chapelle@univfcomte.fr

1 Introduction

The use of composite materials has become a current practice in gas transport and storage structures due to their lightweight, relative low cost and mainly their high strength over metallic materials. Moreover, composite materials can provide their function with the presence of damage rather to metallic materials [1–3]. This latter characteristic is a great technological leap for the design of composite structures, which will minimize the hazard and increase the lifetime of structures. This property is one of the fundamental interests of our work.

Nevertheless, the literature shows that, there is many design variables for the structural design of composite structures [4–6]. These variables are induced first by the variations of material properties, where the composite materials are characterized by a high variability of the mechanical and geometrical properties due to the heterogeneous composition of the components, the load condition and finally the effects of the uncertainties in the manufacturing process according to the winding time, fiber tension, the winding pattern, the delivery system and the curing cycle, which can improve up to 30 %, the performance of composite structure by optimizing this process factors. As a first contribution, this work focuses on the effects of uncertainty (random variables-*RV*) of the different parameters on the static fracture behavior of multilayer plates via the finite element method. It will estimate the probability of failure of the composite structure studied.

2 Approach and Formulation Reliability

The theory of reliability is based on a probabilistic approach to structural safety. It aims to assess the probability of failure of the structure: knowing the structure of a limit state criterion and the variability of the parameters involved in this test, the probability of failure is defined as the probability that this criterion is exceeded.

The structure is finally considered safe if the probability of failure is less than a reference value called the acceptable probability of failure [4]. To achieve our aim, we propose a reliability-mechanical study represented by the Probabilistic Design System (*PDS*) and an *FE* model implanted under the commercial code ANSYS “*APDL*.” The following diagram (Fig. 1) shows the approach of our reliability-mechanical model.

The present work takes place in two main steps. Initially, the *FE* model is realized. Finally probabilistic modeling with Monte Carlo method is implemented to calculate the probability of failure P_f of the studied structure.

This probability is defined by the integral (1) as a function of a random variable X vector, which represents the uncertainty in model [5].

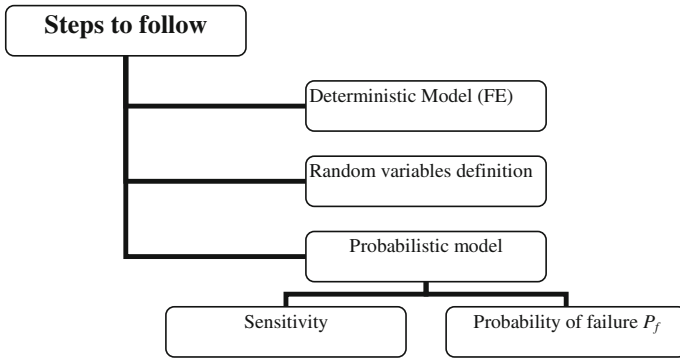


Fig. 1 Reliability-mechanical analysis steps

$$p_f = \int_{G(X_i) \leq 0} f_x(X) dX \tag{1}$$

where:

f_x : Distribution function associated

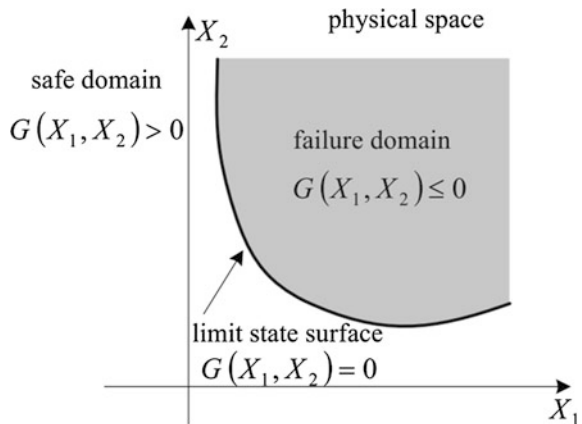
$G(X_i)$: Performance function

$G(X_i) = 0$: Boundary surface between the failure domain ($G(X_i) > 0$) and the security field ($G(X_i) > 0$), as shown in Fig. 2

To reach our objective, we realize a print run of N samples of X vectors to evaluate the limit state function G . Then we calculate Pf which is defined as the ratio between the number of prints $G(X_i)$ where ($G(X_i) \leq 0$) and the total number of prints.

$$p_f = \frac{N_{G \leq 0}}{N_{totale}} \tag{2}$$

Fig. 2 Security and failure areas for two random variables $\{X\} = \{X_1, X_2\}$ [5]



where the probability of failure for each ply is obtained via the Tsai-Wu criterion below.

$$\left(\frac{1}{X_t} - \frac{1}{X_c}\right)S_x + \left(\frac{1}{Y_t} - \frac{1}{Y_c}\right)S_y + \frac{S_x^2}{X_t X_c} + \frac{S_y^2}{Y_t Y_c} + \frac{S_{xy}^2}{S_{XY}^2} - \frac{S_x S_y}{\sqrt{X_t X_c Y_c Y_t}} \leq 1 \quad (3)$$

where the limit state function $G(X)$ is expressed by the following equation:

$$G(X_i) = R(X_i) - S(X_i) \quad (4)$$

with:

$R(X_i)$: Structural strength $R(X) = 1$ in this case.

$S(X_i)$: Loading (maximum value for the Tsai-Wu criterion).

3 Finite Element Model

All Finite element simulations have been performed under the ANSYS.12 software. In order to analyze the variation of the stresses through the thickness, a multilayer 3D element *SOLID186* type of 20 nodes (Fig. 3) was chosen for the mesh of that plate. A uniform mesh characterizes this simulation of the plate, with nodes 803 and 100 elements.

The plane structure considered consists of ten alternating layers $[\pm 55]_5$, of 0.27 mm thickness for each layer glass/epoxy. The material properties of the material are shown in Table 2. The presentation of the stacking sequence is shown by Fig. 4 (Table 1).

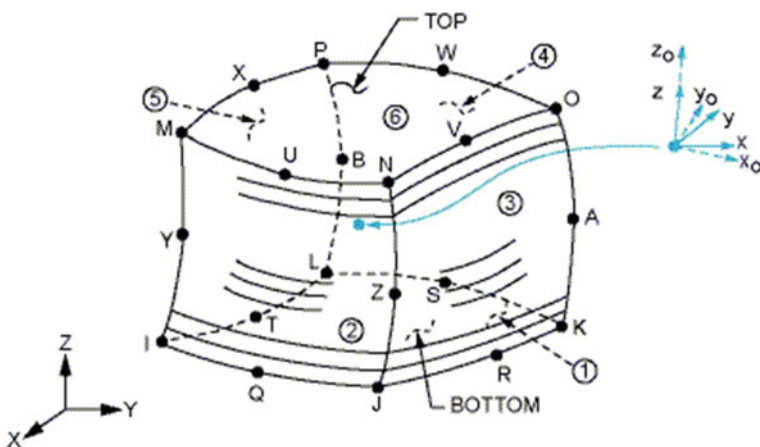


Fig. 3 SOLID186 multilayer element [6]

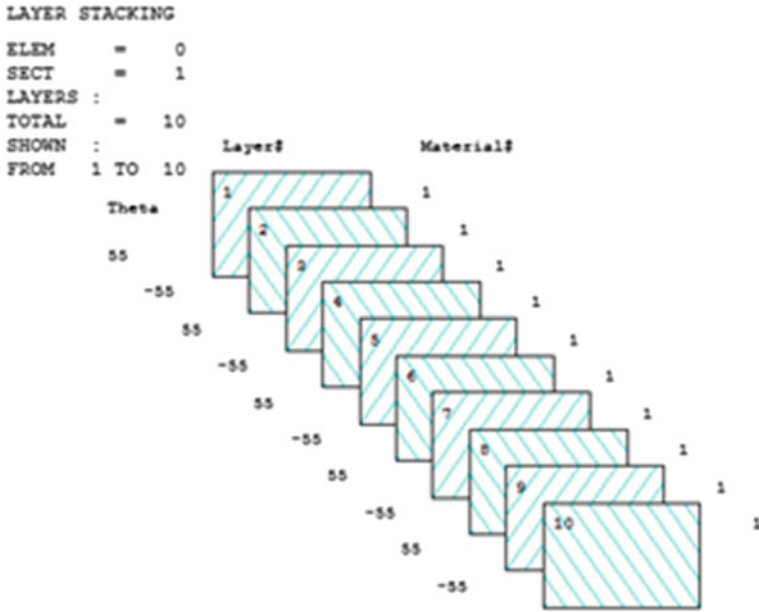


Fig. 4 Representation of the multilayer plate studied

Table 1 Parameters of the probabilistic modeling

Input parameters			
Ex	Longitudinal Young’s modulus	Xt	Longitudinal tensile strength
Ey	Transverse Young’s modulus	Xc	Longitudinal compressive strength
Gxy	Shear modulus in the plane (xy)	Yt	Transverse tensile strength
Gyz	Shear modulus in the plane (yz)	Yc	Transverse compressive strength
Gxz	Shear modulus in the plane (xz)	SXY	Shear strength
NUxy	Poisson module in the plane (xy)	Tita	Orientation of the fibers
NUyz	Poisson module in the plane (yz)	Pr	Loading tensile (MPa)
NUxz	Poisson module in the plan (xz)	EP	Thickness of each pleat (mm)
H	Plate height (mm)	L	Width of the plate (mm)
N	Number of sample prints	R	Ration (H/L)
Sxy	Stress in the plane (xy)	Ux	Displacement in the X direction (mm)
Sx	Stress in the X direction	Uz	Displacement in the Z direction (mm)
Sz	Stress in the Z direction	Sy	Stress in the Y direction

The uncertainty parameters are defined as random input variables and are characterized by their type of distribution (Gaussian, log normal, uniform etc.) and their distribution parameters (mean values, standard deviation, etc.). The data from parameters concerned are expressed in Table 3.

Table 2 Unidirectional elastic properties of composite layer

Mechanical and strengths properties								
E_1 (MPa)	E_2 (MPa)	G_{12} (MPa)	ν_{12}	X_t	X_c	Y_t	Y_c	S_{xy}
380000	90000	36000	0.3	2000	750	60	160	200

Table 3 Specifications random input variables

	Name	Distribution	Parameter 1	Parameter 2
1	EP (mm)	Uniforme	0.26	0.28
2	Ex (MPa)	Gaussian	3.8E+07	1.52E+06
3	Ey (MPa)	Gaussian	9E+06	3.6E+05
4	Gxy (MPa)	Gaussian	3.6E+06	1.44E+05
5	Gyz (MPa)	Gaussian	6.727E+06	2.691E+05
6	H (mm)	Uniforme	990	1010
7	L (mm)	Uniforme	990	1010
8	PR (MPa)	Gaussian	100	5
9	TITA	Uniforme	53	57
10	NUxy	Uniforme	0.30	0.34
11	NUyz	Uniforme	0.49	0.585
12	SXY (MPa)	Gaussian	200	10
13	Xt (MPa)	Gaussian	2000	100
14	Yt (MPa)	Gaussian	60	4
15	Yc (MPa)	Gaussian	-160	10
16	Xc (MPa)	Gaussian	-750	30

4 Results and Analysis

4.1 Deterministic Model

Deterministic analysis is implemented in order to calculate first the mechanical response in terms of stresses and displacements, and last to check the reliability of the structure by the Tsai-Wu criterion. Figures 5 and 6 show the sensitivity of the failure criterion Tsai-Wu to the variation of the load and the dimensions of the structure studied. The results obtained showed a symmetry to the mean plane of the laminated plate, which as an example the computation of Tsai-Wu criterion for each loading elevation for the first layer is identical with the last layer number 10, as shown in Fig. 5. Figure 6 below clearly shows that the damage is initiated from the outer layer to the inner and it is very important to raise the positive windings are more susceptible to damage than negative.

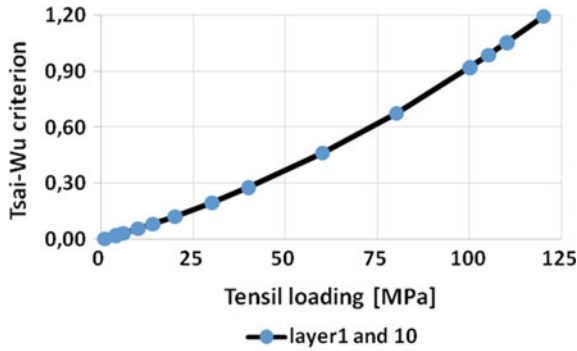


Fig. 5 Change Tsai-Wu criterion depending on the applied load; for (R = 1)

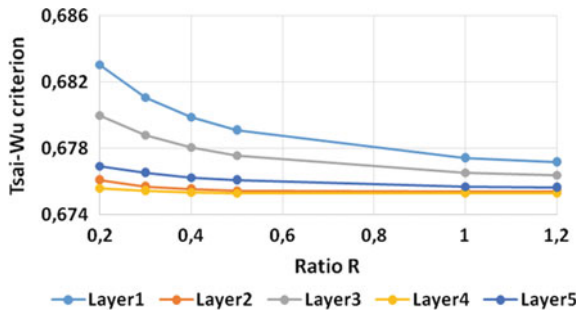


Fig. 6 Tsai-Wu criterion Variation of the ratio R; for a load of 80 (MPa)

4.2 Probabilistic Model

Table 4 shows the statistical random output parameters of the inner layer until the last outer layer.

4.3 Sensitivity

The sensitivity analysis shown in Figs. 7, 8 and 9 illustrates the influence of different random parameters on distribution of axial stress and displacement and on the threshold of Tsai-Wu criterion. These results are calculated for a thickness ratio $R = 1$ and a tensile load $P_r = 100$ MPa. According to the results, we may conclude that the parameters that have a great influence on the safety of the structure are first: fiber orientation angle and loading, as well as the tensile strength. Then, the mechanical properties of the material.

Table 4 Statistics random parameters fold output 1 and 10

	Designation (MPa)	Mean	Standard deviation	Minimum	Maximum
1	Sx max	44.18	4.596	30.1	59.26
2	Sxy max	-50.92	2.76	-61.79	-39.3
3	Sz max	1.651E-02	5.130E-03	3.734E-03	3.512E-2
4	Sy max	56.04	4.879	42.25	74.71
5	Ux max (mm)	5.407E-03	3.251E-04	4.146E-03	6.7E-03
6	Uz max (mm)	6.64E-06	5.131E-07	4.84E-06	8.697E-06
7	Tsai-Wu Criterion of layer 1 and 10	0.922	0.11	0.627	1.38

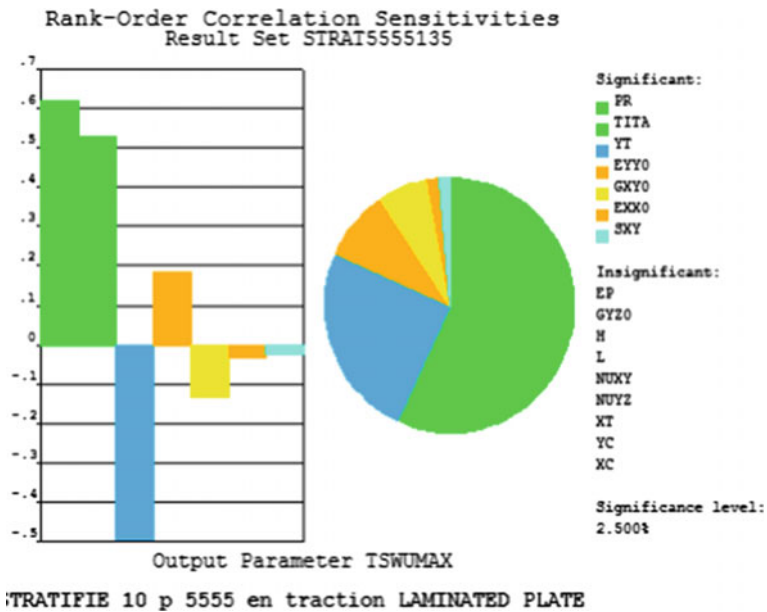


Fig. 7 Tsai-Wu Criterion Sensitivity of layer 1 and 10

4.4 Probability of Failure

On the other hand, Fig. 10 shows a great influence of the load applied P_r on the probability of failure P_f , where one can note that a 5 % change of P_r causes increased 0.2 per P_f .

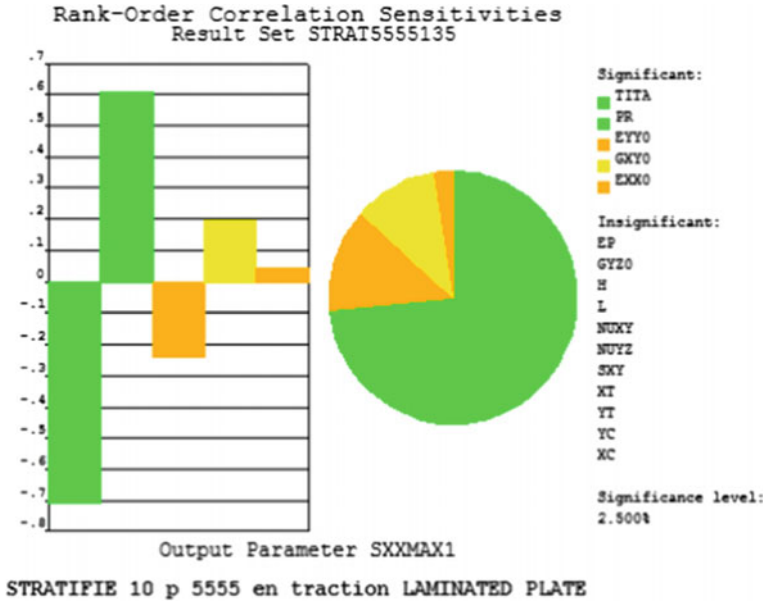


Fig. 8 Axial stress Sx Sensitivity of layer 1 and 10

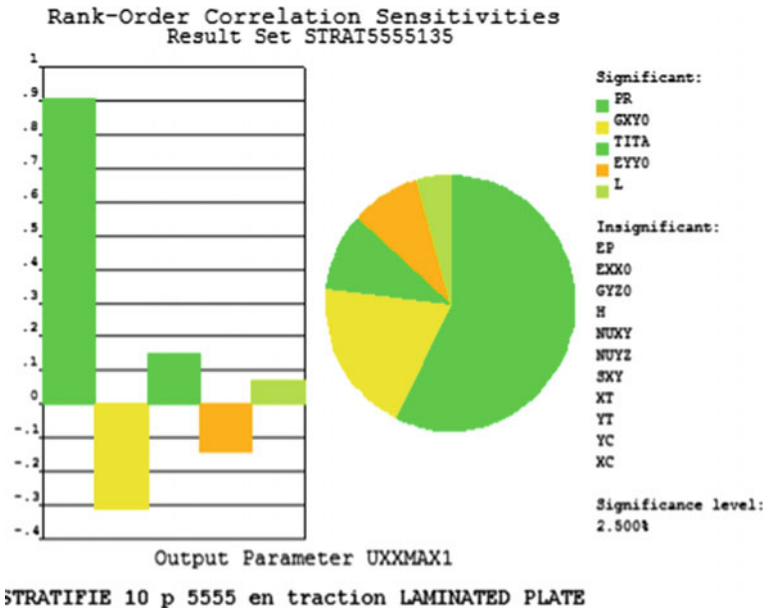
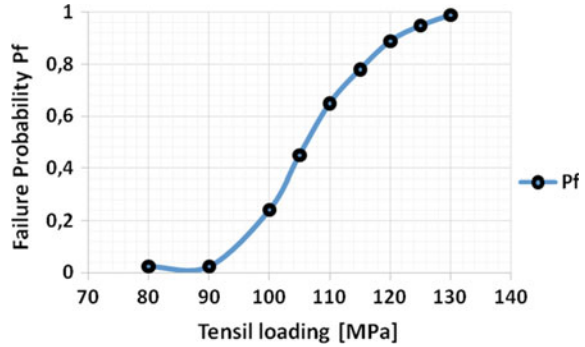


Fig. 9 Radial displacement Ux Sensitivity of layer 1 and 10

Fig. 10 Probability of failure as a function of the tensile load



5 Conclusions and Perspectives

The objective of our work is the development of a numerical model in commercial *FEM* platform ANSYS, which allows the mechanical reliability-study of a multilayer composite plate. In this study, the effects of uncertainty (random variables) of the various settings, including mechanical properties, the load and geometry on the failure behavior of said structure were analysed.

The probabilistic model, which was implemented, has enabled, first to identify the dominant and important design parameters for our structure sensitivity analysis. Secondly, we succeeded to compute the probability of failure P_f for a variation of the applied load; this allows estimating the maximum capacity of our plate.

This work has enabled us to identify the reliability zone without going into the failure zone. Finally, the only disadvantage of this approach is the present digital computation time that is too heavy, due to the use of the Monte Carlo method, which requires a large number of draws, on the other hand made in our probabilistic model ANSYS.12 does not directly calculate P_f .

Acknowledgments The collaboration of the research team structures and new materials laboratory Controls Tests, Measurements and Simulations with Mechanics Department DMA of the mechanical department of the FEMTO-ST Institute is much appreciated. This work was supported by the M2SC team where the Algerian side wishes to express their sincere gratitude to team leaders in experimental research and numerical simulations.

References

1. Stani, C.: Contribution aux Calculs Fiabilistes sur des Structures Composites, PhD thesis at the University of Franche -Comté, N°:1063, France (2005)
2. Boubakar, M.L., Trivaudey, F., Perreux, D., Vang, L.: A meso—macro finite element modelling of laminate structures Part I: time-independent behavior. *Compos. Struct.* **58**, 271–286 (2002) (France)

3. Boubakar, M.L., Vang, L., Trivaudey, F., Perreux, D.: A meso—macro finite element modelling of laminate structures Part II: time-dependent behavior. *Compos. Struct.* **60**, 275–305 (2003) (France)
4. Riccio, A., Russo, T., Scaramuzzino, F.: Impact damage management of composite laminated structures by a probabilistic approach. *Open Mater. Sci. J.* **7**, 8–22 (2013) (University of Naples, via Roma n 29, 81031, Italy)
5. Dehmous, H., Weleman, H.: Multi-scale reliability analysis of composite structures—application to the Laro in footbridge. *Eng. Fail. Anal.* **18**(3), 988–998 (2011). ISSN 1350-6307
6. Ansys.12, help, Element Reference, Element Library, SOLID186

Analysis of Deflection in Isotropic and Orthotropic Rectangular Plates with Central Opening Under Transverse Static Loading

Ahmed Abdelatif Bouzgou, Abdelouahab Tati and Abdelhak Khechai

Abstract In this study, the transverse deflection in orthotropic composite plates as well as in isotropic plates with circular hole subjected to transverse loading is studied. This study was made numerically by using a quadrilateral finite element of four nodes with 8 degrees of freedom at each node, previously developed for the bending and mechanical buckling of laminated composite plates. The main purpose of this study is to demonstrate the accuracy of the present element for analyzing the effect of (D/A) ratio (where (D) is hole diameter and (A) is plate width) upon the transverse deflection in isotropic and orthotropic plates with different support conditions. The numerical results obtained by the present element and the finite element software 'Abaqus' compare favorably with those obtained by the analytic approaches and the numerical results published in literature.

Nomenclature

D	Hole diameter
L, A, e	Length, width and thickness of the plate studied
$N_i(\xi, \eta)$	Linear interpolation functions
$H_{00}, H_{01}, H_{10}, H_{11}$	Interpolation functions of the parent element
$L_w, L_{0x}, L_{0y}, L_{0xy}, L_{0xx}, L_{0yy}$	Interpolation functions of the real element
U	Potential energy of deformation
V	Potential energy due to transverse loads
UZ	Deflection of a plate provided with an opening
UZ^*	Deflection plain plate

A.A. Bouzgou (✉) · A. Tati
Laboratoire de Génie Energétique et Matériaux, LGEM, Université de Biskra,
B.P. 145, R.P. 07000 Biskra, Algeria
e-mail: latif_civil@hotmail.fr

A. Tati
e-mail: abdelatati@yahoo.fr

A. Khechai
Laboratoire de Génie Civil, LRG, Université de Biskra, B.P. 145, R.P.,
07000 Biskra, Algeria
e-mail: abdelhak_khechai@hotmail.fr

1 Introduction

Isotropic, orthotropic and composite plates are increasingly used in various engineering fields (e.g. civil engineering, aerospace, automobile and mechanical). This use is due to the fact that these materials have several advantages, among which we note the high strength and stiffness relative to their weight, low maintenance, a manufacturing time as short as possible; they can increase the duration life of some equipment due to their mechanical properties [1]. Therefore, it is necessary to have a good understanding of their behaviors such as bending, buckling and the stress distribution in the vicinity of geometric singularities, etc. [2]. Our work is the analysis of the mechanical behavior of two-dimensional thin orthotropic plates (glass epoxy) with geometric singularities under external loading (transverse distributed load) using numerical methods and modeling based on the finite element method (*FEM*). This article essentially comprises two parts; the first is devoted to a presentation of the finite element formulation, as well as an example in order to validate the ability of the present element. The numerical results obtained by the present element and the finite element software Abaqus compare favorably with those obtained by the analytic approaches and the numerical results published in literature. In the second part, a parametric study is carried out in order to show the hole diameter effect on the central deflection of the orthotropic composite plate.

2 Finite Element Formulation

The finite element method is an approximate method we use to solve the partial differential equations. For the implementation of this method in analysis, we are using two different numerical tools:

- A *FORTRAN 77* program. In this program, the formulation of the finite element was programmed (Quadrilateral plate element first order Hermite interpolation *Q4*).
- The finite element software Abaqus for the confrontation, when we were using the finite element *S4R* (4 nodes shell element with reduced integration).

2.1 Interpolation Functions of the Reference Element

The transverse displacement w of the element of reference is expressed as a product of one dimensional first order Hermitian interpolation polynomials [3, 4].

$$w(\zeta, \eta) = H_{00}w_i + H_{10} \frac{\partial w_i}{\partial \zeta} + H_{01} \frac{\partial w_i}{\partial \eta} + H_{11} \frac{\partial^2 w_i}{\partial \zeta \partial \eta} \tag{1}$$

$$H_{00} = \frac{1}{16} (\zeta + \zeta_0)^2 (\zeta \zeta_0 - 2) \cdot (\eta + \eta_0)^2 (\eta \eta_0 - 2)$$

$$H_{10} = -\frac{1}{16} \zeta_0 (\zeta + \zeta_0)^2 (\zeta \zeta_0 - 1) \cdot (\eta + \eta_0)^2 (\eta \eta_0 - 2)$$

where: (2)

$$H_{01} = -\frac{1}{16} (\zeta + \zeta_0)^2 (\zeta \zeta_0 - 2) \cdot \eta_0 (\eta + \eta_0)^2 (\eta \eta_0 - 1)$$

$$H_{11} = -\frac{1}{16} \zeta_0 (\zeta + \zeta_0)^2 (\zeta \zeta_0 - 1) \cdot \eta_0 (\eta + \eta_0)^2 (\eta \eta_0 - 1)$$

2.2 Interpolation Functions of the Real Element

The derived geometrical interpolation functions will be calculated by the following formula:

$$\begin{aligned} \frac{\partial N_i}{\partial x} &= \frac{\partial N_i}{\partial \zeta} \frac{\partial \zeta}{\partial x} + \frac{\partial N_i}{\partial \eta} \frac{\partial \eta}{\partial x} \\ \frac{\partial N_i}{\partial y} &= \frac{\partial N_i}{\partial \zeta} \frac{\partial \zeta}{\partial y} + \frac{\partial N_i}{\partial \eta} \frac{\partial \eta}{\partial y} \end{aligned} \tag{3}$$

Or in matrix form by:

$$\begin{Bmatrix} \frac{\partial N_i}{\partial x} \\ \frac{\partial N_i}{\partial y} \end{Bmatrix} = \begin{bmatrix} \frac{\partial \zeta}{\partial x} & \frac{\partial \eta}{\partial x} \\ \frac{\partial \zeta}{\partial y} & \frac{\partial \eta}{\partial y} \end{bmatrix} \begin{Bmatrix} \frac{\partial N_i}{\partial \zeta} \\ \frac{\partial N_i}{\partial \eta} \end{Bmatrix} \tag{4}$$

The derived $\frac{\partial \zeta}{\partial x}$, $\frac{\partial \zeta}{\partial y}$, $\frac{\partial \eta}{\partial x}$ and $\frac{\partial \eta}{\partial y}$ are determined from the inverse of the Jacobian matrix J^{-1} .

The Jacobian matrix is given by:

$$J = \begin{bmatrix} \frac{\partial x}{\partial \zeta} & \frac{\partial y}{\partial \zeta} \\ \frac{\partial x}{\partial \eta} & \frac{\partial y}{\partial \eta} \end{bmatrix} = \sum_{i=1}^4 \begin{bmatrix} \frac{\partial N_i}{\partial \zeta} x_i & \frac{\partial N_i}{\partial \zeta} y_i \\ \frac{\partial N_i}{\partial \eta} x_i & \frac{\partial N_i}{\partial \eta} y_i \end{bmatrix} \tag{5}$$

The interpolation functions of the real quadrilateral plate element are determined from the interpolation functions of the reference element by introducing the geometrical interpolation functions:

$$\begin{aligned}
 \frac{\partial w}{\partial \xi} &= \frac{\partial w}{\partial x} \frac{\partial x}{\partial \xi} + \frac{\partial w}{\partial y} \frac{\partial y}{\partial \xi} \\
 \frac{\partial w}{\partial \eta} &= \frac{\partial w}{\partial x} \frac{\partial x}{\partial \eta} + \frac{\partial w}{\partial y} \frac{\partial y}{\partial \eta} \\
 \frac{\partial^2 w}{\partial \xi \partial \eta} &= \frac{\partial^2 w}{\partial x^2} \left(\frac{\partial x}{\partial \xi} \frac{\partial x}{\partial \eta} \right) + \frac{\partial^2 w}{\partial y^2} \left(\frac{\partial y}{\partial \xi} \frac{\partial y}{\partial \eta} \right) + \frac{\partial^2 w}{\partial x \partial y} \left(\frac{\partial x}{\partial \xi} \frac{\partial y}{\partial \eta} + \frac{\partial y}{\partial \xi} \frac{\partial x}{\partial \eta} \right) \\
 &\quad + \frac{\partial w}{\partial x} \left(\frac{\partial^2 x}{\partial \xi \partial \eta} \right) + \frac{\partial w}{\partial y} \left(\frac{\partial^2 y}{\partial \xi \partial \eta} \right)
 \end{aligned} \tag{6}$$

By introducing the expression (6) in the expression for w , we obtain:

$$\begin{aligned}
 w = H_{00}w_i &= H_{10} \left(\frac{\partial w}{\partial x} \frac{\partial x}{\partial \xi} + \frac{\partial w}{\partial y} \frac{\partial y}{\partial \xi} \right) + H_{01} \left(\frac{\partial w}{\partial x} \frac{\partial x}{\partial \eta} + \frac{\partial w}{\partial y} \frac{\partial y}{\partial \eta} \right) \\
 &\quad + H_{11} \left[\begin{aligned}
 &\frac{\partial^2 w}{\partial x^2} \left(\frac{\partial x}{\partial \xi} \frac{\partial x}{\partial \eta} \right) + \frac{\partial^2 w}{\partial y^2} \left(\frac{\partial y}{\partial \xi} \frac{\partial y}{\partial \eta} \right) \\
 &+ \frac{\partial^2 w}{\partial x \partial y} \left(\frac{\partial x}{\partial \xi} \frac{\partial y}{\partial \eta} + \frac{\partial y}{\partial \xi} \frac{\partial x}{\partial \eta} \right) \\
 &+ \frac{\partial w}{\partial x} \left(\frac{\partial^2 x}{\partial \xi \partial \eta} \right) + \frac{\partial w}{\partial y} \left(\frac{\partial^2 y}{\partial \xi \partial \eta} \right)
 \end{aligned} \right]
 \end{aligned} \tag{7}$$

Then, after transformation, the expression of the transverse displacement $w(x, y)$ at any point of coordinates (x, y) of the real element is given by [1]:

$$w(x, y) = L_w w_i + L_{\theta_x} \frac{\partial w_i}{\partial x} + L_{\theta_y} \frac{\partial w_i}{\partial y} + L_{\theta_{xy}} \frac{\partial^2 w_i}{\partial x \partial y} + L_{\theta_{xx}} \frac{\partial^2 w_i}{\partial x^2} + L_{\theta_{yy}} \frac{\partial^2 w_i}{\partial y^2} \tag{8}$$

Or in matrix form by:

$$w(x, y) = [L_w \ L_{\theta_x} \ L_{\theta_y} \ L_{\theta_{xy}} \ L_{\theta_{xx}} \ L_{\theta_{yy}}] \left[w_i \ \frac{\partial w_i}{\partial x} \ \frac{\partial w_i}{\partial y} \ \frac{\partial^2 w_i}{\partial x \partial y} \ \frac{\partial^2 w_i}{\partial x^2} \ \frac{\partial^2 w_i}{\partial y^2} \right]^T \tag{9}$$

where $L_w \ L_{\theta_x} \ L_{\theta_y} \ L_{\theta_{xy}} \ L_{\theta_{xx}}$ and $L_{\theta_{yy}}$ are the interpolation functions of the real element given by:

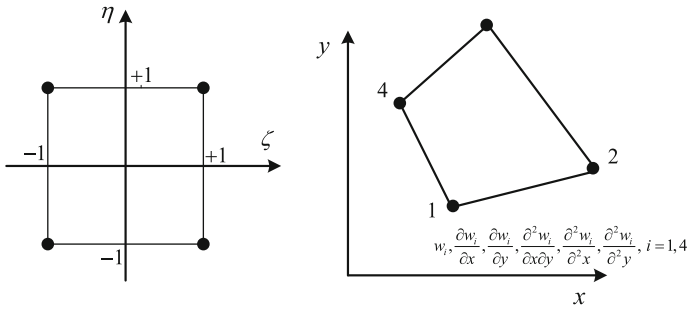


Fig. 1 Plate element

$$\begin{aligned}
 L_w &= H_{00} \\
 L_{\theta_x} &= H_{10} \frac{\partial x}{\partial \xi} + H_{01} \frac{\partial x}{\partial \eta} + H_{11} \frac{\partial^2 x}{\partial \xi \partial \eta} \\
 L_{\theta_y} &= H_{10} \frac{\partial y}{\partial \xi} + H_{01} \frac{\partial y}{\partial \eta} + H_{11} \frac{\partial^2 y}{\partial \xi \partial \eta} \\
 L_{\theta_{xy}} &= H_{11} \left(\frac{\partial x}{\partial \xi} \frac{\partial y}{\partial \eta} + \frac{\partial x}{\partial \eta} \frac{\partial y}{\partial \xi} \right) \\
 L_{\theta_{xx}} &= H_{11} \frac{\partial x}{\partial \xi} \frac{\partial x}{\partial \eta} \\
 L_{\theta_{yy}} &= H_{11} \frac{\partial y}{\partial \xi} \frac{\partial y}{\partial \eta}
 \end{aligned} \tag{10}$$

It can be seen that the interpolation functions of the real element are a function of coordinates x_i and y_i of the nodes $i = 1, 2, 3$ and 4 (Fig. 1).

2.3 Flexion Formulation

The total potential energy of deformation of a plate subjected to a distributed transverse loading is given by:

$$\Pi = U + V \tag{11}$$

The equilibrium configuration is defined by minimizing the total potential energy which means the cancellation of the first variation:

$$\delta\Pi = \delta U - \delta V = 0$$

$$\int_{-1}^1 \int_{-1}^1 \{\partial q\}^T \left\{ \begin{array}{l} [S_\varepsilon]^T [A] [S_\varepsilon] + [S_\varepsilon]^T [B] [S_K] + \\ [S_K]^T [B] [S_\varepsilon] + [S_K]^T [B] [S_K] \end{array} \right\} \{q\} |J| d\xi d\eta - \int_{-1}^1 \int_{-1}^1 P[L] \{\partial q\} |J| d\xi d\eta = 0 \quad (12)$$

This allows getting the following equilibrium equation:

$$[k^e] \{q\} = \{F^e\} \quad (13a)$$

with:

$$[K^e] = \int_{-1}^1 \int_{-1}^1 \left\{ \begin{array}{l} [S_\varepsilon]^T [A] [S_\varepsilon] + [S_\varepsilon]^T [B] [S_K] + \\ [S_K]^T [B] [S_\varepsilon] + [S_K]^T [B] [S_K] \end{array} \right\} |J| d\xi d\eta \quad (13b)$$

The matrix $[K^e]$ can be written in the form:

$$[K^e] = [K_1^e] + [K_2^e] + [K_3^e] + [K_4^e] \quad (14)$$

with:

$$\begin{aligned} [K_1^e] &= \int_{-1}^1 \int_{-1}^1 [S_\varepsilon]^T [A] [S_\varepsilon] |J| d\xi d\eta \\ [K_2^e] &= \int_{-1}^1 \int_{-1}^1 [S_\varepsilon]^T [B] [S_k] |J| d\xi d\eta \\ [K_3^e] &= \int_{-1}^1 \int_{-1}^1 [S_k]^T [B] [S_\varepsilon] |J| d\xi d\eta \\ [K_4^e] &= \int_{-1}^1 \int_{-1}^1 [S_k]^T [D] [S_k] |J| d\xi d\eta \end{aligned} \quad (15)$$

$[K_1^e]$: Membrane elementary stiffness matrix.

$[K_2^e]$ and $[K_3^e]$: Elementary stiffness matrix membrane-flexion coupling.

$[K_4^e]$: Flexural elementary stiffness matrix.

$$\{F^e\} = \int_{-1}^1 \int_{-1}^1 P[L] |J| d\xi d\eta \quad (16)$$

The components of the stiffness matrix and force vectors are determined by numerical integration using 2×2 Gauss points. With $[K^e]$ and $\{F^e\}$ are respectively the elementary stiffness matrix of size 32×32 and the elementary force

vector of dimension 32×1 . The assembly of the stiffness matrix and vectors elementary forces provides the following equation:

$$[K]\{X\} = \{F\} \tag{17}$$

With $[K]$ is the global stiffness matrix, $\{F\}$ is the global Force vector and $\{X\}$ is the vector of the global displacements of the nodes of the plate.

2.4 Validation of Present Element

In this study, a numerical test is considered in this section to assess the performance of the proposed element. Isotropic plates without hole are considered for validating the present element by comparing the numerical results with analytical solutions. In this test, we consider a simply supported plate on all its edges and subjected to uniformly distributed loading $P = 10^{-6}$ MPa in transverse direction (Fig. 2). The mechanical and geometrical properties of the plate are summarized in Table (1).

where: $P = Q/(L \cdot A)$

P : The pressure or the distributed load applied to the plate.

The thickness e and the pressure P and Q are the values given by the reference [5].

The analytical solution of adimensional transverse displacement \bar{W} is given by the formula [6]: $\bar{W} = W \left(\frac{100 E h^3}{q a^4} \right)$. In the Table (2), we compare the numerical results obtained by the present element and the element *S4R* of Abaqus with the analytic results. For different meshes, the convergence of \bar{W} obtained is traced as graphs (Fig. 3).

The Fig. (3) presents the variation of adimensional transverse displacement \bar{W} at the center of the isotropic plate studied according to a number of elements. We note that for a number of elements less than 64 the convergence of adimensional transverse displacement \bar{W} given by this element is fast towards to that given theoretically.

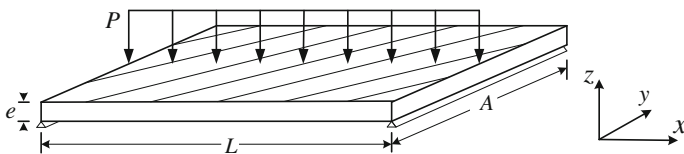


Fig. 2 Isotropic plate simply supported under transverse load

Table 1 Mechanical and geometrical properties of the isotropic plate

Materials	Mechanical and geometrical properties							
	E_1 (MPa)	E_2 (MPa)	G_{12} (MPa)	ν_{12}	L (mm)	A (mm)	P (MPa)	e (mm)
isotropic	39000	39000	15000	0.3	200	10	10^{-6}	1

Table 2 Adimensional transverse displacement of an isotropic plate without opening

Materials	Isotropic					The analytical adimensional displacement
	(2 × 2)	(4 × 4)	(6 × 6)	(8 × 8)	(10 × 10)	
Present element	1.38E-2	1.03E-2	1.03E-2	1.02E-2	1.01E-2	1.01E-02
Abaqus	9.86E-3	1.04E-2	1.02E-2	1.02E-2	1.01E-2	
Error (%)	-36.63	-1.98	-1.98	-0.99	0.00	

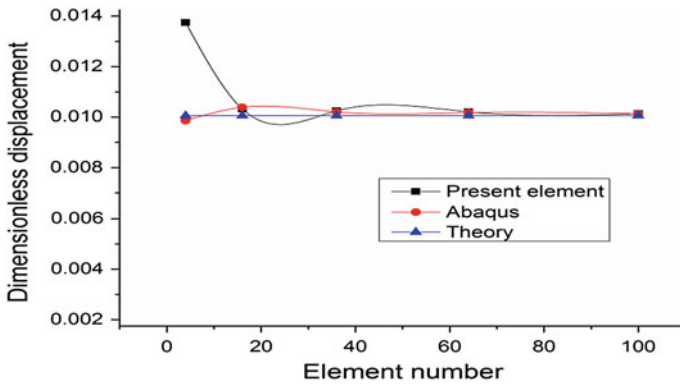


Fig. 3 Convergence of adimensional transverse displacement for an isotropic plate without opening

In the same previous interval, it is observed that there is a convergence of \bar{W} given by the element *S4R* of Abaqus to the theoretical result. For a number of elements greater than 64, it is noted that there is equality between the theoretical result and those given by the two elements used.

3 Parametric Study

In this section we will conduct a parametric study to highlight the report effect of D/A on the report of the deflection U_z/U_z^* in orthotropic epoxy-glass plate provided with a circular hole centered. The plate has a rectangular shape with a circular central hole. The latter solicited transversely evenly distributed static load (Fig. 4).

This study was made for three types of boundary conditions:

- Plate simply supported on four sides *SSSS* (Fig. 5a).
- Clamped plate with four sides *CCCC* (Fig. 5b).
- Plate simply supported on two sides and Clamped to both others *SCSC* (Fig. 5c).

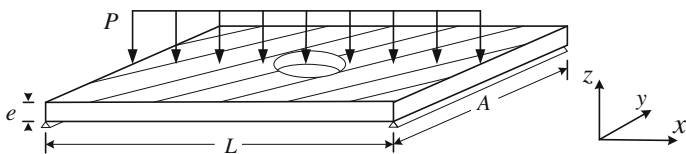


Fig. 4 Orthotropic plate with a centered circular hole subjected to transverse load P

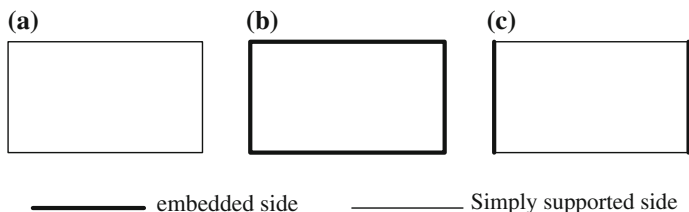


Fig. 5 Boundary conditions adopted

Table 3 Mechanical and geometrical characteristics of the plates tests

Materials	Mechanical and geometrical properties							
	E_1 (MPa)	E_2 (MPa)	G_{12} (MPa)	ν_{12}	L (mm)	A (mm)	P (MPa)	e (mm)
Orthotropic	39000	8600	3800	0.28	200	10	10^{-6}	1

The mechanical and geometrical characteristics of the plates are presented in the Table (3).

- Glass epoxy plate with a circular central hole

The curves of Figs. 6, 7 and 8 presented the variation of the deflection U_z/U_z^* ratio in function of D/A ratio for various boundary conditions. The results presented herein were obtained by the present element, the element *S4R* of Abaqus and the element *Shell93* of ANSYS [5]. According to the two Figs. 6 and 8, one can observe that the results obtained by the present element, the element *S4R* of Abaqus and the element *Shell93* of ANSYS are practically close.

In Fig. 7 where the studied plate is Clamped in all its edges, we note that the curve given by the element *Shell93* of ANSYS takes a different look compared to those given by the two other elements used. This curve increases when D/A is less than 0.8 and after this value, the curve decreases. For trend curves, I calculated the report U_z/U_z^* (the deflection of a perforated plate on the deflection of a full plate) for each report D/A . When using the report U_z^*/U_z the curve starts with a decrease. The black curve in the three figures is given by Jain and Mittal [5] who

Fig. 6 The effect of D/A report on U_z/U_z^* report in case SSSS

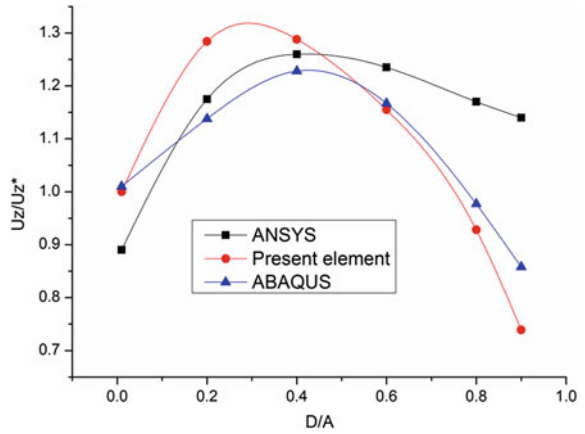


Fig. 7 The effect of D/A report on U_z/U_z^* report in case CCCC

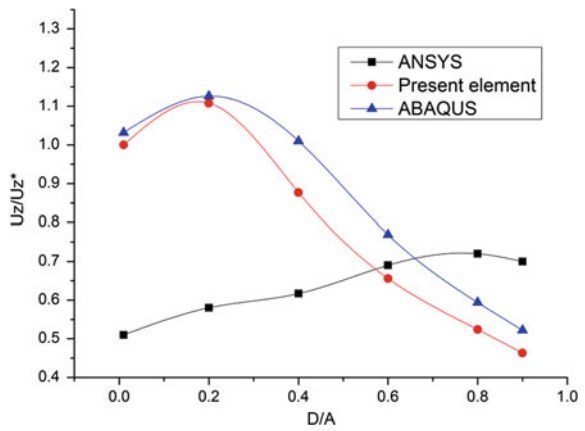
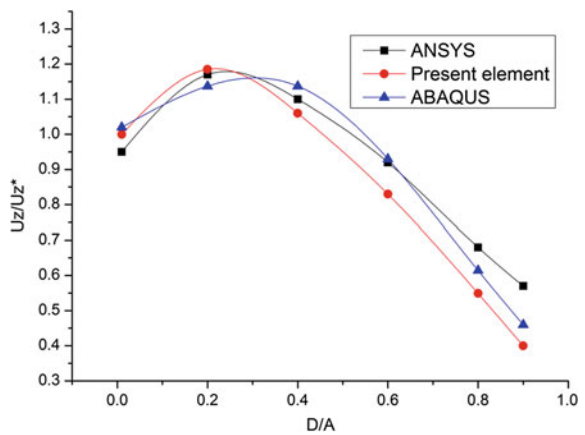


Fig. 8 The effect of D/A report on U_z/U_z^* report in case SCSC



we compare with them (our results are obtained except by the present element and the element *S4R* of Abaqus).

4 Conclusion

Through different examples studied, we conclude that the present element gives very good results for isotropic and composite plates under transverse loading, which prompting us to undertake a parametric study to highlight the effect of D/A ratio on U_z/U_z^* ratio. According to this parametric study, it is noted that the values of U_z/U_z^* depending on the D/A ratio is maximum for the *SSSS* case of boundary conditions and minimum in *CCCC* and when the boundary conditions of the plate are of type *SCSC*, the values of U_z/U_z^* depending on the D/A report take values between the two previous cases.

References

1. Khechai, A., et al.: Finite Element Analysis of Stress Concentrations in Isotropic and Composite Plates with Elliptical Holes, in Design and Modeling of Mechanical Systems-II, pp. 427–436. Springer (2015)
2. Belarbi, M.O., Tati, A., Khechai, A.: Efficient Layerwise Finite Element Model for Multilayer Sandwich Plates Analysis, in Design and Modeling of Mechanical Systems-II, pp. 305–314. Springer (2015)
3. Khechai, A., Tati, A., Guettala, A.: Finite element analysis of stress concentrations and failure criteria in composite plates with circular holes. Front. Mech. Eng. **9**(3), 281–294 (2014)
4. Dhatt, G., Touzot, G.: Une présentation de la méthode des éléments finis 1981: Presses Université Laval
5. Jain, N.K., Mittal, N.: Analysis of stress concentration and deflection in isotropic and orthotropic rectangular plates with central circular hole under transverse static loading. In: 52th International Meet World Academy of Science, Engineering and Technology, Bangalore (2009)
6. Timoshenko, S.P., Gere, J.M.: Theory of elastic stability. McGrawHill-Kogakusha Ltd, Tokyo (1961)

Diffusive Behavior in Polymer-Local Organomodified Clay Matrix

Ali Makhloufi, Djelloul Gueribiz, Djamel Boutassouna,
Frédéric Jacquemin and Mustapha Zaoui

Abstract Composite materials based on organic polymers reinforced by clay nanosheets experience an exceptionally significant expansion due to their characteristics and performance which are continuously in improvement from a day to another. These materials have the ability to be used in various industrial applications. In this context, and as part of a development of natural resources in our region, local clay is treated in different ways and then incorporated, with specific percentages, in a polymer to obtain a polymer-clay matrix. The material obtained is then characterized by different analytical techniques (XRD, FTIR...) to check the nano-polymer/clay structure. Samples of this material are subjected to the moisture tests gain to get an idea of its diffusive behavior and durability in wet environments.

1 Introduction

An intense awareness nowadays has emerged to the development of reinforced nanoscale polymer materials called nanocomposites. This class of materials can be described as an ultrafine dispersion of fillers, having at least one dimension in the nanometer range within a polymer medium. It is the transition from the “micro” to the “nano” that offers to these materials the very superior and possibly unexpected

A. Makhloufi (✉) · D. Boutassouna · M. Zaoui
Faculté de Technologie, Département de génie des procédés,
Université Amar Télidji de Laghouat, Laghouat, Algeria
e-mail: ali.makh1988@gmail.com

D. Gueribiz
Faculté de Technologie, Département de génie mécanique,
Université Amar Télidji de Laghouat, Laghouat, Algeria

F. Jacquemin
IUT de Saint-Nazaire, 58 rue Michel Ange, BP 420, 44606 Saint-Nazaire, France

functional properties compared to conventional composites [1, 2]. The transport properties of small molecules, especially in the presence of impermeable nanofillers and the multiplication of charges/polymer interfaces, can lead to an improvement of the barrier properties by the tortuosity effect associated to the control of the diffusion rate at interfaces [3–6].

Different types of particles of various nature and form can be incorporated into polymer matrices, and these particles are frequently inorganic particles, especially minerals fillers [7, 8]. Natural clays are among the inorganic fillers used, and which are easy to extract further. They represent the perfect competitor for polymer matrix reinforcement [9, 10]. This feature explains the development of composites with organic matrix compared to their counterparts with ceramic and metal matrixes. In this framework, this study has two main objectives: the first is the synthesis and characterization of polymer-clay nanocomposites using local organomodified clay. The second is the study of diffusion behavior and durability of synthesized composites when subjected to moisture loads.

2 Experimental Part

Two kinds of matrices were selected: a thermoplastic matrix (the polystyrene PS commercialized by Arkema with a molecular weight $M_w = 348800$ g/mol), and a Thermosetting matrix polyester resin provided by Polymir company, which has a density of 1.8–2.2 g/cm³ and a viscosity of 300–400 cps, and the styrene content in this matrix is 32–42 %. The raw clay used in this work is local clay from the region of Sidi Makhlouf north of the wilaya of Laghouat. CTAB cetyltrimethylammonium bromide ($M = 364.45$ g/mol) is used in the organophilic modified clay.

2.1 Sodium Clay (Clay-Na) Preparation

The preliminary treatment of the raw clay by sodium homoionisation is not only to eliminate all crystalline phases (quartz, calcite ...), but also to replace all the exchangeable cations of various kinds with identical sodium cations [11, 12]. To obtain sodium homoionic clay (*clay-Na*), 100 g of clay are introduced into a beaker containing a sufficient amount of sodium chloride solution (1 N), the suspension is then stirred for 6 h. This operation is repeated *03 times*, and then the clay undergoes several washing with distilled water to remove excess salt. To pick up the clay particles of size smaller than 2 μm , by a simple calculation based on Stokes law [13].

2.2 Organic Modification of the Clay

In an Erlenmeyer flask, 10 g of arg-Na is placed with 1 L of distilled water and magnetically stirred for 30 min at room temperature. In another Erlenmeyer flask, 20 mmol of cetyltrimethylammonium bromide (CTAB) are dissolved in 100 ml of distilled water using a magnetic stirrer. The two solutions are mixed up vigorously for 1 h with an ultrasound device and stirred for 3 h at 80 °C. After leaving to stand the solution overnight, the precipitate is filtered and washed several times with hot distilled water (80 °C) until disappearance of Br ions detected by an AgNO₃ solution (0.1 M). It is then dried at 60 °C for 24 h. The organomodified clay OM-clay is ground in a mortar and particle size less than 2 μm were collected for the preparation of nanocomposites [14, 15].

2.3 Elaboration of Polymer-Clay Nanocomposite

2.3.1 Thermoplastic Matrix (Polystyrene/Organomodified Clay)

As Polystyrene/organomodified clay nanocomposites were prepared by means of solvent process, using chloroform as solvent. In a volumetric flask, 10 g of PS were dissolved in 100 ml of chloroform and mixed with the aid of a magnetic stirrer for 4 days at room temperature. In another volumetric flask, the calculated amount of the organophilic clay (3, 5 and 10 %) is well dispersed in 60 ml of chloroform using a magnetic stirrer for 4 days at 60 °C. After a swelling for 4 days, the suspension and the solution are mixed by means of ultrasonic bath for 2 h. Finally the mixtures were dried at room temperature for 5 days to let evaporate the solvent and then placed in a vacuum oven for 24 h at 60 °C [16, 17].

The following flowchart (Fig. 1) summarized the method of preparation of the nanocomposite polystyrene/organomodified clay.

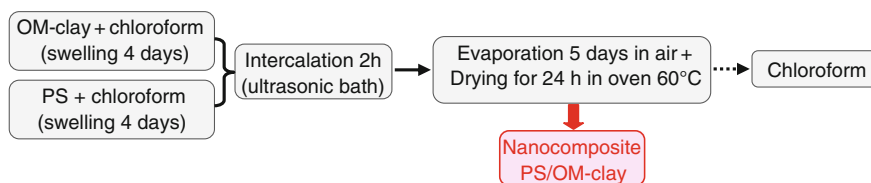


Fig. 1 PS/OM-clay system implementation procedure by the solvent process

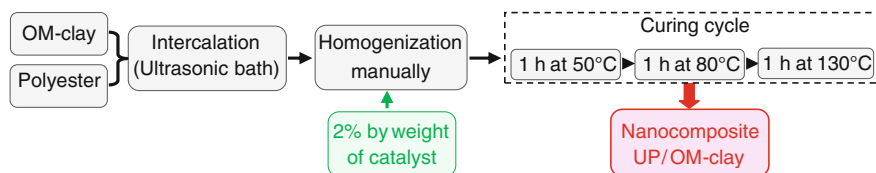


Fig. 2 UP/OM-clay system implementation procedure by the solvent process

2.3.2 Thermosetting Matrix (Polyester/Organomodified Clay)

Sufficient amounts of polyester resin *UP* and different amounts (3, 5 and 10 % *in weight*) of selected clays (previously dried in a vacuum oven) were added up. The mixture was stirred in an ultrasonic bath at room temperature for the time necessary to obtain a homogeneous dispersion. Next, 2 % in weight catalyst were added and the mixture was homogenized manually, and thereafter, the plates were prepared by pouring the mixture into a mold.

The cure cycle was performed in an oven, first for 1 h at 50 °C to remove trapped air, then for 1 h at 80 °C to produce the crosslinking, and finally for 1 h at 130 °C to ensure complete conversion [18]. The full procedure of the synthesis of the polyester-clay films is illustrated in the diagram below (Fig. 2).

2.4 Characterization Methods

2.4.1 X-ray Diffractometry

The *XRD* is a method widely used when studying clays to determine their structure as well as their basal spacing. However, in our work, the analysis by *XRD* was carried out only to determine the nature of the clay embedded in the composites. We used for all the *XRD* characterizations a PHILIPS brand PANalytical X'PertPRO diffractometer. The X-ray source is a ceramic tube equipped with a copper anode supplied with a 45 kV voltage with a current of 40 mA. The wavelength used is 1.54 Å.

2.4.2 Fourier-Transform Infrared Spectrophotometry

Infrared analyses were performed using a Fourier-transform spectrophotometer brand Perkin Elmer 1720-X", on a range of 500–4000 cm^{-1} with a resolution of 2 cm^{-1} . The samples were conditioned in the form of a dispersion in KBr tablet (1/200 in weight). The study of water diffusion in composites has a great

importance, essentially if we consider that in certain cases, the swelling has a major effect on these composites and their properties.

In this study, we will try to investigate the kinetics of diffusion of distilled water in our nanocomposites and determine the water diffusion coefficient in the developed nanocomposites. Tests of water diffusion were carried out by immersing the sample in distilled water at room temperature. All samples were predried under vacuum till a constant weight. The samples were then pulled out from the water, carefully dried with a tissue paper and weighed at predetermined lapses of times. The amount diffused each time is calculated by:

$$M_t (\%) = \frac{M_t - M_0}{M_0} \quad (1)$$

The effective diffusion coefficient (D_{eff}) is obtained according to the following equation [6, 18]:

$$D_{eff} = \pi \left(\frac{h}{4M_{max}} \right)^2 \left(\frac{dM}{d\sqrt{t}} \right)^2 \quad (2)$$

where

$\left(\frac{dM}{d\sqrt{t}} \right)$ is the slope of the initial part (linear) of the curve $M_t (\%)$ with respect to $t^{1/2}$. M_{max} is the maximum amount of adsorbed water, h is the sample thickness.

3 Results and Discussion

3.1 Organophilic Clay

3.1.1 XRD Analysis

The diffraction curves for the raw clay, sodium clay and the organomodified clays are shown in Fig. 3. Sodium clay diffractogram confirms an excellent purification of the clay with a loss of some lines characteristic of the crystalline phases (in the form of impurities). We also note that the interlayer spacing has decreased (9.97 Å in the raw clay to 8.51 Å in the Sodium clay). This decline is due to the removal of Ca^{2+} , Mg^{2+} et K^+ cations replaced by smaller atomic radius Na^+ . Organophilic clay Xray diffractogram shows 2θ angle shifting that passes from 10.38° to 5.48° indicating this way an increase of the interlayer spacing from 8.51 Å for the Sodium clay to 16.10 Å for the organophilic clay, confirming the intercalation of the alkylammonium ions into the space originally occupied by sodium ions (Fig. 4).

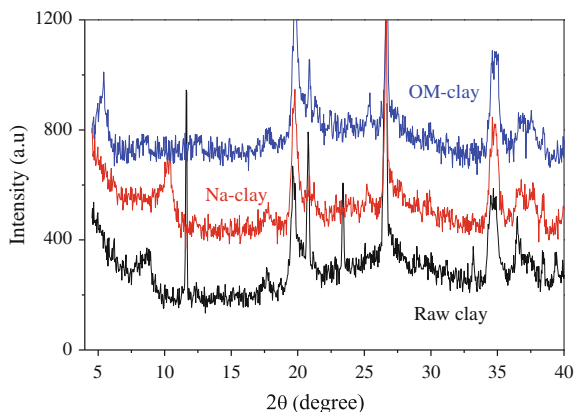


Fig. 3 X-ray diffractograms of raw, sodium and organomodified clays

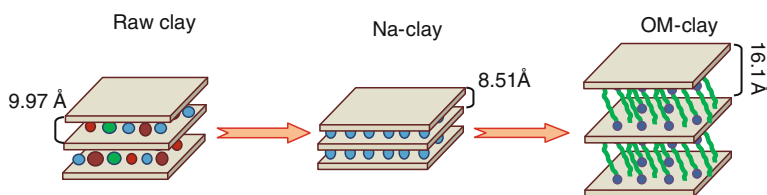


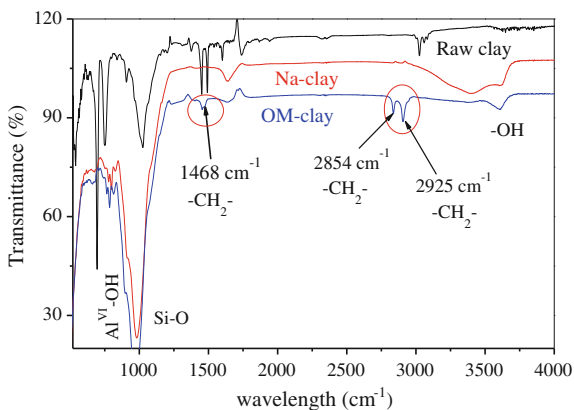
Fig. 4 Overview of the alkyl chains disposition in the organophilic clay

3.1.2 FTIR Analysis

Results of the clays *FTIR* analysis (raw, sodium, organophilic) are presented in Fig. 5.

On the infrared spectrum of sodium clay, we note a disappearance of some bands characterizing crystalline phases (impurities), as an example bands such as 915, 798

Fig. 5 IR spectra of raw, sodium and organomodified clays



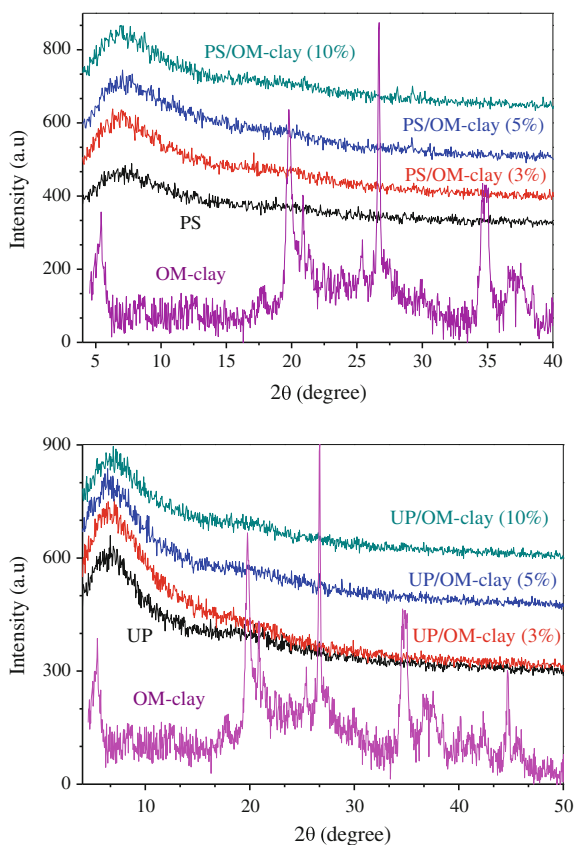
and 694 cm^{-1} characterizing quartz and 1394 cm^{-1} characterizing calcite CaCO_3 . This spectrum actually asserts a good purification of the clay. The review of the organophilic clay spectrum revealed new absorption peaks located at 2925 and 2854 cm^{-1} attributed to valence vibrations of CH_2 groups, the band located at 1468 cm^{-1} is related to the deformation vibration of the same group, and this indicates that the organic group is present within the clay.

3.2 Polymer-Clay Nanocomposites

3.2.1 XRD Analysis

The results of the characterization by XRD of the polystyrene-organomodified clay and the polyester-organomodified clay nanocomposites are shown in Fig. 6. On the

Fig. 6 X-ray diffractograms of: organomodified clay, nanocomposites PS/OM-clay and nanocomposites UP/OM-clay for different fillers rates

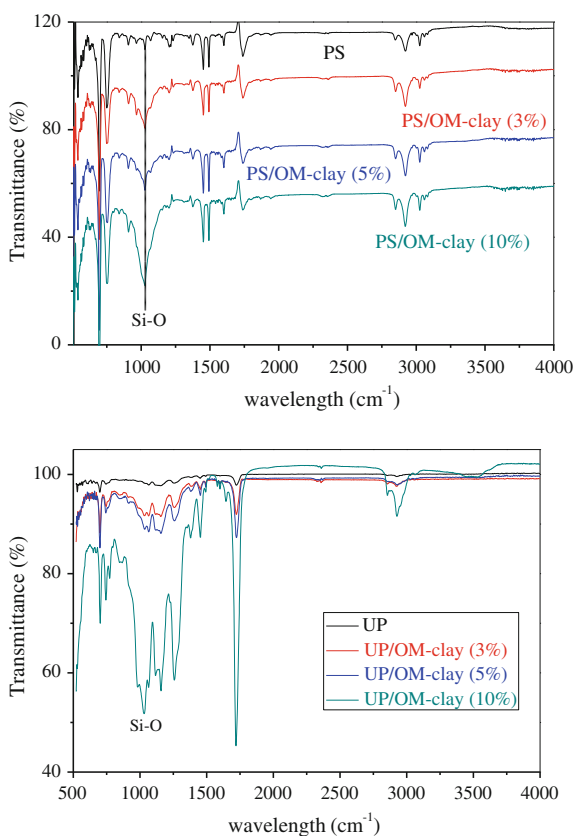


X-ray diffractograms of nanocomposites *PS/OM-clay* and nanocomposites *UP/OM-clay*, we notice two wide peaks corresponding to the polymer but no peak corresponding to the clay appears, and thus we figure out that an exfoliation of the clay happened in the polymer matrix.

3.2.2 FTIR Analysis

The obtained results are represented in Fig. 7. IR spectra of nanocomposites *PS/OM-clay* and *UP/OM-clay* (Fig. 7) show the appearance of a band at 1028 cm^{-1} corresponding to the elongation of the Si-O bond, whose intensity increases with the fillers rate, and which proves the existence of the clay within the polymer matrix.

Fig. 7 IR spectra of nanocomposites *PS/OM-clay* and nanocomposites *UP/OM-clay* at different fillers levels



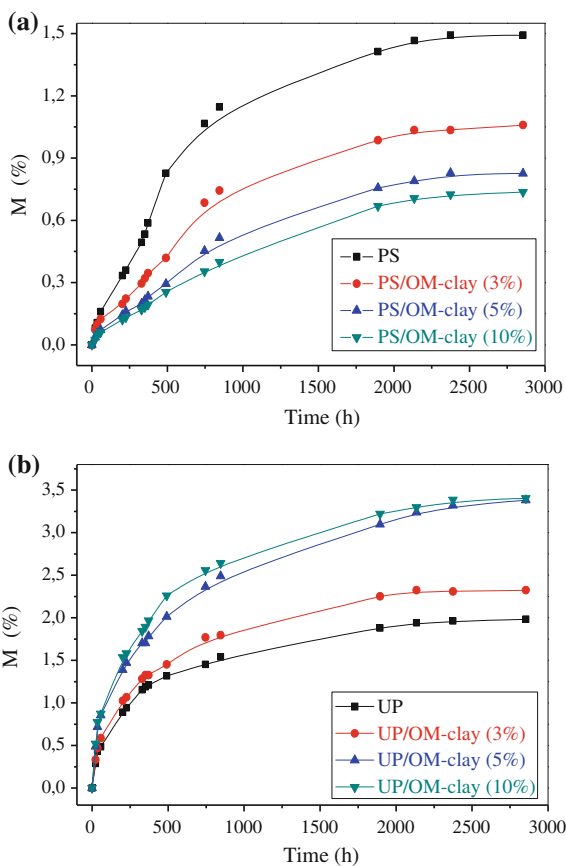
3.3 Diffusion in Nanocomposites

3.3.1 Kinetic Study

Figure 8 presents the kinetics of water diffusion in nanocomposites (*polystyrene-OM clay*, *polyester-OM clay*) at room temperature. The eight diffusion kinetics curves exhibit the same behavior. However one can notice that the curves can be divided into two parts: a first part that represents a significant and rapid increase in the diffusion rate over time, and this part is characterized by an increase in mass and volume (diameter and thickness) of the sample, and as time elapses the diffusion of water molecules within the network takes place. These molecules will try to balance the concentration within the network as well as the on the outside.

After a certain time the swelling ratio takes a maximum value that does not change over time, this is the second part that characterizes the appearance of these swelling curves. At the sample stage, we note that the mass and the volume of the

Fig. 8 Kinetics of diffusion of water in the nanocomposites:
a UP/OM-clay,
b PS/OM-clay



network remains the same: we can say that there is a manifestation of a thermodynamic equilibrium. This equilibrium is at a molecular level due to the elasticity of the macromolecular chains which, once reached the maximum of their stretching, they will oppose to the penetration of water within the network. This phenomenon may be influenced by the chain length in the case of linear polymers or the length of the chain between crosslinking points. Accordingly the influence of the rate of the network crosslinking is very important, and very small amounts may change the network mechanical properties.

3.3.2 Diffusion Coefficient

Figure 9 presents the evolution of the mass ratio M_t (%) with respect to the time squared root (in $s^{1/2}$) for the diffusion test of water in the two nanocomposites

Fig. 9 Diffusion curve of water in the two nanocomposites:
a UP/OM-clay,
b PS/OM-clay

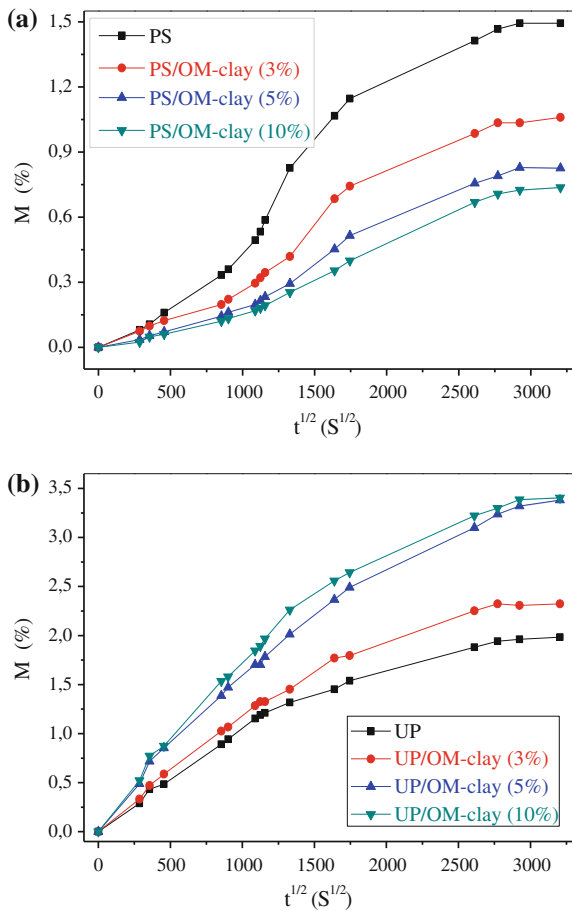


Table 1 Water amount M_{∞} (%) at equilibrium and the effective diffusion coefficient (D_{eff}) for the nanocomposites PS/OM-clay and UP/OM-clay immersed in water with respect to the content in clay

Content in clay (%)	Polystyrene/OM-clay		Polyester/OM-clay	
	M_{∞} (%)	D_{eff} ($\times 10^{-8}$ mm ² /s)	M_{∞} (%)	D_{eff} ($\times 10^{-7}$ mm ² /s)
0	1.493 \pm 0.00060	1.147 \pm 0.459	1.982 \pm 0.00066	11.791 \pm 1.395
3.0	1.059 \pm 0.00051	1.312 \pm 0.515	2.324 \pm 0.00069	8.096 \pm 1.018
5.0	0.826 \pm 0.00045	1.600 \pm 0.640	3.382 \pm 0.00077	5.933 \pm 0.853
10.0	0.736 \pm 0.00042	1.846 \pm 0.738	3.403 \pm 0.00077	4.525 \pm 0.758

(*polystyrene/OM-clay*, *polyester/OM-clay*). Table 1 presents the effect of the clay addition on the water amount absorbed by the nanocomposites and on the diffusion coefficients.

Values of Table 1 show that the addition of clay reduces water adsorption capacity in the nanocomposites *PS/organomodified clay* (1.4933 \rightarrow 0.7367 %) and increases the value of the diffusion coefficient ($1.147 \times 10^{-8} \rightarrow 1.312 \times 10^{-8}$ mm²/s). This is mainly due to the intercalation of the polymer in the clay galleries via hydrogen bridges that are formed between the polymer hydroxyl groups and the OH groups of the clay. As a result, the number of sites able to attract water molecules will decrease.

In the case of polyester-clay nanocomposite, the reverse is quite noted (Table 1), and many authors have reported that the diffusion of water in the polyester-clay nanocomposites is primarily influenced by two factors:

- The first is based on the fact that the clay body is itself rich in water, and thus absorbs more water than almost all polymers used as matrix, which leads to an increase of the equilibrium water content as a function of the clay amount.
- The other factor is that the clay layers dispersed in nanometer scale within the matrix can reduce the mean free path of water molecules to pass through the nanocomposite network in comparison to the pure matrix, which leads to lower absorption of water.

Thus, it is difficult to predict the overall effect of the nano incorporation of clays on the behavior towards the water absorption by the polymer matrixes. Although some studies have shown that moisture and water absorption can be reduced by the incorporation of nano-clays in thermosetting matrixes, the consequences of the modification of the clay on the water absorption and the mechanisms that govern the diffusion processes have not been fully clarified. As an example, Ollier et al. [18] explained that the ability of compounds to absorb water is low and increases with the content in bentonite. This increase of water absorption is due to the ability of the bentonite to maintain water molecules.

4 Conclusion

The aim of this work was the development and characterization of polymer-clay nanocomposites and the study of diffusion in these nanocomposites. We first carried out the modification of the clay by introduction of an alkyl ammonium groups. This modification has two interests:

- Improve the affinity of the clay with regard to the polymer as the synthesis of the nanocomposites takes place in an organic medium.
- Increase the basal spacing of the clay to permit insertion of the polymer between its layers.

FTIR analysis showed that there was definitely a change in the clay, with the appearance of new absorption bands related to the functional groups of the intercalation agent.

The *XRD* analysis revealed an increase in the lattice spacing which was 8.51 Å for the sodium clay and reached 16.1 Å for the organophilic clay.

These two analysis results let to state that the modifying of the clay was thoroughly successful. Nanocomposites obtained were characterized by *XRD* and *FTIR*:

1. The *XRD* revealed no clay diffraction peak in the two matrixes, which is a sign of an exfoliated structure, and that the stacking of the sheets is no more performed on a regular basis; consequently, the interlayer distance may become too large for the limits of the device.
2. The *FTIR* showed that there is indeed clay in the matrix composites by appearance of the absorption characteristics bands of the clay. The intensity of the bands increases with the fillers rate.

The study of the diffusion of water in polystyrene/organophilic clay nanocomposite showed that the addition of amounts of clay reduces the water adsorption capacity and increase the value of the diffusion coefficient. We note the opposite in the case of polyester-clay nanocomposite. These two results are mainly related to the insertion of the polymer in the clay galleries.

References

1. Yehia, A.A., et al.: *J. Mater. Des.* **33**, 11–19 (2012)
2. Kredatusová, J., Brožek, J.: *J. Appl. Clay Sci.* **62–63**, 94–100 (2012)
3. Kim, J.K., et al.: *J. Compos. Technol.* **65**, 805–813 (2005)
4. Almari, H.: *J. Mater. Des.* **42**, 214–222 (2012)
5. Becker, O., et al.: *J. Eur. Polymer* **40**, 187–195 (2004)
6. Kaushik, A., Ahuja, D., Salwani, V.: *J. Compos. Part A* **42**, 1534–1541 (2011)
7. Utracki, L.A.: *J. Nanosci. Nanotechnol.* **8**, 1582–1596 (2008)
8. Lai, S.Q., et al.: *J. Macromol. Mater. Eng.* **290**(3), 195–201 (2005)
9. LeBaron, P.C., Wang, Z., Pinnavaia, T.J.: *J. Appl. Clay Sci.* **15**, 11–29 (1999)
10. Thostenson, E.T., Li, C., Chou, T.W.: *J. Sci. Technol* **65**, 419–516 (2005)

11. Bouras, O.: Thèse de doctorat. L'université de Limoges, France (2003)
12. Tan, W., Zhang, Y., Szeto, Y.S., Liao, L.: *J. Compos. Sci. Technol.* **68**, 2917–2921 (2008)
13. Ghanshyam, V.J., Bhavesh, D.K., Hasmukh, A.P., Bajaj, H., Raksh, V.J.: *Int. J. Pharm.* **45**, 248–253 (2009)
14. Zenasni, M.A., Meroufel, B., Benfarhi, S., Chehimi, M., Molina, S., George, B., Ragoubi, M., Merlin, A.: *Int. J. Chem.* **03**, 2306–6415 (2013)
15. El-Shafie, M., Ibrahim, I.M., Abd El Rahman, A.M.M.: *Egypt. J. Petrol.* **21**, 149–154 (2012)
16. Ngo, T.T.V.: Thèse de doctorat, l'institut national des sciences appliquées de Lyon, France (2007)
17. Benson, S.D., Moore, R.B.: *J. Polymer* **51**, 5462–5472 (2010)
18. Ollier, R., Rodriguez, E., Alvarez, V.: *J. Compos. Part A* **48**, 137–143 (2013)

Effect of Grain Size of Nano Composite on Raman and Magnetic Proprieties

Abderrahmane Younes, Nacer Eddine Bacha, Mourad Zergoug, Mokrane Gousmine, Heider Dehdouh and Amirouche Bouamer

Abstract Based Iron–cobalt alloys exhibit particularly interesting Raman and magnetic properties, with high Curie temperatures, the highest saturation magnetizations, high permeability, and low losses and is relatively strong and partial oxidation of Fe and Co. The cost of these alloys has confined them, since their discovery by Elmen in 1929, to applications where the volume is small and high magnetic performances are critical. Sintering is the procedure of formation and compaction of a material. We have prepared the nano crystalline alloy by the mechanical milling process in a high energy planetary ball-mill PM400. Morphological, micro-structural, magnetic characterizations of the powders milled several times were investigated by scanning electron microscopy, X-ray diffraction, vibrating manometers sample and Raman spectroscopy. The coercivity value increase during millingtime from 0.018 to 185.9 Oe and saturation magnetization value from 42.7 to 51.1 emu/g, respectively.

A. Younes (✉) · M. Zergoug · M. Gousmine · H. Dehdouh · A. Bouamer
Research Center in Industrial Technologies, CRTI, P.O. Box 64,
16014 Cheraga, Algiers, Algeria
e-mail: a.younes@csc.dz

M. Zergoug
e-mail: m.zergoug@csc.dz

M. Gousmine
e-mail: m.gousmine@csc.dz

A. Bouamer
e-mail: a.bouamer@csc.dz

A. Younes · N.E. Bacha
Laboratory of Surface Treatment & Materials,
University of Saad Dahleb, Ouled Yaïch, Blida, Algeria
e-mail: younesabdo11@gmail.com

H. Dehdouh
Ceramics laboratory, University of frères mentouri, Ain El-Bey
Road (25000), Constantine, Algeria
e-mail: h.dehdouh@csc.dz

1 Introduction

Iron Cobalt alloy are significant soft magnetic materials that have been usually used in industry. Compared to polycrystalline, the nano-structured materials have showed superior magnetic properties, such as higher permeability and lower coercivity due to the single domain configuration [1, 2]. However, magnetic properties of nano-materials are affected by their microstructure like the grain size, internal strain and crystal structure [3–5]. The microstructure of nano-structured materials is an important factor for enhancement of magnetic properties. Mechanical Alloying (*MA*) is a method with an advantage that it can be easily operated and produces large amounts of nano-structured powders in small time [6].

In the present work, the effect of microstructure in the magnetic and optical properties was studied by different techniques. The FeCo mixture was prepared by mechanical alloying (*MA*), the microstructure of mixture was analyzed by a scanning electron microscope (*SEM*) and X-ray diffraction (*XRD*), the magnetic and optical properties were characterized by vibrating sample magnetometer (*VSM*) and Raman analysis respectively.

2 Results and Discussion

High purity (>99 %) iron and cobalt obtained were used as unrefined materials. They were independently mixed and weighted to obtain the preferred composition of Iron Cobalt (wt%). The mechanical alloying process was performed in planetary high-energy ball mill pm400. The powders were sealed in cylindrical vial with stainless steel balls. The ball-to-powder weight ratio was 15:1, and the vial rotation speed was 300 rpm. The milling time was ranged from 0 to 40 h to investigate its effect on the properties of the obtained powders. To avoid excessive heating during milling, the process of milling was followed with 15 min of pause every 30 min of

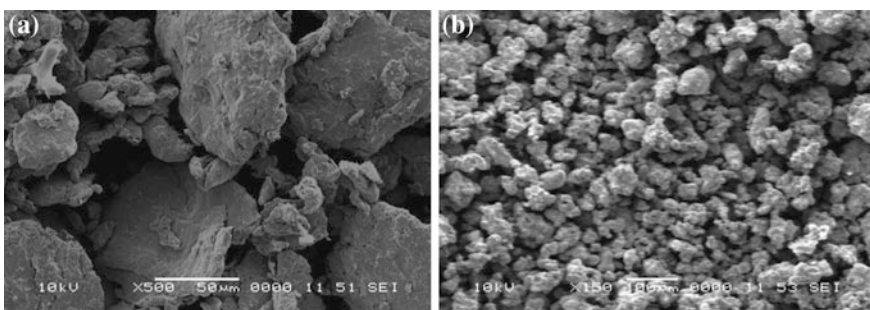


Fig. 1 SEM micrographs of FeCo powder for various milling times: **a** 5 h, **b** 40 h

work. There are three stages of the mechanical alloying which are the initial, the intermediate and the final stage.

Figure 1 presents the morphology of the powder at different milling times. In the first time of milling, the particles of the FeCo powder are flattened by the compression force due to the collision of the balls. Simultaneously, different particle sizes were observed. The process of welding and fracture is significant and the formation of lamellar structures is obtained by plastic deformation. After longer time of milling a considerable refinement and a decrease in the size of particles are noticed at this time. The shape and particles size are more homogeneous compared to the first time of milling.

2.1 Raman Analysis

The analyses with μ -Raman spectroscopy carried out on our samples, with $\lambda = 532$ nm as excitation source and optical excitation of 10 mW. All these peaks were obtained by using an objective x50. By increasing the volume of analysis from x10, the spectra

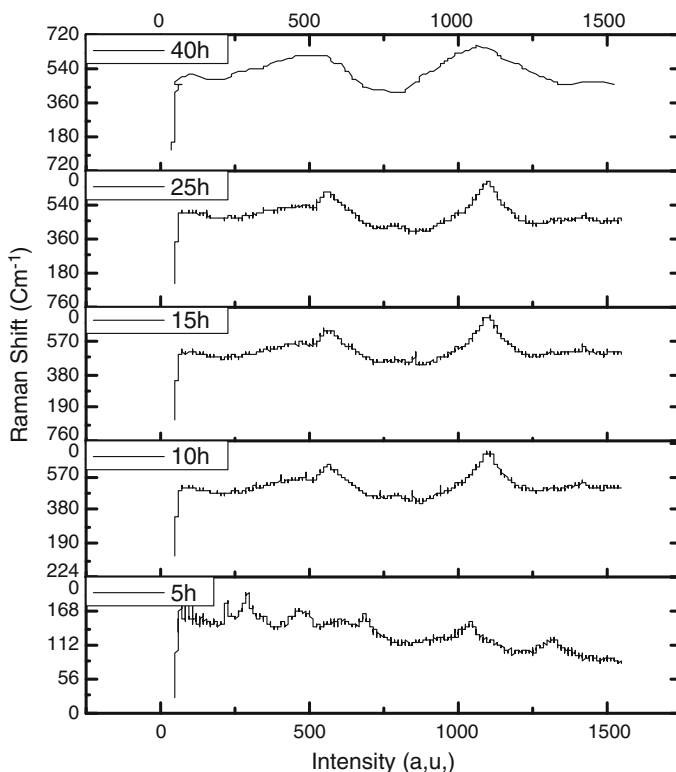


Fig. 2 μ -Raman spectrum of the FeCo alloy at different time of milling (5, 10, 15, 25 and 40 h)

confirm the observations of different modes. Figure 2 shows the representative Raman spectrum of Fe–Co samples with different milling time from 5 to 40 h (5, 10, 15, 25 and 40 h). The activate modes iron oxides appears at around 226 and 296 cm^{-1} for $\alpha\text{-Fe}_2\text{O}_3$, at around 568 cm^{-1} of Fe_3O_4 and at around 686 of CoFe_2O_4 . These results are already discussed by the literature [7, 8]. The peak situated at around 1330 cm^{-1} of D band [9, 10], the presence of this lather confirms the incorporation of Cobalt from the bath of growth during making of our alloy by milling, we notice that the formation starting from 10 h of milling, wish confirm the formation of Fe–Co nano composite.

2.2 Structure Analysis

The kinetics of formation and evolution of the crystallites size, internal strain and the lattice parameters of the Iron Cobalt powder during the milling process have been monitored using the X-ray technique.

The average of crystallites size and the internal strain is determined by the method of Hall Williamson (Fig. 3). After 40 h of milling, the crystallites size decreased until 15 nm while the internal strain increased. Figure 4 shows the evolution of the lattice parameter of the Iron Cobalt alloy as a function of milling time. A rapid increase in the lattice parameter up to 12 h of milling has been noticed and then remained constant up to 40 h. This behavior is explained in the first stage, by the diffusion of cobalt in the matrix of the iron and/or the deformations induced during milling. The weakening in the second stage is explained by a dynamic equilibrium between the milling effects and the material restoration.

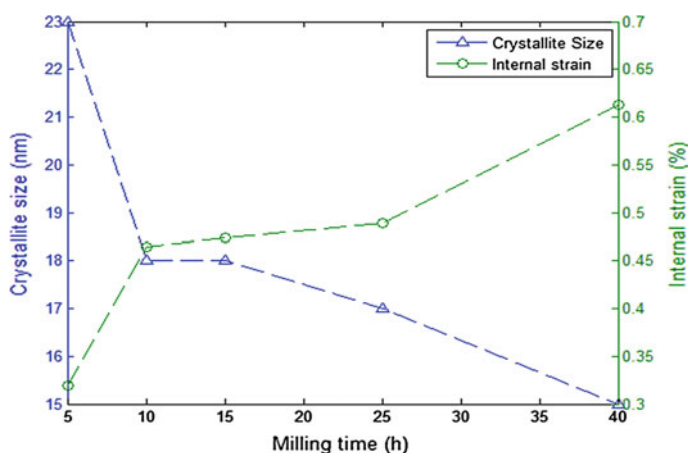


Fig. 3 The crystallite size and internal strain of the FeCo powder during milling time

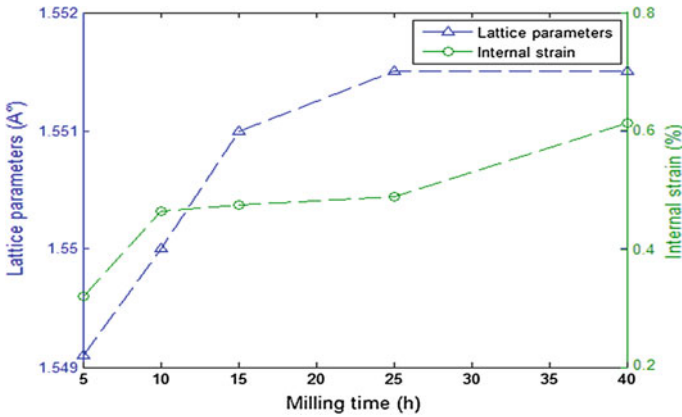


Fig. 4 The lattice parameter and internal strain of the FeCo powder during milling time

2.3 Magnetic Response

The magnetic property is an important factor for identification of soft magnetic behavior. High coercivity is due to the internal strain, pore, impurity, and defect which are introduced during milling. Figure 5 shows the magnetization curves of FeCo alloy mixture, and the related magnetic properties such as saturation magnetization (M_S), coercivity (H_C) and remanent magnetization (M_r) can be obtained.

The inset shows the corresponding magnification of hysteresis loops near the origin. It shows the varying trend in saturation magnetization (M_S), coercivity (H_C) and remanent magnetization (M_r), etc.

The saturation magnetization is generally regarded as independent of the microstructure and strongly depends on the chemical composition. M_S which are the other important parameter from a magnetic point of view are increases when milling time is increased. As shown in Fig. 6, the M_S reaches its maximum value at the milling time of 5 h, and then decreases with increasing milling time after 10 h. The H_c before sintering shows a general increase tendency with milling, in contrast with M_S . This could be certainly attributed to the reduction in magneto-crystalline anisotropy due to the grain refinement, which leads to an easier rotation of the domain walls [11].

The grain refinement diminishes the magneto-crystalline anisotropy that is due to the averaging effect of magnetization over randomly oriented nano-size grains. Such magnetic behavior is similar to the dependence of mechanical strength on the grain size. This can be understood in terms of analogous effects of the grain size on the motion of domain walls and dislocations, respectively, under magnetic and stress fields [12]. The saturation magnetization (M_S) is strongly depending on the

chemical composition of the local environment of atoms and their electronic structures. The MS increases slightly from at the early stage up to 10 h. This trend is attributed to the formation of solid solution of α -Fe Co and charge transferring between Fe, and Co atoms [13].

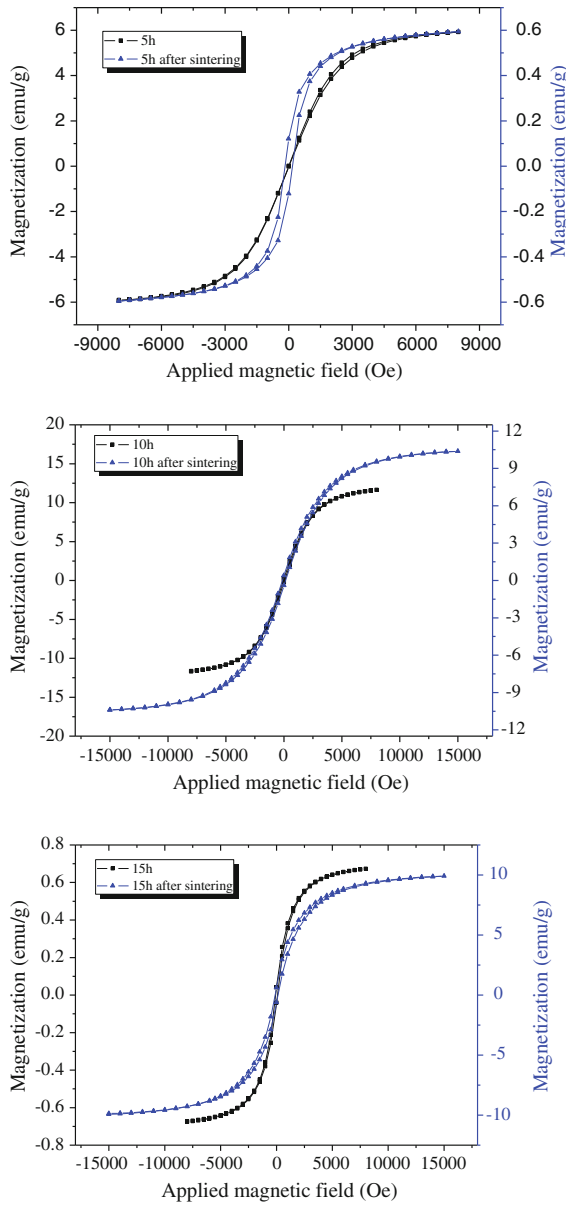


Fig. 5 Hysteresis loops of Fe–Co powders milled for different times before and after sintering

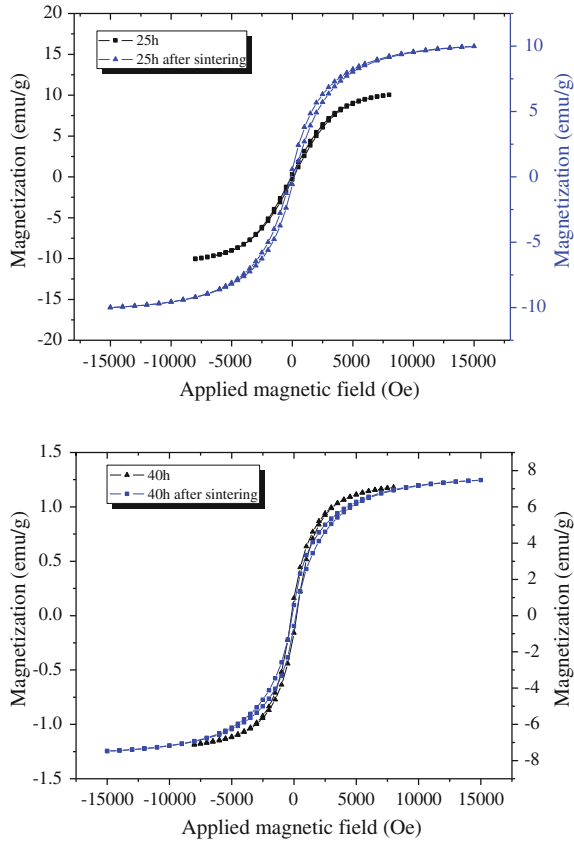


Fig. 5 (continued)

Fig. 6 The variation of the M_s with milling time before and after sintering

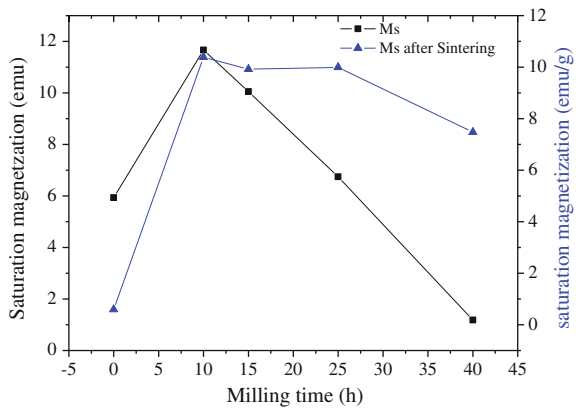


Fig. 7 The variation of the M_r/M_s with milling time before and after sintering

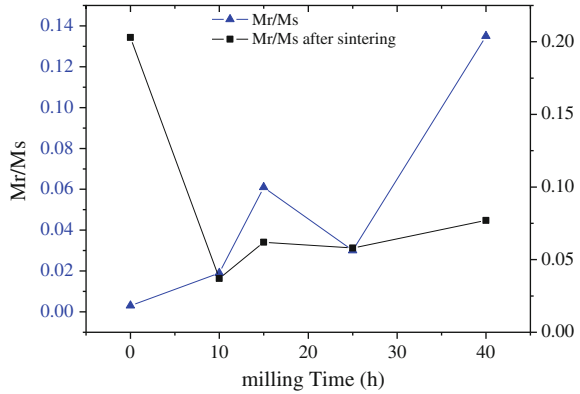
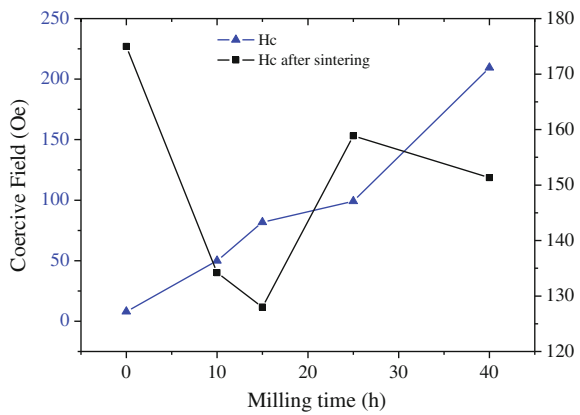


Fig. 8 The variation of the H_c with milling time before and after sintering



The M_r/M_s show increased zigzag tendencies with the increased milling time before sintering see Fig. 7. The value of coercivity before sintering increases during the milling from 0.018 to 185.9 Oe, but after the sintering, we have one decrease until 15 h then there is an increase until 40 h (Fig. 8).

3 Conclusion

The structural, optical and magnetic parameters of magnetic nanostructure materials elaborated by mechanical alloying could be determined using non destructive testing methods. The microstructural factors such as the grain size change the magnetic properties. The coercivity value increase during milling from 0.018 to 185.9 Oe and saturation magnetization value from 42.7 to 51.1 emu/g, respectively, the coercivity of the FeCo alloy strongly depends on the microstructure. The M_s reaches its maximum value at the milling time of 10 h and then decreases with

increasing milling time after 10 h. The H_c before sintering shows a general increase tendency with milling, in contrast with M_s . The saturation magnetization (M_s) is strongly depending on the chemical composition of the local environment of atoms and their electronic structures. The process of sintering and milling influences the magnetic property of the FeCo alloy.

Characterization by Raman technique confirms the incorporation of Co starting from the bath of growth during the formation of FeCo alloy during milling time. Starting from 10 h of milling, the widening of peak at 1338 cm^{-1} for 10, 15, 25 and 40 h samples is a result of the refinement of the particle that reaches the nanoscale.

References

1. Lesile-Pelecky, D.L., Rieke, R.D.: Magnetic properties of nanostructured materials. *Chem. Mater.* **8**(8), 1770–1783 (1996)
2. Herzer, G.: Nanocrystalline soft magnetic materials. *J. Magn. Magn. Mater.* **157**(158), 133–136 (1996)
3. Gleiter, H.: Nanostructured materials: state of the art and perspective. *Nanostruct. Mater.* **6**, 3–14 (1995)
4. Turgut, Z., Scott, J.H.M.Q., Huang Majetich, S.A., Mchenry, M.E.: Magnetic properties and ordering in C-coated $\text{Fe}_x\text{Co}_{1-x}$ alloy nanocrystals. *J. Appl. Phys.* **83**(11), 6468–6470 (1998)
5. Yu, R.H., Basu, S., Zhang, Y., Xiao, J.Q.: Magnetic domains and coercivity in FeCo soft magnetic alloys. *J. Appl. Phys.* **85**(8), 6034–6036 (2000)
6. Fecht, H.J.: Nanostructure formation by mechanical attrition. *Nanostruct. Mater.* **6**, 33–42 (1995)
7. Da Silva, S.W., Melo, T.F.O., Soler, M.A.G., Lima, E.C.D., Da Silva, M.F., Morais, P.C.: Stability of Citrate-Coated Magnetite and Cobalt–Ferrite Nanoparticles Under Laser Irradiation: A Raman Spectroscopy Investigation. *IEEE transactions on magnetics.* **39**(5), 2645–2647 (2003)
8. Kumar, H., Ghosh, S., Srivastava, P., Kabiraj, D., Avasthi, D.K., Olivi, L., Aquilanti, G.: Stabilization of FeCo alloy phase in FeCo–SiO₂ nanocomposites. *Adv. Mat. Lett.* **4**(6), 390–397 (2013)
9. Yamada, M., Okumura, S., Takahashi, K.: Synthesis and Film Formation of Magnetic FeCo Nanoparticles with Graphitic Carbon Shells. *J. Phys. Chem. Lett.* <http://www.sciencedirect.com/science/journal/00086223/77/supp/C> **1**, 2042–2045 (2010)
10. Holodelshikov, E., Perelshtein, I., Gedanken, A.: Synthesis of Air Stable FeCo/C Alloy Nanoparticles by Decomposing a Mixture of the Corresponding Metal–Acetyl Acetonates under Their Autogenic Pressure. *Inorg. Chem.* **50**, 1288–1294 (2011)
11. O’Handley R.C.: *Modern Magnetic Materials (Principles and Applications)*, p. 367. Wiley-Interscience (2000)
12. Bahrami, A., Madaah Hosseini, H.R.: Preparation of nanocrystalline Fe–Si–Ni soft magnetic powders by mechanical alloying. *Mater. Sci. Eng.* **B123**, 74 (2005)
13. Karimi, L., Shokrollahi, H.: *J. Alloys Compd.* **509**, 6571–6577 (2011)

Finite Element Based on Layerwise Approach for Static and Dynamic Analysis of Multi-layered Sandwich Plates

Mohamed-Ouejdi Belarbi, Abdelouahab Tati, Houdayfa Ounis
and Abdelhak Khechai

Abstract The present work deals with the development of a new layerwise quadrilateral finite element model for static and free vibration analyses of multi-layered sandwich plates. Unlike any other layerwise models, the number of variables is independent of the number of layers. The proposed model assumes higher-order displacement field for the core and first-order displacement field for the face sheets. Compatibility conditions are imposed at face sheets/core interfaces to satisfy the interlaminar displacement continuity. The performance of the proposed formulation is demonstrated by comparing the authors' results with available analytical solutions and finite element models.

1 Introduction

Sandwich structures attract the increasing attention in the various engineering disciplines such as civil, automobile, marine and aerospace applications due to their low weight, high stiffness and high strength properties. Despite the many advantages of sandwich structures, their behavior becomes very complex due to the large variation of rigidity and material properties between the core and the face sheets. Different plate theories have been proposed to study the behavior of sandwich

M.-O. Belarbi (✉) · A. Tati · H. Ounis
Laboratoire de Génie Énergétique et Matériaux, LGEM, Université de Biskra,
B.P. 145, R.P. 07000 Biskra, Algeria
e-mail: belarbi.m.w@gmail.com

A. Tati
e-mail: abdelmati@yahoo.fr

H. Ounis
e-mail: houdayfa.ounis@gmail.com

A. Khechai
Laboratoire de Génie Civil, LRG, Université de Biskra,
B.P. 145, R.P. 07000 Biskra, Algeria
e-mail: abdelhak_khechai@hotmail.fr

structures. These plate theories may be grouped as equivalent single layer (*ESL*) approach (where all the layers are referred to the same variables) and layerwise (*LW*) approach. The *ESL* approach can be divided into three major theories, namely, the:

1. classical laminated plate theory (*CLPT*);
2. first order shear deformation theory (*FSDT*);
3. higher order shear deformation theories (*HSDT*).

However, *ESL* approach fail to capture precise the local behavior of sandwich structures. This drawback in *ESL* was circumvented by the layerwise theories in which the displacements are assumed at the mid surface of each laminate and maintaining the continuity of the displacements at the layer interface [1].

In the finite elements (*FE*) development, many researchers have adopted the *LW* approach for the sake of a good description of sandwich structures. On this topic, we can distinguish the work of Oskooei and Hansen [2] and Nabarrete et al. [3], where a *3D* layerwise *FE* model is developed for static and free vibration analysis, respectively, of sandwich plates. They used the *FSDT* to model the face sheets and the *HSDT* was adopted to model the core. Ramtekkar et al. [4] presented *3D*, mixed, 18-node *FE* model (assuming 6 degrees of freedom (*DOF*) per node) for an accurate evaluation of transverse stresses in laminated sandwich. The continuity of displacements as well as the transverse stresses is satisfied. In addition, Linke et al. [5] developed a layerwise *FE* formulation for static and stability analysis of sandwich plates. Later on, a 45-nodes triangular element having 7-*DOF* per node was developed by Ramesh et al. [6] for accurate prediction of interlaminar stresses in laminated composite plates. Elmalich and Rabinovitch [7] have undertaken an analysis of dynamics on sandwich plates, using a four-node rectangular element. More recently, Pandey and Pradyumna [1] presented a new layerwise plate formulation based on higher-order *FE* model for static and free vibration analyses of laminated composite and sandwich plates.

The goal of this work is to propose a new *2D* layerwise *FE* formulation for static and free vibration analyses of multi-layered sandwich plates. Unlike layerwise models, the number of variables in the present model is independent of the number of layers. The results obtained from this investigation will be useful for a more understanding of the bending and free vibration behavior of sandwich laminates plates.

2 Mathematical Formulation

Sandwich plate is a structure composed of three principal layers as shown in Fig. 1, two face sheets (top-bottom) of thicknesses (h_t , h_b) respectively, and a central layer named core of thickness (h_c) which is thicker than the previous ones. Total

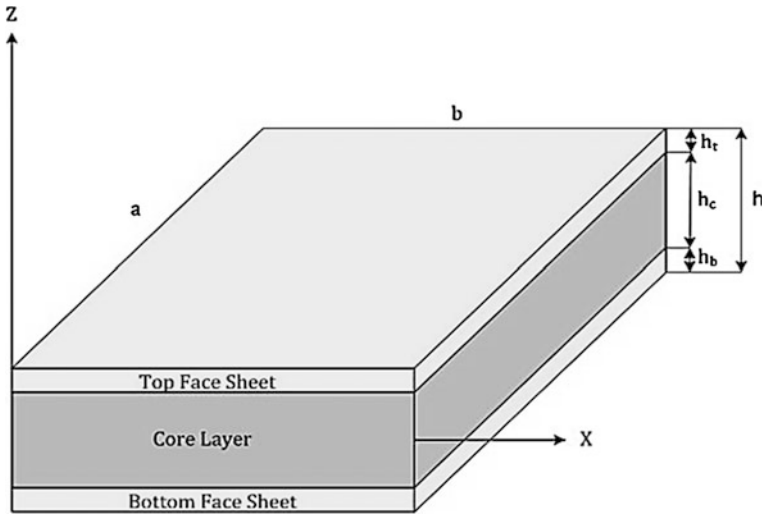


Fig. 1 Geometry and notations of a sandwich plate

thickness (h) of the plate is the sum of these thicknesses. The plane (x, y) coordinate system coincides with mi-plane plate.

2.1 Displacement Field of the Core

In the present model, the *HSDT* is adopted for the core layer. Hence, the displacement field is written as a third-order Taylor series expansion of the in-plane displacements in the thickness coordinate, and as a constant one for the transverse displacement:

$$\begin{aligned}
 u_c &= u_0 + z\psi_x^c + z^2\eta_x^c + z\zeta_x^c \\
 v_c &= v_0 + z\psi_y^c + z^2\eta_y^c + z\zeta_y^c \\
 w_c &= w_0
 \end{aligned}
 \tag{1}$$

where u_0 , v_0 and w_0 are in-plane and transverse displacement components at the mid-plane of the sandwich plate, respectively. ψ_x^c and ψ_y^c represent normal rotations about the x and y axis respectively. The parameters η_x^c , η_y^c , ζ_x^c and ζ_y^c are higher-order terms the Taylor's series expansion.

2.2 Strain-Displacement Relations

The kinematic relations for the core are given by:

$$\begin{aligned}
 \varepsilon_{xx}^c &= \frac{\partial u_0}{\partial x} + z \frac{\partial \psi^c}{\partial x} + z^2 \frac{\partial \eta_x^c}{\partial x} + z^3 \frac{\partial \zeta_x^c}{\partial x} \\
 \varepsilon_{yy}^c &= \frac{\partial v_0}{\partial y} + z \frac{\partial \psi_y^c}{\partial y} + z^2 \frac{\partial \eta_y^c}{\partial y} + z^3 \frac{\partial \zeta_y^c}{\partial y} \\
 \gamma_{xy}^c &= \left(\frac{\partial u_0}{\partial y} + \frac{\partial v_0}{\partial x} \right) + z \left(\frac{\partial \psi_x^c}{\partial y} + \frac{\partial \psi_y^c}{\partial x} \right) + z^2 \left(\frac{\partial \eta_x^c}{\partial y} + \frac{\partial \eta_y^c}{\partial x} \right) + z^3 \left(\frac{\partial \zeta_x^c}{\partial y} + \frac{\partial \zeta_y^c}{\partial x} \right) \\
 \gamma_{yz}^c &= \psi_y^c + \frac{\partial w_0}{\partial y} + z \cdot 2\eta_y^c + z^2 \cdot 3\zeta_y^c \\
 \gamma_{xz}^c &= \psi_x^c + \frac{\partial w_0}{\partial x} + z \cdot 2\eta_x^c + z^2 \cdot 3\zeta_x^c
 \end{aligned} \tag{2}$$

2.3 Displacement Field of the Face Sheets

The face sheets are modeled using the *FSDT*. The compatibility conditions as well as the interlaminar displacement continuity (face sheets/core), leads to the following improved displacement fields:

2.3.1 Top Face Sheet

$$\begin{aligned}
 u_t &= u_0 + \left(\frac{h_c}{2} \right) \cdot \psi_x^c + \left(\frac{h_c^2}{4} \right) \cdot \eta_x^c + \left(\frac{h_c^3}{8} \right) \cdot \zeta_x^c + \left(z - \frac{h_c}{2} \right) \cdot \psi_x^t \\
 v_t &= v_0 + \left(\frac{h_c}{2} \right) \cdot \psi_y^c + \left(\frac{h_c^2}{4} \right) \cdot \eta_y^c + \left(\frac{h_c^3}{8} \right) \cdot \zeta_y^c + \left(z - \frac{h_c}{2} \right) \cdot \psi_y^t \\
 w_t &= w_0
 \end{aligned} \tag{3}$$

2.3.2 Bottom Face-Sheet

$$\begin{aligned}
 u_b &= u_0 - \left(\frac{h_c}{2} \right) \cdot \psi_x^c + \left(\frac{h_c^2}{4} \right) \cdot \eta_x^c - \left(\frac{h_c^3}{8} \right) \cdot \zeta_x^c + \left(z + \frac{h_c}{2} \right) \cdot \psi_x^b \\
 v_b &= v_0 - \left(\frac{h_c}{2} \right) \cdot \psi_y^c + \left(\frac{h_c^2}{4} \right) \cdot \eta_y^c - \left(\frac{h_c^3}{8} \right) \cdot \zeta_y^c + \left(z + \frac{h_c}{2} \right) \cdot \psi_y^b \\
 w_b &= w_0
 \end{aligned} \tag{4}$$

2.4 Strain-Displacement Relations

The kinematic relations for the top face sheet can be written as follows:

$$\begin{aligned}
 \epsilon_{xx}^f &= \frac{\partial u_i}{\partial x} = \frac{\partial u_0}{\partial x} + \left(\frac{h_c}{2}\right) \cdot \frac{\partial \psi_x^c}{\partial x} + \left(\frac{h_c^2}{4}\right) \cdot \frac{\eta_x^c}{\partial x} + \left(\frac{h_c^3}{8}\right) \cdot \frac{\zeta_x^c}{\partial x} + \left(z - \frac{h_c}{2}\right) \cdot \frac{\psi_x^f}{\partial x} \\
 \epsilon_{yy}^f &= \frac{\partial v_i}{\partial y} = \frac{\partial v_0}{\partial y} + \left(\frac{h_c}{2}\right) \cdot \frac{\partial \psi_y^c}{\partial y} + \left(\frac{h_c^2}{4}\right) \cdot \frac{\eta_y^c}{\partial y} + \left(\frac{h_c^3}{8}\right) \cdot \frac{\zeta_y^c}{\partial y} + \left(z - \frac{h_c}{2}\right) \cdot \frac{\psi_y^f}{\partial y} \\
 \gamma_{xy}^f &= \frac{\partial u_i}{\partial x} + \frac{\partial v_i}{\partial y} = \left(\frac{\partial u_0}{\partial y} + \frac{\partial v_0}{\partial x}\right) + \left(\frac{h_c}{2}\right) \cdot \left(\frac{\partial \psi_x^c}{\partial y} + \frac{\partial \psi_y^c}{\partial x}\right) + \left(\frac{h_c^2}{4}\right) \cdot \left(\frac{\eta_x^c}{\partial y} + \frac{\eta_y^c}{\partial x}\right) \\
 &\quad + \left(\frac{h_c^3}{8}\right) \cdot \left(\frac{\zeta_x^c}{\partial y} + \frac{\zeta_y^c}{\partial x}\right) + \left(z - \frac{h_c}{2}\right) \cdot \left(\frac{\psi_x^f}{\partial y} + \frac{\psi_y^f}{\partial x}\right) \\
 \gamma_{yz}^f &= \frac{\partial w_0}{\partial y} + \psi_y^f \\
 \gamma_{xz}^f &= \frac{\partial w_0}{\partial x} + \psi_x^f
 \end{aligned} \tag{5}$$

The same steps are followed to elaborate the strain-displacement relationships of the bottom face sheet.

2.5 Constitutive Relationships

In this work, the two face sheets (top and bottom) are considered as laminated composite. Hence, the stress-strain relations for *k*th layer in the global coordinate system are expressed as:

$$\begin{Bmatrix} \sigma_{xx}^f \\ \sigma_{yy}^f \\ \tau_{yz}^f \\ \tau_{xz}^f \\ \tau_{xy}^f \end{Bmatrix}^{(k)} = \begin{bmatrix} \bar{Q}_{11} & \bar{Q}_{12} & 0 & 0 & \bar{Q}_{16} \\ \bar{Q}_{21} & \bar{Q}_{22} & 0 & 0 & \bar{Q}_{21} \\ 0 & 0 & \bar{Q}_{44} & \bar{Q}_{45} & 0 \\ 0 & 0 & \bar{Q}_{54} & \bar{Q}_{55} & 0 \\ \bar{Q}_{61} & \bar{Q}_{62} & 0 & 0 & \bar{Q}_{66} \end{bmatrix}^{(k)} \begin{Bmatrix} \epsilon_{xx}^f \\ \epsilon_{yy}^f \\ \gamma_{zy}^f \\ \gamma_{xz}^f \\ \gamma_{xy}^f \end{Bmatrix}^{(k)} \quad \text{f = top, bottom} \tag{6}$$

The core is considered as an orthotropic composite material, and the stress-strain relationships can be defined as follows:

$$\begin{Bmatrix} \sigma_{xx}^c \\ \sigma_{yy}^c \\ \tau_{yz}^c \\ \tau_{xz}^c \\ \tau_{xy}^c \end{Bmatrix} = \begin{bmatrix} \bar{Q}_{11} & \bar{Q}_{12} & 0 & 0 & \bar{Q}_{16} \\ \bar{Q}_{21} & \bar{Q}_{22} & 0 & 0 & \bar{Q}_{21} \\ 0 & 0 & \bar{Q}_{44} & \bar{Q}_{45} & 0 \\ 0 & 0 & \bar{Q}_{54} & \bar{Q}_{55} & 0 \\ \bar{Q}_{61} & \bar{Q}_{62} & 0 & 0 & \bar{Q}_{66} \end{bmatrix} \begin{Bmatrix} \epsilon_{xx}^c \\ \epsilon_{yy}^c \\ \gamma_{zy}^c \\ \gamma_{xz}^c \\ \gamma_{xy}^c \end{Bmatrix} \tag{7}$$

The efforts resultants of the core are obtained by integration of the stresses through the thickness direction of laminated plate. Hence, the constitutive equations can be written in the following contracted form:

$$\begin{aligned}
 \begin{Bmatrix} N \\ M \\ \bar{N} \\ \bar{M} \end{Bmatrix} &= \begin{bmatrix} [A] & [B] & [D] & [E] \\ [B] & [D] & [E] & [F] \\ [D] & [E] & [F] & [G] \\ [E] & [F] & [G] & [H] \end{bmatrix} \begin{Bmatrix} \varepsilon^{(0)} \\ \chi^{(1)} \\ \chi^{(2)} \\ \chi^{(3)} \end{Bmatrix} \\
 \begin{Bmatrix} V \\ S \\ R \end{Bmatrix} &= \begin{bmatrix} A^s & B^s & D^s \\ B^s & D^s & E^s \\ D^s & E^s & F^s \end{bmatrix} \begin{Bmatrix} \gamma_s^{(0)} \\ \chi_s^{(1)} \\ \chi_s^{(2)} \end{Bmatrix}
 \end{aligned} \tag{8}$$

where the components of the reduced stiffness matrices of the core are defined by:

$$\begin{aligned}
 (A_{ij}, B_{ij}, D_{ij}, E_{ij}; F_{ij}, G_{ij}, H_{ij}) &= \int_{-\frac{h_c}{2}}^{\frac{h_c}{2}} \bar{Q}_{ij}(1, z, z^2, z^3, z^4, z^5, z^6) dz |_{i,j=1,2,6} \\
 (A_{ij}^s, B_{ij}^s, D_{ij}^s, E_{ij}^s; F_{ij}^s, G_{ij}^s, H_{ij}^s) &= \int_{-\frac{h_c}{2}}^{\frac{h_c}{2}} \bar{Q}_{ij}(1, z, z^2, z^3, z^4) dz |_{i,j=4,5}
 \end{aligned} \tag{9}$$

According to the theory *FSDT*, the constitutive equations for the face sheets are:

$$\begin{Bmatrix} N^f \\ M^f \\ T^f \end{Bmatrix} = \begin{bmatrix} A^f & B^f & 0 \\ B^f & D^f & 0 \\ 0 & 0 & A^f \end{bmatrix} \begin{Bmatrix} \varepsilon_m^f \\ \varepsilon_f^f \\ \gamma_c^f \end{Bmatrix} \tag{10}$$

3 Finite Element Formulation

In the present study, a C^0 four-node isoparametric element, named *QSFT52* (Quadrilateral Sandwich First Third with 52-*DOF*), with thirteen *DOF* per node has been developed. Each node contains: two rotational *DOF* for each face sheet, six rotational *DOF* for the core, while the three translations *DOF* are common for sandwich layers (Fig. 2).

The displacements vectors at any point of coordinates (x, y) of the plate are given by:

$$\delta(x, y) = \sum_{i=1}^n N_i(x, y) \cdot \delta_i \tag{11}$$

where δ_i is displacement vector corresponding to node i , containing

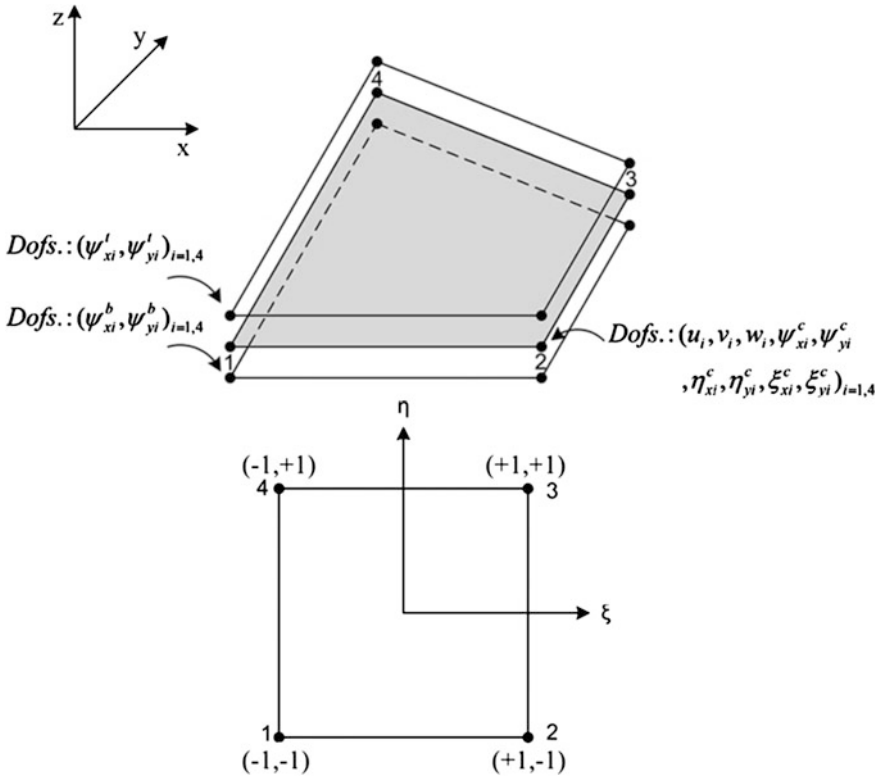


Fig. 2 Geometry and corresponding degrees of freedom of the QSFT52 element

$$\delta_i = \left\{ u_i \ v_i \ w_i \ \psi^c_{xi} \ \psi^c_{yi} \ \eta^c_{xi} \ \eta^c_{yi} \ \xi^c_{xi} \ \xi^c_{yi} \ \psi^t_{xi} \ \psi^t_{yi} \ \psi^b_{xi} \ \psi^b_{yi} \right\}^T \quad (12)$$

Hamilton's principle is used in order to formulate governing static and free vibration problems considered in this work, which is given as:

$$\delta \Pi = \delta \int_{t_1}^{t_2} (\delta U - \delta T) dt = 0 \quad (13)$$

where t is the time, U is the strain energy of the system and T is the kinetic energy of the system. The strain energy is the summation of contribution from the two face sheets and from the core as:

$$\begin{aligned}
\delta U = & \int_{A_c} \int_{\frac{-h_c}{2}}^{\frac{h_c}{2}} \left(\sigma_{xx}^c \delta \varepsilon_{xx}^c + \sigma_{yy}^c \delta \varepsilon_{yy}^c + \tau_{xy}^c \delta \varepsilon_{xy}^c + \tau_{xz}^c \delta \varepsilon_{xz}^c + \tau_{yz}^c \delta \varepsilon_{yz}^c \right) dV_c \\
& + \int_{A_t} \int_{\frac{h_c}{2}}^{\frac{h_c}{2} + h_t} \left(\sigma_{xx}^t \delta \varepsilon_{xx}^t + \sigma_{yy}^t \delta \varepsilon_{yy}^t + \tau_{xy}^t \delta \varepsilon_{xy}^t + \tau_{xz}^t \delta \varepsilon_{xz}^t + \tau_{yz}^t \delta \varepsilon_{yz}^t \right) dV_t \quad (14) \\
& + \int_{A_b} \int_{-\left(\frac{h_c}{2} + h_b\right)}^{-\frac{h_c}{2}} \left(\sigma_{xx}^b \delta \varepsilon_{xx}^b + \sigma_{yy}^b \delta \varepsilon_{yy}^b + \tau_{xy}^b \delta \varepsilon_{xy}^b + \tau_{xz}^b \delta \varepsilon_{xz}^b + \tau_{yz}^b \delta \varepsilon_{yz}^b \right) dV_b
\end{aligned}$$

The variation of kinetic energy of the three layers sandwich plate can be expressed as:

$$\begin{aligned}
\delta T = & \int_{V_t} \rho_t \left(\ddot{u}_t \delta u_t + \ddot{v}_t \delta v_t + \ddot{w}_t \delta w_t \right) dV_t \\
& + \int_{V_c} \rho_c \left(\ddot{u}_c \delta u_c + \ddot{v}_c \delta v_c + \ddot{w}_c \delta w_c \right) dV_c \quad (15) \\
& + \int_{V_b} \rho_b \left(\ddot{u}_b \delta u_b + \ddot{v}_b \delta v_b + \ddot{w}_b \delta w_b \right) dV_b
\end{aligned}$$

Using the standard finite element procedure, the governing differential equations of motion can be rewritten as:

$$[M_T] \left\{ \ddot{\delta} \right\} + [K_T] \{ \delta \} = 0 \quad (16)$$

where $[M_T]$ and $[K_T]$ denote the element mass matrix and the element stiffness matrix, respectively, for the three layers sandwich plate.

$$[K] = \sum_e \int_{-1}^1 \int_{-1}^1 \begin{pmatrix} [B^t]^T & [D^t] & [B^t] \\ + [B^c]^T & [D^c] & [B^c] \\ + [B^b]^T & [D^b] & [B^b] \end{pmatrix} \det(J) \cdot d\xi d\eta \quad (17)$$

and the element mass matrix can be written as:

$$[K] = \sum_e \int_{-1}^1 \int_{-1}^1 \begin{pmatrix} [N]^T & [m^{(t)}] & [N] \\ + [N]^T & [m^{(c)}] & [N] \\ + [N]^T & [m^{(b)}] & [N] \end{pmatrix} \det(J) \cdot d\xi d\eta \quad (18)$$

Now, after evaluating the stiffness and mass matrices for all elements, the governing equations for free vibration analysis can be stated in the form of generalized eigenvalue problem.

$$[K_T]\{\chi\} - \omega^2[M_T]\{\chi\} = 0 \tag{19}$$

4 Results and Discussions

4.1 Unsymmetric Laminated Square Sandwich Plate Subjected to Sinusoidal Load

For static analysis, an un-symmetrical laminated sandwich plate (0/90/C/0/90), all four edges clamped and subjected sinusoidal load, is studied. The mechanical properties of materials used are listed in Table 1. The thickness of each laminate layer is 0.05h, whereas the thickness of the core is 0.8h, where *h* is the total thickness of the plate. The analysis is performed for different thickness ratios (*h/a* = 0.25, 0.1 and 0.05) and different mesh sizes (8 × 8, 12 × 12 and 16 × 16).

The values of non-dimensional transverse displacement (*w*) and transverse shear stresses (τ_{xz}, τ_{yz}) are presented in Table 2 with those obtained from the literature.

$$\bar{w} = \frac{100 E_2 h^3}{a^4 q_0} w \left(\frac{a}{2}, \frac{b}{2} \right), (\bar{\tau}_{xz}, \bar{\tau}_{yz}) = \frac{h}{q_0 a} (\tau_{xz}, \tau_{yz}) \tag{20}$$

It is clear, from the Table 2, that the results obtained from present finite element model, especially for the transverse shear stresses, are in good agreement when compared with those obtained by the nine-node quadratic finite element solution (FEM-Q9), based on higher-order zigzag plate theory (HZZT) by Khandelwal et al. [8], Chalak et al. [9] and Pandit et al. [10]. These results show clearly the performances and convergence of the proposed formulation.

Table 1 Material property for sandwich plate

	Elastic properties						
	Location	E ₁	E ₂	G ₁₂	G ₁₃	G ₂₃	$\nu_{12} = \nu_{21}$
sandwich Plates	Core	0.04E	0.04E	0.016E	0.06E	0.06E	0.25
	Face	25E	E	0.500E	0.5E	0.20E	0.25

Table 2 Normalized maximum deflection and transverse shear stresses of a clamped square laminated sandwich plate under distributed load of sinusoidal

h/a	Reference	$\bar{w}\left(\frac{a}{2}, \frac{b}{2}, 0\right)$	$\bar{\tau}_{xy}\left(0, \frac{b}{2}, 0\right)$	$\bar{\tau}_{yz}\left(\frac{b}{2}, 0, 0\right)$	$\bar{w}\left(\frac{a}{2}, \frac{b}{2}, 0\right)$
0.05	Present element (8 × 8)	QSFT52	0.1639	0.1639	0.4166
		QSFT52	0.1694	0.1694	0.4226
	Present element (12 × 12)	QSFT52	0.1682	0.1682	0.4245
		Q9-HOZT	0.1828	0.1828	0.4296
	Present element (16 × 16)	Q9-HOZT	0.1568	0.2319	0.4283
		Q9-HOZT	0.1661	0.1661	0.4299
	Pandit et al. [10]				
Chalak et al. [9]					
Khandelwal et al. [8]					
0.1	Present element (8 × 8)	QSFT52	0.1518	0.1518	1.0538
		QSFT52	0.1513	0.1513	1.0451
	Present element (12 × 12)	QSFT52	0.1474	0.1474	1.0443
		Q9-HOZT	0.1587	0.1586	1.0489
	Present element (16 × 16)	Q9-HOZT	0.1308	0.2175	1.0484
		Q9-HOZT	0.1380	0.1383	1.0513
	Pandit et al. [10]				
Chalak et al. [9]					
Khandelwal et al. [8]					
0.25	Present element (8 × 8)	QSFT52	0.1325	0.1325	5.2499
		QSFT52	0.1279	0.1279	5.2157
	Present element (12 × 12)	QSFT52	0.1227	0.1227	5.2046
		Q9-HOZT	0.1157	0.1766	5.2305
	Present element (16 × 16)	Q9-HOZT	0.1228	0.1231	5.2470
	Chalak et al. [9]				
Khandelwal et al. [8]					

4.2 Free Vibration Analysis of Sandwich Plate Having Un-symmetric Laminated Face Sheets

A simply supported square sandwich plate with un-symmetric laminated face sheets (0/90/C/0/90) is considered to assess the performance of our model to the thin as well as thick plate. The mechanical properties of the sandwich plate are presented in Table 3. The thickness ratio (a/h) is considered to vary from 2 to 100, where the ratio of thickness of core to thickness of face sheet (h_c/h_f) is considered as 10.

Table 3 Material properties for laminated sandwich plate

Material	Elastic properties (GPa)						
	E ₁₁	E ₂₂	G ₁₂	G ₁₃	G ₂₃	ν ₁₂	ρ (Kg/m ³)
Faces	131	10.34	6.9	6.9	6.9	0.22	1627
Core	0.0069	0.0069	0.0034	0.0034	0.0034	10 ⁻⁵	97

Fig. 3 Simply supported square sandwich plate with un-symmetric laminated face sheets for different thickness ratios (a/h). Comparison of natural frequencies

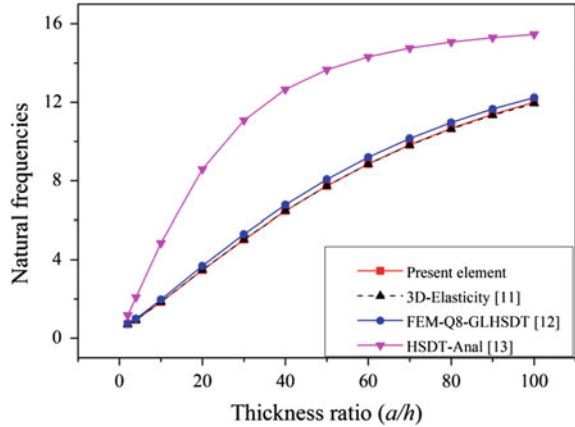
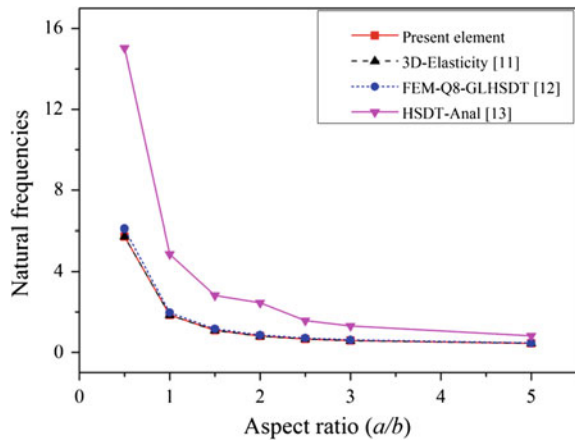


Fig. 4 Simply supported square sandwich plate with un-symmetric laminated face sheets for different aspect ratios (a/b). Comparison of natural frequencies



The comparison of the non-dimensional results of natural frequencies $\bar{\omega} = \omega b^2 / h \sqrt{\rho_c / E_{22f}}$, considering mesh size (12×12), are shown in Fig. 3, with those obtained by the 3D-elasticity solution [11], the analytical results based on HSDT [12], and those obtained with the FEM-Q8 solution based on global-local higher order shear deformation theory (GLHSDT) [13].

On the other hand, the same sandwich plate was analyzed for different aspect ratios (a/b) keeping the same reports $a/h = 10$ and $h_c/h_f = 10$. It can be seen, from the Figs. 3 and 4, that the present FE model gives more accurate results than the other models which confirm the good performance and robustness of the proposed formulation.

5 Conclusion

In this work, a new layerwise quadrilateral finite element model is proposed for static and free vibration analyses of multilayer sandwich plates. The present model satisfies interlaminar displacement continuity. The results obtained by our model were compared with those obtained by the analytical results and other finite element models available in the published literature. These results showed the performance, the simplicity and the stability of the developed element *QSFT52*. Hence, the potential of the element can be used to generate a number of new results, which are expected to be useful to the future research in this field.

References

1. Pandey, S., Pradyumna, S.: A new C0 higher-order layerwise finite element formulation for the analysis of laminated and sandwich plates. *Compos. Struct.* **131**, 1–16 (2015)
2. Oskooei, S., Hansen, J.: Higher-order finite element for sandwich plates. *AIAA J.* **38**(3), 525–533 (2000)
3. Nabarrete, A., De Almeida, S.F.M., Hansen, J.S.: Sandwich-plate vibration analysis: three-layer quasi-three-dimensional finite element model. *AIAA J.* **41**(8), 1547–1555 (2003)
4. Ramtekkar, G., Desai, Y., Shah, A.: Application of a three-dimensional mixed finite element model to the flexure of sandwich plate. *Comput. Struct.* **81**(22), 2183–2198 (2003)
5. Linke, M., Wohlers, W., Reimerdes, H.-G.: Finite element for the static and stability analysis of sandwich plates. *J. Sandwich Struct. Mater.* **9**(2), 123–142 (2007)
6. Ramesh, S.S., et al.: A higher-order plate element for accurate prediction of interlaminar stresses in laminated composite plates. *Compos. Struct.* **91**(3), 337–357 (2009)
7. Elmalich, D., Rabinovitch, O.: A high-order finite element for dynamic analysis of soft-core sandwich plates. *J. Sandwich Struct. Mater.* **14**(5), 525–555 (2012)
8. Khandelwal, R., Chakrabarti, A., Bhargava, P.: An efficient FE model based on combined theory for the analysis of soft core sandwich plate. *Comput. Mech.* **51**(5), 673–697 (2013)
9. Chalak, H.D., et al.: An improved C0 FE model for the analysis of laminated sandwich plate with soft core. *Finite Elem. Anal. Des.* **56**, 20–31 (2012)
10. Pandit, M.K., Sheikh, A.H., Singh, B.N.: An improved higher order zigzag theory for the static analysis of laminated sandwich plate with soft core. *Finite Elem. Anal. Des.* **44**(9), 602–610 (2008)
11. Rao, M., et al.: Natural Vibrations of Laminated and Sandwich Plates. *J. Eng. Mech.* **130**(11), 1268–1278 (2004)
12. Zhen, W., Wanji, C., Xiaohui, R.: An accurate higher-order theory and C0 finite element for free vibration analysis of laminated composite and sandwich plates. *Compos. Struct.* **92**(6), 1299–1307 (2010)
13. Kant, T., Swaminathan, K.: Analytical solutions for free vibration of laminated composite and sandwich plates based on a higher-order refined theory. *Compos. Struct.* **53**(1), 73–85 (2001)

Tool Life Evaluation of Cutting Materials in Turning of X20Cr13 Stainless Steel

Lakhdar Bouzid, Mohamed Athmane Yallese, Salim Belhadi and Lakhdar Boulanouar

Abstract The aim of this experimental study is to evaluate the tool life of each cutting material used in dry turning of X20Cr13 steel. The tests of straight turning were carried out using the following cutting materials: CVD coated carbide (GC2015) and PVD coated carbide (GC1015). Experimental results enable us to study the influence of machining time on flank wear VB of these cutting materials and to determine their lifespan for this cutting regime (depth of cut $a_p = 0.2$ mm, feed rate $f = 0.08$ mm/rev and cutting speed $V_c = 280$ m/min). It arises that CVD coated carbide (insert GC2015) is more resistant to wear than cutting materials. Its tool life is 65 min and consequently, it is the most powerful.

1 Introduction

The definition of a tool life (T) according to ISO 3685: “It is the total time of a cutting tool needed to achieve a specific life test” [1]. Practically the lifespan is evaluated by the measure of the flank wear. If it increases quickly, the lifespan becomes very short and vice versa. In finish turning, tool life is measured by the

L. Bouzid (✉) · M.A. Yallese · S. Belhadi
Mechanics and Structures Laboratory (LMS), 8 May University of Guelma,
BP. 401, 24000 Guelma, Algeria
e-mail: issam.bouzid@yahoo.com

M.A. Yallese
e-mail: yallese.m@gmail.com

S. Belhadi
e-mail: belhadi23@yahoo.fr

L. Bouzid
University of Larbi Ben M'Hidi, Oum El Bouaghi, Algeria

L. Boulanouar
Research Laboratory of Advanced Technologies in Mechanical Production (LRTAPM),
Badji Mokhtar University of Annaba, Annaba, Algeria
e-mail: lakhdar.boulanouar@univ-annaba.org

machining time taken by the same insert until the flank wear reaches its allowable limit of 0.3 mm. Wear is an important technological parameter of control in the machining process. It is the background for the evaluation of the tool life and surface quality [2, 3].

Yaltese et al. [4] have shown that for the *100Cr6* steel, the machined surface roughness is a function of the local damage form and the wear profile of the *CBN* tool. When augmenting V_c , tool wear increases and leads directly to the degradation of the surface quality. In spite of the evolution of flank wear up to the allowable limit $VB = 0.3$ mm, arithmetic roughness Ra did not exceed $0.55 \mu\text{m}$. A relation between VB and Ra in the form $Ra = k \cdot e^{\beta \cdot (VB)}$ is proposed. Coefficients k and β vary within the ranges of 0.204–0.258 and 1.67–2.90, respectively. It permits the follow-up of the tool wear.

The aim of the present study is to evaluate flank wear and to determine the lifespan of each cutting material on *X20Cr13* steel. Machining tests were carried out under dry conditions with the following materials: *GC2015* and *GC1015* (these are “Sandvik Coromant grades”) [5].

A model, predicting the flank wear VB of *CVD* coated carbide tool (*GC2015*) was developed. To calculate the constants of this model, the softwares *Minitab 16* and *Design-Expert 8*, analysis of variance (*ANOVA*), multiple linear regression and response surface methodology (*RSM*), were exploited. The analysis of variance *ANOVA* is a computational technique that enables the estimation of the relative contributions of each of the control factors to the overall measured response. *RSM* is a collection of mathematical and statistical techniques that are useful for the modelling and analysis of problems in which response of interest is influenced by several variables and the objective is to optimize the response [6, 7].

2 Experimental Procedure

The material used in this study was a martensitic stainless steel designated as *X20Cr13*. The reference chemical composition is shown in Table 1. Because of its relatively important corrosion resistance and fair hardness (about *180HB*), it is widely employed for many applications such as tools for food processing, surgery, chemical containers and transportation equipment. The work pieces were used in the form of round bars having 75 mm diameter and 300 mm length. The machining experiments were performed under dry conditions using a conventional lathe type *SN 40C* with 6.6 kW spindle power.

The cutting inserts used were *CVD* coated carbide *GC2015* and *PVD* coated carbide *GC1015*. These inserts were removable, of square form with eight cutting

Table 1 Chemical composition of *X20Cr13* stainless steel (wt %)

C	Cr	Ni	Si	Al	S	Mo	Mn	Sn	Cu	P	Fe
0.36	13.87	0.19	0.28	0.005	0.018	0.04	0.52	0.005	0.04	0.019	rest

edges. The tool holder (designation *PSBNR2525K12*) has geometry of the active part, characterized by the following angles: major cutting edge angle $\chi = 75^\circ$, relief angle $\alpha = 6^\circ$, rake angle $\gamma = -6^\circ$, inclination angle $\lambda = -6^\circ$. A microscope model *Visual Gage 250* was adapted to measure flank wear of different tools.

3 Experimental Results and Discussion

3.1 Effect of Machining Time on Flank Wear VB

The tests of long duration of straight turning on *X20Cr13* steel were carried out. The purpose of these operations was to determine the wear curves as a function of machining time and therefore the tool life of various cutting materials used. Figure 1 shows the evolution of the flank wear *VB* versus machining time at $f = 0.08$ mm/rev, $ap = 0.2$ mm and $Vc = 280$ m/min.

According to the curve of *CVD* coated carbide ($TiN + Al_2O_3 + Ti(C, N)$) *GC2015* and for a machining time of 7 min, the flank wear *VB* of this insert reaches a value of 0.076 mm. At the end of machining $t = 69$ min, the flank wear is 0.321 mm. This change represents an increase of 322.36 %. The tool life of this insert is 65 min.

The first machining test done with the *PVD* coated carbide ($TiN + TiAlN$) *GC1015* generates a flank wear of 0.06 mm. For a machining time of 15 min, its wear *VB* is 0.35 mm, which defines the lifespan of this tool 13 min.

3.2 Tool Life of Cutting Materials

Figure 2 illustrates the tool life of each cutting material. The lifetimes of *CVD* coated carbide *GC2015* and *PVD* coated carbide *GC1015* are respectively 65 and 13 min.

Fig. 1 *VB* of cutting materials versus machining time t

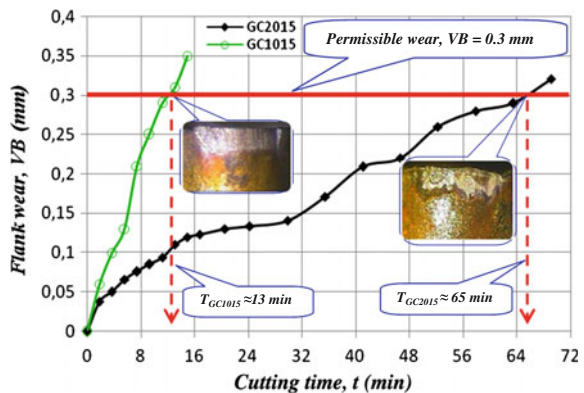
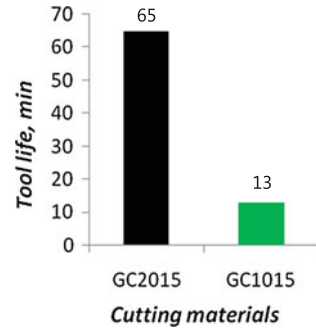


Fig. 2 Tool life of cutting materials



The tool life of *PVD* coated carbide represents 20 % of the tool life of *CVD* coated carbide. These results prove that the *CVD* coated carbide TiN + Al₂O₃ + Ti (C, N) is more efficient than *PVD* coated carbide tool.

3.3 Flank Wear VB of GC2015

CVD coated carbide tool TiN + Al₂O₃ + Ti(C, N) was more efficient than other cutting materials in terms of wear resistance. This is why we felt it necessary to analyse the behaviour of this nuance in terms of flank wear *VB*. Based on the 3² factorial design, a total of 9 tests were carried out. The range of each parameter is set at three different levels, low, middle and high. Results are given in Table 2. Mathematical model of flank wear *VB* of *GC2015* is:

$$VB = 0.0212 - 0.000272 \cdot Vc + 0.011984 \cdot t + 1.464 \cdot 10^{-5} Vc \cdot t + 7.2917 \cdot 10^{-7} Vc^2 - 0.000694 \cdot t^2 \quad (1)$$

where *Vc* is the cutting speed; $R^2 = 99.64\%$.

Table 2 Flank wear of GC2015

Test no	Vc (m/min)	t (min)	VB (mm)
1	160	4	0.043
2	160	7	0.06
3	160	11	0.072
4	280	4	0.056
5	280	7	0.083
6	280	11	0.092
7	400	4	0.088
8	400	7	0.12
9	400	11	0.142

3.3.1 3D Surface Plot for Flank Wear VB of the GC2015 Insert

The 3D Surface of GC2015 flank wear VB versus cutting speed V_c and cutting time t is plotted in Fig. 3. This figure was obtained using RSM according to its mathematical model.

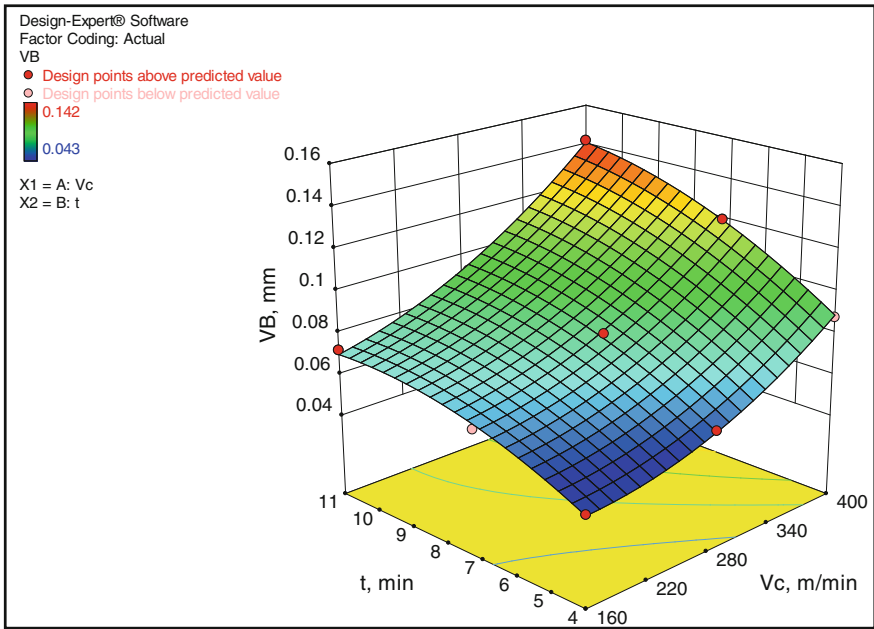


Fig. 3 3D Surface plot for flank wear VB of GC2015 versus V_c and t

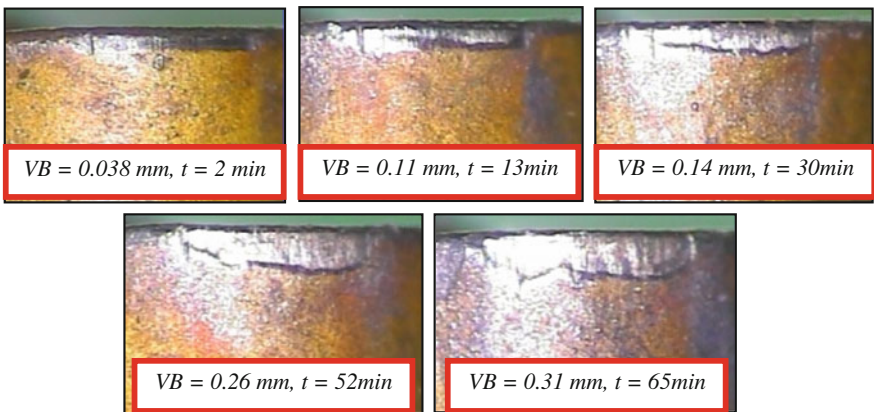


Fig. 4 Micrographs for VB of GC2015 at $a_p = 0.2 \text{ mm}; f = 0.08 \text{ mm/rev}$ and $V_c = 280 \text{ m/min}$

3.3.2 Micrographs for Flank Wear *VB* of the GC2015 Tool

For the considered regime ($V_c = 280$ m/min, $a_p = 0.2$ mm and $f = 0.08$ mm/rev), flank wear *VB* of the *CVD* coated carbide *GC2015* spreads regularly. Figure 4 shows the micrographs for *VB* of *GC2015* insert.

4 Conclusion

The following conclusions can be derived from this experimental study of dry turning of *X20Cr13* steel, machined by the following cutting materials: *CVD* coated carbide tool *GC2015* and *PVD* coated carbide tool *GC1015*.

1. The tool life of the *CVD* coated carbide *GC2015* is 65 min. As for the *PVD* coated carbide *GC1015*, its tool life is 13 min.
2. Cutting speed influences flank wear *VB* of *GC2015* more significantly than the cutting time.
3. This experimental study confirms that in dry turning for the cutting regime tested, the *CVD* coated carbide *GC2015* is the most powerful tool in terms of wear resistance and lifespan.

References

1. Bouchelagheme, H.: Etude du comportement des outils CBN lors de l'usinage de l'acier fortement allié AISI D3. Thesis University of Guelma, Algeria (2011)
2. Fnides, B., Yallese, M.A., Aouici, H.: Comportement à l'usure des céramiques de coupe ($Al_2O_3 + TiC$ et $Al_2O_3 + SiC$) en tournage des pièces trempées. Algerian J. Adv. Mater **5**, 121–124 (2008)
3. Uvaraja, V.C., Natarajan, N.: Optimization on friction and wear process parameters using Taguchi technique. Int. J. Eng. Technol. **2**, 694–699 (2012)
4. Yallese, M.A., Chaoui, K., Zeghib, N., Boulanouar, L., Rigal, J.F.: Hard machining of hardened bearing steel using cubic boron nitride tool. J. Mater. Process. Technol. **209**, 1092–1104 (2009)
5. SANDVIK Coromant: Catalogue Général, Outils de coupe SandvikCoromant, Tournage – Fraisage – Perçage – Alésage – Attachements (2009)
6. Dogra, M., Sharma, V.S., Sachdeva, A., Suri, N.M., Dureja, J.S.: Tool wear, chip formation and workpiece surface issues in CBN hard turning: a review. Int. J. Precis. Eng. Manuf. **11**, 341–358 (2010)
7. Fnides, B., Yallese, M.A., Mabrouki, T., Rigal, J.F.: Application of response surface methodology for determining cutting force model in turning hardened AISI H11 hot work tool steel. Sadhana **36**, 109–123 (2011)

Importance of Physical Modeling for Simulations of Turbulent Reactive Flows

Vincent Robin, Michel Champion, Arnaud Mura and Q.N. Kim Kha

Abstract The physical models implemented in practical computational tools are not systematically required for the numerical simulations of turbulent flows. When the grid is sufficiently refined, satisfactory numerical results can be obtained even if the smallest characteristic scales are not solved. However, when reactive flows are considered, the physical mechanisms occurring at the smallest scales may control the main characteristics of the flow such as the flame velocity propagation. Therefore, the development of new physical models is still needed for practical numerical simulations of turbulent reactive flows. A recent work that describes the inner structure of turbulent flames as composed of different layers is presented. This study also evidences the necessity to understand in details the transition between a slow chemistry layers to a fast chemistry layer. The behavior of the scalar variance and turbulent scalar flux between these two limit cases is presented.

1 Introduction

The rapid development of computational tools for fluid dynamics associated with the increase of the calculation speed of computers allows envisaging in the near future the direct numerical simulations of realistic turbulent flows. However, the complexity of most industrial or natural turbulent flows involves such a wide range of characteristic scales that the mesh used for the numerical simulations of these flows are still unable to represent the smallest physical processes such as the viscous dissipation or the molecular diffusion of species. Accordingly, the statistical Reynolds Averaged Navier-Stokes (*RANS*) representation or the filtered Large Eddy Simulations (*LES*) are still required to proceed with practical numerical simulations. The use of such simulation methods therefore implies modeling efforts to represent the effects of the unresolved phenomena. Although models are essential for *RANS* approaches, they do not seem systematically required in *LES* simulations.

V. Robin (✉) · M. Champion · A. Mura · Q.N.K. Kha
Institut Pprime - UPR 3346 - CNRS - ENSMA, Université de Poitiers, Poitiers, France
e-mail: vincent.robin@ensma.fr

Without models, the unresolved convection; molecular diffusion and viscous dissipation are considered negligible or counterbalanced by the non-physical diffusion and dissipation of the numerical schemes used in simulations. In this case, sufficiently refined meshes are needed. Thus, the permanent increase of computational speed raises the question of the usefulness of physical models to perform numerical simulations of turbulent flows.

However, several arguments highlight the importance of the development of physical models. First, the cost of high performance computations associated to the equipment and specific technical skills required for numerical simulations make these tools unreachable to the majority of practical use. Furthermore, the basis of the models always requires a detailed understanding of the physical phenomena involved in the flow. Although this understanding is not mandatory to perform numerical simulations, it is essential to analyze results and to propose technical innovations. Thus, the physical modeling is useful and even essential whatever the performance of computation tools.

Eventually, the development of models is specifically required in turbulent reactive flows because the characteristic scales of flames correspond to the smallest scales of the flow. Moreover, the strong heat release induced by chemical reactions is a source of kinetic energy at the smallest scales and has a significant impact on all the scales of the flow. The thermal expansion leads also to counter gradient transport that is a segregative mechanism opposite to the turbulent diffusion. Therefore, these phenomena occurring at the smallest scales of the flow cannot be counterbalanced by the non-physical diffusion and dissipation of the numerical schemes.

The first part of this study concerns the main modeling strategies of the mean chemical rate in turbulent premixed flames. The two limit cases where the flame structures are respectively infinitely thin and infinitely large in comparison with the mesh size are introduced. Then, the inability of these limit models to describe some parts of the flow leads us to propose a more refined description of the internal structure of turbulent flames. The flame brush is thus described as composed of different layers. Eventually, the main difficulties associated to the modeling of turbulent transports in these variable density flows are discussed.

2 Basic Consideration of the Modeling of Chemical Production Rate in Turbulent Premixed Flames

The detailed representation of the reactions mechanism in combustion of hydrocarbon fuels can involve hundreds of chemical species and thousands of chemical reactions. The combustion simulation problem therefore requires as many scalar equations as chemical species considered and each reaction of the chemical mechanism must be included in the production rates expressions of the species involved.

Provided now that the smallest scales are not resolved by the computational mesh, the transport equation for the mass fraction of the chemical species i must be averaged or filtered:

$$\frac{\partial \bar{\rho} \tilde{Y}_i}{\partial t} + \frac{\partial}{\partial x_k} (\bar{\rho} \tilde{u}_k \tilde{Y}_i) = - \frac{\partial}{\partial x_k} (\overline{\rho u_k y_i} - \bar{\rho} \tilde{u}_k \tilde{Y}_i) + \frac{\partial}{\partial x_k} \left(\overline{\rho D_i \frac{\partial Y_i}{\partial x_k}} \right) + \overline{\omega_i(Y_{k,k=1,N}, T)} \quad (1)$$

where u_k denotes the velocity field, ρ the density of the mixture, D_i the molecular diffusion coefficient of the species and ω_i is the chemical reaction rate. The Arrhenius laws used for the chemical rates expressions are for example:

$$\omega_i = \rho Y_i A T^b \exp\left(-\frac{Ea}{RT}\right) \quad (2)$$

where A is the pre-exponential factor, b a parameter, Ea the activation energy and R the universal constant of gases. The strong density variations occurring in flames impose the use of Favre averaged or filtered variables: $\bar{\rho} \tilde{Y}_i = \overline{\rho Y_i}$. The modeling of the unresolved convection term $(\overline{\rho u_k Y_i} - \bar{\rho} \tilde{u}_k \tilde{Y}_i)$ of Eq. 1 will be discussed in the last section.

2.1 Combustion Simulation Without Model

Different strategies can be considered to model the source term representing the mean chemical production rates. The simplest one in the sense of modeling is to consider that the mean chemical rates are equal to the chemical rates of the mean values:

$$\overline{\omega_i(Y_{k,k=1,N}, T)} = \omega_i(\tilde{Y}_{k,k=1,N}, \tilde{T}) \quad (3)$$

The use of Eq. (3) allows keeping the detailed description of the chemical kinetic mechanism and thus allowing the tracking of minor chemical species as pollutants. This expression is justified either if the chemical rates are assumed linearly dependent on the mass fractions and temperature or if the scalar mixing at unresolved scales is assumed perfect, i.e. $\tilde{Y}_k = Y_k$ and $\tilde{T} = T$. However, in turbulent flames, neither the latter assumption hold because the chemical reactions are represented by strongly non linear Arrhenius laws, see Eq. (2), nor the former assumption because the flame structures are not resolved by the mesh. Thus, this modeling strategy is obviously inappropriate for simulations of combustion, albeit numerical results may be qualitatively acceptable if the parameters of the Arrhenius laws are adjusted to each practical case considered. However, the adjustment of so

many parameters may be very difficult to achieve when a detailed chemical kinetic scheme is considered.

Moreover, the consideration of Arrhenius laws for the mean chemical rates also constrains the propagation mechanism of the reactive wave as explained in the next section. Eventually, although Eq. 3 may lead to acceptable qualitative results, it does not allow being predictive and does not explain the physical mechanisms that allow the flame to propagate in a turbulent flow.

2.2 Combustion Considering the Flame as an Interface

Accordingly, more sophisticated models than the one given by Eq. (3) are required for the closure of the mean chemical rates. Nevertheless, the consideration of such sophisticated models for all chemical rates that are interrelated due to the chemical kinetic scheme and that involve a wide range of characteristic time scales is unconceivable. Thus, the first necessary step to avoid the use of Eq. 3 is to reduce the number of the scalar transport equations solved. To do so, the chemical mechanism can be reduced to a few steps or even to a single global step. In some cases, a detailed chemical kinetic scheme can still be used if a typical flame structure can be preserved in the flow. The structure is then preliminary calculated and results are stored in tables, see for example [1, 2]. This technique allows the use of a single progress variable $c(x_k, t)$, defined to be $c \equiv 0$ in the fresh unburned mixture and $c \equiv 1$ in combustion products. The corresponding balance equation is:

$$\frac{\partial \bar{\rho} \tilde{c}}{\partial t} + \frac{\partial}{\partial x_k} (\bar{\rho} \tilde{u}_k \tilde{c}) = \frac{\partial}{\partial x_k} (\overline{\rho u_k c} - \bar{\rho} \tilde{u}_k \tilde{c}) + \frac{\partial}{\partial x_k} \left(\overline{\rho D \frac{\partial c}{\partial x_k}} \right) + \bar{\omega}(\tilde{c}) \quad (4)$$

The production of minor species as pollutant cannot be precisely evaluated using this single progress variable. However, this variable is perfectly suited to characterize the main heat release zone of the flame provided that a closure model for the mean chemical rate $\bar{\omega}$ is used.

As discussed in the previous paragraph, when the scalar mixing at unresolved scales is assumed perfect, Eq. (3) can be considered valid. The opposite limit is to assume the flame structure infinitely thin in comparison with the mesh scale.

In this case, the unresolved scalar fluctuations $\left(\overline{\rho c'^2} - \bar{\rho} \tilde{c}^2 \right)$ —the variance $\overline{\rho c'^2}$ in RANS—reaches its maximum:

$$\overline{\rho c'^2} \rightarrow \bar{\rho} \tilde{c} (1 - \tilde{c}) \quad (5)$$

In this case the probability density function of the progress variable c becomes almost bimodal. The flame front thus appears as an interface separating fresh reactants from fully burned gases and may be described as a geometrical entity. Different *geometrical formalisms* have been proposed to deal with such a picture of

turbulent premixed flames. Some are based on a field equation (G -field transport equation), as introduced by Williams [3], while others rely on the flame surface density (FSD) concept or on flame wrinkling descriptions. Others strategies incorporate the influence of unresolved scalar fluctuations thanks to *statistical approaches* often through the consideration of one-point one-time probability density functions [4] or at the level of a conditional moment closure. Finally, when the variance reaches its maximum value, the mean burning rate becomes related to the *scalar dissipation rate*; see for instance references [5–7]. It can also be related to the segregation factor defined as follow:

$$S = \frac{\overline{\rho c'^2}}{\rho \tilde{c}(1 - \tilde{c})} \quad (6)$$

The mean chemical rate expression thus becomes:

$$\bar{\omega} = \rho \tilde{c}(1 - \tilde{c}) \cdot (1 - S)I \quad (7)$$

where I depends on the properties of the flame structures [8]. All these strategies that consider the flame front as an interface require the use of transport equations for the flame surface density, the scalar dissipation rate or second order moments. The mean chemical rate is then obtained from the knowledge of these additional quantities provided that the structure of the interface is known. For example in the case of the flamelet regime of turbulent combustion, the interface is considered as a laminar flame structure. In most of practical simulations, considering the flame as an interface is much more realistic than considering perfect mixing at small scales. However, the additional equations involve many modeling parameters that are difficult to relate to physical quantities and that must be adapted to each flow configuration. Therefore, results obtained with such strategies cannot be retained for practical predictive use. Moreover, these models do not explain the propagation mechanism of the reactive wave. It can even be demonstrated that, in the corresponding solutions, the velocity propagation is imposed by physical phenomena that are not taken into account in the models: those occurring at the leading edge [9, 10].

Eventually, both limit cases: (i) the slow chemistry limit where the scalar mixing at unresolved scales is assumed perfect, i.e. $S \rightarrow 0$, and (ii) the fast chemistry limit where the flame structure is infinitely thin in comparison with the mesh scale, i.e. $S \rightarrow 1$, fail to predict the behavior of turbulent flames. These modeling strategies cannot explain the flame propagation mechanism.

3 Structure of Turbulent Premixed Flames

Both models respectively based on slow and fast chemistry limits are necessary to describe the whole flow. In the flamelet regime of turbulent combustion, these limits are both reached but at different location in the reactive flow. At the fresh gases and burned gases sides of turbulent flames, the reactive processes are slow enough to consider Eq. (3) to be valid. A detailed chemical scheme can be used in these parts of the flow. However, inside the flame brush, the reactive processes are fast enough to consider the flame as an interface. Thus, in numerical simulations, the turbulent flame structure should be composed of a slow chemistry layer where Eq. (3) holds, followed by a fast chemistry bimodal layer where Eq. (7) holds. Figure 1 shows those different layers. The iso- c lines are tightened in the fast chemistry layer and spaced in the slow chemistry layer.

In the slow chemistry layer, the propagation mechanism is controlled by the equilibrium between turbulent transports and chemical production $\bar{\omega}$. It is similar to the propagation mechanism of laminar premixed flame which is controlled by the equilibrium between molecular diffusion and chemical production $\omega(c)$ occurring at the burnt gas side. Accordingly, the propagation mechanism of the slow chemistry layer is controlled by the physical phenomena occurring at its burnt gas side where the fast chemistry layer is located. Thus, the fast chemistry layer pushes the slow chemistry layer.

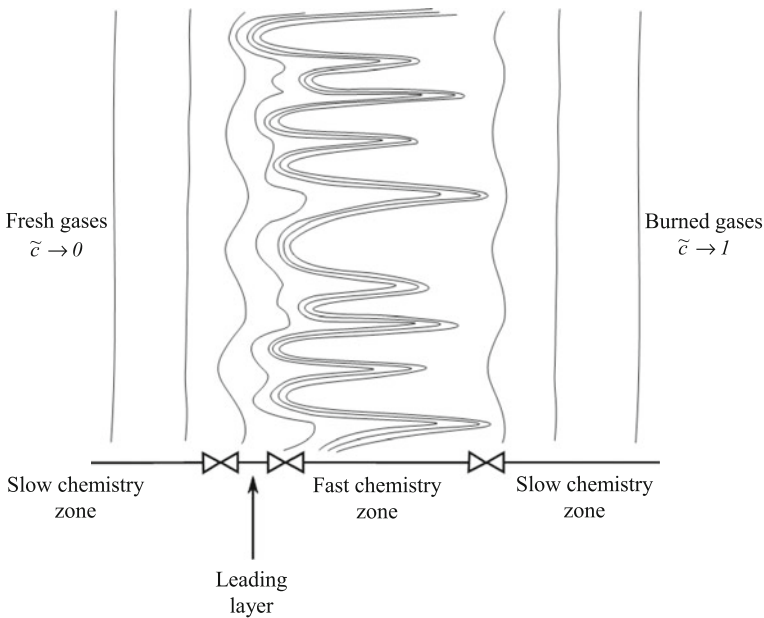


Fig. 1 Schematic iso- c lines in one dimensional turbulent flame propagating towards fresh gases and the layers that composes its structure

In the fast chemistry layer where Eq. 7 holds, the propagation mechanism is controlled by the physical phenomena occurring at the fresh gas side where the slow chemistry layer is located, see the early study of *KPP* [9]. Thus, the slow chemistry layer pulls the fast chemistry layer.

Therefore, the study of the propagation mechanism in both layers independently leads to a paradoxical result: the propagation of each layer is controlled by the other one.

To avoid this paradox, a first possibility is to propose a single expression for the mean chemical rate that is continuous from the slow to the fast chemistry layers. Then, depending on the expression of the mean chemical rate retained, pushed or pulled flames are obtained; see the recent work of Sabelnikov and Lipatnikov [10]. Another possibility is to consider that the transition between these two layers occurs in a third zone: the leading layer. Thus, this transition layer controls the propagation of the two other ones: it pushes the slow chemistry layer and, it pulls the downstream fast chemistry layer, see Fig. 1. Therefore, the physical phenomena involved in this layer are essentials to understand the propagation mechanism of the flame brush. This approach is consistent with the leading point theory [11].

Although the propagation mechanism is still not understood, a recent work describes in details the structure of turbulent premixed flames [12]. The evolution of the segregation rate through the leading layer is studied in the case of the flamelet regime of turbulent combustion. An analytical expression is found by Kha et al. [12] for high values of the activation energy. In the limit case where the fast chemistry layer is composed of infinitely thin flame structures, the segregation rate becomes related to the mean progress variable following these expressions:

$$S = \frac{1}{2}\chi, \quad \chi < 1 \quad (8)$$

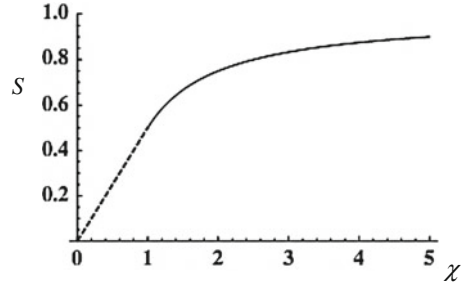
$$S = 1 - \frac{1}{2}\chi, \quad \chi > 1 \quad (9)$$

where the stretch variable introduced is defined as follow:

$$\chi = \frac{\tilde{c}}{\delta_c} \quad (10)$$

The small parameter δ_c is the characteristic thickness of the leading layer in the composition space. Equation (8) corresponds to the appearance of the first flame structure in the leading layer. And Eq. (9) corresponds to the increase of the segregation rate towards the bimodality limit. Figure 2 shows the evolution of the segregation rate in the leading layer. In this limit case, the slow chemistry layer corresponds to $\chi \rightarrow 0$ and the fast chemistry layer corresponds to $\chi \rightarrow \infty$. Kha et al. [12] also study different cases corresponding to finite thickness of the flame structures. It is also found in [12] that the thickness of this leading layer is of the same order of magnitude than the smallest turbulent scales. Therefore, in the

Fig. 2 Evolution of the segregation rate through the leading layer, *dashed line* Eq. (8) and *solid line* Eq. (9)



context of practical numerical simulations, this layer cannot be resolved by the mesh. A law, similar to those used for wall boundary layers, should be introduced in computational tools. Eventually, this recent description brings into question the ability of current computational tools to represent the most important characteristic of a premixed turbulent flame, namely its propagation.

This outcome leads us to focus on simpler algebraic expressions for the mean chemical rate itself instead of solving additional transport equations [13]. In this context, the detailed description of the structure of a turbulent premixed flame can be used to identify the most important parameters of an algebraic expression of the mean chemical rate.

4 Density Variation Effects

Whatever the model used for the mean chemical rate, the velocity propagation of the reactive wave is also directly related to the turbulent induced diffusion mechanism represented by unresolved convection term of Eq. (4). However, it is known [14–16] that this scalar flux behaves completely differently depending on the values of the segregation rate. In the one hand, for small values of S , i.e. slow chemistry layer, this flux is classically modeled by a gradient law:

$$(\overline{\rho u_k \tilde{c}} - \tilde{\rho} \tilde{u}_k \tilde{c}) = -\rho D_T \frac{\partial \tilde{c}}{\partial x} \quad (11)$$

Thus, the unresolved convection is assumed analogous to molecular diffusion. In the other hand, for large values of the segregation rate, i.e. fast chemistry layer, the existence of a bimodal *PDF* of the scalar c leads to:

$$(\overline{\rho u_k \tilde{c}} - \tilde{\rho} \tilde{u}_k \tilde{c}) = -\rho (u_k^b - u_k^f) \cdot \tilde{c}(1 - \tilde{c}) \quad (12)$$

where u_k^f and u_k^b are the conditional velocities in fresh and burned gases respectively.

Accordingly, the unresolved scalar flux is no more proportional to the gradient of the mean progress variable. In constant density flows, this unresolved convection is associated to a mixing process even if the segregation rate is large. Thus, under the influence of turbulent mixing, the pockets of burned gases tend to get closer to the pockets of fresh gases. In this case, the velocity difference $(u_k^b - u_k^f)$ has the same direction as the scalar gradient. Then, although the shapes of the expressions of Eqs. (11) and (12) are very different, their modeling in the context of constant density flows are usually considered as a diffusion mechanism whatever the values of the segregation factor.

However, in reactive flows, the thermal expansion induced by chemical reactions leads to strong accelerations. This unresolved expansion phenomenon may override the turbulent mixing effect so that the pockets of burned and fresh gases move away one from each other. Consequently, the velocity difference $(u_k^b - u_k^f)$ has an opposite direction of the gradient law. In this case, the unresolved convection is counter- gradient. This phenomenon is well known in turbulent premixed flames [14–16] but has been only scarcely studied in non premixed flames [17], see Fig. 3.

The density variations that are responsible for the unresolved accelerations are fully correlated to the scalar fluctuations through the state law of gases. Thus, the unresolved accelerations can be directly related to the fluctuations of the scalar c [15–17]. This is the direct effect of thermal expansion, see Fig. 3. However, the density variations occurring in flames also induce streamline curvatures elsewhere in the flow field. This indirect effect of thermal expansion causes additional unresolved accelerations, see Fig. 3.

In addition to this counter-gradient process, the unresolved accelerations that are obviously oriented towards a privileged direction, see Fig. 3, are strongly anisotropic at small scales and provide kinetic energy. Therefore, the thermal expansion effects are opposite to the diffusive and dissipative mechanisms observed in non reactive turbulent flows. Accordingly, these effects cannot be counterbalanced by the artificial diffusion and dissipation induced by the numerical schemes used in computational tools.

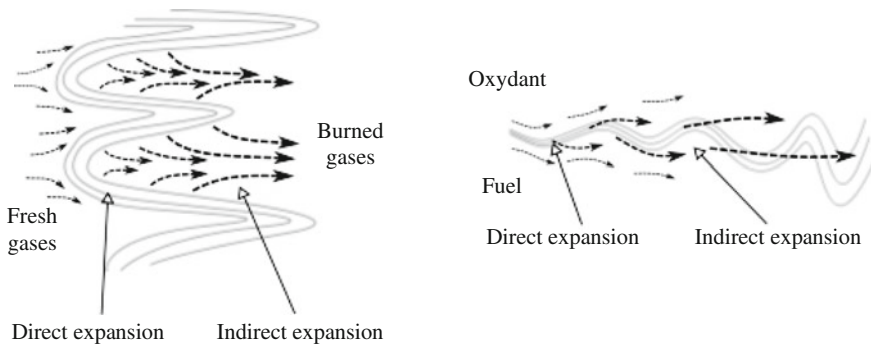


Fig. 3 Direct and indirect expansion in premixed and non premixed turbulent flames

Eventually, taking into account these mechanisms in numerical simulations is essential to predict the velocity propagation of reactive waves as well as the production of turbulence. A good evaluation of the level of turbulent mixing is indeed crucial to evaluate minor species formations, such as pollutant, downstream of the flame brush where the chemistry process becomes slow again, see Fig. 1. However, as for the chemical rate models, the turbulent transport models must change their form, from the slow chemistry layer, i.e. Eq. (11) to the fast chemistry layer, i.e. Eq. (12). The transition between these two limits occurring in the leading layer will also be essential to obtain relevant results from numerical simulation of practical flows.

5 Conclusion

The physical modeling of turbulent reactive flows is still necessary despite the increase of the calculation speed and the associated accuracy of computation tools. Whatever the grid refinement, as long as a *DNS* is not reached, the main practical characteristic of turbulent flames, i.e. its velocity propagation and the pollutant production, cannot be solved by numerical simulations without the use of models. Moreover, the development of models makes the computational cost decrease significantly so that this tool becomes accessible to a wider community of users. However, the development of models requires a detailed understanding of the physical phenomena involved in reactive flows. The main challenges identified are: (i) the understanding of the propagation mechanism and the associated description of the leading layer (ii) taking into account the leading layer in practical simulations, (iii) taking into account the thermal expansion effects on unresolved convection terms.

References

1. Pope, S.: Computationally efficient implementation of combustion chemistry using in situ adaptive tabulation. *Combust. Theor. Model.* **1**, 41–63 (1997)
2. Oijen, J.V., Goey, L.D.: Modelling of premixed laminar flames using flamelet-generated manifolds. *Combust. Sci. Technol.* **161**, 113–137 (2000)
3. Williams F.A., *Combustion Theory*, 2nd edn. Benjamin Cummings (1985)
4. Pope, S.: Pdf methods for turbulent reactive flows. *Prog. Energy Combust. Sci.* **11**, 119–192 (1985)
5. Mantel, T., Borghi, R.: A new model of premixed wrinkled flame propagation based on a scalar dissipation equation. *Combust. Flame* **96**, 443–457 (1994)
6. Mura, A., Borghi, R.: Towards an extended scalar dissipation equation for turbulent premixed combustion. *Combust. Flame* **133**, 193–196 (2003)
7. Bray, K.N.C., Swaminathan, N.: Scalar dissipation and flame surface density in premixed turbulent combustion. *C.R. Mec.* **334**, 466–473 (2006)

8. Bray, K.N.C., Champion, M., Libby, P.A., Swaminathan, N.: Finite rate chemistry and presumed pdf models for premixed turbulent combustion. *Combust. Flame* **146**, 665–673 (2006)
9. Kolmogorov, A.N., Petrovskii, I., Piskunov, N.: A study of the diffusion equation with increase in the amount of substance and its application to a biology problem. *Bull. Univ. Moscow Ser. Int.* **A1**, 1–16, see also selected works of A.N. Kolmogorov (Tikhomirov, V.M. ed.) vol. I, pp. 242, Kluwer Academic Publishers, London (1991) (1937)
10. Sabelnikov, V., Lipatnikov, A.: Transition from pulled to pushed premixed turbulent flames due to countergradient transport. *Combust. Theory Model.* **17**(6), 1154–1175 (2013)
11. Kuznetsov, V.R., Sabel'nikov, V.: *Turbulence and Combustion*. Hemisphere Publishing, New York (1990)
12. Kha, K.Q.N., Robin, V., Mura, A., Champion, M.: Implications of laminar flame finite thickness on the structure of turbulent premixed flames. *J. Fluid Mech.* **787**, 116–147 (2016)
13. Kha, K.Q.N., Losier, C., Robin, V., Mura, A., Champion, M.: Relevance of basic turbulent premixed combustion models for accurate simulations of v-shaped flames. In: *International Conference on Dynamics of Explosions and Reactive Systems*, Leeds, England (2015)
14. Veynante, D., Trounev, A., Bray, K.N.C., Mantel, T.: Gradient and counter-gradient scalar transport in turbulent premixed flames. *J. Fluid Mech.* **332**, 263–293 (1997)
15. Robin, V., Mura, A., Champion, M.: Direct and indirect thermal expansion effects in turbulent premixed flames. *J. Fluid Mech.* **689**, 149–182 (2011)
16. Robin, V., Mura, A., Champion, M.: Algebraic models for turbulent transports in premixed flames. *Combust. Sci. Technol.* **184**, 1718–1742 (2012)
17. Serra, S., Robin, V., Mura, A., Champion, M.: Density variations effects in turbulent diffusion flames: modeling of unresolved fl

Influence of Diverging Section Length on the Supersonic Jet Delivered from Micro-nozzle: Application to Cold Spray Coating Process

Abderrahmane Belbaki and Yamina Mebdoua-Lahmar

Abstract Supersonic jet delivered from a micro-nozzle was used for a new deposition process named cold spray. The undertaken aims to well understand the jet in order to improve the process efficiency. A 2D numerical investigation was carried out, using the commercial software ANSYS Fluent 15.0, predicting the effect of the diverging section length on the supersonic jet before and after the nozzle exit. It is shown that the expansion gradient within the nozzle is inversely proportional to the diverging section length, and shock diamonds after the nozzle exit are stronger for the short lengths than the longer ones.

1 Introduction

Cold spray process (*CSP* for Russian scientific comity, and Cold Gas Dynamic Spray Method *CGSM* for American scientific community) is a technique that belongs to the coating processes family, Fig. 1. It was accidentally developed in the early 1980s, in the Institute of Theoretical and Applied Mechanics of the Siberian Branch of the Russian Academy of sciences [2, 9]. It consists on accelerating small particles, with diameters below 50 μm , of the material to be deposited on the substrate to velocities ranging from 300 to 1200 m/s, by injecting them into a supersonic jet of specific gas: air, helium, Nitrogen, or a gas mixture. At these high velocities particles become plastically deformed and this facilitates their adherence to the substrate. However, there exists a velocity above which particles could be deposited, which depends on several parameters, among other, gas flow.

Grujicic et al. [3] studied the influence of the nozzle shape on particles acceleration by applying a one-dimensional isentropic model. An increase of particle velocities at the nozzle exit was achievable, by designing an appropriate nozzle in such a way that at each axial location the acceleration of the particles should be

A. Belbaki (✉) · Y. Mebdoua-Lahmar
Centre de Développement des Techniques Avancées (CDTA),
20 août 1956, B.P. 17, Baba Hassen, Algiers, Algeria
e-mail: abelbaki@cdta.dz

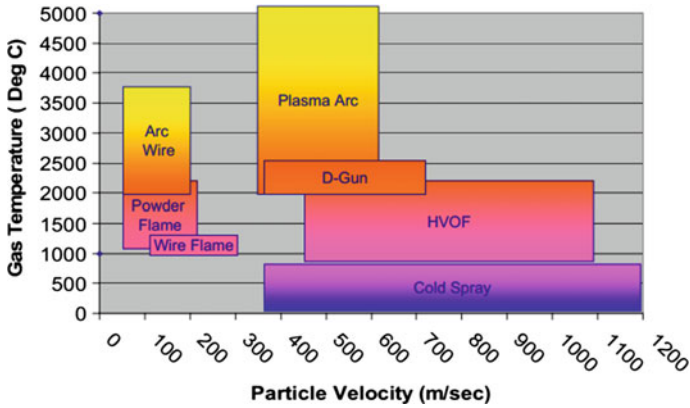


Fig. 1 Different industrial coating processes

maximal. They found also that the use of helium as carrier gas yields a substantially higher exit velocities than air. Jen et al. [4] conducted a numerical investigation on the possibility of the nano- and microsize particles deposition via cold spray process, and observed that the existence of the bow shocks near the substrate avoids the smaller size particles—less than $0.5 \mu\text{m}$ —from penetrating, which leads to poor coating.

For the use of an extended straight section after the nozzle exit, they reported that its optimal length may depend on particle sizes [4]. Li and Li [6] performed a numerical analysis involving the effect of nozzle expansion ratio, gas type, and operational gas conditions on cold sprayed coating efficiency. Their results confirm the feasibility of optimal design for a spray gun nozzle used in a limited space. Karimi et al. [5] presented a numerical model of the cold spray process, where an oval-shaped supersonic nozzle was used instead of circular one.

They also included the effect of the substrate orientation on particle deposition efficiency. Li et al. [7] tried to optimize the exit diameter of the nozzle under different spray conditions, and revealed that the latter is influenced by several parameters including, gas conditions, particle size, nozzle diverging section length, and throat diameter. Samareh and Dolatabadi [11] developed a three-dimensional model of modeling a cold gas dynamic spray system with a peripheral non-axisymmetric powder feeder.

They found that the stagnation pressure alters for different standoff distances due to the nature of the supersonic flow interactions with the substrate. They also reported that the optimum substrate location for any given operating condition is the one that results in minimum pressure buildup on the substrate. Li et al. [8] investigated the effect of the standoff distance on coating deposition characteristics and found that the deposition efficiency decreases with the increase of standoff distance. Pattison et al. [10] studied the effect of the standoff distance on the bow shock phenomenon.

They found that there exists a direct relationship between standoff distance, bow shock and deposition efficiency. Samareh et al. [12] developed a numerical model for modeling the interactions between the gas and the particles. Significant agreement between the predicted results and the experimental data was found for the geometrical gas flow structure, the resulting particle velocities, and the dependence of the two-phase flow on the particulate phase mass loading.

In the present study the effect of the length of the supersonic diverging section on the flow field before and after the nozzle exit was numerically investigated, using ANSYS Fluent 15.0 software, which helps to optimize the design of the cold spray gun.

2 Numerical Procedure

2.1 Geometry and Meshing Strategy

The geometry used for the present investigation, as shown in Fig. 2, is a converging-diverging DeLaval nozzle, which produces a supersonic jet at the nozzle exit. The converging part, with a 20 mm length and a 2.7 mm in diameter of throat section, was stuck to longitudinal duct named a stagnation chamber with a diameter of 14 mm and a length of 30 mm. This type of nozzles was constructed with the particular aim of reaching a sonic velocity at the throat section ($M = 1$).

For the diverging part, the nozzle exit section has a diameter of 8.36 mm, and four different lengths are chosen in the present study, $L = 59.9, 69.9, 79.9,$ and 89.9 mm, respectively. The second case corresponds exactly to the nozzle specifications used in [12] which is used for validation task. The external domain (aft the nozzle exit), was extended to 30 mm in both axial and radial directions. Note that for all cases, the nozzle has circular cross section. Other forms may be considered for further investigations.

Due to geometric simplicities: axial single phase fluid flow, no swirl motion, the axisymmetric assumption was opted resulting on substantial diminishing of the numerical cost. Figure 3 displays the considered geometry meshed with quadrilateral elements with variable densities (high density near to the nozzle walls and low density elsewhere) with the aim of well catching the strong gradients of flow parameters in wall proximity. Table 1 summarizes the mesh parameters for the used nozzles.

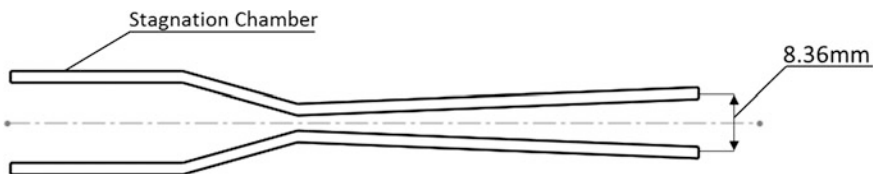


Fig. 2 Two-dimensional visualization of DeLaval nozzle

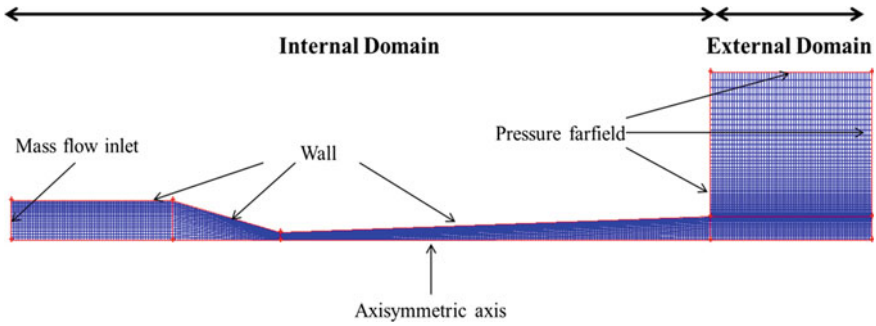


Fig. 3 Meshing strategy and boundary conditions

Table 1 Mesh characteristics

Nozzle	Internal domain		External domain	
	Axial	Radial	Axial	Radial
Nozzle 1: 59.9 mm	220	20	60	70
Nozzle 2: 69.6 mm	240	20	60	70
Nozzle 3: 79.9 mm	260	20	60	70
Nozzle 4: 89.9 mm	280	20	60	70

2.2 Boundary Conditions

Mass flow inlet was chosen as nozzle inlet boundary, with a flow rate of 25.4 g/s under a static pressure of 30 bars and a total temperature of 614 K—in the stagnation chamber, the flow velocity is negligible, so total and static pressures are almost equal—Turbulent effect was also taken into account, with turbulence intensity of 1 % and the length scale is set to be 20 % of the throat diameter at the inlet. The nozzle edges are stationary and assumed to be adiabatic due to the high velocity flow in the axial direction (as result the heat flux dissipation in radial direction is negligible). On all surrounding boundaries, since they are far enough to have no effect on the flow field, pressure is set to the atmospheric pressure, and the medium axis was chosen as the axisymmetric axis.

Note that these flow operational conditions are the same used in the experiments of Samareh et al. [12].

2.3 Numerical Model and Equations Discretization

Due to the supersonic flow regime, compressibility effects are present, thus density based solver was considered. Also for such flow regime turbulence has a meaningful effect on fluid behavior, to get close to these effects the $k-\omega$ turbulent model

was used. The $k-\omega$ is a closure model for the Reynolds-averaged Navier-Stokes equations (*RANS*), which attempts to predict turbulence by adding two equations for two variables, k and ω . While the first variable is the turbulence kinetic energy (k), the second (ω) being the specific rate of dissipation of the turbulence kinetic energy [13]. Air is used as operational fluid for the present investigation, where density is calculated via ideal gas equation, and the viscosity was evaluated by Sutherland’s three coefficients law, which quantifies viscosity as function of fluid temperature—resulted from a kinetic theory by Sutherland (1893) using an idealized intermolecular-force potential [1]. Implicit formulation was used for resolving coupled equations of steady $2D$ axisymmetric flow. Green-Gauss node based method was used for gradient discretization while, for different variables estimation at cell centers, second order upwind method was applied.

3 Results

To verify the validity of the numerical approach, our results are compared with the experiments in [12]. Figure 4 shows a qualitative comparison of the flow behavior aft the nozzle exit, between the present predictions and the experimental results in [12]. The fluid behavior was visualized by means of pressure gradient, where it appears that, for both Fig. 4A, B, at nozzle exit a series of oblique shock waves were formed, followed by a succession of shock diamonds. The shock diamonds are composed of a succession of compression waves and Prandtl-Meyer expansion waves, with the unique object of decelerating the fluid jet to the same surrounding fluid conditions.

Figures 5, 6 and 7, display the evolution of different flow parameters along the centerline from the stagnation chamber until a distance of 30 mm aft the nozzle exit

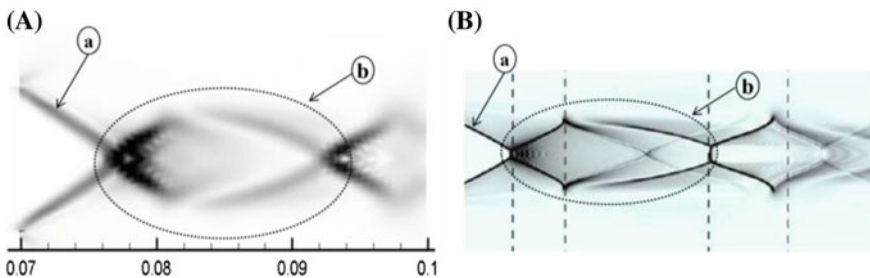


Fig. 4 A Predicted and B Measured pressure gradient contours of the flow behind nozzle exit at constant gas flow rate 25.4 g/s, with (a) oblique shock waves and (b) shock diamond

Fig. 5 Evolution of Mach number along the centerline for DeLaval nozzle with different diverging section lengths

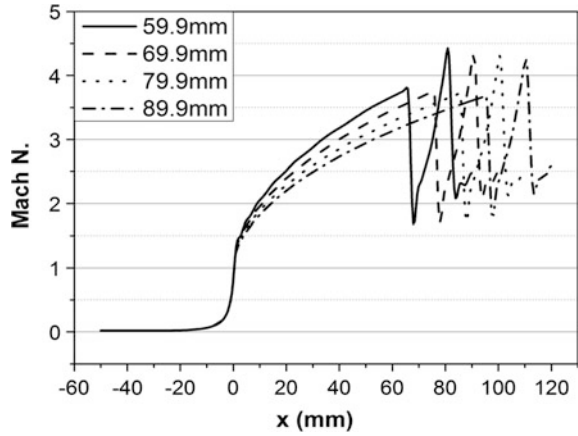


Fig. 6 Evolution of static pressure along the centerline for DeLaval nozzle with different diverging section lengths

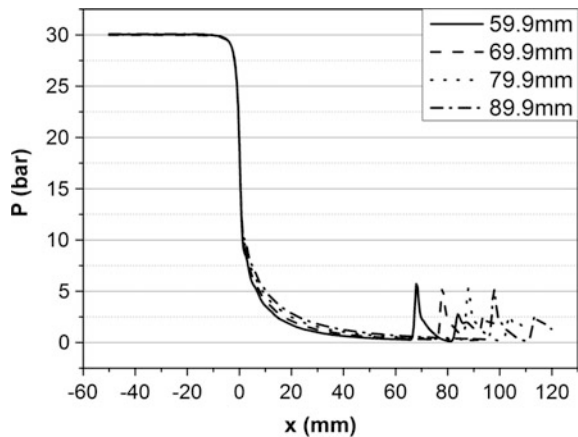
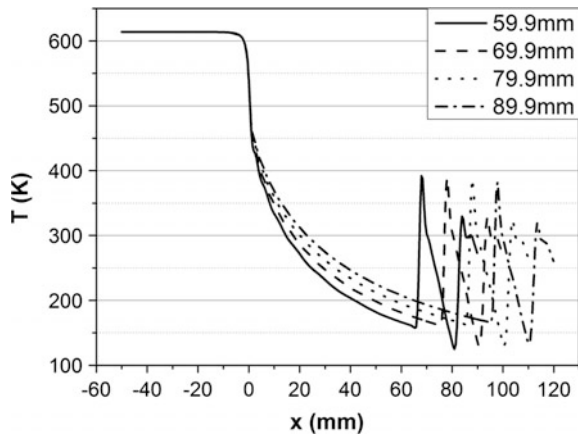


Fig. 7 Evolution of static temperature along the centerline for DeLaval nozzle with different diverging section lengths



for DeLaval nozzle with four different diverging lengths. From Mach number evolution (Fig. 5), it is clear that, for all tested nozzles, the Mach number has approximately a vanished value in the stagnation chamber (fluid at rest $V \approx 0$ and $M \approx 0$), and its value begins to rise just after entering the converging section till the throat where it becomes equal to unity ($M = M^* = 1$). It continues to rise in the diverging section and after the nozzle exit until reaching a maximum value in the range (4–5).

Then it drops down sharply influenced by the presence of the oblique shock waves. It continues to drop down before increasing rapidly due to expansion and compression waves (Fig. 4). This procedure is repeated twice—sign of two shock diamonds. At distance of 30 mm aft the nozzle exit and for all cases, Mach number reaches a value of 2.5, approximately. It is also perceived that; the Mach number gradient within the nozzle is inversely proportional to the divergent length while the value of Mach number at the distance of 30 mm aft the nozzle exit and the divergent length are proportional.

Static pressure and static temperature evolutions follow the same trend (Figs. 6 and 7), where they seem to be practically constant at the stagnation chamber. Then both of them decrease inside the nozzle and continue to decrease after the nozzle exit until reaching the shock diamonds where their values decrease (expansion wave) and increase (compression wave), consecutively. It is also noted that pressure and temperature gradients (between the inlet and the outlet of the nozzle) are inversely proportional to the diverging section length, and through compression or expansion waves.

This is due to the fact that the flow, through long distances, reaches the surrounding conditions gradually, while the one passing through short distances achieves that quickly. At the distance of 30 mm aft the nozzle exit, both the static pressure and the static temperature decrease when the divergent length increases.

Figure 8 displays the supersonic flow behavior by means of contour of static pressure, for the fourth used nozzles. Despite of the pressure amplitudes, there is no real difference between the considered cases. As earlier mentioned, shock diamonds are composed of Prandtl-Meyer expansion waves (symbol—a—in Fig. 8) and compression waves (symbol—b—in Fig. 8). Also for all cases the oblique shock waves occur after the nozzle exit section.

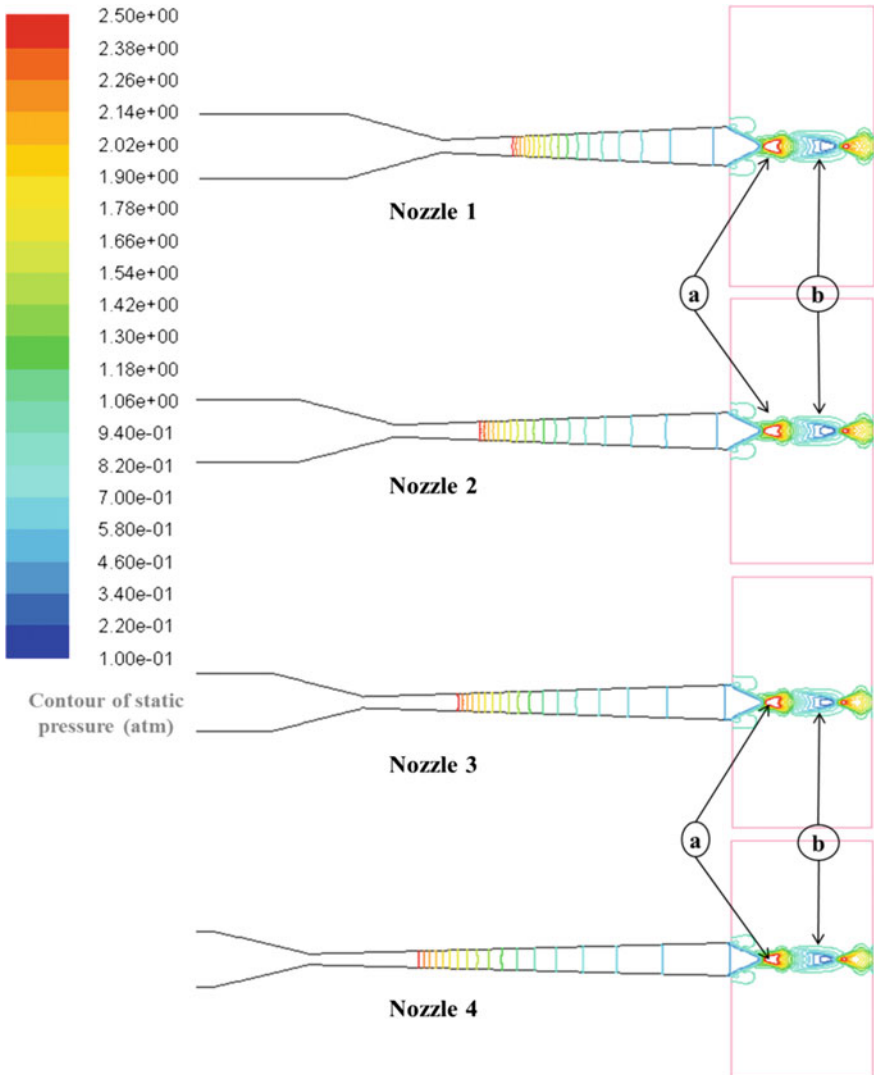


Fig. 8 Contour of static pressure inside and outside DeLaval nozzle with different diverging section lengths

4 Conclusions

The cold spray deposition process is based on gas-dynamic acceleration of fine particles to supersonic velocities and high kinetic energies. Therefore a well understanding of gas flow behavior and different parameters affecting this flow is with great importance for the success of the coating operation. A numerical

investigation that considers the effect of diverging section length on the supersonic jet behavior was carried out. The results show that the expansion gradient within the nozzle is inversely proportional to the divergent length, and the intensity of shock diamonds after the nozzle exit evolves in reverse proportionality with the growth of the diverging section length. In the present work, a free jet was considered, which did not reflect the cold spray process. Thus, the effect of the particle flow, the presence of the substrate and their consequences on the above-discussed phenomena should be taken into account for further investigations.

References

1. Ansys documentation section 2.7.4 (2012). ANSYS Inc
2. Alkhimov, A.P., Anatoly, N., Kosarev, V.F., Nesterovich, N.I., Shushpanov, M.M.: Gas-dynamic spraying method for applying a coating. 5302414 United States Patent (1994)
3. Grujicic, M., DeRosset, W.S., Helfritch, D.: Flow analysis and nozzle-shape optimization for the cold-gas dynamic-spray process. *J. Eng. Manuf.* **217**, 1603–1616 (2003)
4. Jen, T.-C., Li, L., Cui, W., Chen, Q., Zhang, X.: Numerical investigations on cold gas dynamic spray process with nano- and microsize particles. *Int. J. Heat Mass Transf.* **48**, 4384–4396 (2005)
5. Karimi, M., Fartaj, A., Rankin, G., Vanderzwet, D., Birtch, W., Villafuerte, J.: Numerical simulation of the cold gas dynamic spray process. *J. Therm. Spray Technol.* **15**(4), 518–523 (2006)
6. Li, W.-Y., Li, C.-J.: Optimal design of a novel cold spray gun nozzle at a limited space. *J. Therm. Spray Technol.* **14**(3), 391–396 (2005)
7. Li, W.-Y., Liao, H., Douchy, G., Coddet, C.: Optimal design of a cold spray nozzle by numerical analysis of particle velocity and experimental validation with 316L stainless steel powder. *Mater. Des.* **28**, 2129–2137 (2007)
8. Li, W.-Y., Zhang, C., Guo, X.P., Zhang, G., Liao, H.L., Li, C.-J., Coddet, C.: Effect of standoff distance on coating deposition characteristics in cold spraying. *Mater. Des.* **29**, 297–304 (2008)
9. Papyrin, A., Kosarev, V., Klinkov, S., Alkhimov, A.P., Fomin, V.: *Cold Spray Technology*. Elsevier Ltd., Netherlands (2007)
10. Pattison, J., Celotto, S., Khan, A., O’Neill, W.: Standoff distance and bow shock phenomena in the Cold Spray process. *Surf. Coat. Technol.* **202**, 1443–1454 (2008)
11. Samareh, B., Dolatabadi, A.: A three-dimensional analysis of the cold spray process: the effects of substrate location and shape. *J. Therm. Spray Technol.* **16**(5–6), 634–642 (2007)
12. Samareh, B., Stier, O., Luthen, V., Dolatabadi, A.: Assessment of CFD modeling via flow visualization in cold spray process. *J. Therm. Spray Technol.* **18**(5–6), 934–943 (2009)
13. Wilcox, D.C.: Formulation of the k-omega turbulence model revisited. *AIAA J.* **46**(11), 2823–2838 (2008)

Turbulent Combustion Modeling in Compression Ignition Engines

Mohamed Bencherif, Rachid Sahnoun and Abdelkrim Liazid

Abstract Reduction of pollutant emissions in diesel engines passes through a perfect knowledge and control of all phenomena related to combustion. This can be done by experimental observations and physical modeling for simulation of turbulent reactive flows using CFD tools. This paper presents a synthesis of numerical investigations performed for two direct injection diesel engines. The first one is a laboratory single-cylinder diesel engine and the second one is a serial turbocharged heavy duty diesel engine with six cylinders. Three combustion modeling approaches were used and computations were achieved using different versions of Kiva code. The first one uses the Westbrook combustion model with a one-step single kinetic reaction. The second approach is based on the generic chemical mechanism Shell coupled to the model of characteristic time of combustion. The last approach is based on modeling combustion-turbulence interactions using generalized PaSR concept. In the last approach a skeletal mechanism with 246 equations and 60 chemical species has been used. A set of simulations was carried out for five loads at 1500 rpm for the laboratory engine and 1400 rpm for the serial engine under partial load. Results and comments are presented and discussed.

1 Introduction

Combustion into diesel engines is controlled by simultaneous interactions of several physical and chemical processes. Indeed, it consists in a turbulent flow in which a diphasic fuel jet leads to the formation of a strongly exothermic reactive mixture.

M. Bencherif (✉)
USTO-MB, P.B. 1505 El M'naouer, Oran 31000, Algeria
e-mail: m_bencherif@yahoo.fr

R. Sahnoun · A. Liazid
LTE Laboratory, ENPO P.B.1523 El M'naouer, Oran 31000, Algeria
e-mail: r_sahnoun@yahoo.fr

A. Liazid
e-mail: ab-liaz@hotmail.fr

Table 1 Engines characteristics

Parameters	Specifications	
Engine type	Laboratory engine	Serial engine
Cylinder number	One cylinder	6 cylinders
Engine speed (RPM)	1500	1400
Maximal power (tr/min)	5.4 kW @ 1800	264 kW @ 2400
Piston diameter (mm)	95.25	120
Piston stroke (mm)	88.5	145
Connecting rod length (mm)	165	227
Injection angle (CAD)	-18°	-8°
Compression ratio	18:1	17:1
Engine loads (%)	20, 40, 60, 80 and 100	60

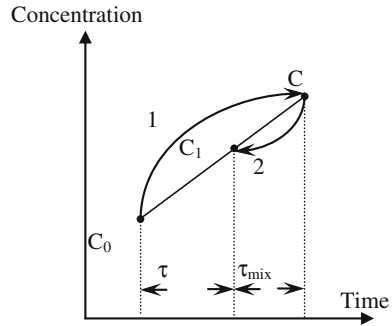
The interactions between the three aspects Combustion-Turbulence-Spray are determining for performances and emissions levels in diesel engines [1, 2]. Currently, simulation offers an interesting alternative for the prediction of performances and emissions of the internal combustion engines. It allows a better knowledge of the various processes brought into combustion chamber, the exploration of new solutions and the reduction of costs [3, 4].

In addition it was shown that knock phenomenon in spark ignited engines, auto-ignition process in compression ignited engines and in homogeneous charge engines are widely governed by reaction mechanism and thus chemical kinetics [5]. This work focuses on numerical simulation of turbulent combustion in direct injection diesel engines. A particular interest is related to the approaches of combustion modeling and the level of turbulence during combustion process. The characteristics of the considered engines are shown in Table 1.

2 Combustion Modelling and Simulation

In the present paper several versions of Kiva3v code were used. In fact, Kiva3v is the basic version developed by Amsden and O’rourke at Los Alamos National laboratory. It is one of the most used codes for reciprocating engine combustion simulation. The flow configuration in the combustion chamber is considered as three-dimensional and the transport equations [6] are resolved using the RANS formulation. The mesh generation is completed by several structured blocks. A Lagrangian-Eulerian approach is used in the code [6–9]. The structure of the two-phase jet with coalescence, breakup and evaporation of fuel droplets are

Fig. 1 Schematic PaSR concept [12]



provided by the famous *TAB* (Taylor Analogy Break-up) model developed by Reitz [10]. Illustrations of meshes related to each engine are shown in Fig. 1. Combustion model describes the source term of species Eq. (1) through the advancement rate of overall reaction to a step.

$$\frac{\partial \rho_i}{\partial t} + \nabla(\rho_i u) = \nabla \left[\rho D \nabla \left(\frac{\rho_i}{\rho} \right) \right] + f_i + \dot{\rho}_i^s \delta_{i1} \tag{1}$$

where ρ_i is the mass density of species i , ρ is the averaged mass density of the gas, u is the speed of the gas, f_i is the chemistry source term, $\dot{\rho}_i^s$ is the source term due to spray evaporation. Chemical species 1 and 2 correspond respectively to fuel and oxidant species. D is the mass diffusion coefficient issue from Fick's law.

Furthermore, the released version of the code (Kiva3v2r) includes new sub-models adapted by Valeri Golovitchev and Niklas Nordin [11–13] in order to use tabulated reaction mechanisms for more accurate and realistic combustion prediction. An approach based on the extension of Magnussen-Hjertager model (*EDC*) to a generalized *PaSR* model is integrated in Kiva3v2r code. The PaSR model is conceptually developed to achieve quantitatively the link between the sub-grid information and the computation cell level. In fact, the chemical characteristic time located at the sub grid scale, Fig. 1, is modeled by the physical characteristic time related to the turbulent scale $\tau_{mix} = C_{mix} \frac{k}{\epsilon}$. The detailed description of this approach can be found in the Ref. [12]. The main relation in this model is represented by the Eq. (2):

$$\frac{C_1 - C_0}{\tau} = \frac{C - C_1}{\tau_{mix}} = f_i(C) \tag{2}$$

As required by Golovitchev and Nordin, the appropriate turbulence model is the *RNG-kε* and n-heptane is a typical fuel recommended for simulating the combustion

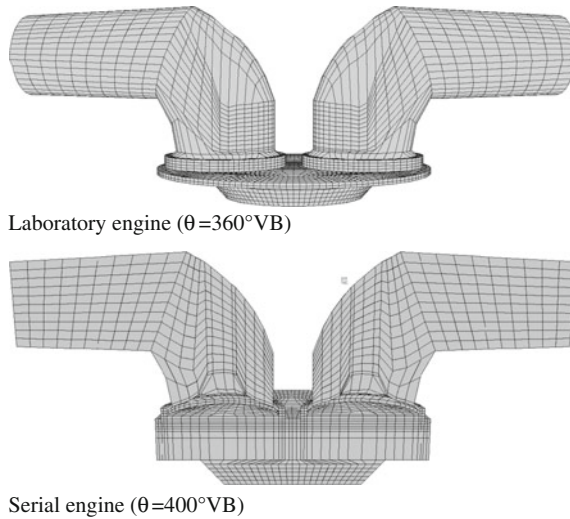


Fig. 2 Engines meshes

in diesel engines because its cetane number is approximately 56 which is similar to the cetane number of the conventional diesel fuels. The Fig. 2 represents the numeric 3D meshes of the engines.

The laboratory studies of the combustion kinetic in partially stirred reactors showed that at a temperature close 1000 K, H_2O_2 species decomposes as quickly as it appears which prevents the concentration of H_2O_2 to achieve an appreciable level to initiate auto-ignition [14].

For diesel engines the temperature reached just at injection timing is about 700 K. Indeed, at this temperature level the reaction mixture produces a small amount of heat which causes H_2O_2 decomposition and simultaneously the beginning of the combustion by ignition is observed [5, 14].

The reaction mechanism used in this work is the reduced mechanism of n-heptane. It is composed by a global equation and 245 coupled equations describing the kinetics of 60 reactive species [15]. The sub-models as well as the type of physical approach used for combustion modeling are summarized in Table 2.

Table 2 Sub-models and reaction mechanisms

Sub-models	Kiva3v standard	Kiva3v Shell-CTC	Kiva3v2r
Combustion	Westbrook	Shell /characteristic time	PaSR
Turbulence	k-ε	k-ε	RNG k-ε
Break-up	TAB	KH-RT	TAB
Reaction mechanism	1 Global equation	8 Generic equations [16]	Reduced mechanism of n-heptane [15]
Fuel	C ₁₂ H ₂₆ -C ₁₄ H ₃₀	C ₁₄ H ₃₀	C ₇ H ₁₆

3 Results and Discussions

The code calibration is achieved by the comparison between experimental of in-cylinder averaged pressure curves and those obtained by simulation. The Figs. 3, 4, 5 and 6 represent averaged evolutions of in-cylinder pressure, temperature and as well as CO₂, H₂O, CO and OH species obtained by the *Shell-CTC* and the

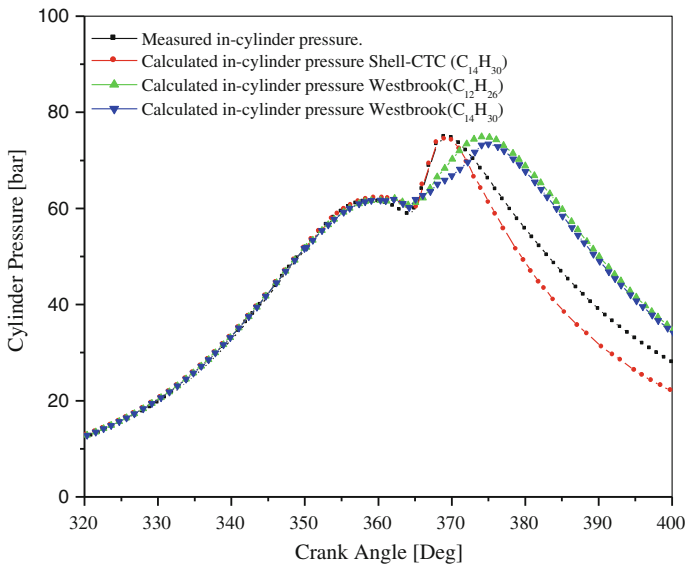


Fig. 3 Averaged in-cylinder pressure (serial engine)

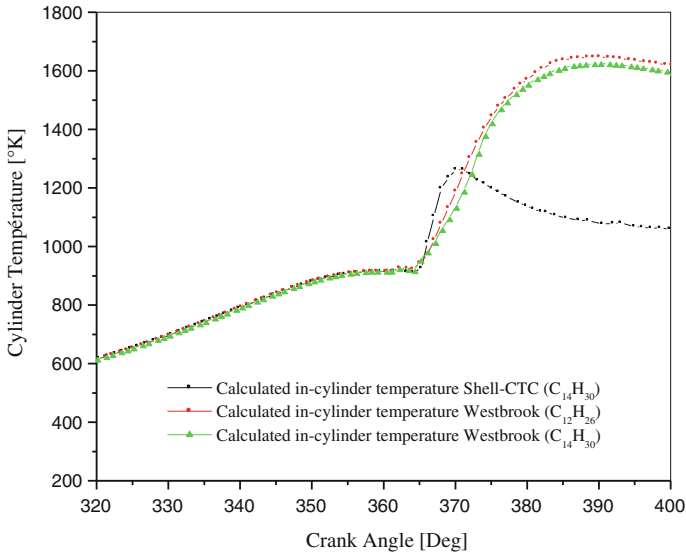


Fig. 4 Averaged in-cylinder temperature (serial engine)

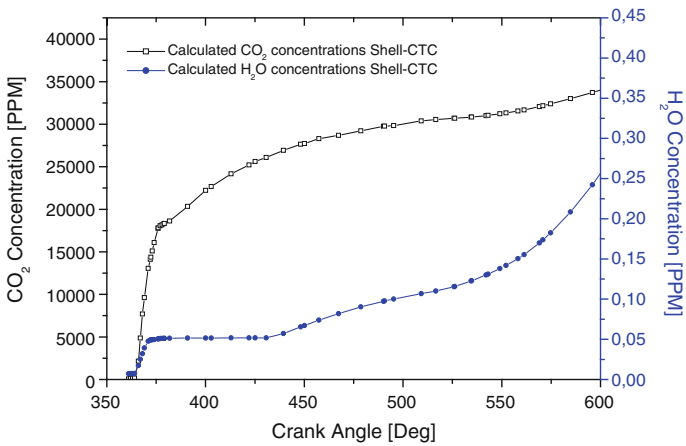


Fig. 5 CO₂ and H₂O concentration evolutions during combustion (serial engine)

Westbrook models. The Shell-CTC combustion model provides better predictions of in-cylinder averaged pressure during combustion process. Moreover, in-cylinder averaged temperature obtained by *Shell-CTC* combustion model is more realistic.

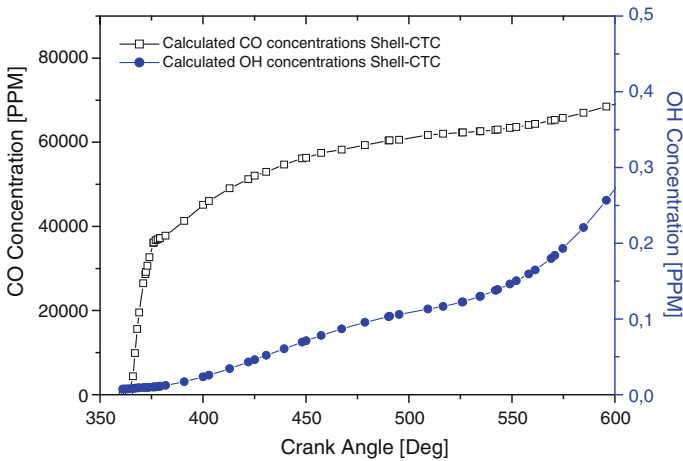


Fig. 6 CO and OH concentration evolutions during combustion (serial engine)

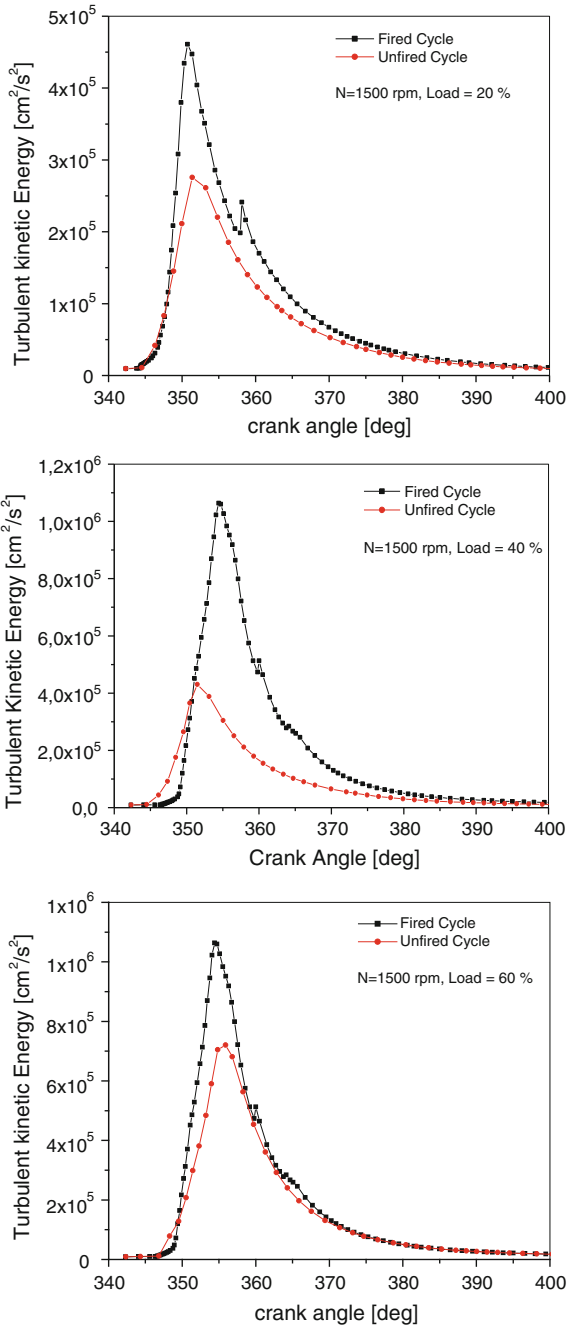
This is mainly due to that standard combustion model (*Westbrook*) with one step-one reaction does not consider the kinetic aspect of combustion and neglects dissociation of radicals and other intermediate species during the combustion which implicitly leads to an overestimation of average in-cylinder temperature. Thus, the standard model gives an incorrect interpretation of thermal levels and it is not capable to predict the evolution of the reaction mixture during combustion.

The Fig. 7 represents the turbulent kinetic energy evolutions for different loads corresponding to the laboratory engine for fired (using the *PaSR model*) and unfired cycles. It can be observed that the pic position of turbulent kinetic energy remains practically unchanged and it is located at the auto-ignition timing. This can permit to perform a correlation for auto-ignition delay using the empirical relationship (3) describing the turbulence intensity as a function of the average velocity of the engine piston proposed by Heywood [1].

$$\frac{\sqrt{k_{max}}}{S_p} = 243 e^{0.01(T/T_{max})} \tag{3}$$

Therefore, another way to estimate directly the time of auto-ignition can be provided with the maximum value of the turbulent kinetic energy as follows:

Fig. 7 Turbulent kinetic energy (laboratory engine)



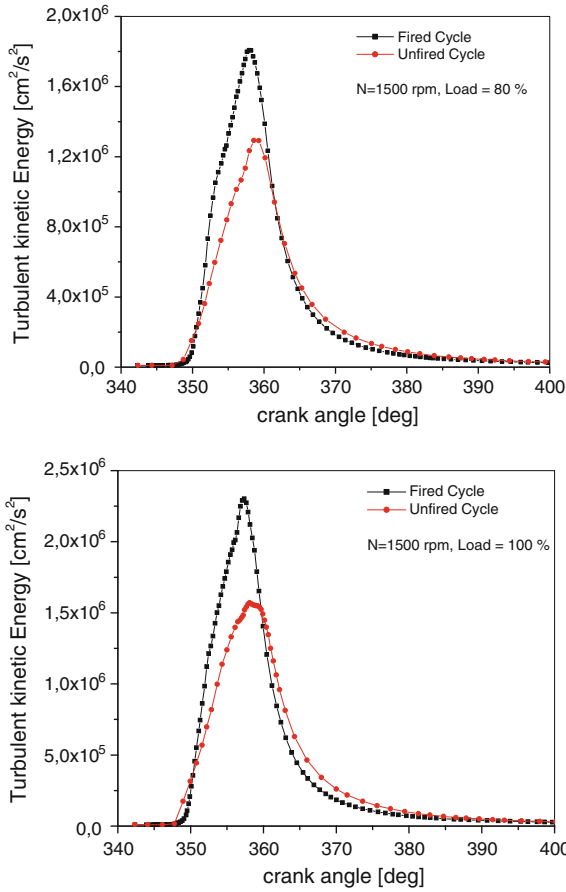


Fig. 7 (continued)

$$\tau_{id} = 0.065 \left[\frac{k_{max}}{(k_{max})_{full\ load}} \right] \tag{4}$$

Indeed, the above equations represent an attempt to estimate auto-ignition delay of the rapid combustion avoiding chemical and thermodynamic parameters (temperature, pressure and the activation energy). The confirmation of the previous relationship requires a greater number of engines testing which is a perspective.

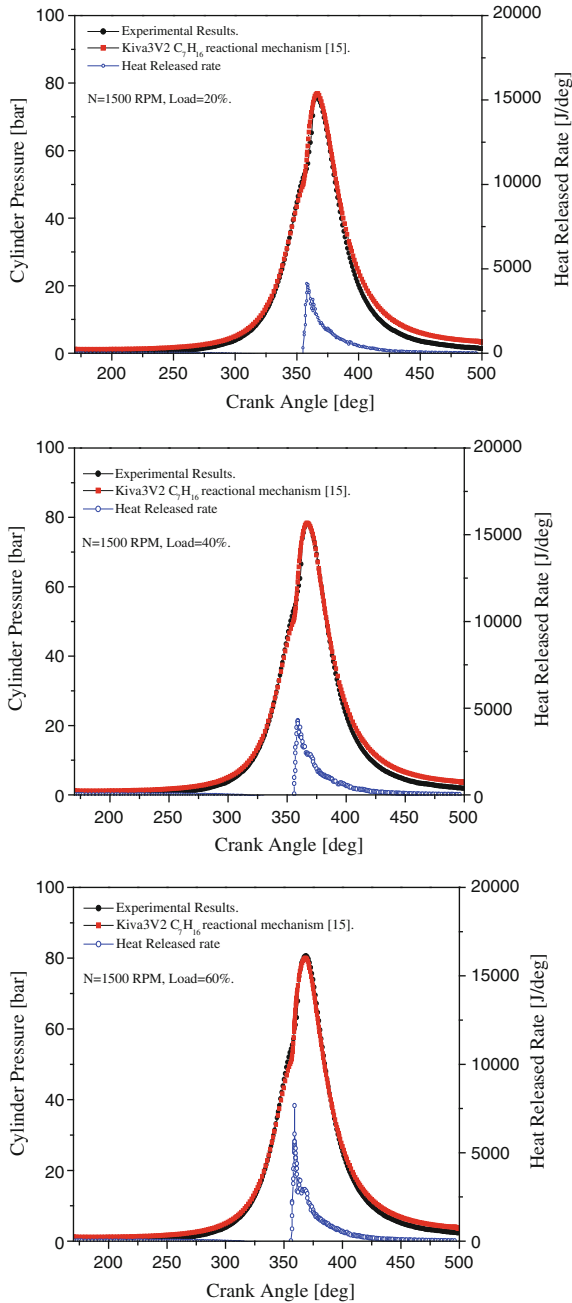


Fig. 8 Averaged in-cylinder pressure evolutions (laboratory engine)

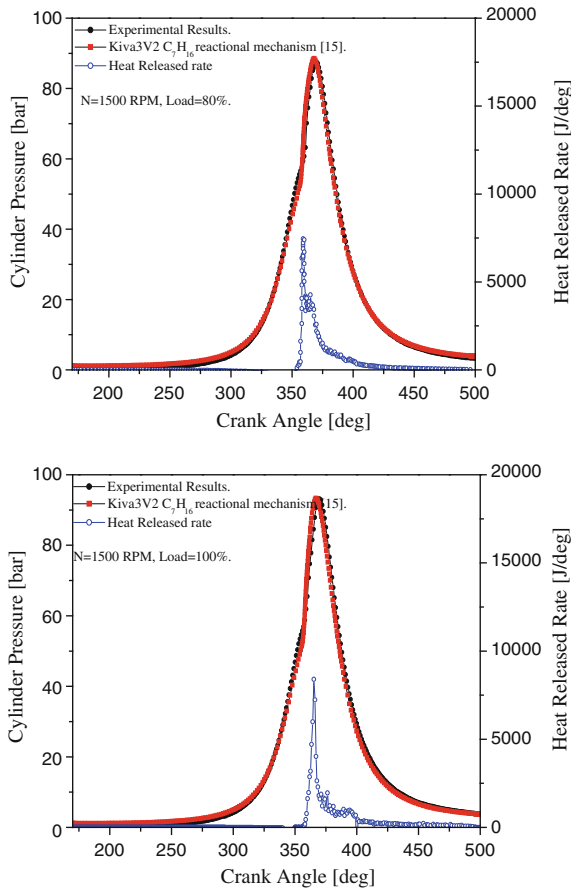
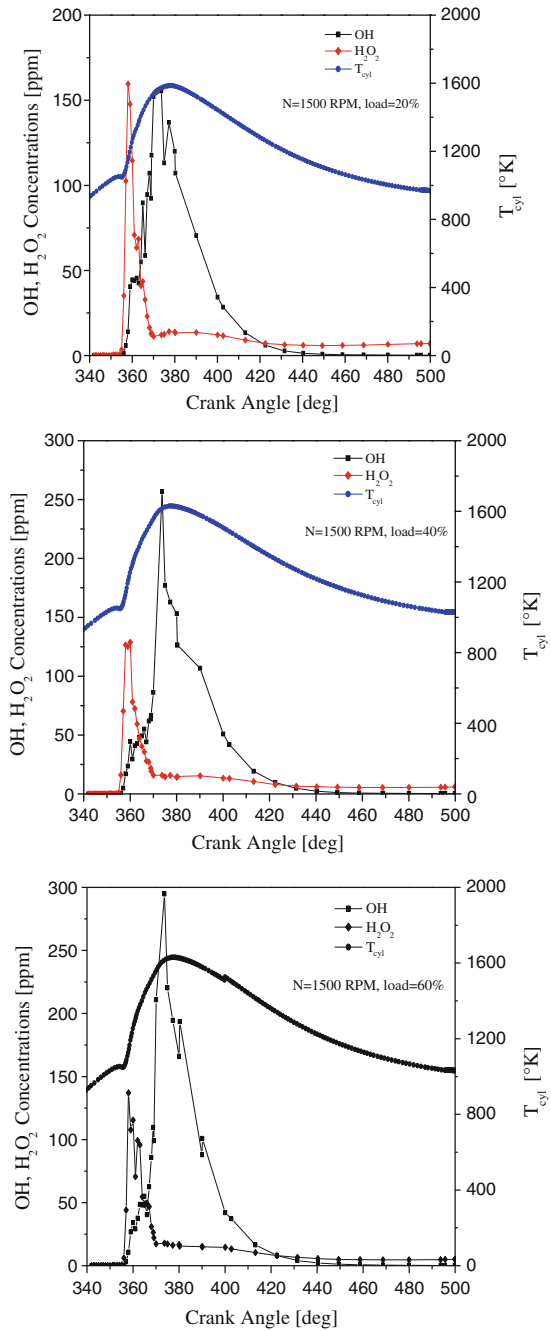


Fig. 8 (continued)

Figure 8 shows the computed (using *PaSR model*) and measured averaged in-cylinder pressures and heat released rate for all considered laboratory engine loads. A good agreement can be noticed between the measured pressures and those obtained by simulation during the compression before injection and during combustion. Also, it can be seen that heat released rate decreases after injection. This is mainly due to the evaporation of fuel.

Figure 9 represents the averaged in-cylinder temperature and calculated concentrations of OH and H₂O₂ evolutions for all loads obtained by the second reduced mechanism of n-heptane. As presented above, one can notice that, whatever

Fig. 9 Averaged in-cylinder temperature, OH and H₂O₂ concentrations (laboratory engine)



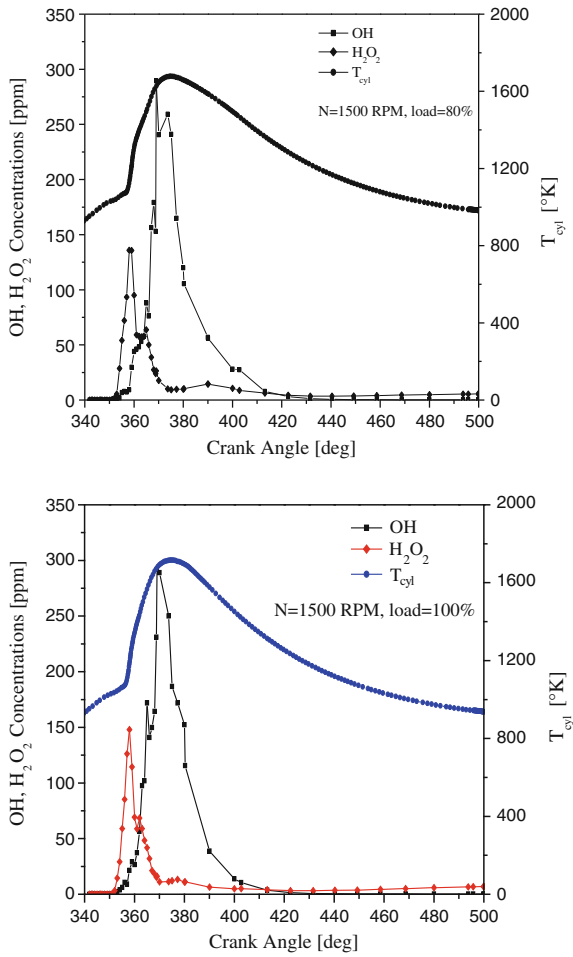


Fig. 9 (continued)

triggered exothermicity, the temperature levels are close 1000 K. This corresponds to the instant when the concentration of Per-hydroxide species H₂O₂ is quit sufficient to initiate combustion and coincides with the time when the heat release rate reaches its maximum. The same results are found for the serial turbocharged heavy duty diesel engine, Fig. 10.

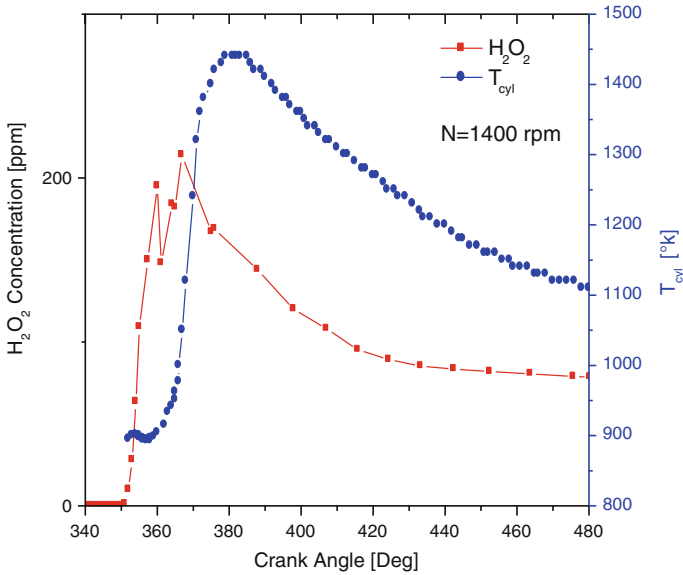


Fig. 10 Averaged in-cylinder temperature and H₂O₂ concentrations (serial engine)

4 Conclusion

This article summarizes numerical investigations of combustion in both experimental and industrial direct injection diesel engines. Three combustion modeling approaches were tested. The classical Westbrook model, the approach using the generic *Shell-CTC* model and finally the approach based on reduced kinetic mechanisms of n-heptane. All these approaches involve three versions of kiva3 code with the aim of predicting the evolutions of averaged in-cylinder pressure and temperature and averaged concentrations of some chemical species involved during the combustion phase. A comparison between results obtained by the Westbrook model and those obtained by the *Shell-CTC* model was presented.

The *Shell-CTC* model taking into account dissociation provides a better prediction of combustion as those obtained by the Westbrook combustion model. Based on the sub-model describing the combustion turbulence interactions proposed by Golovitchev and Nordin leading to a generalized PaSR concept, a correlation for auto-ignition delay estimation is obtained using an empirical relationship of the maximum value of the turbulent kinetic energy during combustion phase as a function of the mean speed of the engine piston. Otherwise, according to the literature [14] it is confirmed that the changes in concentrations of H₂O₂ species is directly related to the phenomenon of self-ignition in diesel engines.

References

1. Heywood, J.B.: *Internal Combustion Engine Fundamentals*. McGraw-Hill Inc, New York (1983)
2. Ramos, J.I.: *Internal Combustion Engine Modeling*. Hemisphere Publishing Corporation (1989)
3. Bencherif, M., Liazid, A., Tazzerout, M.: Pollution duality in turbocharged heavy duty diesel engine. *Int. J. Veh. Des.* **50**(1/2/3/4), 182–195 (2009)
4. Xiao, F., Liu, C., Karim, G.: The 3D simulation with detailed chemical kinetics of the turbulent combustion a pre-chamber indirect injection diesel engine. In: 7th International Conference on CFD in the Minerals and Process Industries CSIRO, Melbourne, Australia. 9–11 December 2009
5. Westbrook, C.K.: Chemical kinetics of hydrocarbon ignition in practical combustion systems. In: *Proceeding of the Combustion Institute*, vol. 28, pp. 1563–1577 (2000)
6. Amsden, A.A., O'Rourke, P.J., Butler, T.D., KIVA-II: A Computer Program for Chemically Reactive Flows with Sprays. LA-11560-MS. Los Alamos National Laboratory, Los Alamos (1989)
7. Amsden, A.A.: KIVA-3: A KIVA Program with Block-structured Mesh for Complex Geometries. Technical Report, Los Alamos National Laboratory, LA-12503-MS (1993)
8. Amsden, A.A.: KIVA-3 V: A Block-structured KIVA Program for Engines with Vertical or Canted Valves. Technical Report, Los Alamos National Laboratory, LA-13313-MS (1997)
9. Amsden, A.A.: KIVA-3 V: Released 2, Improvements to Kiva-3v. Technical Report, Los Alamos National Laboratory, LA-13608-MS (1999)
10. Reitz, R.D., Rutland, C.J.: Development and testing of diesel engine CFD models. *Prog. Energy Combust. Sci.* **21**, 173–196 (1995)
11. Golovitchev, V., Nordin, N.: 3-D KIVA simulations using new detailed chemistry diesel spray combustion model. In: Presented at the Workshop Combustion Modeling in I.C.E., Cassino, Italy. 14–15 December 1999
12. Golovitchev, V.I., Nordin, N., Jarnicki, R., Chomiak, J.: 3-D Diesel Spray Simulations Using a New Detailed Chemistry Turbulent Combustion Model. SAE 00FL-447 (2000)
13. Golovitchev, V.I., Nordin, N., Tao, F.: Modelling of Spray Formation, Ignition and Combustion in Internal Combustion Engines. Chalmers University of Technology, Department of Thermo and Fluid Dynamics. ISSN 1101-9972, Annual Report, Göteborg, December 1998
14. Westbrook, C.K., Pitz, W.J., Herbinet, O., Curran, H.J., Silke, E.J.: A Detailed Chemical Kinetic Reaction Mechanism for n-Alkane Hydrocarbons From n-Octane to n-Hexadecane. *Combustion and Flame*, LLNL-JRNL-401196, February 11, 2000
15. Site Web: www.tfd.chalmers.se/_nordin/KJS/Patches/D'tailed Chemistry, 2003
16. Bencherif, M., Liazid A.: Modélisation et Simulation de la Combustion dans un Moteur Diesel à Injection Directe à l'aide du Modèle Shell-CTC. In: *Proceedings of 1st International Conference on Aeronautics Sciences (ICAS'01)*, USTO-MB, Oran, Algeria, 27–28 Mai, 2013

On the Thermal Characterization of a Fire Induced Smoke-Layer in Semi-confined Compartments

Abdallah Benarous, Souhila Agred, Larbi Loukarfi
and Abdelkrim Liazid

Abstract The present work deals with a comparative study on various methods for thermal characterisation of a fire-induced smoke layer. A focus is made on models predicting both excess temperature and mean thickness of the smoke layer. These models are either thermodynamic based model, dynamic based-model or experimental based-model. According to the considered models, a preliminary dimensioning is performed for smoke and heat evacuation systems (SHEVS). The obtained results are discussed and confronted with those provided by thermodynamic calculations based on US and European standards.

List of Symbols

A_i, A_{NV}^t	Ventilation area
c, c_p	Specific heat, calorific specific capacity at constant pressure
C_e, C_i, C_V	Thermodynamic model constants
g	Sea level gravity
H	Ceiling height
\dot{h}	Instantaneous thermal release rate
K	Mc Caffrey model constant
\dot{m}, \dot{M}	Mass flow rate
p	Hydrodynamic pressure
P_f	Pool fire perimeter
\dot{Q}, \dot{Q}_c	Fire heat release rate (HRR), Convective part of HRR
r	Radial distance from the fire axis
T	Static temperature
V	Volume

A. Benarous (✉) · S. Agred · L. Loukarfi
Department of Mechanical Engineering, Hassiba Benbouali University, Chlef, Algeria
e-mail: a.benarous@univ-chlef.dz

S. Agred · L. Loukarfi
LCEMSM Laboratory, Hay Essalem, Chlef, Algeria

A. Liazid
LTE Laboratory, National Polytechnic School (E.N.P), Oran, Algeria

\vec{v}	Velocity vector
Z, z_0	Vertical distance, virtual fire source height
η	Mc Caffrey model constant
γ	Smoke isentropic ratio
ρ	Density
Π	Dynamic pressure
∞	Ambient (fresh air) conditions
NV	Natural ventilation
S	Smoke conditions
Steady	Steady state conditions

Acronyms

FDS	Fire Dynamic Simulator
LES	Large Eddy Simulation
NIST	National Institute of Standards and Technology
RANS	Reynolds Averaged Navier-Stokes
SHEVS	Smoke and Heat Evacuation Systems

1 Introduction

Fire engineering is a field that lies on a common interface between reactive flows, heat transfer and structural mechanics. This field has crossed the boundaries of academic research to establish itself as a fundamental prerequisite in the profession exercise for fire fighters, building engineers and industrial safety policies [1]. Fire safety engineering strategies are specifically managed at the design step of industrial infrastructure, public buildings (ERP) as well as collective homes. The complex and coupled phenomena involved in fire engineering require not only experimental investigations but also multiphysics modelling in order to ensure safety for people and reliability for structures. In this context, particular attention is paid to thermal and dynamic characterization of smoke flows that unlike flames are not localized but contribute to heat and toxic gases spreading. It is also important to know how to carry out predictive calculations for SHEVS in order to evacuate or at least, to control the flow of these substances. Owing to the permanent competitiveness between buoyancy and inertial force, both natural and mechanical ventilation are required to achieve a global design for SHEVS. Regarding engineering aspect, calculations are still based on thermodynamic models (OD) that are currently established according to continental standards (USA, EU) [2].

These methods are not very suitable for fire resistance studies of structures, but have the advantage of predicting the thermal field (temperature, average thickness) of the smoke layer and the characteristic dimensions of SHEVS [3]. As for smoke dynamics, several correlative models were developed to characterize both fire-induced plumes [4–6] and ceiling jets [7–9] in stationary regimes.

For transient conditions describing flashover or extinction phases, thermodynamic based-models called ‘zone models’ have been developed for characterizing the hot layer, which is supposed to be installed above an interface that lies under the ceiling [10].

Dynamic based-models called ‘Field models’ are based on numerical solution of the Navier-Stokes turbulent equations. They provide spatial and temporal informations (3D) that remain highly dependent on boundary conditions imposed at the domain limits. For thermal characterization of smoke layer, the available literature does not sufficiently provide studies for comparative analysis between models. It seems that there are no academic works devoted to SHEVS design procedures based on non-thermodynamic models.

This work is a numerical attempt towards providing some answers on SHEVS-smoke interaction. In the case of a large compartment subjected to 02 MW standard fire, the models are firstly used to predict both excess temperature and mass flow rate within the hot layer. Thermal data are then used to perform a preliminary design of SHEVS in a natural ventilation configuration. For practical use, the models are automated as Matlab routines and implemented within a set of graphical user interfaces (GUI). The developed software also provides several links between thermodynamic and correlative models while it allows an automatic generation of input files for the fire dynamic simulator (FDS) solver.

2 Smoke Layer Modelling

2.1 Thermodynamic Model

For a prescribed heat release rate \dot{Q}_c , mass flow rate of the smoke can be expressed as [2]:

$$\dot{M}_s = \frac{\dot{Q}_c}{c\Delta T} \quad (1)$$

where c , $\Delta T = T_s - T_\infty$ refer respectively to specific heat and excess temperature of the smokes. Buoyancy forces lead to stratification, such that the smoke layer is situated at a distance Y_s from the floor, given by [2]:

$$Y_s = (\dot{M}_s / C_e P_f)^{2/3} \quad (2)$$

The mean thickness δ_s of the smoke layer can be deduced as:

$$\delta_s = H - Y_s \quad (3)$$

To allow for a natural smoke evacuation, a ventilation area A'_{NV} featuring several holes is explicitly expressed with European standard, whereas it requires an implicit calculation for the US norm [2]:

$$A'_{NV}C_v = \frac{\dot{M}_s T_s}{\sqrt{2\rho_\infty^2 g \delta_s T_\infty \Delta T - \frac{\dot{M}_s^2 T_s T_\infty}{(A_i C_i)^2}}} \quad (4)$$

$$A'_{NV}C_v = \frac{\dot{M}_s}{\rho_\infty} \sqrt{\frac{T_s^2 + \left(\frac{A'_{NV}C_v}{A_i C_i}\right)^2 T_\infty T_s}{2g \delta_s T_s \Delta T}} \quad (5)$$

C_v, C_i denote respectively discharge coefficients for ventilation openings and fresh air inlets (gates, windows).

2.2 Zone Models

For the stratified layer, temporal evolution of the static temperature is believed to obey an ordinary differential equation (ODE) [10]:

$$\frac{dT_s^{Zone}}{dt} = \frac{1}{C_p \cdot \rho_s \cdot V_s} \left((\dot{h}_s - \dot{C}p \cdot \dot{m}_s \cdot T_s^{Zone}) + V_s \frac{dp}{dt} \right) \quad (6)$$

The terms h_s, V_s, m_s refer respectively to thermal release rate, volume and mass of the hot gases. The static pressure evolution is modelled as [10]:

$$\frac{dp}{dt} = \frac{\gamma - 1}{V_s} \dot{h}_s + \dot{h}_\infty \quad (7)$$

where \dot{h}_∞ denotes thermal release rate due to fresh air. The previous equation was derived from an isotropic thermal assumption within the smoke layer thickness.

2.3 Correlative Models

Inside the *ISO-834* standard for fires, static temperature of the hot layer is a time dependent quantity, which is given by [1]:

$$T_s^{ISO}(t) = T_\infty + 345 \text{Log}_{10}(8t + 1) \quad (8)$$

For flows induced by smoke plumes, excess temperature as well as smoke flow rates, can be evaluated from one of the following sub-models:

Zukoski model [6]:

$$\Delta T = 5.0 \left(\frac{T_\infty}{g C_p^2 \rho_\infty^2} \right)^{\frac{1}{3}} \dot{Q}_c^{\frac{2}{3}} \cdot Z^{-\frac{5}{3}} \tag{9a}$$

$$\dot{M}_s = 0.2 \left(\frac{\rho_\infty^2 g}{C_p T_\infty} \right)^{\frac{1}{3}} \dot{Q}_c^{\frac{1}{3}} Z^{\frac{5}{3}} \tag{9b}$$

Heskestad et al. model [4]:

$$\Delta T = 9.1 \left(\frac{T_\infty}{g C_p^2 \rho_\infty^2} \right)^{\frac{1}{3}} \dot{Q}_c^{\frac{2}{3}} (Z - z_0)^{-\frac{5}{3}} \tag{10a}$$

$$\dot{M}_s = 0.071 \dot{Q}_c^{\frac{1}{3}} (Z - z_0)^{\frac{5}{3}} + 1.92 \cdot 10^{-3} Q_c \tag{10b}$$

Mc Caffrey model [5]:

$$\Delta T = 9.1 \left(\frac{K}{0.9 \sqrt{2g}} \right)^2 \left(\frac{Z}{\dot{Q}_c^{\frac{2}{3}}} \right)^{2\eta-1} T_\infty \tag{11}$$

As the plume impinges the ceiling, a radial development from the fire axis is observed on the smoke flow. The stratified flow occurs under the ceiling while yielding to a radial gradient for the smoke temperature. Here the maximum temperature in the ceiling vicinity T_s^{\max} can be predicted from one of the following sub-models:

- Alpert model [7]:

$$\begin{aligned} T_s^{\max}(r) &= T_\infty + 16.9 \dot{Q}_c^{\frac{2}{3}} \cdot (H - z_0)^{-\frac{5}{3}}; \quad r \leq 0.18H \\ T_s^{\max}(r) &= T_\infty + 5.38 \frac{\dot{Q}_c^{\frac{2}{3}}}{r} \cdot (H - z_0)^{-1}; \quad r > 0.18H \end{aligned} \tag{12}$$

- Cooper model [8]:

$$T_s^{\max}(r) = T_\infty + 5.77 \dot{Q}_c^{\frac{2}{3}} H^{-\frac{5}{3}} \left(\frac{r}{H} \right)^{-0.88} \tag{13}$$

- Revisited Alpert model [9]:

$$T_s^{\max}(r) = T_\infty + 6.721 \dot{Q}_c^{\frac{2}{3}} \frac{1}{H - z_0} \left(\frac{r}{H - z_0} \right)^{-0.6545} \quad (14)$$

2.4 Field Models

In such models, mass-weighted (*Favre*) decomposition of Navier-Stokes, energy and species transport equations can either be treated according to *RANS* approaches where all turbulence scales are modelled, or filtered for *LES* resolution where large scales are simulated. When smoke is considered as a perfect gas deprived from compressibility effects, continuity and momentum equations can be rearranged to derive a Poisson equation for the dynamic pressure [12]:

$$\nabla^2 \Pi = \Psi(u, v, w, \rho); \quad \Pi = p / \rho_\infty + (1/2) |\vec{V}|^2 \quad (15)$$

Several fluid dynamic solvers (as *NIST-FDS*) use the previous equation to predict firstly the dynamic pressure and the velocity components followed by the temperature and density. Other solvers (as *Ansys-Fluent*) still continue to use pressure-velocity coupling strategies.

3 Results and Discussions

The application case considered in this work is a large compartment, with 24 m length, 24 m width and 12 m height [11]. The compartment features four (4) gates (10 m × 2 m) and is subjected to a 2 MW fire of category 2 (2 m × 2 m) located in its middle (Fig. 1).

As correlative models as well as *SHEVS* design relations are mainly based on stationary considerations, it is important to predict a relaxation time for which thermal stratification would be timely independent. As depicted in Fig. 2a, b, temporal evolution of the smoke temperature reveals a stationary-like behaviour from $t_{Steady}^{Zone} = 4200$ s in the case of the *CFAST* zone model while it requires $t_{Steady}^{ISO834} = 4800$ s (80 min) for the *ISO-834* standard.

FDS computations predict also a thermal stratification on a point-sensor located 20 cm beneath the ceiling. The corresponding relaxation time for static temperature was evaluated at $t_{Steady}^{FDS} = 4600$ s [12]. Towards a *SHEVS* design strategy, it is important to consider either the excess temperature ΔT_s , or a mean value of the

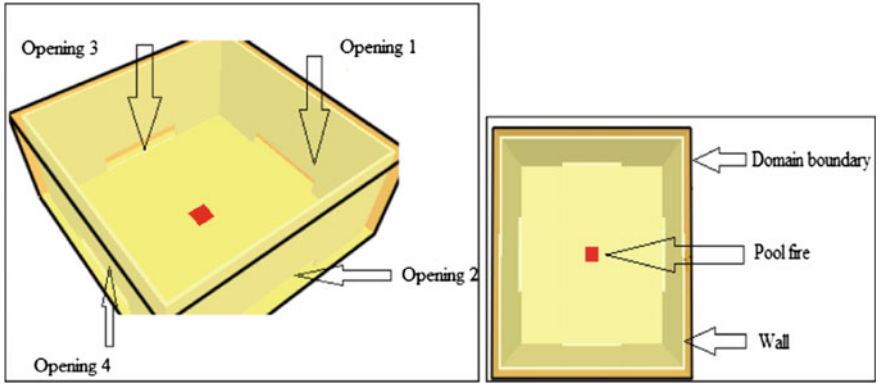


Fig. 1 3D representation of the compartment

Fig. 2 a Temperature evolution according to ISO-834. b Stratification temperature as predicted by a zone model (CFAST)

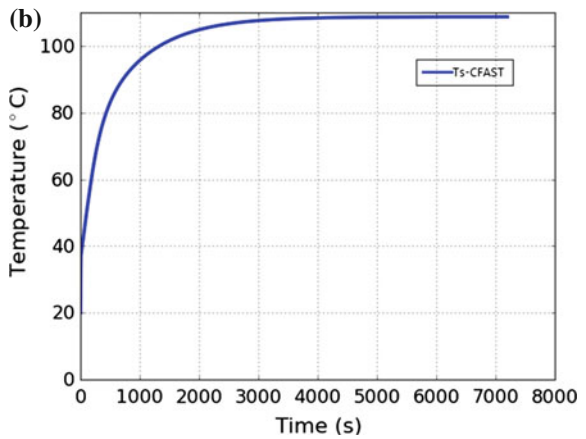
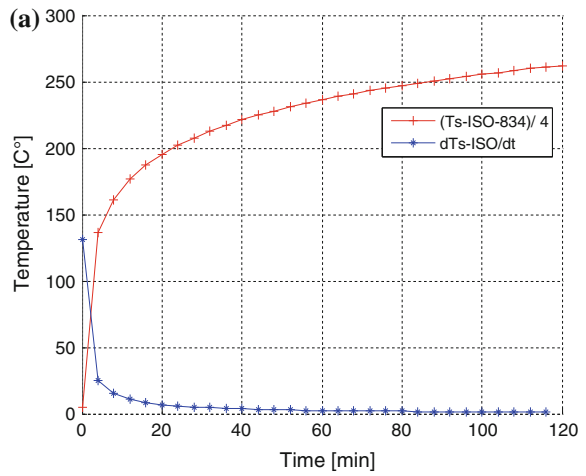
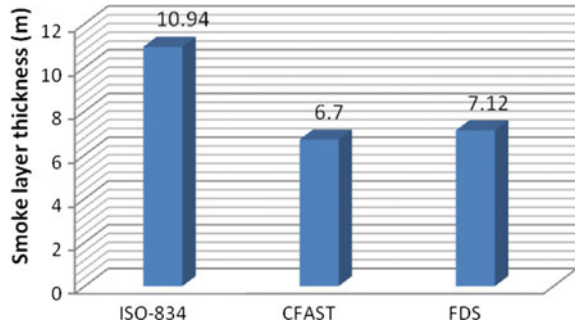


Fig. 3 Mean thickness of the smoke layer



smoke thickness δ_s . The first procedure is more realistic since most of models provide spatial or temporal evolution of the static temperature.

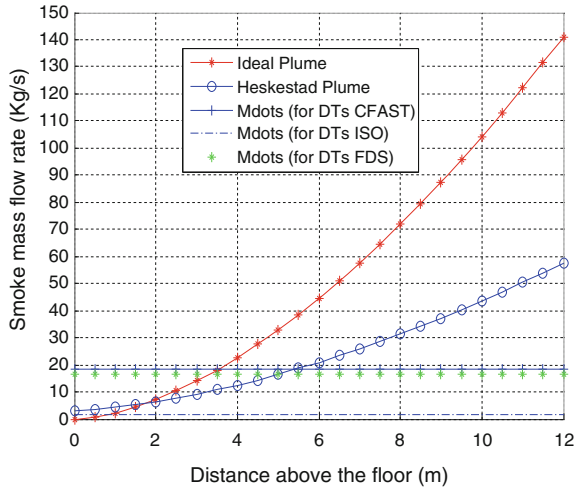
Let us take a prescribed value for the excess temperature as predicted by the standard (*ISO-834*), the *CFAST* (zone model) and the *FDS* (field model) formulations. This coupling process between manual calculations and modeling, will design the *SHEVS* on different considerations than those relating to thermodynamic models [13]. Excess temperatures as predicted by the previous models, are respectively $\Delta T_s^{ISO834} = 968^\circ\text{C}$, $\Delta T_s^{CFAST} = 88^\circ\text{C}$ and $\Delta T_s^{FDS} = 97^\circ\text{C}$, they are mandatory for predicting mean thickness of the stratified layer. It is noticed that *ISO-834* formulation provides a non realistic value ($>900^\circ\text{C}$) for the smoke temperature.

This result is due to the lack of considering the smoke dilution by fresh air in the *ISO-834* formulation. Furthermore, *ISO-834* standard contains no spatial variable and assumes an absolute homogeneity of the temperature. This obviously makes the formulation inappropriate to predict the thermal stratification phenomenon. By imposing the previous excess temperatures, several values for the mean smoke thickness are depicted in Fig. 3.

It should be noticed that the mean thickness $\delta_s^{Zone} = 8.4\text{ m}$ was predicted by solving an *ODE* in the zone model formulation, Eq. (6). One notices that the thickness recovered by *ISO-834* standard exhibits a huge overestimation with regards to ceiling high $H = 12\text{ m}$ and therefore, cannot be considered for design calculations. When imposing a constant value for the smoke temperature $T_s^{CFAST} = 108^\circ\text{C}$, the corresponding mean thickness $\delta_s^{CFAST} = 6.7\text{ m}$ seems slightly lower ($\sim 20\%$) than that predicted value from a zone model calculation. As predicted by a field model computation, the mean thickness $\delta_s^{FDS} = 7.1\text{ m}$ remains more realistic since stratification is fully considered and no assumption is issued on thermal homogeneity.

The discrepancy noticed between excess temperature values directly affects the prediction of smoke flow rates. Indeed, it is noticed that for a prescribed heat release rate, smoke mass flow rates are inversely proportional to the temperature rise (Fig. 4). As expected, the smoke flow rate as predicted by the *ISO-834* standard seems non realistic (1.65 kg/s) according to the compartment dimensions and the fire heat release rate (02 MW). It is also worthy noticing that the thermodynamic

Fig. 4 Evolution of the smoke flow rate



models involved in European and US standards, predict several values for the smoke flow rate which are constant and do not relate to the elevation from the floor. This tendency is obvious since no spatial information is required to evaluate excess temperatures within thermodynamic formulations.

A slight discrepancy (~9 %) is noticed between the smoke flow rate values predicted by means of *CFAST* and *FDS* models since both formulations account for smoke dilution by fresh air. In fact, smoke flow rates evaluated by correlative formulations show a proportional tendency to the vertical distance above the floor. This behavior can be related to the physical trend of these models which account for air entrainment by the plume while it develops in the vertical direction.

For the Heskestad plume model, fire dimensions are considered via the virtual source height z_0 while radiative losses are accounted thanks to the convective part \dot{Q}_c of the fire heat release. Consequently, at a prescribed elevation above the floor, the corresponding smoke flow rate is lower than that predicted by the Zukoski (ideal) model, Eq. (9a and b). For SHEVS design purposes, it is important to notice that the overall equivalence ratio, as defined by Mc Grattan et al. is $\phi = 0.11$ [14]. This value means that the compartment is under ventilated and an additional evacuation is mandatory for smoke clearance. Figure 5 depicts global ventilation area required for a naturally evacuation strategy of the compartment. Area values allow for the prediction of either number or dimensions of the natural ventilation openings.

On a basis of a combined *SHEVS* design procedure, involving thermodynamic calculations of excess temperature with plume-based calculations of smoke flow rates, one can bring out several cases regarding ventilation area prediction (Fig. 5). Owing to an important under estimation of ventilation area, the *ISO-834* cannot be considered in such design procedure. The Zukoski (ideal) plume model in which the excess temperature is provided from *CFAST* or *FDS* approaches, recovered a quite

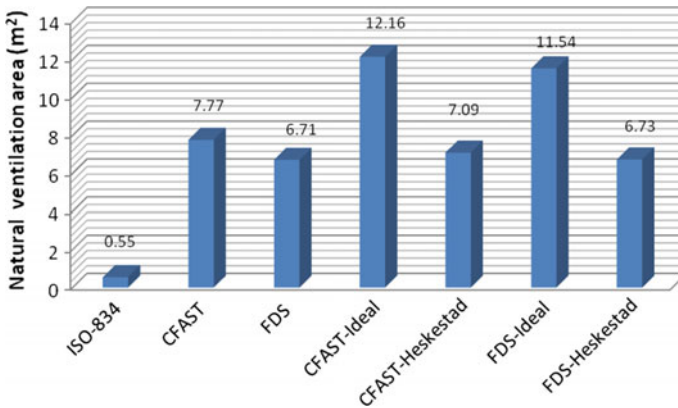


Fig. 5 Minimum number of the ventilation openings

high value $A_{NV} = 11 \text{ m}^2$ for the ventilation area. In fact, the Heskestad plume model combined with *CFAST* or *FDS* thermal calculations seems more adequate for *SHEVS* design since it predicts a value $A_{NV} \approx 7 \text{ m}^2$ for the ventilation area that is quite close to that estimated by standard calculations.

4 Conclusion

In the present work, several modelling strategies were investigated in the aim of characterizing the thermal behaviour of a smoke layer. A large compartment was considered as an application case. Special emphasis was made on numerical values for excess temperature, smoke layer thickness and mass flow rates. Combining input data as well as output values for state variables of the different models, it reveals that for the studied case, zone model and field model are well suited for thermal prediction within the hot layer. Furthermore, the Heskestad plume model succeeds in recovering realistic dimensions for *SHEVS* elements in a naturally ventilation case.

References

1. Purkiss, J.A.: Fire Safety Engineering: Design of Structures, 2nd edn. Butterworth-Heinemann Publications (2007)
2. Merci, B., Van Maele, K.: J. Fire safety **43**, 495–511 (2008)
3. Merci, B., Shipp, M.: J. Fire safety **57**, 3–10 (2013)
4. Heskestad, G., Delichatios, M.A.: The Initial Convective Flow in Fire. The combustion Institute, Pittsburg, USA, pp. 1113–1123 (1978)

5. Mc Caffrey, B.J.: Purely Buoyant Diffusion Flames: Some Experimental Results. NBSIR 79-1910, National Bureau of Standards (1979)
6. Zukoski, E.E., Kubota, T.B.: *Fire Saf. J.* **3**, 107–121 (1980)
7. Alpert, R.L.: *Fire Technol.* **8**, 181–195 (1972)
8. Cooper, L.Y.: Ceiling Jet-Driven Wall Flows in Compartment Fires, NBSIR 87 - 3535 (1987)
9. Alpert, R.L.: the fire-induced ceiling-jet revisited. In: 5th FireSeat Symposium, Edinburgh, Scotland (2011)
10. Peacock, R.D, Forney, G.P, Reneke, P.A.: CFAST: A Consolidated Model for Fire Growth and Smoke Transport, NIST Technical Report No.1026 R1, USA
11. Yu, D, LiG, Q.: *Fire Saf. J.* **54**, 113–120 (2012)
12. Tahri, F.Z.: Smoke Movements Analysis Within Semi-Confined Compartments: A Correlative-CFD Comparison, Master Thesis in Mechanical Engineering, Hassiba Benbouali University, Chlef, Algeria (2015)
13. Agred, S., Benarous, A., Loukarfi, L., Naji, H.: *Nat. Technol. Rev. (ISSN 2437-0312)*, Issue C-13, 23–27 (2015)
14. Mc Grattan, K., Myers, T.: A way to characterise the range of validity of a fire model. In: Proceeding of Fire and Evacuation Modelling Conference, Maryland, USA (2011)

Numerical Study of Twin-Jets Impinging Against a Smooth and Flat Surface

Rachid Sahnoun and Abdelkrim Liazid

Abstract The present study is focused on the analysis of the statistical quantities (mean and rms quantities) of the dynamical field along the central axis of a twin-jets impingement against a flat and smooth surface without recirculation. The study is achieved using the RANS approach associated with the popular turbulence model ($k - \epsilon$). The jet opening ratio is $H/e = 10$ and the Reynolds Number $Re = 14000$. The results are compared to those of experimental measurements found in the literature. The model exhibits good agreement with the experimental data. Some discussions are performed.

1 Introduction

Impinging jets are frequently found in several industrial applications because of their highly localized heat and mass transfer, compared with those achieved for the same amount of fluid flowing parallel to the object surface. Air curtains are separation devices based on the discharge of a plane air stream to isolate from each other two adjacent air volumes with different climatic characteristics. Most of the time, air-curtains consist of one or several jets blown vertically or obliquely downwards. After the jet hits the floor, the supplied air simply spills into the regions on either side of the jet. In many cases, the geometrical aspect ratio of the rectangular discharge nozzle is such that air curtains may be regarded as two-dimensional plane jets. Gupta [1] Investigated smoke confinement in tunnels studying the air curtain by means of *PIV* measurement. Loubière, Pavageau, Gupta and others [2–5] have analyzed the structures in jet development for various geometrical and cinematic configurations, using Particle Image Velocimetry (*PIV*). The purpose of this study is to simulate the twin-jets air impinging against a fixed smooth and flat surface

R. Sahnoun (✉) · A. Liazid (✉)
LTE, ENP – Oran, BP 1523 El-M'naouer, 31000 Oran, Algeria
e-mail: r_sahnoun@yahoo.fr

A. Liazid
e-mail: ab-liaz@hotmail.fr

using the RANS approach associated with the classical turbulence model ($k - \varepsilon$) model. The study is performed in 2D dimensional space. The dimension of the computational domain adopted is the same given by experimental [1]. The results are expected to reveal the detailed flow structure.

2 Basic Equations and Method of Solution

The jet flow characteristics are governed by the well-known balance equations of mass and momentum.

2.1 Mathematical Formulation

The average continuity and momentum equations for incompressible flow are:

$$\frac{\partial \bar{u}_i}{\partial x_i} = 0 \quad (1)$$

$$\frac{\partial \bar{u}_i}{\partial t} + \frac{\partial}{\partial x_j} (\bar{u}_i \bar{u}_j) = - \frac{\partial \bar{p}}{\partial x_i} - \frac{\partial \tau_{ij}}{\partial x_j} + \frac{1}{R_e} \frac{\partial^2 \bar{u}_i}{\partial x_i \partial x_j} \quad (2)$$

with:

$$R_e = \frac{U_0 \cdot e}{\vartheta} \quad (3)$$

Based on the Boussinesq assumptions, the turbulent stresses are expressed according to the mean velocity using the turbulent viscosity μ_t . The components of the modeled turbulent stresses are expressed according to the linear deformation as:

$$\tau_{ij} = -\rho \cdot \overline{u_i u_j} = \mu_t \left(\frac{\partial \bar{u}_i}{\partial x_j} + \frac{\partial \bar{u}_j}{\partial x_i} \right) \quad (4)$$

Applying the same approach as the mixing length model, we specify the turbulent viscosity as:

$$\mu_t = C_\mu \rho \frac{k^2}{\varepsilon} \quad (5)$$

The selected standard ($k - \varepsilon$) model [6] is described by two equations. The first one is for the turbulent kinetic energy k and the second one is for the dissipation rate ε .

$$\frac{\partial(\rho k)}{\partial t} + \frac{\partial(\rho k U_i)}{\partial x_i} = - \frac{\partial}{\partial x_j} \left[\left(\mu + \frac{\mu_t}{\sigma_k} \right) \frac{\partial k}{\partial x_j} \right] + \mu_t \left(\frac{\partial U_i}{\partial x_j} + \frac{\partial U_j}{\partial x_i} \right) \frac{\partial U_i}{\partial x_j} - \rho \varepsilon \quad (6)$$

$$\frac{\partial(\rho \varepsilon)}{\partial t} + \frac{\partial(\rho \varepsilon U_i)}{\partial x_i} = - \frac{\partial}{\partial x_j} \left[\left(\mu + \frac{\mu_t}{\sigma_\varepsilon} \right) \frac{\partial \varepsilon}{\partial x_j} \right] + C_{1\varepsilon} \frac{\varepsilon}{k} \mu_t \left(\frac{\partial U_i}{\partial x_j} + \frac{\partial U_j}{\partial x_i} \right) \frac{\partial U_i}{\partial x_j} - C_{2\varepsilon} \rho \frac{\varepsilon^2}{k} \quad (7)$$

The Eqs. (5), (6) and (7) contain five adjustable constants. The standard ($k - \varepsilon$) model employs values for these constants deduced from a comprehensive data fitting for a wide range of turbulence flows:

$$C_{1\varepsilon} = 1.44, C_{2\varepsilon} = 1.92, C_\mu = 0.09, \sigma_k = 1.0, \sigma_\varepsilon = 1.3.$$

2.2 Numerical Method

The Fig. 1 illustrates the numerical computational domain. For numerical runs and experiments the height (H) of the tunnel is 0.3 m; the jet opening ratio H/e is equal to 10. The blowing unit consists of two fully independent feeding circuits converging to form a twin-jet nozzle. Each jet is 0.015 m wide so that the total width (e) of the twin-jet nozzle is 0.03 m. The left-hand side far end of the tunnel is located at a distance of $5H$ from the air curtain center plane (1.5 m) and the right-hand side at $15H$ (4.5 m). The y -axis is oriented downwards.

No slip conditions were applied on every wall. The right outlet was set to atmospheric pressure while a relative pressure of 0.2 Pa was set at the left tunnel outlet. The numerical simulations were performed using the CFD code FLUENT 6.0 [7].

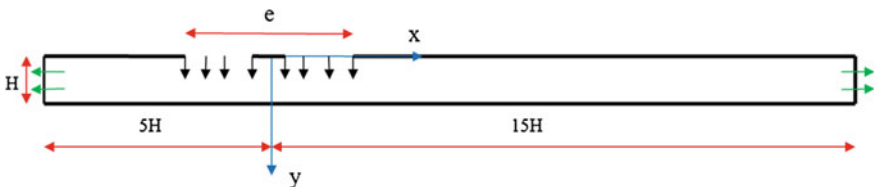


Fig. 1 Schema of the computational domain

3 Computational Results

The Reynolds number $Re = \frac{U_0 \cdot e}{\nu}$ (U_0 is the maximum inlet velocity and ν is the kinematic viscosity) is fixed to 14,000 to achieve a fully turbulent flow. The discretized equations in standard $(k - \epsilon)$ model for the pressure-velocity coupling were solved by using the SIMPLEC algorithm. Pressure was solved using a second order discretization scheme, for wall treatment the standard wall functions is employed; it is based on the proposal of Launder and Spalding. A power law discretization method was used for the other variables. A segregated solver was employed along with a second order unsteady explicit formulation and standard under-relaxation parameters. A refined mesh in the jet flow region is achieved especially near the wall impingement and at jet axe; the whole of our computational domain is with 80000 cells.

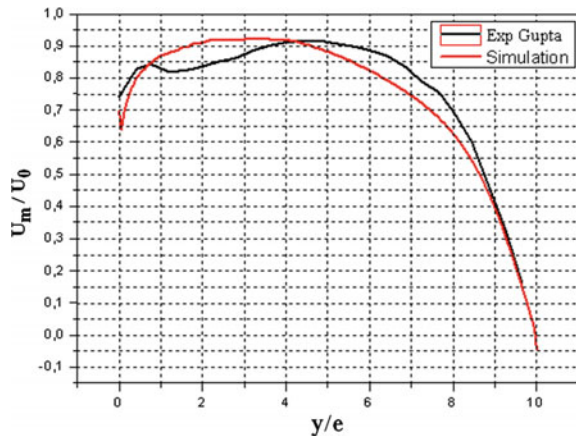
4 Mean Flow and Turbulence Statistics

In the Fig. 2, the obtained results are compared with those experimental ones published by Gupta [1].

From the profiles of mean velocity U_m along the jet centerline, Fig. 2, it is observed that the selected numerical models give a good agreement with experimental data. The Fig. 3a, b shown the iso-vector spaced and iso-contours of the mean velocity. It can be observed the deviation of the jet axis like experimental measures shown on the Fig. 3c, d.

The turbulent intensity in the x-direction, Fig. 4 shows that the simulation overestimates the velocity close the impact region $\frac{y}{e} \geq 7$. This is a direct consequence of a smaller expansion rate, revealing lower transversal diffusion of

Fig. 2 Mean velocity profile in the y direction



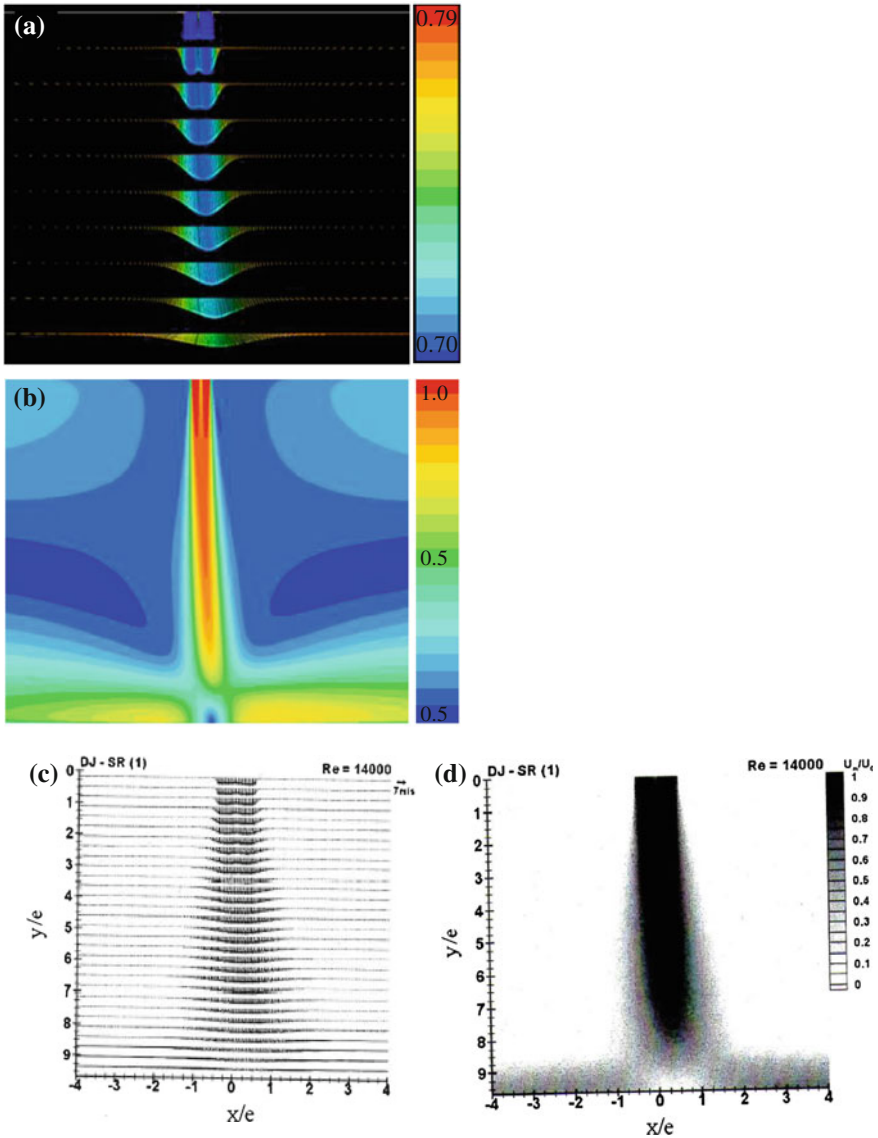
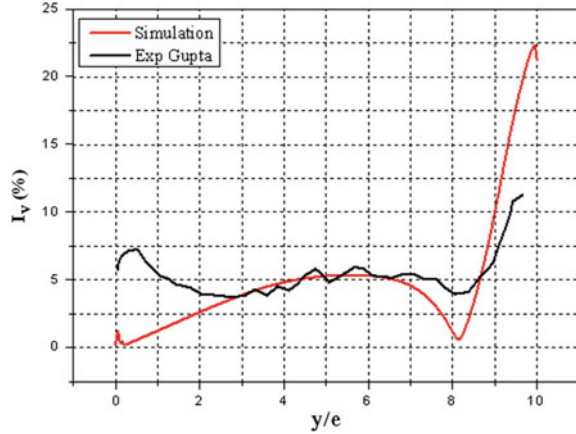


Fig. 3 **a** Mean velocity iso-vector along the jet axis; **b** mean velocity magnitude iso-contours in the y-direction; **c** experimental mean velocity iso-vector; **d** experimental mean velocity magnitude iso-contours

momentum. As numerical investigation is achieved in 2D space, smaller expansion rate of jet is also related with eventual non three-dimensional effects that could be present within the real flow. In the initial flow region, between $\frac{y}{e} = 2$ and $\frac{y}{e} = 7$, the model give values close to those obtained in the experimentation. The standard

Fig. 4 Turbulent intensity in the x direction



$(k - \varepsilon)$ model seems to better match the experimental results. However the model fails to correctly describe the flow region immediately upstream the nozzle, from $\frac{y}{e} = 0$ to $\frac{y}{e} = 2$, due to the non-uniform and poorly known profiles of turbulence and velocity at nozzles and considered uniform in the simulation.

5 Conclusion

A 2D RANS approach associated with the $(k - \varepsilon)$ turbulence model has been used to simulate the impinging twin-jets from a rectangular slot nozzle. The computed results show flow structures of the impinging jets. Evolution of the axial velocity and the turbulence intensity has been reported. The predicted results of root-mean-square normal velocity are verified with the available experimental results. The model is able to predict subtle features of turbulence production rate.

References

1. Gupta, S.: Etude expérimentale du comportement dynamique et des performances de rideaux d'air en vue de la conception de systèmes de confinement cellulaire. Thèse de doctorat, Ecole des mines de Nantes, France (2005)
2. Loubière, K., Pavageau, M.: Educing coherent eddy structures in air curtain systems. Chem. Eng. Process. **47**, 435–448 (2008)
3. Felis, F., Pavageau, M., Elicer-Cortés, J.C., Dassonville, T.: Simultaneous measurements of temperature and velocity fluctuations in a double-stream twin-jet air curtains for heat confinement in case of tunnel fire. Int. Commun. Heat Mass Transf. **37**, 1191–1196 (2010)
4. Elicer-Cortés, J.C., Demarco, R., Valencia, A., Pavageau, M.: Heat confinement in tunnels between two double-stream twin-jet air curtains. Int. Commun. Heat Mass Transf. **36**, 438–444 (2009)

5. Gupta, S., Pavageau, M., Elicer-Cortés, J.C.: Cellular confinement of tunnel sections between two air curtains. *Build. Environ.* **42**, 3352–3365 (2007)
6. Fernandez, J.A., Elicer-Cortés, J.C., Valencia, A., Pavageau, M., Gupta, S.: Comparison of low-cost two-equation turbulence models for prediction flow dynamics in twin-jets devices. *Int. Commun. Heat Mass Transf.* **34**, 570–578 (2007)
7. Copyright © 2006 Fluent Inc, by Macrovision Corporation. Flexible license Manager. FLUENT 6.3.26

Heat and Mass Transfer into a Porous Annulus Found Between Two Horizontal Concentric Circular Cylinders

**Karim Ragui, Abdelkader Boutra, Rachid Bennacer
and Youb Khaled Benkahla**

Abstract This numerical work refers to the study of natural convection driven by cooperating thermal and solutal buoyancy forces, into a porous annulus found between a cold (less concentric) outer circular enclosure and a hot (concentric) inner cylinder. The physical model for the momentum conservation equation makes use of the Brinkman extension of the classical Darcy equation, the set of coupled equations is solved using the finite volume method and the SIMPLER algorithm. To account for the effects of the main parameters such the Lewis number, the buoyancy ratio and the cylinders aspect ratio as well, heat and mass transfer characteristics are inspected. Summarizing the numerical predictions, the dynamic, thermal and solutal fields are found strongly dependent on the governing studied parameters. It is to note that the validity of the computing code used was ascertained by comparing our results with the numerical ones already available in the literature.

List of symbols

- C Dimensional mass fraction
- D Mass diffusivity, $m^2 s^{-1}$
- D_{int} Inner cylinder diameter, m
- D_{ext} Outer cylinder diameter, m

K. Ragui (✉) · A. Boutra · Y.K. Benkahla
Laboratory of Transport Phenomena, USTHB, 16111 Algiers, Algeria
e-mail: ragui-karim@live.fr

A. Boutra
e-mail: aeknad@yahoo.fr

Y.K. Benkahla
e-mail: youbenkahla@yahoo.fr

A. Boutra
Preparatory School of Science and Technology, 16111 Algiers, Algeria

R. Bennacer
LMT, Superior Normal School Cachan, 94235 Cedex, France
e-mail: rachid.bennacer@ens-cachan.fr

Da	Darcy number, (K/D_{ext}^2)
K	Porous medium permeability, m^2
Le	Lewis number
N	Buoyancy ratio, (β_C/β_T)
p^*	Pressure, Pa
P	Dimensionless pressure
Pr	Prandtl number (ν/α)
Ra	Thermal Rayleigh number $(g \beta_T \Delta T D_{\text{ext}}^3/\nu^2)$
Ra*	Porous thermal Rayleigh number $(Ra \text{ Da})$
T	Dimensional Temperature, K
u	V, Velocity components, m s^{-1}
U	V, Dimensionless velocity components
x	Y, Cartesian coordinates, m
X	Y, Dimensionless Cartesian coordinates

Greek letters

α	Thermal diffusivity, $\text{m}^2 \text{ s}^{-1}$
β_T	Thermal expansion coefficient, K^{-1}
β_C	Solutal expansion coefficient
ε	Porosity of the porous medium
ν	Kinematic viscosity, $\text{m}^2 \text{ s}^{-1}$
ϕ	Dimensionless concentration
θ	Dimensionless temperature
Ψ	Stream function

Subscripts

h	Hot
c	Cold

Superscript

+	Concentric
-	Less concentric

1 Introduction

Over the past four decades, double-diffusive natural convection analysis in porous enclosures has been the subject of a very intense research activity, due to the importance of related industrial and technological applications such as grain storage installation, geothermal energy, fibrous insulating materials, heat exchangers, catalytic reactor and some modes of assisted oil recuperation [1–4]. Nevertheless, in

engineering applications, the enclosures are often more complicated, as the cylindrical muffle furnace and the fibrous insulator which covers a cylindrical tube [5].

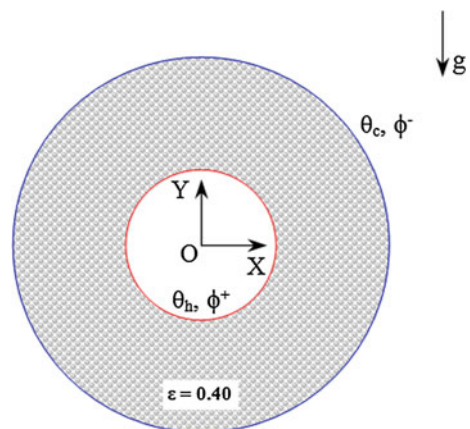
Many investigations have dealt with the influence of the porous annulus width on natural heat and mass transfer. Cited, for example, the papers of Mojtabi et al. [6, 7] in which a two-dimensional steady state natural convection into a rectangular porous annulus was conducted, and the Burns et al. [8] paper in which the natural convection into a porous medium bounded by concentric spheres and horizontal cylinders was examined. Using the finite element method, Badruddin et al. [9] carried out the natural convective heat transfer in a saturated porous medium contained in a square annulus. The outer boundaries of the annulus are exposed to cooler isothermal temperature when the inner walls are maintained at hot one. The effects of the porous width ratio and the Rayleigh number were the main object of this investigation.

By employing the control volume method, Xu et al. [10] studied numerically the transient natural convective heat transfer of liquid gallium from a heated horizontal circular cylinder to its coaxial triangular enclosure. The Grashof number was varied from 10^4 to 10^7 to predict its effect on the convection phenomenon. Motivated by the numerous practical applications of double-diffusive natural convection into porous annulus, and by the fact that the investigation on this subject may less common in the available literature, this paper will discuss the results of laminar flows into a porous annulus bounded by two concentric cylinders.

2 Problem Statement and Mathematical Formulation

The studied configuration, shown in Fig. 1, consists of a cold (less concentric) outer circular porous enclosure containing a hot (concentric) inner cylinder. The fluid filled the porous medium is assumed to be Newtonian, its thermo-physical

Fig. 1 Simulation domain with its boundary conditions



properties are presumed to be constant except the density variation, in the buoyancy term, which depends linearly on both the local temperature and concentration.

$$\rho_{(T,C)} = \rho_0[1 - \beta_T(T - T_0) - \beta_C(C - C_0)] \quad (1)$$

where β_T and β_C are the thermal and concentration expansion coefficients:

$$\beta_T = -\frac{1}{\rho_0} \left(\frac{\partial \rho}{\partial T} \right)_{p,C}, \quad \beta_C = -\frac{1}{\rho_0} \left(\frac{\partial \rho}{\partial T} \right)_{p,T} \quad (2)$$

The solid matrix is supposed to be isotropic, homogeneous and in thermal equilibrium with the fluid. Soret and Dufour effects on the heat and mass diffusion are neglected; the permeability of the porous medium K is kept uniform, when the porosity ε is about 0.40. The dimensionless conservation equations, describing the transport phenomena inside the porous annulus, can be written as:

$$\frac{\partial U}{\partial X} + \frac{\partial V}{\partial Y} = 0 \quad (3)$$

$$\frac{1}{\varepsilon} \left(U \frac{\partial U}{\partial X} + V \frac{\partial U}{\partial Y} \right) = -\frac{\partial P}{\partial X} - \frac{Pr}{Da} U + Pr \left(\frac{\partial^2 U}{\partial X^2} + \frac{\partial^2 U}{\partial Y^2} \right) \quad (4)$$

$$\frac{1}{\varepsilon^2} \left(U \frac{\partial V}{\partial X} + V \frac{\partial V}{\partial Y} \right) = -\frac{\partial P}{\partial Y} - \frac{Pr}{Da} V + Pr \left(\frac{\partial^2 V}{\partial X^2} + \frac{\partial^2 V}{\partial Y^2} \right) + Ra Pr (\theta + N \phi) \quad (5)$$

$$U \frac{\partial \theta}{\partial X} + V \frac{\partial \theta}{\partial Y} = \left(\frac{\partial^2 \theta}{\partial X^2} + \frac{\partial^2 \theta}{\partial Y^2} \right) \quad (6)$$

$$U \frac{\partial \phi}{\partial X} + V \frac{\partial \phi}{\partial Y} = \frac{1}{Le} \left(\frac{\partial^2 \phi}{\partial X^2} + \frac{\partial^2 \phi}{\partial Y^2} \right) \quad (7)$$

where Da is the Darcy number, Le is the Lewis number, N is the buoyancy ratio, Pr and Ra are the Prandtl and the thermal Rayleigh numbers.

3 Numerical Procedure and Validation

The governing conservation equations are discretized in space using the finite volume approach, when the convection-diffusion terms were treated with a Power-Law scheme. The resulting algebraic equations, with the associated boundary conditions, are then solved using the line by line method. As the momentum equation is formulated in terms of the primitive variables (U , V and P), the iterative procedure includes a pressure correction calculation method, namely SIMPLER [11], to solve the pressure-velocity coupling. Compared to other velocity-pressure coupling

approaches, such *SIMPLE* and *SIMPLEC*, the *SIMPLER* approach has proven to be faster, (*about 30 to 50 % fewer iterations*). The convergence criterion for the temperature, the concentration, the pressure and the velocity as well, is given as:

$$\frac{\sum_{j=1}^m \sum_{i=1}^n \left| \zeta_{i,j}^{t+1} - \zeta_{i,j}^t \right|}{\sum_{j=1}^m \sum_{i=1}^n \left| \zeta_{i,j}^{t+1} \right|} \leq 10^{-5} \tag{8}$$

where both *m* and *n* are the numbers of grid points in the *X* and *Y* directions, respectively, ζ is any of the computed field variables and *t* is the iteration number.

The performance of the using code via the double-diffusive natural convection problem in a confined porous medium is accomplished by comparing predictions with other numerical results, and by verifying the grid independence of the present results. In the first, the present results are consistent with previous computations, namely those of Hadidi et al. [12]. By taking into account the same hypotheses, Tables 1 and 2 demonstrate a comparison of the mean Nusselt and Sherwood numbers computed with various values of the buoyancy ratio *N* and the porous thermal Rayleigh number *Ra**, respectively. As we can see, the present results and those of Hadidi et al. [12] are in excellent agreement with a maximum discrepancy of about 2 %.

Then, to check the numerical code validity with the inner cylindrical results those obtained by Kim et al. [13] for a cold enclosure containing a centred hot cylinder have been selected. Figure 2 displays the comparison between the numerical Kim et al. predictions and the present ones in term of streamlines and Isotherm plots. A great agreement between the both works is observed through the last figure what validates our code via the cylindrical configuration.

Table 1 Average Nusselt and Sherwood numbers obtained with our computer code and those of Hadidi et al. [12]. *Ra* = 10⁶, *Pr* = 7, *Da* = 10⁻⁴, *Le* = 10

N	Hadidi et al. [12]		Present Work	
	Nu	Sh	Nu	Sh
0	2.83	10.25	2.79	10.29
10	3.95	26.30	3.91	26.33
15	4.57	29.75	4.56	29.81

Table 2 Average Nusselt and Sherwood numbers obtained with our computer code and those of Hadidi et al. [12]. *Pr* = 7, *Da* = 10⁻⁴, *Le* = 10, *N* = 10

<i>Ra*</i>	Hadidi et al. [12]		Present Work	
	Nu	Sh	Nu	Sh
1	1.02	3.28	1.04	3.30
100	3.95	26.30	3.91	26.33

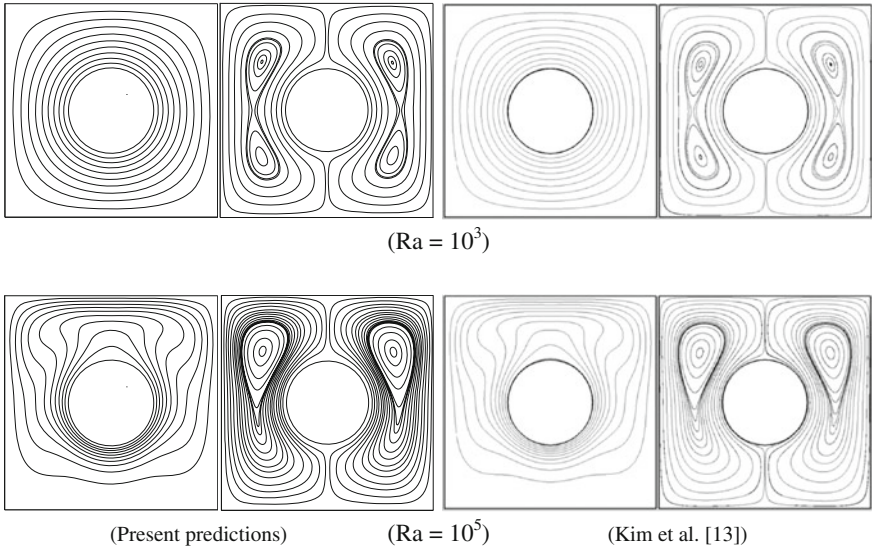
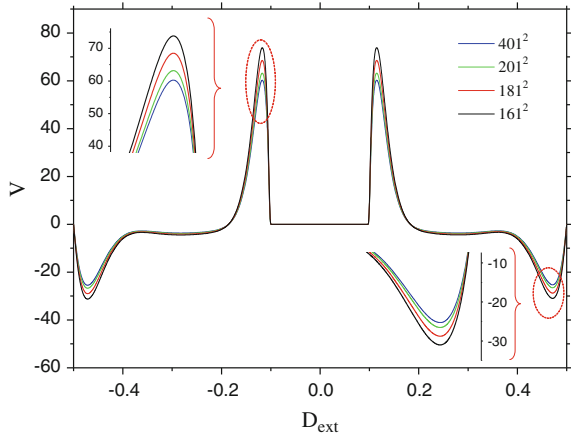


Fig. 2 Comparison of the present results with those reported by Kim et al. [13] for different Rayleigh numbers, $Pr = 0.71$

In order to determine a proper grid for the numerical simulations, a grid independence study is conducted for the double-diffusive natural convection into the porous annulus, previously shown in Fig. 1. Several mesh distributions ranging from 161^2 to 401^2 were tested and the central V-velocity profile, for the above uniform grids, is presented in Fig. 3. It is observed that a 201^2 uniform grid is adequate for a grid independent solution. However, a fine structured mesh of 401^2 is used to avoid round-off error for all other calculations in this investigation.

Fig. 3 V-velocity at $Y = 0$ for different uniform grids, $D_{int}/D_{ext} = 0.10$, $Le = 10$, $N = 10$, $Ra^* = 100$



4 Results and Discussion

In the present work the calculations are performed for various values of Lewis number ($1 \leq Le \leq 50$), buoyancy ratio ($1 \leq N \leq 30$) and cylinders aspect ratio ($0.10 \leq D_{int}/D_{ext} \leq 0.40$). Both, Darcy and Prandtl numbers are fixed at 10^{-3} and 10 , respectively. Figure 4 displays the Streamlines, the Isotherms and the Iso-concentration plots for different values of the Lewis number and that, at $N = 10$. For the all cases, at this buoyancy ratio, the plots follow the shape of inner and outer walls. Two symmetrical counter-rotating cells are formed into the porous annulus for a Lewis number equals 1 and 10 , when two lower secondary vortices show on when the later (Le) is greater than 20 . These secondary vortices are generated by the cold, (less concentric), fluid that remains confined in a small region created by the two primary cells.

On the other hand, the Isotherm plots represented for $Le > 1$ are found to be nearly the some demonstrating a dominated-conduction heat transfer regime, unlike the Isoconcentration plots where the thin concentric boundary layer nearer the porous walls decreases with the increasing Lewis number. Regarding the effect of the buoyancy ratio, Fig. 5 illustrates the Streamlines, the Isotherms and the Iso-concentration plots for different values of the latter and that, for a Lewis number equals 10 . Once again, and except for $N = 30$, two symmetrical counter-rotating eddies are formed into the porous annulus. Its absolute stream function value increases by increasing the buoyancy ratio as the fluid motion becomes stronger.

The heat transfer into the saturated porous medium is found to be more pronounced by increasing N what indicates the transition from the conduction regime (at $N = 1$) to the convective one (see $N = 30$). Then, the Iso-concentration plots are very affected by the enhancement of the buoyancy ratio.

Thin mass boundary layers are formed around the upper part of the outer cylinder and all around the inner one, indicating large concentration gradients along these surfaces, the thickness of the boundary layer is found to be a decrease function of the enhanced value of the buoyancy ratio. It is to note that unlike the other values, when the buoyancy ratio is about 20 , two lower secondary vortices raise, as this part of the annulus contains only a very cold and very less concentric fluid. For more clarification, the hydrodynamic, the thermal and the solutal behaviors are summarized in Fig. 6, where the V-velocity, the temperature and the concentration profiles along the horizontal mid-plane of the porous annulus are presented.

The examination of the magnitude of V at different values of the Lewis number confirms the results previously obtained from analysing the streamlines. The V-velocity profiles verify the existence of clockwise and anti-clockwise circulating cells inside the annuli. The decrease of the velocity magnitude with increasing Lewis number is an indication of weak buoyant flows at high values of the latter. The mass transfer mechanism is, therefore, expected to be more pronounced as

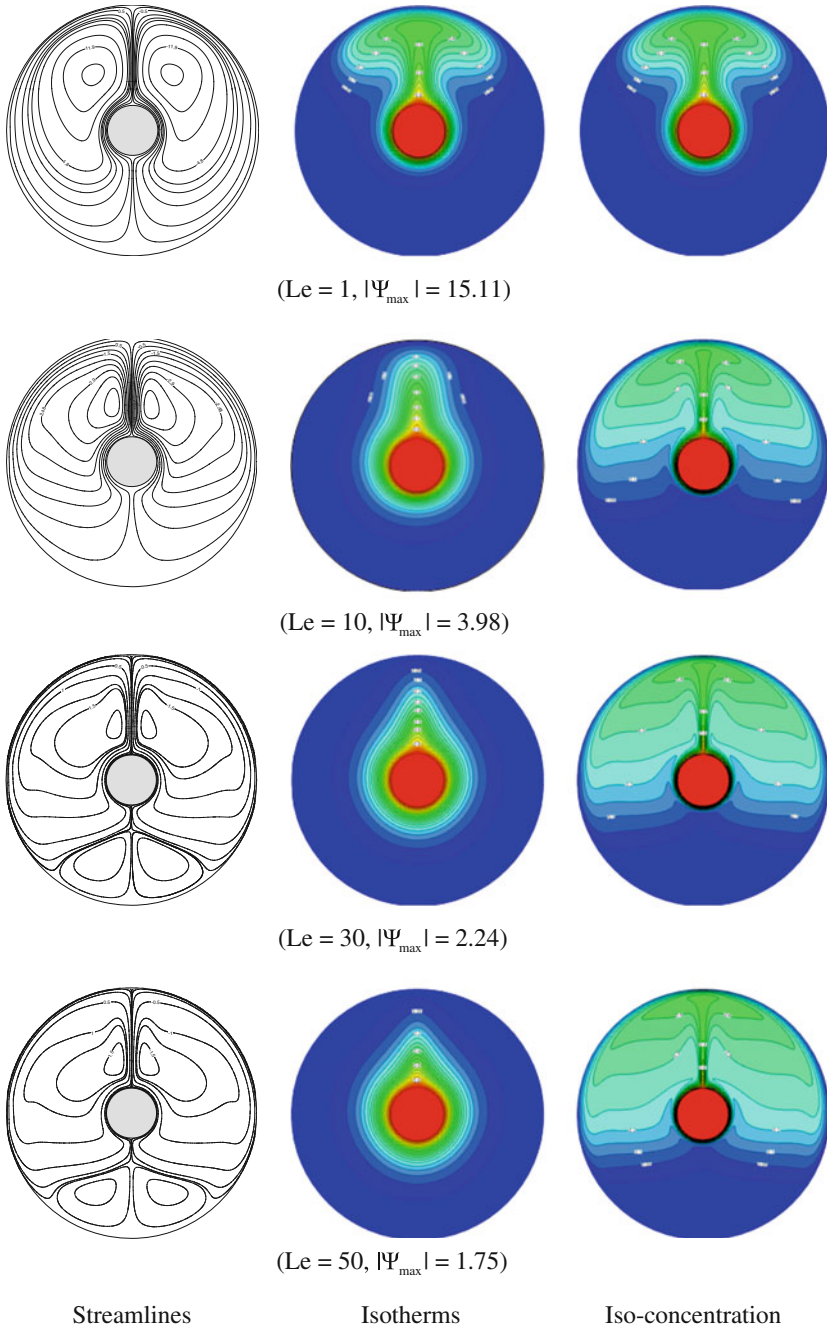


Fig. 4 Effect of Lewis number, $N = 10$, $Ra^* = 100$, $D_{int}/D_{ext} = 0.10$

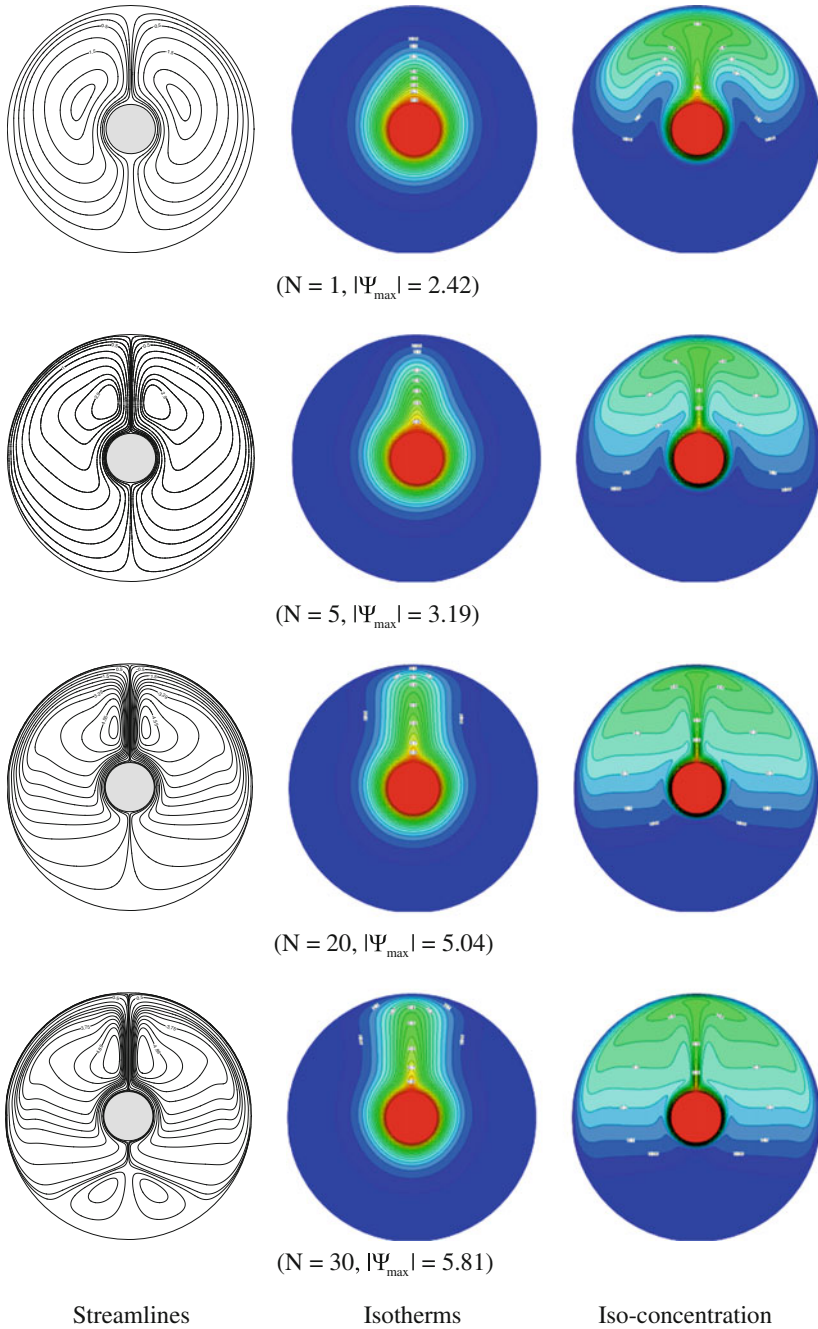


Fig. 5 Effect of the buoyancy ratio, $Le = 10$, $Ra^* = 100$, $D_{\text{int}}/D_{\text{ext}} = 0.10$

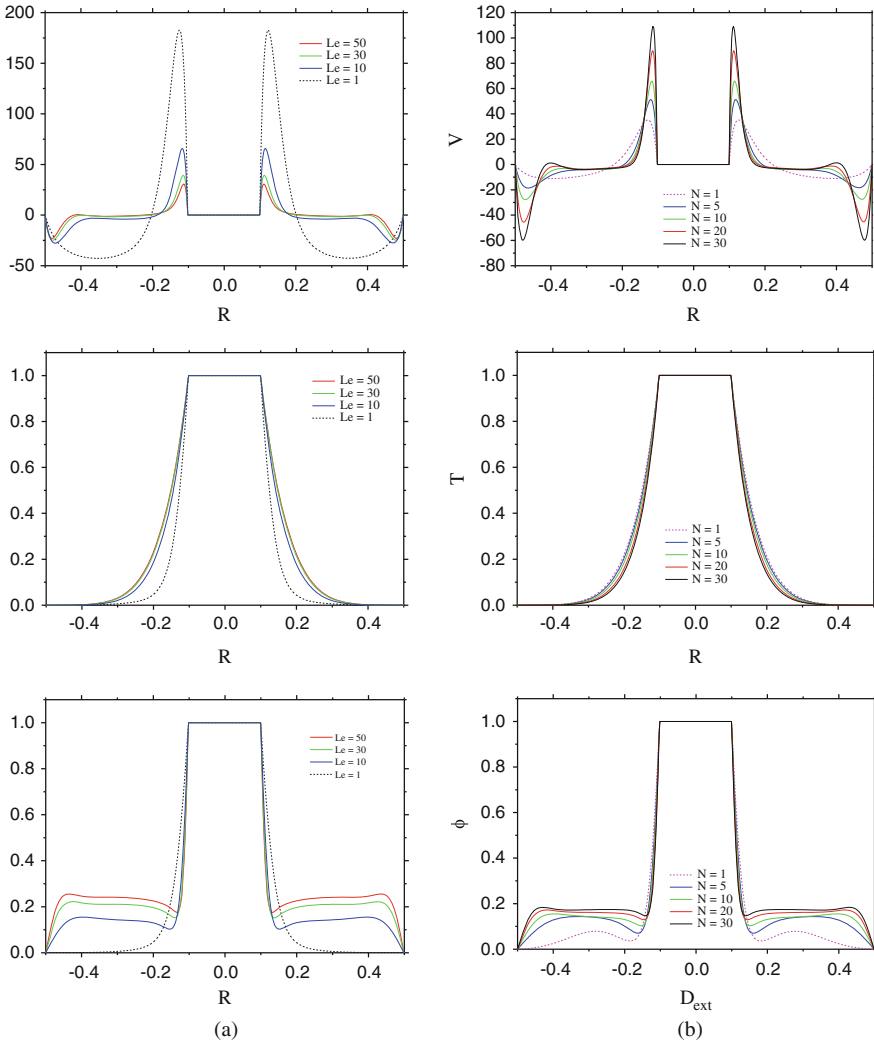


Fig. 6 V-Velocity, Temperature and Concentration profiles at $Y = 0$ for different values of the Lewis number (a) and the buoyancy ratio (b). $Ra^* = 100$, $D_{int}/D_{ext} = 0.10$

illustrated via the concentration profiles while conduction is responsible for the heat transfer. Once again, the buoyancy ratio is proved to be an amplifier of the flow velocity and the mass transfer, when its effect on the heat transfer regime still less pronounced (See Fig. 6b).

The effect of the aspect ratio, D_{int}/D_{ext} , is shortly investigated. Figure 7 displays the Streamlines, the Isotherms and the Iso-concentration plots for different values of

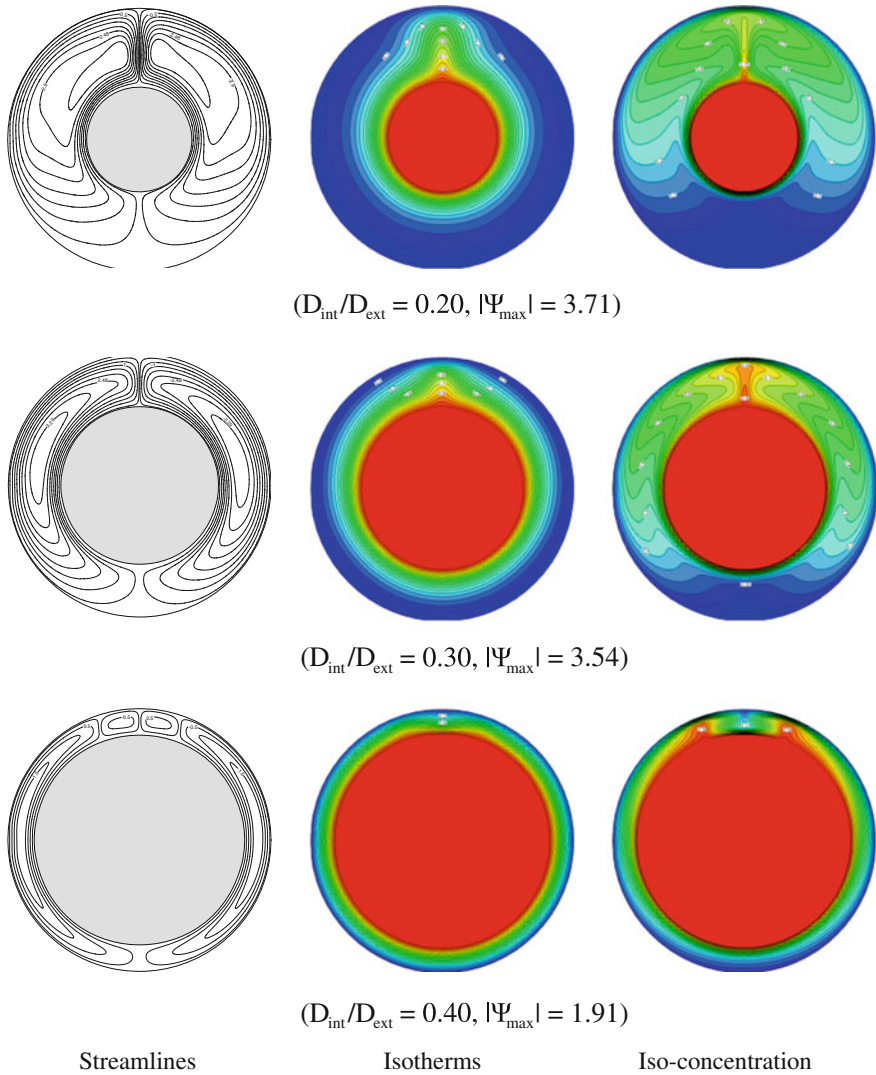


Fig. 7 Effect of the inner cylindrical radius, $Le = 10$, $N = 10$, $Ra^* = 100$

the aspect ratio and that, for a fixed Lewis and buoyancy ratio, taken as 10. As we can see, the increase in the inner radius decrease the flow motion into the porous annulus, and makes the conduction regime more dominated. A further increase in the radius value to 0.40 causes a rise of a two secondary vortices, which become responsible for the top Iso-concentration disturbance.

5 Conclusion

The analysis of double-diffusive natural convection phenomenon inside a square Darcy-Brinkman porous annulus was numerically realized in this paper. Taking into account effects of various parameters, such the Lewis number, the buoyancy ratio and the inner radius, the predictions may resume as follows:

- Into the saturated porous annulus, the fluid velocity becomes more powerful by increasing value of the buoyancy ratio, unlike the Lewis number.
- The heat transfer is a quiet function of the buoyancy ratio, and doesn't much depend on the Lewis number unlike the mass transfer, which is a function of the both; Lewis and buoyancy ratio.
- The increase in the inner radius decreases the fluid motion and makes the conduction regime more pronounced.

References

1. Trevisan, O., Bejan, A.: *Int. J. Heat Mass Transf.* **30**, 2341–2356 (1987)
2. Benard, C., Gobin, D., Thevenin, J.: In: ASME, R.K., Shah, (eds.) pp. 249–254, New York (1989)
3. Rachid, B.: Ph.D. Thesis, Pierre and Marie Curie, Paris (1993)
4. Nield, D.A., Bejan, A.: Springer, Berlin (1992)
5. Ait, Saada M., Chikh, S., Campo, A.: *Int. J. Heat Fluid Flow* **28**, 483–495 (2007)
6. Charrier-Mojtabi, M.C., Caltagirone, J.P.: *First Int. Conf. Numer. Meth. Non-Linear Problems*, pp. 821–828 (1980)
7. Mojtabi, A., Quazar, D., Charrier-Mojtabi, M.C.: *Int. Conf. Numer. Meth. Thermal Probl* **5**, 644–654 (1987)
8. Burns, P.J., Tien, C.L.: *Int. J. Heat Mass Transf.* **22**, 929–939 (1979)
9. Badruddin, I.A., Abdullah, A., Salman Ahmed, N.J., Kamangar, S., Jeevan, K.: *Int. J. Heat Mass Transf.* **55**, 7175–7187 (2012)
10. Xu, X., Yu, Z.T., Hub, Y.C., Fan, L.W., Cen, K., Flint, J.: *Heat Mass Transf.* **55**, 995–1003 (2012)
11. Patankar, S.V.: *Numerical heat transfer and fluid flow*. Mc Grow, New York (1980)
12. Hadidi, N., Ould Amer, Y., Bennacer, R.: *Energy* **51**, 422–430 (2013)
13. Kim, B.S., Lee, D.S., Ha, M.Y., Yoon, H.S.: *Int. J. Heat Mass Transf.* **51**, 1888–1906 (2008)

Heat and Mass Transfer in the Growth of Titanium Doped Sapphire Material with the μ -PD Technique

Hanane Azoui, Abdellah Laidoune, Djamel Haddad
and Derradji Bahloul

Abstract In this work we have studied the heat and the mass transfer of titanium doped sapphire in the growth domain. The growth of this material ($\text{Ti}^{+3}: \text{Al}_2\text{O}_3$) is performed using a relatively recent growing technique that is the micro-pulling down (μ -PD) [1]. This method presents several advantages over other growing methods [2] and allows a stable growth of shaped material with very good quality [3]. In this study we established a numerical, two-dimensional finite volume model in cylindrical coordinates with an axisymmetric configuration. The flow, the thermal transfer and the mass transfer are modeled by the differential equations of conservation of the mass, of quantity of the movement, energy and the species. This problem, which takes into account the convection-diffusion coupling, is discretized using the Finite Volumes Method (FVM). We focus on the physical properties of the molten zone and on the radial and axial distribution of titanium in the sapphire crystal fiber. Our model is in good agreement with experimental results.

1 Introduction

Titanium doped sapphire is a very important material because of its exceptional chemical and physical (mechanical, optical, thermal and dielectric) properties [1]. For this reason titanium doped sapphire is most used in several military, medical, and industrial applications [4]: wafer for micro-electronics or *LED*, windows, watch and cellular phone glasses, optic fibers and wave guides for surgery [1]. Many growing techniques have been used to grow this material such as Heat exchanger method (*HEM*) [5], Czochralski [6]. The geometry, the shape and the quality of the

H. Azoui (✉) · A. Laidoune · D. Bahloul
Département de sciences de la matière, Université de Batna 1,
1 rue Chahid Boukhrouf Mohamed El-Hadi, Batna 05000, Algeria
e-mail: anhanane@gmail.com

D. Haddad
Département de mécanique, Université de Batna 2, Batna, Algeria
e-mail: djamel_hd2@yahoo.fr

material play an important role in the choice of the growing technique [3]; in this work we have performed a numerical simulation of the growth process with micro-pulling down μ -PD technique. This method allows the control of the thermal gradient (heat transfer), and has become a major method for growing materials of good quality [2]. The theoretical analysis of heat and mass transfer in the growth of Ti doped Al_2O_3 is conducted using the mass, momentum, energy and solutal concentration conservation laws.

The study of the problem is simplified to an incompressible flow of a viscous fluid in the molten zone governed by the Navier-Stokes, heat transfer and concentration equations under the Boussinesq approximation. A schematic diagram and a computational domain of the micro-pulling down are illustrated in Figs. 1 and 2.

Fig. 1 Schematic diagram of the μ -PD

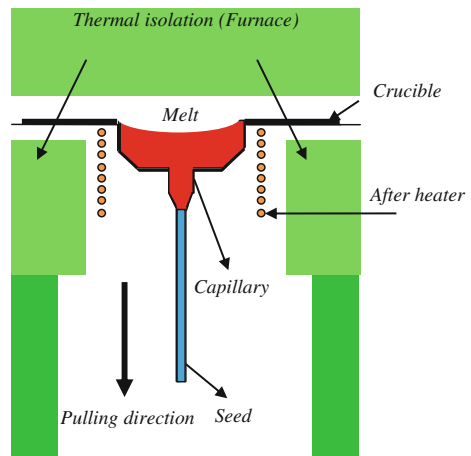
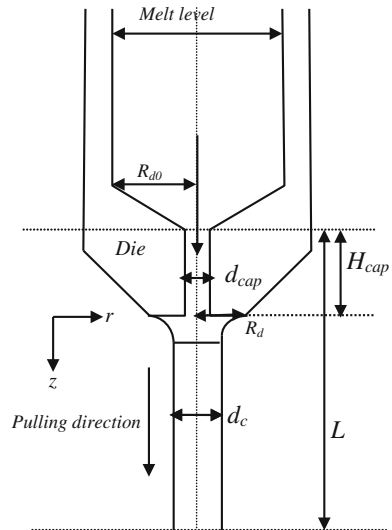


Fig. 2 Computational domain



In the next section we present the mathematical formulation of our model that is the governing equations, and the numerical scheme used in our simulations. Section 3 is devoted to the results and discussion, followed by conclusions in Sect. 4.

2 Mathematical Formulation

In this study we established a two-dimensional finite volume model in cylindrical coordinates, with an axisymmetric configuration. The flow, thermal and mass transfer are modeled by the differential equations of conservation of the mass, of quantity of the movement, energy and concentration.

2.1 Governing Equations

In this report the melt is assumed incompressible and Newtonian, while the flow is laminar. Dimensionless variables are defined by scaling lengths by R_d , velocity by α_m/R_d , temperature by the melting point T_m , and concentration by C_0 , where α_m is the thermal diffusivity of the melt and R_d is the radius of the die of the crucible [7]. We have used a two dimensional axisymmetric model because of the cylindrical symmetry of the problem. The flow, the heat transfer and the mass transfer are modeled by the dimensionless differential equations:

Equation of radial component of the momentum:

$$\frac{\partial u}{\partial t} + u \frac{\partial u}{\partial r} + v \frac{\partial u}{\partial z} = -\frac{\partial P}{\partial r} + P_r \left(\left(\frac{1}{r} \frac{\partial}{\partial r} (r \cdot u) \right) + \frac{\partial}{\partial z} \left(\frac{\partial u}{\partial z} \right) \right) \quad (1)$$

Equation of axial component of the momentum:

$$\begin{aligned} \frac{\partial v}{\partial t} + u \frac{\partial v}{\partial r} + v \frac{\partial v}{\partial z} = & -\frac{\partial P}{\partial z} + P_r \frac{\partial}{\partial r} \left(\frac{1}{r} \frac{\partial}{\partial r} (rv) \right) + P_r \frac{\partial}{\partial z} \left(\frac{\partial v}{\partial r} \right) \\ & - P_r RaT + \frac{Pr^2}{Sc} Ra_S C \end{aligned} \quad (2)$$

Conservation equation:

$$\nabla V = \frac{1}{r} \frac{\partial (ru)}{\partial r} + \frac{\partial v}{\partial z} = 0 \quad (3)$$

Energy equation:

$$r \frac{\partial T}{\partial t} + \frac{\partial}{\partial r}(r \cdot uT) + \frac{\partial}{\partial z}(r \cdot vT) = \frac{\partial}{\partial r} \left(r \cdot \alpha_i(T) \frac{\partial}{\partial r} \right) + \frac{\partial}{\partial z} \left(r \cdot \alpha_i(T) \frac{\partial}{\partial z} \right) \quad (4)$$

Dopant concentration equation:

$$r \frac{\partial C}{\partial t} + \frac{\partial}{\partial r}(r \cdot uC) + \frac{\partial}{\partial z}(r \cdot vC) = \frac{Pr}{Sc} \left(\frac{\partial}{\partial r} \left(r \cdot \frac{\partial C}{\partial r} \right) + \frac{\partial}{\partial z} \left(r \cdot \frac{\partial C}{\partial z} \right) \right) \quad (5)$$

where

- Pr is the Prandtl number ($Pr \equiv v_m/\alpha_m$),
- v_m is the kinematic melt viscosity,
- Sc is the Schmidt number ($Sc \equiv v_m/D$),
- D the diffusivity of titanium in the melt,
- α_i is the thermal diffusivity of phase i , $i = c$ for crystal and $i = m$ for melt,
- Ra_T, Ra_S Ra_s the thermal and solutal Rayleigh number respectively, are two important dimensionless variables in the source term of the equation of motion they are defined as follows [7]:

$$Ra_T = \frac{g\beta_T T_m R_d^3}{\alpha_m v_m}; \quad Ra_S = \frac{g\beta_S C_0 R_d^3}{\alpha_m v_m} \quad (6)$$

The thermal and solutal expansion coefficients are β_T and β_S respectively, and g is the gravitational acceleration. The governing equations with their associated boundary conditions are discretized by a finite volume method (FVM). Boundary conditions are also required to solve the above governing equations. The boundary conditions used in our simulations that are the same in Refs. [7, 8].

To solve numerically the above equations, the physical domain in axisymmetric cylindrical coordinates (r, z) is subdivided into a finite number of contiguous volumes (CV) of volume V , which are bounded by cell faces located about halfway between consecutive nodal points. Figure 3 represent the numerical scheme or mesh grid that has been used.

2.2 Boundary Conditions

It is assumed that the solute is uniformly distributed in the melt reservoir and its concentration is C_0 . The solute diffusion in the solid phase is neglected. These governing equations with their associated boundary conditions are discretized by a finite volume method (FVM). We present below a detailed description about the boundary conditions used in our simulations that are the same in Ref. [7]. Some important boundary conditions are described here.

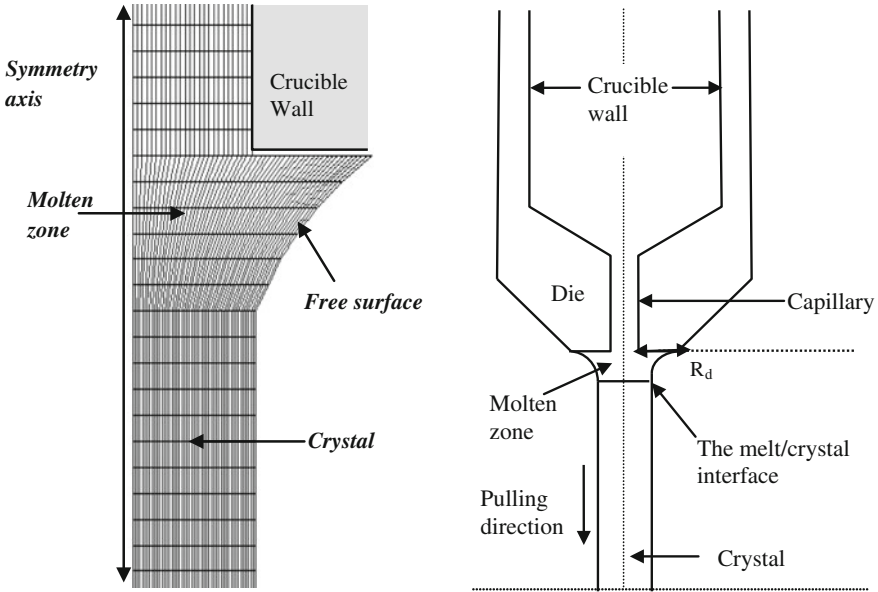


Fig. 3 Portion of a sample mesh (numerical scheme) for calculation

2.2.1 Boundary Conditions at the Symmetric Axis

In our two dimensional axisymmetric model, the boundary condition at the symmetric axis for the physical quantities is set as follows:

$$\frac{\partial \Phi}{\partial r} = 0 \tag{7}$$

In the above equations Φ is the physical propriety velocities (u, v), temperature T and concentration C . The boundary conditions for heat and mass transfer are set as follows.

2.2.2 Temperature Boundary Conditions

At the top entrance the temperature is set by the radio frequency generator it's about $\Delta T \approx 20\text{--}30$ K above the melting point T_m of sapphire.

$$T = T_m + \Delta T \tag{8}$$

At the wall inside the capillary, the die temperature T_d is assumed as a linear function of the axial distance:

$$T_d(z) = T_d|_0 - (T_d|_{H_{cap}} - T_d|_0) \cdot \frac{z}{H_{cap}} \quad (9)$$

At the surface of the material, heat transfer from the system to the ambient is by convection according to the energy balance along the material surface:

$$\vec{n} \cdot k_i \vec{\nabla} T = -B_i(T - T_a) \quad (10)$$

where

n is the unit normal vector on the melt or crystal surface pointing outwards,

k_i is the ratio of thermal conductivity of phase i to the conductivity of melt K_m ,

$B_i = hR_d/k_m$ is the Biot number

In this study the ambient temperature T_a is set to be a constant. At the liquid-solid interface the boundary condition is:

$$\rho_c \Delta H v_c + K_m \vec{\nabla} T_m \cdot \vec{n} = K_c \vec{\nabla} T_c \cdot \vec{n} \quad (11)$$

ΔH is the latent heat of sapphire,

v_c is the growth velocity,

ρ_c the crystal density,

K_c the thermal conductivity of crystal

At the end of the fiber $z = L$ using the fixed-temperature boundary condition, i.e. $T = T_a$ (T_a is the ambient temperature).

2.2.3 Solute Concentration Boundary Conditions

At the top entrance ($z = -H_{cap}$) the solute boundary condition is given by:

$$\vec{e}_z \cdot \vec{\nabla} C = \left(\frac{Sc}{Pr} \right) \cdot Pe_m (C - 1) \quad (12)$$

where e_z is the unit vector along the z axis and ∇C is the gradient of the concentration. The Neumann condition is imposed at the melt/crystal interfaces:

$$\vec{n} \cdot \vec{\nabla} C = \left[\left(\frac{\rho_c}{\rho_m} \right) - K \right] \left(\frac{Sc}{Pr} \right) Pe_c \cdot C (n \cdot e_z) \quad (13)$$

where: K is the segregation coefficient according to the phase diagram, ρ_c and ρ_m are the crystal and melt densities, respectively. The Peclet numbers of the melt and crystal respectively are:

$$Pe_m = \frac{v_m R_d}{\alpha_m}; \quad Pe_c = \frac{v_c R_d}{\alpha_m} \quad (14)$$

ρ_c, ρ_m respectively the crystal and melt densities,
 v_m, v_c respectively the melt and growth velocity.

3 Results and Discussion

In the present study, we are interested only in cases with concentration less than 0.1 % of titanium in the melt (sapphire) which was used in the previous experiments [1]. The physical properties (Table 1) of $Ti^{3+}: Al_2O_3$ and some input parameters used in calculations are listed here [1, 9].

3.1 Masse Transfer (Distribution) of the Titanium in the Sapphire Crystal

3.1.1 Axial Mass Transfer

The distribution of the dopants concentration of titanium along the axis of the crystal of titanium-doped sapphire (solid) for various pulling rate is illustrated in the Fig. 4. The pulling rates used in our simulation are the same in the experimental work [1] Fig. 5: (0.3, 0.5, 0.81 mm/min).

In Fig. 4, we notice that the longitudinal distribution of the Ti^{3+} is homogeneous along the axis of the fiber ($z > 0.6$: the crystal). For the μ -PD technique the dopants distribution remains homogeneous although the pulling rate is relatively high. These results is in good agreement with experimental results shown in the Fig. 5

Table 1 Physical Properties of $Ti^{3+}: Al_2O_3$

Physical properties
$Cp_c = 1300 \text{ J/kg K}$
$Cp_m = 765 \text{ J/kg K}$
$K_c = 17.5 \text{ W/m K}$
$K_m = 3.5 \text{ W/m K}$
$\mu_m = 0.0475 \text{ kg/m s}$
$T_m = 2323 \text{ K}$
$\beta_T = 0.0475 \text{ K}^{-1}$
$\Delta H = 1.8 \times 10^{-5} \text{ J/kg}$
$K = 1$
$\rho_c = 3960 \text{ kg/m}^3$
$\rho_m = 3500 \text{ kg/m}^3$
$\Phi_0 = 17^\circ$

Fig. 4 Results of our simulation

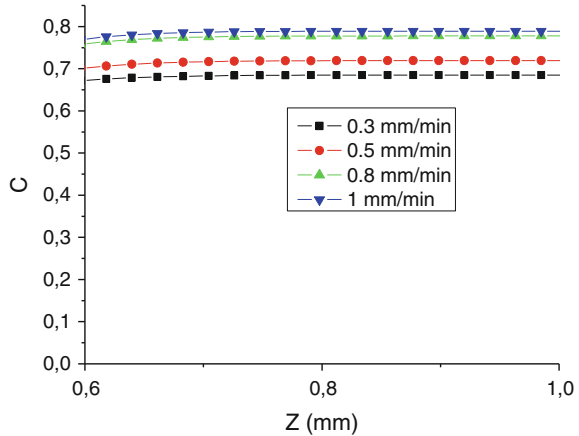
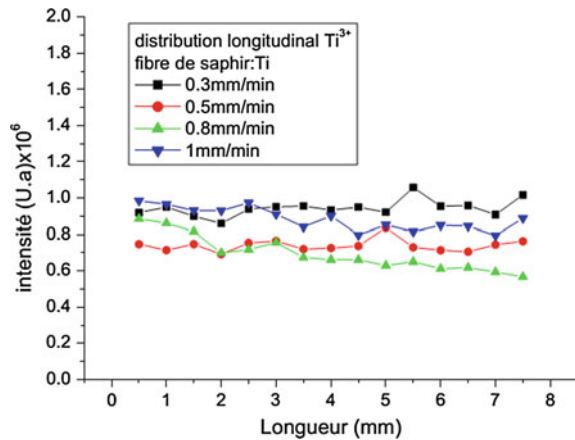


Fig. 5 Results of experimental [1]



[1], and give a good optical quality of crystal for various applications, especially for optoelectronics and laser applications.

3.1.2 Radial mass transfer

Figure 6 illustrates the radial distribution in the center $r = 0 \mu\text{m}$ and in the periphery $r = 0.310^3 \mu\text{m}$ of the crystal of sapphire. We notice the increasing of Ti^{+3} radial concentrations with the increasing of the pulling rate in the case of our simulation. This result agrees again with the experimental results for the three pulling rate: 0.5, 0.8 and 1 mm/min, shown at the Fig. 7. We add another result that regards by the distribution of Ti^{+3} in the periphery $r = 0.310^3 \mu\text{m}$ where this distribution almost zero and this is avoids the problem of segregation.

Fig. 6 Dopants radial mass transfer

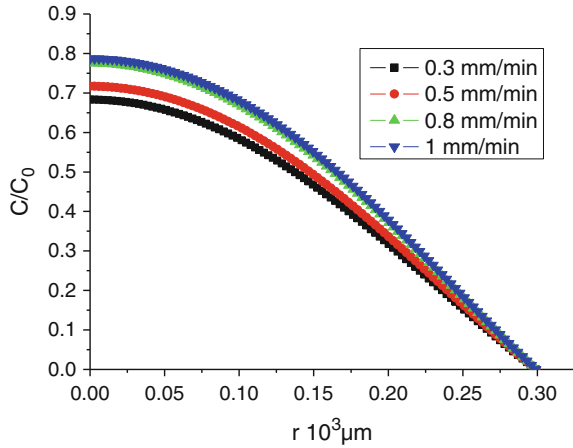
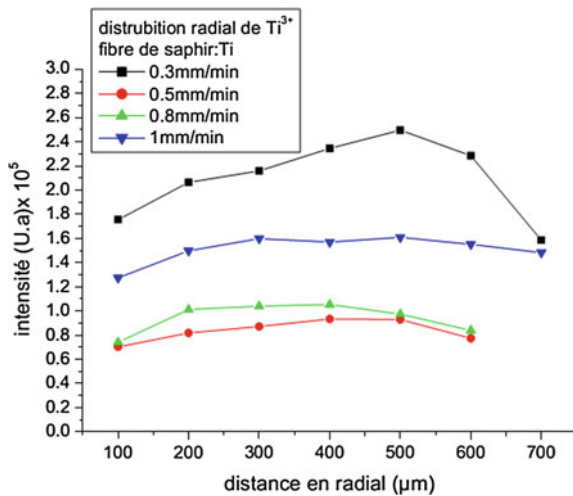


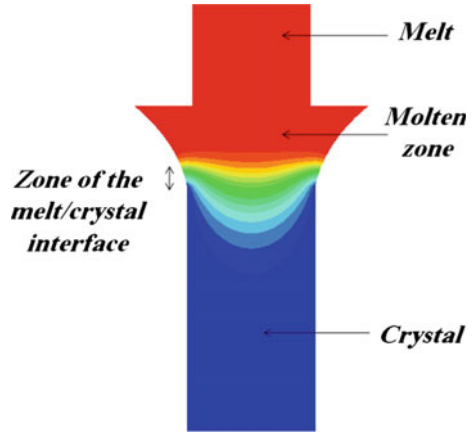
Fig. 7 Experimental radial mass transfer [2]



3.2 Heat Transfer in the Growth System of μ -PD

The quality of the crystals is governed by many factors, citing the dynamics of drawing, thermal transfer, effect of convection, the geometry of the melt/crystal interface. The melt/crystal interface shape plays an important role for the quality of the material drawn. The shape of this interface is essentially determined by the heat transfer in the growing system [10]. Figure 8 shows the heat transfer (Temperature contour plot) in the μ -PD system, such as blue color shows the solid or crystal and red color shows the fluid or the melt. According to these results the melt/crystal interface has a flatshape. This important result from the melt-crystal interface agrees with the experiment observation [1].

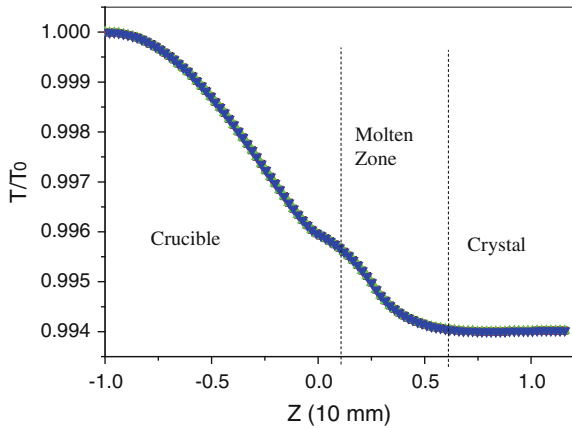
Fig. 8 Heat transfer showing the melt/crystal interface



3.3 The Thermal Field

The evolution of temperature fields is shown in Fig. 9, where we represent the axial distribution of the dimensionless temperature along the growth axis ($z(\text{mm})$). The temperature fields in the molten sapphire decreases with the growth axis of the crystal, i.e., there is a solidification of the fluid particles. The temperature of the melt (Sapphire) is elevated in the upper part of the crucible, also in the molten zone and it decreases when the fluid particles solidifies or cools and this in the crystal of sapphire. This result is in a good agreement with the Ref. [9].

Fig. 9 Axial evolution of temperature fields



4 Conclusion

We have developed a numerical model to analyze the heat and the mass transfer of titanium doped sapphire material by the micro-pulling-down (μ -PD) technique. The steady state heat and mass transfer, melt flow, interface shapes, are computed simultaneously using a Finite Volumes Method (FVM). We conclude that:

- The longitudinal mass transfer of the Ti^{3+} remains homogeneous along the axis of the crystal even for relatively high pulling rates. Our results are in good agreement with experimental results, and this homogeneity gives a material with a good quality for several applications.
- The radial mass transfer of titanium (dopants radial distribution) increase in the crystal drawn when the pulling rate increases.
- The heat transfer gives information on the shape of the melt/crystal interface, which plays an important role for the quality of the material drawn. The flat shape of the melt-crystal interface agrees with the experiment observation.
- The geometry of the micro-pulling down avoids the segregation problem of the dopants towards the periphery, and pulling rate helps the gathering of dopants in the center of the crystal.

References

1. Laidoune, A.: Croissance des fibres cristallines pour usage dans l'optoélectronique. Université de Batna, Thèse de doctorat (2010)
2. Martial, I., Sangla, D., Aubry, N., Didierjean, J.: Lasers à fibres cristallines dopées Nd et Yb: point sur les avancées récentes (2009)
3. Fukada, T., Rudolph, P.: In: Uda, S. (eds.) Fiber Crystal Growth from the Melt. Springer (2003)
4. Nubling, R., Harrington, J.: Optical properties of single crystal sapphire fibers. Appl. Opt. **36** (24) (1997)
5. Joyce, D.B., Schmid, F.: Progress in the growth of large scale Ti: sapphire crystals by the heat exchanger method (HEM) for petawatt class lasers. J. Cryst. Growth **312**(2010), 1138–1141 (2010)
6. Li, H., Ghezal, E.A., Alombert-Goget, G., Breton, G., Ingargiola, J.M., Brenier, A., Lebbou, K.: Qualitative and quantitative bubbles defects analysis in undoped and Ti-doped sapphire crystals grown by Czochralski technique. Opt. Mater. **37**, 132–138 (2014)
7. Lan, C.W., Uda, S., Fukuda, T.: Theoretical analysis of the micro-pulling-down process for Ge_xSi_{1-x} fiber crystal growth. J. Cryst. Growth **193**, 552–562 (1998)
8. Lan, C.W.: Effect of axisymmetric magnetic fields on radial dopant segregation of floating-zone silicon growth in a mirror furnace. J. Cryst. Growth **169–269** (1996)
9. Lee, W.J., Lee, Y.C., Jo, H.H., Park, Y.H.: Effect of crucible geometry on melt convection and interface shape during Kyropoulos growth of sapphire single crystal. J. Cryst. Growth **V324**, 248–254 (2011)
10. Lu, C.-W., Chen, C.-H., Chen, J.-C.: Effects of RF coil position on the transport processes during the stages of sapphire Czochralski crystal growth. J. Cryst. Growth **312**, 1074–1079 (2010)

Cooperating Double Diffusion Natural Convection in a Square Enclosure with Partially Active Vertical Wall

Abdennacer Belazizia, Smail Benissaad and Said Abboudi

Abstract Steady, laminar, double diffusion natural convection flow in a square enclosure with partially active vertical wall is considered. The enclosure is filled with a binary fluid and subjected to horizontal temperature and concentration gradients. The flow is driven by cooperating thermal and solutal buoyancies. Finite volume method is used to solve the dimensionless governing equations. The physical problem depends on five parameters: thermal Rayleigh number ($Ra_t = 10^3-10^6$), Prandtl number ($Pr = 7$), Schmidt number ($Sc = 240$), buoyancy forces ratio ($N = 1$) and the aspect ratio of the enclosure ($A = 1$). The active location takes three positions in the left wall: top (T), middle (M) and bottom (B). The main focus of the study is on examining the effect of Rayleigh number on fluid flow and heat and mass transfer rates. The results including the streamlines, isotherm and iso-concentration patterns, flow velocity and the average Nusselt and Sherwood numbers for different values of Ra_t . The obtained results show that the increase of Ra_t leads to enhance heat and mass transfer rates. The fluid particles move with greater velocity for higher thermal Rayleigh number. Also by moving the active location from the top to the bottom on the left vertical wall, convection and heat and mass transfer rates are more important in case (B). Furthermore for high Rayleigh number ($Ra_t = 10^6$), Convection mechanism in (T) case is principally in the top of the enclosure, whereas in the remaining cases it covers the entire enclosure.

Keywords Active location · Binary fluid · Cooperate buoyancies · Thermosolutal natural convection

Nomenclature

Symbols

- A Aspect ratio H/L
C Dimensionless concentration $(C^* - C_{min})/\Delta C^*$
Le Lewis number, $Le = \alpha/D$

A. Belazizia (✉) · S. Benissaad · S. Abboudi
Université Kasdi Merbah, Ouargla, Algeria
e-mail: nacer.belazizia@gmail.com

\overline{Nu}	Average Nusselt number, Eq. (7a, b)
N	Buoyancy ratio number $(\beta_s \Delta C^*) / (\beta_t \Delta T)$
P	Dimensionless pressure $p / (\alpha / H)^2$
Pr	Prandtl number of the fluid ν / α
Ra_t	Thermal Rayleigh number $g \beta_t H^3 \Delta T / \nu \alpha$
Sc	Schmidt number ν / D
\overline{Sh}	Average Sherwood number Eq. (7a, b)
t	Dimensionless time $t^* / (H^2 / \alpha)$
U, V	Dimensionless velocity components $u / (\alpha / H), v / (\alpha / H)$
X, Y	Non-dimensional cartesian coordinates $x / H, y / H$

Greek symbols

θ	Non-dimensional temperature, $(T - T_{\min}) / \Delta T$
ψ	Non-dimensional stream function, $U = \partial \psi / \partial Y$
ΔT	Temperature difference $(T_{\max} - T_{\min})$
ΔC^*	Concentration difference, $(C_{\max} - C_{\min})$

1 Introduction

Natural convection, in which the buoyant forces are due both to temperature and concentration gradients, is generally referred to as thermosolutal convection or double-diffusive convection. Various modes of convection are possible depending on how temperature and concentration gradients are oriented relative to each other as well as to gravity. The stratified fluid can be subjected to horizontal or vertical temperature and concentrations gradients [1]. This phenomenon is of considerable interest in a very wide range of fields. In nature such flow is encountered in the oceans, pollution dispersion in lakes, shallow coastal waters and the atmosphere [2]. Thermosolutal convection is also important in crystal growth processes. It is induced when the non uniform distribution of impurities occurs in the fluid phase. The quality of the growing crystal is severely affected by the melt convection and any oscillations are disadvantageous [3].

Convection in binary fluids is more complex than in pure fluids because of the difference in time scale diffusion between energy and species [4]. The species gradients may be induced by the solutal boundary conditions applied on the system (double diffusive problem) (Ostrash et al. [5], Lee et al. [6], Benacer et al. [7], Gobin et al. [8] and Sezai et al. [9]). It can also be induced by thermal gradients via the Soret effect [2, 3].

Thermosolutal convection was widely experimentally and numerically studied for several non-dimensional parameters namely the Lewis and Prandtl numbers, the buoyancy ratio, and for either cooperating or opposing heat or mass gradients. We shall refer to some important works that may serve as background for the present work.

Kamotani et al. [1] studied experimentally the phenomenon of natural convection in rectangular enclosures with combined horizontal temperature and concentration gradients. Various complex flow patterns are observed with different experimental conditions. Temperature distributions, mass transfer rates and flow instability are also reported.

An analytical and numerical studies of natural convection in enclosures filled with binary fluids with Neuman boundary conditions are studied by Ouriemi et al. [2, 3]. Both double diffusive convection and Soret induced convection are considered. The authors proposed an analytical solution based on the parallel flow approximation.

In the above studies thermosolutal convection is due to the imposed temperature and concentration gradients between the opposite walls of the enclosure taking the entire vertical wall to be thermally active. But in many engineering applications such as solar energy collectors it is only a part of the wall which is thermally activated.

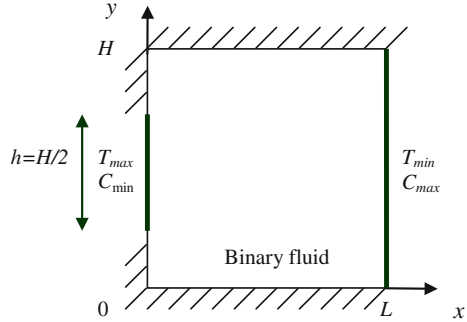
Many articles concerning natural convection in enclosures with partially active walls had been published. For example Nithyadevi et al. [10] studied numerically the effect of double diffusive natural convection of water in a partially heated enclosure with Soret and Dufour coefficients for either cooperating or opposing heat or mass gradients.

In this work we present a numerical study of laminar thermosolutal natural convection in a square enclosure filled with a binary fluid and submitted to horizontal temperature and concentration gradients. The main focus is on examining the effect of thermal Rayleigh number on fluid flow and heat and mass transfer in the enclosure. The rate of heat and mass transfer in the enclosure is measured in terms of the average Nusselt and Sherwood numbers.

2 Problem Geometry

The geometry of the problem is shown in Fig. 1. The partially heated active vertical left side wall ($h = H/2$) and fully heated active vertical right side wall of the enclosure are maintained at two different but uniform temperatures and concentrations: ($T_{max} > T_{min}$) and ($C_{max} > C_{min}$). The remaining boundaries of the enclosure are impermeable and thermally insulated.

Fig. 1 Physical configuration



The flow in the enclosure is assumed to be two-dimensional. All fluid properties are constant. The fluid is considered to be incompressible and Newtonian. The Boussinesq approximation is applied: $\rho(T, C^*) = \rho_0 [1 - \beta_t(T - T_0) - \beta_s(C^* - C_0^*)]$.

Viscous dissipation, heat generation, radiation and Soret effects are neglected. The governing non-dimensional mass, momentum, energy and concentration equations are as follows, respectively:

- at $t = 0$: $U = V = 0$; $\theta = 0$; $C = 0$; $0 \leq X \leq 1$; $0 \leq Y \leq 1$
- for $t > 0$;

$$\frac{\partial U}{\partial X} + \frac{\partial V}{\partial Y} = 0 \tag{1}$$

$$\frac{\partial U}{\partial t} + U \frac{\partial U}{\partial X} + V \frac{\partial U}{\partial Y} = -\frac{\partial P}{\partial X} + Pr \nabla^2 U \tag{2}$$

$$\frac{\partial V}{\partial t} + U \frac{\partial V}{\partial X} + V \frac{\partial V}{\partial Y} = -\frac{\partial P}{\partial Y} + Pr \nabla^2 V + Pr \cdot Rat(\theta - NC) \tag{3}$$

$$\frac{\partial \theta}{\partial t} + U \frac{\partial \theta}{\partial X} + V \frac{\partial \theta}{\partial Y} = \nabla^2 \theta \tag{4}$$

$$\frac{\partial C}{\partial t} + U \frac{\partial C}{\partial X} + V \frac{\partial C}{\partial Y} = \frac{Pr}{Sc} \nabla^2 C \tag{5}$$

The boundary conditions in the dimensionless form are:

$$X = 0 : U = V = 0, \quad For 0 \leq Y \leq 1 \tag{6a}$$

$$X = 0 : \theta = 1, C = 0, \quad \text{For } Y \geq 1/2, \quad 3/4 \geq Y \geq 1/4 \text{ Or } Y \leq 1/2 \quad (6b)$$

$$X = 1 : U = V = 0, \quad \theta = 0, \quad C = 1, \quad 0 \leq Y \leq 1 \quad (6c)$$

$$Y = 0 : U = V = 0, \quad \frac{\partial \theta}{\partial X} = \frac{\partial C}{\partial X} = 0, \quad \text{For } 0 \leq X \leq 1 \quad (6d)$$

$$Y = 1 : U = V = \frac{\partial \theta}{\partial Y} = \frac{\partial C}{\partial Y} = 0, \quad \text{For } 0 \leq X \leq 1 \quad (6e)$$

The average Nusselt and Sherwood numbers are:

$$\text{Left wall : } \overline{Nu} = - \int_h^1 \frac{\partial \theta}{\partial X} dy \quad \overline{Sh} = \int_h^1 \frac{\partial C}{\partial X} dy \quad (7a)$$

$$\text{Right wall : } \overline{Nu} = - \int_0^1 \frac{\partial \theta}{\partial X} dy \quad \overline{Sh} = \int_0^1 \frac{\partial C}{\partial x} dy \quad (7b)$$

3 Numerical Methode

The governing Eqs. (1)–(5) associated with the boundary conditions (6a–e) are solved numerically using the finite volume method described by Patankar [11]. A uniform mesh is used in X and Y directions. A hybrid scheme and first order implicit temporally discretisation is used. Because of the nonlinearity of the momentum equations, the velocity pressure coupling, and the coupling between the flow and the energy and concentration equations, an iterative solution is necessary. The SIMPLER algorithm and Tri-Diagonal Matrix algorithm iteration procedure [11] are used to solve the algebraic equations. The iteration process is terminated under the following conditions:

$$\sum_{i,j} \left| \phi_{i,j}^n - \phi_{i,j}^{n-1} \right| / \sum_{i,j} \left| \phi_{i,j}^n \right| \leq 10^{-5} \quad (8)$$

where ϕ represent: U , V , θ and C ; n denotes the iteration step.

$$\overline{Nu}|_{X=0} = \overline{Nu}|_{X=1} \quad (9a)$$

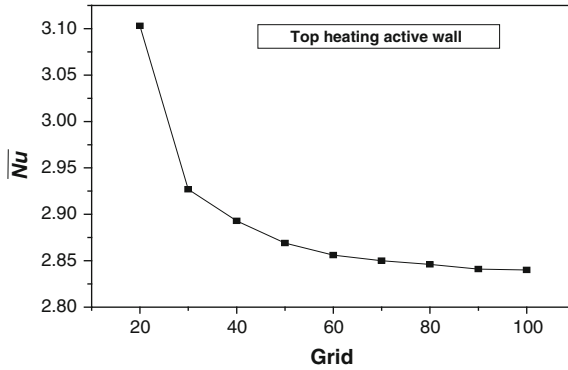


Fig. 2 Average Nusselt number for different grid sizes

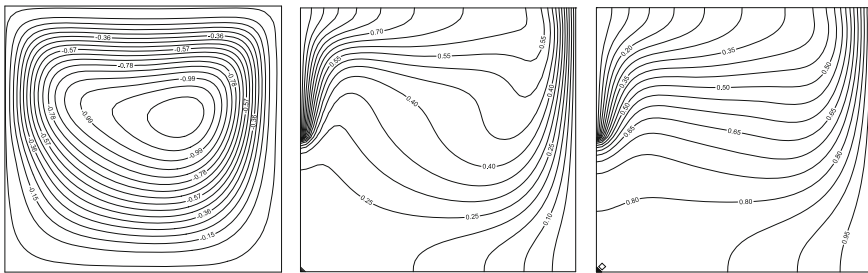


Fig. 3 Steady state of streamlines (*left*), isotherms (*middle*) and iso-concentration (*right*) for top heating active wall. $N = 1$, $Sc = 5$, and $Ra_t = 10^5$

$$\overline{Sh}|_{x=0} = \overline{Sh}|_{x=1} \tag{9b}$$

In order to obtain a precise results a (90×90) grid was selected and used in all the computations Fig. 2. A good agreement between the obtained results and thows reported in literature [10] are observed (Fig. 3).

4 Results and Discussions

Figure 4 (a, b and c) shows the effect of thermal Rayleigh number on fluid motion inside the enclosure for different active locations in the left vertical wall: top (*T*), middle (*M*) and bottom (*B*). A single cell rotating in clockwise direction ($\psi < 0$)

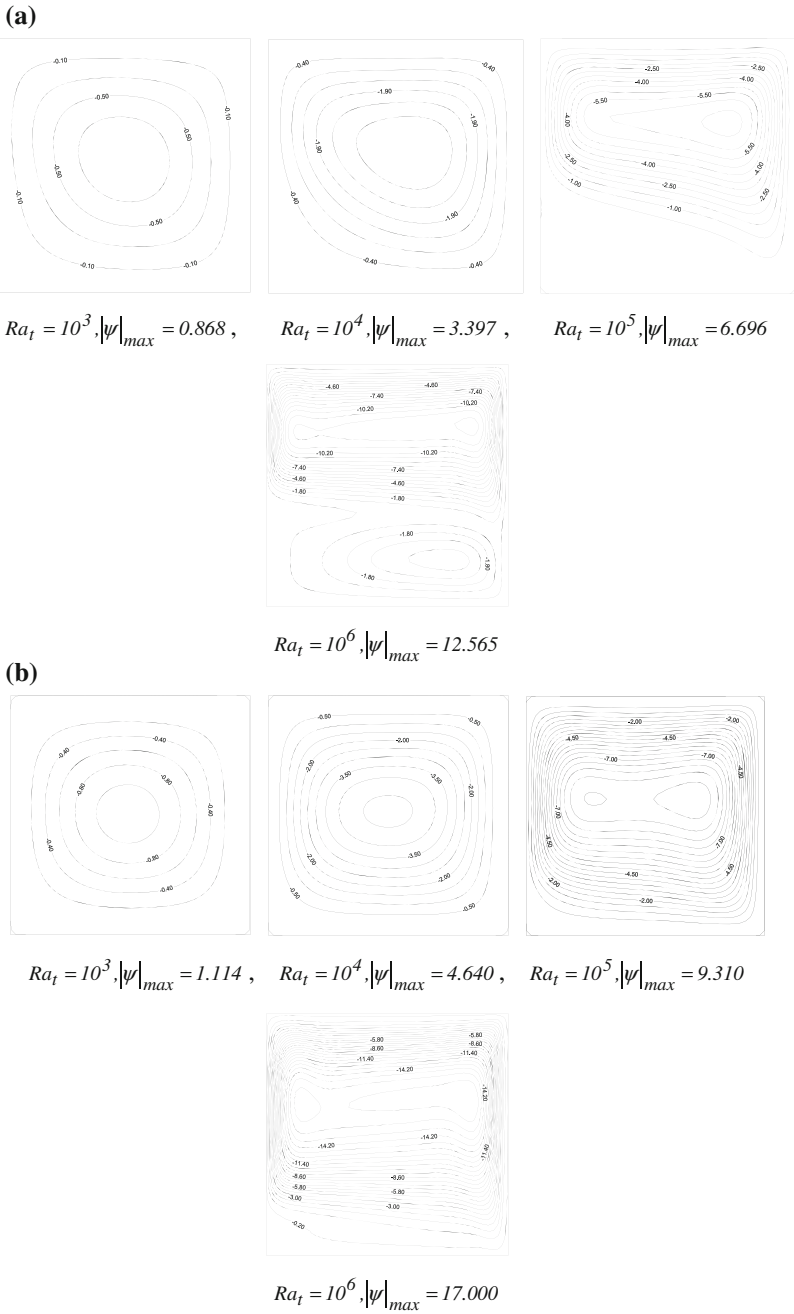
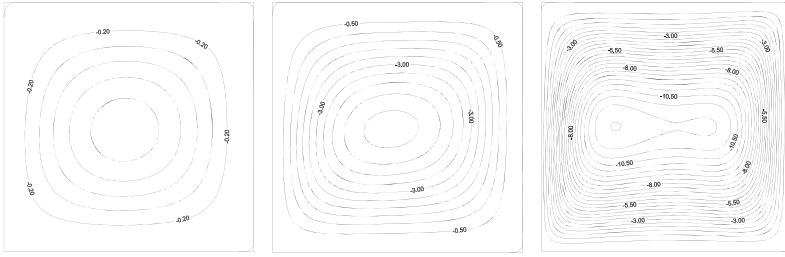
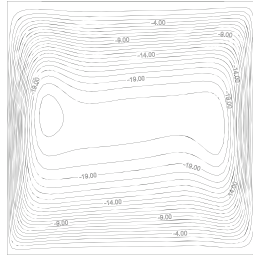


Fig. 4 Steady state of streamlines: top (a), middle (b) and bottom (c) active wall for different values of thermal Rayleigh number

(c)



$$Ra_t = 10^3, |\psi|_{max} = 1.125, \quad Ra_t = 10^4, |\psi|_{max} = 5.204, \quad Ra_t = 10^5, |\psi|_{max} = 12.022$$



$$Ra_t = 10^6, |\psi|_{max} = 22.430$$

Fig. 4 (continued)

appears inside the enclosure. Except for the case (*T*) when $Ra_t = 10^6$ we observe that the principal cell is pushed to the top of the enclosure and a weak cell rotating in the same direction is formed in the lower part indicating a weak convection in this region Fig. 4a. While for the remaining cases (*M* and *B*) and for $Ra_t \geq 10^5$ Fig. 4b, c streamlines cover the entire enclosure and the centre of each cell is elongated and two secondary vertices appear inside it. As shown by Fig. 4a–c for the three cases (*T*, *M* and *B*) we observe that the maximum absolute value of the stream function $|\psi|_{max}$ increase with the increase of Rayleigh number. Which means natural convection is strength. In addition by moving of the active location from the top to the bottom, $|\psi|_{max}$ in the case (*B*) is the greatest. Therefore convection is more important for this location.

It is observed that the fluid particles move with greater velocity for higher thermal Rayleigh number, as mentioned in Fig. 5 showing the effect of Ra_t on mid-height vertical velocity profiles. The velocity peaks especially near the vertical walls are more important for both high Ra_t and bottom (b) location.

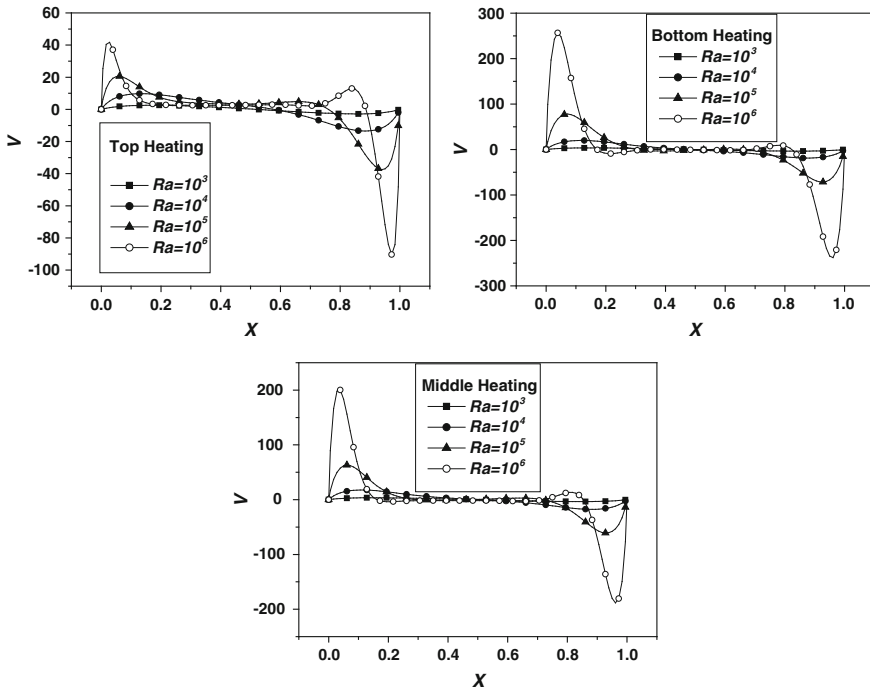


Fig. 5 Axial velocity U at $X = 0.5$ and vertical velocity V at $Y = 0.5$

The effect of thermal Rayleigh number on thermal and solutal fields is illustrated in Figs. 6 and 7. The isotherms and iso-concentration are crowded around the active location on the left side of the enclosure. The fluid rises along the hot wall and falls along the right cold wall, so thermal and concentration gradients are very important in these regions. Convection mechanism in T case is principally in the top of the enclosure for high Rayleigh number $Ra_t = 10^6$, whereas in the remaining cases it covers the entire enclosure. As the buoyancy ratio $N = 1$ and the Lewis number $Le = \alpha/D = 34.28$, natural convection is dominated by thermal buoyancy. For low Ra_t the isotherms shown in Fig. 6 are almost parallel to the vertical walls, indicating that most of the heat transfer is by heat conduction.

For moderate and high Rayleigh number $Ra_t = 10^5$ and 10^6 there is a temperature stratification in the vertical direction and the thermal boundary layer is well established along the side walls Fig. 6 indicating the dominant heat transfer mechanism. Whereas the iso-concentrations are more confined to the vertical walls

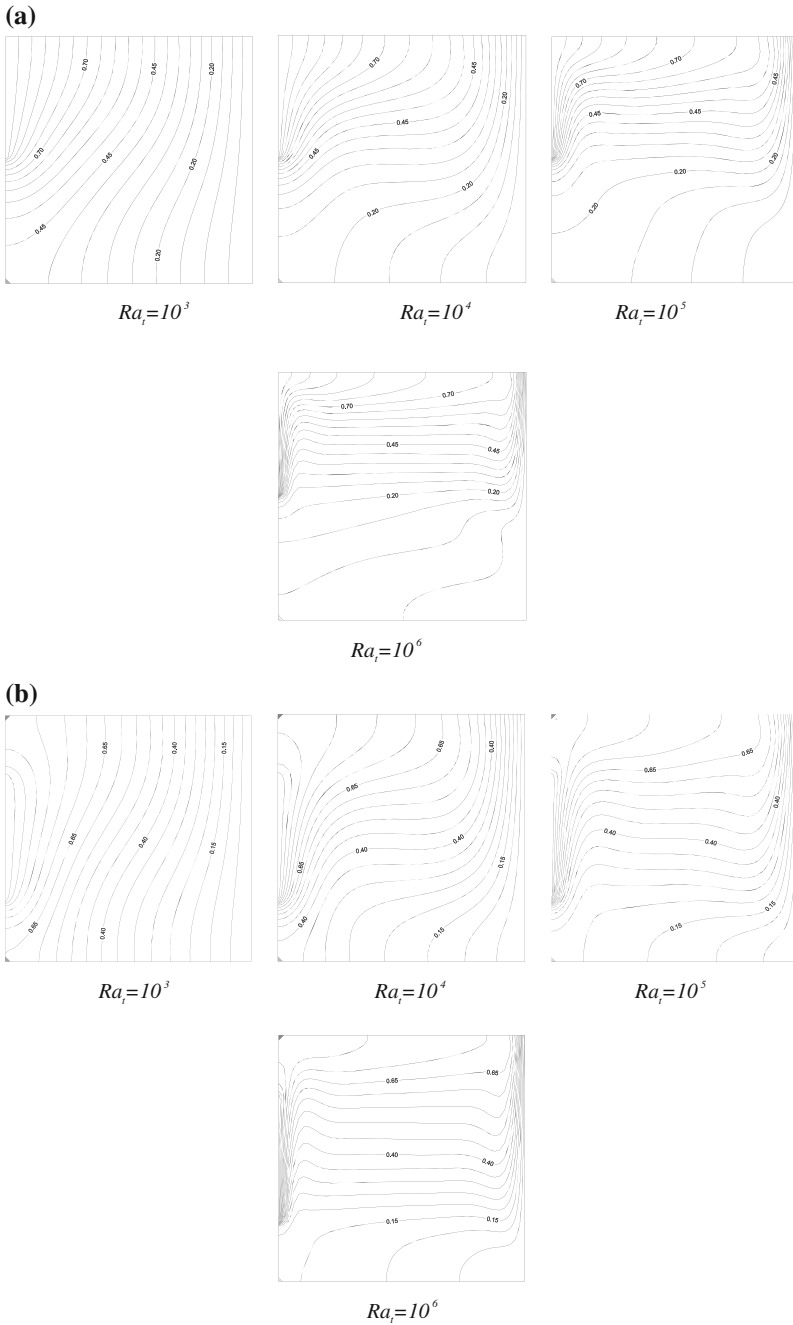


Fig. 6 Steady state of isotherms: top (a), middle (b) and bottom (c) active wall for different values of thermal Rayleigh number

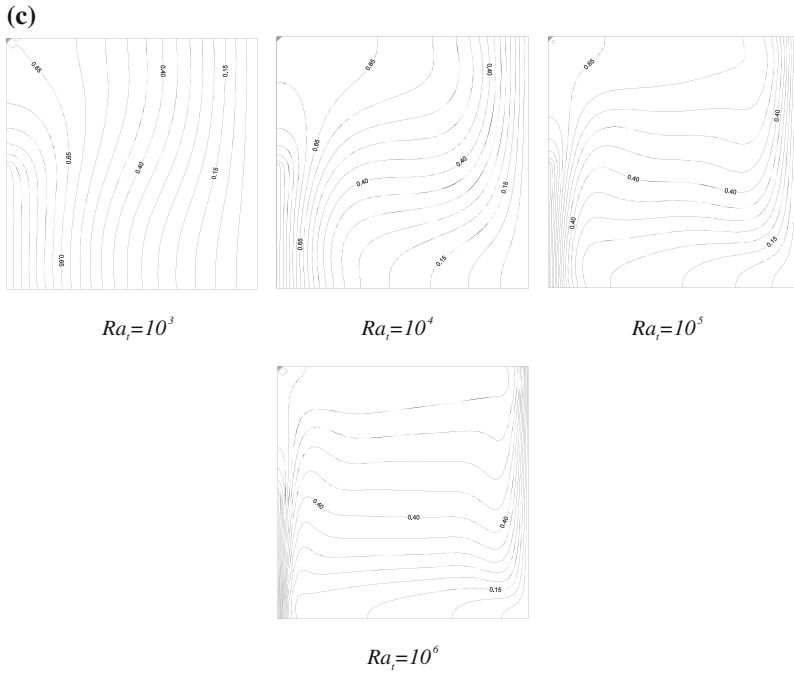


Fig. 6 (continued)

indicating that concentration gradient is very important in these regions and the concentration in the middle of the enclosure is almost constant (is nearly the same in the interior).

The rate of heat and mass transfer across the cavity is obtained by evaluating the average Nusselt and Sherwood numbers at the cavity walls. Figure 8 presents the effect of thermal Rayleigh number on \overline{Nu} and \overline{Sh} for various active locations in the left vertical wall: It is clear from this figure that for a given active location the average Nusselt and Sherwood numbers are increasing with Rayleigh number. Comparing the three cases (T , M and B) \overline{Nu} and \overline{Sh} are nearly the same for low Rayleigh number ($Ra_t = 10^3$). This indicates that most of heat and mass transfer are dominated by diffusion mode. While for $Ra_t > 10^3$ heat and mass transfer are less important in (T) case and they are nearly the same in the remaining cases (M and B).

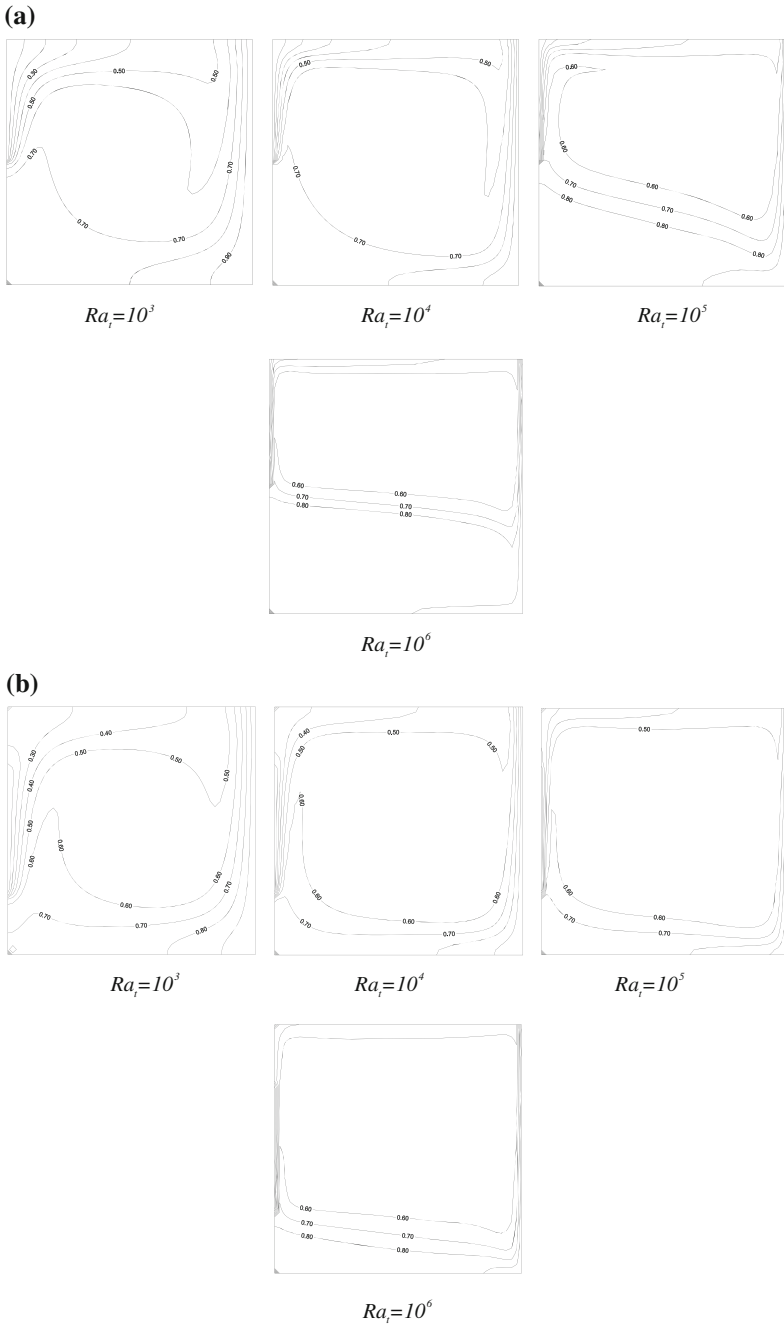


Fig. 7 Steady state of iso-concentration: top (a), middle (b) and bottom (c) active wall for different values of thermal Rayleigh number

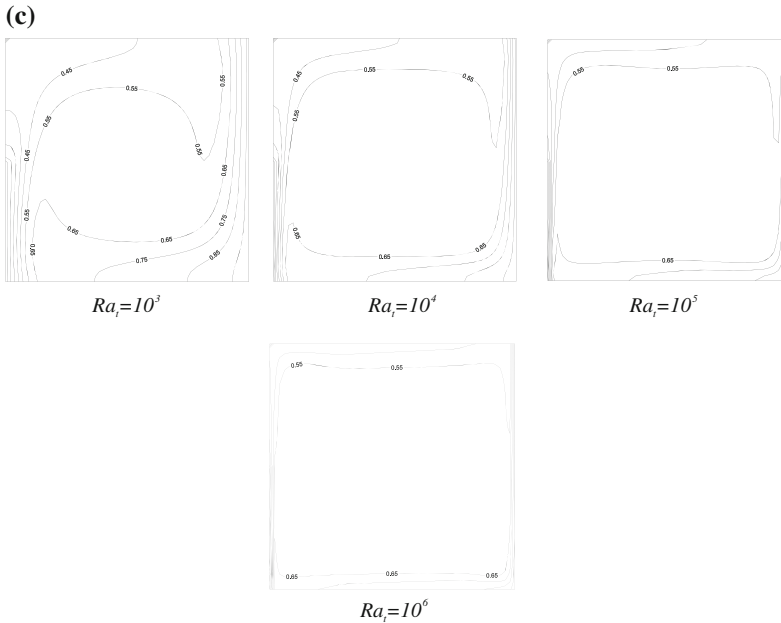


Fig. 7 (continued)

In consequence we can note that the position of the active location has a noticeable effect on the rate of heat and mass transfer and fluid velocity.

5 Conclusion

A numerical study of thermosolutal natural convection was employed to analyze the flow, heat and mass transfer in a square enclosure. A binary fluid is considered and the vertical left wall is partially heated and soluted: in the top (*T*), in the middle (*M*) or in the bottom (*B*). The flow is driven by cooperating thermal and solutal buoyancies. The following conclusions are summarized:

- The position of the active location has a noticeable effect on the flow and heat and mass transfer rates.
- For the three cases (*T*, *M* and *B*), the increase of thermal Rayleigh number, leads to increase flow convection and heat and mass transfer rates.
- In all cases, most of heat and mass transfer are dominated by diffusion mode and the average Nusselt and Sherwood numbers are nearly the same for low Rayleigh number.
- For moderate and high Rayleigh number ($Ra_t > 10^3$), by moving of the active location from the top to the bottom, the rate of heat and mass transfer in case (*T*) is less important comparing with the other cases (*M* and *B*).

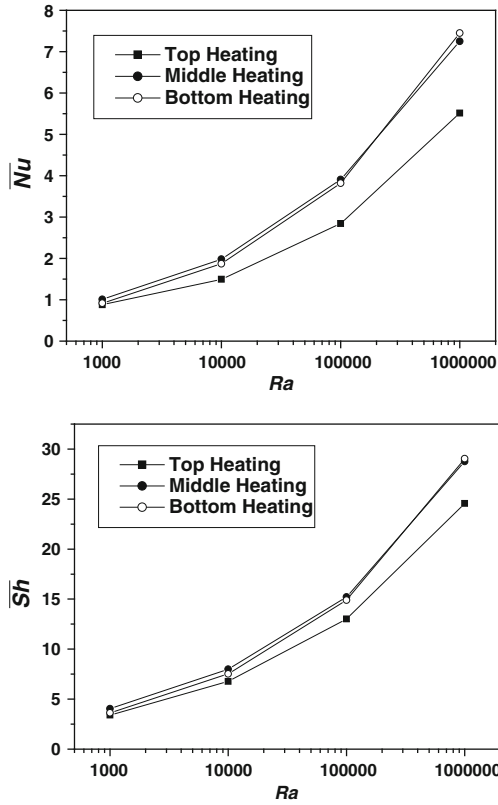


Fig. 8 Average Nusselt and Sherwood numbers versus thermal Rayleigh number

- For the case (T), when $Ra_t = 10^6$ convection is principally in the top and a weak cell is formed in the lower part.

Finally it is very important to study the same problem with considering the opposing thermal and solutal buoyancies. The effect of buoyancy ration number in this case can also be considered.

References

1. Kamotani, Y., Wang, J.S., Ostrah, S., Jiang, H.D.: Experimental study of natural convection in shallow enclosures with horizontal temperature and concentration gradient. *Int. J. Heat Mass Transf.* **28**(1), 165–173 (1985)
2. Ouriemi, M., Vasseur, P., Bahloul, A., Robillard, L.: Natural convection in a horizontal layer of a binary mixture. *Int. J. Thermal Sci.* **45**, 752–759 (2006)

3. Borjini, M.N., Aissia, H.B., Halouani, K., Zeghamati, B.: Effect of optical properties on oscillatory hydromagnetic double-diffusive convection within semitransparent fluid. *Int. J. Heat Mass Transf.* **49**, 3984–3996 (2006)
4. Yahiaoui, M.A., Bahloul, A., Vasseur, P., Robillar, L.: Natural convection of a binary mixture in a vertical closed annulus. *Chem. Eng. Commun.* **194**, 924–937 (2007)
5. Ostrach, S.: Natural convection with combined driving forces. *Physico-chem Hydrodyn.* **1**, 233–247 (1980)
6. Lee, J., Hyun, M.T., Kim, K.W.: Natural convection in confined fluids with combined horizontal temperature and concentration gradients. *Int. J. Heat Mass Transf.* **31**, 1969–1977 (1988)
7. Bennacer, R., Gobin, D.: Cooperating thermosolutal convection in enclosures-I. Scale analysis and mass transfer. *Int. J. Heat Mass Transf.* **39**(13), 2671–2681 (1996)
8. Gobin, D., Bennacer, R.: Cooperating thermosolutal convection in enclosures-II. Heat transfer and flow structure. *Int. J. Heat Mass Transf.* **39**(13), 2683–2697 (1996)
9. Sezai, I., Mohamed, A.A.: Double diffusion convection in a cubic enclosure with opposing temperature and concentration gradients. *Phys. Fluids* **12**, 2210–2223 (2000)
10. Nithyadevi, N., Yang, R.J.: Double diffusive natural convection in a partially heated enclosure with Soret and Dufour effects. *Int. J. Heat Fluid Flow.* **30**, 902–910 (2009)
11. Patankar, S.V.: *Numerical Heat Transfer and Fluid Flow*. Hemisphere, McGraw-Hill, Washington, DC (1980)

Increased Risk of Accidents Due to Human Behavior

Martina J. Mazankova

Abstract The human factor is a cause of a big portion of the traffic accidents. The article presents an example of the traffic accident that was caused by a human factor. The increased social danger of the presented type of the accidents lies in the fact that one of the cars in the traffic accident was a car of the police whose crew was in a hurry to a police action. The police car could not continue the way to the police action because of the accident that was not necessary and was caused by irresponsibility of the other drivers. The possibilities of the ward off collision were analyzed. It was stated among other that in the case that the drivers of the civilian cars enabled the drive through the column of the cars the accident would not happen. The breaking of the traffic law and laws generally is becoming a serious problem in the traffic safety. The experience of the police drivers using the blue lights when going to the police actions is presented, too.

1 Introduction

The road traffic accidents caused by the human factor [1] form 57 % of all of the traffic accidents. The human factor together with the road environment factors cause 26 %, together with vehicle factors cause 6 %, and combination of all the above mentioned factors causes 4 % of the road traffic accidents. The human factor participates together in 93 % of the road traffic accidents.

Some of accidents were originated due to the faults of the drivers of the crashed vehicles. The here presented accident was caused by disrespecting of the laws by several drivers. The drivers were neither in the crash, nor were found out and penalized. It is clear that the sufficient behavior of the drivers in the case was to slow down the velocity or to stop the cars and to stand on the side of the road for a while and let the police vehicle with the blue light drive through as the law sets down. The accident would not happen.

M.J. Mazankova (✉)
Cvrcovice 57, 691 23 Pohorelice, Czech Republic
e-mail: martinam57@yahoo.com

The goal of the here presented work is to show the danger of the behavior of some drivers who participate on the origin of the traffic accidents with impunity.

2 Technical Data

A road accident happened at the crossroad to the hotel Star in August in the night time according to the report of a road accident. The personal motor vehicle Renault and the motor vehicle Volkswagen in the police version were in the collision. The driver of the vehicle Renault was turning from the main road to the left to the hotel Star. The police vehicle Volkswagen had the warning blue light on together with the acoustical device. Its driver was overtaking the vehicles driving in the same direction in the left line. The driver of the police vehicle hit the front left door by the front part of the service vehicle. The vehicle Renault remained staying in the left part of the road after the accident. The police vehicle drove out of the road to the left grass. Any technical fault of the vehicles was not found or reported.

The damage of the vehicle Renault: a deformation of the front left fender, the front left wheel arch, the front left wheel disk, the front left shield of the wheel disk, the grazed painting of the front left door, the dented front left door, the destroyed window of the front left door, the left mirror.

The damage of the vehicle Volkswagen: the front radiator cover, the front bumper, the front window, the fog head lamp, the front right direction indicator, the front right headlight, a deformation of the front right fender, the grazed painting of the rear right door.

The accident happened in the crossroad of the road of the 1st class and the road to the parking lots of the hotel. The width of the whole road was 11.60 m. The width of the right line was 3.50 m. The width of the right side lay-by was 2.10 m. The width of the left line was 3.80 m. The width of the left side lay-by was 2.20 m. The right and left lines in the crossroad were separated by the dashed line. In front and behind the crossroad was the continuous line. The vertical traffic signs Speed Limit 60 km/h and Do Not Pass were in the driving direction of both vehicles in front of the crossroad. The informational signs Parking, Restaurant, and Hotel with the direction of arrival were nearer the crossroad. The traffic signs Side Road and Crossing were behind the informational signs. The crash barrier was along the right side of the road behind the lay-by. A slight left turning of the road was changed in the straight direction before the crossroad. The surface of the road was in good technical state without visible defects. The visibility of the traffic signs was good. A slight rain was in the time of the accident. There were no street lights in the space of the crossroad.

The initial point of measurement was the right end of the concrete canalization block. The auxiliary point of measurement was the right edge of the road. The traces of the traffic accident are depicted in the Fig. 1. The trace *No. 1*—the blocking trace, *No. 2*—the groove trace, *No. 3*—the trace from the left wheels of

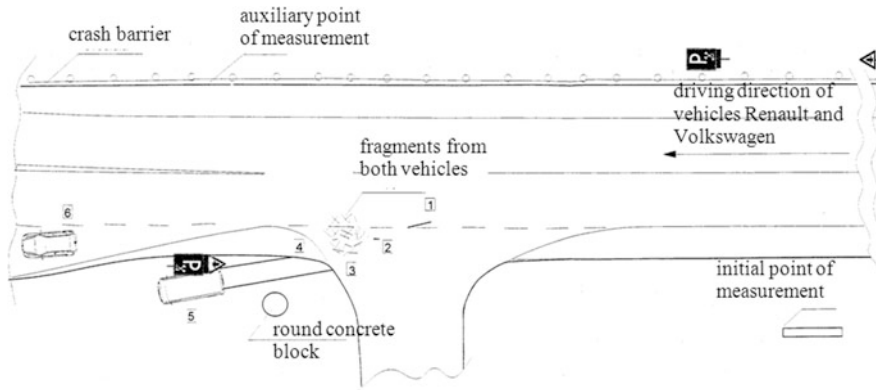


Fig. 1 The plan of place of accident

the vehicle Volkswagen, No. 4—the trace from the right wheels of the vehicle Volkswagen, No. 5—the vehicle Volkswagen, No. 6—the vehicle Renault.

The important evidences for technical analysis of the accident are underneath described.

The driver of the vehicle Renault stated: He drove by the velocity of about 70 km/h. He turned on the left direction indicator and decreased the vehicle velocity, looked in the opposite direction and in the backward mirror and turned left. He saw no vehicle in the backward mirror and in the opposite direction. He saw only the vehicles driving behind him. It was dark. There were no street lights. He had low beam on. He did not know about the fact that another vehicle was overtaking him. The vehicles driving behind him continued in their way after the accident.

He registered the police vehicle with the blue lights on just before the collision. He noticed the police vehicle in the last moment, about 1 s before the accident. There were several vehicles behind him. He saw about 30 m behind him in the backward mirror.

The driver of the vehicle Volkswagen stated that he drove the vehicle Volkswagen to the police action. He turned the blue light on. It was night time and it was raining. He did not remember how many vehicles he overtook to the accident place. He did not know what his vehicle velocity was because he was concentrated on the traffic in front of him. He came to a column of about four vehicles in the left turn. No one driver of the vehicles reacted to the blue light. They did not slow down. They did not react to the high beam. He decided to overtake the column after a control that nobody was on the crosswalk. When he was near the crossroad to the hotel Star, he registered two blinks of the left direction indicator of the white vehicle that was in the column. The vehicle started to turn immediately. The vehicle did not react and continued slowly turning. He stepped on the braking pedal sharply and tried to prevent the collision by turning. He did not manage to prevent the collision and hit the left door of the white vehicle by the front part of the police car.

He drove out the road to the grass on the left side. He and his colleague assured that they had not injury and he went to ask if the people in the white car were not injured.

A witness said that there drove several vehicles in front of the vehicle Renault and several vehicles behind it. There were more than three vehicles in front and more than three vehicles behind the vehicle Renault including trucks. There were no vehicles in the opposite direction. The vehicle Renault was approximately in the middle of the vehicles column. The police vehicle was overtaking the column and had the blue light on and it was possible to hear the alarm.

3 Methods

The movement of the vehicles was analysed by two methods. The collision was solved by the modified diagram of balance of momentum and impulses (combination of graphical and analytical solution) [2]. Checking of results was calculated using energy conservation equation. Analytical calculation of the movement of the vehicles after the collision was made as well as the movement of the vehicles before the collision. Second method was the simulation using software Virtual Crash v 2.2 [3].

4 Accident Analysis and Results

The technical analysis was judged from the traces, the damages of the vehicles, the final positions of the vehicles and the technically acceptable evidences of the accident participants and the witness.

The correspondence of the damages of the vehicles and the collision was deduced from the photo-documentation, the report of the road accident, the plan of the place of the accident, and the final positions of the vehicles.

The front part of the vehicle Volkswagen (Fig. 2) and the left side of the vehicle Renault (Fig. 3) was in the collision. The schemes of the vehicles damages are depicted on the Figs. 4 and 5. The angle between the vehicles was about 35°. The consequence of the collision was the damage of the front left door, the left doorsill, the left A pillar, the dash behind the A pillar, knock off of the left mirror of the vehicle Renault and the damage of the right compound headlight, the fog head lamp, the hood, and the fender of the vehicle Volkswagen.

The place of the collision (the yellow area) is located at the end of the braking traces of the vehicle Volkswagen and in front of the groove trace of the vehicle Renault (Fig. 6).

The technically acceptable result of the collision of the vehicles Renault and Volkswagen is following. The collision velocity of the vehicle Renault was from 0 to 7 km/h. The collision velocity of the vehicle Volkswagen was from 30 to 41 km/h. The equivalent energetic velocity—*EES* that demonstrates the part of the



Fig. 2 Damage of vehicle Renault

Fig. 3 Damage of vehicle Volkswagen



kinetic energy that was changed in the plastic deformation was evaluated according to the source [4] and the Eq. 1.

$$EES_{Vehicle} = EES_{Etalon} \cdot \sqrt{\frac{m_{Etalon}}{m_{Vehicle}}} \quad (1)$$

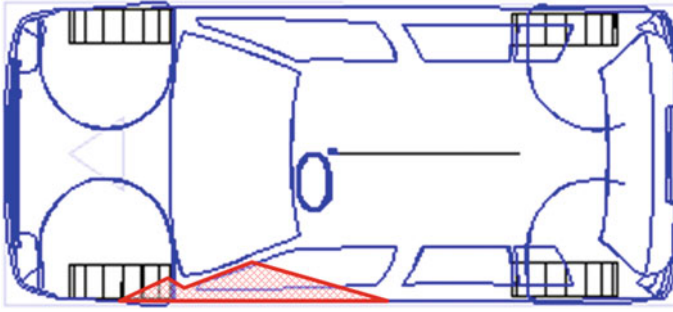


Fig. 4 Scheme of damage of vehicle Renault

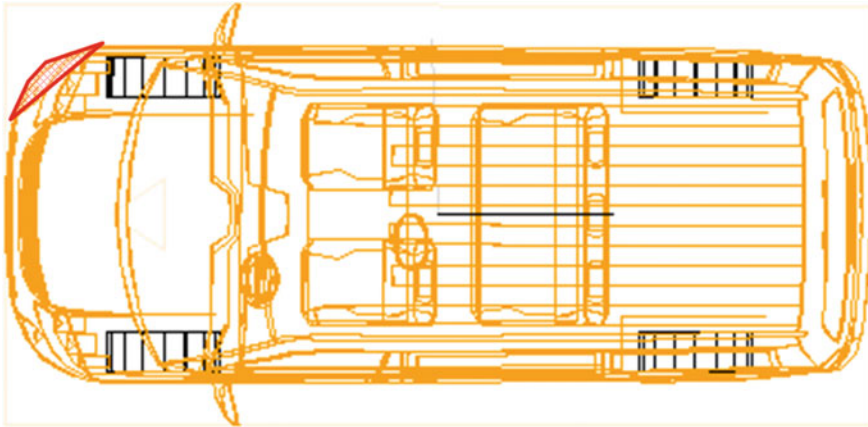


Fig. 5 Scheme of damage of vehicle Volkswagen

where $EES_{Vehicle}$ (km/h) is the EES of the measured vehicle, EES_{Etalon} (km/h) is the EES of the known etalon, $m_{Vehicle}$ (kg) is the instant weight of the vehicle, and m_{Etalon} (kg) is the curb weight of the etalon. The EES corresponding to the damage of the vehicle Renault is considered from 15 to 23 km/h. The EES corresponding to the damage of the vehicle Volkswagen is considered from 9 to 15 km/h.

The traces *No. 3* and *4* were from the rolling of wheels of the vehicle Volkswagen and the trace *No. 2* was the groove trace from the vehicle Renault after the collision. The vehicle Renault rotated to the right after the collision and ended in the final position turned about the angle about 47° as corresponds to the calculation and the report of the road accident. The vehicle Volkswagen turned about the angle about 3° and stopped in the final position as documented and derived.

The conclusions from the analysis of the motion of the vehicles before the collision are following:

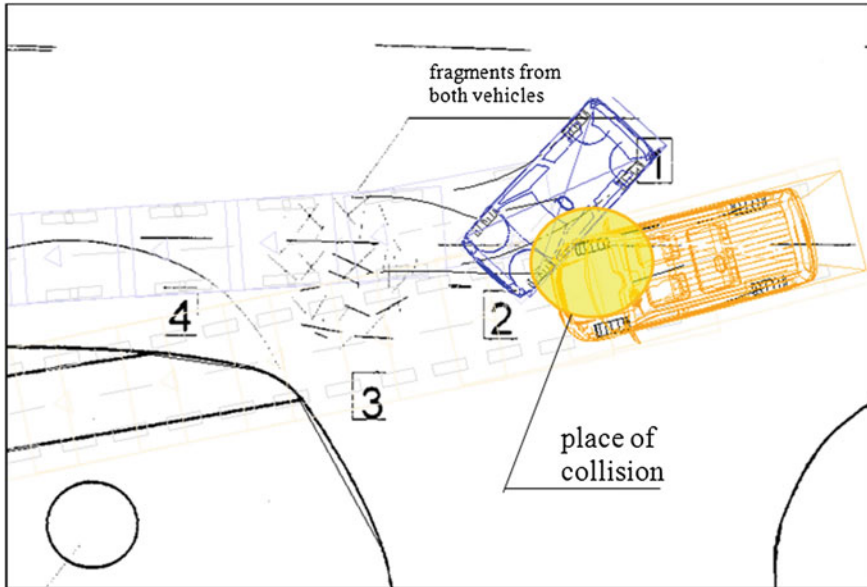


Fig. 6 Place of collision of vehicles

- The vehicle Renault drove maximally with the velocity of 7 km/h before the collision. It came to the place of the collision from the main road turning to the left in the direction to the parking place. It could move with a constant velocity on the arch in the time 3.9 s. It could stop in the place of collision after the driver saw the vehicle Volkswagen with intense braking with a deceleration from 7.5 to 8.5 m/s² on the distance from 0.22 to 0.25 m (during the time from 0.23 to 0.26 s).
- The vehicle Volkswagen drove with the velocity of 30 to 41 km/h before the collision. It braked intense according to the documented braking traces on the distance 1.6 m. The vehicle could brake with the average deceleration from 7.5 to 8.5 m/s², with the time to the full braking 0.2 s from the velocity from 38 to 48 km/h.
- The driver of the vehicle Volkswagen tried to avert the collision with the go around maneuver to the left. It was needed minimum from 0.8 to 1.0 s to deviate 2 m from the straight direction. The driver of the vehicle Volkswagen could react 1 s before the go around maneuver. The driver could start the go around maneuver and braking in the same instant. He would brake from the velocity from 55 to 62 km/h.

5 Possibilities to Avert Collision

The possibilities to avert the collision and the accident could be deduced from the analysis.

5.1 Possibilities of Driver of Vehicle Renault to Avert Collision

It is possible to deduce by the analysis of the motion of the vehicles before the collision that the driver of the vehicle Renault could see the vehicle Volkswagen only in the case if the vehicle Volkswagen started overtaking in the distance at least 115 m before the crossroad. In the case that the vehicle Volkswagen started overtaking nearer the crossroad, the driver of the vehicle Renault started turn to the left earlier than the vehicle Volkswagen got to the opposite direction line. The possibility of glare was not excluded, too.

The driver of the vehicle Renault could not avert the collision in the case that the vehicle Volkswagen started overtaking near than 115 m in front of the crossroad. It is not possible to exclude the possibility of glare from the vehicles behind him and than the impossibility to see the overtaking vehicle Volkswagen in the case that the vehicle Volkswagen started overtaking farther than 115 m before the crossroad.

5.2 Possibilities of Driver of Vehicle Volkswagen to Avert Collision

It is possible to deduce by the analyze of the motion of the vehicles before the collision that in the case that behind the vehicle Renault were only two vehicles and one of them was a truck, the vehicle Volkswagen could start the overtaking in the distance 56 m before the place of collision. The driver of the vehicle Volkswagen would not finish the maneuver of going around and he would react to the vehicle Renault turning to the left. He could avert the collision only in the case that he would not start overtaking.

The vehicle Volkswagen could start overtaking at the level of the traffic sign Speed Limit 60 km/h in the distance 120 m before the crossroad in the case of longer column behind the vehicle Renault. The driver of the vehicle Volkswagen could see the vehicle Renault when it was 7.5 m before the place of collision (it was driving in the opposite direction line), e.g. in the time 3.9 s before the place of collision. In the case that the driver of the vehicle Volkswagen saw the vehicle Renault when it was driving in the opposite direction line and the driver would react in the time 1 s, he could stop in front of the vehicle Renault with the deceleration 3.36 m/s^2 .

In the case that the driver of the vehicle Volkswagen did not start overtaking nearer than 87 m before the place of collision, e.g. 83 m before the crossroad, he could avert the collision by braking with the deceleration 5.0 m/s^2 , that is required for the trucks with respect to their technical roadworthiness.

The driver of the vehicle Volkswagen could avert the collision of the vehicles by braking with the maximum deceleration 8.5 m/s^2 in the case that he did not start the overtaking nearer the crossroad than 75 m before the place of collision, e.g. 71 m before the crossroad. In the case that he started overtaking of the vehicles nearer than 75 m before the place of collision, he had no possibility to avert the collision.

5.3 Possibilities of Other Drivers to Avert Collision

The vehicle Volkswagen had the blue light on together with the warning sound according to the report of the road accident. The vehicles in front of the vehicle Volkswagen had to enable free driving to him by departing from the line to the right side, vehicle by vehicle. The driver of the vehicle Renault could decide if to depart from the line to the right side or to turn to the left and he would leave the driving corridor of the vehicle Volkswagen. The collision would not happen.

6 Coment from Practice

It was learned by discussion that the policemen state decreasing respect of law from drivers in the last years. It is not an exceptional case that the drivers do not enable the police vehicles with blue lights a safety driving through.

The drivers of the crashed vehicles are punished in most cases. Nobody deals neither with the fact that the primary reason of the traffic accident caused somebody else nor that he broke the law.

Nobody from the vehicles driving behind the vehicle Renault stopped to find out that someone was hurt in the accident.

7 Conclusions

The article presents one of the traffic accidents that was caused by disrespecting of law. The drivers driving just in front of the police vehicle with blue light had to drive to side of the road and enable the drive through to the police vehicle. The width of the road enabled to the drives safety driving out of the driving line and to the lay-by. Consequently every vehicle in front of the police vehicle had to enable the safety drive through to the police vehicle.

Nobody of the drivers driving between the vehicles Renault and Volkswagen provided the first aid. Nobody from the drivers that drove away was punished and they gained the experience that they may repeat.

The knowledge of law and the willingness to respect it decreases generally. The risk of traffic accidents increases from the same reason.

References

1. PIARC: Road Safety Manual—Recommendations from the World Road Association (PIARC). Paris (2003)
2. Bradac, A., et al.: Forensic Engineering. CERM Academic Press, Brno (1999)
3. Virtual Crash v 2.2: <http://www.vcrash3.com> (2008)
4. Melegh, G.: AutoExpert - CD EES 4.0. Budapest (2002)

Statistic of Police of Czech Republic Influence on Risk Assessment of Road Traffic

Martina J. Mazankova

Abstract The number of the road accidents and the appraisal of the damage fluctuate in Czech Republic. A dependence of the number of the registered traffic accidents on the law changes can be found out from the analyses of the number of accidents. The fatal traffic accidents and accidents entailed personal injuries are registered. The obligation of registration of the accidents with damage only was adapted several times in the last years. The influence of the law is significant with respect to the number of the registered road traffic accident. It can modulate the results of the risk assessment in the road traffic.

1 Introduction

All the human activities that people consider to be useful are accompanied by certain risks. The road traffic has its own risks, too. The road traffic enables the transfer of people and material on one side, there is a risk of accidents and environment pollution on the other side. The consequences of the accidents are death, personal injuries, and damages on vehicles, roads, and technical equipments of roads, environment and others. The individual and social losses from the traffic accidents are huge.

The appraised material damage from the road traffic accidents in Czech Republic registered by the Police of Czech Republic (*PCR*) in the year 2013 was 493817000 CZK, i.e. 189060893 EUR (calculated with a rate of Czech National Bank on *November 31st, 2013*).

M.J. Mazankova (✉)
Cvrcovice 57, 691 23 Pohorelice, Czech Republic
e-mail: martinam57@yahoo.com

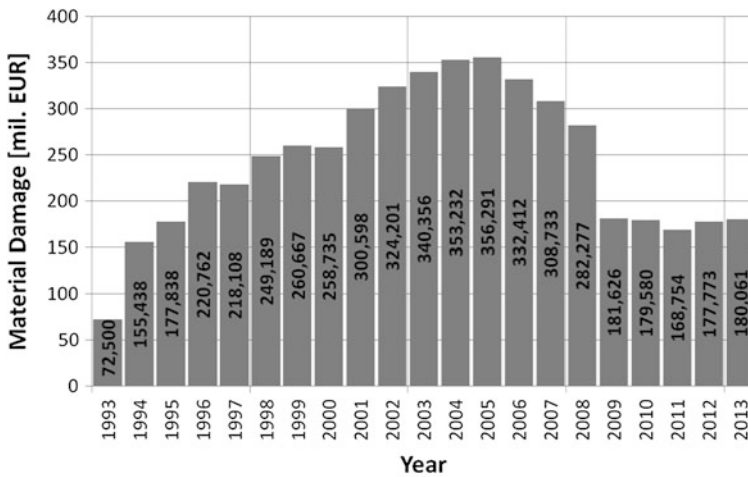


Fig. 1 Appraised material damage from traffic accidents in Czech Republic

2 Material Damage from Road Traffic Accidents

The Fig. 1 shows the material damage from the road traffic accidents in Czech Republic registered by PCR [1]. That is the damage appraised by the policeman on the material, especially on the vehicles. The graph contains the data starting from 1993.

The Czechoslovak Federative Republic was divided to Czech Republic and Slovakia on *January 1st, 1993*. The road traffic grew in Czech Republic in the 90th years. It was connected with the transfer of a part of the railway cargo to the trucks. The individual personal transport grew fast, especially the transport to work. The damage from the road traffic accidents grew consequently. The material damage from accidents grew to the year 2005 and then it decreased according to the graph on the Fig. 1. The biggest decrease is shown in the year 2009. The damage decreased to 64.34 % comparing with the year 2008 and to 50.98 % comparing with the year 2005. What is the real reason of such a fall of the value of damage from the road traffic accidents? The following chapters answer the question.

3 Numbers of Road Traffic Accidents

The Fig. 2 depicts numbers of the traffic accidents registered by PCR every year from 1980 [1]. The number of the traffic accidents increased in the years 1989–1999 according to the statistic. The number of the accidents decreased in the years 2000 and 2001. Next decrease is shown in the years 2006–2008. A significant decrease is

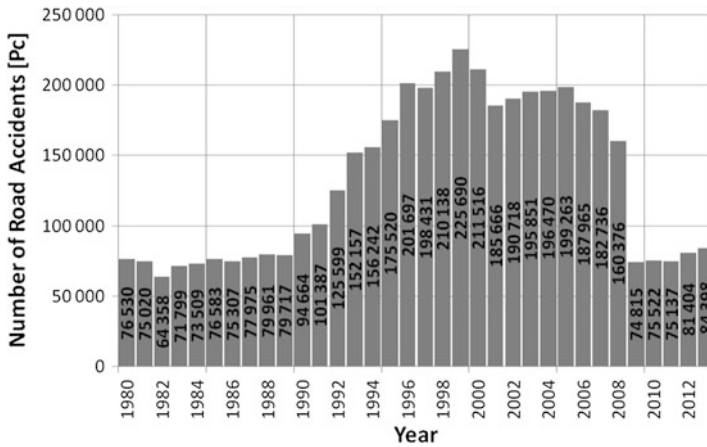


Fig. 2 Numbers of traffic accidents registered by PCR in Czech Republic

noticeable in the year 2009. The number of the accidents falls to 46.65 % comparing with the previous year 2008 and to 33.15 % comparing with the year 1999.

Not all the traffic accidents are registered in every country and some of the registered ones may contain mistakes [2]. The type of the registered accidents depends on the law valid in the country. The minimum limit of the registered accidents with the material damage only can be different country by country.

The essential law for the announcement of the road accidents in Czech Republic is the law No. 361/2000 of the Collection of laws, about road traffic and alteration of some laws, in the latest reading [3]. The origin of the apparent decreases of the traffic accidents in the statistic can be found in the changes of the law.

The law No. 361/2000 of the Collection of Laws, about road traffic and alteration of some laws, in the latest reading [3], became effectual on *January, 1st, 2001*. The duty to announce a traffic accident was limited only to the accidents:

- with the damage on an individual vehicle and its load was obviously bigger than 20000 CZK (729 EUR),
- with killing or injury,
- in the case when the participants of the accident were not in agreement about the matter who was responsible for the accident, or
- in case of the damage of the property of the third person.

The law No. 361/2000 of the Collection of Laws, about road traffic and alteration of some laws, in the latest reading [3], was amended by the law No. 411/2005 of the Collection of Laws [4] on *July, 1st, 2006*. The duty to announce a traffic accident was limited only to the accidents:

- in the case when the damage on individual vehicle and its load was obviously bigger than 50000 CZK (1 823 EUR),
- with killing or injury,

- in case of the damage of the property of the third person, or
- in the case when the participants of the accident were not in agreement about the involvement who and how much was responsible for the accident.

A new more strict system of sanctions for the drivers that repeated law breaking was introduced at the same time. The drivers can lose the driving license for some period of time because of law breaking.

The law No. 274/2008 of the Collection of Laws [5] amended the law No. 361/2000 of the Collection of Laws [3] with the effectiveness since *January, 1st, 2009*. The duty to announce a traffic accident was limited only to the accidents:

- in the case when the damage on an individual vehicle and its load was obviously bigger than 100000 CZK (3 646 EUR),
- with killing or injury, and
- with damages on a property of a third person with an exception to the damage on the vehicle or the load of the participant of the road accident,
- with damages on a road or an equipment of a road or the environment, and
- in the case when the participants of the accident could not renew the continuous traffic.

The participants of the traffic accident that is not necessary to announce have to fill in the European traffic accident form—Agreed Statement of Facts on Motor Vehicle Accident since *January 1st, 2009*, which is for the insurance companies. The police fill in the European traffic accident form in the case of accident with the damage lower than 100000 CZK (3 646 EUR). Such accidents are considered to be only misprisions.

The Fig. 3 presents a graph showing the numbers of the road traffic accidents registered by PCR since the year 1989 and the estimation of the real number of the

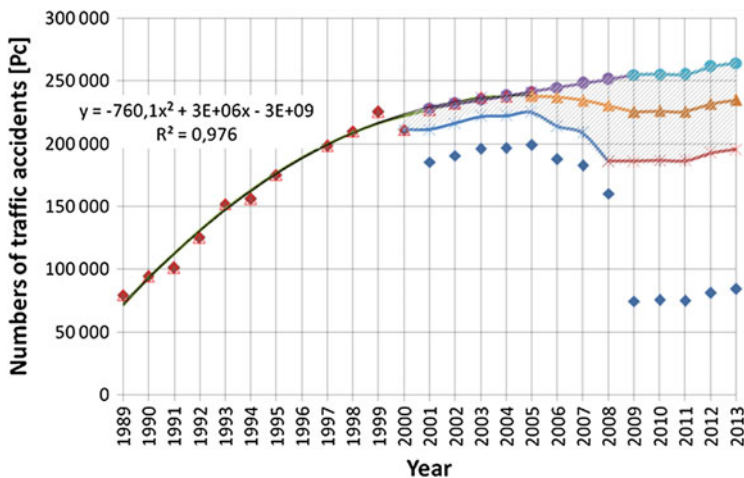


Fig. 3 Estimated annual numbers of traffic accidents in Czech Republic

traffic accidents. The rhombs represent the concrete numbers of the accidents registered by *PCR* annually.

It is clear from the above mentioned that the numbers of the registered accidents by *PCR* do not correspond to the real numbers of the accidents. It was made the estimation of the real numbers of the accidents to enable the comparison of the real numbers of the accidents with the registered ones.

An assumption that the numbers of the accidents correspond to the real numbers in the years from 1989 to 2000 was made. Only a small amount of the accidents was not announced and reported. Such accident contain the ones with small damage only when the drivers prefer to avoid bureaucracy and wish to avoid the insurance company penalties. More serious accidents can be missing from those announced in the case that the offender drives away from the place of the accident, the victim is unaware to announce the accident because of the injury, and the offender is not found.

As the relevant data about the real numbers of the accidents are not available temporarily, the estimations are made starting with the year 2001. A minimum version, a maximum version, and an expert estimation were evaluated.

The minimum expected numbers of the traffic accidents is depicted by stars in the graph. An assumption that in the year 2001 was the number of the accidents was the same as in the year 2000 as no decrease is expected from the practical experience. The number of the accidents in the following years till the year 2008 was shift by the difference between the real and the minimum value of the expected traffic accident in the year 2001. It is complicated to asses the minimum number of accidents in the years 2006–2009. The law change was effective in the middle of the year 2006. Several factors influenced the reported number of accidents progressively. The tendency was let sustentative as reported. The minimum expected number of accident from the year 2009 was shift by the difference between the real number of the traffic accidents in the year 2009 and the minimum expected traffic accident in the year 2008.

The maximum expected numbers of the traffic accidents are depicted by the circles in the graph. The estimation of the trend of the traffic accidents was made by extrapolation of the join of the trend of the traffic accidents from the years 1989 to 2000. A quadratic interpolation curve was calculated. The extrapolated value in the year 2001 is higher than the maximum value from the years 1989 to 2000. The maximum expected number of accidents in the years 2002–2005 was shift by the difference between the real and the maximum expected number of the traffic accidents in the year 2001. The maximum expected numbers of the traffic accidents in the years 2006–2009 was assessed as the linear extrapolation from the years 2001 to 2005 as the maximum values of the traffic accidents are not expected to have decreasing tendency. The number of the accidents in the following years was shift by the difference between the real and the maximum value of the expected traffic accident in the year 2009.

An expert assessment of the numbers of the traffic accidents since the year 2001 is depicted in the graph by triangles. A slight decrease of the traffic accidents in the years 2006–2009 is admitted. The expert estimation of the value in the year 2001 is obtained by the extrapolation of the approximation parabolic curve from the years 1989 to

2000. The numbers of the traffic accidents in the years 2002–2005 was shift by the difference between the real and the expected number of the traffic accidents in the year 2001. The estimated number of the traffic accidents in the years 2006–2009 is the extrapolation of the parabolic approximation curve from the years 1989 to 2005. The expert assessment of the traffic accidents in the following years was increased by the difference between the real and the estimated values in the year 2009.

The estimated numbers of the traffic accidents in the years 2001–2013 is expected to be in the shaded area on the graph. The expert assessment of the traffic accidents in the year 2013 is 235033. The registered number 84398 makes only 35.91 % of the expert assessed accidents. The minimum estimated number of the accidents is 195809, which is more optimistic version. The registered number makes 43.10 % of the minimum estimated number of the accidents. The maximum estimated number of the accidents is 264418, which is more pessimistic version. The registered number makes 31.92 % of the maximum estimated number of the accidents.

4 Risks of Road Traffic Accidents

A natural effort of the people is to minimize the risks while spending adequate budget. The risk management enables to regulate the risk of the road traffic accidents. The statistics of the road traffic accidents are one of the primary resources for the risk analyses. Those are particularly the statistics registered by *PCR* in Czech Republic. The numbers of the accidents that can be found in the database are:

- fatal,
- with injury, and,
- with material damage only.

Most of the fatal and with injury traffic accidents are registered. Exceptions can make for example some of the victims' disabled announcing in the time. Only a portion of the traffic accidents with material damage only is registered. Many of the traffic accidents with material damage only are not reported due to the legal exclusion from the announcement. It is not sufficient to make the risks analyses from statistics only.

5 Conclusions

The risk analysis of the road traffic accidents based on the statistics of the police in the Czech Republic is not complete. It is distort and insufficient. It is estimated that it is registered about 35.91 % of the whole number of the traffic accidents only, in

the extent (31.92; 43.10 %). The origins of the traffic accidents with smaller extent of the material damage up to 100000 CZK (3 646 EUR) on an individual vehicle and its load is necessary to trace in another way. The statistics of the Police of Czech Republic contain the relatively complete data only about the fatal and with injuries accidents.

References

1. Stulikova, E., Lerch, T.: Statistic of Traffic Accidents in Czech Republic in 2013. <http://www.doipo.cz/aktuality/statistika-dopravnich-nehod-za-rok-2013-ceske-republice/> (2014). Accessed 10 Dec 2014
2. PIARC: Road Safety Manual—Recommendations from the World Road Association (PIARC), Paris (2003)
3. Law No. 361/2000 of the Collection of Laws, about road traffic and alteration of some laws. Collection of Laws, Prague
4. Law No. 411/2005 of the Collection of Laws. Collection of Laws, Prague
5. Law No. 274/2008 of the Collection of Laws. Collection of Laws, Prague

Author Index

A

Abboudi, Said, 535
Adjal, Yassine, 179
Agred, Souhila, 491
Ait Shgir, Khalid, 239
Ait Tahar, Kamal, 355
Ait Taleb, Souad, 355
AL-Badour, Fadi, 129
Amara, Idriss, 289
Antoni, Jerome, 251
Aouad, Razika, 289
Atzori, Bruno, 9
Ayadi, Sami, 227
Azouaoui, Krime, 375
Azoui, Hanane, 523

B

Babouri, Mohamed Khemissi, 299
Bacha, Nacer Eddine, 425
Bahloul, Derradji, 523
Bazoune, Abdelaziz, 129
Belarbi, Mohamed-Ouejdi, 435
Belattar, Adel, 25
Belazizia, Abdennacer, 535
Belbaki, Abderrahmane, 465
Belhadi, Salim, 275, 447
Benarous, Abdallah, 491
Bencherif, Mohamed, 475
Benissaad, Smail, 535
Benkahla, Youb Khaled, 511
Benlamnouar, Mohamed Farid, 365
Bennacer, Rachid, 511
Bennaceur, Hamza, 323
Benzidane, Rachid, 179
Boivie, Klas, 67
Bouamer, Amirouche, 425
Bouazaoui, Oussama, 169

Boucherit, Septi, 299
Boukerroum, Said, 331
Boukharouba, Taoufik, 51
Boulanouar, Lakhdar, 447
Bouledroua, Omar, 101
Bourenane, Hocine, 311
Boutassouna, Djamel, 411
Boutra, Abdelkader, 511
Bouyakoub, Samira, 345
Bouzgou, Ahmed Abdelatif, 399
Bouزيد, Lakhdar, 275, 447
Branci, Taïeb, 345
Brik, Mouaad, 41

C

Capelle, Julien, 87
Chabane Chaouche, Malek, 41
Champion, Michel, 453
Chapelle, David, 387
Chouaf, Abdelkrim, 169

D

Dehdouh, Heider, 425
Dehmous, Hocine, 387
Demri, Boualeme, 365
Djamaa, Mohamed Cherif, 251, 299
Djebala, Abderrazek, 219, 251, 267, 299
Djebbar, Ahmed, 1
Djordjevic, Branislav, 117
Dron, Jean Paul, 239

E

Elmiloudi, Khled, 101

F

Fizi, Yazid, 193
Fréour, Silvain, 311

G

Gousmine, Mokrane, 365, 425
 Gueribiz, Djelloul, 311, 411
 Guesmi, Mohamed, 157

H

Habib, Sadam Houcine, 157
 Haboussi, Mohamed, 157
 Hachi, Brahim Elkhalil, 157
 Haddad, Djamel, 523
 Hadj Meliani, Mohamed, 87
 Hadj Meliani, Mohammed, 101
 Haj Taïeb, Ezzeddine, 227
 Hamzaoui, Nacer, 205, 219, 267, 331
 Hocine, Abdelkader, 387

J

Jabbar Hassan, Ammar, 51
 Jacquemin, Frédéric, 311, 411
 Jana, Horníková, 67

K

Kebabsa, Tarek, 251
 Kerrar, Gihad, 129
 Kha, Q.N. Kim, 453
 Khechai, Abdelhak, 399, 435
 Khettabi, Raid, 251

L

Lahmar, Hadj, 193
 Laidoune, Abdellah, 523
 Lechelal, Ramzi, 51
 Liazid, Abdelkrim, 475, 491, 503
 Loukarfi, Larbi, 491

M

Maizia, Abdelhakim, 387
 Makhloufi, Ali, 411
 Mazankova, Martina J., 551, 561
 Mebdoua, Yamina, 193
 Mebdoua-Lahmar, Yamina, 465
 Meneghetti, Giovanni, 9
 Merah, Nesar, 129
 Merzoug, Mustapha, 239
 Milosevic, Milos, 117
 Miloudi, Abdelhamid, 239
 Milović, Ljubica, 139
 Miroslav, Piška, 67
 Miroud, Djamel, 51, 365

Mouedden, Kada, 25
 Mouhoubi, Said, 375
 Mura, Arnaud, 453

O

Ouali, Nourdine, 51
 Ouelaa, Nouredine, 219, 251, 267, 299
 Ould-M'beirick, Mohamed, 101
 Ounis, Houdayfa, 435
 Outtas, Toufik, 323

P

Pavel, Šandera, 67
 Pavlína, Trubačová, 67
 Pluvinaud, Guy, 87, 101

R

Ragui, Karim, 511
 Ramtani, Salah, 323
 Ricotta, Mauro, 9
 Robin, Vincent, 453

S

Sadou, Mohamed, 101
 Sahnoun, Rachid, 475, 503
 Sedmak, Simon A., 117
 Sereir, Zouaoui, 179
 Shuaib, Abdelrahman Nasr, 129
 Si Salem, Abdelmadjid, 355

T

Taleb, Lakhdar, 25, 41
 Tati, Abdelouahab, 399, 435
 Tatic, Uros, 117
 Titouche, Nacer-eddine, 51

V

Vucetic, Filip, 117

Y

Yallese, Mohamed Athmane, 275, 447
 Younes, Abderrahmane, 365, 425
 Younes, Ramdane, 219, 267

Z

Zaoui, Mustapha, 411
 Zergoug, Mourad, 425
 Zerti, Oussama, 275